eman ta zabal zazu

Universidad del País Vasco

Euskal Herriko Unibertsitatea

Ingeniaritza Goi Eskola Teknikoa
Escuela Técnica Superior de Ingeniería
Bilbao

TRIBOCORROSION OF HIGH-STRENGTH LOW-ALLOY STEELS AND COATINGS USED IN OFFSHORE APPLICATIONS

Ph.D Thesis
In Materials Engineering

Ainara López Ortega

November, 2018

Supervisors:
Dr. José Luís Arana Bilbao
Dr. Raquel Bayón González

Departamento de Ingeniería Minera y Metalúrgica y Ciencia de los Materiales

eman ta zabal zazu

Universidad del País Vasco

Euskal Herriko Unibertsitatea

University of the Basque Country

Ph.D. Thesis

TRIBOCORROSION OF HIGH-STRENGTH LOW-ALLOY STEELS AND COATINGS USED IN OFFSHORE APPLICATIONS

Ainara López Ortega

Bilbao, November 2018

IK4 TEKNIKER

Research Alliance

eman ta zabal zazu

Universidad del País Vasco

Euskal Herriko Unibertsitatea

University of the Basque Country

Departamento de Ingeniería Minera y Metalúrgica y Ciencia de los Materiales

Programa de Doctorado:

Ingeniería de Materiales y de Procesos Sostenibles
Engineering of Materials and Sustainable Processes

Ph.D. Thesis

TRIBOCORROSION OF HIGH-STRENGTH LOW-ALLOY STEELS AND COATINGS USED IN OFFSHORE APPLICATIONS

Presented by

Ainara López Ortega

Supervisors

Dr. José Luís Arana Bilbao

Dr. Raquel Bayón González

Acknowledgments

This work has been developed within the frame of the following projects: Fondeo Adhoc ("*Soluciones de fondeo ad hoc para plataformas offshore de oil and gas*", INNPACTO 2012, IPT-2012-1167-120000), MECOFFBI (ELKARTEK 2016, KK-2015/00071), FRONTIERS III (ELKARTEK 2017, KK-2017/00096), FRONTIERS IV (ELKARTEK 2018, KK-2018/00108), and the EMAITEK financed by the Basque Government.

I would like to thank IK4-TEKNIKER for the opportunity given to fulfill this Ph.D. Thesis, and the Education, Linguistic Politics and Culture Department of the Basque Government for its support through the grant "*Programa Predoctoral de Formación de Personal Investigador No Doctor* (PRE_2017_2_0088)".

I would also like to thank my thesis supervisors and all the laboratory colleagues from IK4-TEKNIKER that have contributed to the success of this work, through their personal and professional support.

Abstract

The use of High-Strength Low-Alloyed steels (HSLA) in offshore applications has risen considerably during the last decade. The increasing demand for lighter steels with higher strength has led to the development of steel grades with ultimate strengths up to 1100 MPa. However, the high strength of these steels is achieved in detriment of other properties, and they are very susceptible to corrosion in marine environments, which comprise one of the most aggressive atmospheres. The likelihood of these steels of suffering substantial degradation with corrosion-related phenomena is high, and involves significant costs of maintenance and replacement of damaged structures. In order to protect steel from marine corrosion, protective measures have been successfully employed. One of the most recurrent solutions has been the use of coatings.

On the other hand, materials in offshore structures are also subjected to mechanical stresses such as fatigue, abrasion, impact, and wear generated by waves, wind, ocean currents, floating objects, and so on. Wear is another degradation mechanism that is related to high material losses in offshore applications. When wear and corrosion take place simultaneously, the process is known as tribocorrosion. There is a synergism between wear and corrosion, since the material loss when the two processes take place simultaneously can be considerably larger than when they occur alone. This leads to material losses higher than those collected in the design codes, which can have significant implications on the long-term integrity of components and structures. Therefore, a closer understanding of the tribocorrosion and the synergistic effect that it involves in HSLA steels is necessary to reestablish the wear-corrosion allowances in the design phase, in order to better predict the durability of high-performance materials in such adverse working conditions.

In this context, the first part of the present thesis deals with the assessment of tribocorrosion of HSLA steels used in chains of offshore mooring lines, which have been reported to be profoundly affected by both wear and corrosion during their service life. Up to know, tribocorrosion of passive materials has been widely reported, e.g., stainless steels, aluminum alloys, and titanium alloys. However, little investigations have been carried out on the response of active materials, such as HSLA steels of low corrosion resistance in the marine environment. In this regard, the present study aims to address the tribocorrosion of these materials on the basis of the procedures employed in passive materials, adapting and redesigning the protocols available in the standards and literature.

Additionally, the second part of the thesis is focused on the evaluation of protective coatings employed for the protection of steel components and structures from corrosion. Up to now, the selection of the coatings has been made mainly considering their effectiveness against corrosion, neglecting their performance against wear. For instance, organic coatings with high corrosion resistance due to their polymeric nature have been the most employed solution. However, their wear resistance is rather low, and any damage generated on the coating can considerably decrease their efficiency. In this framework, tribocorrosion studies have been performed for different coatings currently employed in the protection of offshore mooring lines, to verify their suitability against wear-corrosion requirements. Finally, a widely employed coating system has been functionalized through different surface modification techniques, to enhance its performance against wear and corrosion, and provide it with additional abilities such as superhydrophobicity and a biocide ability against certain bacteria.

All in all, the outcomes of this work show the importance of the synergism between wear and corrosion on the degradation of the HSLA steels, evincing the necessity of tribocorrosion related studies to increase the knowledge on this synergism and reestablish the allowances included in the design codes.

Resumen

El uso de aceros de alta resistencia y baja aleación (HSLA, por sus siglas en inglés) en aplicaciones offshore ha aumentado considerablemente durante la última década. La creciente demanda por parte de la industria de aceros más ligeros con mayor resistencia ha dado lugar al desarrollo de nuevas aleaciones con tensiones de rotura de hasta 1100 MPa. Sin embargo, la alta resistencia de estos aceros se consigue en detrimento de otras propiedades, por lo que su resistencia a corrosión en ambientes marinos, uno de los entornos más hostiles de trabajo, es relativamente baja. La probabilidad de fallo de componentes de aceros HSLA por mecanismos relacionados con la corrosión es alta, lo que da lugar a elevados costes de mantenimiento y reemplazo de estructuras dañadas. Con el fin de proteger las estructuras de acero frente a la corrosión se han tomado diversas medidas, siendo una de las más comunes el uso de recubrimientos protectores.

Por otro lado, los materiales en estructuras offshore también se encuentran sujetos a solicitaciones mecánicas, siendo la fatiga, la abrasión, el impacto y el desgaste las más habituales. Estos fenómenos suelen ser generados por las olas, el viento, las corrientes marinas, los objetos flotantes y otras cargas climáticas. El desgaste es un mecanismo de degradación que conlleva una gran pérdida de material en aplicaciones offshore. Cuando la corrosión y el desgaste tienen lugar simultáneamente, el proceso generado se conoce como tribocorrosión. Existe un efecto sinérgico entre corrosión y desgaste, dado que la pérdida de material cuando ambos fenómenos ocurren a la vez puede ser considerablemente mayor que cuando actúan por separado. Esto tiene como consecuencia pérdidas de material mayores a las consideradas en los códigos de diseño, lo que podría tener una gran repercusión en la integridad a largo plazo de componentes y estructuras. Por lo tanto, es necesario ampliar el conocimiento en el comportamiento frente a tribocorrosion, y el efecto sinérgico que éste fenómeno conlleva, en aceros HSLA, para poder restablecer los márgenes de tolerancia de pérdida de material por corrosión y desgaste de los códigos de diseño. Con ello se conseguiría predecir de forma más fidedigna la durabilidad de materiales de alta prestaciones en condiciones adversas de trabajo, como el entorno offshore.

En este contexto, la primera parte de esta tesis doctoral se centra en el estudio de la tribocorrosion de los aceros HSLA utilizados en la fabricación de cadenas para líneas de fondeo de estructuras flotantes, los cuales se encuentran sometidos a solicitaciones de corrosión-desgaste durante su vida útil. Hasta la fecha, se han realizado numerosas investigaciones sobre la tribocorrosión en materiales denominados pasivos, como las aleaciones de aluminio, titanio o aceros inoxidables, de alta resistencia a corrosión. Sin embargo, no existe información en sobre el comportamiento frente a tribocorrosion de materiales activos, como los aceros HSLA de baja resistencia a corrosión en ambientes marinos. Por lo tanto, el presente estudio pretende evaluar la tribocorrosion de estos materiales partiendo de los procedimientos de ensayo utilizados en materiales pasivos, adaptando y rediseñando los protocolos disponibles en la normativa y en la literatura.

Además, la segunda parte de la tesis se centra en la evaluación del comportamiento de recubrimientos utilizados en la protección de componentes y estructuras de acero frente a la corrosión. Hasta el momento, la selección de recubrimientos se realiza considerando su efectividad en la protección frente a la corrosión, obviando su comportamiento frente al desgaste. Por ejemplo, entre los recubrimientos más utilizados se encuentran los de naturaleza orgánica, que poseen una alta resistencia a corrosión. Sin embargo, su resistencia al desgaste es baja, y su eficacia puede disminuir considerablemente si se encuentran sometidos a ambos fenómenos simultáneamente. A este respecto, se han realizado estudios del comportamiento frente a tribocorrosion

en recubrimientos actualmente utilizados en la protección de componentes de líneas de fondeo, para verificar su aptitud frente a solicitaciones de corrosión y desgaste. Por último, se ha realizado la funcionalización de un sistema de recubrimiento típicamente utilizado mediante distintas técnicas de modificación superficial, con el objetivo de mejorar su resistencia a la corrosión y al desgaste, y proporcionarle propiedades adicionales, como la superhidrofobia y la respuesta biocida ante cierto tipo de bacterias.

En definitiva, los resultados principales de este trabajo muestran la importancia del sinergismo entre la corrosión y el desgaste en la degradación de los aceros HSLA, poniendo en evidencia la necesidad de realizar estudios de tribocorrosión para ampliar el conocimiento sobre dicho sinergismo, y poder aplicarlo en los requerimientos de los códigos de diseño.

Abbreviations

General terms

Abbr	Description
AC	Alternating current
AF	Antifouling
AHT	Alternating humidity and air temperature
AISI	American Iron and Steel Institute
API RP	American Petroleum Institute, Recommended Practices
APPs	Antifouling paint particles
ASTM	American Society for Testing Materials
AT	Alternating air temperature
CE	Counter electrode
CH	Constant humidity
COF	Coefficient of friction
DIN	Deutsches Intitut für Norming
DLC	Diamond Like Carbon
DNV-GL	Det Norske Veritas and Germanischer Lloyd
DP	Dynamic Position mooring
EEC	Electric Equivalent Circuit
EPS	Extracellular polymeric substances
FBS	Fetal Bovine Serum
FBW	Flash Butt Welding
FC	Ferric corrosion
FOWTs	Floating offshore wind turbines
FPS	Floating Production and Storage
FPSO	Floating Production Storage and Offloading
FPSs	Floating Production Systems
GNP	Gross National Product
HAWTs	Horizontal axis wind turbines
HBSS	Hank's Balanced Salt Solution
HF	High frequency
HR	Relative humidity
HSE	Health and Safety Executive
HSLA	High-Strength Low-Alloy Steels
HSS	High Strength Steels
IACS	International Association of Classification Society
ISO	International Organization for Standardization
LF	Low frequency
MF	Middle frequency
MIC	Microbiologically Induced Corrosion
MODUs	Mobile offshore drilling units
NCS	Norwegian Continental Shelf
OWEAs	Offshore wind energy devices
OX	Oxidized form of a meta
PBS	Phosphate Buffered Solution
PVD	Physical Vapor Deposition
PWHT	Post Welding Hear Treatment
R4	HSLA steel grade denomination according to the classification societies
R5	HSLA steel grade denomination according to the classification societies
RE	Reference electrode
RED	Reduced form of a metal
Redox	Reduction-oxidation reaction
SCE	Saturated Calomel Electrode
SHE	Standard Hydrogen Electrode
SRB	Sulphate reducing bacteria
TBT	Tributyltin oxide
TLP	Tension Leg Platform
TSA	Thermally Sprayed Aluminum
TSC	Thermally Sprayed Coatings
TSCC	Thermally Sprayed Carbide Coatings
TWh	Terawatt hours
UNE	Una Norma Española
WE	Working electrode

WS	White salts	ZRA	Zero Resistance Ammeter

Chemical Compounds

Abbr	Description	Abbr	Description
Ag/AgCl	Silver/Silver chloride	KCl	Potassium chloride
Al	Aluminum	Mg	Magnesium
$Al(OH)_3$	Aluminum hydroxide	Mn	Manganese
Al_2O_3	Alumina	Mo	Molybdenum
Al^{3+}	Aluminum (III) ion	Na	Sodium
C	Carbon	NaCl	Sodium chloride
Ca	Calcium	Ni	Nickel
Cl	Chlorine	O	Oxygen
Cl^-	Chloride ion	P	Phosphorus
CoCr	Cobalt chromium	S	Sulphur
Cr	Chromium	Si	Silicon
Cu_2O	Copper (II) oxide	SiO_2	Silicon dioxide
Cu_2O	Copper oxide	TaN	Tantalum nitride
Fe	Iron	Ti	Titanium
Fe^{3+}	Ferric (III) ion	V	Vanadium
$FeO(OH)_3$	Iron (III) oxyhydroxide (monohydrated)	WC	Tungsten carbide
		Zn	Zinc
FeOOH	Iron oxyhydroxide	ZrO_2	Zirconium dioxide
H	Hydrogen	α-FeO(OH)	Goethite
K	Potassium	γ -FeO(OH)	Lepidocrocite

Experimental techniques

Abbr	Description	Abbr	Description
BSE	Back-Scattered Electrons	LDS	Laser Diffraction Spectrometry
EDS	Energy Dispersive Spectroscopy	MAO	Micro Arc Oxidation
EIS	Electrochemical Impedance Spectroscopy	OCP	Open Circuit Potential
		OD	Optical Density
EN	Electrochemical Noise	PDP	Potentiodynamic Polarization
FE-SEM	Field Emission Scanning Electron Microscope	PEO	Plasma Electrolytic Oxidation
		SEI	Secondary Electron Imaging
ICP-OES	Inductive Plasma Optical Emission Spectroscopy	SEM	Scanning Electron Microscope

Symbol	Description	Units
A_0	Exposed surface area	cm^2
A_{act}	Area of active material in the wear track	cm^2
A_t	Average common logarithm of the number of viable bacteria recovered after 24 hours from the untreated samples	$cell/cm^2$
B	Constant	12-15mV
C_0	Electrochemical corrosion rate in absence of wear	mm/yr
CPE	Constant Phase Element	
CPE-n	Potential factor of the CPE	
CPE-Y_0	Admittance constant of the CPE	$F/cm^{-2}s^{-n}$
C_w	Electrochemical corrosion rate during corrosive wear process	mm/yr
EC_{50}	Concentration of test substance resulting in a decrease of 50% in the algal growth	mg/L
E_{corr}	Corrosion potential	V
EL_{50}	Concentration of leachate resulting in a decrease of 50% in the algal growth	Vol.%
E_{pit}	Pitting potential	V
E^s_{oc}	Stable potential during sliding	V
F	Faraday's constant (9500)	C
f	Frequency	Hz
HV	Vickers hardness	
i_{corr}	Corrosion current density	A/cm^2
I_{corr}	Corrosion current	A
i_p	Current density in the passive domain	A/cm^2
i_{pass}	Corrosion current density of a passivated material	Ω
I_{pass}	Passivation current	A
M	Molar mass	g/mol
n	Number of electrons taking place in a reaction	
R	Antibacterial activity	$cell/cm^2$
R(%)	Antibacterial activity in percentage	
Ra	Roughness	µm
R_{act}	Active polarization resistance	Ω
R_p	Polarization resistance	Ω
R_{pass}	Passive polarization resistance	Ω
r_{pass}	Specific polarization resistance	Ω
R_{pore}	Pore resistance	Ω
R_{ps}	Polarization resistance during sliding	Ω

R_s	Solution resistance	Ω
S	Synergistic component	mm/yr
T	Total material loss rate	mm/yr
U_t	Average common logarithm of the number of viable bacteria recovered after 24 hours from the untreated samples	cell/cm^2
v_{corr}	Corrosion rate	mm/yr
V_{corr}	Material loss due to corrosion in the unworn area	cm^3
V_{pc}	Material loss due to pure corrosion in the unworn area	cm^3
V_{tot}	Total material loss in volume	cm^3
V_{tr}	Material loss due to tribocorrosion in the wear track	cm^3
V_{wac}	Material loss due to wear-accelerated corrosion in the unworn area	cm^3
W_0	Wear rate in absence of corrosion	mm/yr
W^c	Volume of material removed by the effect of corrosion	cm^3
W^c_{act}	Material loss due to corrosion in the wear track	cm^3
W^{cm}	Effect of corrosion on wear	cm^3
W^m	Volume of material removed by the effect of wear	cm^3
W^m_{act}	Material loss due to mechanical wear in the wear track	cm^3
W^{mc}	Effect of wear on corrosion	cm^3
W^s	Synergistic effect between wear and corrosion	cm^3
wt%	Mass fraction as weight percentage	
W_{tr}	Total volume of removed material or wear track volume	cm^3
W-Y_0	Warburg admittance	F/cm^{-2}s$^{-1/2}$
Z	Total impedance of the system	Ω cm^2
Z’	Real component of the impedance	Ω cm^2
Z’’	Imaginary component of the impedance	Ω cm^2
ΔC_W	Change in electrochemical corrosion rate due to wear	mm/yr
ΔW_C	Change in mechanical wear due to corrosion	mm/yr
ω	Angular frequency	rad/s

Table of contents

Chapter 1

General introduction

Chapter 1: General Introduction

1.1 MOTIVATION

The most employed structural material is steel, usually mild or low-alloyed, which easily corrode in the marine environment or submerged in seawater. These steels are relatively cost-effective, compared to other alloyed steels with higher corrosion resistances [1]. High-Strength Low-Alloyed (HSLA) steels, for instance, are widely used due to their high mechanical properties, with yield strengths in the range of 460-950 MPa, and relatively low weight [2,3]. The increasing demand of lighter and higher strength steels has led to an increase in the use of HSLA steels in offshore applications, from less than 10% to over 40% in less than a decade [4]. They are used in the fabrication of offshore structures such as jack-ups and legs, also in pipelines and tethering attachments for floating structures in tension leg platforms (TLPs), or mooring lines of semi-submersible structures, among others [2,5,6]. Typical HSLA steels employed currently are the R4 and R5 steel grades[i], of ultimate strengths of 960 and 1000 MPa [7], respectively. As a consequence of the high demand for steels with increased strength, new steel grades have been recently developed. This is the case of the recently approved R6 grade, with an ultimate strength of 1100 MPa [7,8].

However, the achievement of such high mechanical properties in terms of strength, toughness, and weldability, can be detrimental to other properties. The strength of these steels is controlled by their microstructure, which depends on the chemical composition, the heat treatment, and the deformation processes undergone during their production. In this context, the metallurgy of the steels is accurately controlled, and they usually contain alloying elements in a range of 1 to 5 % in weight. Despite containing manganese, chromium, nickel, and molybdenum, their amount is not high enough to provide them with a high corrosion resistance, as in the case of stainless steels in which some of these elements exceed the 15 % in weight. Therefore, HSLA steels are very susceptible to corrosion, especially in marine environments that comprise one of the most aggressive atmospheres. For instance, the corrosion rate of mild steel in seawater has been reported to be 250 microns per year [9,10]. Consequently, the likelihood of HSLA steels of suffering substantial degradation with corrosion-related phenomena, such as corrosion-fatigue, stress corrosion cracking, or hydrogen embrittlement, is considerably high. The high dissolution rate of HLSA involves significant costs on maintenance and replacement of damaged surfaces and, what is worse, the risk of premature deterioration of infrastructures or components that can lead to catastrophic failures, even taking human lives in the worst-case scenario.

In fact, corrosion is one of the phenomena that worst affect the deterioration of materials in offshore applications. A 30% of failures in ships and other marine equipment are the consequence of marine corrosion, with an annual cost of over EUR 1.5 trillion[ii] [1]. Marine corrosion is particularly aggressive, due to the salt content and low electrical resistivity of seawater [11]. The chlorides present in seawater depassivate metals and alloys such as stainless steels, aluminum alloys, or titanium alloys; even in the absence of oxygen. Chlorides are also present in marine atmospheres, which can lead to corrosion of non-submerged materials and structures [12]. There are other factors affecting corrosion in seawater and marine environments, e.g., temperature, dissolved oxygen concentration,

---

[i] *Denomination according to the International Association of Classification Society (IACS)*
[ii] *Currency expressed in American trillion (10^{12})*

pH, the presence of microorganisms, and so on [1,13-16]. Temperature and salinity of seawater, as well as dissolved oxygen concentration, vary depending on the geographical location. Temperature and oxygen concentration also vary with water depth [1,13,14,17,18]. In fact, corrosion has been reported to be more severe some meters above and below the water level, i.e., the splash zone, where the concentration of oxygen is higher [9,15,19]. With the aim of minimizing the material loss rate of corrosion-susceptible materials such as HSLA steels, protective measures have been successfully employed. Among the existing options, the use of coatings has been the most recurrent solution, and especially organic coatings with high corrosion resistance [20].

On the other hand, in certain applications, materials are also subjected to mechanical stresses that can lead to premature failure of components and structures. This is the case of Oil&Gas platforms, wind towers, renewable energy extraction systems, and mooring lines, inter alia. Fatigue, abrasion, impact, and wear generated by waves, wind, ocean currents, floating objects, sand, and heavy waves are the major stress types [1,9,21]. Mooring lines, for instance, are subjected to severe wear degradation in the connection between links and accessories, as consequence of the relative movement generated between components by waves, wind, and ocean currents [15,22,23]. Offshore structures, as well as mooring lines, are also exposed to abrasion and impact in the splash zone generated by heavy waves, floating wastes, sand particles, and other contaminants present in seawater [1,9,21].

Wear and corrosion are two processes that lead to an irreversible degradation, and whenever they take place simultaneously, the process is known as tribocorrosion [24-26]. Tribocorrosion involves a synergism between wear and corrosion, since the total material loss when the two processes occur simultaneously is greater than when they act alone [24,27,28]. While the tribocorrosion behavior of passive metals and alloys has been widely studied over the last decades [24-28], tribocorrosion of active materials, i.e., low-alloyed steels with high corrosion rates, is poorly documented. The lack of knowledge in this field, along with the unpredictable behavior of materials under the large number of degradation phenomena occurring simultaneously in marine environments, has led to slow progress in the development of offshore technologies. Up to now, the reliability of structures minimizing the risks of catastrophic failures has been achieved by oversized designs of components and structures. This, together with the high in-situ maintenance costs of metallic structures and protective coatings, entail large investments. Furthermore, the insufficient knowledge of materials behavior impedes the geographical expansion of offshore technologies, limiting the location of platforms and structures to low depths close to shore.

For all these reasons, a closer understanding of the behavior of active steels under wear-corrosion requirements could provide a better insight into materials performance in offshore environments. In turn, this knowledge could be used in the design phase, reducing both materials and maintenance costs. With this aim, in the present thesis, the tribocorrosion behavior of active materials is addressed. The thesis is focused in the specific case of mooring lines for Oil&Gas platforms, where wear and corrosion have been reported to be one of the main failure causes of chains and components [29-37]. The materials, i.e., HSLA steel grades, and the mechanical loads, have been selected according to this application. Nevertheless, the knowledge generated can be extrapolated to other offshore applications, where similar structural materials are usually employed.

This is the case of offshore technologies related to renewable energies. Oceans cover over 70% of the surface area of the earth and represent a rich source of renewable

energy. Therefore, the energetic resources available in the ocean have been found to be very attractive for the generation of renewable energy, due to the effectiveness of the marine environmental conditions, i.e., stronger wind, fewer turbulences, strong swell, currents, etc. It is estimated that ocean energy could produce from 20000 to 80000 TWh of electricity a year, covering the 100-400% of the current global demand [1]. The designs of onshore structures and the knowledge acquired in Oil&Gas and naval fields during the last decades have been used to develop current offshore technologies. However, ocean energy development is still in an early stage, and far from other renewable energies such as onshore wind power or photovoltaic solar [1], due to the harsher offshore environmental conditions. The better comprehension of materials performance in marine atmospheres is a crucial factor to achieve the expansion of both Oil&Gas platforms and renewable energy extraction systems and structures to key locations with higher resources. This could lead to a higher energy generation to meet the demand and fulfill the H2020 objectives: a 20% of the consumed energy in Europe to be obtained from renewable sources by 2020, and at least the 27% by 2030 [38].

Finally, it should be considered that the protective systems, i.e., coatings, are also subjected to tribocorrosion conditions [39,40], but they are usually selected mainly to protect steel structures and components from corrosion. Besides, the 45% of the mechanical damage in coatings is mainly generated in transport and erection operations [21], which can considerably reduce their durability in life service. Therefore, the performance of these coatings should also be addressed regarding tribocorrosion resistance, and the second part of this thesis deals with this matter. The selection of an adequate corrosion-wear resistant coating should also be a key issue in the design of offshore structures and components, to enhance the durability of coated systems against the great deterioration phenomena in marine environments.

1.2 STRUCTURE OF THE THESIS

This thesis is composed of 7 chapters. In this section, the structure of the thesis is explained, linking the different publications, and briefly describing the main topic addressed in each chapter. The main purpose of the present chapter, chapter 1, is to introduce the main motivation of the thesis.

Chapter 2 reviews the state of the art related to the main topics treated in the thesis. The problematics of offshore applications, focused on the specific case of mooring lines, their working conditions, and failures causes are presented. In the second part of this section, basic definitions of the main degradation mechanisms in offshore applications are provided. Wear, corrosion, and tribocorrosion phenomena are described, and the experimental techniques for the evaluation of tribocorrosion are explained. It is worth mentioning that this section is part of a review paper written and published in the frame of this thesis, used as a state of the art of techniques and test protocols employed in the tribocorrosion assessment of passive materials. Although it is not presented as a main contribution in the core body of the thesis, the review is included in Annex 2, with the rest of the published contributions. Finally, the last section of this chapter provides an insight into the protective systems and coatings used in offshore applications, as well as the standards and test protocols employed for their selection, evaluation, and validation.

After introducing the motivation and the state of the art, chapter 3 outlines the main objectives of the thesis and the key challenges that have been dealt with in its execution.

Chapter 4 explains the different methodologies employed in the thesis, briefly describing the type of characterization performed in each stage of the study.

The main results of the thesis are presented in the form of 7 scientific papers. Some of these contributions have already been published in international journals, while the rest have been submitted for publication and are currently under review process. These contributions are collected in chapter 5. The core of the thesis can be divided into two main blocks. In the first part, from chapter 5.1 to chapter 5.3, the tribocorrosion behavior of active materials is assessed. In the second part, from chapter 5.4 to chapter 5.7, the evaluation of currently employed protective coatings in terms of corrosion and tribocorrosion is addressed.

The first findings in the tribocorrosion behavior of active steels are presented in chapter 5.1. In this paper, two HSLA steel grades used in offshore mooring chain manufacturing, i.e., grades R4 and R5, were evaluated. As briefly explained in chapter 2, there are two standardized test procedures for the assessment of tribocorrosion of passive materials (ASTM G119 [41] and UNE 112086 [42]). In this chapter, the procedure of ASTM G119 standard was employed to evaluate the synergism between wear and corrosion for these steel grades in synthetic seawater. The results obtained in this work provided a first interesting insight into the response of active steels, showing a significant difference with respect to the better-known passive materials.

In chapter 5.2, the response of the R4 and R5 steels was evaluated using the test protocol described in the more recently published standard for tribocorrosion of passive materials (UNE 112086). Since seawater temperature is well known to vary with the geographical location and water depth, the influence of this parameter in the tribocorrosion resistance of the steels has been evaluated in this chapter. For this aim, the tests were performed at two temperatures, i.e., 23 ºC representing seawater temperature in the Gulf of Mexico, and 2º C to reproduce the low temperature in the North Sea. The results obtained from this work demonstrated the suitability of the test procedure, but the material loss quantification for passive materials could not be used for active materials.

In the last chapter from the first part of the thesis core, chapter 5.3, the tribocorrosion behavior of a passive AISI 316 steel and the active R4 steel grade is compared. In this chapter, the Zero Resistance Ammeter (ZRA) technique was employed, to simultaneously record information on the potential and corrosion current evolution during the wear test. The experiments were performed at different rotation speeds, so as to evaluate the influence of electrolyte agitation on the tribocorrosion response of both materials. The passive steel was found to be unaffected by the agitation, whereas the active steel showed a considerable acceleration of corrosion on the unworn surface with higher rotation speeds.

The second part of the thesis, regarding the assessment of protective systems, starts in chapter 5.4. In this chapter, three commercial coatings currently employed in offshore submerged component protection were evaluated. Currently, the coatings are selected by their corrosion properties, and little is known about their performance against wear-corrosion conditions. The corrosion and tribocorrosion performance of the coatings was studied, in order to compare the behavior of three physically different coatings and select the more suitable option for its use in severe working conditions, i.e., under wear-corrosion requirements.

The study of chapter 5.4 was completed with the aging tests presented in chapter 5.5. At present, the suitability of a coating for its use in atmospheres of different corrosivity is

verified subjecting the coated samples to different conditions in climatic chambers according to certain standards (ISO 12944 [43], NORSOK M501 [44]). The three commercial coatings were aged following these specifications. From the results obtained in chapter 5.4 and chapter 5.5, one of the three coatings was found to have the best performance in all the tests. This was a Thermally Sprayed Aluminum (TSA) coating with an organic topcoat.

Based on the results of the two previous chapters, the last two chapters aimed to provide the commercial TSA/organic-topcoat coating system with enhanced properties. In chapter 5.6, the TSA coating was treated by Plasma Electrolytic Oxidation (PEO) technique, in order to improve the low wear resistance of the aluminum layer. The newly generated duplex TSA/PEO coating system was evaluated in terms of corrosion, dry abrasion, and tribocorrosion tests in synthetic seawater. Based on the results, the corrosion, the wear and the tribocorrosion mechanisms of the oxide layer were proposed. The PEO treatment was found to be an effective solution to enhance the wear and tribocorrosion behavior of the TSA coating.

The last scientific work of the thesis is presented in chapter 5.7. In this paper, the organic topcoat applied to the TSA coating was functionalized to provide the system with antifouling abilities. The topcoat paint formulation was modified by adding SiO_2 nanoparticles to increase the hydrophobicity, and Cu_2O nanoparticles to make it bactericide. The former property aims to avoid the attachment of fouling and microorganisms into the submerged components, whereas the latter intends to annihilate any organism that gets to stick on the surface. The newly formulated topcoat applied on the duplex TSA/PEO coating was evaluated in terms of wettability, bactericide activity, and ecotoxicity tests. Finally, the whole coating system was aged according to the coating validations standards previously mentioned.

In chapter 6, the main deductions obtained from the outcomes of the seven previous chapters are discussed. At the end of this section, the final conclusions of the thesis are presented.

Finally, the future work and studies that could be performed to improve this work, and to gain new insights into the tribocorrosion behavior of active materials are proposed in chapter 7.

At the end of the document, two annexes are presented. In Annex I, the instrumental techniques employed in the execution of the thesis are described. In Annex II, the main contributions and dissemination activities derived from this thesis are listed.

1.3 REFERENCES

[1] M.R. Dhanak, N.I. Xiros (Eds.). *Springer Handbook of Ocean Engineering*. Springer (2016) ISBN: 978-319-16648-3

[2] M. Lannuzzi, A. Barnoush, R. Johnsen. *Materials and corrosion trends in offshore and subsea oil and gas production*. NPJ Materials Degradation (2017) 2

[3] Y. Weng, H. Dong, Y. Gan (Eds.). *Advanced Steels. The Recent Scenario in Steel Science and Technology*. Springer (2011) ISBN: 978-3-642-17664-7

[4] J. Billingham, J.V. Sharp, J. Spurrier, P.J. Kilgallon. *Review of the performance of high strength steels used offshore*. Research Report 105. Prepared by Cranfield University for the Health & Safety Executive. ISBN: 0-7176-2205-3 (2003)

[5] H. Zhang, X. Wang, R. Jia, J. Hou, W. Guo. *Investigation on stress corrosion cracking behavior of welded High-Strength Low-Alloy steel in seawater containing various dissolved*

oxygen concentrations. International Journal of Electrochemical Science 8 (2013) 1262-1273

[6] D.A. Skobir. *High-Strength Low-Alloy (HSLA) Steels*. Materials and technology 45 (2011) 294-301

[7] DNVGL-OS-E302. *Offshore mooring chain*. July 2018

[8] B. Albisu, I. Salado, A. Arredondo, D. Bilbao, M. Abrisketa, J.L. Arana, Z. Idoyaga, M.C. Carcedo. OTC 27024 MS: *New Grades of High Strength Steel for Offshore Mooring Chains: R5S 1100MPa and R6 1200 MPa*. Offshore Technology Conference (2016) Houston, Texas, USA

[9] A.W. Momber, P. Plagemann, V. Stenzel. *Performance and integrity of protective coating systems for offshore wind power structures after three years under offshore site conditions*. Renewable Energy 74 (2015) 606-617

[10] P. Ault. *The use of coatings for corrosion control on offshore oil structures*. Journal of Protective Coatings and linings 23 (2006) 42-47

[11] R. Winston Revie, Hebert H. Uhlig. *Corrosion and Corrosion Control. An Introduction to Corrosion Science and Engineering (4th edition)*. Wiley-Interscience (2008) ISBN: 978-0-471-73279-2

[12] (Ed.) L.L. Shreir, R. A. Jarman & G.T. Burstein. *Corrosion. Volume 2, Corrosion Control (3rd edition)*. Butterworth-Heinemann (1994) ISBN: 0-7506-1077-8

[13] R. Baboian (Ed.). *ASTM corrosion tests and standards. Application and Interpretation (2nd edition)*. ASTM International (2006) ISBN: 0-8031-2098-2

[14] ASM Handbook. *Volume 13. Corrosion*. ASM International (1987) ISBN: 0-87170-007-7

[15] R.E. Melchers, T. Moan, Z. Gao. *Corrosion of working chains continuously immersed in seawater*. Journal of Marine Science and Technology 12 (2007)102-110

[16] P.R. Roberge. *Corrosion Engineering. Principles and Practice*. Mc Graw Hill (2008) ISBN: 0-07-164087-8

[17] D. Talbolt, J. Talbolt. *Corrosion science and technology*. CRC Press US (1998). ISBN: 0-8493-8224-6

[18] C. Guedes Soares, Y. Garbatov, A. Zayed. *Effect of environmental factors on steel plate corrosion under marine immersion conditions*. Corrosion Engineering, Science and Technology (2011) Vol 46, No 4

[19] M. Kutz (Ed.). *Handbook of environmental degradation of materials (2nd edition)*. Elsevier (2012) ISBN: 978-1-4377-3455-3

[20] K. Mühlberg. *Corrosion Protection of Offshore Wind Turbines. A Challenge for the Steel Builder and Paint Applicator*. Hempel Protective. Published in JPCL (2010)

[21] W. Momber, T. Marquardt. *Protective coatings for offshore wind energy devices (OWEAs): a review*. Journal of Coatings Technology and Research 15 (2018) 13-40

[22] A.O. Vazquez-Hernandez, G.B. Ellwanger, L.V.S. Sagrilo. *Reliability-based comparative study for mooring lines design criteria*. Applied Ocean Research 28 (2006) 398–406

[23] A.O. Vázquez-Hernández, G.B. Ellwanger, L.V.S. Sagrilo. *Long-term response analysis of FPSO mooring systems*. Applied Ocean Research 33 (2011) 375– 383

[24] J.-P. Celis, P. Ponthiaux (Ed.). *Testing tribocorrosion of Passivating Materials Supporting Research and Industrial Innovation: Handbook*. Maney Publishing UK (2012). ISBN 978-1-907975-20-2

[25] D. Landolt, S. Mischler, M. Stemp. *Electrochemical methods in tribocorrosion: a critical appraisal*. Electrochimica Acta 46 (2001) 3913-3929

[26] S. Mischler. *Triboelectrochemical techniques and interpretation methods in tribocorrosion: A comparative evaluation*. Tribology international 41 (2008) 573-583

[27] P. Ponthiaux, F. Wenger, J.-P. Celis. *Tribocorrosion: Material Behaviour Under Combined Conditions of Corrosion and Mechanical Loading*, Corrosion Resistance, in: Dr. Shih (Ed.), In Tech (2012) ISBN: 978-953-51-0467-4

[28] D. Landolt, S. Mischler (Ed.). *Tribocorrosion of Passive Materials and Coatings*. Woodhead Publishing (2011). ISBN: 978-1-84569-966-6

[29] F. Yaghin, R.E. Melchers. *Long-Term inter-link wear model of mooring chains*. Marine Structures 44 (2015) 61-84

[30] Noble Denton Europe Limited. *Floating production systems. JIP FPS mooring integrity*. Health & Safety Executive(HSE) (2006). Research report 444.

[31] R.B. Gordon, M.G. Brown, E. M. Allen. *OTC 25134: Mooring Integrity Management: A State-of-the-Art Review*. Offshore Technology Conference (2014) Texas, USA
[32] M. Brown, A. Comley, M. Eriksen, I. Williams, P. Smedley, S. Bhattacharjee. *OTC 20613: Phase 2 Mooring Integrity JIP: Summary of Findings*. Offshore Technology Conference (2010) Houston, Texas, USA
[33] M.G. Brown, T.D. Hall, D.G: Marr, M. English, R.O. Snell. *OTC 17499: Floating Production Mooring Integrity JIP: Key Findings*. Offshore Technology Conference (2005), Houston, Texas, USA
[34] A. Kvitrud. *Anchor Line Failures. Norwegian Continental Shelf 2010-2014*. Petroleumstilsynet (2014) Report no 992081
[35] Z. Gao, T. Moan, S.E. Heggelund. *Time variant reliability of mooring system considering corrosion deterioration*. Proceedings of 24th conference on Offshore Mechanics and Arctic Engineering, OMAE (2005) Halkidiki, Greece
[36] S. Majhi, R. D'Souza. *OTC 24181: Application of Lessons Learned From Field Experience to Design, Installation and Maintenance of FPS Moorings*. Offshore Technology Conference (2013) Houston, Texas, USA
[37] ABSG Consulting Inc. *Study on Mooring System Integrity Management for Floating Structures. Final Report.* Submitted to The Bureau of Safety and Environmental Enforcement (BSEE) (2015) Project PS-003-14/ 3365033. Contract E14PC00038.
[38] Horizon 2020. *Work Programme 2016-2017. 10. 'Secure, Clean and Efficient Energy*. European Commission Decision C (2017) 2468 of 24 April 2017
[39] R.J.K. Wood. *Tribocorrosion of coatings: a review*. Journal of Physics D: Applied Physics 40 (2007) 5502-5521
[40] R.J.K. Wood, J.A. Wharton. *Coatings for tribocorrosion protection*, in *Tribocorrosion of Passive Metals and Coatings*, D. Landolt, S. Mischler (Eds.), Woodhead Publishing (2011), ch. 11, pp. 296-333, ISBN: 978-1-94569-96
[41] ASTM G119-09. *Standard Guide for Determining Synergism Between Wear and Corrosion*. vol. 03, ASTM, 02 August 2013
[42] UNE 112086:2016. *Ensayos de tribocorrosión en materiales pasivos*. 07 September 2016
[43] ISO 12944:1-9 *Paints and varnishes. Corrosion protection of steel structures by protective paint systems*. November 2017- January 2018
[44] NORSOK M-501. *Surface preparation and protective coating*. February 2012

Chapter 2

State of the art

Chapter 2: State of the art

2.1 OFFSHORE APPLICATIONS: CASE STUDY OF MOORING LINES

2.1.1 Mooring lines

Mooring lines are employed to maintain floating structures in a fixed position, within acceptable limits, ensuring the safe operation of the units. Mooring systems consist of a number of lines that are attached to different points of the floating structure. They have a physical contact with seabed providing restoring forces that act against the environmental solicitations that push the unit off station [1,2]. In operable platforms, the environmental forces cannot be withstood by a single mooring line, so typically 3 or 4 lines are employed. Mooring lines can be of different configurations, depending on the type of unit, the water depth, the seabed layout, the geographical location, etc. The different kind of moorings are [2,3]:

- **Catenary mooring:** consist of one single line or several lines in a radial fashion. The position of the floating units is maintained by the weight of the line.
- **Taut mooring:** usually consist of synthetic fibre ropes, which are prestressed forming angles of 30-45º with the seafloor. In this case, the elastic properties of the ropes maintain the structure in place.
- **Tension leg mooring:** They are a set of vertical tendons attached to the platform and the seabed, usually made of steel tubes and ropes.
- **Dynamic Position mooring (DP):** active thrusters are employed to oppose drifting caused by the natural forces acting on the unit.

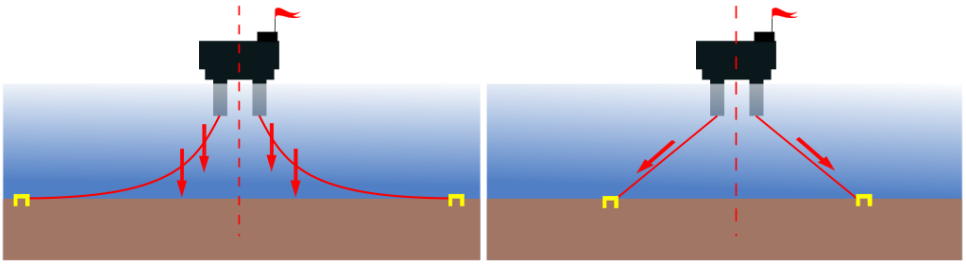

Fig. 2.1 Schematics of a catenary mooring arrangement, using the weight as restoring force (left) and a taut mooring arrangement employing the elastic properties of prestressed ropes to maintain the position (right) (Image based on [4])

The predominantly employed mooring types have been the catenary and the tensioned mooring or taut mooring systems [5] (see Fig. 2.1). Catenary moorings can be composed of chains, wires, and fiber ropes. Chains can be used as a sole component in a mooring line, but they are usually combined with wires and ropes of steel, natural fiber or synthetic fiber [6]. The benefit of such materials combination is a synergy of stiffness provided by the heavy chain, and a reduction of dead load an increased flexibility provided by the rope. Chains are typically used at the bottom of the line connected to the anchor, and at the top connected to the floating structure. The splash zone and the thrash zone, i.e. the top and bottom of the line, respectively, are particularly exposed to corrosion, wear, axial load and bending, and the use of robust chain is preferred for such harsh conditions.

2.1.2 Mooring lines in offshore floating platforms and facilities

The earliest moorings were employed as anchoring system for boats, ships, and vessels, to keep them from drifting freely in the ocean. These moorings consisted mainly of rope

or chains locket at a heavy anchor. As oceanic technologies developed to higher depths, moorings have been adapted and redesigned for their use in huge and heavy floating system station keeping operations.

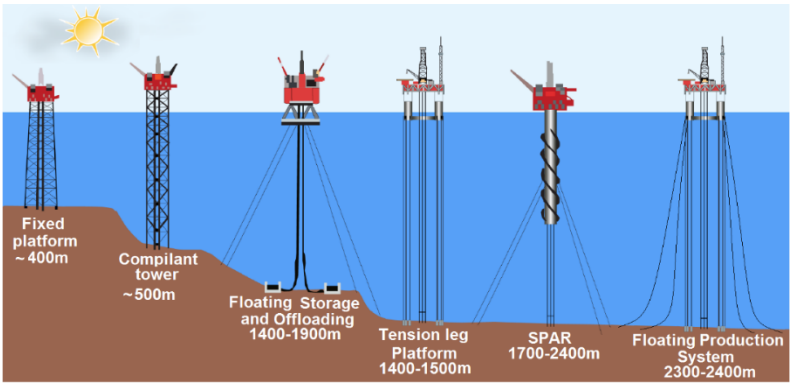

Fig. 2.2 Schematic of foundations and moorings employed in Oil&Gas production (Based on [7,8])

Regarding floating structures, the most ancient sector in ocean resources exploitations has been the petroleum industry. Oil&Gas continues to be the major source of energy in the 21st century. Oil&Gas Floating Production Systems (FPSs) are placed all over the world, and there has been an exponential growth in the number of facilities during the last decades. For instance, the number of FPSs increased from 277 in 2013 [9] to around 370 in 2017 [10]. FPSs are usually employed for water depths above 1500 m, where fixed structures are not economically viable, so mooring systems are employed to keep the platforms in a stable position during years. In Fig. 2.2, different platform types employed in Oil&Gas production are presented, i.e. FPS (Floating Production and Storage), FPSO (Floating Production Storage and Offloading), Semi-Submersibles, Spar, and TLP (Tension Leg Platform). Furthermore, the image shows different attachments to seabed employed in the different units: catenary, tension leg, or taut. Unlike trading ships, FPSs must stay fixed in the same position for years. The misplace of a stable position may lead to a malfunctioning of the platform, failure of components, or even catastrophic failures.

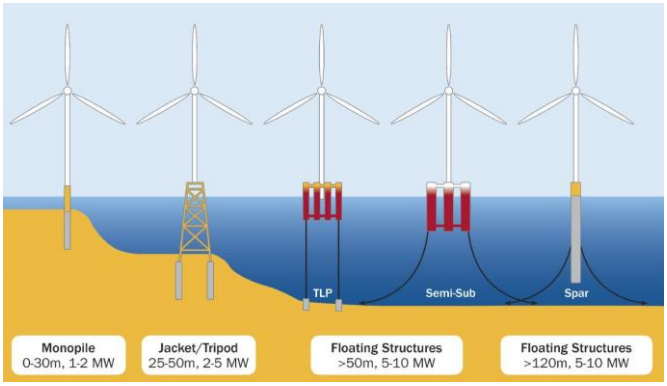

Fig. 2.3 Types of wind turbine foundations, showing floating structures adapted from Oil&Gas industry [13]

On the other hand, the growing interest in renewable energies has led to the development of new technologies for the generation of energy from the ocean natural resources. This is the case of offshore wind energy. The earliest offshore wind turbines where built close to shore in fixed structures. The need to increase the generated energy is leading to wind farm movement further offshore, into deeper waters, where better wind resources are available. Similarly to Oil&Gas platforms, fixed structures in depths greater than 50 m are not an economically viable option. This has led to a transition from fixed to floating support structures [5,11-13]. Floating offshore wind turbines (FOWTs) are the

most promising technologies among all the available wind energy harvesting facilities [12,14]. The knowledge acquired from the Oil&Gas industry has been employed in the design of different technologies for wind energy [15], including the mooring systems for FOWTs [5,11-13] (see Fig. 2.3). Chain catenary moorings have been already employed in floating horizontal axis wind turbines (HAWTs), e.g. Windfloat [11] and Hywind [16] prototypes. The former is located 20 km offshore in water depths of 150m [11], whereas the latter is placed 24 km offshore in water depths of 220 m [17]. Both facilities use three-catenary-chain line mooring systems for each wind tower of the farm.

Another less known example where mooring is also necessary are fish cage structures. Nowadays, the fish consumption coming from aquaculture is on the 35 %, which has led to an increase of a 10% per year in volume within the food industry sector. Chain-composed moorings are commonly employed to keep these platforms on a static specific position. The failure of mooring systems in these facilities results in fish scape, with the consequent economical loss [18,19].

2.1.3 Steel grades used in mooring chain links

Chains have been used in offshore mooring lines for decades in catenary configuration. The high strength of steel to resist the imposed loads, and the weight of the chains to be used as position restoring, make these components a good choice for mooring operations. A mooring line can be composed of over 1,500 links, and the weight of each link in water can be around 474 kg for 165 mm diameter chain, and 550 kg for 178 mm diameter chain [20]. Usually more than one line is employed for each floating platform, so the weight of the mooring systems can be considerably high, over thousand tones.

The steels used in mooring system components contain between 1 and 5 % of alloying elements by weight and are commonly referred to as High-Strength Low-Alloy Steels (HSLA). Links are manufactured from rolled steel bars, which are bent and joint by flash butt welding process. After welding, the links are heat treated, to achieve a proper microstructure and homogeneity. The heat treatments consist of two processes, namely quenching and tempering. The high mechanical properties, in terms of strength and toughness requited for mooring applications, are achieved through chemical composition and heat treatments [21,22]. Therefore, the properties of the steels can be controlled by adjusting the temperatures and the cooling rates of the heat treatments. There are two main types of chain links: stud links and studless links. The former are commonly employed in semi-submersible drilling platforms, whereas the latter are used in permanent moorings of FPSO, FPS and Spars [6]. The design of stud links is standardized and described in the ISO 1704 [23], whereas the design of studless link is not standardized, but the recommendations provided by the IACS W22 [24] are commonly considered. During manufacturing process, the links must undergo non-destructive tests to ensure the absence of irregularities, and the finished chains must also be inspected, checking their dimensions to discard any anomality undergone during manufacturing stages [21]. The classification societies classify the HSLA steels in different grades depending on their mechanical properties. The International Association of Classification Society (IACS) denotes the steel grades with an “R” followed by a number. The required minimum properties for each steel grade are presented in Table 2.1.

After the last highest grade R5 was approved by the Classification Societies in 2005, great efforts have been made to design new steel grades, with higher strength [25]. Recently, a new standard including a new steel grade has been approved: the R6 grade, with 1100 MPa of ultimate strength [21]. The properties of these steels are included in Table 2.1.

Table 2.1 Mechanical properties of the different steel grades used in mooring chains [21]

Steel grade	Quality assurance ISO 9000	Ultimate Strength min. (MPa)	Yield Strength min. (MPa)	Reduction of area min. (%)	Elongation min. (%)
API 0RQ	Required	641	-	40	17
R3	Required	690	410	50	17
R3S	Required	770	490	50	15
R4	Required	860	580	50	12
R4S	Required	960	700	50	12
R5	Required	1000	760	50	12
R6	Required	1100	850	50	12

It is worth noting that the steel components and structures in offshore industry are commonly protected against marine corrosion by coatings and/or cathodic protection. The case of mooring lines where the steel components are mainly unprotected is rather special [22]. More about coatings for the protection of submerged components will be addressed in the following section of this chapter.

2.1.4 Offshore working conditions

Offshore structures and their moorings are exposed to harsh environmental conditions, including high loadings coming from storms, waves, wind, ocean currents, marine growth, ice, and so on. Mooring lines can extent for several hundred meters undersea, and the weight of the catenary becomes very heavy. The environmental loads applied on the stationed unit are resisted by this high weight [2,26,27]. When the unit is forced to move in one direction, the mooring line stretches in the opposite direction, lifting from the seabed, and adding more weight to the line. The lifting and dropping of the line in the thrash zone can cause wear and abrasion damage in the links, by rubbing them against the sand in the seabed [2]. The combination of seawater with oxygen can generate considerable material loss of steel by corrosion. The sea behaviour results in cyclic loadings inducing the risk of fatigue. Since this fatigue takes place in a hostile environment, i.e. seawater, it corresponds to corrosion-fatigue phenomenon, which is a type of fatigue enhanced by corrosion. Therefore, mooring systems must withstand mechanical and environmental loads maintaining a stable position in the sea, ensuring the functionality of the FPSs [1,26-28]. Usually, mooring lines are designed for an operational life of 20 years [2,26,29], but the adversities in seawater environment can reduce the designed lifetime of these structures several years, resulting in unpredicted failures. Since moorings of fixed structures are not frequently inspected and repaired in dry conditions, periodic inspections are essential to monitor their structural integrity.

2.1.5 Mooring line failure causes

The mooring line is as strong as its weakest link. Therefore, the longer the chain the higher the probability that a link has a weakness that might lower its strength [26,27]. The failure of one or more lines results in an increase in the loading on the remaining lines, which can exceed their capacity, leading to failure of these lines. In 2000, the potential FPSOs hazards were identified and ranked in a report prepared by the Norwegian University of Science and Technology (NTNU) for Health and Safety Executive (HSE), based on frequency as well as consequence. In this report, multiple failures in mooring systems were ranked as safety critical risk category 1, which corresponded to the highest category [3].

Since the oldest offshore technology corresponds to FPSO industry, the most reported mooring incidents of floating units are associated with Oil&Gas production units. Premature line replacements as well as single or multiple line breakages have been reported [1,9,30-33]. Just in the period between 2010 and 2014, 16 failures were

reported on the Norwegian Continental Self [30]. Mooring line failures have occurred due to a range of motives, but the main causes are fatigue, corrosion and mechanical issues, including wear [1,2,9,26-30,33]. The most reported failure types are classified into the following major groups:

- **Corrosion-fatigue:** Fatigue damage accumulates in mooring line components as a result of cyclic loading. As consequence of the low frequency generated by waves (0.1-0.5 Hz) [34,35], there is plenty of time for corrosion to occur, and the phenomenon shall be therefore referred to as corrosion-fatigue.

Fig. 2.4 Chain failure by corrosion-fatigue crack propagation in the crown (left [36] and middle [37]), and fatigue crack initiation in the crown (right) [37]

- **Electrochemical corrosion:** Corrosion is an electrochemical process where metallic atoms are oxidized. In steel components, iron atoms oxidize into positive ions (Fe^{2+}) that react with other ions and molecules present in seawater to form oxides and salts [22]. Iron dissolution corresponds to the anodic reaction, whereas the dominant cathodic reaction is the oxygen reduction. Iron ions can react forming different oxides or hydroxides, creating a rust layer in the surface of the steel. The most common corrosion product for steel in seawater has been found to be iron oxyhydroxide (FeOOH) [38-42], which can be present in different structures: goethite (α-FeO(OH)), lepidocrocite (γ-FeO(OH)), or monohydrated ($Fe(OH)_3$). Magnetite has also been found under high iron ion and low oxygen concentrations [22,42].

Fig. 2.5 Chain links presenting general corrosion (left) [2], chain covered by fouling (middle) [45], and chains showing localized corrosion due to MIC (right) [44]

There are several corrosion types that can affect mooring components, from locally concentrated to generally extended over a wide surface. Localized corrosion, commonly referred to as pitting corrosion, causes typically 2-3 mm of metal loss with isolated areas of deeper pits [2]. This type of corrosion has been reported to be mainly consequence of the presence of microorganisms, what is known as Microbiologically Induced Corrosion (MIC) [9,22,33,42-47]. MIC has been found to reduce up to a 35% of the cross-sectional area of a chain link after 7 years of operation in West Africa [43]. Corrosion of steel in seawater is a function of many

factors including water temperature, salinity, water velocity, oxygen concentration, and surface roughness, inter alia [1,28,47,48]. Some of these factors vary with the geographical location, the year season, or the water depth. For instance, an increment water temperature of 10 degrees can increase the corrosion rate of low alloy steels by a factor of 1.5 or even 2 [22,42]. Furthermore, corrosion is also known to be more aggressive some meters above and below the water level, i.e. in the splash zone, where more oxygen is available for corrosion reactions [22,31,33,42,46,48]. Galvanic corrosion is another major concern in such applications were the combination of dissimilar materials is employed [2,22,33,42]. Therefore, corrosion rate of mooring chains is not a simple function of exposure period, but it is influenced by several variables hard to predict.

- **Wear and abrasion:** The cyclic loads generated by environmental factors can lead to wear, and fatigue-wear, which can result in premature failure of components. Chain wear is more severe in the inter-link contact, particularly in the upper chain links [1,42,47] and in the sea floor or thrash zone [2,9,22,33,47]. The high wear in the less heavily loaded leeward lines is attributed to a greater inter-link rotation occurring in the thrash zone [26,27,33]. Furthermore, sand and other foreign materials can be trapped in the inter-link contact, aggravating the abrasion between links [1,30,49,50]. Some studies have reported wear rates up to 3-4 mm per year in chain links [22,26]. The main wear mechanisms found in the interaction between links in mooring lines have been found to be adhesive wear, abrasive wear, and surface fatigue wear [22,47]. The considerable reduction of the chain section results in a loss of strength, and the links might not resist the imposed load failing prematurely.

Fig. 2.6 Chain links showing severe wear in the inter-link contact (left) [51], and wear and pitting corrosion (right) [2]

- **Tribocorrosion (wear and corrosion):** Wear in inter-link contacts removes the corrosion products formed in the chains surface, leading to higher material loss in the inter-link zone than elsewhere [1,2]. The oxide formed in HSLA steels, mainly iron oxyhydroxide, is porous and loose [38-41]. However, its presence slows down the corrosion rate of the steel, strongly limiting the Fe^{3+} iron transport from the steel to water, and the oxygen transport from the water to the steel [52-54]. On the other hand, the salts present in seawater can precipitate on the surface of the steel, reducing its corrosion rate from 0.6 mm/yr to 0.1-0.2 mm/yr [22]. The removal of these oxides and deposits from the surface exposes the underlying steel, which can corrode faster [1,2,22,42]. The detached particles can be trapped in the contact between links enhancing the wear extent by a three-body abrasion mechanism. On the other hand, corrosion can increase the surface roughness, altering the contact forces and affecting the wear of the links. There is a synergistic effect between wear

and corrosion, where the material loss when the two processes take place simultaneously is higher than when they take place alone [22,42].

- **Overloading:** Overloading is a common cause of mooring line failure, which often occurs during meteorological phenomena, i.e. storms, gales, etc. Under these circumstances, the chain links experience a far larger loading, which can exceed their maximum strength [9,30,55].
- **Design errors and manufacturing defects:** The unawareness of the potential threats in the design phase is usually behind the failures related with design errors. The uncertainties produced by a lack of knowledge, and the unpredictable behavior of materials in such unsteady environment, often make the design process difficult and imprecise [9,28]. Inappropriate chain manufacture is another issue of concern. Some reports indicated the failure of components by improper heat treatment resulting in low toughness [22,56-58]. Finally, a high number of mooring integrity issues and interventions have been consequence of installation related shortcomings, especially in the first years of service [29].

As consequence of the diverse working conditions of mooring lines, the above mentioned failure causes can interact leaving to complex failure mechanisms. For instance, the material loss due to wear or corrosion, changing the cross-sectional geometry of the links, can lead to premature failure by faster crack propagation under corrosion-fatigue conditions. Excessive corrosion or wear can lead to the initiation of fatigue cracks under cyclic loading [22,42]. Furthermore, depending on the material, or steel grade in this case, the deterioration concerning wear and corrosion will be different. Corrosion and wear properties of the chain links will be influenced by the chemical composition, microstructure, hardness and surface conditions, in terms of roughness and oxides presence [22]. At present, little data is available related to the influence of wear and corrosion on the degradation of long-term mooring components of HSLA steels, and the reduction of their break strength [9].

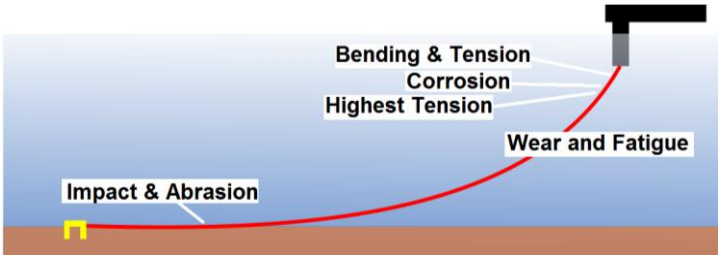

Fig. 2.7 Main degradation processes and their location on a catenary mooring line (based on [2,9])

Some of the degradation mechanism that long-term mooring systems must withstand are presented in Fig. 2.7. As observed in the picture, the fairlead or chain stopper, i.e. the upper part of the line, is subjected to high tension with additional bending and twisting stresses. The twisting can also lead to inter-link wear in the contacts. The links located in the splash zone are exposed to highly oxygenated water, where high rate aerobic corrosion processes take place [31]. Finally, the touchdown or the links placed in the bottom of the line in contact with the sea floor, are exposed to severe wear, impact and abrasion [1,30,49,50].

On the other hand, the different degradation mechanisms in a single chain link are presented in Fig. 2.8. Links are exposed to particle erosion in the whole surface. Fatigue cracks are generated due to cyclic tension and compression loads. Inter-link wear takes place in the crowns, and it can be aggravated by the presence of foreign particles, sand,

or iron oxides removed during wear. Corrosion affects the whole component, and in the areas where wear processes take place the material loss is accelerated (tribocorrosion).

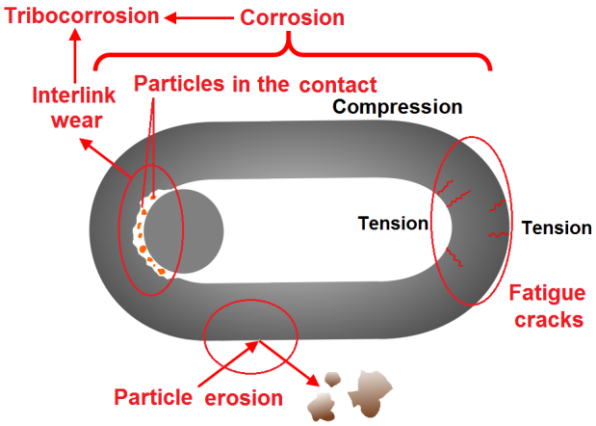

Fig. 2.8 Schematic of the different degradation mechanisms in a chain link (based on [33,50])

2.1.5.1 Reported failures: statistics of failure types and causes

Over the years, there has been an increase in the number of mooring line failures, which has been proportional to the increase of the FPSO population [31]. Most of the reported failures have been related to a single line failure, but some multiple line failures and even catastrophic failures have also been reported. Furthermore, in most cases, the assets presented integrity issues requiring intervention, which resulted in partial or complete line replacements [29,31]. Mooring line failure frequency follows a classic U-shaped curve, presenting a high number of failures in the first 5 years of operation, a decrease during the following years, and a final increase in the late life above 15 years of operation [29]. The early life failures are consequence of poor design, defects on manufacture process, or damages originated during installation operations. The late life failures are often related with the aging of components, which is accelerated by the harsh environmental and mechanical working conditions, i.e. corrosion, wear, fatigue, etc [29,31,57].

Many authorities have gathered information on mooring line failures and their causes. Most of the data available is from the North Sea, where there are statutory requirements for reporting mooring-related incidents to the UK HSE (Health and Safety Executive) [9]. The surveys presented by the HSE showed different failure times depending on the structure type [2,30,55,59]. For FPSOs and FSOs, a line failure for every seven and seventeen operating years was expected, respectively. Drilling semi-submersible and Production semi-submersible units presented one failure every four and eight operating years, respectively. More frequent failures are expected for drilling ships, every year and a half. The shorter expected time to failure on non-permanent platforms, i.e. MODUs (mobile offshore drilling units), might be due to rougher handling of the lines, since they are more frequently installed and uninstalled when switching locations. Taking under consideration that mooring lines are designed to last for more than 20 years, the expected failure rate of mooring systems is rather high. Furthermore, giving the substantial increase in the number of FPSs installed during the last years, and the increasing age of the already installed ones, the probability of failure might increase in the near future.

In 2014, a survey was carried out by E. Fontaine gathering information on the incidences related to pre-emptive replacements, reported degradations, and mooring failures, either single or multiple for ship-shaped FPSs [31]. According to this survey, the highest number of failures have been reported from the North Sea, followed by West Africa. The latter also presented the highest pre-emptive replacements. On the other hand, there was little data available from other locations such as Brazil or Asia, which were thought

to be an under reporting of failures rather than a lack of incidents [31]. As shown in Fig. 2.9a, the survey revealed the highest failure event types to be single line failures (42%), followed by pre-emptive replacements (39%). Multiple line failures represented the 8% of the cases. The 19% of these failures led to a production shutdown (Fig. 2.9b). The reported root causes of the failures are presented in Fig. 2.9c. The most prevalent failure reasons were fatigue and corrosion, which together represented the 45% of the cases. Installation failures represented the 16%, which comprising residual mechanical damage, design issues, manufacturing defects, and so on. In Fig. 2.9d, it can be seen how most of failures took place during operation processes (49%), followed by installation (22%) and design (19%) related causes. The breakdown of mooring component type associated with single line failures and the prevalent failure modes for chain links are presented in Fig. 2.9e and f. Single line failures are mostly consequence of chain links failure (54%). In turn, chain link failures are dominated by corrosion (20%) and corrosion fatigue (19%), followed by fatigue (17%) [31]. Regarding the location of the failure along the length of the mooring line, most of the failures took place on the terminations (e.g. fairleads and anchor), in the touchdown regions on the seafloor, and at connectors [9,60].

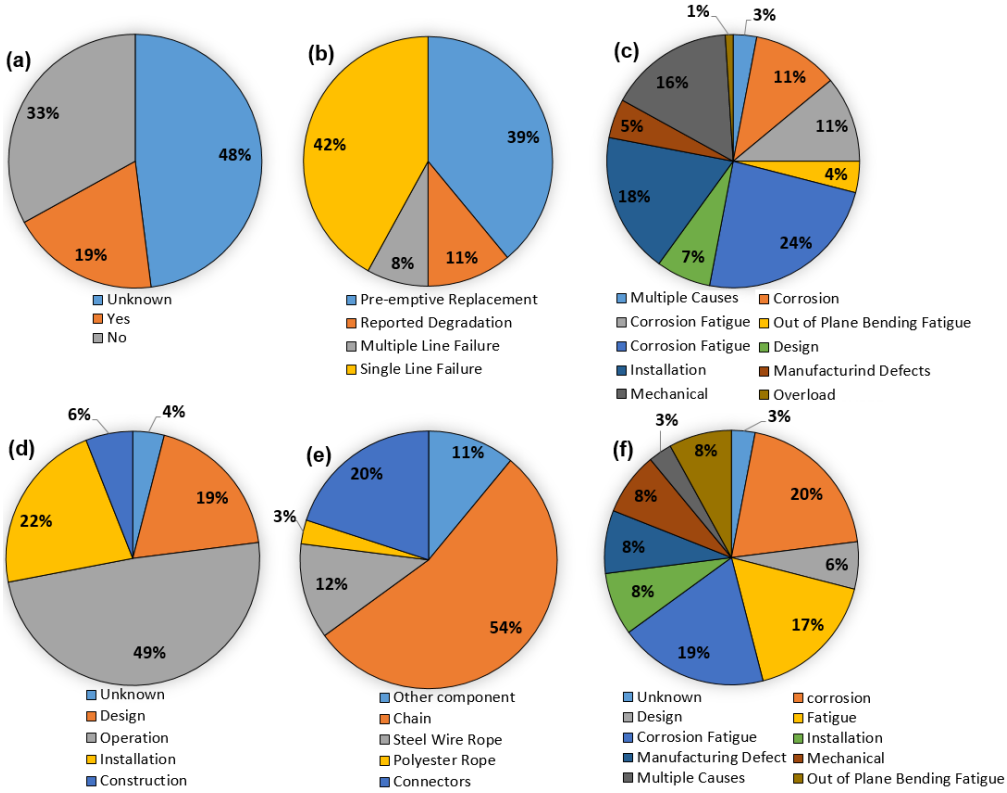

Fig. 2.9 (a) Failure event type, (b) effect of failures on the production of the units, (c) main causes of failures, (d) proportion of failure associated to each project phase of mooring line, (e) component type associated with single line failures, and (f) failure causes for steel chain links (from [31])

2.1.6 **Impact of mooring line failures**

A mooring line failure, which in turn can lead to the platform failure, can have a major impact on the local environment, the company economics, financial losses, and welfare of human lives [1,2,9,26,27]. The consequences connected to mooring failure are diverse, from damaging subsea equipment, to completely uncontrolled platform drifting in the sea. This was the case of Transworld 58, the first semi-submersible platform, which after 6 years of operation broke away in 1981 when a single mooring line failure was followed by multiple line failures. Another example is the Fulmar SALM, which broke free in the North Sea in 1988 after 7 years of service [2]. The free drifting of a platform could

also affect other units in the proximity, increasing the losses. Mooring systems failure represent the 77% of all FPSO losses. For the operational losses of FPSOs reported from 2001 to 2016, a total of EUR 3.6 billion[iii] was registered for around 300 losses. A 37% of the losses (EUR 1.3 billion[iii]) were attributed to mooring line failures, whereas those corresponding to risers were the 16% (EUR 0.6 billion[iii]) [61].

The financial costs associated with mooring line failure can be extremely large. The replacement of a broken mooring line with a new one, or the production shutdown of the moored structure for a short period involves a considerable economic impact for offshore industries. The full replacement of a mooring may well take several months, due to lack of spares and procedures, and also to a possible non-availability of suitable vessels [27].

The failure of a mooring line can lead to the rupture of risers or drilling pipes, allowing a large spill of hydrocarbons into the ocean. Hydrocarbon release might cause a severe environmental contamination, which can be difficult to treat. The presence of hydrocarbons can disturb the marine ecosystem, affecting the fish growth [62], or being lethal to certain organisms inducing the loss of habitat of marine species [63]. A worse and more catastrophic incident would be an explosion of a platform as consequence of hydrocarbons ignition after a leak in a broken drilling pipe. This would generate the loss of expensive equipment, and also the loss of human lives in the worst-case scenario.

2.1.7 Mooring line design codes: specifications and limitations

Permanent mooring systems are typically designed to last 15 to 20 years [2,26,29]. The considerable number of assets that have require mooring replacement, or the premature failure of mooring lines, evince that the intended design performance of moorings does not meet the operational performance in real service conditions [29].

Corrosion is one key issue that must be considered in mooring line design. However, certain uncertainties will always be present as corrosion process depends on diverse causes that are not always constant, e.g. temperature, salinity, presence of microorganisms, etc. This results in different corrosion rates that depend on the geographical location, depth, or year season, inter alia. Therefore, the influence of all these variables make the prediction of the corrosion behaviour of steel components markedly challenging [2,33]. Furthermore, the constant movement of the mooring line, the relative movement generated between the links, the graze generated in the seabed, and the impact of sand and other objects present in the ocean, can lead to considerable material loss by wear process. This produces a fairly reduction in the effective section of the chain links, which eventually might not withstand the loads failing prematurely. Therefore, a key factor in the long-term integrity of a mooring system is the correct accountancy of wear and corrosion in the design process.

There are several design codes and standards that present design requirements considering wear and corrosion of steel chains. The early design and operational protocols were based on the knowledge acquired from the North Sea cold-water reported experience. All this knowledge is reflected in the most current requirements specified by the Classification Societies [47]. The oldest design codes did not include corrosion allowance or fatigue life calculation requirements, as in the case of POSMOOR code (1989) [64]. Back then, mooring lines were design just with load allowances, so there was no much margin to assure the durability of the links that could no longer meet allowable loads due to the degradation occasioned by wear and corrosion.

[iii] *Currency expressed in American billion (10^9)*

Current industry practice is to increase the chain diameter several millimetres per service year. The wear and corrosion allowances for mooring line designs of more recent offshore-related standards are compiled in Table 2.2. As observed in the table, the allowances depend on the exposure zone of the mooring line. The parts of the mooring line are divided as splash zone, catenary, and bottom [65]. The splash zone is defined as 5 m above and 4 m below the still water level, the Catenary is the suspended length of the mooring line between the splash zone and the bottom, and the bottom is the line length in contact with the hard bottom sea-bed. According to the DNVGL-OS-E301 [65] and NORSOK M-001 standards [66], the design in the splash zone must be more conservative comparted to the remaining exposure zones, due to the aggressiveness of corrosion in this region with high oxygen concentration. The allowance of the bottom of the line should be increased if bacterial corrosion is suspected.

Table 2.2 Chain wear-corrosion allowance requirements of different standards

Codes/Standards		Chain wear-corrosion allowance referred to chain diameter (mm/yr)		
		Splash zone	Catenary	Bottom
API RP 2SK		0.2-0.4	0.1-0.2	0.2-0.4
ISO 19907-1		0.2-0.8	0.1-0.2	0.2-0.8
NORSOK M-001		0.4	0.1	-
DNVGL-OS-E301	No inspection	0.4	0.3	0.4
	Regular inspection	0.2	0.2	0.3
	Requirements of the Norwegian shelf	0.8	0.2	0.2
	Requirements for tropical water	1.0	0.3	0.4

API RP 2SK [67] recommends an increase of 0.1-0.2 mm in the mid-catenary, and of 0.2-0.4 mm in the splash zone and the hard bottom sea-bed. On the other hand, API RP 2I [68] has been used in the design of long-term FPS moorings, but it does not take into consideration wear and corrosion allowances. The inconsistency of chain dimensions requirements of the two API standards has drawn the attention of the sector [69]. The ISO 19907-1 standard [70] recommends an increase of 0.2 mm to 0.8 mm per service year in the splash zone and the hard bottom sea-bed. Similarly, the NORSOK M-001 prescribes 0.4 mm for the splash zone and 0.1 mm for fully submerged conditions. The requirements of NORSOK cover the regulations of the Norwegian Continental Shelf (NCS), which are stricter than the requirements of other locations around the world. The DNVGL-OS-E301 presents high-level requirements regarding in-service inspection programs. The standard states that corrosion allowance should depend on inspection schedules. The allowances are lower compared to other standards, since the lines are designed to be inspected with higher frequency, and states that the lines should be replaced when the diameter is reduced by 2%.

2.1.8 Challenges in the mooring line design

Dimensional checks carried out on FPSs placed on the North Sea have demonstrated that wear and corrosion are significantly higher than that specified in most mooring design codes. For instance, the worn areas in the thrash zone of a failed line showed a reduction of 10 mm due to wear and corrosion over 16 years of service. This corresponded to a material loss rate of 0.615 mm/yr, being a 50% higher than the value specified in the DNVGL-OS-E301 [2,26]. If the material loss due to combined wear and corrosion processes is higher than that specified in mooring design codes, which could also have significant implications for the true long-term integrity of FPS moorings [27].

On the other hand, corrosion rate is also different depending on the corrosion mechanism. The localized corrosion induced by sulphate reducing bacteria (SRB) [29],

or by galvanic reaction when two distinct metals are in electrical contact, lead to fast metal dissolution, overcoming the values in the design codes. Other failure mechanisms such as friction induced bending fatigue appears to be a significant issue which has been somehow neglected and require further investigation [2,6]. The design codes offer little guidance about the influences of climatic, environmental, and operational conditions [47]. Finally, the synergistic effect of the combination of several degradation phenomena make the prediction a complicated issue. Awareness of corrosion, wear, and relevant loading conditions during design phase will certainly improve offshore structural components, guaranteeing their correct functioning and extending their service life.

2.2 ANALYSIS OF THE DETERIORATION MECHANISMS IN OFFSHORE APPLICATIONS. TRIBOCORROSION

2.2.1 Introduction

Materials working in offshore applications, are subjected to very harsh environmental conditions. Often several phenomena can take place simultaneously shortening the useful life of structural materials, leading to unpredicted failures. In the case of mooring systems, tribocorrosion plays an important role in terms of premature failure of components [71]. On one hand, the relative motion between chain links and connectors generated by waves, wind and ocean currents [72,73] leads to a continuous wear process in the contact surfaces. Moreover, the components that are continuously submerged or located in the splash zone of offshore structures, are subjected to high rate corrosion processes [48].

2.2.2 Wear

Wear is the removal of material from one or both of two solid surfaces in a solid-state contact. It occurs when solid surfaces are in a sliding, rolling, or impact motion relative to one another, through surface interactions at asperities [74,75]. The generation and circulation of wear debris can enlarge the total amount of wear [76,77]. In extreme conditions of mechanical or environmental stress, wear can lead to fatigue or fatigue-corrosion failure of the material [78]. Wear has a significant economic impact on modern industrial society. Several studies estimate that the cost associated with wear damage corresponds approximately to a 1-22% GNP, so it plays a vital role from a socioeconomic standpoint [75]. Depending on the nature of the damage, the factors causing wear, and the combination of materials, wear damage on materials can be classified into the following wear modes [75,78,79]:

- **Adhesive wear:** It is common in metal/metal, metal/polymer, and metal/ceramic contacts, and occurs when asperities on sliding surfaces interact to form cold welds. When the adhesion strength of the weld points exceeds the cohesive strength of the contacting materials, one material is transferred to the other and adhesion takes place.
- **Abrasive wear:** Abrasion is the most common type of wear (55-60% of all wear). It occurs when one of the sliding materials is much harder than its counterpart, typically with a difference higher than a 20%. In such a case, known as two-body abrasion, surface asperities on the harder surface can easily abrade the softer material. Another kind of abrasion called three-body abrasion is caused by the particles confined in the tribological contact. In this case, the particle shape and hardness play a major role in the overall wear rate.

- **Oxidation wear:** Oxidation wear is commonly observed on oxide forming materials at high temperatures. In general, oxides on the surface of a metal can be released as wear particles once the oxide layer reaches a critical thickness.
- **Erosion wear:** Erosion wear occurs when hard particles or fluids droplets impinge on a material. The erosion with particles is termed particle erosion, whereas erosion caused by the impingement of liquid droplets is called liquid erosion.
- **Fatigue wear:** This type of wear occurs when materials are subjected to cyclic stresses.
- **Fretting:** It is a special type of corrosive wear, that includes corrosion damage of surface asperities on contacting surfaces and involves micro-movements.
- **Cavitation wear:** Fluid dynamic effects cause the formation and collapse of gas bubbles near the surface. Cavitation wear occurs therefore due to the collapse of those gas bubbles at the surface of the material, as consequence of the violent pressure impulses generated by their rapid collapse.

2.2.3 Corrosion

Corrosion is another surface degradation phenomenon that is known to generate high material losses in diverse applications. Corrosion can be defined as the chemical or electrochemical reaction of a metal or an alloy with its surrounding media with the consequent deterioration in properties [75,80,81]. Corrosion occurs in every aspect of the modern life, affecting areas of the economy, from the integrated circuit to structural constructions made of steel or reinforced concrete [82-84]. The cost of corrosion in developed countries has been estimated to be between the 3.5 and 4.5% of the GNP [78,80-82,85]. Furthermore, replacement of corrosion-deteriorated materials implies material extraction from nature, with its subsequent environmental damage [80-83].

When an electric union between two different metals is made, i.e. by immersing them in the same conductive solution; an electrical current is generated due to the difference of electrochemical potential of both metals. As consequence, there is a charge transfer through the liquid. The surface of the metal prone to dissolution (anode) is corroded in a process in which metallic atoms leave electrons in the core of the metal and pass to the solution as positive ions. On the other hand, the surface less prone to dissolution (cathode) receives the electrons liberated in the anode through the metallic mass remaining immune to the corrosive attack [72,75,78,80,81]. The oxidation reaction taking place in the dissolving anode, necessarily needs to be accompanied by a reduction process in the cathode (Fig. 2.10). The impurities and heterogeneities in the surface of a metal lead to electrochemically differentiated zones within the same material, and thus, corrosion can take place without the necessity of another metal to be in electrical contact [78,81,86].

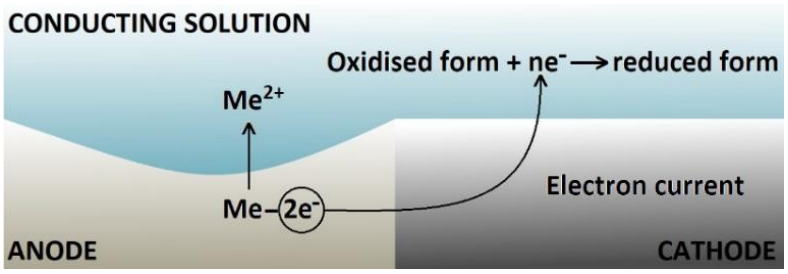

Fig. 2.10 Schematic representation of the electrochemical corrosion process for a divalent metal [78]

The basic electrochemical reactions are the following:

- Anode (oxidation): $M_e \Longrightarrow M_e^{n+} + ne^-$
- Cathode (reduction): $OX + ne^- \Longrightarrow RED$

The oxidation reaction involves the loss of electrons or an increase in the oxidation state of a molecule, atom or ion: $Fe \Longrightarrow Fe^{2+} + 2e^-$. It causes either dissolution of the metal as metal ions in the surrounding environment or, alternatively, the formation of an oxide protective layer [75]. The reduction reaction is the gain on electrons or decrease in the oxidation state of molecule, atom or ion. A cathodic reaction is often related with the development of oxygen and hydrogen, depending on the solution:

- Non-aerated acid dissolutions: $2H^+ + 2e^- \Longrightarrow H_2$
- Non-aerated neural or alkaline dissolutions: $2H_2O + 2e^- \Longrightarrow H_2 + 2OH^-$
- Aerated acid dissolutions: $O_2 + 4H^+ + 4e^- \Longrightarrow 2H_2O$
- Aerated neutral or alkaline dissolutions: $O_2 + 2H_2O + 4e^- \Longrightarrow 4OH^-$

There are different types of corrosion [75,79,82,83,86,87]:

- **General or uniform corrosion**: It is the most general type of corrosion and refers to a loss of material uniformly distributed over the entire surface exposed to a corrosive environment. For uniform corrosion attacks, metals can be classified into three groups according to their corrosion rates:
  - <0.15 mm/yr: Good corrosion resistance, and they are suitable for critical parts (e.g. valve seats, impellors, pump shafts…)
  - 0.15-1.5 mm/yr: Satisfactory performance, whenever higher corrosion rates can be tolerated (e.g., tanks, piping, valve bodies…)
  - >1.5 mm/yr: Not satisfactory.
- **Localized corrosion**: This type of corrosion occurs on specific sites of the metal surface, under specific environmental conditions. There are several types of localized corrosion: pitting, fretting, crevice, filiform and cavitation.
- **Galvanic corrosion**: It is also called bimetallic corrosion, and results from the formation of an electrochemical cell between two metals, due to the potential difference between them.

Finally, there are forms of corrosion where two effects are overlapped, one chemical or electrochemical and another mechanical one. Erosion-corrosion or stress corrosion cracking are some examples.

2.2.4 Tribocorrosion

All in all, wear and corrosion are two processes that lead to a surface damage due to a progressive material loss as a result of mechanical and electrochemical processes, respectively. When these two degradation processes occur in a simultaneous way, it is known as tribocorrosion [77,88,89]. Tribocorrosion can be defined as the irreversible transformation of materials resulting from the simultaneous action of mechanical loading (e.g., friction, erosion, abrasion) and chemical/electrochemical interactions with the surrounding environment (corrosion attack). It combines two major scientific areas: Tribology and Corrosion. The former comprises the study of friction, wear, and lubrication, whereas the latter is related to the chemical aspects of material degradation [76,88,90-99].

Tribocorrosion involves a synergism between wear and corrosion, since the degradation caused by the combined action of mechanical and electrochemical processes is larger than the sum of each of them acting separately [76,88,90-100]. This synergism can be either beneficial or detrimental, depending on the surface reactions that take place in the

tribological contact [90,94]. The reaction products formed on the surface can protect the surface by forming self-lubricating layers, or accelerate the material degradation by third-body effect, for instance [76,90,94,95,101-105]. The synergy between wear and corrosion can be defined as:

$$W_t = W^m + W^c + W^s \quad (2.I)$$

Where W_t is the total volume removed, and W^m and W^c are the volume of material removed separately by the effects of wear and corrosion, respectively. W^s represents the synergistic effect between wear and corrosion which can account for 20-70% of the total volume of material removed [77]. The previous equation may also be written as follows:

$$W_{tr} = W^m + W^c + W^{cm} + W^{mc} \quad (2.II)$$

Where W^{cm} is the effect of corrosion on wear and W^{mc} the effect of wear on corrosion.

The origin of tribocorrosion is closely related to the presence of a passive film on material surfaces subjected to wear and the modifications of these surfaces by friction or any other form of mechanical loading. In very general terms, the passive film, mainly oxide, is considered to be snatched in the contact area [88].

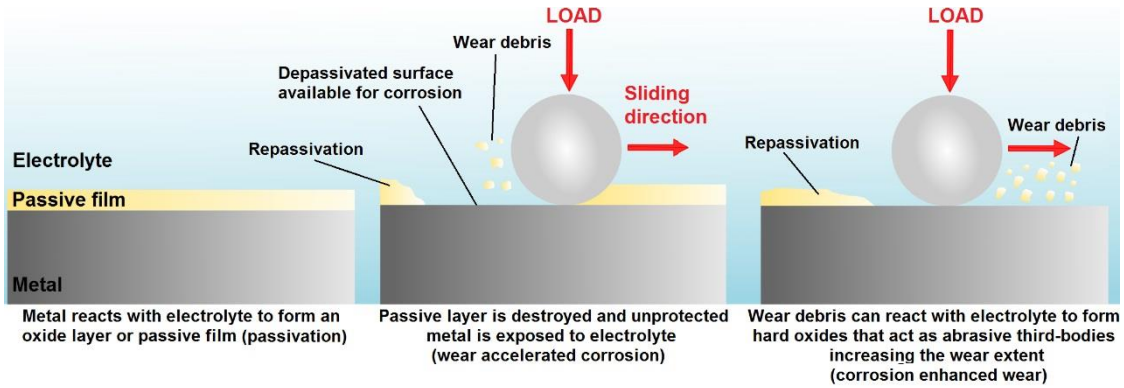

Fig. 2.11 Schematic representation of the synergism in tribocorrosion: passive layer is removed promoting corrosion (wear-accelerated corrosion) and the oxidized wear debris can increase the wear extent (corrosion enhanced wear)

The degradation of material due to tribocorrosion may occur under a variety of wear mechanisms (erosion, abrasion, microabrasion, fatigue, fretting, sliding wear, etc.) interacting with corrosion. Furthermore, contacts between surfaces in tribocorrosion can be both two-body or three-body contacts, and there are different contact modes such as sliding, fretting, rolling, impact, etc. The relative motion between surfaces can be either unidirectional or reciprocating [76,90,91,94,95,99].

2.2.5 Evaluation of tribocorrosion: electrochemical techniques and test procedures

Tribocorrosion encompasses several industrial sectors, e.g., material processing, energy conversion, transportation, oil and gas exploration, medical and dental implants, surgical devices, among others [90,94,95]. Due to its impact on daily life and potential economic benefits, interest in the study of tribocorrosion phenomenon has increased over the last few decades [77,91,105]. As a consequence, several electrochemical techniques have been adapted to be applied to tribocorrosion research and crucial improvements have been achieved through a better interpretation of triboelectrochemical results [94,96]. There are two standards available for the assessment of tribocorrosion: ASTM G119 [100] and UNE 112086 [106], published in 1994 and 2016, respectively. Nevertheless,

the knowledge acquired on tribocorrosion has been achieved by performing and combining different electrochemical techniques before, during, and after the wear process, to evaluate the influence of wear on corrosion, and vice versa.

2.2.5.1 Tribocorrosion test apparatus

For tribocorrosion, the test equipment shall allow monitoring and controlling both mechanical and electrochemical parameters. The apparatus used to measure tribological properties is named tribometer. A tribometer creates relative motion, either unidirectional (rotatory) or bidirectional (reciprocating), rubbing two surfaces against each other. On the other hand, electrochemical cells are used to record and control the electrochemical parameters. These cells are usually composed of three electrodes: a reference electrode (RE), a counter electrode (CE), and the working electrode (WE). The reference electrode has a stable, well-defined potential, and it is used to register the potential of the working electrode, i.e., the test sample. Typical reference electrodes are Saturated Calomel Electrodes (SCE) and Silver/Silver Chloride electrodes (Ag/AgCl). The counter electrode is used to measure or control the current and is usually made of inert materials such as platinum, gold, or graphite. The electrodes are connected to a potentiostat to register the potential between the reference electrode and the working electrode, or the current between the counter electrode and the working electrode. A typical tribocorrosion test set-up is schematically shown in Fig. 2.12, for a unidirectional tribometer under a ball-on-disc configuration. There is no standardized test apparatus for tribocorrosion tests, which makes the interlaboratory comparability difficult for results [90]. Generally, existing tribometers are modified to incorporate the electrochemical cell.

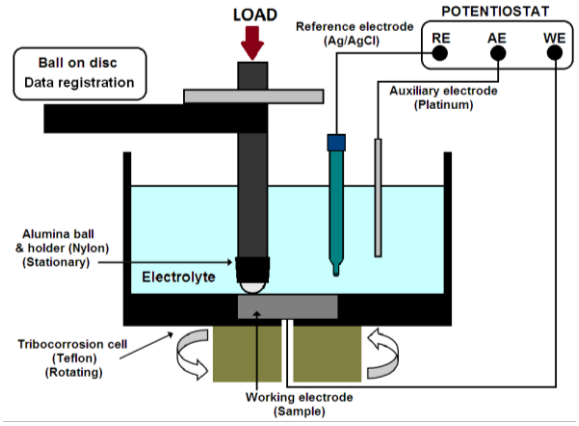

Fig. 2.12 Schematic of a unidirectional tribocorrosion ball-on-disc experimental setup

2.2.5.2 Electrochemical techniques for tribocorrosion

The test procedures employed to assess tribocorrosion behaviour of passive materials involve performing and combining different electrochemical techniques. In general, tribocorrosion tests consist of analysing the electrochemical behaviour of surfaces before, during, and after the tribological process, in order to evaluate how wear influences the electrochemical response of materials exposed to specific corrosive media, under determined mechanical conditions. The most widely-used electrochemical techniques in tribocorrosion evaluation are potentiodynamic and potentiostatic tests, electrochemical impedance spectroscopy (EIS), open circuit potential registration (OCP) and electrochemical noise (EN) analysis.

Potentiodynamic polarization tests

The potentiodynamic polarization (PDP) technique is one of the most widely-used test methods to evaluate corrosion. It consists of imposing a potential between the reference

and working electrodes, in a potential difference range from the cathodic to the anodic domain at a constant sweep rate, while registering the current being produced. In these tests, the current represents the rate of the anodic or cathodic reactions that are taking place on the working electrode surface, i.e. the studied metal exposed to the corrosive electrolyte. The registered current is typically expressed in terms of current per unit area of the working electrode, that is, the current density [107]. This technique provides information about the different corrosion processes taking place on the surface of a metal, such as pitting occurrence susceptibility, passive layer formation, plus the cathodic behaviour of an electrochemical system. It is the most useful method to evaluate the active/passive behaviour of the materials at different potentials and to determine the kinetics of ongoing reactions, i.e., the corrosion rate [76,104,108].

Performing potentiodynamic polarization tests during wear experiments can be used to evaluate the effect of wear on the electrochemical reactions on the surface of the working electrode, as a function of the potential applied, while being rubbed against an insulating body. Therefore, it is a quick and useful tool to detect the possible effects of friction on the electrochemical kinetics of the system, and vice versa [96,109]. As a first approach, the current registered during potentiodynamic polarization in a material subjected to a sliding process is the sum of two components, namely the currents of the worn and unworn areas. Furthermore, the coefficient of friction usually varies with applied potential during a potentiodynamic scan, due to the electrochemical changes taking place in the surface state of the material in the tribological contact [88,91].

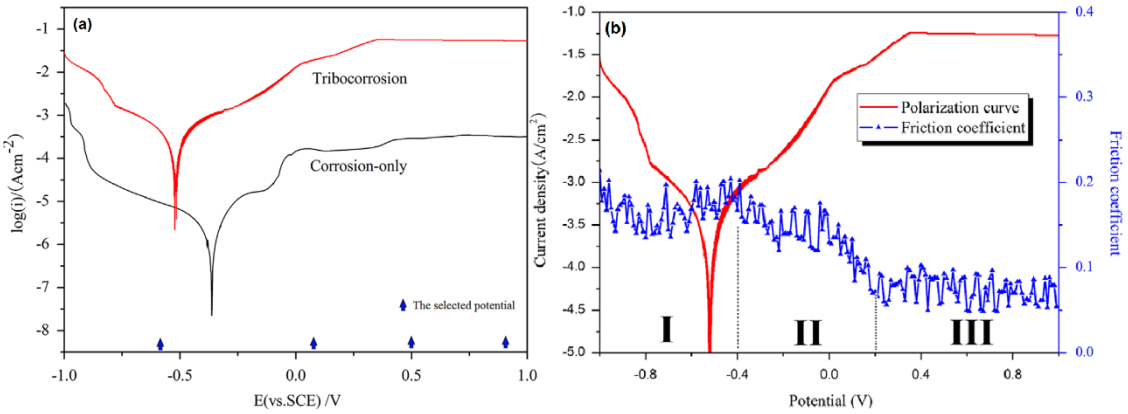

Fig. 2.13 (a) Polarization curves of a Monel K500 alloy in artificial seawater obtained in corrosion-only and tribocorrosion conditions. (b) Polarization curve of Monel K500 alloy in artificial seawater and evolution of coefficient of friction obtained during measuring [110]

Fig. 2.13a shows the polarization curve obtained for a Monel K500 alloy in artificial seawater under corrosion-only and tribocorrosion (wear and corrosion) conditions. It can be clearly seen that, under tribocorrosion conditions, the corrosion potential is shifted to more cathodic potentials, and the corrosion current density is increased by two orders of magnitude [110]. Furthermore, there is a correlation between the coefficient of friction and the current density arising from the polarization imposed (Fig. 2.13b). In this case, the coefficient of friction decreases at higher anodic potentials, as a consequence of oxide films forming on the surface [110]. Thus, the potentiodynamic polarization technique performed with and in the absence of sliding provides interesting information on both the effect of wear on corrosion, and the influence of corrosion on wear behaviour.

Potentiostatic polarization tests

Electrochemical polarization is used to simulate the oxidising action of a corrosive environment. This technique consists of imposing a fixed potential between the reference and the working electrodes. The current is measured as a function of time, to evaluate

the evolution of electrochemical kinetics of reactions occurring on the electrode surface [96]. The potential value being applied determines the dominant electrochemical reactions taking place. The polarization curve of passive materials can be divided in three regions:

- **Active region:** where the metal dissolves directly in contact with the solution.
- **Passive region:** where a protective passive film of few nanometres is grown on the surface, protecting the bare material from dissolution.
- **Transpassive region:** at high anodic potentials, where the current increases sharply with potential, as a consequence of the non-stable state of the oxide layer and the breakdown of this film.

These three regions are clearly observed in the polarization curve represented in Fig. 2.14; with i_{corr} the corrosion current density, E_{corr} the corrosion potential, i_p the current density in the passive state, and E_{pit} the potential at which pitting processes begin in the passive layer.

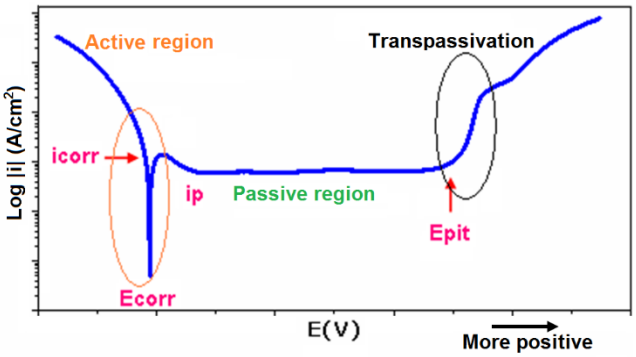

Fig. 2.14 Typical Polarization curve of a passive material showing the active, passive and Transpassive regions

Imposing a fixed potential on rubbing surfaces gives information on the potential effect on the wear behaviour [94]. The current registered during rubbing mainly flows through the wear track area, which constitutes a very small area compared to the complete metal surface exposed to the electrolyte [96]. The measured current value corresponds to the sum of the anodic and cathodic currents, due to all electrochemical reactions occurring on the exposed surface. It is thus possible to simulate different corrosion conditions by imposing appropriate potentials [94,96,109]. At cathodic potentials, the corrosion is inhibited, and the material loss after the tribocorrosion tests is attributed to pure mechanical wear. On the contrary, at anodic or passive potentials, the metal is covered by an oxide film whose thickness is controlled by the applied potential. This layer reduces the dissolution rate of the metal to negligible values and affects the friction response of the material. During sliding, the registered anodic current increases due to the local damage or removal of the passive layer exposing the base material surface to the electrolyte and, thus, to an active dissolution [91].

Additionally, this technique can also quantify the metal dissolution rate, i.e. the corrosion rate, from the corrosion current density (i_{corr}) registered using Faraday's law [92,94,96,98,108,111,112]:

$$v_{corr} = \frac{i_{corr}.M}{n.F} \qquad \text{(2.III)}$$

where v_{corr} is the corrosion rate, M the atomic mass, n the number of electrons taking part in the process and F the Faraday constant (96500 coulomb per electron mol). More details on calculating corrosion rates from electrochemical measurements can be found in the ASTM G102 [113] Standard.

The evolution of current transient and coefficient of friction during sliding wear tests at different fixed potentials are shown in Fig. 2.15, for an AISI 304 stainless steel in 0.5M NaCl solution [114]. Sliding results in a shift of current transient towards more positive values due to the removal of the passive layer, and this shift becomes higher as greater potential is applied. Moreover, the coefficient of friction value is also variable depending on the potential.

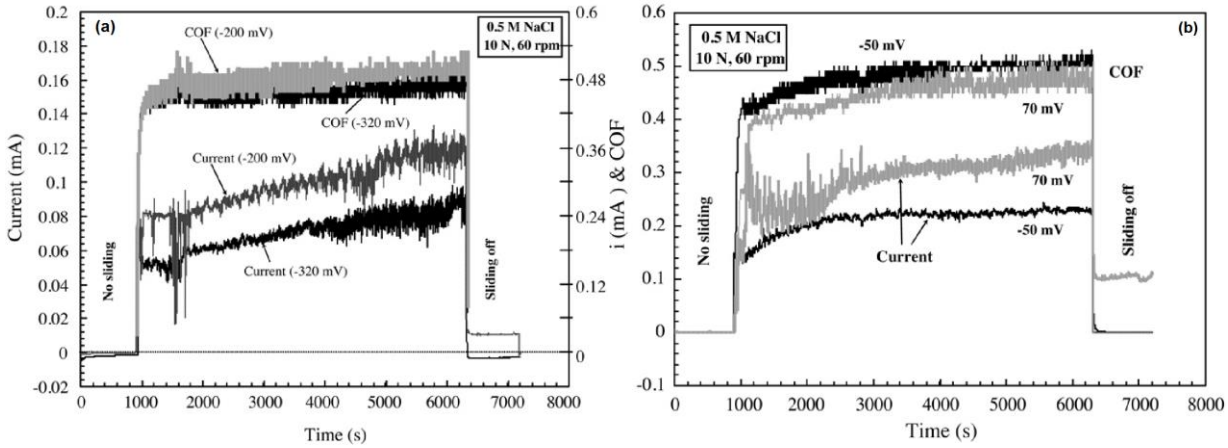

Fig. 2.15 Current transients and coefficients of friction (COF) recorded before, during and after sliding wear test at fixed potentials for an AISI 304 stainless steel in 0.5M NaCl solution: (a) -320 mV and -200 mV, (b) -50 mV and 70 mV [114]

Open Circuit Potential monitoring

The open circuit potential (OCP) monitoring is the simplest electrochemical method for corrosion evaluation, although it does not provide quantitative information on the interaction between wear and corrosion. To study the effect of wear, the potential is monitored before, during and after the sliding. Before the sliding test, the samples are immersed in the electrolyte until a steady-state is achieved. Several authors have performed experiments with an hour of stabilisation [76,91,96,104]. However, the stabilisation period depends on the material and electrolyte used and should be selected considering the system being studied. The potential evolution registered during the stabilisation period provides information on the electrochemical reactivity of the material in the test solution. An increase in the potential with immersion time reaching stable values after several minutes of immersion indicates the formation of a passive oxide layer on the surface. This layer of a few nanometres protects the material underlying from corrosion. This phenomenon is known as passivation [76,91,96,104]. On the other hand, a decrease of potential with immersion time suggests that general corrosion has occurred. Finally, short term potential fluctuations are attributed to localized corrosion processes such as pitting. These fluctuations are a consequence of the successive breakage of the passive layer and subsequent growth of the film in the affected zone [76,97,115].

OCP measurement during sliding can also provide information on the evolution of surface state when the material is subjected to wear-corrosion conditions. Once sliding begins, the potential has been observed to shift towards more negative values, indicating the initiation of electrochemical activity. Change in potential is a consequence of removing the passive layer in the tribological contact, thus exposing the bare material to corrosion. During wear, galvanic coupling between the active worn area and passive unworn area is generated [76,91,96,104]. According to Ponthiaux et *al*. [104], there are four parameters that affect the corrosion potential during rubbing:

- The intrinsic corrosion potentials of the unworn and worn surfaces. The electrochemical state of the worn surface is disturbed by the removal of the passive layer and the mechanical strain caused by sliding.
- The ratio between worn and unworn surface areas.
- The relative position between worn and unworn areas.
- The mechanisms and kinetics of the anodic and cathodic reactions involved in the worn and unworn areas.

After sliding, the potential usually tends to increase again reaching values close to pre-sliding figures, as a consequence of the re-formation of the passive layer in the depassivated area. The potential restoration process gives information on the material's ability to recover after sliding, which is known as repassivation.

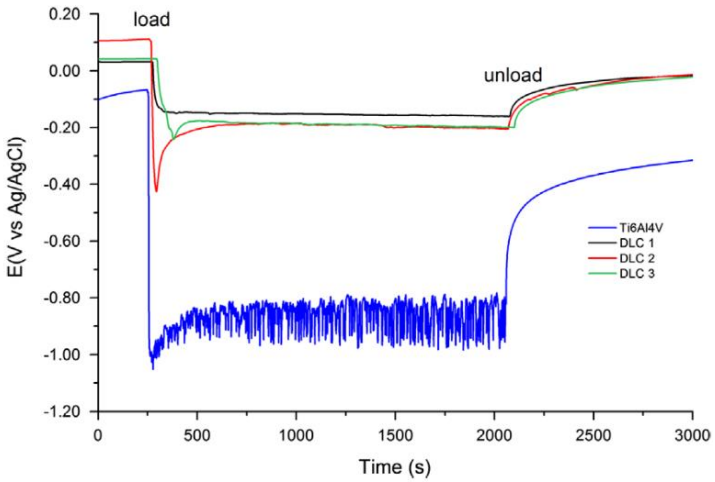

Fig. 2.16 Evolution of the open circuit potential before, during and after sliding wear test for a Ti6Al4V alloy with different DLC coatings in PBS solution [116]

The shift in potential due to the action of wear can be clearly observed in Fig. 2.16, for a Ti6Al4V alloy with several DLC (Diamond Like Carbon) coatings in Phosphate Buffered Solution (PBS) [116]. As soon as the countermaterial begins to slide against the test materials, a depassivated area is created in the surface leading to a decrease of potential due to the galvanic couple generated between the worn and unworn surfaces. Once sliding ends, the potential increases again to reach potential values close to those before wear process, as a consequence of the repassivation of the surface.

Electrochemical Impedance Spectroscopy

The Electrochemical Impedance Spectroscopy (EIS) technique consists of exciting the system using an AC potential or small amplitude current sinusoidal signal over a wide range of frequencies and measuring the current or potential response obtained. This technique is usually performed at free potential, with the requirement that the material should be electrochemically stable, in terms of the open circuit potential. Therefore, a small amplitude, usually 5-10 mV, is employed to maintain the system in a (quasi-) equilibrium state. Thus, the system can be evaluated without imposing significant perturbations. The impedance spectrums are obtained by plotting the electrochemical impedance, i.e. the potential and current ratio, over the frequency range being studied. The spectrums are then modelled using equivalent electric circuits that combine passive electric elements such as resistors, inductors, and capacitors. Combining the elements reproduces the electrochemical behaviour of the electrode surface. Information on the elementary steps occurring in the electrochemical reactions and their kinetics can also be obtained from the impedance diagrams [76,91,104,117-119].

One of the diagrams used to represent impedance data is the so-called Nyquist plot, where the imaginary impedance, indicative of capacitive response, is represented versus the real impedance, which indicates a resistive response. Fig. 2.17 shows typical Nyquist diagrams, together with the electrochemical equivalent circuit used in each curve to fit the impedance data. Fig. 2.17a represents a bare metal without any coating, (b) shows the response of a metal or alloy with mixed activation and diffusion control, and (c) is the case of a metal with a protective oxide layer or a porous coating on the surface. In the equivalent circuits, R_s represents the solution resistance, *CPE* is the constant phase element representing the capacitive properties of the electrolyte/metal interface, and R_{ct} is the charge transfer resistance in the electrolyte/metal interface, which determines the kinetics of the reaction. The Warburg impedance (*W*) in Fig. 2.17b indicates the occurrence of reactant diffusion to the corroding surface, as a consequence of reactant concentration gradients in the solution. In the last circuit (Fig. 2.17c), CPE_1 corresponds to the capacitance of the coating, whereas CPE_2 is related to the capacitive properties of the electrolyte/metal interface. Finally, R_{pore} is the resistance of the paths generated in the coating, i.e. the resistance in the pores and defects.

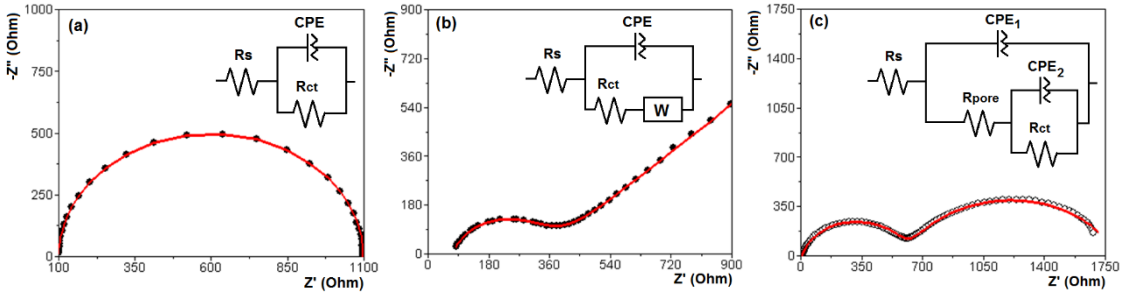

Fig. 2.17 Nyquist plots for impedance data and equivalent circuits used to fill each curve for a metal or alloy (a) without any coating, (b) without a coating showing diffusion of reactants, and (c) with a passive oxide layer or a porous coating on the surface

This technique can be used to study the role of intermediate species adsorbed in the surface, the properties of the passive films generated, and also the changes in the metal/electrolyte interface. The high frequency loop is associated with the charge transfer taking place in the interface, whereas the low frequency loop is attributed to diffusion of dissolved oxygen from the electrolyte to the metal/electrolyte interface [104,108].

By performing impedance measurements during sliding, it is possible to study the influence of wear on the elementary processes involved in the corrosion mechanism. Analysing the changes in the impedance diagrams with sliding parameters, i.e. normal force or sliding speed, it is possible to develop a model taking into account the effects of sliding in the corrosion mechanism [76,88]. On the other hand, the EIS measurements after sliding provide information on the recovery of the material in post-wear damage. The approximate value of corrosion current (I_{corr}) or passivation current (I_{pass}) of a metal or alloy, can be determined from the polarization resistance (R_p). This value is obtained from the impedance diagrams. EIS is the most accurate technique among the different methods available to measure the polarization resistance [76]. Furthermore, the reduction in the corrosion resistance of the studied material during sliding can be quantified, by comparing the polarization resistances from the EIS data obtained before and during sliding.

The effect of wear on corrosion can be observed in the Nyquist and Bode plots in Fig. 2.18. The results correspond to EIS measurements performed before and during sliding

of a TaN-coated and uncoated titanium alloy in PBS solution [120]. The electrochemical data was fitted with the so-called Randles equivalent circuit (Fig. 2.17a).

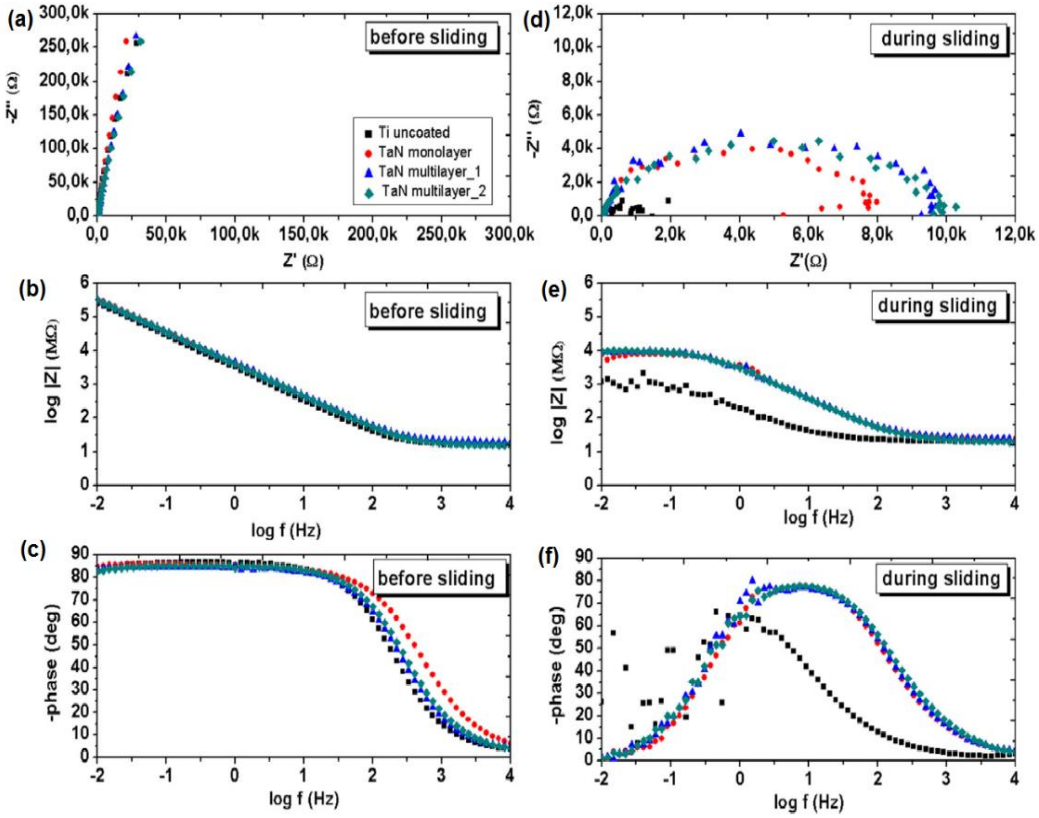

Fig. 2.18 Nyquist and Bode plots of the EIS measurements performed before (a,b,c) and during (d,e,f) sliding process, for a Titanium alloy and a TaN-coated titanium alloy in PBS solution [120]

Electrochemical noise analysis

Electrochemical noise (EN) can be defined as the spontaneous potential and current fluctuations taking place in a metal exposed to an aggressive medium. Most corrosion processes in metals are electrochemical and, thus, are likely to generate electrochemical noise [78,121,122]. EIS and EN are commonly used when the corrosion process takes place in a series of stages. In this case other techniques such as potentiodynamic polarization just provides information on the corrosion rate of the controlling reaction, which is not enough to understand the mechanism of the reaction taking place [78].

The previously explained electrochemical techniques, i.e., potentiodynamic polarization, potentiostatic tests, and EIS, require an external potential source to perturb the system, by either accelerating or inhibiting the corrosion kinetics. The main advantage of the EN technique is that the corrosive system is not disturbed externally by the measurement process, so the system is kept in the natural corrosion potential. Thus, it allows potential and current fluctuations to be registered simultaneously, so it is possible to obtain information on the thermodynamics from the potential noise, and kinetics information from the current noise. EN measurements allow the early stages of localized corrosion to be detected and studied and can isolate the individual events related to film breakdown in the sliding zone [76,122-124]. The electrochemical noise is a low frequency (<10 Hz) potential or current fluctuation of small amplitude, originating from the variation of electrochemical reaction rates in a corrosion process. There are several noise sources in corrosion [122-124]: atoms exchange kinetics in the electrode surface, the formation and release of bubbles on the surface, mechanical effects, formation of pits, etc.

There are two main experimental configurations for simultaneous registration of potential and current signals. The configuration that has been most widely used in tribocorrosion assessment is schematically shown in Fig. 2.19a. It consists of using two working electrodes made of the same material (WE_1, WE_2). CE and RE are the counter electrode and reference electrode, respectively. It is necessary to connect the two working electrodes through a Zero Resistance Ammeter (ZRA), which can measure the current whilst maintaining both working electrodes at a negligible potential difference. Two electrodes coupled through a ZRA will basically behave as a single electrode. The registered current signal corresponds to the current flowing between the two working electrodes, whereas the potential measured is the potential difference between both working electrodes and the reference electrode [122-125].

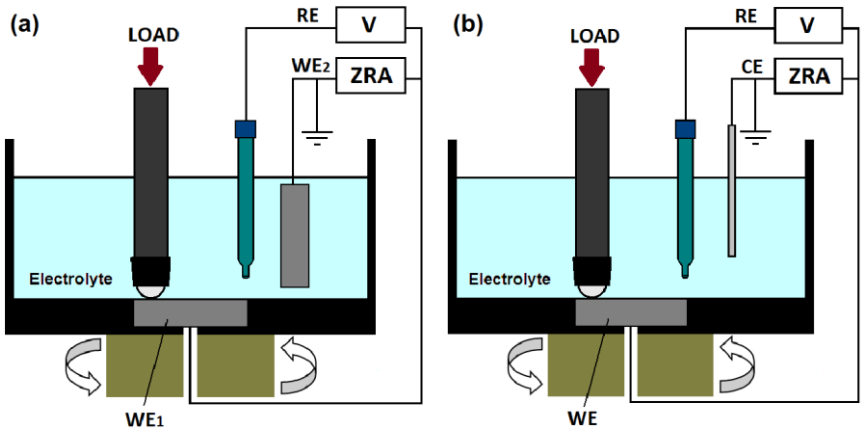

Fig. 2.19 Schematic setup configuration for potential and current noise registration using: (a) two nominally identical electrodes, and (b) asymmetrical electrodes

The local potential variations of each working electrode generate small variations in the mixed potential of the system. Therefore, the working electrodes must be nominally identical with the same surface preparation, since any difference would generate a galvanic couple, accelerating the oxidation of the more active electrode [121,123]. In a tribocorrosion test, however, the electrodes are identical right until sliding wear process is initiated. Once wear is generated, the removal of the passive layer makes the worn electrode more active compared to the undamaged one. Therefore, the mechanical activation leads to galvanic coupling between the worn (anode) and unworn (cathode) electrodes. The latter acts as the cathode of the reaction, accelerating the corrosion-wear process on the worn sample [91,122,124,126].

Sometimes, the different electrochemical characteristics presented in nominally identical electrodes generate asymmetry between them. In order to assess this drawback, several researchers have used asymmetric electrodes intentionally, measuring the electrochemical noise and studying the electrochemical processes taking place just in one of the working electrodes. For this purpose, platinum microcathodes have been widely used [121,122,124]. The configuration is schematically represented in Fig. 2.19b. The platinum microelectrode area must be small enough to avoid polarization of the working electrode, ensuring that the tribocorrosion process is not accelerated, and thus, current variations registered are the result of the mechanically influenced electrochemical process. Therefore, the electrochemical noise registered mainly belongs to the worn working electrode.

Fig. 2.20 shows the response of current and potential before, during and after sliding measured by EN technique for a bare and duplex treated (plasma nitriding and deposition of CrN coatings) AISI 304 stainless steel in a Hank's Balanced Salt Solution

(HBSS) [127]. In this study, the working electrode was coupled with a platinum microcathode through a ZRA.

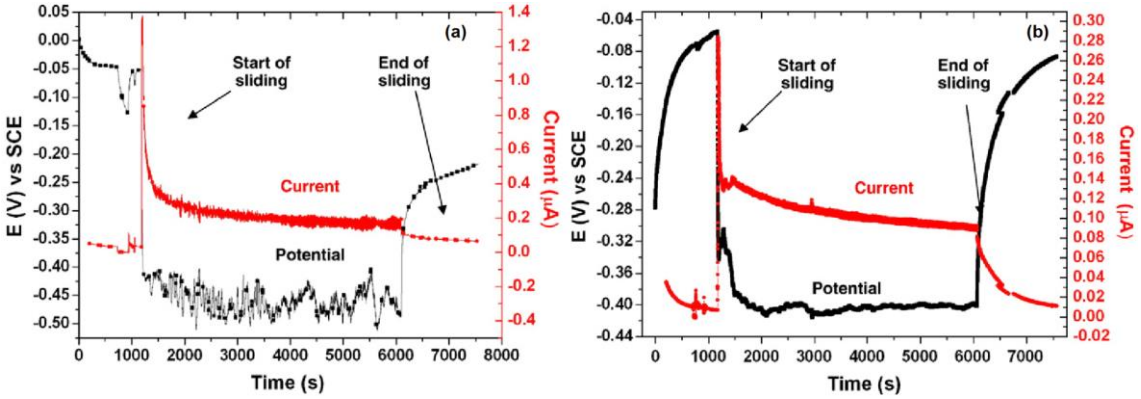

Fig. 2.20 Potential and current response measured by Electrochemical Noise Technique on (a) AISI 304 stainless steel and (b) duplex treated 304 against corundum in HBSS [127]

2.2.5.3 Standardized tribocorrosion test procedures for passive materials

From approximately 1980 onwards, many researchers studied the synergism between wear and corrosion [92], but no tribocorrosion mechanism in sliding contacts was proposed until the 1990s [91]. Tribocorrosion mechanisms have been evaluated through different approaches: synergistic, mechanistic, third body and nanochemical wear approaches [91]. After several previous studies, Madsen [92,128,129] developed a standard guide in 1994 [100], to quantify the synergism between wear and corrosion. This is known as the synergistic approach, where the material loss is the sum of the material loss due to corrosion, the material loss due to wear, and a synergetic component. In order to assess some drawbacks of the synergistic approach collected in the ASTM G119 standard reported by some authors [91,97,98,115], a test procedure based on the mechanistic approach was developed. According to this approach, the material loss due tribocorrosion is considered to be composed of two main contributions: anodic dissolution and mechanical removal of material. This test procedure was standardized in 2016 as a UNE 112086 standard [106]. The third-body approach in tribocorrosion, was proposed by Mischler, *et al*. in 2001 [112], based on the third-body concept defined by Godet [130] in 1984 for dry sliding contacts. In this approach, the metal volume loss due to tribocorrosion is the sum of three contributions, namely the mechanically detached material (abrasion, adhesion, or delamination), the chemically removed material (metal ions dissolved in the electrolyte), and the metal oxidized to form the passive film. In turn, the metal particles in the track can be ejected from the contact, oxidized, or smeared and transferred to the metal surface. Finally, the most recent nanochemical wear approach considers subsurface deformation of the material in the contact under the mechanical solicitations. In dry sliding contacts, the plastic deformation leads to formation and movement of dislocations, leading to a recrystallization of the material and the modification of the mechanical behaviour in the contact [91,131,132].

Wear and corrosion synergism evaluation procedure (ASTM G119)

The ASTM standard consists of four tests where the mechanical and electrochemical conditions were modified: corrosion only, wear only, and a combination of corrosion and wear. According to the standard, the total material loss (*T*) corresponds to the total degradation due to wear and corrosion, i.e., tribocorrosion. The term includes the contributions from mechanical wear, corrosion dissolution and the interaction between them, and can be defined as follows:

$$T = W_0 + C_0 + S \qquad (2.IV)$$

with W_0 the rate of material loss in the absence of corrosion, C_0 the electrochemical corrosion rate when no mechanical wear is applied, and S the synergetic component. Since wear affects corrosion, and corrosion affects wear, the synergetic component can be further divided into two components; namely, the increase in the mechanical wear due to corrosion (ΔW_c), and the increase in corrosion due to mechanical wear (ΔC_w):

$$S = \Delta W_c + \Delta C_w \quad \text{(2.V)}$$

Where ΔW_c and ΔC_w can be calculated as follows:

$$\Delta W_c = W_c - W_0 \quad \text{(2.VI)}$$

$$\Delta C_w = C_w - C_0 \quad \text{(2.VII)}$$

With W_c the total wear component of T, and C_w the electrochemical corrosion during corrosive wear.

The above-mentioned parameters can be calculated, as specified in the ASTM G119 standard, as follows:

- T: material loss after a corrosion-wear test at open circuit potential.
- W_0: can be obtained from the material loss after a wear test in the absence of corrosion. For this aim, the sample must be cathodically polarized one volt with respect to the free corrosion potential, so that corrosion is inhibited.
- C_w: calculated from the corrosion current obtained in a potentiodynamic polarization test under mechanical wear, by using Faraday's law (Eq. I).
- C_0: is calculated similarly to C_w from the corrosion current obtained from a potentiodynamic polarization test without mechanical wear.

Finally, the standard defines three dimensionless factors to describe the degree of wear-corrosion synergism:

- The total synergism factor: $\frac{T}{(T-S)}$ (2.VIII)
- The corrosion augmentation factor: $\frac{(C_0+\Delta C_w)}{C_0}$ (2.IX)
- The wear augmentation factor: $\frac{(W_0+\Delta W_c)}{W_0}$ (2.X)

Tribocorrosion test procedure for passive materials (UNE 112086:2016)

In spite of growing interest and enhancement of electrochemical techniques, the only existing standard until 2016 was the ASTM G119 [100]. In order to assess the drawbacks of the ASTM standard [91,97,98,115], different approaches were developed, and a new standard was developed in 2016. The ASTM [100] standard involves wear testing under anodic and cathodic polarization, whereas the new UNE 112086 [106] standard comprises wear tests at open circuit potential.

The main shortcoming of the ASTM G119 standard reported by several authors [91,97,98,115], is that the methodology employed does not separate measurements of the different contributions to the total material loss. According to the ASTM, material loss due to wear is obtained by performing sliding tests at cathodic potentials, where corrosion is negligible. However, the material loss measured does not necessarily represent the real conditions correctly since the contribution of corrosion products to the mechanical response of the surface cannot be considered in the absence of corrosion [76,97]. Furthermore, the wear volume depends on the cathodic potential selected and

could vary by an order of magnitude due to the sensitivity to hydrogen embrittlement of the metal [133]. On the other hand, the standard does not consider the galvanic couple generated between the worn and unworn areas during sliding either. Another considerable drawback, is that the standard does not provide information on the different processes occurring within the wear track [76,97].

The protocol of the UNE standard can be used to identify and quantify the different mechanical and electrochemical mechanisms leading to material loss. Furthermore, it can also be used to identify the origin of material loss from different parts of the wear track, that is, from the active areas and partially or fully repassivated areas inside the track [91,97,98,115]. The new approach consists of a series of successive steps during which essential data on tribocorrosion behaviour of materials is acquired:

1. Open circuit potential registration until a steady-state is reached.
2. Electrochemical impedance spectroscopy: The polarization resistance (R_p) value obtained from this measurement is then used to calculate the corrosion current density (i_{pass}) of the passivated material as follows:

$$r_{pass=}R_p.A_0 \quad \text{(2.XI)}$$

$$i_{pass} = \frac{B}{r_{pass}} \quad \text{(2.XII)}$$

   Where r_{pass} is the specific polarisation resistance of the passive material, A_0 the exposed surface area, and B a constant with typical values between 13 and 15 mV for metallic materials.
3. First sliding wear test: Determination of the corrosion rate of the depassivated material inside the wear track. For this purpose, a sliding wear test should be performed in order to remove the passive layer and keep the material in the wear track in a continuous active state. The potential is registered during the sliding process, and the stable potential during sliding (E_{oc}^{s}) is calculated.
4. Second sliding wear test and second EIS measurement: The effect of sliding on the corrosion resistance can be evaluated by performing an EIS measurement during sliding. In order to assure the stable state during sliding, EIS data is registered imposing a fixed potential on the system, which corresponds to E_{oc}^{s}, calculated in the previous step. The polarization resistance during sliding (R_{ps}) obtained is a combination of two polarisation resistances, namely the resistances corresponding to the active (R_{act}) and passive areas (R_{pass}):

$$\frac{1}{R_{ps}} = \frac{1}{R_{act}} + \frac{1}{R_{pass}} \quad \text{(2.XIII)}$$

$$R_{act} = \frac{r_{act}}{A_{act}} \quad \text{(2.XIV)}$$

$$R_{pass} = \frac{r_{pass}}{A_0 - A_{act}} \quad \text{(2.XV)}$$

   Since r_{pass} is known from equation (IX), r_{act} can be calculated as follows:

$$r_{act} = \frac{A_{tr}.R_{ps}.r_{pass}}{r_{pass} - R_{ps}.(A_0 - A_{act})} \quad \text{(2.XVI)}$$

   The corrosion current density of the active material (i_{act}) can be obtained from the next equation:

$$i_{act} = \frac{B}{r_{act}} \quad \text{(2.XVII)}$$

The material loss due to corrosion in the wear track (W_{act}^{c}) can be calculated using Faraday's law:

$$W_{act}^{c} = i_{act}.A_{act}.\frac{M}{n.F.\rho}N.t_{lat} \quad \text{(2.XVIII)}$$

With M the molecular weight, n the number of electrons involved in the anodic process, ρ the density and F the Faraday constant (96500 C). N corresponds to the number of cycles and t_{lat} is the latency time of the sliding test. The material loss due to wear and corrosion (W_{tr}) can be obtained from the volume of the wear track generated after the tribocorrosion test. Finally, the material loss due to mechanical wear in the wear track (W_{act}^{m}) can be calculated from the following equation:

$$W_{tr} = W_{act}^{c} + W_{act}^{m} \quad \text{(2.XIX)}$$

2.2.6 Historical background in tribocorrosion of passive materials and coatings, and future challenges

The earliest studies in the passivation phenomenon were performed using acidic solutions (e.g. sulphuric acid), and they were focused on understanding the formation of the passive film and its behaviour under corrosion-wear solicitations [99,111,112,134]. The electrolyte and materials used in tribocorrosion tests were reasonably well-adapted to the technological interests, so saline solutions began to be used more in order to reproduce industrial applications [113,135-138], and thus predict the useful life of components more accurately. Remarkable developments in the marine industry have also promoted tribocorrosion studies in synthetic seawater in later years [110,139-143]. On the other hand, developing coatings with enhanced wear and corrosion properties has also aroused interest, and a great number of tribocorrosion studies have taken place over the last decade to evaluate the performance of coatings produced by different depositing techniques (HVOF, PVD, etc.) [137,144,145]. Finally, the increasing impact and growing interest of biomedicine over the last decade has led to a great number of studies involving biomedical alloys used in orthopaedic and dental implants [90,115,122,146], which are subjected to both corrosion and wear as a result of human daily activity. Biomedical materials such as the CoCrMo [147-149] alloy or titanium alloys [150-152] have been widely studied in simulated body fluids (SBF), e.g., artificial saliva, NaCl solutions, phosphate buffer saline (PBS) solutions, or foetal bovine serum (FBS) solutions.

A major challenge in the study of tribocorrosion to be addressed is adapting test procedures for passive materials to assessment of tribocorrosion in active materials, such as the HSLA employed in offshore structures and components. Unlike passive materials, active materials do not generate a protective oxide layer on the surface when in contact with a corrosive media. On the contrary, the oxide layer in the surface is rather porous with low adherence. Therefore, the material loss is a consequence not only of wear and corrosion processes taking place in the wear track, but also of pure corrosion in the unworn surface. Tribocorrosion of passive materials has been widely studied, whereas the response of active materials is less documented. A closer understanding on the tribocorrosion degradation mechanism of active metals and alloys could provide better awareness of the use of these materials, with or without protective coatings, in order to enlarge their useful life in applications where passive materials are not suitable for use, i.e. higher costs and lower mechanical properties.

2.3 COATINGS EMPLOYED IN THE PROTECTION OF STEEL IN OFFSHORE APPLICATIONS

2.3.1 Marine Corrosion

Corrosion is one of the phenomena that worst affects the deterioration of materials in offshore applications. A 30% of failures in ships and other marine equipment are consequence of marine corrosion, with an annual cost of over EUR 1.5 trillion[iv] [153]. Marine corrosion is particularly aggressive, due to the salt content and low electrical resistivity of seawater [81,153]. The salt particles present in marine atmospheres, containing chlorides, combined with moisture initiate corrosion processes by the formation of galvanic or differential aeration cells [86]. Chlorides depassivate metal and alloys such as stainless steels, aluminum alloys or titanium alloys; even in absence of oxygen. They are also present in marine atmospheres, leading to corrosion of non-submerged materials and structures [154]. Fig. 2.21 shows the corrosion rate of steel at different sodium chloride solutions, where a maximum peak in corrosion rate can be observed at around 3% of NaCl. The salinity of seawater is 3.5 %, making it the one of the most corrosive chloride salt solution [153,155]. The amount of chlorides and, thus, the corrosion rate of metals decrease with increasing distance from ocean, and it is influenced by the wind direction and velocity [87,155].

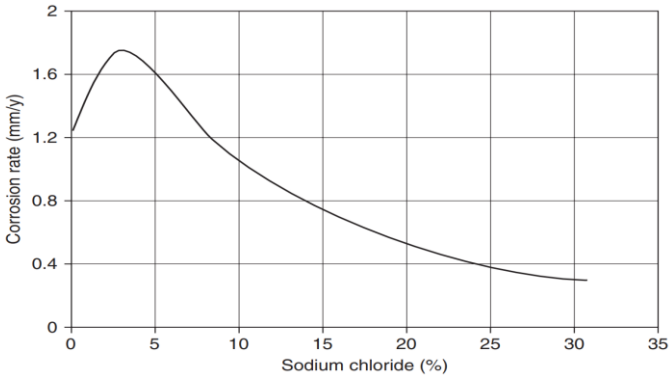

Fig. 2.21 Corrosion rate of Steel in various sodium chloride solutions [155]

There are other factors affecting corrosion in seawater and marine environments, i.e., temperature, dissolved oxygen concentration, pH, presence of microorganisms, and so on. The corrosion reaction rate in seawater increases with increasing temperature. Dissolved oxygen has a major influence on the corrosion rate of metals, since it is the principal reactant involved on the cathodic reaction, and also on the passive layer formation of several metals and alloys in seawater, e.g. stainless steel, titanium or aluminum. Seawater temperature varies depending on the geographical location and ocean currents, ranging from -2 ºC in the poles to 35 ºC in the equator. Furthermore, temperature and oxygen concentration vary with water depth, with the lowest temperatures close to 0 ºC and lowest oxygen at the higher depths [79,87,153,156,157]. The solubility of oxygen depends on the temperature, decreasing with increasing temperature [48,79,87,153]. Oxygen concentration on the seawater surface in the North Pacific Ocean is 1.4 times higher than that in the North Atlantic Ocean. However, both temperature and salinity are lower in the North Pacific Ocean and reach similar values with high depths below 15000 m [79]. Therefore, it is difficult to predict the deterioration of materials in seawater, and the results obtained from corrosion studies performed with

[iv] *Currency expressed in American trillion (10^{12})*

synthetic seawater in the laboratory are not easy to correlate with that observed in real applications.

2.3.2 Use of coatings to protect steel structures and components in marine applications

It is estimated that one third of the cost produced by corrosion could be saved by using the actual knowledge on corrosion-control measures [81,82,84]. In order to avoid or prevent unpredictable failures, coatings have been successfully used to minimize corrosion losses in steel structures. The requirements of protective coatings and their application procedures vary significantly depending on the installation location, i.e., onshore or offshore, and exposition zone. The coatings repair operation costs in hard accessibility places and locations, such as offshore structures, can be 50 times higher than the initial application cost of the protective system [158]. This is the case of Oil&Gas platforms, offshore wind energy devices (OWEAs), jack-ups, mooring systems, and so on. Therefore, it is of great interest to have an awareness of the performance of the coatings in a certain environment, in order to assure their proper functioning and plan an adequate maintenance strategy, without putting in risk the service life of structures.

The high economic impact of corrosion has served as a motivation for the study of the phenomenon during the last decades. A better comprehension of corrosion mechanisms has been achieved thanks to advancements of corrosion evaluation techniques and characterization technologies. This, in turn, has make possible to develop different corrosion preventive measures [82]. As highlighted before, one third of the costs produced by corrosion could be saved by applying corrosion-control measures [81,82,84].

The goal of the fight against corrosion is to guarantee the predetermined life of a structure, component or device at minimum cost, considering both the investment and maintenance costs. The solution must also be compatible with environmental regulations, allowing recycling of components at the end of their life. There are several approaches to minimize corrosion of engineering structures, i.e., preventive measures (appropriate design and correct election of materials) or protective measures (use of corrosion inhibitors, protective coatings or electrochemical protection) [83]. Corrosion protective measures consist of stopping one or more of the electrochemical or transport processes involved in the substrate corrosion [159], and they can be either active or passive. An active protection is achieved by changing the electrochemical properties of the substrate to avoid electrochemical corrosion; whereas passive protection is achieved by providing the metals with a barrier that inhibits or slows down corrosion. Protective measures can be applied alone or by combining different methods, e.g., the application of coating in conjunction with cathodic protection [82,84,153].

Cathodic protection

Cathodic protection consists of applying a sufficiently negative potential to the metal, so its corrosion rate becomes negligibly small or zero. This kind of protection is widely used to protect heavy steel structures against corrosion [82,83,155,159,160]. There are two methods of cathodic protection: by sacrificial anode and by impressed current. A sacrificial anode is a metal with more negative potential value than the metal to be protected in the corroding electrolyte. Magnesium, zinc, and aluminum are typical sacrificial anodes used to protect steel structures. Cathodic protection by impressed currents involves the use of an external power source to polarize the metal to a potential range in which it does not corrode.

Protective coatings

Protective coatings are probably the most employed corrosion-control measure [85,160]. An 89% of the money spent in corrosion prevention nowadays corresponds to coating service sector [84]. The main objective of protective coatings is not to provide the structural materials with strength or improved mechanical properties, but to assure a long-term protection under a wide range of corrosive conditions, by isolating the corroding materials from the corrosive environments. The quality of a coating depends on many factors, including the nature of the materials that comprises it [160]. On the other hand, coatings are designed to withstand different service conditions, so they can be single-layered or more robust multilayered coatings [82]. The use of different multifunctional layers provides the coating system with more effectiveness for a wide range of corrosion mechanisms. There are different types of coatings, depending on their nature [82,83,87,76,160]:

- **Metallic coatings:** This kind of coatings can provide the substrate not only with corrosion protection, but also with higher wear resistance. Metallic coatings can be divided into two groups: more noble and less noble than the substrate. Chromium, nickel, and copper are usually used as more noble coatings than steel substrates, whereas zinc, cadmium and aluminum are used less noble coatings. Coating metals less noble than the substrate act as a sacrificial anode and dissolve in the electrolyte, whereas coating metals more noble than the substrate act as the cathode of the reaction and accelerate the dissolution of the substrate.
- **Inorganic non-metallic coatings:** They can be divided into two groups: conversion coatings (anodizing, phosphatizing, or chromatizing) and contact coatings (Physical Vapor Deposition (PVD) or electroplating techniques).
- **Organic coatings:** they can be divided in bituminous coatings, polymer coatings, and paints and varnishes. Paint systems usually consist of various layers, including the primer, intermediates and topcoat. Organic coatings are widely employed in offshore applications, since they offer a barrier effect to the corrosive environment due to their polymeric nature.

2.3.3 Selection of coating system for different exposition zone in offshore applications

Since offshore installations are exposed to very severe corrosion conditions, the most effective corrosion control system is required. There are five exposure zones, in which the corrosion rate of steel is different [79,81,82,87,159,161,162], as shown in Fig. 2.22. Protective coatings used for marine environment strongly depend on the exposure zone, and they are selected considering whether the protected system will be subjected to marine atmosphere (atmospheric zone), continuous immersion (immersed zone), or intermittent exposure to marine atmosphere and seawater (splash and tidal zones). Depending on the exposure zone, the coatings must provide the system with specific properties to guarantee infrastructures durability. Furthermore, it is common to combine protective measures such as cathodic protection and organic coatings [82,83,163]:

- **Atmospheric zone:** it is above the sea level, so it is not continuously wetted or affected by the rise of tidal waves. There is a direct relationship between atmospheric salt content and corrosion rate. On the other hand, materials are also exposed to solar radiation, which deteriorates the performance of organic coatings. Corrosion protection is usually achieved with organic coatings based on zinc rich epoxy primer (60-100µm), an epoxy intermediate layer (100-120 µm), and a polyurethane top-coat (50-80 µm). The coating must provide the structural materials with anti-corrosion, anti-

erosion, anti-icing, and UV-resistant properties. Given that this zone is not in contact with the electrolyte, the coating does not need to be complimented by cathodic protection.

- **Splash zone:** section in the structure that is intermittently exposed to seawater. Tides and wind are responsible for wetting this zone. Since it is constantly being wetted, chlorides can concentrate in the surface while the water films dry. The corrosion rate of metals in this zone is the highest, due to the aerated condition, which makes the access of dissolved oxygen for electrochemical reactions easy. The corrosion protection is achieved through the combination of a high-performance coating system supplemented by a cathodic protection system. Typical organic coatings are based on 2 or three epoxy coats (200-250 µm), with a polyurethane top-coat (50-70 µm). The coating used in this exposure frame must provide the structural materials with properties that combine the atmospheric exposure (corrosion, erosion, UV radiation, icing…) and the submerged exposure (corrosion, wear, fouling…)
- **Tidal zone:** the materials are alternatively submerged and exposed to the splash zone, as the tide fluctuates. In the submerged condition, materials are exposed to a well-aerated seawater, which favors the attachment and growth of biofouling. In some materials, fouling can protect the metals, e.g. steel; whereas in other cases such as for stainless steels, biofouling can accelerate localized corrosion attack. The corrosion rate is influenced by the tidal flow, with higher corrosion rates with increasing movements. The coatings employed in the splash and tidal zone usually are the same.
- **Submerged zone:** section of structure that is below the end of the splash zone and always below the sea level. This zone is always immersed in the electrolyte. The corrosion rate in this zone depends on the availability of oxygen to be transported to the cathodic sites of materials surfaces. As oxygen concentration varies with depth, decreasing with increasing distance to surface, the corrosion rate is also slower at higher depths. Similarly to the splash and tidal zones, protective coatings are used together with cathodic protection. The coatings for submerged structures and components are epoxy-based (200-250 µm), with lower thicknesses that those in the splash and tidal components. The coatings should have anti-corrosion, anti-wear, and antifouling properties.

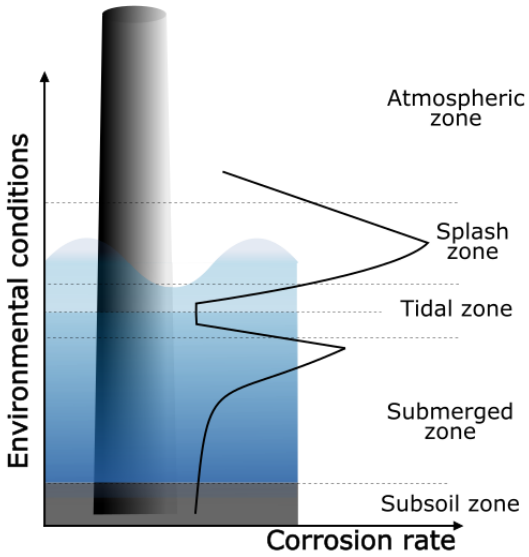

Environmental zone	Corrosion rate
Splash zone	0.40 mm/yr
Tidal zone	0.25 mm/yr
Submerged zone	0.20 mm/yr
Subsoil	0.10 mm/yr

Fig. 2.22 (left)Zones of corrosion for Steel piling in seawater, and relative loss in thickness depending on the exposure zone [164], and (right)the corrosion rate of steel depending the exposure zone [161,165]

The most widely employed corrosion-control measure for metallic materials in marine environments are organic coatings (250-300 µm thick), due to their high corrosion

resistance. However, the low wear resistance of these coatings is a drawback in certain offshore applications. On the other hand, Thermally Sprayed Coatings (TSC) have recently been used in offshore applications [166,167]. For instance, Thermally Sprayed Aluminum (TSA) coatings with organic sealant systems (250-300 µm thick) have widely been applied in submerged components [161,168], providing effective service life of coated systems for 30 years in different exposure zones [159,168,169]. The aluminum layer deposited on top of the steel provides the substrate with an additional cathodic protection via the sacrificial anodic reaction of the aluminum. The NORSOK M-501 [170] standard recommends the use of an organic sealant on top of the sprayed aluminum to fill the pores and irregularities present in the coating and enhance the coating lifetime. When an additional wear resistance is required, Thermally Sprayed Carbide Coatings (TSCC) have also been used. This kind of coating protects the substrates against wear due to their high hardness, also providing the system with enhanced corrosion resistance.

2.3.4 Evaluation and validation of protective coatings for different corrosivity atmospheres

Currently, the protection systems used in offshore structures are regulated by several standards, among which the ISO 12944 (2008) [171] and the NORSOK M 501 (2012) [170] can be found. The selection of the protective system deeply depends on the location of the component. According to ISO 9223 [172] and ISO 12944 (part two), there are five corrosivity categories; from the C1 corresponding to a non-corrosive atmosphere, to industrial and marine corrosive categories (C5-I and C5-M). There are also IM1 and IM3 categories, to describe the water and soil corrosivities, respectively. ISO 12944 standard has been recently revised, and a new part has been published in January 2018 (part 9). In this new part, entitled "*Protective paint systems and laboratory performance test methods for offshore and related structures*", new categories have been added to refer to extreme conditions in offshore applications: CX-offshore for atmospheric exposure, CX-offshore/Im4 for splash and tidal zones, and Im4 for immersion zone. ISO 9223 classifies the corrosivity atmospheres and provides information on the material loss of different metals (carbon steel, zinc, copper, and aluminum) for a year of exposition to each category. On the other hand, ISO 12944 consists of nine different parts, that comprise from substrate preparation, design considerations, coating system selection, and so on. Based on the corrosivity categories of ISO 9223, ISO 12944 proposes several aging tests in climatic chambers, with different exposure durations depending on the corrosivity category, which are used to validate the effectiveness of coatings to be used in real applications. ISO 12944 also considers the durability, or the time for the first major maintenance of the coating systems as:

- Low (L): 2 to 5 years
- Medium (M): 5 to 15 years
- High (H): 15 to 25 years
- Very High (VH): >25 years

In order to obtain the protection grades specified in the ISO 12944 (C5-M/Im2), the standard recommends employing multilayer coatings with thickness between 320 and 500 µm for a C5-M category in the atmospheric zone, and between 480 and 1000 µm for the splash zone and submerged components (Im2). According to the standard, these specifications should be enough to assure a component durability of 15 years [171]. On the other hand, the NORSOK standard does not specify a coating thickness range, but a minimum thickness. Therefore, a coating requiring a C5-M category should be at least

280 µm, whereas submerged components should have a minimum of 350 µm for a Im2 category [170].

Typical coating systems employed in offshore applications [163] with the desired properties depending on the exposure zone are compiled in Table 2.3. The coatings used in the splash and submerged zones are usually combined with a well-designed cathodic protection, either by sacrificial anodes or impressed currents; in order to protect steel structures against the aggressive corrosion conditions in marine environment [82,84,153,161].

Table 2.3 Typical coating systems employed in offshore applications in the different exposure zones [163], with the desired properties and corrosivity category required (ISO 12944)

Exposure zone	Coating system		Desirable coating properties
Atmospheric zone C5-M (ISO 12944)	Zinc rich epoxy primer Epoxy intermediate layer Polyurethane top-coat	(60-100 µm) (100-120 µm) (50-80 µm)	Corrosion-resistant, erosion-resistant, anti-icing, UV-resistant
Splash and tidal zones C5-M/Im2 (ISO 12944)	Two or three epoxy-based coats Polyurethane top-coat	(>1000 µm in total) (50-80 µm)	Combination of atmospheric and submerged coatings´ properties
Submerged zone Im2 (ISO 12944)	Two or three epoxy-based coats	(>450 µm in total)	Corrosion-resistant, antifouling, wear-resistant

2.3.5 **Antifouling coatings**

2.3.5.1 Biofilms and Biofouling

Marine biofouling can be defined as the undesirable accumulation of microorganisms, algae and animals on submerged structures in seawater [173,174]. When bacteria attach themselves onto metallic surfaces, they start to form a thin film known as biofilm. This film consists of immobilized microorganisms that are held together with excreted slime, referred to as extracellular polymeric substances (EPS). EPS is composed of sticky, high molecular weight compounds and is abundantly produced by many microorganisms, rapidly coating the surface of steel in natural environments [175,176]. The active metabolism of microorganisms consumes oxygen and produces metabolites. The net result of the biofilm formation is that it usually creates concentration gradients of chemical species across the thickness of the biofilm, which can enhance the corrosion in the metal surface [175-177].

2.3.5.2 Microbiologically Induced Corrosion (MIC)

Microbiologically Influenced Corrosion (MIC) is a corrosion process that is initiated and/or accelerated by the activity of microorganisms. The presence of biofilms on the material surface is linked to the degradation process. The microorganisms that adhere to the interfaces have influence on the corrosion kinetics of the metals by initiating, facilitating or accelerating the reactions through the interaction of the three components that make up the system: metal, solution and microorganisms. The term “microorganism” refers to bacteria, cyanobacteria, algae, lichens and fungi [175,177]. Some researchers have found MIC to accelerate corrosion, e.g. impeding passivation of pits; but others have reported that the biofilm formed could have a protecting rather than a deteriorating effect [175]. Bacterial activity can result in local acidification, which can threaten the stability of the oxide layer of steels, enhancing corrosion [42]. MIC has been reported to cause 2-3 mm of materials loss in steel components in the form of pits [2,43].

2.3.5.3 Antifouling paints

The accumulation of biomass results in the formation of microenvironments that may encourage corrosion and increase the weight of components. Besides, the inspection and maintenance operations of immersed surfaces is complicated [173]. In order to prevent the colonization of microorganisms, antifouling (AF) paints have been widely employed in marine environments [173,174,178]. These paints were firstly used in boat hulls, where the presence of fouling increases the drag friction and weight, thus, increasing the fuel consumption up to a 40% [179,180], and reducing the speed in a 70% [173,178]. AF paints have also been used in static structures such as buoys, pipelines, drilling platforms and submerged components [181,182], in order to reduce MIC occurrence. The use of AF protection can save up to EUR 4.8 billion[v] per year worldwide [173,183,184].

The former AF paints were formulated adding extremely toxic organotin, e.g. tributyltin oxide (TBT). However, TBT was found to affect a wide variety of organisms, including invertebrates and fish or water birds that feed on intoxicated marine species. This made the consumption of marine foods an important route to human exposure [173,183]. The use of TBT was banned in 2003 in the EU territory, and globally in 2008 by the Maritime Organization [173,182,185,186]. Different formulations and technologies have been used thenceforth. Copper has been the predominant biocide after the ban of TBT [174,179,183,187]. Copper can be found naturally in marine environments, and it is an essential element in the metabolic functioning of many organisms. However, it becomes toxic when exceeding the threshold of the organism tolerance of marine species. Copper can be naturally found in concentrations of 0.5-3 µg/L, but it can be raised up to 21 µg/L in contaminated areas [183]. The use of copper-based AF paints is regulated in some countries based on the copper release rate. For instance, the allowance in Canada is of 40 µg/cm^2/day, whereas that in Denmark is 200 µg/cm^2 over the first 14 days [183]. AF paints are usually loaded with high amounts of copper oxide (Cu_2O) and algaecide co-biocides or boosters, e.g. Irgarol 1051, diuron or chlorothalonil, among others [173,178,182,183,186,188]. Inorganic zinc, as zinc oxide or zinc acetate, has been employed in combination with copper to increase the toxicity and to ease the leaching process [178,181,188,187]. Currently, there are approximately 23 boosters in use [186], and some of them have been restricted in some countries [173,183,185].

Some non-toxic silicone-based coatings have been developed, which are best known as foul release coatings [182,183]. These shelf-polishing paints rely on the controlled formation of seawater soluble salts within the paint matrix, which allows a controlled release of biocides or algaecides [173]. The use of biocide releasing paints and their effect on marine environment after the release is an issue of concern. This is because the concentration of this components can be considerable in high activity areas [173,181,183,189]. Since AF paints are designed to slowly release the biocides to seawater, they lose their efficiency over time. Therefore, they have to pe replaced periodically, leading to antifouling paint particles (APPs) generation, due to the removal of the old coating. APPs have been found to be a source of contamination [181,186,190]. Unlike the self-releasing biocides, those bonded to particles on the paint matrix are more persistent and more likely to be a long-term threat for the environment [189].

[v] *Currency expressed in American billion (10^9)*

2.3.6 Challenges in the protection of submerged components

Coatings are one of the best routes to achieve the proper protection of submerged steel components and structures from marine corrosion. Up to now, the coating selection has been mainly made considering the efficiency of the coating in terms of corrosion protection. However, the threats in marine environments are diverse, often combining mechanical solicitations, such as wear and fatigue, as previously explained. The protective system should as well resist these solicitations to ensure their correct functioning. The most employed coatings are usually polymeric, with low mechanical properties. This kind of soft coatings have been found to be damaged in transport and erection operations [158], which reduces their effectiveness from the beginning of immersion. Therefore, the long-term durability of the coatings is uncertain and must not be established solely based on exposition tests specified in the ISO 12944 and NORSOK standards. Awareness of the tribological and wear-corrosion (tribocorrosion) performance of protective systems will improve the selection of the most suitable option depending on the application and solicitations that it will be subjected to. On the other hand, the development of proper AF paints has become a challenge for the paint industry, as a good active substance for antifouling paint should be not only technically and economically viable, but also environmentally friendly [185].

2.4 REFERENCES

[1] A.F. Yaghin, R.E. Melchers. *Long-Term inter-link wear model of mooring chains*. Marine Structures 44 (2015) 61-84

[2] Noble Denton Europe Limited. *Floating production systems. JIP FPS mooring integrity*. Health & Safety Executive (HSE) (2006). Research report 444.

[3] Norwegian University of Science and Technology (NTNU). *Operational Safety of FPSOs: Initial Summary Report*. Health & Safety Executive (HSE) (2000). Research report 086

[4] J. Mohanraj, S. Cawthorne, S. Calverley, S.L. Fletcher, J. Verwaayen. *OTC 22494 Development of a New Generation of Innovative Synthetic Wire Mooring Ropes*. Offshore Technology Conference (2011) Rio de Janeiro, Brazil

[5] M. Borg, M. Collu, A. Kolios. *Offshore floating vertical axis wind turbines, dynamics modelling state of the art. Part II: Mooring line and structural dynamics*. Renewable and Sustainable Energy Reviews 39 (2014) 1226-1234

[6] I.M.L. Ridge, R.E. Hobbs, J. Fernandez. *OTC 17789 Predicting the Torsional Response of Large Mooring Chains*. Offshore Technology Conference (2006) Texas, USA

[7] F. Rusco. *Offshore oil and gas resources. Information on Infrastructure Ddecommissioning and Federal Financial Risk*. United States Government Accountability Office (GAO) 2017(GAO-17-642T)

[8] M. Palmquist. *Hurricanes enter the offshore oil drilling debate*. Pacific Standard (2008). Available at (June 2018): https://psmag.com/news/hurricanes-enter-the-offshore-oil-drilling-debate-4236

[9] R.B. Gordon, M.G. Brown, E.M. Allen. *OTC 25134: Mooring Integrity Management: A State-of-the-Art Review*. Offshore Technology Conference (2014) Texas, USA

[10] EMA. *2012-2021 FPS Outlook report*. January 2017. Avaiable at (June 2018): https://www.marinemoney.com/system/files/media/2017-07/1505%20MMO%202017-EMA-Floating%20Production%20Outlook%202017-2021.pdf

[11] D. Roddier, C. Cermelli, A. Aubault, A. Weinstein. *WindFloat: A floating foundation for offshore wind turbines*. Journal of Renewable and Sustainable Energy 3 (2010) 1–34.

[12] Y. Li, Q. Zhu, L. Liu, Y. Tang. *Transient response of a SPAR-type floating offshore wind turbine with fractured mooring lines*. Renewable Energy 122 (2018) 576-588

[13] H. Bailey, K.L. Brookes, P.M. Thompson. *Assessing environmental impacts of offshore wind farms: lessons learned and recommendations for the future*. Aquatic Biosystems 10 (2014) 1-13

[14] C.B. Li, J. Choung, M.H. Noh. *Wide-banded fatigue damage evaluation of Catenary mooring lines using various Artificial Neural Networks models*. Marine Structures 60 (2018) 186-200

[15] G.H. Hansen. *Offshore oil and gas firms' involvement in offshore wind: Technological frames and undercurrents*. Environmental Innovation and Societal Transitions 17 (2015) 1-14

[16] B. Skaare, T.D. Hanson, F.G. Nielsen, R. Yttervik, A.M. Hansen, K. Thomsen, T.J. Larsen. *Integrated dynamic analysis of floating offshore wind turbines*. Proceedings of the 25th International Conference on Offshore Mechanics and Arctic Engineering, OMAE (2006) Hamburg, Germany

[17] N. Ren, Y. Li, J. Ou. *The Effect of Additional Mooring Chains on the Motion Performance of a Floating Wind Turbine with a Tension Leg Platform*. Energies 4 (2012) 1135-1149

[18] H.M. Hou, T.J. Xu, G.H. Dong, Y.P. Zhao, C.W. Bi. *Time-dependent reliability analysis of mooring lines for fish cage under corrosion effect*. Aquacultural Engineering 77 (2017) 42-52

[19] H.M. Hou, G.H. Dong, T.J. Xu, Y.P. Zhao, C.W. Bi, F.K. Gui. *Fatigue reliability analysis of mooring systems for fish cage*. Applied Ocean Research 71 (2018) 77-89

[20] Vicinay Cadenas S.A. *Offshore mooring chain*. Information available on the company website (June 2018): http://www.vicinaycadenas.net/mooring-chain/offshore-mooring-chain.asp

[21] DNVGL-OS-E302. *Offshore mooring chain*. July 2018

[22] Joint Industry Project Steering Committee. *Mooring Integrity for Floating Offshore Installations Joint Industry Project: Phase 2 Summary*. Health & Safety Executive (HSE) (2017). Research report 1090.

[23] ISO 1704. *Ships and marine technology. Stud-link anchor chains*. 2008

[24] *Requirements Concerning Materials and Welding, W22 Offshore Mooring Chain*. International Association of Classification Societies (IACS) Rev. 6 June 2016

[25] B. Albisu, I. Salado, A. Arredondo, D. Bilbao, M. Abrisketa, J.L. Arana, Z. Idoyaga, M.C. Carcedo. OTC 27024 MS: *New Grades of High Strength Steel for Offshore Mooring Chains: R5S 1100MPa and R6 1200 MPa*. Offshore Technology Conference (2016) Houston, Texas, USA

[26] M. Brown, A. Comley, M. Eriksen, I. Williams, P. Smedley, S. Bhattacharjee. *OTC 20613: Phase 2 Mooring Integrity JIP: Summary of Findings*. Offshore Technology Conference (2010) Houston, Texas, USA

[27] M.G. Brown, T.D. Hall, D.G: Marr, M. English, R.O. Snell. *OTC 17499: Floating Production Mooring Integrity JIP: Key Findings*. Offshore Technology Conference (2005), Houston, Texas, USA

[28] Z. Gao, T. Moan, S.E. Heggelund. *Time variant reliability of mooring system considering corrosion deterioration*. Proceedings of 24th conference on Offshore Mechanics and Arctic Engineering, OMAE (2005) Halkidiki, Greece

[29] S. Majhi, R. D'Souza. *OTC 24181: Application of Lessons Learned From Field Experience to Design, Installation and Maintenance of FPS Moorings*. Offshore Technology Conference (2013) Houston, Texas, USA

[30] A. Kvitrud. *Anchor Line Failures*. Norwegian Continental Shelf 2010-2014. Petroleumstilsynet (2014) Report no 992081

[31] E. Fontaine, A. Kilner, C. Carra, D. Washington, F.T. Ma, A. Phadke, D. Laskowski, G. Kusinski. *OTC 25273 MS: Industry Survey of Past Failures, Pre-emptive Replacements and Reported Degradations of Mooring Systems of Floating Production Units*. Offshore Technology Conference (2014) Houston, Texas, USA

[32] G.J. Shoup, R.A. Muller. *OTC 4764: Failure analysis of a calm buoy anchor chain system*. Offshore Technology Conference (1984) Houston, Texas, USA

[33] ABSG Consulting Inc. *Study on Mooring System Integrity Management for Floating Structures. Final Report*. Submitted to The Bureau of Safety and Environmental Enforcement (BSEE) (2015) Project PS-003-14/ 3365033. Contract E14PC00038.

[34] H. Yu, J. Li, K. Wu, Z. Wang, H. Yu, S. Zhang, Y. Hou, R.M. Kelly. *A global high-resolution ocean wave model improved by assimilating the satellite altimeter significant wave height*. International Journal of Applied Earth Observation and Geoinformation 70 (2018) 43-50

[35] N.V. Viet, Q. Wang. *Ocean wave energy pitching harvester with a frequency tuning capability*. Energy 162 (2018) 603-617

[36] J. Fernández, W. Storesund, J. Navas. *Fatigue Performance of Grade R5 and R5 mooring chains in seawater*. Proceedings of the 33rd International Conference on Ocean, Offshore and Artic Engineering, OMAE (2014) San Francisco, California

[37] Joint Industry Project Steering Committee. *Mooring Integrity for Floating Offshore Installations Joint Industry Project Phase 2: An assessment of proof load effect on the fatigue life of mooring chain for floating offshore installations*. Health & Safety Executive (HSE) (2017). Research report 1093

[38] J. K. Saha. *Corrosion of Constructional Steels in Marine and Industrial Environment*. Springer India (2013). ISBN: 978-81-322-0719-1

[39] K. Xiao, C.F. Dong, X.G. Li, F.M. Wang. *Corrosion Products and Formation Mechanism during Initial Stage of Atmospheric Corrosion of Carbon Steel*. Journal of Iron and Steel Research International 15 (2008) 42-48

[40] J.G. Castaño, C.A. Botero, A.H. Restrepo, E.A. Agudelo, E. Correa, F. Echeverría. *Atmospheric corrosion of carbon steel in Colombia*. Corrosion Science 52 (2010) 216-223

[41] H. Möller, E.T. Boshoff, H. Froneman. *The corrosion behaviour of a low carbon steel in natural and synthetic seawaters*. The Journal of The South African Institute of Mining and Metallurgy, Volume 106 (August 2006) 585-592

[42] Joint Industry Project Steering Committee. *Mooring Integrity for Floating Offshore Installations Joint Industry Project Phase 2: The effect of wear and corrosion of steel components on the integrity of mooring systems for floating offshore installations*. Health & Safety Executive (HSE) (2017). Research report 1096

[43] E. Fontaine, A.E. Potts, R.E. Melchers, A. Arredondo, K.T. Ma. *Investigation of Severe Corrosion of Mooring Chain in West Africa Waters*. Proceedings of the 22nd International Offshore and Polar Engineering Conference, ISOPE (2012), Rhode, Greece

[44] E. Fontaine, A.E. Potts, R.E. Melchers, A. Arredondo, K.T. Ma. *OTC 23012: SCORCH JIP: Examination and Testing of Severly-Corroded Moorng Chians from West Africa*. Offshore Technology Conference (2012), Houston, Texas, USA

[45] E. Fontaine, J. Rosen, A. Potts, K.T. Ma, R.E. Melchers. OTC 25234: *Feedback on MIC and pitting corrosion from field recovered mooring chain links*. In: Offshore Technology Conference (2014) Houston, Texas, USA

[46] R.E. Melchers. *Long-term immersion corrosion of steels in seawaters with elevated nutrient concentration*. Corrosion Science 81 (2014) 110-116

[47] R.E. Melchers, A.E. Potts. *Data based materials numerical modelling for FPSO safety and reliability optimization*. Proceedings of the 11th World Congress on Structural and Multidisciplinay Optimisation (2015) Sydney, Australia

[48] R.E. Melchers, T. Moan, Z. Gao. *Corrosion of working chains continuously immersed in seawater*. Journal of Materials Science and Technology 12 (2007) 102-110

[49] J. De Pauw, P. De Baets, Y. Perez Delgado, J. Sukumaran, W. Ost. *A full scale test rig for assessment of abrasive wear of shackle chains*. Wear 302 (2013) 1017-1025

[50] D.V. Steenkiste, S. Plasschaert, P. De Baets, J. De Pauw, Y. Perez Delgado, J. Sukumaran. *Abrasive wear of link chains*. Sustainable Construction and Design 2 (2011) 338-396

[51] Energy Global. *Monitoring mooring reliability*. Energy Global Oilfield Technology (2015). Available at (June 2018): https://www.energyglobal.com/upstream/special-reports/20082015/monitoring-mooring-reliability

[52] R.E. Melchers, R. Jeffrey. *Early corrosion of mild Steel in seawater*. Corrosion Science 47 (2005) 1678-1693

[53] R.E. Melchers. *Effect of marine immersion corrosion of carbon content of low alloy Steels*. Corrosion Science 45 (2003) 2609-2625

[54] J. Bhandari, F. Khan, R. Abbassi, V. Garaniya, R. Ojeda. *Modelling of pitting corrosion in marine and offshore Steel structures-A technical review*. Journal of Loss Prevention in the Process Industries 37 (2015) 39-62

[55] A. Kvitrud. *Lessons learned from the Norwegian line failures 2010-2013*. Proceedings of the 33rd International Conference on Ocean, Offshore and Arctic Engineering, OMAE (2014) California, USA

[56] P. Hughs, W. Flores. *OTC 20909: The Effects of Large Scale Forgings and Heat Treatment on the Mechanical Performance of Mooring Connectors*. Offshore Technology Conference (2010) Houston, Texas, USA

[57] K.T. Ma, H. Shu, P. Smedley, D. L'Hostis, A. Duggal. *OTC 24025: A Historical Review on Integrity Issues of Permanent Mooring Systems*. Offshore Technology Conference (2013) Houston, Texas, USA

[58] A. Ku, D. Gallagher. *OTC 24391: Assessment and Mitigation of Low-Toughness Forger Mooring Components for Floating Structures*. Offshore Technology Conference (2013) Houston, Texas, USA
[59] C. Morandini, F. Legerstee. *Consistent Integrity of Mooring Systems*. Proceedings of the 29th International Offshore and Polar Engineering Conference, ISOPE (2009) Osaka, Japan.
[60] D. Denney. *Post-Mortem analysis of MODUs in Hurricanes Katrina and Rita*. Journal of Petroleum Technology 62 (2010) 1-2
[61] Willis Towers Watson. *Energy Loss Database*. (2017) Available at (June 2018): www.willis.com
[62] T. Bakke, J. Klungsoyr, S. Sanni. *Environmental impacts of produced water and drilling waste discharges from the Norwegian offshore petroleum industry*. Marine Environmental Research 92 (2013) 154-169
[63] IPIECA-IOGP. *Impacts of oil spills on marine ecology. Good practice guidelines for incident management and emergency response personnel*. IOGP (2015) Report 525
[64] *DNV Rules for Classification of Mobile Offshore Units. Special Equipment and Systems Additional Class*. *Part 6 Chapter 2: Position Mooring (POSMOOR).* July 1989.
[65] DNVGL-OS-E301. *Position Monitoring*. July 2015.
[66] NORSOK M-001. *Materials Selection*. November 2002
[67] API RP 2SK. *Design and Analysis of Stationkeeping Systems for Floating Structures*. 3rd edition, October 2005.
[68] API RP 2I. *In-service Inspection of Mooring Hardware for Floating Structures*. 3rd edition, April 2008.
[69] M. Wang and R. D'Souza. *Mooring Chain Corrosion Design Considerations for an FPSO in Tropical Water*. Proceedings of the 23rd International Conference on Offshore Mechanics and Arctic Engineering, OMAE (2004) Vancouver, Canada
[70] ISO 19901-7. *Petroleum and natural gas industries. Specific requirements for offshore structures. Part 7: Stationkeeping systems for floating offshore structures and mobile offshore units*. February 2018.
[71] E. Fontaine, A. Kilner, C. Carra, D. Washington, K.T. Ma, A. Phadke, D. Laskowski, G. Kusinski. *Industry Survey of Past Failures, Pre-emptive Replacement and Reported Degradations of Mooring Systems of Floating Production Units*, Offshore Technology Conference, Houston, Texas, USA, 5-8 May 2014
[72] A.O. Vázquez-Hernández, G.B. Ellwanger, L.V.S. Sagrilo. *Long-term response analysis of FPSO mooring systems*. Applied Ocean Research 33 (2011) 375– 383
[73] A.O. Vazquez-Hernandez, G.B. Ellwanger, L.V.S. Sagrilo. *Reliability-based comparative study for mooring lines design criteria*. Applied Ocean Research 28 (2006) 398–406
[74] B. Bhushan. *Principles and Applications of Tribology*. 2nd edition. A Wiley-Interscience Publication (2013). ISBN: 978-1-119-94454-6
[75] P. Moller, L.P. Nielsen. *Advanced Surface Technology*. Volume 01. NASF (2013). ISBN: 978-87-92765-24-6
[76] F. Díaz del Castillo. *Tribología: fricción, desgaste y lubricación*. Facultad de estudios superiores Cuautitlán. Lecturas de ingeniería 2.
[77] J.-P. Celis, P. Ponthiaux (Eds.), *Testing Tribocorrosion of Passivating Materials Supporting Research and Industrial Innovation: Handbook*. Maney Publishing, UK, 2012, ISBN: 978-1-907975-20-2.
[78] J.J. Damborenea, A.J. Vázquez. Consejo Superior de Investigaciones Científicas. *Ciencia e ingeniería de la superficie de los materiales metálicos*. Raycar (2000). ISBN: 978-84-00-07920-8
[79] R. Baboian (Ed.). *ASTM corrosion tests and standards. Application and Interpretation (2nd edition)*. ASTM International (2006) ISBN: 0-8031-2098-2
[80] E. McCafferty. *Introduction to Corrosion Science*. Springer (2010) ISBN: 978-1-4419-0454-6
[81] E.O. Huerta. *Corrosión y degradación de materiales*. Síntesis (2001). ISBN: 84-7738-518-1
[82] R. Singh. *Corrosion Control for Offshore Structures. Cathodic Protection and High-Efficiency Coatings*. Gulf Professional Publishing, Elsevier (2014) ISBN: 978-0-12-404615-3

[83] D. Landolt. *Corrosion and Surface Chemistry of Metals*. CRC Press (2007) ISBN: 978-0-8493-8233-8
[84] C. Smith, T. Siewert, B. Mishra, D. Olson, A. Lassiegne (Eds.). *Coatings for Corrosion Protection: Offshore Oil and Gas Operation Facilities, Marine Pipeline and Ship Structures*. National Institue of Standards and Technology (2004) doi: https://dx.doi.org/10.6028/NIST.sp.1035
[85] A. Amirudin, D. Thierry. *Application of electrochemical impedance spectroscopy to study the degradation of polymer-coated metals*. Progress in Organic Coatings 26 (1995) 1-28
[86] R.W. Revie, H.H. Uhlig. *Corrosion and Corrosion Control. An Introduction to Corrosion Science and Engineering (4th edition)*. Wiley-Interscience (2008) ISBN: 978-0-471-73279-2
[87] ASM Handbook. *Volume 13. Corrosion*. ASM International (1987) ISBN: 0-87170-007-7
[88] H. Shih (Ed.). *Corrosion Resistance*. In Tech (2012). ISBN 978-953-51-0467-4
[89] D. Landolt, S. Mischler, M. Stemp. *Electrochemcial methods in tribocorrosión: a critical appraisal*. Electrochimica Acta 46 (2001) 3913-3929
[90] M.T. Mathew, P. Srinivasa Pai, R. Pourzal, A. Fischer, M.A. Wimmer. *Significance of Tribocorrosion in Biomedical Applications: Overview and Current Status*. Advances in Tribology (2009) doi:10.1155/2009/250986, article ID 250986
[91] D. Landolt, S. Mischler (Eds.), *Tribocorrosion of Passive Metals and Coatings*. Woodhead Publishing, Cambridge, 2011, ISBN: 978-1-84569-966-6
[92] S.W. Watson, F.J. Friedersdorf, B.W. Madsen, S.D. Cramer. *Methods of measuring wear-corrosion synergism*. Wear 181-183 (1995) 476-484
[93] S. Mischler, E.A. Rosset, D. Landolt. *Effect of Corrosion on the Wear Behaviour of Passivating Metals in Aqueous Solutions*. Tribology Series 25 (1993) 245-253
[94] D. Landolt. *Electrochemical and materials aspects of tribocorrosion systems*. Journal of Physics, D 39 (2006) 3121-3127
[95] D. Landolt, S. Mischler, M. Stemp. *Electrochemical methods in tribocorrosion: a critical appraisal*. Electrochimica Acta 46 (2001) 3913-3929
[96] S. Mischler. *Triboelectrochemical techniques and interpretation methods in tribocorrosion: A comparative evaluation.* Tribology International 41 (2008) 573-583
[97] N. Diomidis, J.-P. Celis, P- Ponthiaux, F. Wenger. *A Methodology for the Assessment of the Tribocorrosion of Passivating Metallic Materials*. Lubrication Science 21 (2009) 53-67
[98] N. Diomidis, J.-P. Celis, P- Ponthiaux, F. Wenger. *Tribocorrosion of Stainless Steel in Sulfuric Acid: Identification of Corrosion-Wear Components and Effect of Contact Area*. Wear 269 (2010) 93-103
[99] S. Mischler, P. Ponthiaux. *A round robin on combined electrochemical and friction tests on alumina/stainless steel contacts in sulphuric acid*. Wear 248 (2001) 211-225
[100] ASTM G119-09. *Standard Guide for Determining Synergism Between Wear and Corrosion*. vol. 03, ASTM, 02 August 2013.
[101] R.I. Trezona, D.N. Allsopp, I.M. Hutchings. *Transitions between two-body and three-body abrasive wear: influence of test conditions in the microscale abrasive wear test*. Wear 225-229 (1999) 205-214
[102] D. Landolt, S. Michler, M. Stemp, S. Barril. *Third body effects and material fluxes in tribocorrosion systems involving a sliding contact*. Wear 256 (204) 517-524
[103] N. Diomidis, S. Mischler. *Third body effects on friction and wear during fretting of steel contacts*. Tribology International 44 (2011) 1452-1460
[104] P. Ponthiaux, F. Wenger, D. Drees, J.P. Celis. *Electrochemical techniques for studying tribocorrosion processes*. Wear 256 (2004) 459-468
[105] G. Stachowiak, M. Salasi, G. Stachowiak. *Three-Body Abrasion Studies of High-Cr Cast Irons: Benefits and Limitations of Tribo-electrochemical Methods*. Journal of Bio- and Tribo-Corrosion (2015) 1:6
[106] UNE 112086:2016. *Ensayos de tribocorrosión en materiales pasivos*. 07 September 2016
[107] R. Baboian (Ed.). *ASTM corrosion tests and standards*. ASTM International (2005) ISBN: 0-8031-2098-2
[108] A.I. Muñoz, L.C. Julián. *Influence of electrochemical potential on the tribocorrosion behaviour of high carbon CoCrMo biomedical alloy in simulated body fluids by electrochemical impedance spectroscopy*. Electrochimica Acta 55 (2010) 5428-5439
[109] S. Mischler, A. Spiegel, D. Landolt. *The role of passive oxide films on the degradation of steel in tribocorrosion systems*. Wear 225-229 (1999) 1078-1087

[110] J. Chen, J. Wang, F. Yan, Q. Zhang, Q.A. Li. *Effect of applied potential on the tribocorrosion behaviours of monel K500 alloy in artificial seawater*. Tribology International 81 (2015) 1-8
[111] M. Stemp, S. Mischler, D. Landolt. *The effect of contact configuration on the tribocorrosión of stainless steel in reciprocating sliding under potentiostatic control*. Corrosion Science 45 (2003) 625-640
[112] S. Mischler, A. Spiegel, M. Stemp, D. Landolt. *Influence of passivity on the tribocorrosion of carbon steel in aqueous solutions*. Wear 251 (2001) 1295-1307
[113] ASTM G102-89. *Standard Practice for Calculation of Corrosion Rates and Related Information from Electrochemical Measurements*
[114] Y. Sun, V. Rana. *Tribocorrosion behaviour of AISI 304 Stainless steel in 0.5M NaCl solution*. Materials Chemistry and Physics 129 (2011) 138-147
[115] Y. Yan (Ed.), *Bio-Tribocorrosion in Biomaterials and Medical Implants*, Woodhead Publishing (2013), ISBN: 978-0-85709-540-4
[116] R. Bayón, A. Igartua, J.J. González, U. Ruiz de Gopegui. *Influence of the carbon content on the corrosion and tribocorrosion performance of Ti-DLC coatings for biomedical alloys*. Tribology International 88 (2015) 115-125
[117] S.I. Pyun, H.C. Shin, J.W. Lee, J.Y. Go. *Electrochemistry of Insertion Materials for Hydrogen and Lithium*. *Chapter 2: Electrochemical Methods* (pp 11-31). Springer (2012) ISBN: 978-3-642-29463-1
[118] A. Lasia. *Electrochemical Impedance Spectroscopy and its Applications*. Springer (2014) ISBN: 978-1-4614-8932-0
[119] F. Scholz (Ed.). *Electroanalytical Methods, Guide to Experiments and Applications*. Springer (2010). ISBN: 978-642-02914-1
[120] L. Mendizabal, A. López, R. Bayón, P. Herrero-Fernandez, J. Barriga, J.J. González. *Tribocorrosion response in biological environments of multilayer TaN films deposited by HPPMS*. Surface & Coatings Technology 295 (2016) 60-69
[121] J.B. Pedemonte, M.M. Bárcena, A.A. Villero. *Ruido electroquímico: Métodos de análisis*. Septem Ediciones (2002) ISBN: 84-95687-33-X
[122] A. de Frutos Rozas. *Tribocorrosión de biomateriales metálicos modificados superficialmente mediante técnicas de vacío*. PhD Thesis, Universidad autónoma de Madrid, Facultad de ciencias, June 2010
[123] J.M. Sánchez-Amaya, M. Berthencourt, L. González-Rovira, F.J. Botana. *Medida de ruido electroquímico para el estudio de procesos de corrosión de aleaciones metálicas*. Revista de Metalurgia 45 (2009) 143-156
[124] P.Q. Wu, J.-P. Celis. *Electrochemical noise measurements on stainless Steel during corrosion-wear in sliding contacts*. Wear 256 (2004) 480-490
[125] R.J.K. Wood, J.A. Wharton, A.J. Speyer, K.S. Tan. *Investigations of erosion-corrosion processes using electrochemical noise measurements*. Tribology International 35 (2002) 631-641
[126] F. Galliano, E. Galvanetto, S. Mischler, D. Landolt. *Tribocorrosion behaviour of plasma nitrided Ti-6Al-4V alloy in neutral NaCl solution*. Surface and Coatings Technology 145 (2001) 121-131
[127] A. de Frutos, M.A. Arenas, G.G. Fuentes, R.J. Rodríguez, R. Martínez, J.C. Avelar-Batista, J.J. de Damborenea. *Tribocorrosion behaviour of duplex Surface treated AISI 304 stainless steel*. Surface & Coatings Technology 204 (2010) 1623-1630
[128] B. W. Madsen. *Measurement of wear and corrosion rates using a novel slurry wear test*. Materials Performance 26 (1987) 21-28
[129] B. W. Madsen. *Measurement of erosion-corrosion synergism with a slurry wear test apparatus*. Wear 123 (1988) 127-142
[130] M. Godet. *The third-body approach: A mechanical view of wear*. Wear 100 (1984) 437-452
[131] J.-P. Celis, P. Ponthiaux, F. Wenger. *Tribo-corrosion of materials: Interplay between chemical, electrochemical and mechanical reactivity of surfaces*. Wear 261 (2006) 939-946
[132] D. Shakhvorostov, B. Gleising, R. Brüscher, W. Dudzinski, A. Fischer, M. Scherge. *Microstructure of tribologically induced nanolayers produced at ultra low wear rates*. Wear 263 (2007) 1259-1265
[133] S. Akonko, D.Y. Li, M. Zomiek-Moroz. *Effect of cathodic protection on corrosive wear of 304 stainless steel*. Tribology Letters 18 (2005) 405-410
[134] P. Jemmely, S. Mischler, D. Landolt. *Electrochemical modeling of passivation phenomena in tribocorrosion*. Wear 237 (2000) 63-76

[135] X.Y. Wang, D.Y. Li. *Application of an electrochemical scratch technique to evaluate contributions of mechanical and electrochemical attacks to corrosive wear of materials*. Wear 259 (2005) 1490-1496
[136] Y. Sun, R. Bailey. *Improvement in tribocorrosion behavior of 304 stainless steel by surface mechanical attrition treatment.* Surface & Coatings Technology 253 (2014) 284-291
[137] R. Pileggi, M. Tului, D. Stocchi, S. Lionetti. *Tribo-corrosion behavior of chromium carbide based coatings deposited by HVOF*. Surface & Coatings Technology 268 (2015) 247-251
[138] A.C. Vieira, A.R. Ribeiro, L.A. Rocha, J.P. Celis. *Influence of pH and corrosion inhibitors on the tribocorrosion of titanium in artificial saliva*. Wear 261 (2006) 994-1001
[139] J. Chen, F.Y. Feng. *Tribocorrosion behaviours of Ti-6Al-4V and monel K500 alloys sliding against 316 stainless steel in artificial seawater*. Transactions of Nonferrous Metal Society of China 22 (2012) 1356-1365
[140] Y. Zhang, X. Yin, J. Wang, F. Yan. *Influence of microstructure evolution on tribocorrosion of 304 SS in artificial seawater*. Corrosion Science 88 (2014) 423-433
[141] J. Chen, Q. Zhang, Q.A. Li, S.L. Fu, J.Z. Wang. *Corrosion and tribocorrosion behaviours of AISI 316 stainless steel and Ti6Al4V alloys in artificial seawater*. Trans. Nonferrous Met. Soc. China 24 (2014) 1022-1031
[142] Y. Zhang, X. Yin, F. Yan. *Effect of halide concentration on tribocorrosion behavior of 304SS in artificial seawater*. Corrosion Science 99 (2015) 272-280
[143] Y. Zhang, X.Y. Yin, F.Y. Yan. *Tribocorrosion behavior of Type S31254 steel in seawater: identification of corrosion-wear components and effect of potential*. Materials Chemistry and Physics 179 (2016) 273-281
[144] Y. Sun, E. Haruman. *Tribocorrosion behaviour of low temperature plasma carburized stainless steel in 0.5M NaCl solution*. Corrosion Science 53 (2011) 4131-4140
[145] B.A. Obadele, M.L. Lepule, A. Andrews, P.A. Olubambi. *Tribocorrosion characteristics of laser deposited Ti-Ni-ZrO2 composite coatings on AISI 316 Stainless steel*. Tribology International 78 (2014) 160-167
[146] M. Azzi, J.A. Szpunar. *Tribo-electrochemical technique for studying tribocorrosion behaviour of biomaterials*. Biomolecular Engineering 24 (2007) 443-446
[147] X. Luo, X. Li, Y. Sun, H. Dong. *Tribocorrosion behaviour of S-phase surface engineered medical grade Co-Cr alloy*. Wear 302 (2013) 1615-1623
[148] Z. Guo, X. Pang, Y. Yan, K. Gao, A.A. Volinsky, T-Y Zhang. *CoCrMo alloy for orthopedic implant application enhanced corrosion and tribocorrosion properties by nitrogen ion implantation*. Applied Surface Science 347 (2015) 23-34
[149] A.M. Ribeiro, A.C. Alves, L.A. Rocha, F.S. Silva, T. Toptan. *Synergism between corrosion and wear on CoCrMo-Al2O3 biocomposites in a physiological solution*. Tribology International 91 (2015) 198-205
[150] Z. Doni, A.C. Alves, F. Toptan, J.R. Gomes, A. Ramalho, M. Buciumeanu, L. Palaghian, F.S. Silva. *Dry sliding and tribocorrosion behavior of hot pressed coCrMo biomedical alloy as compared with the cast CoCrMo and Ti6Al4V alloys*. Materials and Design 52 (2013) 47-57
[151] V.G. Pina, A. Dalmau, F. Devesa, V. Amigó, A.I. Muñoz. *Tribocorrosion behavior of beta titanium biomedical alloys in phosphate buffer saline solution*. Journal of the Mechanical Behavior of Biomedical Materials 46 (2015) 59-68
[152] I. Hacisalihoglu, A. Samancioglu, F. Yildiz, A. Alsaran. *Tribocorrosion properties of different type titanium alloys in simulated body fluid*. Wear 332-333 (2015) 679-686
[153] M.R. Dhanak, N.I. Xiros (Ed.). *Springer Handbook of Ocean Engineering*. Springer (2016) ISBN: 978-319-16648-3
[154] L.L. Shreir, R. A. Jarman, G.T. Burstein (Ed.). *Corrosion. Volume 2, Corrosion Control (Third edition)*. Butterworth-Heinemann (1994) ISBN: 0-7506-1077-8
[155] P.R. Roberge. *Corrosion Engineering. Principles and Practice*. Mc Graw Hill (2008) ISBN: 0-07-164087-8
[156] D. Talbolt, J. Talbolt. *Corrosion science and technology*. CRC Press US (1998). ISBN: 0-8493-8224-6
[157] C. Guedes Soares, Y. Garbatov, A. Zayed. *Effect of environmental factors on steel plate corrosion under marine immersion conditions*. Corrosion Engineering, Science and Technology 46 (2011) 524-541
[158] A.W. Momber, T. Marquardt. *Protective coatings for offshore wind energy devices (OWEAs): a review*. Journal of Coatings Technology and Research 15 (2018) 13-40

[159] M. Kutz (Ed.). *Handbook of environmental degradation of materials (2nd edition)*. Elsevier (2012) ISBN: 978-1-4377-3455-3
[160] Pierre. R. Roberge. *Handbook of Corrosion Engineering*. Mc Graw-Hill (2000) ISBN: 0-07-076516-2
[161] A.W. Momber, P. Plagemann, V. Stenzel. *Performance and integrity of protective coating system for offshore wind power structures after three years under offshore site conditions*. Renewable Energy 74 (2015) 606-617
[162] D. Santos, C. Brites, M.R. Costa, M.T. Santos. *Performance of Paint systems with polyurethane topcoats, proposed for atmospheres with very high corrosivity category*. Progress in Organic Coatings 54 (2005) 344-352
[163] K. Mühlberg. *Corrosion Protection of Offshore Wind Turbines. A Challenge for the Steel Builder and Paint Applicator*. Hempel Protective. Published in JPCL (2010)
[164] R. Baboian (Ed.). *NACE Corrosion Engineer's Reference Book. Third edition*. NACE International (2002) ISBN: 978-1-57590-127-5
[165] P. Ault. *The use of coatings for corrosion control on offshore oil structures*. Journal of Protective Coatings and linings 23 (2006) 42-47
[166] R.J.K. Wood. *Tribocorrosion of coatings: a review*. Journal of Physics D: Applied Physics 40 (2007) 5502-5521
[167] R.J.K. Wood, J.A. Wharton. *Coatings for tribocorrosion protection, in Tribocorrosion of Passive Metals and Coatings*, (eds.) Landolt D. And Mischler S, Woodhead Publishing (2011), ch. 11, pp. 296-333, ISBN: 978-1-94569-966-6
[168] S. Shrestha, A. Sturgeon. *Characteristics and electrochemical corrosion behaviour of thermal sprayed aluminum (TSA) coatings prepared by various wire thermal spray processes*. Eurocorr Proceedings, 2005
[169] K.P. Fisher, W.H. Thomanson, T. Bosbrook, J. Murali. *Performance of Thermal-Sprayed Aluminum Coatings in Offshore Service*. Materials Performance 34 (1995) 27-35
[170] NORSOK M-501. *Surface preparation and protective coating*. February 2012.
[171] ISO 12944:1-9 *Paints and varnishes. Corrosion protection of steel structures by protective paint systems*. November 2017- January 2018.
[172] ISO 9223. *Corrosion of metals and alloys. Corrosivity atmospheres. Guiding values for the corrosivity categories*. June 2017.
[173] C. Hellio, D. Yebra (Ed.). *Advances in marine antifouling coatings and technologies*. Woodhead publishing (2009) ISBN: 978-1-84569-631-3
[174] I. Amara, W. Miled, R.B. Slama, N. Ladhari. *Antifouling processes and toxicity effects of antifouling paints on marine environment. A review*. Environmental Tocixology and Pharmacology 57 (2018) 115-130
[175] R. Javaherdashti. *Microbiologically Influenced Corrosion. An Engineering Insight*. Springer (2008) ISBN: 978-1-84800-073-5
[176] K.M. Usher, et al. Critical Review: *Microbially Influenced Corrosion of Buried Carbon Steel Pipes*. International Biodeterioration & Biodegradation 93 (2014) 84-106
[177] D. Feron (Ed.). *Nuclear corrosion science and engineering*. Woodhead Publishing Series in Engineering (2012). ISBN: 978-1-84569-765-5. Chapter 8: *Microbiologically influenced corrosion (MIC) in nuclear power plant systems and components*. B. Tribollet. Pages 230-261
[178] R. Parks, M. Donnier-Marechal, P.E. Frickers, A. Turner, J.W. Readman. *Antifouling biocides in discarded marine paint particles*. Marine Pollution Bulletin 60 (2010) 1226-1230
[179] D.M. Yebra, S. Kiil, K. Dam-Johansen. *Antifouling technology- past, present and future steps towards efficient and environmentally friendly antifouling coatings*. Progress in Organic Coatings 50 (2004) 75-104
[180] N. Voulvoulis, M.D. Scrimshaw, J.N. Lester. *Comparative environmental assessment of biocides used in antifouling paints*. Chemosphere 47 (2002) 789-795
[181] A. Turner. *Marine pollution from antifouling paint particles*. Marine Pollution Bulletin 60 (2010) 159-171
[182] D. Carteau, K. Vallé-Réhel, I. Linossier, F. Quiniou, R. Davy, C. Compère, M. Delbury, F. Faÿ. *Development of environmentally friendly antifouling paints using biodegradable polymer and lower toxic substances*. Progress in Organic Coatings 77 (2014) 485-493
[183] K. A. Dafforn, J.A. Lewis, E.L. Johnston. *Antifouling strategies: History and regulation, ecological impacts and mitigation*. Marine Pollution Bulletin 62 (2011) 453-465

[184] D. M. Yebra, S. Kiil, K. Dam-Johansen, C. Weinell. *Reaction rate estimation of controlled-release antifouling paint binders: Rosin-based systems*. Progress in Organic Coatings 53 (2005) 256-275
[185] J. Wang, T. Shi, X. Yang, W. Han, Y. Zhou. *Environmental risk assessment on capsaicin used as active substance for antifouling system on ships*. Chemosphere 104 (2014) 85-90
[186] S. Soroldoni, F. Abreu, I.B. Castro, F.A. Duarte, G.L. Pinho. *Are antifouling paint particles a continuous source of toxic chemicals to the marine environment?*. Journal of Hazardous Materials 330 (2017) 76-82
[187] M. Lagertröm, J.F. Lindgren, A. Holmgvist, M. Dahlström, E. Ytreberg. *In situ release rates of Cu and Zn from commercial antifouling paints at different salinities*. Marine Pollution Bulletin 127 (2018) 289-296
[188] B.T. Watermann, B. Daehne, S. Sievers, R. Dannenberg, J.C. Overbeke, J.W. Klijnstra, O. Heemken. *Biassays and selected chemical analysis of biocide-free antifouling coatings*. Chemosphere 60 (2005) 1530-1541
[189] K.V. Thomas, M. McHugh, M. Hilton, M. Waldock. *Increased persistence of antifouling paint biocides when associated with paint particles*. Environmental Pollution 123 (2003) 153-161
[190] S. Soroldoni, S.E. Martins, I.B. Castro, G.L.L. Pinho. *Potential ecotoxicity of metals leached from antifouling paint particles under different salinities*. Ecotoxicology and Environmental Safety 148 (2018) 447-452

Chapter 3

Objectives

Chapter 3: Objectives

As previously mentioned in the state of the art (chapter 2), High-Strength Low-Alloys steel components in offshore mooring lines are exposed to tribocorrosion conditions during their service life. A better understanding of this phenomenon could be used to improve the design of steel structures in extreme conditions, such as those in marine environments. In fact, the wear and corrosion allowance requirements specified on the mooring design codes are below the actual material loss registered after real service of components, as highlighted in chapter 2. In this context, the main objective of the first part of this thesis is to provide a closer insight into the tribocorrosion behavior of HSLA steels, i.e., active materials, in offshore applications. Up to now, the existing knowledge on tribocorrosion field has been related to materials and alloys with considerably high corrosion resistance in aggressive media, such as stainless steels or titanium alloys, commonly referred to as passive materials. Therefore, the work developed within this thesis would provide a first insight into the tribocorrosion of active materials, for which new test protocols and procedures need to be developed, on the basis of those employed in the assessment of passive materials.

On the other hand, in light of the common use of protective coatings to protect steel components and structures, the second part of the thesis deals with this matter. Coherently with the information gathered in chapter 2, the coatings are exposed to the same threats as the steel structures, including wear and fatigue, among others. However, the selection of the coatings is mainly made by considering their efficiency in terms of corrosion, and little is known on their tribocorrosion performance. Considering that the effectiveness of a coating system can be compromised once it has been damaged by mechanical means, further investigations on tribocorrosion of coatings should be performed. For all these reasons, the evaluation of protective coatings behavior in terms of wear-corrosion requirements is the second goal of the thesis.

All in all, the aim of this work was achieved through a multidisciplinary approach, by fulfilling the main objectives that can be summarized as follows:

- Evaluation and understanding of **the tribocorrosion phenomenon in active materials**, i.e., HSLA steels used in mooring line systems.
- Design of **suitable testing procedures** for the assessment of tribocorrosion in active materials, considering the influence of test parameters and conditions.
- **Evaluation of the suitability of currently employed coatings** for the protection of steel structures and components against extreme conditions.
- **Development of enhanced wear-corrosion resistant coatings**, by means of functionalization of pre-existing solutions.

Chapter 4

Methodology

Chapter 4: Methodology

The studies performed within this thesis, can be divided into two major parts. In the first one, the tribocorrosion behavior of active materials, i.e., High-Strength Low-Alloy (HSLA) steels employed in offshore applications, has been investigated. The second part, in turn, can be divided into two principal approaches: the performance evaluation of different coatings currently employed in the protection of structural steel in offshore applications, and the development or improvement of the existing coating systems. For this aims, different technologies and equipment have been employed.

The different methodologies used in this thesis can be divided into different categories depending on the type of activity or characterization performed. Fig. 4.1 shows the methodology employed in the different steps of the investigation performed in the thesis. Additional information on the instrumental techniques and equipment is included in Annex I.

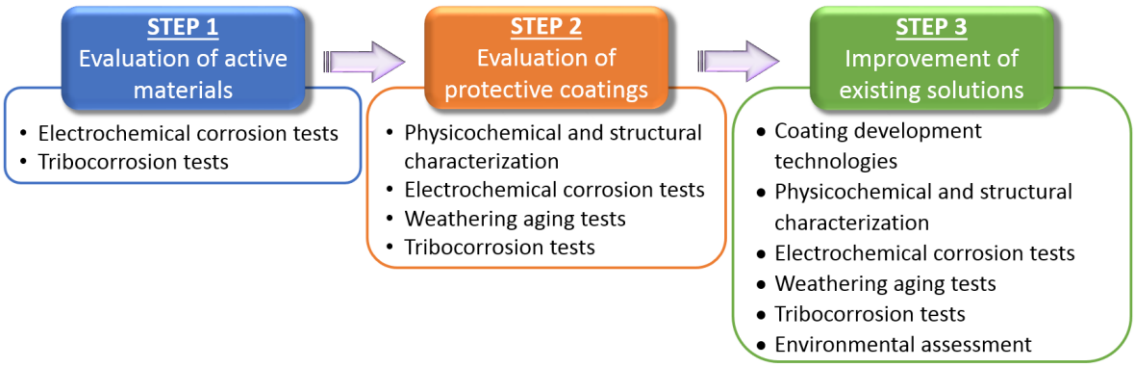

Fig. 4.1 Schematic representation of the methodology employed in the different steps of the investigation performed in the thesis

4.1 ELECTROCHEMICAL CORROSION TESTS

The electrochemical corrosion tests were employed to evaluate the corrosion behavior in synthetic seawater of the uncoated HSLA steels, the steels coated with the coatings currently employed in offshore applications, and also the new solutions developed in the last section of this work.

The corrosion behavior evaluation was carried out by performing different electrochemical techniques in a three-electrode electrochemical test set-up connected to an Autolab-Metrohm PGSTAT302N potentiostat equipped with FRA32M and EDC modules.

The surface of the samples was evaluated after the tests by means of an Olympus GX71 optical microscope and a ZEISS ULTRA plus Field Emission Scanning Electron Microscope (SEM) with EDS and BSE microanalysis from OXFORD INCA synergy.

4.2 TRIBOCORROSION

For the tribocorrosion behavior evaluation the HSLA steels and the different coating systems in synthetic seawater, a rotatory MicroTest MT/10/SCM tribometer was employed, under ball-on-disc configuration. The tribometer was connected to the Autolab-Metrohm PGSTAT302N potentiostat for the control and registration of the

electrochemical parameters. The reciprocating UMT-CETR3 tribometer connected to the potentiostat was also employed for testing HSLA steels.

After the tests, the worn surface of the samples was evaluated through different microscopic techniques. The total material loss was quantified by weighing the samples before and after the tests in a Mettler Toledo XP205 balance. The material loss in the wear tracks was calculated from the cross-section profiles obtained with a Nikon ECLIPSE ME600 and a Sensofar S Neox confocal microscopes. The tribocorrosion mechanisms were proposed by analyzing the test surfaces with the above-mentioned optical and SEM microscopes.

4.3 WEATHERING AGING TESTS

The protective effectiveness of the commercial coatings and the newly developed solutions was assessed by performing weathering aging tests in different climatic chambers:

- Julabo ED thermostatic bath for water immersion tests (ISO 2812-2 [1])
- ASCOTT 2000S chamber for the salt-fog exposure tests (ISO 9227[2])
- Kesternich HK300-800 S/M humidostatic chamber for the water condensation tests (ISO 6270-2 [3])
- WEISS C340/70 climatic chamber for the low-temperature exposure (ISO 12944-9 [4], NORSOK M501 [5])
- Atlas UVTest weathering device with type II UV lamps (UVA-340) of 340 nm (ISO 16474-3 [6])

The exposure types and durations were based on different standards currently employed for the evaluation of the coatings performance and validation for different corrosivity atmospheres (ISO 12944-6 [7], ISO 12944-9 [4], NORSOK M501 [5]).

After the aging in the different chambers, the surface of the coatings was analyzed with the Olympus GX71 optical microscope.

4.4 COATINGS DEVELOPMENT TECHNOLOGIES

The development of the improved solutions for the protection of HSLA steels for offshore submerged components was achieved through two main steps.

The wear and tribocorrosion resistance of the Thermally Sprayed Aluminum (TSA) coating was enhanced with the Plasma Electrolytic Oxidation (PEO) technique, by growing a hard aluminum oxide layer in a KERONITE KT 20-50 (20KW AC power supply) instrument.

On the other hand, the organic sealant applied on top of the TSA coating was functionalized to provide it with antifouling properties by incorporating nanoparticles. The nanoparticles selected were the silicon dioxide (SiO_2) to obtain superhydrophilicity, and copper II oxide (Cu_2O) to provide the paint with antibacterial ability. The nanoparticles were dispersed using an ultrasonic homogenizer (Vibracell-VCX750), incorporated into the paint formulation, and applied by spray technique.

4.5 PHYSICOCHEMICAL AND STRUCTURAL CHARACTERIZATION

The physicochemical and structural characterization of the coatings was assessed with the following equipment and methodologies:

- The thickness of the coatings was measured from the cross-section profile in the Olympus GX71 optical microscope (UNE-EN ISO 1463 [8]).
- For the hardness determination, the Akashi AVK-A and Future-Tech FM-700 testers equipped with Vickers indenters were employed (UNE-EN ISO 6507-1 [9])
- The roughness was determined in a Perthometer M2 (Mar GmBH) profilometer (DIN EN-ISO 4288 [10]).
- The adhesion of the coating systems was evaluated by means of pull-off adhesion tests with a PosiTest AT-A equipment (ISO 4624 [11])
- The microstructure of the coatings was analyzed with the above-mentioned SEM microscope
- The chemical composition was also analyzed in the SEM microscope, equipped with Energy Dispersive Spectroscopy (EDS) technique
- The phases of the newly generated PEO coating were analyzed by X-ray diffraction (XRD) in a D8 Advance diffractometer from Bruker, equipped with a Cr-Kα1 radiation source.
- The hydrophobicity or hydrophilicity grade of the organic sealants with nanoparticle addition was evaluated in a SURFTENS universal goniometer.
- Inductive Coupled Plasma Optical Emission Spectroscopy (ICP-OES) technique was employed to quantify the particle release of the sealant with nanoparticles, in an ULTIMA 2 HORIBA Jobin Yvon instrument.

4.6 ENVIRONMENTAL ASSESSMENT

The environmental related assessment was performed to evaluate the antibacterial activity and ecotoxicity of the organic sealant with nanoparticle addition, to determine its suitability to be employed in the marine environment.

The antibacterial activity tests were performed according to JIS Z2801 [12] standard, and its equivalent ISO 22196 [13], with *Escherichia coli* ATCC 8739 (*E. Coli*) microorganism.

The ecotoxicological analysis performed was the algal growth inhibition tests following the ISO 10253 standard [14], with the MARINE ALGALTOXKIT recommended. The marine algae employed was the *Phaeodactylum tricornutum* (MICROBIOTESTS Inc.). The algal growth inhibition was determined by measuring the optical density (OD) at 670 nm in a Jenway 6300 spectrophotometer.

4.7 REFERENCES

[1] ISO 2812-2. *Paints and varnishes. Determination of resistance to liquids*. Second edition, January 2007
[2] ISO 9227. *Corrosion tests in artificial atmospheres. Salt spray test*. Fourth edition, March 2017
[3] ISO 6270-2. *Paints and varnishes. Determination of resistance to humidity*. Second edition, November 2017
[4] ISO 12944-9. *Paints and varnishes. Corrosion protection of steel structures by protective paint systems. Part 9: Protective Paint systems and laboratory performance test methods for offshore and related structures*. First edition, January 2018
[5] NORSOK M-501. *Surface preparation and protective coating*. Sixth edition, February 2012

[6] ISO 16474-3 *Paints and varnishes. Methods of exposure to laboratory light sources. Fluorescence UV lamps.* September 2014
[7] ISO 12944-6. *Paints and varnishes. Corrosion protection of steel structures by protective paint systems. Part 9: Laboratory performance test methods*. Second edition, January 2018
[8] UNE-EN ISO 1463. *Metallic and oxide coatings: Measurement of coating thickness. Microscopical method*. Second edition, March 20115
[9] UNE-EN ISO 6507-1. *Metallic materials. Vickers hardness tests. Part I: Test method*. Third edition, November 2006
[10] DIN EN ISO 4288. *Geometrical products specifications (GPS). Surface texture: Profile method. Rules and procedures for the assessment of surface texture*. July 2008
[11] ISO 4624. *Paints and varnishes. Pull-of test for adhesion*. February 2016
[12] JIS Z2108:2012. *Antibacterial Products-Test for antibacterial activity and efficacy*. May 21, 2012
[13] ISO 22196:2011. *Measurement of antibacterial activity on plastics and other non-porous surfaces*. August 1, 2011
[14] ISO 10253. *Water quality: Marine algal growth inhibition test with Skeletonema sp. And Phaeodactylum tricornutum*. Third edition, November 2011

Chapter 5

Results and discussion

Part I

Tribocorrosion of HSLA steels (active materials) in offshore applications

Contribution 1

Tribocorrosion behavior of mooring High-Strength Low-Alloy steels in synthetic seawater

Wear 338-339 (2015) 1-10

Contribution 1: Wear 338-339 (2015) 1-10

5.1. TRIBOCORROSION BEHAVIOR OF MOORING HIGH STRENGTH LOW ALLOY STEELS IN SYNTHETIC SEAWATER

A. López[a], R. Bayón[a], F. Pagano[a], A. Igartua[a], A. Arredondo[b], J.L. Arana[b], J.J. González[c]

[a]*IK4-TEKNIKER, Eibar, Spain*
[b]*Department of Metallurgical and Materials Engineering, University of the Basque Country, Spain*
[c]*Vicinay Marine Innovación, Spain*

ABSTRACT

Offshore components of High-Strength Low-Alloy Steel (HSLA) are frequently exposed to tribological and corrosion effects during their working life. In the present work, several experiments have been performed to study the tribocorrosion behavior of two steel grades, under unidirectional sliding in synthetic seawater. Sliding wear tests were performed under potentiodynamic and potentiostatic conditions at different applied potentials. The wear tracks were analyzed by means of optical microscope and profilometry. The wear-corrosion synergism was quantified according to the ASTM G119 standard. Sliding promotes the wear accelerated corrosion of the unworn area in both alloys. Furthermore, the coefficient of friction of the steels is strongly influenced by the corrosion products and the applied potential.

Keywords: *High Strength Steel; Tribocorrosion; Corrosion; Seawater*

5.1.1 Introduction

The main energetic sources used nowadays are oil and gas, especially those generated offshore. The platforms used for this aim have a great impact at environmental, social and economic levels. Offshore platforms are tied up to the sea bottom through mooring systems, which are composed of chains, anchor systems, and connectors.

High strength steels (yield strength from 460 MPa to 960 MPa) are increasingly being used in offshore structural applications. These steels offer some advantages over conventional steels, especially when the weight plays an important role.

When immersed in the ocean, the chains are subjected to high corrosion rates [1] especially in the splash zone, where the concentration of oxygen is high. Moreover, the floater motions induced by the environmental actions due to waves, wind and current movements of the sea [2,3] involves the links to be in relative motion with each other leading to a continuous wear in the surfaces in contact [1]. Wear and corrosion are two processes that lead to a surface damage due to a progressive material loss as a result of mechanical and electrochemical processes, respectively [4]. When these two degradation processes occur in a simultaneous way, it is known as tribocorrosion.

In accordance with the ASTM G40 Standard [5], tribocorrosion can be defined as a form of solid surface alteration that involves the joint action of relatively moving mechanical contact with chemical reaction in which the result may be different in effect than either process acting separately. In other words, it is the process leading to an irreversible transformation of the material resulting from the simultaneous physic-chemical and mechanical surface interactions occurring at a tribological contact [6-11]. In passive materials, the origin of tribocorrosion is closely related to the presence of a protective oxide film of few nm thick on material surfaces [11-13]. Under tribocorrosion conditions two main mechanisms contribute to material removal from the surface of the material:

wear accelerated corrosion and mechanical removal from the sliding contact [4,7,13,14,15]. Tribocorrosion involves numerous synergy effects between mechanical and chemical or electrochemical phenomena [6-11].

The tribocorrosion behavior of passive materials such as stainless steels or titanium has been widely studied [16,17,18] during years in different solutions. It is well known that these passive materials form a protective layer of few nanometers thick, which is mostly composed of oxides as a consequence of a spontaneous reaction when immersed in aqueous solutions [11-13].

As for low alloy steels, like those used in mooring line chains, the content in alloy elements is not enough to form such protective layer, and the major oxide formed is the ferric oxyhydroxide (FeOOH). The rust layer formed in carbon steels has a complex morphology and it is generally porous, with poor adherence and cracked in the outer part [19-21]. Unlike that formed on stainless steels, the film is not protective in the presence of corrosive electrolytes and it usually breaks down [22], so the electrolyte and the corrosive species can easily penetrate the porous rust layers to the substrate where corrosion reactions proceed continuously [19].

While a good understanding of the tribocorrosion behavior of passive materials has been achieved, little is known about the behavior of active materials, such as the steels used in offshore components.

The present investigation was carried out with the aim to further comprehend the behavior of two steel grades commonly used in mooring lines. The tribocorrosion behavior of the steels under unidirectional sliding in synthetic seawater was studied using a rotatory tribometer under ball-on-disc configuration, equipped with an electrochemical cell placed over the rotating plate. The combination of mechanical and electrochemical techniques allowed an in-situ characterization of the surface state of that material and its evolution during sliding tests [23,24]. The tests were performed under laboratory conditions that simulated as close as possible to those that the chains are subjected to. A series of experiments have been performed to study the effect of applied potential on the tribocorrosion behavior of the steels. Furthermore, a surfaces examination was conducted to study the materials degradation mechanisms involved.

5.1.2 **Experimental Procedures**

5.1.2.1 Materials and sample preparation

The steel grades used in the manufacture of chains and accessories that form the mooring lines are approved by the current Classification Societies. The steels are classified by specified minimum ultimate tensile strength into five grades: R3, R3S, R4, R4S and R5 [25]. The present work studies the tribocorrosion behavior of the steel grades R4 and R5.

High strength steel (HSS) grades, such as the R4, R4S and the R5, are manufactured with the chemical compositions of low and medium alloy steels (Cr, Ni, Mo, V…), using alloying percentages that depend on the hardenability (mass effect) and the specific mechanical characteristics of each grade. The chains are welded by flash butt welding (FBW) process, followed by a post-welding heat treatment (PWHT).

The samples used in the tests were discs of 7.9 mm thickness obtained by cutting 24 mm diameter bars from a real chain component. The discs were mirror polished in order to obtain a surface with low roughness (Ra=0.05μm). Prior to the tests, the samples were cleaned with ether and acetone in an ultrasonic bath, dried with air and adequately stored

in a desiccator in order to avoid corrosion and contamination. The exposed surface of the samples was of 2.54 cm^2.

5.1.2.2 Tribocorrosion tests with in situ electrochemical measurements by ball on disc rotatory system

Frictional tests were carried out using a unidirectional tribometer shown schematically in Fig. 5.1.1. An electrochemical cell is placed on the rotatory plate of the tribometer in order to perform the tribocorrosion tests by controlling both mechanical and electrochemical parameters simultaneously. The tribocorrosion test system was composed of a ball-on-disc MicroTest MT/10/SCM tribometer and an Autolab-Metrohm PGSTAT30 potentiostat.

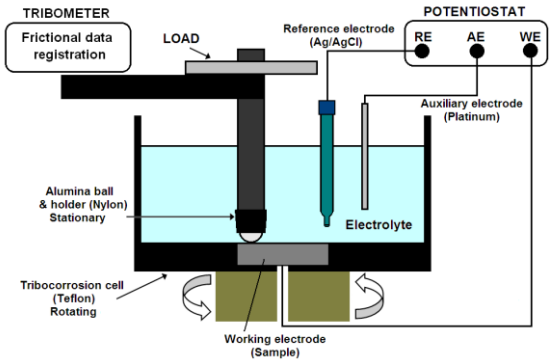

Fig. 5.1.1 Schematic of tribocorrosion ball-on-disc experimental setup used in this work [15]

The samples were fixed in the electrochemical cell, which rotates ensuring the contact between the stationary counterbody and the specimen under controlled load, radius and speed conditions. An alumina ball of 10 mm in diameter (G28) was used as the counterbody. The cell and the ball holder were made of Teflon and nylon, respectively. These insulating and corrosion resistant materials ensure the electrical isolation of the specimen from the metallic components of the tribometer.

The electrolyte used for the test was synthetic seawater with heavy metals, which was prepared in accordance with ASTM D1141. The test cells were filled with 150 ml of this dissolution. A commercial Ag/AgCl (KCl 3M) electrode and a platinum wire were placed 5 mm above the exposed surface of the sample to act as the reference electrode and the auxiliary electrode, respectively. The sample was connected as the third electrode (working electrode). The potential of the reference electrode is of 207 mV versus standard hydrogen electrode (SHE), and all the potentials registered in this work are referred to this electrode.

During the wear experiments the frictional forces, as well as the current and potential are continuously monitored. The coefficient of friction was obtained by dividing the frictional force measured during the test by the normal force applied. Sliding was used in this study to represent the conditions when the links in the chains move with relative movement to one another causing wear in the contact points. The contact conditions of the surfaces were calculated using the Hertzian Contact Theory [26], considering the real contact pressure between the links in real applications. The normal force used in the tests was of 5 N, which corresponded to an average Hertzian pressure of 930 MPa with a contact radius of 50.5 μm. The ball described a wear track of 5 mm radius, with a rotation speed of 100 rpm.

Potentiodynamic tests were performed at a sweep rate of 1 mVs^{-1}, from -1000 mV to 400 mV. The polarization curves of the two steels were obtained both in the absence of sliding

and with sliding under the mechanical conditions of load, wear track radius and rotation speed mentioned above. Before each potentiodynamic measurement, the open circuit potential (OCP) was measured during 3600 s in order to study the evolution of the potential of the steels with immersion time until its stabilization.

After the potentiodynamic tests, five potentials were selected: two cathodic potentials, two anodic potentials and the OCP of each steel grade. Sliding wear tests under potentiostatic conditions were performed by using the selected potentials, at a constant load of 5 N and 100 rpm for a rubbing time of 2400 s, corresponding to 4000 cycles. All the tests were conducted at room temperature and aerated conditions.

5.1.2.3 Wear and corrosion synergistic experiments

The evaluation of corrosion, wear, and combined wear and corrosion behavior was carried out according to the ASTM G119 Standard [27], which allows quantifying the synergism by calculating the parameters mentioned throughout this section.

The total material loss (*T*), which includes contributions from mechanical wear, corrosion dissolution and the interaction between these two can be defined as:

$$T = W_0 + C_0 + S \quad \text{(5.1.I)}$$

Where W_0 is the rate of material loss in the absence of corrosion, C_0 is the electrochemical corrosion rate when no mechanical wear is applied, and S the synergetic component.

Therefore, mechanical wear affects corrosion, and corrosion affects mechanical wear. The synergetic component can be divided into two components: the increase in the mechanical wear due to corrosion, ΔW_C, and the increase in corrosion due to mechanical wear, ΔC_W, as follows:

$$S = \Delta W_C + \Delta C_W \quad \text{(5.1.II)}$$

Where ΔW_C and ΔC_W can be calculated by using the following equations:

$$\Delta W_C = W_C - W_0 \quad \text{(5.1.III)}$$

$$\Delta C_W = C_W - C_0 \quad \text{(5.1.IV)}$$

Where W_C is the total wear component of *T*, and C_W represents the electrochemical corrosion rate during the corrosive wear and.

In order to obtain the parameters in accordance with the ASTM Standard, the samples tested under potentiodynamic and potentiostatic conditions were weighted before and after each test, using a Mettler Toledo XP205 balance with an accuracy of 0.01mg.

5.1.2.4 Morphology of the worn surface by optic microscope and profilometry

The morphology of all the tested specimens was examined by optical microscopy (Leica DM2500MH). The contact area on the surface of the alumina ball was also examined, but the wear of the ball was not measurable in either test.

After each test, the wear track volume due to the combined action of wear and corrosion of the samples was calculated by using the profiles registered with a confocal microscope (Nikon ECLIPSE ME600). The cross-section of the track was measured in four equidistant locations. Average values of the track width and depth were obtained, and the cross-sectional area of the track was estimated by approaching its shape with a semi-

elliptical geometry [4]. The volume of material loss in the wear track was calculated by multiplying the cross-sectional area by the circumferential length of the wear track.

5.1.3 Results and Discussion

5.1.3.1 Potentiodynamic tests with and without sliding

Potentiodynamic tests were performed to obtain the polarization curves under sliding (tribocorrosion) and without sliding (corrosion), at a sweep rate of 1 mVs^{-1}. The polarization curves under sliding were measured under a load of 5 N and a rotation speed of 100 rpm. Before each polarization measurement, the specimens were stabilized for 3600 s of immersion in the seawater.

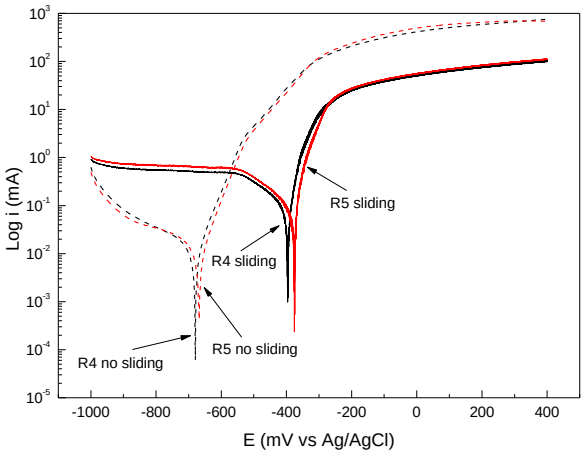

Fig. 5.1.2 Potentiodynamic curves obtained for both steel grades without sliding and under sliding

Fig. 5.1.2 shows the polarization curves obtained under sliding and without sliding. In the curves obtained in the absence of sliding, both steels exhibit similar behavior, with close corrosion potential values and identical anodic currents. No passive region is observed in either curve. Instead, a great activation stretch is observed in the anodic region at potentials above the corrosion potential, where the current increases several orders of magnitudes for small potential variations. Such increase in the current to reach values near 700 mA, indicates that the steels are very active materials and undergo high rate corrosion processes when immersed in seawater, coherently with that observed by other authors [28].

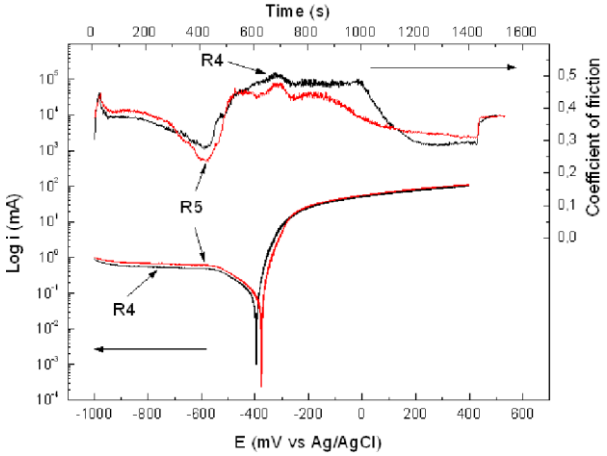

Fig. 5.1.3 Polarization curves and recorded COF during the potentiodynamic tests under sliding for both steel grades

The electrochemical behavior of both steels changes significantly when sliding is applied. The corrosion potential or zero-current potential of both steels is anodically shifted, from -680±25 mV to -395±15 mV for steel grade R4 and from -668±21 mV to -372±13 mV for

steel grade R5. Moreover, a decrease of nearly an order of magnitude in the anodic currents is observed for both steels due to the action of sliding. However, the activation stretch under sliding is smaller than that of the tests performed without sliding, and the anodic currents reach lower values, of around 100 mA. The difference in the values of currents measured with and without sliding suggests that the corrosion kinetic in the track and in the outer part of the track is different, since the continuous action of the counterbody seems to impede the natural trend of corrosion of the material inside the wear track. This peculiar tendency in the current results was observed by the authors in tribocorrosion tests performed under reciprocating sliding with small volumes of seawater dissolution. Therefore, the fluid motion during sliding does not seem to affect the corrosion system and the current tendency registered during the tests.

The coefficients of friction (COF) recorded during the potentiodynamic tests are very similar for both steel grades. The evolution of the COF with the applied potential can be observed in Fig. 5.1.3, where the COF and the polarization curves are plotted together. In the cathodic region, the COF experiences a sudden increase when the potential sweep starts, and the samples are polarized to the cathodic potential of -1000 mV. Then, the COF decreases until the applied potential is close to -600 mV, after what it increases again during the cathodic activation region. At potentials close to the corrosion potential, the COF increases suddenly. More stable values are observed when the slope of the polarization curve changes to the anodic region. At higher anodic potentials the COF decreases again and stabilizes until the end of the sliding when it reaches higher values. Therefore, the COF is reduced when the samples are cathodically protected, and it seems that the formation of the oxide layers in the track when the samples are anodically polarized helps to maintain a low COF.

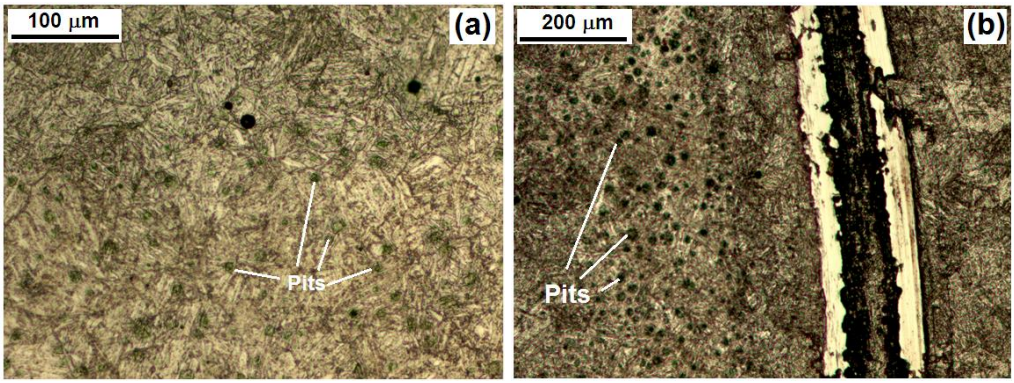

Fig. 5.1.4 Optical micrographs of the steel grade R5 (a) under no sliding condition and (b) under sliding showing the presence of pits, and corrosion products in the wear track

The surface of the samples was examined by means of an optical microscope. The micrographs are shown in Fig. 5.1.4 reveal the existence of generalized corrosion along the surface of the steels, and some localized corrosion in the form of pits. Furthermore, the formation of corrosion products in the wear track is observed in the samples tested under sliding (Fig. 5.1.4b). The degradation and the presence of corrosion products are more evident in the unworn area of the sample tested under sliding, suggesting that sliding accelerates the corrosion kinetics outside the wear track.

5.1.3.2 Potentiostatic sliding tests

After studying the potentiodynamic behavior of the steels, sliding wear tests were performed under potentiostatic conditions at five different potentials. The sliding tests were carried out under a 5N load and a speed of 100 rpm for 4000 cycles. The tests started after an hour of immersion, and once the potential was stable. The potential was applied 2 minutes before the sliding started, and it was maintained for 10 minutes after

the sliding finished, so the total duration of the polarization was of 52 min. In all the tests the current and the COF were registered simultaneously. The tests were performed under the following potential values: two cathodic potentials (-1000 mV and -650 mV), open circuit potential (-395 mV for the R4 steel and -371 mV for the R5 one) and two anodic potentials (0mV and 300 mV), which were selected in accordance with the polarization curves obtained in the potentiodynamic tests under sliding.

Electrochemical behavior under applied potential

The first potentiostatic test was conducted at a cathodic potential of -1000 mV. This potential is below the corrosion potentials measured under both sliding and without sliding conditions for both steels, so the sample is cathodically protected. Therefore, the occurrence of corrosion is impeded, and the contribution of pure mechanical wear to the total material loss from the wear track can be determined [8,14,16]. The recorded currents and COF at -1000 mV are plotted together in Fig. 5.1.5a. The currents measured in both steels are cathodic (negative) before, during and after sliding, confirming that no electrochemical corrosion occurred on the surface of the steels at this potential. The average values of the COF and the currents registered are compiled in Table 5.1.1.

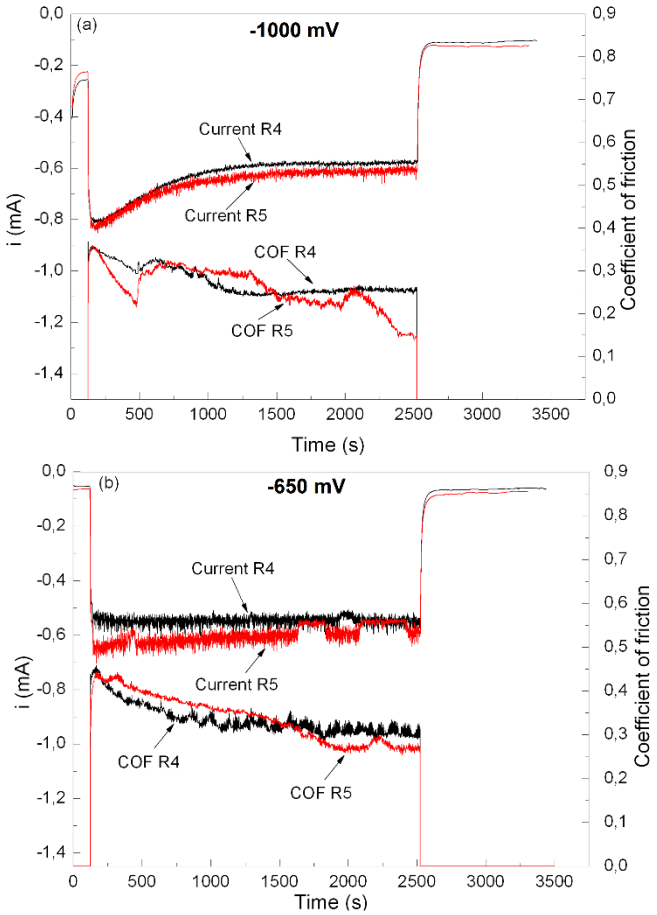

Fig. 5.1.5 Evolution of the current and COF recorded before, during and after sliding for both steel grades under cathodic potentials: (a) -1000 mV and (b) -650 mV

Another test was performed under cathodic protection at -650 mV (Fig. 5.1.5b). The measured currents are still cathodic, indicating that at this potential the material loss is totally attributed to mechanical wear. The currents registered at -650 mV are more stable and slightly higher than those at -1000 mV during the whole test. Wear volumes measured under both cathodic potentials are similar (Table 5.1.2). Therefore, the wear

at those cathodic potentials is purely mechanical, and the negative currents are controlled by the reduction of water and, partially, of dissolved oxygen [12,13,18,24].

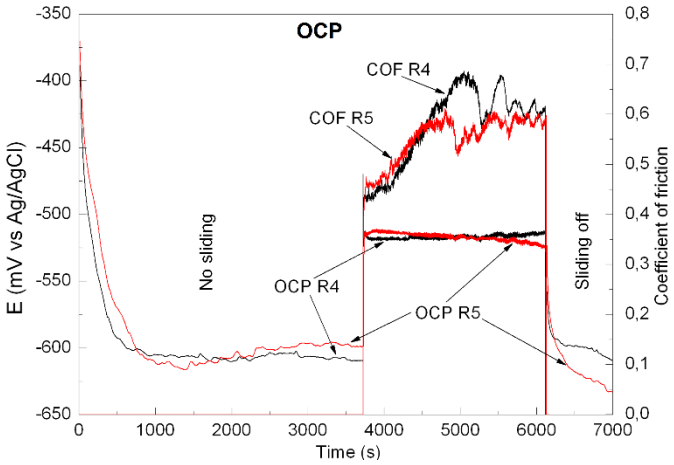

Fig. 5.1.6 Evolution of OCP during the first hour of immersion and the variations of OCP and COF with sliding for both steel grades

For the tests performed under open circuit conditions, the open circuit potential (OCP) was recorded instead of the current. The corrosion currents compiled in Table 5.1.1 for open circuit conditions were obtained by standard Tafel extrapolation in the polarization curves. Before each sliding tests, the OCP of both steels was recorded for the first hour of immersion. Fig. 5.1.6 depicts the evolution of potential during the first hour of immersion and its variation during sliding, plotted together with the evolution of the COF. The tendency of potential during the first hour of immersion in seawater was observed to be the same for both steel grades. The behavior of these steels is the opposite to that observed for passive materials, where the OCP usually shifts towards anodic potentials due to the formation of the protective layer when immersed in some specific electrolytes, and changes again reaching more cathodic potentials when sliding starts, as a consequence of the rupture of that protective layer and the dissolution of the bare material exposed to the electrolyte [4,6,18,23,29,30]. The initial drop in the potential of these active steels to more negative values shown in Fig. 5.1.6 indicates the initiation of corrosion processes in the surface of the steels just after the immersion in seawater. This is attributed to high rate corrosion, since the steel surface at the seawater/metal interface is exposed to the full oxygen concentration of the solution [31]. The microscopic examination of the samples confirmed that corrosion started as localized in the form of pits, and spread until the whole surface is covered by an uniform corrosion. Once the oxygen in the interface has been consumed, a stabilization of the potential is observed since a further diffusion of oxygen from the bulk water to the corroding surface is necessary for corrosion to continue.

As soon as the alumina ball comes into contact with the surface of the steels, the OCP measured towards more positive values. The OCP measurement is a mixture lecture of potentials on the surface of the studied material [4,22,23]. The inhomogeneities in the surface of the materials act as microbatteries due to the difference in the potential with reference to that of the rest of the surface, and the recorded potential is the result of the two differentiated potentials of the cathodic and small anodic regions. The result of the sliding in the surface of the steels is the formation of a macrobattery, where the potential in wear track seems to be more cathodic than that of the unworn area. The continuous action of the alumina ball modifies the kinetics of corrosion in the track, since the material in the top is constantly being removed, slowing down corrosion processes occurring in that area. The modification of the potential in the track increases the difference between the two regions in the sample, and the mixed OCP lecture shifts towards more positive

values. Although the track seems to be less subjected to corrosion, the difference in potentials generated in the two regions affects the corrosion of the unworn area, where the potential is more anodic and, thus, the material is subjected to higher rate corrosion processes. Therefore, sliding results in the formation of a macrobattery in the surface of the steels where the worn area acts as the cathode and the unworn one as the anode.

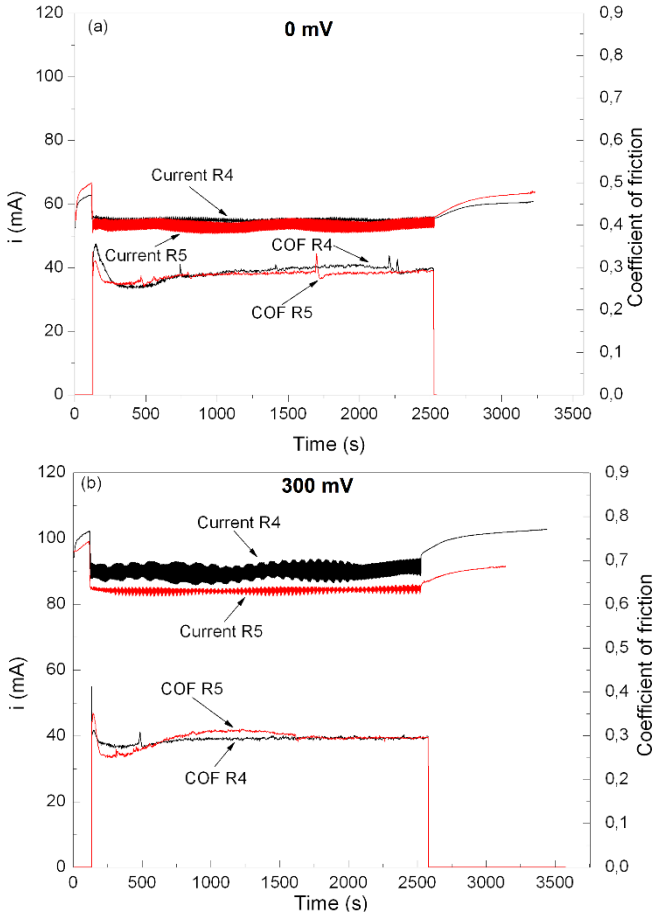

Fig. 5.1.7 Evolution of the current and COF recorded before, during and after sliding for both steel grades under anodic potentials: (a) 0 mV and (b) 300 mV

At anodic potentials, the currents registered during sliding of both steels are positive and further higher when compared to those measured at OCP conditions. As for the previous tests, a decrease in the current is observed during sliding for both steels, as shown in Fig. 5.1.7a and b. At 0 mV, the current values registered before sliding are between 60 and 67 mA for both steel grades, whereas at 300 mV the current values before sliding are close to 100 mA. In both cases, the shift in current due to sliding is of about 15 mA.

In all the tests performed at different potentials the current shifts to lower values when sliding is applied (Fig. 5.1.5 and Fig. 5.1.7). This observation is again against to that observed for passive materials, where the current tends to increase during sliding processes indicating the start of corrosion dissolution processes in the track, where the protective layer has been removed [4,6,18,23,29,30]. The samples of steel grade R4 and R5 immersed in seawater are constantly being dissolved, since no effective protective layer is formed on their surfaces. Hence, that shift in the current indicates that the corrosion kinetics in the track and in the outer part of the track is different. Thus, considering that the shift of current is to more negative values, this suggests that the corrosion rate in the worn area is lower than that of the unworn area. This is a consequence of the continuous action of the alumina ball against the surface of the steel, which removes the bare material and the corrosion products present in the track,

reducing the corrosion kinetics in that area. Therefore, sliding results in wear accelerated corrosion process in the unworn area, leading to high loss of material due to the sum of the material loss by tribocorrosion in track and the material loss by corrosion in the outer part of the track.

Effect of potential on the coefficient of friction

The average current and the average coefficients of friction (COF) obtained in the sliding tests under different potentiostatic conditions are summarized in Table 5.1.1.

Table 5.1.1 Average current and COF obtained from the potentiostatic tests under different potentials for the steel grades R4 and R5

Potential (mV vs Ag/AgCl)	Average current (mA)		Average COF	
	R4	R5	R4	R5
-1000	-0.6175	-0.6190	0.2753	0.2598
-650	-0.5463	-0.5990	0.3341	0.3387
-395 (OCP R4)	0.1134 (I_{corr})*	-	0.5782	-
-371 (OCP R5)	-	0.1032 (I_{corr})*	-	0.5526
0	54.9290	53.3231	0.2894	0.2834
300	90.0013	84.2813	0.2946	0.2931

**Corrosion currents measured from the polarization curves*

The evolution of the coefficients of friction with time and the average values registered of both steel grades are similar for the different applied potentials. In the cathodic region, the friction coefficient recorded is low, and it decreases as the sliding time increases (Fig. 5.1.5a and b). At open circuit conditions, the coefficient of friction increases gradually with increasing sliding time. At anodic potentials, the average COF values are low and practically constant for both steels.

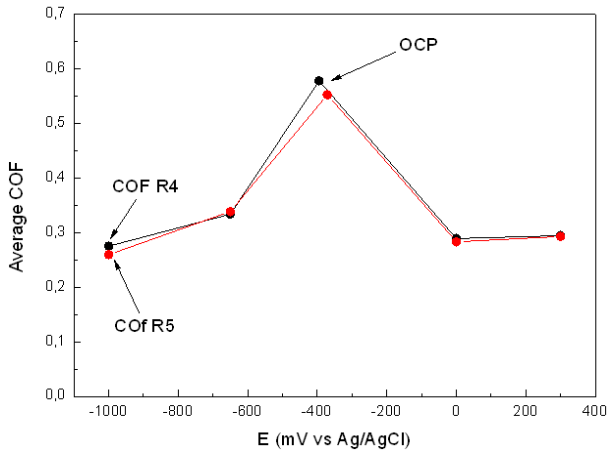

Fig. 5.1.8 Average COF as a function of applied potential

The average COF as a function of applied potential plotted in Fig. 5.1.8 shows how the material and the corrosion products removed from the surface can modify the frictional behavior of the surface and thus, the wear mechanism. The low values of the friction coefficient in the cathodic region for both steels are attributed to the particles detached from the metal that remain between the steel and the ball. These particles are sheared by the continuous action of the counterbody and become smeared in the contact area, where they act as a lubricant accommodating the sliding by shearing [12,13,17,32]. The coefficient decreases with the increasing sliding time, as a consequence of a greater amount of particles smeared in the contact. Furthermore, as part of the material is recirculated but not removed from the contact, the total material loss in the wear track is lowered. Some smeared layers are eventually eliminated from the wear track due to the continuous action of the countermaterial. According to the theory of adhesion [33], the

coefficient of friction corresponds to the shear stress and hardness ratio, being of 0.2 for most metals. The friction coefficients measured for the tests performed at cathodic potentials are close to that value, confirming the prediction made.

At open circuit conditions (OCP), the coefficient of friction increases gradually with increasing sliding time and eventually remains more constant. The increase in the coefficient can be attributed to the continuous superficial modification produced by the sliding which, at first, removes the oxides formed during the first 3600 s of immersion, changing the nature and morphology of the contact area between the countermaterial and the steel. Then, the equilibrium between the oxide formation rate and their removal is reached, and the coefficient acquires more constant values.

At anodic potentials, the average COF values are low and practically constant for both steels. The low values of the coefficients of friction suggest that the layer of corrosion products formed in the surface at high anodic potentials have the ability of reducing the friction and act as a lubricant. The micrographs of the samples tested at anodic potentials show a great amount of corrosion products in the wear tracks, confirming the existence of compact layers of oxides that reduce the frictional forces measured.

Effect of potential on the wear track

The total material loss in volume (V_{tot}) obtained by the weight difference in the samples before and after each test, and the volume of the wear tracks (W_{tr}) measured with the confocal microscope are listed in Table 5.1.2.

Table 5.1.2 Total material loss and wear track volume of the steel grades R4 and R5 tested under different potentials

Potential (mV vs Ag/AgCl)	Total material loss, V_{tot} (mm^3)		Wear track Volume, V_{tr} (mm^3)	
	R4	R5	R4	R5
-1000	0.0128	0.0115	0.0088	0.0074
-650	0.0641	0.0512	0.0116	0.0891
-395 (OCP R4)	0.3333	-	0.0216	-
-371 (OCP R5)	-	0.3205	-	0.0199
0	9.3987	8.6141	0.0794	0.0782
300	12.1721	10.2564	0.0947	0.0923

All the samples were weighed before and after each test, so the total material loss due to tribocorrosion in the wear track and corrosion in the outer part of the track is calculated, and the results are compiled in Table 5.1.2. Fig. 5.1.9 shows the total material loss (V_{tot}) against the applied potential. It is evident that the material loss increases with increasing potential, but that increasing tendency seems to be slightly reduced at high anodic potentials. In passive materials, this is attributed to the transpassive potential [16]. As for the active steels studied in this work, no transpassive region is observed in the polarization curves (Fig. 5.1.2), since the material is constantly dissolving in the electrolyte due to the low protective quality of the rust layer formed on the surface. Therefore, such decrease in the trend of material loss can be attributed to a deceleration of corrosion kinetics due to both the saturation where the oxygen in the electrolyte is almost consumed, and the inhibition of oxygen diffusion to the corroding surface by the oxide layer and corrosion products formed on top of the surface. The seawater solution volume used in the tests is small, and the reduction of dissolved oxygen in small compartments has been found to be noticeable when the corrosion rate is high [34], as in the case of these mooring steels when polarized at anodic potentials. Furthermore, some researchers have observed that the iron oxide layer formed on top of the surface and the pits in carbon steels immersed in NaCl solutions acts as a physical barrier to the

oxygen diffusion to the corroding surface [22], slowing down the rate of corrosion processes.

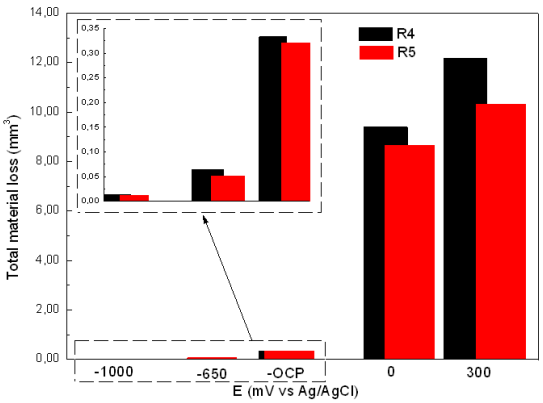

Fig. 5.1.9 Total material loss as a function of applied potential

Fig. 5.1.10 shows cross-section profiles measured across the wear tracks generated in the steels under different potentials. For both steels, the surface of the wear tracks observed in the profiles are smooth at cathodic and open circuit potentials, but an increase of roughness is observed at anodic potentials. The cross-section profiles of the tracks of the steels verify that the track size is increased with increasing potential for both steels. The small wear volumes measured in the samples tested at cathodic potential show the effectiveness of cathodic protection against tribocorrosion. The roughness of the surface of both the worn and unworn areas increases with increasing potentials, since more corrosion processes occur at higher potentials. As it was expected, at higher anodic potentials the major material loss is due to the dissolution of the metal in the outer part of the track rather than the material loss in the wear track due to the simultaneous action of wear and corrosion. This is evidenced when comparing the values of the total material loss (V_{tot}) and the material loss in the track (W_{tr}) in Table 5.1.2.

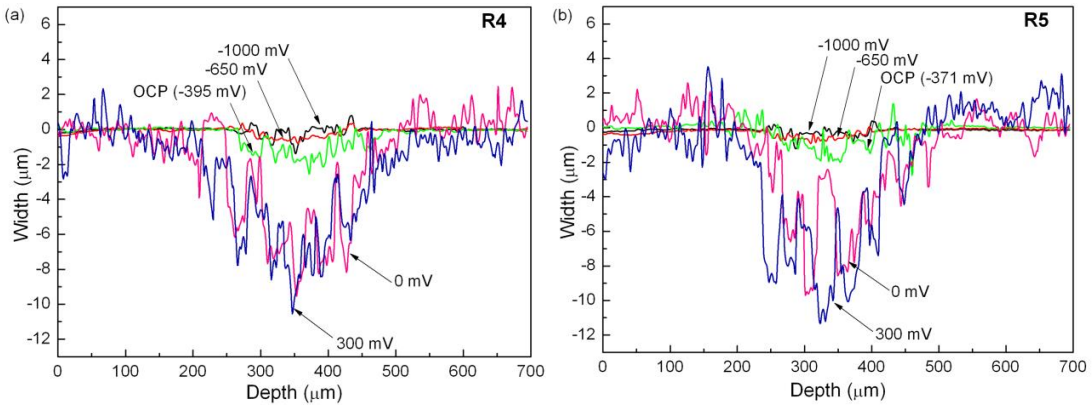

Fig. 5.1.10 Cross section profiles across the wear tracks at different potentials on the steel grades (a) R4 and (b) R5

5.1.3.3 Wear-corrosion synergism

Material loss rate has been obtained by using the equations described in Section 5.1.2.3 (Eqs. (2.I)-(2.IV)). The total material loss (T) is the sum of the wear rate in the absence of corrosion (W_0), the corrosion rate in the absence of wear (C_0) and the synergistic component (S), which is, in turn, the sum of interactions between corrosion and wear processes.

In the tests, T was calculated from the weight loss measured in the samples in the potentiostatic sliding tests at OCP potential, whereas W_0 was obtained from the weight

loss of the samples tested under applied cathodic potential (-1000 mV). C_W and C_0 were calculated from the weight difference in the samples used for potentiodynamic tests under sliding and without sliding conditions, respectively.

The wear and corrosion synergistic data compiled in Table 5.1.3 show that the total material loss (T) is similar in both steels. The higher amount of material loss is found to be due to mechanical wear rather than corrosion dissolution. Corrosion rate (C_W) seems to be influenced by the action of wear, and the change observed in the corrosion rate (ΔC_W) is similar in both steels. The differences between the results obtained for the two steels are negligible. Thus, both steel grades can be considered to have the same tribocorrosion behavior in seawater.

Table 5.1.3 Wear and corrosion synergistic data

Steel grade	Material loss rate, ($mm^3/mm^2/yr$)						
	T	W_0	C_0	C_w	S	ΔC_w	ΔW_c
R4	1.7047	0.6556	0.0581	0.0876	0.9909	0.0295	0.9614
R5	1.6391	0.6228	0.0519	0.0740	0.9643	0.0220	0.9422

5.1.3.4 Surface morphology

Fig. 5.1.11 show the optical micrographs of the wear track of steel grade R4 produced by sliding tests at the different applied potentials. The surface of the sample tested at the first cathodic potential of -1000 mV is smooth, as observed in the cross-section profiles of the wear tracks. The sample is free from corrosion products, and abrasion lines are clearly observed (Fig. 5.1.11a). At -650 mV, the state of the surface is similar to that observed at -1000 mV. Corrosion products are not detected either in the surface nor in the track (Fig. 5.1.11b). However, the track is wider, and the abrasion lines are deeper when comparing to that of the samples tested at -1000 mV, in accordance with the track profiles. In the sample tested at open circuit potential, both worn and unworn areas are covered by large shaped corrosion products (Fig. 5.1.11). Piled material is also observed at the edge of the track, which seems to have undergone corrosion processes. At anodic potentials, the surface of the steel is highly degraded in comparison with the previous samples (Fig. 5.1.11d and e). The surface is completely covered by corrosion products, and corrosion is also present in the tracks. Abrasion is represented by the lines parallel to the sliding movement, but it is less evident than in the samples tested at more cathodic potentials.

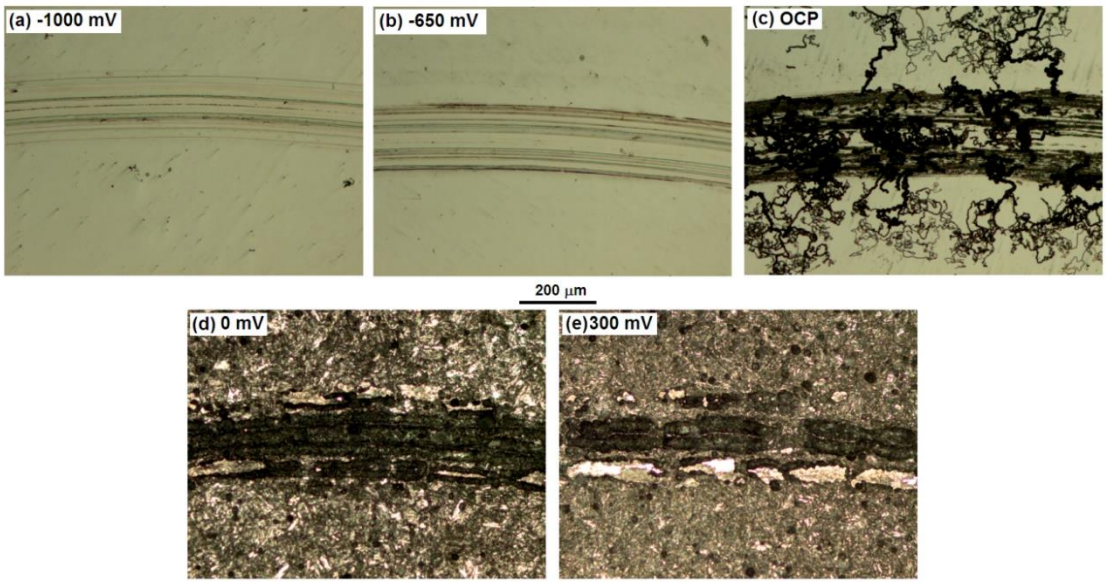

Fig. 5.1.11 Optical micrographs of the wear tracks in the steel grade R4 at different applied potentials

The micrographs of the tracks of steel grade R5 are depicted in Fig. 5.1.12 for all the applied potentials. The results are very similar to those of the steel grade R4. Corrosion is not present in either of the samples tested at cathodic potentials, but the wear tracks are wider, and the abrasion lines are deeper under -650 mV. Similar large shaped corrosion products are formed in the steel grade R5 at open circuit potential. Finally, the degradation observed in the samples at anodic potentials is comparable to that in the samples of steel grade R4. The sizes of the wear tracks of both steels observed by optical microscopy are similar, in agreement with that measured by profilometry.

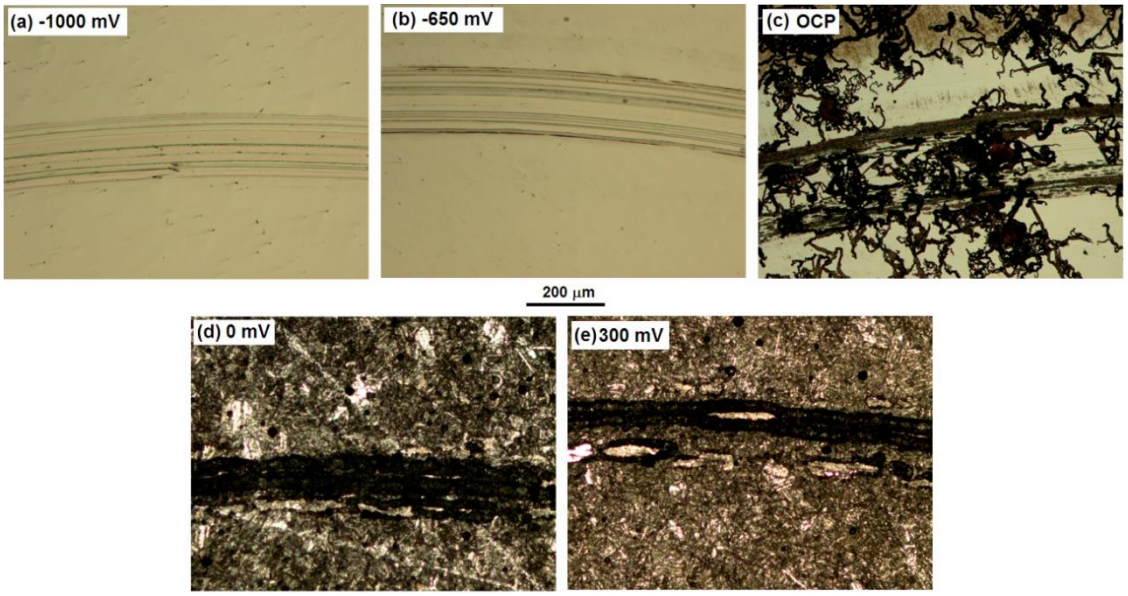

Fig. 5.1.12 Optical micrographs of the wear tracks in the steel grade R5 at different applied potentials

5.1.4 Conclusions

In the present work, the tribocorrosion behavior of the steel grades R4 and R5 used in mooring line components has been studied in synthetic seawater. For this aim, potentiodynamic and potentiostatic tests have been performed. The following conclusions can be drawn:

- The polarization curves obtained with and without sliding present a great activation stretch in the anodic region, where the current increases several orders of magnitude for small potential variations, indicating that the steels are very active materials and undergo high rate corrosion processes when immersed in seawater.
- The evolution of potential and current under the simultaneous action of wear and corrosion is the opposite of that observed for passive materials. Sliding results in an increase in the OCP registered and a decrease in the current measured. This is due to the different corrosion kinetic inside the track, which have more cathodic potential that the outer part of the track, indicating that sliding accelerates corrosion in the unworn area.
- The coefficient of friction of the steels is strongly influenced by the corrosion products and the applied potential. At cathodic potentials, the COF is reduced due to detached particles of the metal that accommodate sliding by shearing. The oxide products film formed at high anodic potential seems to have a lubricating ability.
- The total material loss increases with increasing applied potential. At higher anodic potentials, the major material loss is due to the dissolution of the alloy in the outer part of the track rather than the material loss in the wear track due to the simultaneous action of wear and corrosion.

- The tests performed revealed that both steel grades exhibited a similar tribocorrosion response under the selected testing conditions. The differences in the results obtained for the synergism quantification are negligible and, therefore, both steels can be considered to have the same tribocorrosion behavior in seawater.

5.1.5 Acknowledgments

Authors would like to thank the Spanish Ministry of Economy and Competitiveness for funding the project "*Soluciones de fondeo ad hoc para plataformas offshore de oil and gas*", INNPACTO 2012, IPT-2012-1167-120000. Authors would also like to thank the project partners: Vicinay Marine Innovación A.I.E., Gerdau Aceros Especiales S.L., CSIC-CISDEM and IK4-Azterlan.

5.1.6 References

[1] R.E. Melchers, T. Moan, Z. Gao. *Corrosion of working chains continuously immersed in seawater*. J Mar Sci Technol (2007) 12:102-110

[2] A.O. Vázquez-Hernández, G.B. Ellwanger, L.V.S. Sagrilo. *Long-term response analysis of FPSO mooring systems*. Applied Ocean Research 33 (2011) 375– 383

[3] A.O. Vazquez-Hernandez, G.B. Ellwanger, L.V.S. Sagrilo. *Reliability-based comparative study for mooring lines design criteria*. Applied Ocean Research 28 (2006) 398–406

[4] J.-P. Celis and P. Ponthiaux (Eds.). *Testing tribocorrosion of passivating materials supporting research and industrial innovation: Handbook*. Maney publishing (2012). ISBN: 978-1-907975-20-2

[5] ASTM G40-13. *Standard Terminology Relating to Wear and Erosion*. ASTM International, West Conshohocken, PA, 2013

[6] D. Landolt, S. Mischler, M. Stemp. *Electrochemical methods in tribocorrosion: a critical appraisal*. Electrochimica Acta 46 (2001) 3913-3929

[7] D. Landolt, S. Mischler, M. Stemp, S. Barril. *Third body effects and material fluxes in tribocorrosion systems involving a sliding contact*. Wear 256 (2004) 517–524

[8] S. Mischler. *Triboelectrochemical techniques and interpretation methods in tribocorrosion: A comparative evaluation*. Tribology international 41 (2008) 573-583

[9] P. Jemmely, S. Mischler, D. Landolt. *Electrochemical modelling of passivation phenomena in tribocorrosion*. Wear 237 (2000) 63–76

[10] N. Diomidis, J.-P. Celis, P. Ponthiaux, F. Wenger. *A methodology for the assessment of the tribocorrosion of passivating metallic materials*. Lubrication Science 2009; 21: 53–67

[11] H. Shih (Ed.). *Corrosion Resistance*. InTech (2012). ISBN 978-953-51-0467-4

[12] S. Mischler, A. Spiegel, D. Landolt. *The role of passive oxide films on the degradation of steel in tribocorrosion systems*. Wear 225-229 (1999) 1078-1087

[13] S. Mischler, A. Spiegel, M. Stemp, D. Landolt. *Influence of passivity on the tribocorrosion of carbon steel in aqueous solutions*. Wear 251 (2001) 1295-1307

[14] S.W. Watson, F.J. Friedersdorf, B.W. Madsen, S.D. Cramer. *Methods of measuring wear-corrosion synergism*. Wear 181-183 (1995) 476-484

[15] M.S. Jellesen. *Tribocorrosion properties of metallic materials and effects of metal release*. Ph. D. Thesis, August 2007

[16] Y. Sun, Vipul Rana. *Tribocorrosion behavior of AISI 304 stainless steel in 0.5 M NaCl solution*. Materials Chemistry and Physics 129 (2011) 138–147

[17] J. Chen, F.Y. Yan. *Tribocorrosion behaviors of Ti-6Al-4V and Monel K500 alloys sliding against 316 stainless steel in artificial seawater*. Transactions of Nonferrous Metals Society of China 22(2012) 1356-1365

[18] J. Chen, Q. Zhang, Q.A. Li, S.L. Fu, J.Z. Wahng. *Corrosion and tribocorrosion behaviors of AISI 316 stainless steel and Ti6Al4V alloys in artificial seawater*. Transactions of Nonferrous Metals Society of China 24(2014) 1022−1031

[19] K. Xiao, C.F. Dong, X.G. Li, F.M. Wang. *Corrosion Products and Formation Mechanism During Initial Stage of Atmospheric Corrosion of Carbon Steel*. Journal of Iron and Steel Research, International. 2008, 15(5): 42-48

[20] J.G. Castaño, C.A. Botero, A.H. Restrepo, E.A. Agudelo, E. Correa, F. Echeverría. *Atmospheric corrosion of carbon steel in Colombia*. Corrosion Science 52 (2010) 216-223

[21] H. Möller, E.T. Boshoff, H. Froneman. *The corrosion behavior of a low carbon steel in natural and synthetic seawaters*. The Journal of The South African Institute of Mining and Metallurgy. Volume 106 (August 2006)
[22] L. Cáceres, T. Vargas, L. Herrera. *Influence of pitting and iron oxide formation during corrosion of carbon steel in unbuffered NaCl solutions*. Corrosion Science 51 (2009) 971-978
[23] J.-P. Celis, P. Ponthiaux, F. Wenger. *Tribo-corrosion of materials: Interplay between chemical, electrochemical, and mechanical reactivity of surfaces*. Wear 261 (2006) 939–946
[24] P. Ponthiaux, F. Wenger, D. Drees, J.P. Celis. *Electrochemical techniques for studying tribocorrosion processes*. Wear 256 (2004) 459–468
[25] Offshore Standard DNV-OS-E302, Det Norske Veritas. Offshore Mooring Chain. October 2013
[26] Gwidon W. Stachowiak, Andrew W. Batchelor. *Engineering tribology*. Butterworth Heinemann (2005). ISBN: 978-0-7506-7836-0
[27] ASTM G119-09(2016). *Standard guide for determining synergism between wear and corrosión*. ASTM International, West Conshohocken, PA, 2016
[28] W. Liu, Q. Zhou, L. Li, Z. Wu, F. Cao, Z. Gao. *Effect of alloy element on corrosion behavior of the huge crude oil storage tank steel in seawater*. Journal of Alloys and Compounds 598 (2014) 198–204
[29] C.-O.A. Olsson, D. Landolt. *Passive films on stainless steels: chemistry, structure and growth*. Electrochimica Acta 48 (2003) 1093-1104
[30] X. Luo, X. Li, Y. Sun, H. Dong. *Tribocorrosion behavior of S-phase surface engineered medical grade Co-Cr alloy*. Wear 302 (2013) 1615-1623
[31] R. E. Melchers, R. Jeffrey. *Early corrosion of mild steel in seawater*. Corrosion Sciene 47 (2005) 1678-1693
[32] K. Kato. *Wear in relation to friction-a review*. Wear 241 (2000) 151–157
[33] E. Rabinowicz. *Friction and Wear of Materials. Second edition*. John Wiley and Sons (2013) ISBN 978-0-471-83084-9
[34] M. Fabbricino, G.V. Korshin. *Changes of the corrosion potential of iron in stagnation and flow conditions and their relationship with metal release*. Water Research 62 (2014) 136-146

Contribution 2

Influence of temperature on the corrosion and tribocorrosion behavior of High-Strength Low-Alloy steels used in offshore applications

Tribology International 121 (2018) 341-352

Contribution 2: Tribology International 121 (2018) 341-352

5.2. INFLUENCE OF TEMPERATURE ON THE CORROSION AND TRIBOCORROSION BEHAVIOR OF HIGH-STRENGTH LOW-ALLOY STEELS USED IN OFFSHORE APPLICATIONS

A. López-Ortega[a], R. Bayón[a], J.L. Arana[b], A. Arredondo[c], A. Igartua[a]

[a] *IK4-TEKNIKER, Eibar, Spain*
[b] *Department of Metallurgical and Materials Engineering, University of the Basque Country, Spain*
[c] *Vicinay Marine Innovación, Spain*

ABSTRACT

Tribocorrosion is an important failure cause of High-Strength Low-Alloy steel (HSLA) components in offshore applications due to the synergistic effect of wear and the corrosiveness of seawater. In this work, the effect of temperature on the tribocorrosion behavior of two steel grades has been investigated by performing tribocorrosion tests under reciprocating sliding at two electrolyte temperatures. The total material loss due to corrosion in the unworn surface and due to tribocorrosion in the wear track was quantified. Sliding was found to accelerate the corrosion in the unworn area. Furthermore, temperature was confirmed to have an important effect on the tribocorrosion behavior of the steels, in terms of higher material losses due to corrosion at higher test temperature.

Keywords: *High Strength Low Alloy steel; Tribocorrosion; Seawater; Offshore*

5.2.1 Introduction

The materials working in offshore applications, are subjected to very harsh environmental conditions that accelerate their degradation. In marine environments, several phenomena take place simultaneously, which can shorten the useful life of structural materials leading to unpredicted failures. In the case of mooring systems, for instance, tribocorrosion plays a vital role in terms of premature failure of components [1]. On the one hand, the relative motion between chain links and connectors generated by waves, wind and ocean currents [2,3] leads to a continuous wear process in the contact surfaces. Moreover, corrosion is another important phenomenon to take into consideration in marine environments. The components that are continuously submerged or located in the splash zone of offshore structures, are subjected to high rate corrosion processes [4]. When wear and corrosion take place simultaneously, the process is known as tribocorrosion. There is a synergism between wear and corrosion, since the material loss when the two processes are occurring simultaneously, is greater than when they act separately [5,6].

Tribocorrosion of passive materials, e.g., stainless steels and titanium alloys, has been widely studied during the last decades for different applications and corrosive environments. It is well known that passive materials form a protective oxide layer of few nanometers in the surface [5-7], and that wear locally destroys and removes this layer, exposing the underlying fresh material to the electrolyte. The unprotected material in the track generated by wear undergoes corrosion while the intact protective film in the unworn surface remains undamaged [5-8]. However, the use of passive materials in offshore applications is limited, due to their high cost in comparison with lower alloyed steels, that meet the mechanical requirements at the expense of a higher corrosion resistance. For instance, High Strength Steels (HSS), with yield strength values ranging

from 460 to 960 MPa, are commonly used in offshore structural applications due to the high resistance/weight ratio. Submerged structures, anchor systems, chains and connectors composing mooring systems of offshore oil and gas platforms are predominantly manufactured with HSS steels. This kind of low-alloyed steels do not grow a protective oxide layer in the surface as a consequence of their low content in alloying elements precursors of passive film formation (Cr, Ni, Mo, etc.). The dominant oxide formed on their surface is the ferric oxyhydroxide (FeOOH) compound. This rust film is highly porous and presents week adhesion bonds [9-12], allowing the electrolyte to penetrate through and reach the bare steel leading to continuous corrosion processes and high rates of material loss. Therefore, unlike passive alloys, low alloy steels are subjected to corrosion not only in the regions where the rust layer has been removed due to wear, but also in the remaining surface where the oxide layer does not form an effective barrier. Consequently, the surface degradation experienced in these steels is the sum of the material loss resulting from tribocorrosion in the contact area and the wear-accelerated corrosion process at the unworn area [13].

It is well known that the corrosion rate of metals in seawater is influenced by a series of variables, i.e., salinity, pH, temperature, dissolved oxygen concentration or microorganisms [4,14,15]. The temperature of seawater is not constant but varies depending on the geographical location and ocean currents, ranging from -2 ºC in the poles to 35 ºC in the equator [15-17]. Moreover, there is also a variation of temperature with the depth, reaching values close to 0 ºC at the lower depths [14,15]. Temperature can affect corrosion in several ways. When the corrosion rate is governed by the elementary process of metal oxidation, the corrosion rate increases exponentially with the increase in temperature [15,16]. Therefore, temperature is an important factor to consider in terms of corrosion degradation of the steels that compose submerged components.

Unlike in the case of passive materials, little is known about the tribocorrosion behavior of active materials, e.g., the HSLA steels used in offshore components. Furthermore, while a good understanding of the effect of temperature on corrosion of carbon steels has been achieved, little is known about the effect of temperature when the steels are subjected to the simultaneous action of wear and corrosion.

In the present work, the tribocorrosion behavior of two steel grades commonly used in offshore components is studied at two seawater temperatures. For this aim, reciprocating tribocorrosion tests were performed at room (23 ºC) and low temperature (2 ºC), under ball-on-disc configuration. The temperature of 23 ºC corresponds to the sea temperature in the Gulf of Mexico, whereas the low temperature of 2 ºC was selected in order to reproduce the climatic conditions that mooring lines are subjected to in the North Sea [18].

The tribocorrosion test procedure employed in this work has been used by several researchers in the tribocorrosion assessment of passive materials [8,19-23], and was standardized in 2016 [24]. The procedure was selected both to analyze and comprehend the behavior of active materials as well as to determine the suitability of the procedure designed for passive materials for the evaluation of less-studied active materials. The combination of tribological and electrochemical techniques commonly used in tribocorrosion studies allows the in-situ characterization of the state of the surfaces during the tests [13,25,26].

5.2.2 Experimental Procedures

5.2.2.1 Materials and samples preparation

The present work studies the tribocorrosion behavior of two steel grades commonly used in the manufacturing of offshore components. The steels are the R4 and R5 grades, approved by the Classification Societies [27]. These are High Strength steel grades manufactured with the chemical compositions of low and medium alloy steels (Cr, Ni, Mo, V, etc.). The alloying percentages slightly vary depending on the hardenability (mass effect) and the specific mechanical characteristics of each steel grade. The components manufactured with these steel grades, e.g., mooring chain links, are welded by means of flash butt welding (FBW), and eventually heat treated to reach the desired mechanical properties.

The test samples were discs of 24 mm in diameter and 7.9 mm thick, directly machined from real components. The surface of the samples was mirror-polished to low roughness values (Ra<0.05μm). After polishing the samples and prior to the tests, the discs were cleaned in an ultrasonic bath with ether and acetone, dried with compressed air, and stored in a desiccator to avoid contamination or corrosion.

5.2.2.2 Tribocorrosion tests

The tribocorrosion tests consisted of reciprocating ball-on-disc tests in the tribometer schematically depicted in Fig. 5.2.1. The electrochemical cell was placed in the reciprocating plate of the tribometer, so both electrochemical and mechanical parameters were simultaneously controlled during the tests. The tribocorrosion test system was composed of a ball-on-disc UMT-CETR3 reciprocating tribometer connected to an Autolab-Metrohm PGSTAT30 potentiostat.

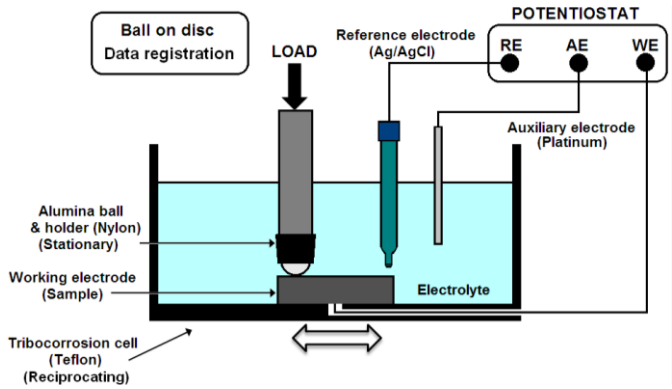

Fig. 5.2.1 Reciprocating tribocorrosion ball-on-disc experimental setup used in this work

The electrolyte used in the tests was synthetic seawater with heavy metals prepared in accordance with the ASTM D1141 standard. 150 ml of this solution was used in each test. A commercial Ag/AgCl (KCl 3M) and a platinum wire were used as the reference electrode and auxiliary electrode, respectively. The test sample was connected as the working electrode. The potential of the reference electrode is of 207 mV versus the Standard Hydrogen Electrode (SHE), and all the potentials presented in this work are referred to the Ag/AgCl electrode. The tests were performed at two electrolyte temperatures and under aerated conditions. The higher temperature, of 23 ºC represented the seawater temperature in the Gulf of Mexico, whereas the low temperature of 2 ºC represented the water temperature in the North Sea [18]. The tests at 23 ºC were performed at laboratory facilities with controlled climatic conditions of 23 ºC and 50% HR. The low temperature of 2 ºC tests were done after introducing the

tribometer in a climatic chamber, controlling both temperature and humidity (0% HR). The exposed surface of the samples was in all cases of 2.54 cm^2.

The countermaterial used in the tests was an alumina ball of 10 mm in diameter (G28). The ball remained stationary as the electrochemical cell oscillated ensuring a proper contact between the countermaterial and the sample under the selected mechanical conditions. The ball holder and the electrochemical cell were made of nylon and polyethylene, respectively, assuring the electrical isolation of the sample from the metallic components of the tribological equipment.

Prior to the tribocorrosion tests, potentiodynamic polarization tests were performed in the potential range from -1000 mV to +400 mV, at a sweep rate of 1 mV/s. Two polarization curves were obtained for each steel grade at each test temperature: in the absence of sliding (corrosion only) and under sliding (tribocorrosion). In the tests performed during sliding, a normal load of 49 N was applied, corresponding to a maximum average Hertzian contact pressure of 2000 MPa with a contact radius of 215 μm. The ball oscillated at a frequency of 2.5 Hz, with a stroke length of 10 mm. Before the potentiodynamic measurements, the Open Circuit Potential (OCP) was stabilized for 60 minutes.

The test procedure employed for tribocorrosion tests, as described elsewhere [8,19-24], consisted of combining OCP registration and Electrochemical Impedance Spectroscopy (EIS) measurements. At the beginning of the tribocorrosion tests, the OCP of the samples was registered during 3600 s of immersion in the electrolyte, and the mean stable potential value was obtained. Two EIS measurements were performed during the tribocorrosion tests, both under a sinusoidal perturbation of ±10 mV amplitude, at a frequency range from 100 kHz to 10 mHz. The first EIS was recorded after the stabilization time of 3600 s in the electrolyte at OCP conditions, whereas the second one was obtained during sliding process under potentiostatic control, in order to obtain stable values. The potential applied in the second EIS was the potential of the steels during sliding, which was calculated by performing a preliminary short wear test of 600 cycles (4 min) after the first EIS. The potential was registered 2 minutes before sliding, 4 minutes during sliding, and 10 minutes after sliding. The mean potential value during sliding was calculated, and the samples were then polarized at this potential to perform a longer sliding wear test of 11400 cycles, during which the second EIS was measured. The coefficient of friction (COF) was simultaneously recorded during this sliding test. The load, sliding speed and the stroke used in tribocorrosion tests was the same as in the potentiodynamic polarization tests under sliding, previously described. The total duration of sliding was of 80 minutes, corresponding to 12000 cycles. Immediately after the second sliding wear test ended, the samples were removed from the cell, rinsed with alcohol and distilled water and dried with compressed air. The samples were kept in a desiccator until the analysis of their surfaces.

After the test, the morphology of the surfaces was examined by optical microscopy (Leica DM2500MH) and by Field Emission Scanning Electron Microscope (FE-SEM), equipped with Energy Dispersive X-ray Spectrometer (EDS), from OXFORD INCA Synergy. The contact area on the surface of the alumina ball was also examined, but the wear of the ball was found to be negligible. The cross-section profiles of the wear tracks were obtained with a Nikon ECLIPSE ME600 and Sensofar S Neox confocal microscopes. Furthermore, indentation hardness tests were performed in an Akashi AVK-A tester equipped with Vickers indentation device, following the UNE-EN ISO 6507-1:2006 Standard. The measurements were performed with a Vickers diamond pyramid indenter, under a load of 1 Kg and an indentation time of 10 s. The hardness was determined in

two zones of each sample; inside the wear track and outside the wear track in a non-tested area, in order to compare the effects of sliding in the hardness of the steels after tribocorrosion tests. Finally, the roughness of the corroded unworn area of the samples was evaluated by means of a Perthometer M2 (Mar GmbH), under the DIN EN-ISO 4288:1998 Standard.

5.2.2.3 Material loss estimation due to tribocorrosion and corrosion phenomena

The material loss due to tribocorrosion in the wear track (V_{tr}) was determined by calculating the volume of the wear tracks from the cross-section profiles obtained with the confocal microscope. Average width and depth values of the wear tracks were obtained from different locations along the wear track length. The cross-sectional area of the track was estimated by approaching its shape with a semi-elliptical geometry [8]. Finally, the volume of material loss was calculated by multiplying the cross-sectional area by the stroke length of the wear track.

The material loss volume due to electrochemical corrosion in the unworn area (V_{corr}) was calculated by subtracting the volume due to tribocorrosion in the wear track (V_{tr}) to the total material loss (V_{tot}):

$$V_{corr} = V_{tot} - V_{tr} \tag{5.2.I}$$

The total material loss in volume (V_{tot}), was obtained by weighting the test samples before and after each test and multiplying this value by the density of the steels.

5.2.3 **Results and Discussion**

5.2.3.1 Polarization curves with and without sliding

The polarization curves of the R4 and R5 steels were obtained under corrosion (no sliding) and tribocorrosion (sliding) conditions at 23 and 2 ºC. All the curves are plotted together in Fig. 5.2.2, and the corrosion potentials and corrosion currents values obtained by standard Tafel extrapolation are given in Table 5.2.1.

Table 5.2.1 Corrosion potentials and currents for the two steel grades in synthetic seawater at 23 and 2 ºC, obtained from the polarization curves with no sliding and under sliding conditions

	No Sliding				**Sliding**			
	R4		**R5**		**R4**		**R5**	
	23 ºC	**2 ºC**	**23 ºC**	**2 ºC**	**23 ºC**	**2 ºC**	**23 ºC**	**2 ºC**
E_{corr} (mV)	-680	-624	-668	-611	-535	-494	-497	-459
i_{corr} (µA/cm²)	9.40	2.58	4.95	2.44	31.47	9.66	13.50	8.14

The curves presented in dashed lines in Fig. 5.2.2 correspond to the tests without sliding at both temperatures. The results obtained at 23 ºC show that the steels present a great activation stretch, with no passive plateau. The current increases rapidly for small potential variations above the corrosion potential, indicating that the steels are very active in seawater and corrode with high corrosion rates. At 2 ºC, the polarization curves are anodically displaced with respect to the ones at 23 ºC. Furthermore, the activation stretch is less pronounced in the curves at 2 ºC, and the anodic currents registered are considerably smaller, indicating that the corrosion kinetics of the steels at low temperature is slower.

The polarization curves obtained under sliding conditions are presented in straight lines in Fig. 5.2.2. In these tests too, the curves of both steels at 2 ºC are anodically displaced with reference to those at 23 ºC. The curve corresponding to the steel grade R4 at 2 ºC and the steel grade R5 at 23 ºC are almost superimposed. The difference in the anodic

currents registered due to temperature is not as pronounced as in the tests performed without sliding, which indicates that the corrosion kinetics of the steel is less influenced by temperature when wear and corrosion are acting simultaneously.

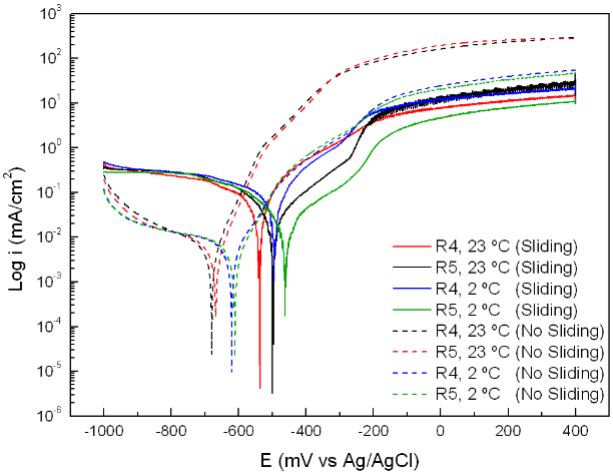

Fig. 5.2.2 Polarization curves of the R4 and R5 steel grades in absence of sliding and under sliding, at 23 ºC and 2 ºC

Sliding has been found to modify the electrochemical behavior of both steels. When comparing all the polarization curves obtained at 23 ºC, the activation stretch in the anodic region is noticeably reduced in the tests performed with sliding. When the samples are subjected to wear, a difference of an order of magnitude is observed between the anodic currents in the range from -100 to 400 mV. At 2 ºC, this difference in the anodic currents is not so pronounced, being less than 100 mA in the same potential ranges. However, there is an increase in the corrosion currents registered in the tests performed with sliding at both temperatures (Table 5.2.1).

The dissimilarity in the current values observed in the absence of sliding at different temperatures confirms the slower corrosion rate at a lower temperature, as previously reported by several researchers [9,14-17]. The same trend is observed in the results with sliding, where the curves at low temperature are shifted towards more positive potential values. On the other hand, the displacement observed for the curves under sliding with reference to those in the absence of sliding at both temperatures, indicates that there is a difference in the corrosion kinetics of the worn and unworn areas. This is a consequence of the continuous mechanical action of the countermaterial above the surface of the steels, which alters the natural trend of corrosion dissolution in the contact area and seems to slow down the corrosion kinetics of the material in the track [13]. However, the higher corrosion currents registered under sliding conditions suggest that wear increases the corrosion rates of the steels.

The surface of the samples was analyzed by means of optical microscopy. The optical micrographs of the samples of the steel grade R4 tested with and without sliding at 23 and 2 ºC are presented in Fig. 5.2.3. The micrographs of the R5 steel were very similar to those of the R4 steel showed in Fig. 5.2.3 and, thus, are not presented in the paper. The micrographs revealed the surface of the steels to be covered by generalized corrosion products, and some localized corrosion in the form of pits is also observed in all the specimens. In the samples tested under sliding conditions, corrosion products can be clearly observed in the wear tracks. The unworn surface of the samples tested under sliding at 23 ºC seems to be more degraded in comparison with those tested at 2 ºC.

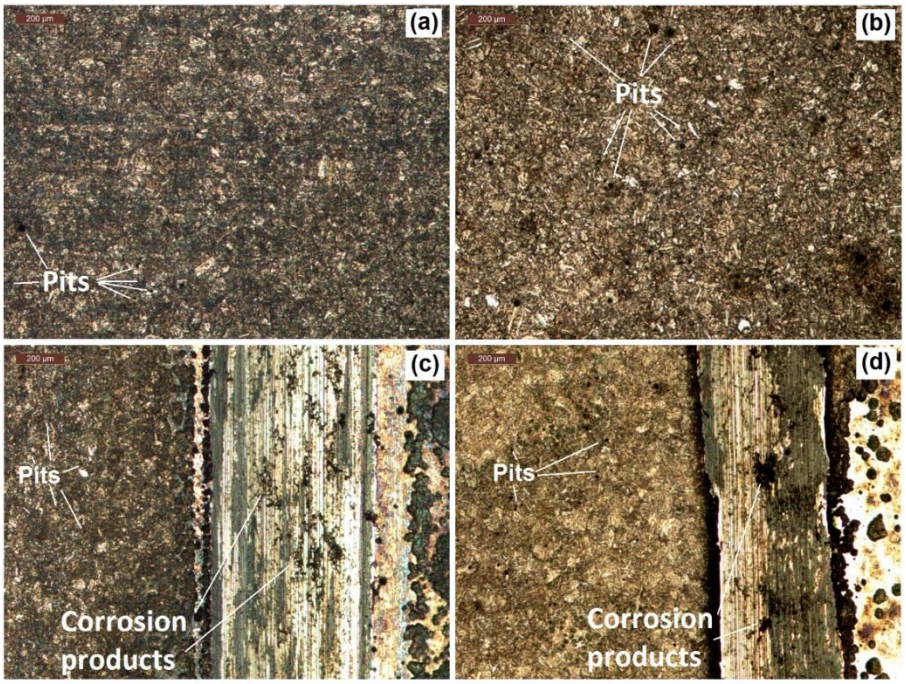

Fig. 5.2.3 Optical micrographs of the R4 steel grade (a) under no sliding condition at 23 ºC, (b) under no sliding condition at 2 ºC, (c) under sliding condition at 23 ºC, and (d) under sliding condition at 2 ºC

5.2.3.2 Tribocorrosion tests

Fig. 5.2.4a depicts the evolution of the open circuit potential (OCP) during the first hour of immersion in synthetic seawater of the two steels at 23 and 2 ºC. There is an initial drop in potential observed in all the samples, followed by a stabilization after 2000 seconds of immersion. This is the opposite response observed for passive materials, where the potential shifts towards nobler values as a consequence of the formation of the characteristic oxide layer in the surface [5,7,8,25,26]. The shift of potential towards negative values observed in these active steels, indicates the initiation of corrosion processes in the surface, which is exposed to the full oxygen concentration of the solution. This is known as phase 0 or activation control [4,28-30], during which a series of phenomena take place simultaneously, e.g., corrosion by activation control. In all the samples, corrosion was observed to start as localized in the forms of pits, which then spread leading to a surface covered by a homogeneous corrosion. The change in the slope of potential curve observed after several minutes of immersion is the consequence of the consumption of oxygen in the metal/electrolyte interface, which involves the further diffusion of oxygen from the bulk electrolyte to the corroding surface to give continuity to corrosion processes. This phase is known as phase 1 or concentration control [4,28-30], as the corrosion rate depends on the supply of oxygen to the corroding surface and the governing factor is the oxygen concentration in the electrolyte. During this phase, the corrosion of the steel leads to the formation of a rust layer in its surface. Eventually, the potential stabilizes in phase 2 or non-linear diffusion control [4,28-30]. In this phase, the further corrosion of the steel involves the diffusion of oxygen through the rust layer, which hinders the access of oxygen. The stable potential values of the samples registered after the hour of immersion are presented Table 5.2.2.The potential drop during the first minutes of immersion is less pronounced in the tests at 2 ºC, and the potential values registered during the whole hour are nobler, which can be attributed to slower corrosion processes taking place at lower temperatures. As previously reported by several researchers [9,14,16,31-34], temperature has an influence on corrosion rate of metals primarily through its effect on factors which control the diffusion rate of oxygen. The increase in temperature leads to an increase in the diffusion coefficient of oxygen and a

decrease in the viscosity of the electrolyte, which entails faster oxygen diffusion to the corroding surface and thus, higher corrosion rates.

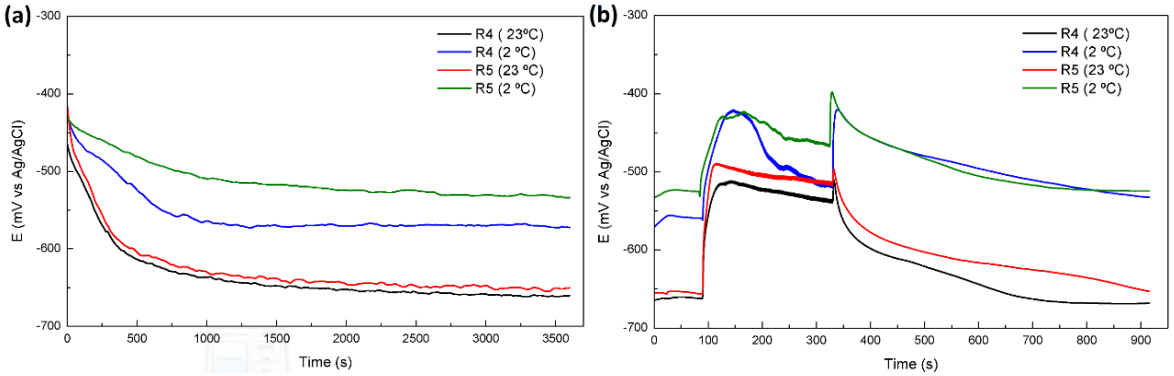

Fig. 5.2.4 Evolution of the open circuit potential with time for the R4 and R5 steel grades at 23 ºC and 2 ºC during the first hour of immersion (a) and before, during and 10 min after sliding (b)

The evolution of potential of both steels at the two temperatures registered during the sliding wear test of 4 minutes, and the stabilization time of 10 minutes after sliding is illustrated in Fig. 5.2.4b. Before the wear test, the potential remains stable, but a shift of potential is observed towards nobler values when the alumina ball comes into contact with the sample surface and sliding begins. In the case of passive materials, it has been widely observed that sliding results in a change of potential to more negative values as a consequence of the partial or total removal of the passive layer, and the subsequent exposure of corrodible fresh material to the electrolyte [5,7,8,25,26]. Active materials such as the R4 and R5 steels, however, do not grow such a protective oxide layer. It is well known that the OCP measurement is a mixed lecture of potential resulting from the different potentials of the anodic and cathodic regions [8,25,26]. Therefore, the shift of potential to more positive values observed in the steels when sliding is applied, suggests that the wear tracks generated, with different potential value than that of the unworn surfaces, possess a nobler potential. This is a consequence of the continuous action of the countermaterial in the worn surface modifying the natural trend of corrosion, due to both material removal and the plastic deformation under a normal load that exceeds the yield strength of the steels. Thus, sliding results in the formation of two electrochemically differentiated areas in the surface. A galvanic couple is established between the wear track and the uncrown surface, where the worn material with more noble potential acts as the cathode of the electrochemical reaction, and the unworn surface as the anode [13]. In other words, sliding results in a wear-accelerated corrosion of the unworn surface. The potential reached during sliding is more positive in the tests at low temperature, but the shift of potential is larger at 23 ºC. A decrease in potential value with sliding time can be observed in all the tests, which is more noticeable at 2 ºC, and especially in the R4 steel. This progressive change in potential can be attributed to both corrosion and structural transformation that are taking place in the tribological contact. The corrosion of the worn surface between successive events of the countermaterial strongly influences the potential lecture after several cycles of sliding. Furthermore, the normal load exceeding the yield strength of the steels (800 MPa and 950 MPa for the R4 and R5 steel grades, respectively [27]), results in a plastic deformation that affects the potential of the samples [25]. This plastic deformation undergone by the steels causes a work hardening of the material in the wear track [35,36,37], which increases with sliding time leading in turn to a gradual decrease in the potential. This work hardening was confirmed by the increase in hardness measured in the worn material with reference to the rest of the surface (Table 5.2.3). Once the wear test ends, there is an increase in potential to positive values, which is attributed to the contribution of the fresh material in

the worn area to the lecture. The continuous material removal taking place during sliding, leaves the worn surface free from corrosion and corrosion products. Therefore, at the end of sliding, the potential of the track material corresponds to the potential of a freshly immersed steel, which corrodes in contact with seawater, leading a decrease in potential and an eventual stabilization reaching values close to those registered before sliding.

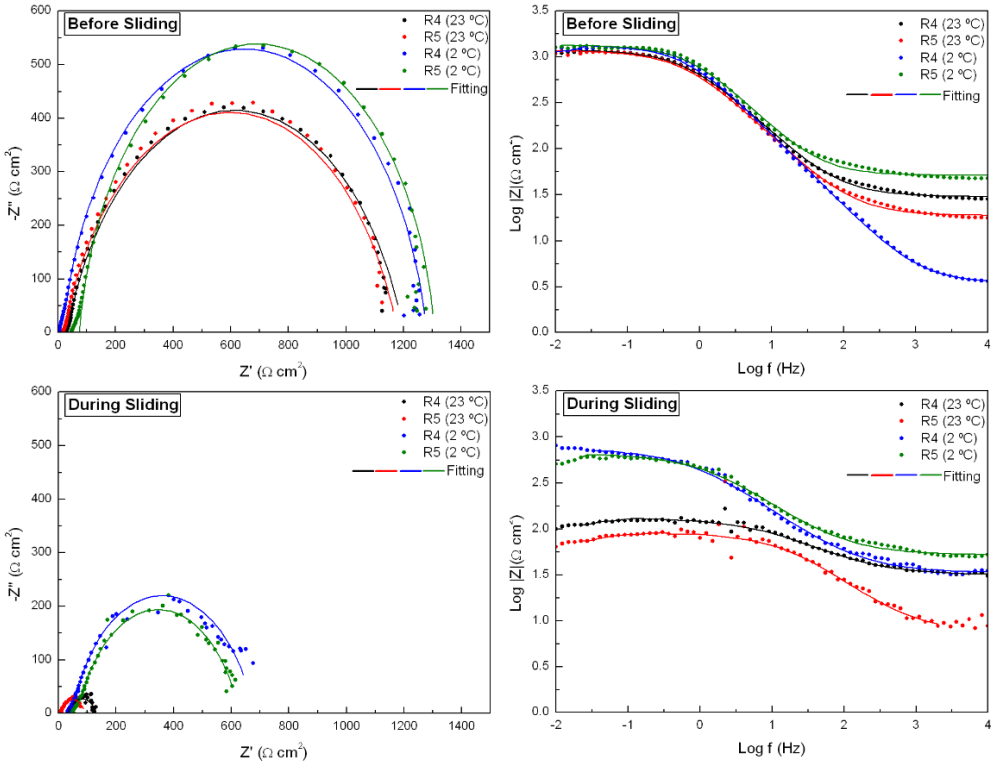

Fig. 5.2.5 Electrochemical impedance spectroscopy diagrams before and during the wear process for the R4 and R5 steels grades at 23 ºC and 2 ºC

The impedance data obtained from the EIS measurements performed before and during sliding are displayed in Fig. 5.2.5 in the form of Nyquist and Bode diagrams. In all the cases, the one single capacitive semicircle at high frequencies present in the Nyquist plot indicates that there is a charge transfer reaction taking place at the electrolyte/steel interface, and hence, the corrosion reaction is controlled by the transfer process. The corrosion resistance of the steels is slightly higher at a lower temperature. The reduction in the Nyquist semicircle and the lowest values of log |Z| in the Bode diagram observed during sliding, indicate a decrease of the corrosion resistance of the steels during wear at both temperatures. However, this decrease is more noticeable at 23 ºC.

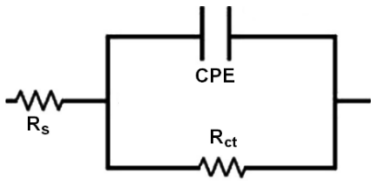

Fig. 5.2.6 Equivalent circuit used in the fitting process of the experimental data of R4 and R5 steel grades before and during sliding at 23 ºC and 2 ºC

The experimental data was analyzed with the Autolab FRA version 4.9 software and fitted to the Randles equivalent circuit of Fig. 5.2.6. Electrical equivalent circuits are widely used to describe the electrochemical behavior of the studied systems. In this circuit, Rs represents the resistance of the electrolyte between the reference and the working electrodes, and R_{ct} corresponds to the charge transfer resistance or the polarization resistance, in the case of these uncoated steels. The Constant Phase

Element (CPE) represents the double layer capacitance at the electrolyte/steel interface. Constant phase elements are used for replacing the simple capacitances for a better fit quality of the experimental data. The impedance of a CPE element can be represented by the following expression as: $Z_{CPE} = 1/Y0\,(i\omega)^n$, where ω is the angular frequency, and i the imaginary number. Y0 and n ($n \leq 1$) are the admittance and the empirical exponent of the CPE, respectively. Whether the surface acts as an ideal capacitor n is equal to unity and Y0 is identical to the double layer capacitance. Table 5.2.2 summarizes the parameters obtained from the fitting process of the impedance data recorded before and during sliding.

Table 5.2.2 OCP values registered and equivalent circuit parameters obtained from the Impedance data before and during sliding in synthetic seawater at 23 ºC and 2 ºC

Steel grade	Temp.	Condition	OCP (mV*)	Rs (Ω cm^2)	CPE-Y0 (F cm^{-2} s^{-n})	CPE-n	R_{ct} (Ω cm^2)
R4	23 ºC	Before sliding	-661	30.05	265.95	0.785	1176.02
		During sliding	-525	31.27	661.81	0.627	100.84
	2 ºC	Before sliding	-572	16.19	239.80	0.805	1371.60
		During sliding	-504	28.47	405.12	0.668	679.96
R5	23 ºC	Before sliding	-650	18.67	292.68	0.780	1196.34
		During sliding	-506	20.46	389.88	0.719	95.25
	2 ºC	Before sliding	-534	51.16	219.61	0.807	1384.30
		During sliding	-445	51.46	377.32	0.660	656.84

V Volts are referred to Ag/AgCl reference electrode*

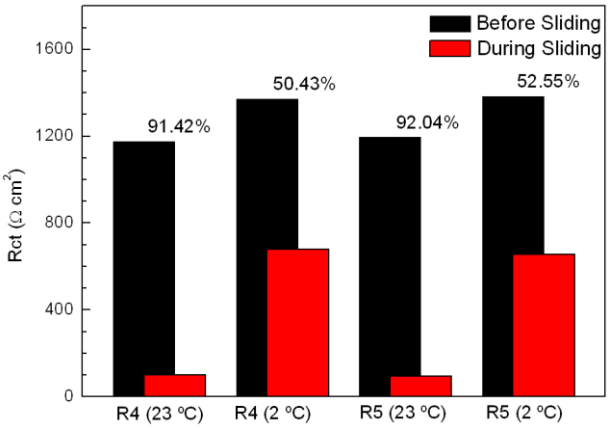

Fig. 5.2.7 Reduction of the corrosion resistance of the R4 and R5 steel grades tested at 23 and 2 ºC due to sliding

Before sliding, the corrosion resistance of the steels is close to 1200 Ω cm^2 and 1380 Ω cm^2 at 23 ºC and 2 ºC, respectively. The difference in the resistance at 23 and 2 ºC can be attributed to the effect of temperature in the diffusivity of oxygen in the electrolyte, which is more favored at higher temperatures, thus leading to slightly smaller corrosion resistance. The corrosion resistance of the steels is considerably affected by sliding, especially at 23 ºC. As observed in Fig. 5.2.7, the corrosion resistance of the steels at 23 ºC decreases in a 92%, reaching values close to 100 Ω cm^2 during sliding, whereas at 2 ºC the reduction is significantly smaller, of a 52%, with values close to 660 Ω cm^2. Hence, sliding has a greater effect in the reduction of corrosion resistance at higher temperature, as a consequence of the faster corrosion processes taking place in the unworn surface at 23 ºC. Analyzing the CPE element in Table 5.2.2, it can be noticed that Y0 increases during sliding, due to the increase in the surface roughness of the samples, due to the corrosion processes taking place [38].

Fig. 5.2.8 depicts the evolution of the coefficient of friction (COF) with time, for the sliding wear test of 11400 cycles (76 min), and coefficient values are given Table 5.2.4.

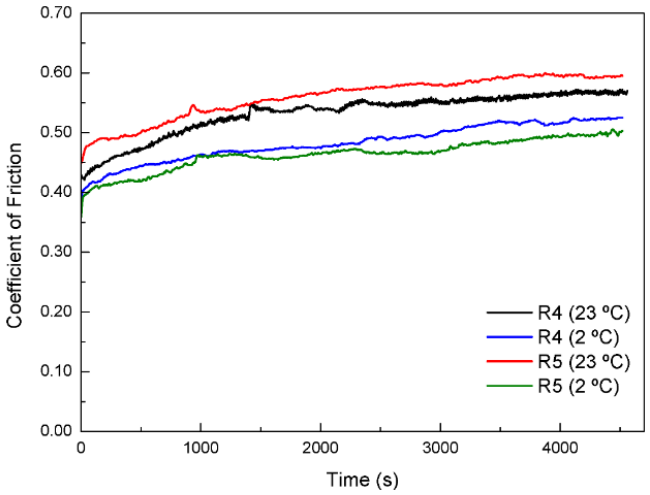

Fig. 5.2.8 Evolution of the COF during the wear processes of 76 min for the R4 and R5 steel grades in synthetic seawater at 23 ºC and 2 ºC.

Table 5.2.3 Mean hardness values obtained inside and outside the wear track, and mean roughness of the surface of the samples before and after the tests for both steel grades at 23 ºC and 2 ºC

Steel grade	Temperature	Hardness (HV_1)			Roughness (µm)	
		Wear track	Outside	Increase (%)	Initial	final
R4	23 ºC	264.00±4.00	258.33±3.51	2.27	0.017±0.002	0.241±0.042
	2 ºC	301.00±6.93	264.33±2.88	12.29	0.018±0.005	0.123±0.040
R5	23 ºC	326.33±4.04	322.00±2.64	1.33	0.016±0.004	0.239±0.034
	2 ºC	338.00±6.25	319.00±6.08	5.62	0.018±0.003	0.125±0.036

In all the samples, the COF was observed to increase with sliding time, as a consequence of the superficial modifications produced by sliding. The countermaterial continuously removes the oxides that are formed in the contact, leading to a change in the wear track morphology and size affecting in this way the contact pressure during the sliding. The higher coefficients of friction were registered for the steels at 23 ºC. This can be attributed to several factors: the lower hardness of the material in the wear tack, the higher amount of corrosion products in the contact, and the lower viscosity of seawater at 23 ºC. On the one hand, the plastic deformation of the material in the track under the applied load that exceeds the yield strength of the steels, leads to an increase in hardness of the 12.29 % (R4) and 5.6 % (R5) at 2 ºC, respectively; and a smaller increase of the 2.27 % (R4) and 1.32 % (R5) at 23 ºC (Table 5.2.3). Thus, the lower hardness of the steels at 23 ºC makes material detachment easier, leading to higher particle adherence in the contact and, in turn, to higher coefficients of friction [39]. On the other hand, the greater particle detachment can lead to larger amount of corrosion products (ferrous oxides) present in the junction, leading again to higher coefficients. The higher amount of corrosion products in the track were confirmed in the microscopic analyses of the samples (Fig. 5.2.9 and Fig. 5.2.10). Finally, temperature affects the viscosity of seawater, which according to literature is of 1.783 $x10^{-3}$ Pa.s at 2 ºC and 1.004 $x10^{-3}$ Pa.s at 23 ºC [40-43]. Therefore, the lower viscosity of the electrolyte at 23 ºC entails a poorer lubricating ability of seawater and, thus, higher coefficients of friction at that temperature [44].

Table 5.2.4 Mean COF values obtained from the sliding test of 76 min, total material loss (V_{tot}), material loss due to tribocorrosion in the wear track (V_{tr}) and material loss due to corrosion in the unworn surface (V_{corr}) for both steel grades at 23 ºC and 2 ºC

Steel grade	Temperature	Mean COF	V_{tot} (x10^{-2}mm^3)	V_{tr} (x10^{-2}mm^3)	V_{corr} (x10^{-2}mm^3)
R4	**23 ºC**	0.533±0.009	23.03±0.76	14.39±0.45	8.64±0.53
	2 ºC	0.483±0.009	13.96±0.55	11.52±0.02	2.44±0.05
R5	**23 ºC**	0.560±0.010	17.27±0.55	12.17±0.06	5.10±0.05
	2 ºC	0.464±0.012	13.48±0.17	11.44±0.31	2.03±0.19

5.2.3.3 Superficial state of the samples after tribocorrosion test

The optical micrographs of the worn surfaces of the steels at 23 and 2 ºC are presented in Fig. 5.2.9 and Fig. 5.2.10, respectively. In all the samples, the unworn area is uniformly corroded. However, the worn surfaces present some differences depending on the test temperature. The wear tracks of the steels tested at 23 ºC (Fig. 5.2.9) are covered by large-shaped corrosion products, whereas those tested at 2 ºC (Fig. 5.2.10) are almost free from corrosion. In all the cases, abrasion lines parallel to sliding motion are also visible in the corrosion-free areas. The wear tracks of the steels at 2 ºC are narrower than those obtained at 23 ºC.

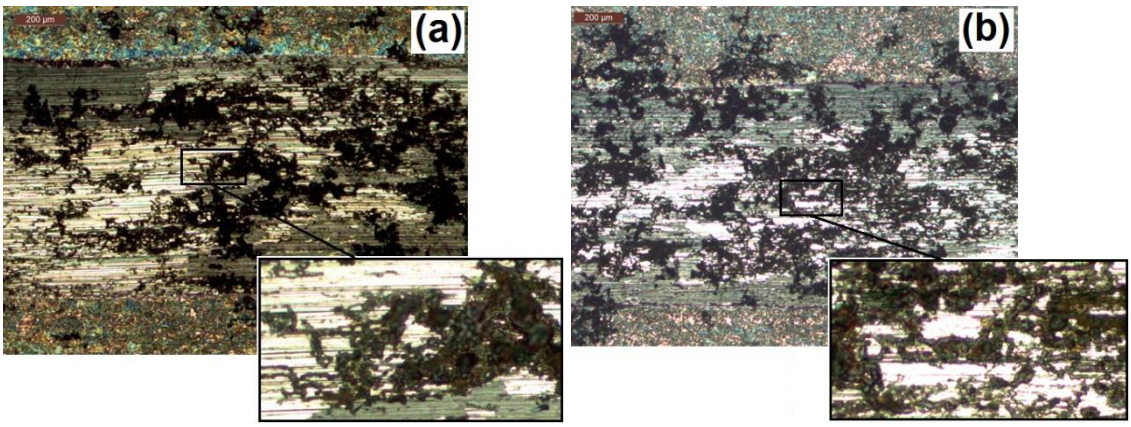

Fig. 5.2.9 Optical micrographs of the samples after the tribocorrosion tests performed at 23 ºC: (a) R4 and (b) R5 steel grades

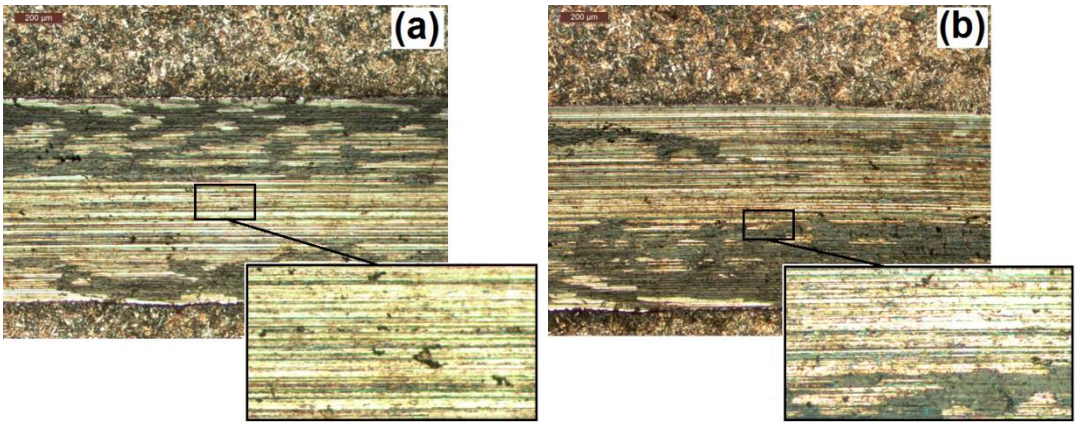

Fig. 5.2.10 Optical micrographs of the samples after the tribocorrosion tests performed at 2 ºC: (a) R4 and (b) R5 steel grades

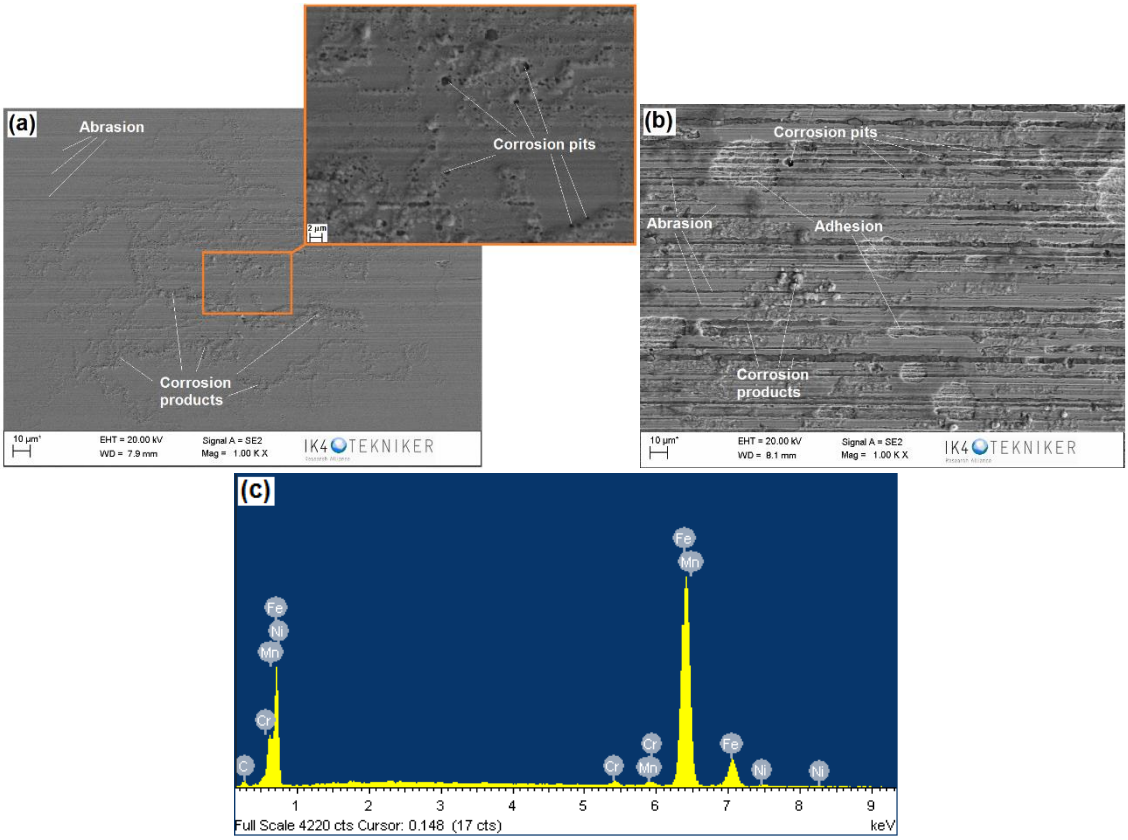

Fig. 5.2.11 SEM images and EDS analysis of the wear tracks in the samples tested at 23 ºC: (a) R4 steel grade, (b) R5 steel grades, and (c) EDS obtained from the R5 steel sample

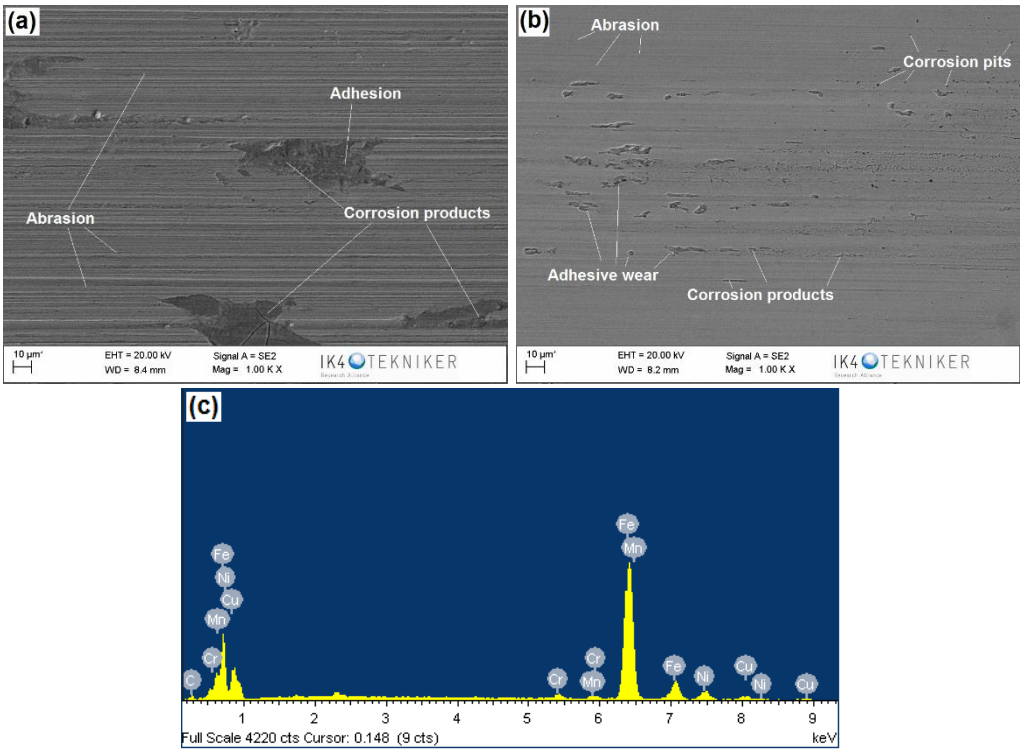

Fig. 5.2.12 SEM images and EDS analysis of the wear tracks in the samples tested at 2 ºC: (a) R4 steel grade, (b) R5 steel grades, and (c) EDS obtained from the R5 steel sample

Fig. 5.2.11 and Fig. 5.2.12 show the SEM images and EDS results of the wear tracks of the specimens at 23 and 2 ºC, respectively. In the images of the samples tested at 23 ºC (Fig. 5.2.11a and b), abrasion lines, corrosion products, and some localized corrosion

in the form of pits can be observed along the wear tracks. The R5 steel sample (Fig. 5.2.11b) presents some whiter areas, which showed low oxygen content in the EDS analysis (Fig. 5.2.11c). Furthermore, the analysis of the wear track in the confocal microscope showed these areas to be hollows (Fig. 5.2.13). Therefore, they correspond to material detachment due to adhesion of the steel on the countermaterial. Some steel and corrosion products were observed in the alumina balls, which corroborated the former statement. No evidence of cracks and fatigue are observed in the SEM images. In the samples tested at lower temperature (Fig. 5.2.12a and b), the wear tracks are almost free from corrosion and abrasion grooves are visible. The darker zones in the tracks showed low oxygen content in the EDS analysis (Fig. 5.2.12c). Similarly to that observed in Fig. 5.2.13 for the R5 steel at 23 ºC, the surface analysis by confocal microscopy confirmed these areas to be caused by material detachment due to adhesive wear occurring in the track.

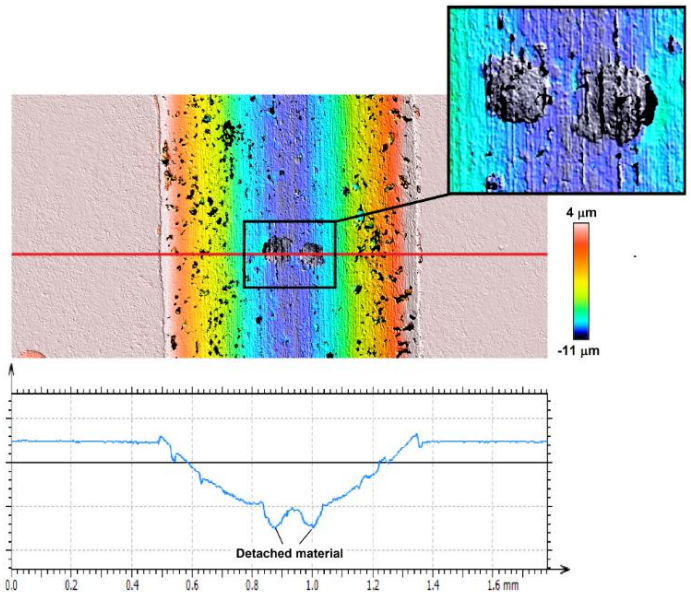

Fig. 5.2.13 Surface topography of the wear track of the R5 steel rested at 23 ºC, showing the presence of hollows in the cross-section profile of the track, corresponding to material detachment during sliding

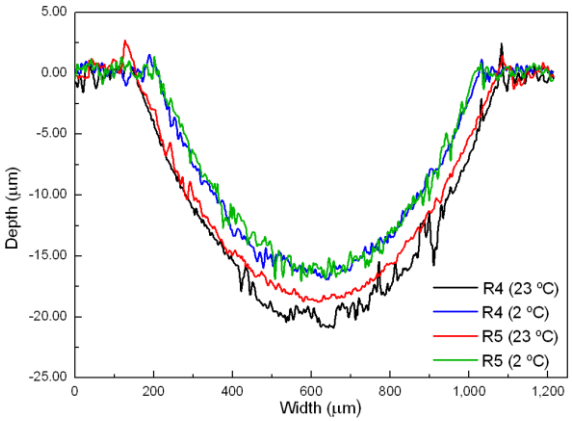

Fig. 5.2.14 Cross section profiles across the wear tracks on the two steel grades tested at 23 ºC and 2 ºC

The cross-section profiles of the wear tracks are depicted in Fig. 5.2.14. The biggest tracks were obtained in the R4 steel at 23 ºC, followed by the R5 steel sample tested at the same temperature. The wear tracks of both steels tested at 2 ºC are identical in size. The difference in the wear track size, which was considerably smaller at 2 ºC, can be attributed to the lower deformation and material detachment, due to the higher superficial hardness of the steels in the tribological contact at 2 ºC [39]. On the other hand, the

roughness in the unworn surface of the samples, which was mirror polished before the tests, increased during the test being comparable to that of the track, especially in the case of the samples at 23 ºC. The roughness of the samples unworn surface was measured after the test, and the mean values are compiled in Table 5.2.3. The increase in roughness confirms the high corrosion undergone by the steels during the test, in accordance with that observed in the optical micrographs.

The protocol described in the UNE 112086 standard [24] allows quantifying the mechanical and electrochemical contributions to material loss in the wear track due to tribocorrosion process. In this procedure, the material loss due to corrosion (W^c) in the wear track is obtained by Faraday's law:

$$W^c = i_{act}.A_{act}.\frac{M}{n.F.\rho}N.t_{lat} \quad (5.2.II)$$

With *M* the molecular weight, *n* the number of electrons involved in the anodic process, *ρ* the density, and *F* the Faraday constant (96500 C). *N* corresponds to the number of cycles, and t_{lat} is the latency time of the sliding test. A_{act} and i_{act} are the area and the current density flowing in the wear track, i.e., the active area. The material loss due to mechanical wear in the wear track (W^m) is then calculated from the following equation:

$$W^m = W_{tr} - W^c \quad (5.2.III)$$

where W_{tr} is the total material loss in the wear track, obtained by calculating the volume of the wear track.

For the calculation of W^c in Eq. 5.2.II, i_{act} must be obtained by means of a set of equations as described elsewhere [8,19,20,23,24]. For this aim, the polarization resistance values obtained in the EIS measurements performed before and during sliding are employed. The basis of the calculations consists of considering the unworn surface of the tested sample to be in the same electrochemical state during the whole test. Since the oxide layer protects the material from corrosion, sliding is considered not to affect this area, that remains undamaged and unaltered during the whole tests. Then, the corrosion current in the wear track is obtained considering that the polarization resistance measured during sliding is the combination of two resistances, corresponding to the worn and unworn areas, where the resistance of the unworn surface is known from the impedance data obtained in tribocorrosion tests before sliding.

In the case of active steels, such as the steels studied in this work, no protective passive film is formed on the surface, so the steels are continuously corroding during immersion. Furthermore, sliding has been observed to increase the corrosion of the unworn surface of the steel samples [13], so the electrochemical state of this area cannot be considered to remain unchanging during the whole test. Therefore, the approach specified in the standard is not applicable to the active steels studied in this work.

In this case, the total material loss is the sum of material loss due to tribocorrosion in the worn area and the material loss due to corrosion in the unworn surface. In turn, the latter is derived from two components: pure corrosion (V_{pc}) and wear-accelerated corrosion (V_{wac}). The total material loss in volume (V_{tot}) was obtained by weighting the samples before and after each test, and multiplying the results by the density of the steels. The wear track volume (V_{tr}) was quantified by calculating the wear track volume from the cross-section profiles obtained by profilometry, as explained in section 5.2.2.3. Finally, the material loss due to corrosion in the unworn area (V_{corr}) was calculated by subtracting the wear track volume to the total material loss (Eq. 5.2.I). In order to estimate the wear-accelerated corrosion of the steels in the unworn surface, additional corrosion tests were

performed to quantify the material loss due to pure corrosion (V_{pc}) in the absence of sliding. For this aim, the samples were immersed in synthetic seawater for the total duration of the tribocorrosion test, and V_{pc} was calculated by weighting the samples before and after the tests. These values were compared with the results from tribocorrosion tests, and the wear-accelerated corrosion (V_{wac}) component was calculated as the difference between V_{corr} and V_{pc}. All the contributions to material loss obtained for both steel grades at 2 and 23 ºC are listed in Table 5.2.4, and the results are depicted in Fig. 5.2.15.

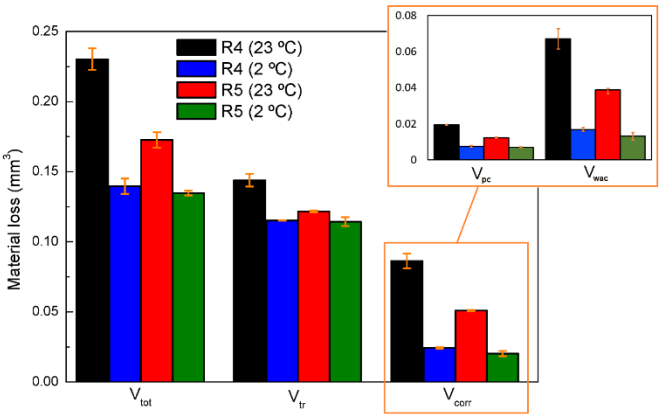

Fig. 5.2.15 Total material loss (V_{tot}), material loss due to tribocorrosion in the wear track (V_{tr}) and material loss due to corrosion in the unworn surface (V_{corr}), in volume. In the detailed image, the material loss due to pure corrosion (V_{pc}) and the wear-accelerated corrosion (V_{wac}) in the unworn surface.

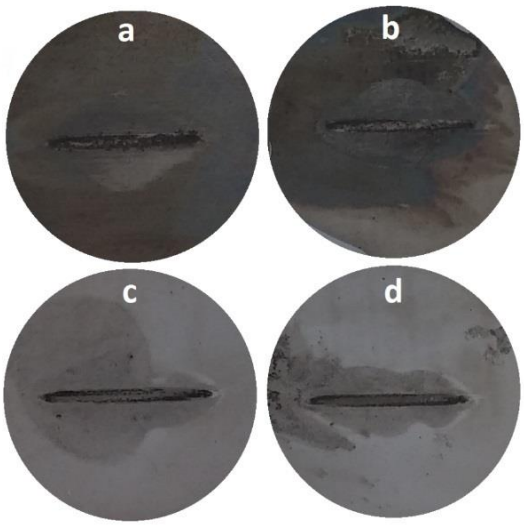

Fig. 5.2.16 Picture of the tested surface of the samples of R4 steel at 23 ºC (a) and 2 ºC (c) and the samples of R5 steel at 23 ºC (b) and 2 ºC (d)

The larger total material loss corresponds to the R4 steel grade at 23 ºC, followed by the R5 steel grade at the same temperature. The material loss of both steels at 2 ºC is similar and considerably smaller than that obtained at 23 ºC. The principal cause of material loss in all the samples is tribocorrosion in the wear track, rather than corrosion in the unworn surface. Furthermore, considering the low amount of corrosion products observed in the wear tracks at 2 ºC, the main contribution to material loss in the tracks seems to be due to mechanical effects. The material loss due to corrosion in the unworn surface (V_{corr}) is larger at 23 ºC for both steels, in accordance with that observed in the surface state of the tested samples in Fig. 5.2.16. The material loss due to corrosion is 3.5 (R4) and 2.5 (R5) times higher at 23 ºC than at 2 ºC. The difference in the material loss due to corrosion in the unworn surface obtained in the tribocorrosion and the corrosion tests, confirms the wear-accelerated corrosion of the unworn surface during

sliding. In fact, V_{corr} is triplicated (2 ºC) and quadruplicated (23 ºC) for both steels when wear is applied. Therefore, wear accelerates the corrosion in the unworn surface, especially at 23 ºC, due to a more favored oxygen diffusion from the bulk solution to the corroding surface at higher temperature.

5.2.4 **Conclusions**

The objective of this work was to investigate the effect of temperature on the tribocorrosion behavior of the R4 and R5 steel grades, commonly used in offshore structural applications. For this aim, reciprocating tribocorrosion tests were performed in synthetic seawater at two electrolyte temperatures, under ball-on-disc configuration. Furthermore, the suitability of the test protocol developed for passive materials (UNE 112086) has been evaluated to be used for active materials. With the results obtained from the tests, the following conclusions can be drawn:

- The increase in the corrosion current observed in the polarization curves when sliding is taking place, suggests that wear promotes the corrosion of the steels.
- Moreover, sliding results in the potential shift to nobler values, indicating that a galvanic coupling is established on the surface of the steels between the worn and unworn surfaces. The former possesses a nobler potential, leading to a wear-accelerated corrosion of the unworn surface.
- The corrosion resistance of the steels before sliding is slightly higher at 2 ºC. Sliding results in a decrease of corrosion resistance in all the cases, increasing the difference between the results at different temperatures, with values more than six times smaller at 23 ºC in comparison with those at 2 ºC.
- The COF registered during tribocorrosion tests were higher for the steels at 23 ºC. The lower hardness of the material led to higher particle detachment and, in turn, to a greater amount of corrosion products remaining in the contact, which led to higher coefficients. Furthermore, the lower viscosity of seawater at 23 ºC also led to higher coefficient lectures, due to a poorer lubricating ability of the electrolyte.
- In all the tests, the principal cause of material loss is tribocorrosion in the wear track. The material loss due to corrosion in the unworn surface is more than two times higher in the steels tested at 23 ºC. Furthermore, the corrosion of the unworn surface is accelerated by wear, being three times and four times higher during sliding at 2 and 23 ºC, respectively.
- Even if sliding accelerates the corrosion of the unworn area of the steels at both temperatures, the effect is more noticeable at 23 ºC, since the access of oxygen is more favored. Therefore, temperature has an influence on the tribocorrosion response of both steels, leading to higher material losses and lower corrosion resistance at a higher temperature.
- Finally, the test procedure of the UNE 112086 standard designed for the assessment of tribocorrosion of passive materials, has been found to be suitable to evaluate the effect of wear in corrosion, and vice versa, in active materials. However, the procedure described in the standard to quantify the contribution of mechanical and electrochemical parameters to the material loss due to tribocorrosion in the wear track, is not appropriate for active materials, since the material loss, in this case, is the sum of three components: pure corrosion and wear-accelerated corrosion in the unworn surface, and tribocorrosion (wear+corrosion) in the wear tack.

5.2.5 Acknowledgments

This work was performed with the financial support of the *MECOFFBI (ELKARTEK 2016, KK-2015/00071)* project and the support of EMAITEK Initiative, both financed by the Basque Country. Authors would also like to acknowledge the Education, Linguistic Politics and Culture Department of the Basque Government for its support through the grant "*Programa Predoctoral de Formación de Personal Investigador No Doctor (PRE_2017_2_0088)*" awarded to the first author.

5.2.6 References

[1] E. Fontaine, A. Kilner, C. Carra, D. Washington, K.T. Ma, A. Phadke, D. Laskowski, G. Kusinski. *Industry Survey of Past Failures, Pre-emptive Replacement and Reported Degradations of Mooring Systems of Floating Production Units*. Offshore Technology Conference, Houston, Texas, USA, 5-8 May 2014

[2] A.O. Vázquez-Hernández, G.B. Ellwanger, L.V.S. Sagrilo. *Long-term response analysis of FPSO mooring systems*. Applied Ocean Research 33 (2011) 375– 383

[3] A.O. Vazquez-Hernandez, G.B. Ellwanger, L.V.S. Sagrilo. *Reliability-based comparative study for mooring lines design criteria*. Applied Ocean Research 28 (2006) 398–406

[4] R.E. Melchers, T. Moan, Z. Gao. *Corrosion of working chains continuously immersed in seawater*. J Mar Sci Technol (2007) 12:102-110

[5] D. Landolt, S. Mischler, M. Stemp. *Electrochemical methods in tribocorrosion: a critical appraisal*. Electrochimica Acta 46 (2001) 3913-3929

[6] P. Ponthiaux, F. Wenger, J.-P. Celis. *Tribocorrosion: Material behavior Under Combined Conditions of Corrosion and Mechanical Loading, Corrosion Resistance*, in: Dr. Shih (Ed.), InTech, 2012, ISBN:978-953-51-0467- 4, http://dx.doi.org/10.5772/35634, Available from: http://www.intechopen. com/books/corrosion-resistance/tribocorrosion-material-behaviour-under- combined-conditions-of-corrosion-and-mechanical-loading.

[7] S. Mischler, A. Spiegel, D. Landolt. *The role of passive oxide films on the degradation of steel in tribocorrosion systems*. Wear 225-229 (1999) 1078-1087

[8] J.-P. Celis, P. Ponthiaux (Ed.). *Testing Tribocorrosion of Passivating Materials Supporting Research and Industrial Innovation: Handbook*. Maney Publishing UK (2012), ISBN: 978-1-907975-20-2

[9] J.K. Saha. *Corrosion of Constructional Steels in Marine and Industrial Environment*. Springer India (2013), ISBN: 978-81-322-0719-1

[10] K. Xiao, C.F. Dong, X.G. Li, F.M. Wang. *Corrosion Products and Formation Mechanism during Initial Stage of Atmospheric Corrosion of Carbon Steel*. Journal of Iron and Steel Research, International 2008, 15(5): 42-48

[11] J.G. Castaño, C.A. Botero, A.H. Restrepo, E.A. Agudelo, E. Correa, F. Echeverría. *Atmospheric corrosion of carbon steel in Colombia*. Corrosion Science 52 (2010) 216-223

[12] H. Möller, E.T. Boshoff, H. Froneman. *The corrosion behaviour of a low carbon steel in natural and synthetic seawaters*. The Journal of The South African Institute of Mining and Metallurgy, Volume 106 (August 2006)

[13] A. López, R. Bayón, F. Pagano, A. Igartua, A. Arredondo, J.L. Arana, J.J. González. *Tribocorrosion behaviour of mooring high strength low alloy steels in synthetic seawater*. Wear 338-339 (2015) 1-10

[14] ASM Handbook. *Corrosion*. Vol 13, ASM International (1987), ISBN 0-87170-007-7.

[15] C. Guedes Soares, Y. Garbatov, A. Zayed. *Effect of environmental factors on steel plate corrosion under marine immersion conditions* Corrosion Engineering, Science and Technology (2011) Vol 46, No 4

[16] D. Talbolt, J. Talbolt. *Corrosion science and technology*. CRC Press US (1998), ISBN: 0-8493-8224-6.

[17] K. Chandler. *Marine and offshore corrosion*. Butterworths US (1985), ISBN 0-408-01175-0

[18] R. Baboian (Ed.). *NACE Corrosion Engineer's Reference Book. Third edition*. NACE International (2002) ISBN: 978-1-57590-127-5

[19] N. Diomidis, J.-P. Celis, P- Ponthiaux, F. Wenger. *A Methodology for the Assessment of the Tribocorrosion of Passivating Metallic Materials*. Lubrication Science 21 (2009) 53-67

[20] N. Diomidis, J.-P. Celis, P- Ponthiaux, F. Wenger. *Tribocorrosion of Stainless Steel in Sulfuric Acid: Identification of Corrosion-Wear Components and Effect of Contact Area*. Wear 269 (2010) 93-103
[21] L. Mendizabal, A. López, R. Bayón, P. Herrero-Fernandez, J. Barriga, J.J. González. *Tribocorrosion response in biological environments of multilayer TaN films deposited by HPPMS.* Surface & Coatings Technology 295 (2016) 60-69
[22] V. Saenz de Viteri, G. Barandika, R. Bayón, X. Fernández, I. Ciarsolo, A. Igartua, R. Pérez Tanoira, J.E. Moreno, C.P. Peremarch. *Development of Ti-C-N coatings with improved tribological behavior and antibacterial properties*. Journal of the Mechanical Behavior of Biomedical Materials 55 (2015) 75-86
[23] F.B. Saada, Z. Antar, K. Elleuch, P. Ponthiaux. *On the tribocorrosion behaviour of 304L stainless steel in olive pomace/tap water filtrate*. Wear 328-329 (2015) 509-517
[24] UNE 112086:2016. *Ensayos de tribocorrosión en materiales pasivos*. 07 September 2016
[25] J.-P. Celis, P. Ponthiaux, F. Wenger. *Tribo-corrosion of materials: Interplay between chemical, electrochemical, and mechanical reactivity of surfaces*. Wear 261 (2006) 939–946
[26] P. Ponthiaux, F. Wenger, D. Drees, J.P. Celis. *Electrochemical techniques for studying tribocorrosion processes*. Wear 256 (2004) 459–468
[27] Offshore Standard DNV-OS-E302, Det Norske Veritas, Offshore Mooring Chains, October 2013
[28] R.E. Melchers, R. Jeffrey. *Early corrosion of mild steel in seawater*. Corrosion Science 47 (2005) 1678–1693
[29] R.E. Melchers. *Effect of marine immersion corrosion of carbon content of low alloy steels*. Corrosion Science 45 (2003) 2609-2625
[30] J. Bhandari, F. Khan, R. Abbassi, V. Garaniya, R. Ojeda. *Modelling of pitting corrosion in marine and offshore steel structures-A technical review*. Journal of Loss Prevention in the Process Industries 37 (2015) 39-62
[31] E. McCafferty. *Introduction to Corrosion Science*. Springer USA (2010), ISBN: 978-1-4419-0454-6.
[32] B.O. Hasan, S.A. Sadek. *The effect of temperature and hydrodynamics on carbon steel corrosion and its inhibition in oxygenated acid-salt solution*. Journal of Industrial and Engineering Chemistry 20 (2014) 297-307
[33] N. Pérez. *Electrochemistry and corrosion science*. Kluwer Academic Publishers, Boston, ISBN: 1-4020-7744-0
[34] C.-O.A. Olsson, D. Landolt. *Passive films on stainless steels: chemistry, structure and growth*. Electrochimica Acta 48 (2003) 1093-1104
[35] N. Diomidis, S. Mischler, N.S. More, Manish Roy. *Tribo-electrochemical characterization of metallic biomaterials for total joint replacement*. Acta Biomaterialia 8 (2012) 852-859
[36] N. Papageprgiu, A. von Bonin, N. Espallargas. *Tribocorrosion mechanisms of NiCrMo-625 alloy: An electrochemical modelling approach*. Tribology International 73 (2014) 177-186
[37] A. Eghlimi, K. Raessi, M. Shamanian. *Tribocorrosion behavior of overlay welded super duplex stainless steel in chloride medium*. Journal of Bio- and Tribo- Corrosion (2015) 1-18
[38] E. Barsoukov, J.R. Macdonald (Eds.). *Impedance Spectroscopy: Theory, Experiment and Applications*. Wiley-Interscience, USA (2005), ISBN: 0-471-64749-7
[39] P. Menezes, S.P. Ingole, M. Nosonovsky, S.V. Kailas, M.R. Lovell (Eds.). *Tribology for Scientists and Engineers*. Springer New York (2013), ISBN: 978-1-4614-1944-0
[40] M.H. Sharqawy, J.H. Lienhard, S.M. Zubair. *Thermophysical properties of seawater: a review of existing correlations and data*. Desalination and Water Treatment 16 (2010) 354-380
[41] L. Seuront, S.C. Leterme, J.R. Seymour, J.G. Mitchell, D. Ashcroft, W. Noble, P.G. Thomson, A.T. Davidson, R. van der Enden, F.J. Scott, S.W. Wright, M. Schapira, C. Chapperon, N. Cribb. *Role of microbial and phytoplanktonic communities in the control of seawater viscosity off East Antartica (30-800º E)*. Deep-Sea Reserch II 57 (2010) 877-886
[42] M.N. Hill (Ed.). *The Sea. Ideas and Observations on Progress in the Study of the Seas*. John Wiley & Sons (1962) ISBN: 0-674-01727-7
[43] ITTC-Recommended Procedures. *Fresh Water and Seawater Properties*. Revision 02 (2011)
[44] T. Ron, S. Lee. *Influence of Temperature on the Frictional Properties of Water-Lubricated Surfaces*. Lubricants 2 (2014) 177-192

Contribution 3

Influence of agitation on the tribocorrosion of active materials

Submitted for publication in Corrosion Science

Contribution 3: Submitted for publication in Corrosion Science

5.3. EFFECT OF AGITATION ON THE TRIBOCORROSION BEHAVIOR OF ACTIVE MATERIALS

A. López-Ortega[a], J.L. Arana[b], R. Bayón[a]

[a] *IK4-TEKNIKER, Eibar, Spain*
[b] *Department of Metallurgical and Materials Engineering, University of the Basque Country, Spain*

ABSTRACT

In this study, the tribocorrosion behavior of an AISI 316 stainless steel (passive) and a Low-Alloyed steel (active) was compared, also evaluating the influence of agitation. Unidirectional ball-on-disc tests were performed in synthetic seawater with the Zero Resistant Ammetry technique. The differences on the currents registered for both materials evinced the high dissolution rate of the active steel even in the absence of sliding when the AISI showed negligible electrochemical activity. The results showed little influence of the agitation for the passive material, but a considerable effect on the wear-accelerated corrosion in the unworn surface of the active steel.

Keywords: *Tribocorrosion; Active materials; Zero-Resistance Ammeter (ZRA); Wear-accelerated corrosion; Seawater*

5.3.1 Introduction

Tribocorrosion can be defined as the irreversible transformation of materials resulting from the simultaneous action of mechanical loading and chemical/electrochemical interactions with the surrounding environment. It combines two major scientific areas: Tribology and Corrosion. Tribology comprises the study of friction, wear, and lubrication, whereas corrosion science is related to the chemical aspects of material degradation [1-5]. Tribocorrosion involves a synergism between wear and corrosion, since the degradation in terms of material loss generated by the two processes acting simultaneously is larger than the sum of each of them acting separately [6-10]. On the one hand, corrosion can be accelerated by the removal of the passive layer by mechanical actions, which expose the bare material where active corrosion can take place. On the other hand, solid products of corrosion resulting from the material loss during wear can act as third body particles in the tribological contact. Those products can oxidize and form hard oxides that induce abrasion of the bare material, in which is known as the third-body effect [3,6,11-14].

The interest on the study of tribocorrosion has increased over the last decades, due to the high impact of tribocorrosion on the daily life, encompassing several industrial sectors such as material processing, energy conversion, transportation, oil and gas exploitations, and medical and dental implants, among others [1,3-7,11]. Tribocorrosion of passive materials has been studied since the late 1970s, when several researchers evaluated abrasion-corrosion, erosion-corrosion or sliding-corrosion in different industrial application systems [1,15]. The earliest studies were focused on understanding the formation of a passive film and its behavior under wear-corrosion solicitations, for which acidic solutions were usually employed [11,16-18]. Over time, the studies were more focused on reproducing tribocorrosion systems on industrial applications in order to predict the useful life of components, using saline solutions as electrolytes [19-22]. With the increasing interest and impact of biomedicine over the last decades, a significant number of tribocorrosion studies in simulated body fluids have been performed for

biomedical alloys such as titanium or CoCrMo alloys [23-28]. These alloys are used in orthopedic and dental implants [6,29-31], which are subjected to both corrosion and wear as a result of the human daily activity.

In short, tribocorrosion of passive materials such as stainless steels or titanium alloys has been widely studied during the last decades, under different mechanical and electrochemical conditions, in a wide range of corrosive electrolytes. However, little research has been done on the assessment of tribocorrosion of active materials. Unlike passive materials, active materials do not grow a protective oxide layer on their surface when in contact with an aggressive environment. On the contrary, active materials are subjected to progressive active dissolution. Low-alloyed steels, with low percentages of nickel, chromium, or molybdenum in their chemical composition are some examples. The rust layer formed on the surface of this kind of steels is somewhat porous with low adhesion bonds [32-36], so it does not provide an effective barrier against the penetration of electrolyte to the bare material surface, where corrosion proceeds unstoppably. As observed in previous works that dealt with the assessment of tribocorrosion of active materials [37-39], the material loss is a consequence not only of wear and corrosion processes taking place in the wear track, but also of pure corrosion on the unworn surface. The results showed a shift of potential towards more positive values during sliding, contrary to that observed in passive materials where the potential changes to more cathodic values due to the removal of the passive layer. In the case of active materials, the wear track was found to be more cathodic than the unworn surface, which led to a formation of a galvanic couple between worn and unworn areas promoting the corrosion of the unworn surface.

In these works, the tribocorrosion performance of High-Strength Low-Alloyed (HSLA) steels used in the manufacturing of mooring lines and components in offshore applications was evaluated in synthetic seawater [37-39]. Low-alloyed steels are highly employed as structural materials, due to their high resistance, and relatively low cost compared to more corrosion resistant materials and alloys [40]. HSLA, for instance, reach yield strengths in the range of 460-960 MPa, with relatively low weight [41,42]. The corrosion rate of low-alloyed steels in seawater has been measured to be around 250 microns per year [43]. Furthermore, the material loss is highly accelerated when the components are exposed to the combined action of wear and corrosion, which can lead to unpredicted premature failures with fatal consequences. Therefore, a closer understanding on the tribocorrosion degradation mechanism of active metals and alloys could provide better awareness of the use of these materials, with or without protective coatings, to enlarge their useful life in applications where passive materials are not suitable for use, i.e., higher costs and lower mechanical properties.

A major challenge in the study of tribocorrosion to be addressed is adapting test procedures for passive materials to the assessment of tribocorrosion in active materials [44]. In this context, the present study deals with the further investigation on the tribocorrosion of HSLA steels in synthetic seawater. In previous works, different tests procedures were employed, i.e., ASMT G119 [45] standard to evaluate the wear and corrosion synergism [37], and the procedure described in the UNE 112086 [46] standard with which the influence of the electrolyte temperature was also evaluated [38]. In the present work, the test procedure employed consisted of using Electrochemical Noise (EN) analysis, to register both the potential and current responses before, during, and after wear tests. The tribocorrosion response of a HSLA steel is compared with that of a passive material, an AISI 316 stainless steel. Furthermore, the influence of the agitation of the electrolyte is evaluated and compared for the active and passive steels.

5.3.2 Materials and methods

5.3.2.1 Materials

The present work compares the tribocorrosion behavior of a passive material and an active material. The passive material was an AISI 316 stainless steel. The active material was an R4 steel grade [47] commonly used in the manufacturing of offshore components. This is a High-Strength Low-Alloyed steel, with the chemical compositions of low and medium alloy steels (Cr, Ni, Mo, V, etc.) and heat treated to reach the desired mechanical properties.

The test samples were discs of 24 mm in diameter and 7.9 mm thick. The surface of the specimens was mirror polished to low roughness values (Ra<0.05μm). After polishing the samples and prior to the tests, the discs were cleaned in an ultrasonic bath with ether and acetone, dried with compressed air, and stored in a desiccator to avoid contamination or corrosion.

5.3.2.2 Potentiodynamic tests with and without sliding

For the electrochemical corrosion tests, a three-electrode set-up was employed, with the test sample as working electrode, a platinum wire as counterelectrode, and a commercial Ag/AgCl (KCl 3M) as reference electrode (+207 mV/SHE). The electrodes were connected to an Autolab-Metrohm PGSTAT302N potentiostat. The corrosion behavior of the two materials was evaluated by means of Potentiodynamic Polarization (PDP) measurements in synthetic seawater with heavy metals (ASTM D1141) at room temperature (23±2 ºC) and aerated conditions. After the stabilization of the Open Circuit Potential (OCP) for an hour of immersion, the polarization curves were recorded in a potential range from -0.4 V to 1.6 V with respect to the open circuit potential (OCP vs. Ag/AgCl) of each sample. The scan rate employed was of 0.166 mV/s (ASTM G5). The samples were placed horizontally in the cell, which was filled with 150 ml of electrolyte. The exposed surface of the samples was of 2.31 cm^2.

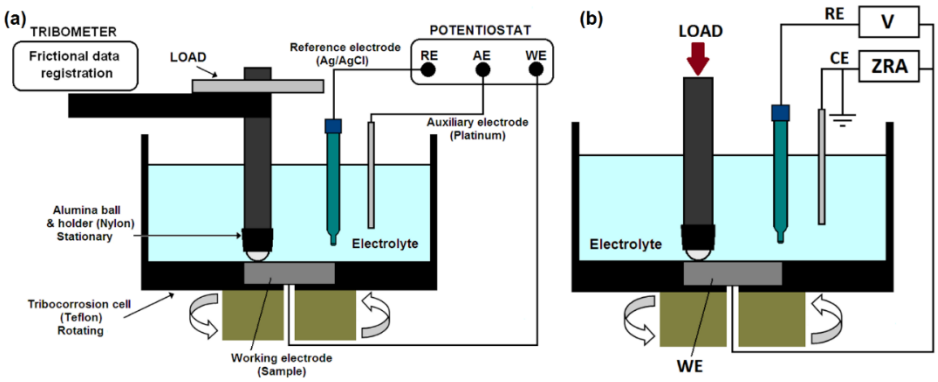

Fig. 5.3.1 Schematics of tribocorrosion ball-on-disc experimental setup used in this work (left) and the setup configuration for potential and current noise registration using two asymmetrical electrodes

The electrochemical cell was placed above the rotatory plate of a MicroTest MT/10/SCM tribometer, in order to perform the tests in rotating conditions with and without sliding. The experimental set-up is schematically depicted in Fig. 5.3.1a. This configuration allows the simultaneous control of both electrochemical and mechanical parameters during the tests. The cell and the ball holder are made of Teflon and nylon, respectively, in order to ensure the electrical isolation of the specimen from the metallic components of the tribometer. The samples were fixed in the electrochemical cell, which rotates ensuring the contact between the stationary counterbody and the specimen under controlled mechanical conditions, i.e., load, radius and rotation speed. The contact

conditions were calculated using the Hertzian Contact Theory [48], considering the actual contact pressure between links in real applications, as already reported in previous works [37-39]. The normal load was of 5 N, corresponding to an average Hertzian pressure of 930 MPa with a contact radius of 50.5 µm. An alumina ball of 10 mm in diameter (G28) was used as the countermaterial. The ball described a wear track of 10 mm in diameter at a rotation speed of 50 and 100 rpm.

In order to evaluate the influence of both agitation and wear, the tests were performed under different conditions: static cell, rotating cell at 50 rpm, rotating cell at 100 rpm, and tribocorrosion conditions under 5 N at 50 and 100 rpm. All the tests were triplicated in order to ensure the reproducibility of the results.

5.3.2.3 Tribocorrosion tests

The electrochemical technique employed in the tribocorrosion tests was the Electrochemical Noise (EN) analysis. The test configuration employed in the experiments is shown in Fig. 5.3.1b, where the working electrode (WE) and the counterelectrode (CE) were connected through a Zero Resistance Ammeter (ZRA). This configuration allows measuring the current whilst maintaining both the WE and CE at a negligible potential difference. A platinum wire of 1mm in diameter was used as the CE, and the test sample was connected as the WE. The reference electrode (RE) was a commercial Ag/AgCl (KCl 3M) electrode. Potential and current signals were recorded at a sampling rate of 1Hz. The potentiostat is equipped with an EDC modulus, that allowed the registration of current and potential variations with a resolution of 100 pA and 0.3 µV, respectively. The electrolyte used for the tests was synthetic seawater with heavy metals prepared in accordance with the ASTM D 1141. For each test, the cell was filled with 150 ml of this solution. The experiments were carried out at room temperature (23±2 ºC) and aerated conditions, and the exposed area of the samples was of 2.31 cm^2.

The test consisted of monitoring both the potential and the current before, during and after wear process. The samples were immersed in the electrolyte, and the potential was stabilized for an hour, after which a sliding wear test was performed under the above-mentioned mechanical conditions, i.e., under 5 N and wear track radius of 5 mm. After the end of sliding, the samples were left in the electrolyte for 15 minutes to register the recovery of the samples after wear. At the end of the tests, the samples were removed from the cells, cleaned with ether and acetone in an ultrasonic bath, and dried with air. The tests were repeated for two rotation speeds, 50 and 100 rpm, under two conditions: the cells rotated just during sliding (still), and the cell was rotating during the whole test (rotating). The duration of sliding for both rotation speeds was of 40 minutes, so the total number of cycles was 2000 for the tests at 50 rpm and 4000 for the one at 100rpm. Three replicates were tested for each material and test conditions to ensure the repeatability of the results.

5.3.2.4 Morphology of the worn surface and material loss quantification

After the tribocorrosion tests, the surface morphology of all the tested specimens was examined by optical microscopy and scanning electron microscopy (FE-SEM / EDS), in order to identify the wear mechanism. The cross-section profile of the wear tracks was obtained with a confocal microscope (Sensofar S Neox). The contact area of the alumina ball was also examined by optical microscopy (Olympus GX71).

The material loss due to tribocorrosion in the wear track (V_{tr}) was determined by calculating the volume of the wear tracks from the cross-section profiles obtained by confocal microscopy. Average width and depth values of the wear tracks were obtained

from different locations along the wear track length. The cross-sectional area of the track was estimated by approaching its shape with a semi-elliptical geometry. Finally, the volume of material loss was calculated by multiplying the cross-sectional area by the circumferential length of the wear track. The material loss volume due to electrochemical corrosion in the unworn surface (V_{corr}) was obtained by subtracting the volume due to tribocorrosion in the wear track (V_{tr}) to the total material loss (V_{tot}) as follows:

$$V_{corr} = V_{tot} - V_{tr} \quad (5.3.I)$$

The total material loss in volume (V_{tot}), was obtained by weighting the test samples before and after each test and multiplying this value by the density of the steels. The density of the steels was calculated by means of a precision balance with bellow weighting capability. All the samples were weighted in a Mettler Toledo XP205 balance with an accuracy of 0.01 mg.

5.3.3 **Results and discussion**

5.3.3.1 Polarization curves with and without sliding

The polarization curves were obtained under corrosion conditions (no sliding) and tribocorrosion conditions (sliding) at different rotation velocities. The curves under tribocorrosion conditions were measured under 5 N of applied load, while the rest of the tests were performed without any load. All the curves are presented in Fig. 5.3.2, separated for each steel type. The electrochemical data obtained from the curves by standard Tafel extrapolation are collected in Table 5.3.1.

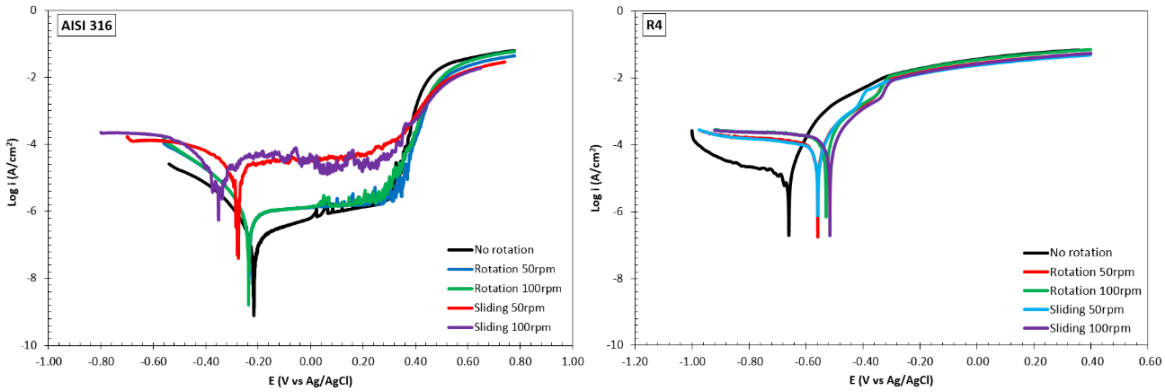

Fig. 5.3.2 Potentiodynamic polarization curves obtained for the AISI 316 stainless steel and R4 steel grade in synthetic seawater under different conditions: no rotation, rotation at 50 and 100 rpm, and tribocorrosion at 50 and 100 rpm under 5N

The curves obtained for the AISI 316 stainless steel possess the typical shape for a passive material, showing a passive plateau and a transpassive domain. The former is observed above the corrosion potential, where the potential remains almost constant for a current range, as a consequence of the formation of a protective oxide layer of few nanometers that protects the bare material from dissolution. The transpassive domain is presented after the plateau when the current increases sharply for small potential variations. The breakdown potential, also named pitting potential, indicates the breakdown of the passive film, which starts to dissolve in the electrolyte due to the occurrence of stable pitting [29,49,50]. The breakdown of the passive film by pitting attack is a typical failure type of stainless steels in seawater, as a consequence of the presence of chloride ions in the solution that can penetrate through the surface film due to their small size [51]. It can be seen that the curve is shifted to more cathodic potentials when changing the test conditions. In the case of the rotating cell without sliding, the zero-current potential or corrosion potential (E_{corr}) moved from -0.216 V to around -0.234

V, and the corrosion current (i_{corr}) increased. This difference in E_{corr} and i_{corr} for the static and rotating conditions might be attributed to a slower passivation of the stainless steel due to the agitation of the electrolyte. However, above 0.100 V, the anodic currents in the passive plateau are similar in both cases. The two curves obtained with the cell rotating at 50 and 100 rpm are superimposed, indicating that there is a small influence of agitation speed on the corrosion of the steel. On the other hand, the curves obtained under tribocorrosion conditions are considerably displaced to lower potentials and higher corrosion currents. The higher shift corresponds to the higher rotation speed. i_{corr} increased in an order of magnitude for the test at 50 rpm, and in two orders of magnitude at 100 rpm. This increase can be attributed to the depassivation of the material in the wear track, which is exposed to the electrolyte were corrosion processes can take place. In all the curves, fluctuations can be observed below and above the pitting potential (E_{pit}). These have been ascribed to metastable pitting activity [52-54], as a consequence of successive passive film breakdown and recovery events. With regard to the pitting potential of the alloy, little variation can be observed in the curves at different conditions. In all the cases, the E_{pit} was close to 0.300 V, indicating that the electrolyte agitation or the action of wear does not promote the breakdown of the passive layer present in the alloy.

Table 5.3.1 Electrochemical data obtained from the potentiodynamic curve by standard Tafel extrapolation

Material	Condition		i_{corr} (μA/cm²)	E_{corr} (V vs Ag/AgCl)	Epit (V vs Ag/AgCl)	R_p (kΩ cm²)	v_{corr} (mm/yr)
AISI 316	No rotation		0.12	-0.216	0.295	159.95	0.001
	Rotation	50 rpm	0.19	-0.234	0.316	81.26	0.002
		100 rpm	0.20	-0.236	0.305	80.27	0.002
	Sliding	50 rpm	9.70	-0.278	0.281	2.18	0.111
		100 rpm	12.73	-0.277	0.297	2.09	0.146
R4	No rotation		18.52	-0.660	-	1.89	0.242
	Rotation	50 rpm	37.13	-0.562	-	0.29	0.427
		100 rpm	71.44	-0.528	-	0.27	0.821
	Sliding	50 rpm	86.93	-0.556	-	0.22	1.101
		100 rpm	94.80	-0.515	-	0.18	1.114

On the curve of the R4 steel grade under no rotation conditions, a great activation stretch is observed in the anodic branch. Above the corrosion potential, the current increases several orders of magnitude for small potential variations. Furthermore, no passive region is observed. This is a typical response of active materials undergoing high rate corrosion processes, i.e., active dissolution [55]. The curves obtained under rotation and tribocorrosion conditions present similar shape, but they are shifted towards more positive potentials. In this case, the curves performed at the same rotation speed are almost superimposed. E_{corr} is shifted from -0.660 V in the static test, to around -0.560 V at 50 rpm and around -0.520 V at 100 rpm. The curves obtained under tribocorrosion conditions are just slightly shifted with respect to those in the rotating cells without sliding. On the other hand, i_{corr} increases with sliding speed, but also when wear is applied. The increase of i_{corr} during tribocorrosion process is attributed to the modifications taking place on the wear track, which natural trend of corrosion dissolution is impeded by sliding. The wear track has been found to have more positive potential than the unworn area, leading to wear-accelerated corrosion of the latter [37,38]. Therefore, the results suggest that the effect of agitation is the main contributor to the acceleration of corrosion of the R4 steel in synthetic seawater. However, the slight increase in the corrosion current leading to lower resistance (R_p) and higher corrosion rates (v_{corr}) indicates that there is also a wear-accelerated corrosion of the unworn surface during sliding.

5.3.3.2 Tribocorrosion tests

Fig. 5.3.3 shows the continuous evolution of potential and current measured through the ZRA configuration during the first hour of immersion, the 40 minutes of sliding, and after sliding.

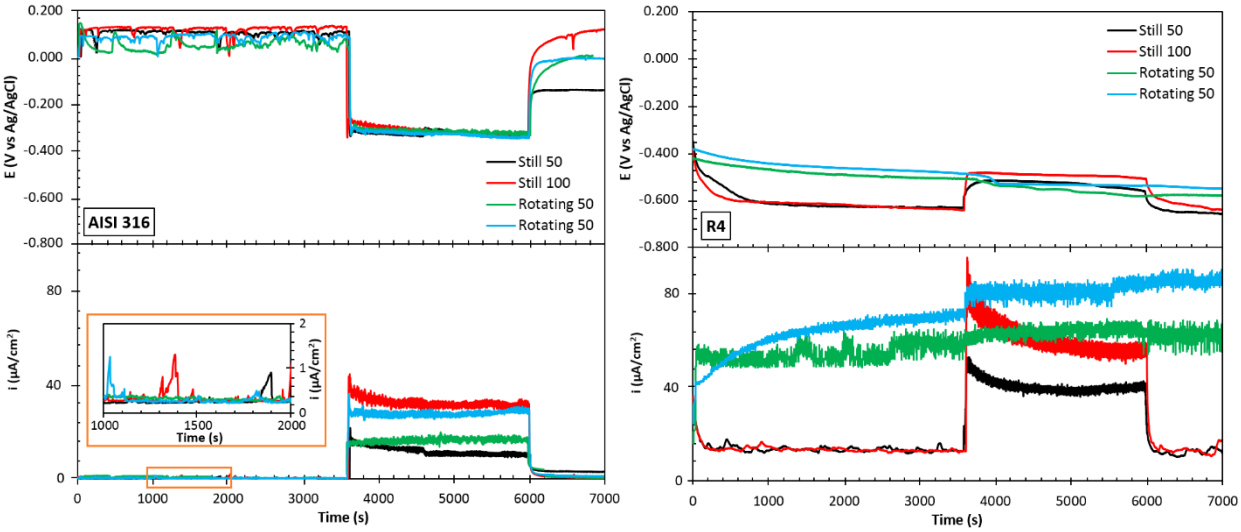

Fig. 5.3.3 Evolution of the potential and current before, during, and after sliding wear test registered by the EN technique through a ZRA for the AISI 316 stainless steel and R4 steel grade

In the results obtained for the AISI 316 stainless steel, during the first hour of immersion the potential fluctuates around 0.01 V. The surface of the steel passivates rapidly in contact with seawater, increasing to reach 0.01 V. The potential fluctuations observed during the first hour can be related to the formation of metastable pits, with successive passive layer breakdown and recovery events. In all the test conditions, the currents registered during this period are around 0.2 μA/cm^2. These small values close to 0 indicate low electrochemical activity on the surface of the steel, just that related to the formation of the metastable pits. Immediately after the steel is submerged in seawater, the surface reacts to form the passive layer, protecting the bare material and impeding its further reaction with the electrolyte resulting in low currents. Once the ball comes into contact with the surface and sliding begins, a sharp drop in the potential towards negative values and an increase in the current is observed. This is the consequence of the damage generated in the passive film, which is removed from the tribological contact, exposing the bare material to the electrolyte [1,3-5,9,21,56-58]. The potential lecture is a mixed potential reflecting the state of the unworn and worn areas. The activation of the worn during sliding leads to a galvanic coupling formation between the worn and unworn surface [1,7,59,60]. The active area is then subjected to local dissolution, and since the potential in this region is more negative, the mixed potential lecture shifts towards negative values. Little difference is observed in the potential of the samples tested at different conditions. In all the cases, the potential during sliding is close to -0.33 V and remains practically constant around that value during the whole test. Similarly, the increase in the electrochemical activity due to the removal of the passive layer and the dissolution taking place in the worn surface leads to an increase in the registered current. The shift in current was found to be larger for the tests at 100 rpm. At 50 rpm, the current was slightly higher for the sample that rotated during the whole test, whereas at 100 rpm it corresponded to the current in the sample that just rotated during sliding. The more considerable increase in the current in the tests at 100 rpm can be attributed to the successive passes of the countermaterial at a higher frequency, with lower time for partial repassivation to take place, maintaining the worn surface in a more active state.

At the end of sliding, the potential increases again, recovering values close to those before sliding. The regeneration of the passive film after sliding is known as repassivation. As the surface repassivates the current decreases to reach values close to 0.

In the case of the R4 steel grade, the shape of the potential evolution is different for that of the stainless steel, being almost the opposite response. In the samples that just rotated during sliding, the potential decreases during the first hour of immersion as a consequence of the initiation of corrosion processes on the steel surface. On the first stage in which the potential decreases sharply, known as phase 0 or activation control, the surface is exposed to the full oxygen concentration of the solution [61-64]. After several minutes, the oxygen on the electrolyte/metal interface is consumed, and the further diffusion of oxygen to the corroding surface is hindered, leading to a change in the slope of potential in what is known as phase 1 or concentration control [61-64]. At this stage, the reaction rate depends on the oxygen supply to the corroding surface, and the governing factor is the oxygen concentration in the electrolyte. A thin corrosion product layer is formed on the surface of the samples, and the potential eventually stabilizes. The common corrosion product forming the rust layer on HSLA steels in seawater has been reported to be composed mainly of iron oxyhydroxide (FeOOH) compound [32-35]. This can be present in different structures, such as goethite (α-FeO(OH)), lepidocrocite (γ-FeO(OH)), or monohydrated ($Fe(OH)_3$). Magnetite has also been found under high iron ion and low oxygen concentrations [36,65]. Even if the oxide layer formed in HSLA steels composed of these oxyhydroxides is porous and loose [32-35], its presence slows down the corrosion rate of the steel, strongly limiting the Fe^{3+} iron transport from the steel to water, and the oxygen transport from the water to the steel [62-64]. This is known as phase 2 or non-linear diffusion control [61-64], where the corrosion of the steel involves the diffusion of oxygen through the rust layer. The current registered during this first hour of immersion follows a similar trend, showing an initial sharp decrease from 33 $\mu A/cm^2$ to 14 $\mu A/cm^2$ during the first 10 minutes of sliding. Afterward, the current remains fluctuating around this value, slowly decreasing to 11 $\mu A/cm^2$ before sliding. This indicates the electrochemical activity on the surface of the steel is slowly reduced as the rust layer is formed on the surface, but not wholly impeded. During sliding, the potential increases to more positive values, as observed in previous works [37,38], showing the opposite response of that in a passive material like the AISI 316 previously explained. This shift has been attributed to the more positive potential of the material on the worn surface, which is free from rust as it is removed by the countermaterial during sliding [37,38]. The increase in the current lecture during sliding confirms the activation of the surface and the occurrence of corrosion reactions of higher rate. In this case, the galvanic coupling formed between the worn and unworn surfaces lead to the wear-acceleration of corrosion of the latter, which constitutes the active area with more negative potential [37,38]. The current increase during sliding is more substantial for the test performed at higher rotation speed, suggesting a more pronounced wear-acceleration corrosion caused by the higher frequency between successive contacts with less time for the worn material to recover. At the end of sliding, the worn surface reacts with the electrolyte leading to potential and current values close to those before sliding, with a decreasing trend similar to that at the beginning of immersion.

In the tests performed for the R4 steel in the rotating cell, the potential evolution differs from that in the static conditions. The initial trend of potential decrease towards more negative values is not so pronounced. This can be ascribed to the continuous rotation of the cell impeding the settlement of corrosion products on the surface of the samples and

pushing them away by centrifugal forces. Therefore, the diffusion of oxygen to the corroding surface is not slowed by the rust layer, but it is further facilitated by the continuous electrolyte agitation. This leads to a lower decrease on the potential and, in turn, to larger corrosion currents evincing higher electrochemical activity on these samples. During sliding, the potential shows a small shift to slightly more negative values, whereas the current increases. The current increase also reflects an acceleration of corrosion during sliding. Furthermore, the larger currents registered for the samples that rotated during the whole test evince higher corrosion rate of the steel during sliding in these samples. This might be related to lower oxides deposited in both the worn and unworn surfaces, which might somehow hinder the access of oxygen in the samples that just rotated during sliding. At the end of sliding, the potential remains in similar values and the current shows a slight increase with time until the end of the test. The current values are slightly higher than those registered before the wear test. This can be a consequence of the reaction of the worn surface with electrolyte after wear, which removed the initially corroded surface during sliding, leaving fresh bulk material to the electrolyte, as well as to the further corrosion of the unworn surface.

When comparing the results obtained for the passive and active steels, apart from the opposite tends on potential evolution previously explained, the more relevant difference between the two materials relies on the current evolution. As it can be noticed, the currents registered for the R4 steel are considerably higher than those of the AISI. Before sliding, the currents on the stainless steel are close to 0, reflecting negligible electrochemical activity after surface passivation. However, in the case of the R4, the current around 14 $\mu A/cm^2$ evinces the reactivity of the steel in seawater despite the rust layer formed in the surface. On the other hand, even if there is a considerable increase of current during sliding in both materials, that of the R4 is larger, which is a consequence of the greater active area corresponding to the unworn surface constituting the anode, rather than the smaller wear track area as in the case of the AISI. After sliding the currents in the passive steel are close to zero, decreasing as the surface repassivates, whereas those in the active steel continue to be higher as the whole surface continues reacting with seawater. Finally, the agitation was found to have low influence on the AISI steel, whereas in the R4 increased the corrosion rate, by both impeding the deposition of corrosion products on the surface and the facilitating the uninterrupted supply of dissolved oxygen to the corroding surface.

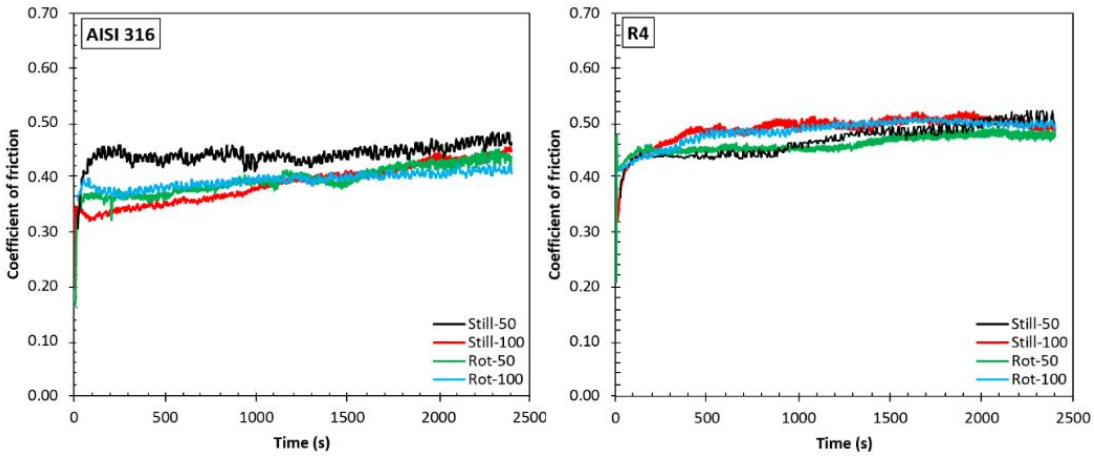

Fig. 5.3.4 Evolution of the coefficient of friction with sliding time for the AISI 316 stainless steel and R4 steel grade in synthetic seawater

The evolution of the coefficient of friction (COF) registered during tribocorrosion tests for both steels is presented in Fig. 5.3.4. The mean COF values are compiled in Table 5.3.2. The curves registered for the AISI 316 steel show a gradual increase of the COF after

an initial running-in period. This trend has been observed in stainless steels and was attributed to the removal of the passive layer and exposure of the fresh surface, increasing the coefficient [57]. The detached material can react with the surface to form oxides that remain in the contact increasing the COF by third body effect [12,13,14,66]. The curves corresponding to the rotating tests and the static test at 100 rpm increase with a similar trend, with close values after 1000 seconds of sliding. The coefficient in the static test at 50 rpm increases sharply during the running-in period, fluctuating around the same value after 200 seconds. The COF of the R4 steel were found to be similar in trend for each speed pair, regardless of the previous cell condition, i.e., static or rotating. The results obtained at 50 rpm seem to remain constant after the running-in period, increasing progressively after around 1000 s of sliding. On the other hand, the curves of the tests at 100 rpm increase from the beginning of the sliding test and fluctuate around 0.5 after 800 seconds. Above 1900 seconds all the curves converge to values close to 0.5. In this case, the increase in the COF is a consequence of the continuous modifications produced by sliding, removing the corrosion products from the wear track and changing the nature and morphology of the contact area [37,38]. In both materials, the fluctuations observed in all the curves are attributed to the formation and ejection of wear debris in the tribological contact [56]. Furthermore, as the sliding time increases, the contact area is enlarged decreasing the contact pressure [38,66].

Table 5.3.2 Mean coefficient of friction values obtained during the tribocorrosion tests, total material loss (V_{tot}), material loss due to tribocorrosion in the wear track (V_{tr}), and material loss due to corrosion in the unworn surface (V_{corr}) for both steel types

Material	Test type	Mean COF	V_{tot} (µm^3)	V_{tr} (µm^3)	V_{corr} (µm^3)
AISI 316	Still-50	0.42±0.03	10.8±0.2	10.7±0.1	0.1±0.0
	Still-100	0.38±0.01	14.6±0.2	14.2±0.2	0.4±0.0
	Rot-50	0.38±0.02	6.1±0.5	5.9±0.6	0.1±0.0
	Rot-100	0.37±0.01	11.4±0.1	11.1±0.2	0.3±0.0
R4	Still-50	0.43±0.01	59. 5±8.5	35.8±0.9	23.6±7.6
	Still-100	0.47±0.03	89.2±7.1	57.0±0.5	32.1±6.5
	Rot-50	0.46±0.03	48.8±2.9	36.9±1.1	11.9±1.8
	Rot-100	0.46±0.01	76.4±4.4	55.2±0.6	21.2±3.8

From the values collected in Table 5.3.2, it can be noticed that the mean coefficients values of each material do not vary significantly for the different test conditions. In the case of the stainless steel, for instance, the COF is around 0.38 for the static tests at 100 rpm and both rotating tests. The coefficient in the static test at 50 rpm is slightly higher, with values of 0.42. The results of the R4 steel are quite higher, being around 0.46 for the static tests and the rotating test at 100 rpm. The coefficient in the rotating test at 50 rpm was lower, around 0.43.

5.3.3.3 Surface analysis of the test surface after tribocorrosion tests

At the end of the tests, the surface of the specimens was analyzed by SEM-EDS and confocal microscopic techniques. The SEM micrographs obtained in the AISI and R4 steel under the different test conditions are presented in Fig. 5.3.5 and Fig. 5.3.6, respectively, and the optical micrographs of the alumina counterbody are shown in Fig. 5.3.7. For both materials, the appearance of the alumina ball was similar for each rotation speed, independently of the cell condition before sliding, i.e., static or rotating. Thus, one representative image is presented in Fig. 5.3.7 for each material and rotation speed.

All the samples of AISI 316 in Fig. 5.3.5 present similar appearance showing ploughing lines parallel to sliding direction and some corrosion in the form of pits inside the wear track. The EDS analysis performed in the worn surface revealed the presence of the

main alloying elements with low oxygen content (66.59wt% Fe, 16.78wt% Cr, 9.16wt% Ni, 2.47wt% Mo, 2.34 wt% C, 1.38wt%Mn, and 1.30wt% O). However, the oxygen concentration on the pits formed inside the wear track was considerable higher, showing also some elements such as chlorine, sodium or magnesium coming from the electrolyte composition, as a consequence of the reaction of the steel with the solution (52.8wt% O, 26.8wt% Fe, 8.57wt% Cr, 3.59wt% C, 3.31wt% Si, 2.05wt% Ca, 1.49wt% Cl, 0.76wt% Na, and 0.63wt% Mg). Furthermore, the analysis made on some grooves of the track revealed the presence of corrosion products with high oxygen content (59.21wt% Fe, 20.1wt% O, 8.23wt% Cr, 8.19wt% Ni, 2.21wt% C, 1.08wt% Mn, 0.75wt% Cl, and 0.23wt% Na). This can be a consequence of the wear debris that react with the electrolyte to form oxides which are smeared and compacted in the tribological contact, filling the ploughs generated during sliding. The unworn surface, however, seems to be free from corrosion, with no pits or corrosion products. The EDS results indicated that this region is mainly composed by the main alloying elements with some oxygen, which corresponds to the passive oxide layer formed during the first hour of immersion in seawater (61.79wt% Fe, 15.27wt% Cr, 9.21wt% Ni, 7.69wt% O, 2.63wt% C, 2.16wt% Mo, 1.23wt% Mn). This is in coherence with that stated by noteworthy researchers, that the passivated surface, i.e., the unworn area, remains unaltered and protected by the passive layer whereas the wear track is subjected to both wear and corrosion due to the removal of the passive layer and the synergism taking place during tribocorrosion [1-10]. The surface analysis performed in the countermaterial after the tests showed the presence of adhered steel that was transferred from the surface of the sample during the tests (Fig. 5.3.7). In spite of the adhesion observed in the balls, no plough or delamination was detected in the tracks, suggesting that the material transferred to the countermaterial corresponded to the debris detached from the worn surface during sliding. Therefore, the tribocorrosion mechanism of the AISI 316 stainless steel in seawater is abrasive-corrosive.

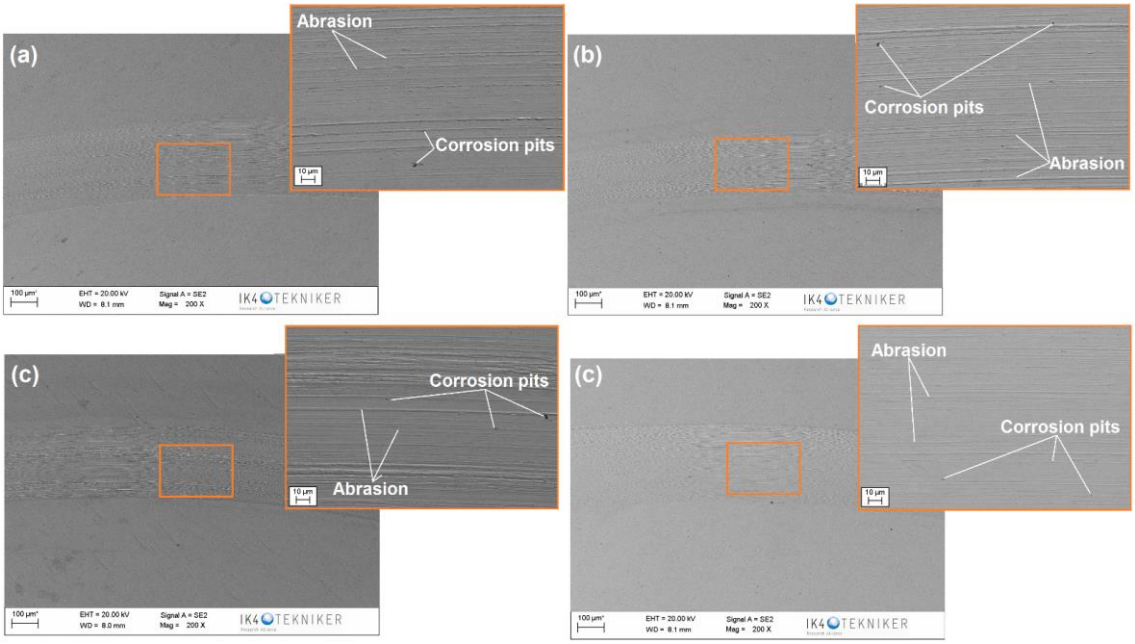

Fig. 5.3.5 SEM images showing the topography of the wear tracks of the AISI stainless steel obtained in the tests with rotation just during sliding at (a) 50 and (b)100 rpm, and the rotating tests at (c) 50 and (d) 100 rpm

In the case of the R4 steel samples, the images show more severe damage in both the wear track and unworn surface comparing with the AISI samples (Fig. 5.3.6). In all the samples, abrasion lines aligned in the direction of the countermaterial movement can be clearly observed. Corrosion pits and corrosion products are also present in both the worn

and unworn areas. The EDS analysis showed similar composition for the pits and corrosion products detected in the samples inside and outside the wear track. In all the cases, apart from a considerable amount of oxygen, certain elements such as chlorine and sodium coming from the reaction with the electrolyte were detected in the pits (51.84wt% Fe, 37.19wt% O, 5.66wt% C, 2.96wt% Cr, 1.43wt% S, 0.50wt% Cl, and 0.41wt% Na) and the corrosion products (61.55wt% Fe, 27.46wt% O, 9.36wt% C, 0.93wt% Cr, and 0.70wt% Cl). Furthermore, the analyses made on the abrasion grooves revealed the presence of corrosion products that might have been smeared during sliding (57.59wt% Fe, 56.72wt% O, 4.17wt% Cr, 3.73wt% C, 1.76wt% S, 0.84wt% Mn, and 0.41wt% Cl). Finally, the EDS results revealed low oxygen concentration on the abraded regions inside the wear track (87.71wt% Fe, 5.45wt% C, 3.70wt% O, 1.18wt% Cr, 0.85wt% Mn), whereas the worn surface showed higher oxygen content (74.58 wt% Fe, 15.29wt% O, 7.11 wt% C, 1.34 wt% Cr, 0.95 0.75 wt% Mn). This evinces the degradation of the unworn surface by corrosion both before and during the wear test. The evaluation of the countermaterial surface revealed the transference of material during the test, but no adhesive detachment was observed in the tracks. No abrasion or wear was observed in the ball. Therefore, the tribocorrosion mechanism of the R4 steel in seawater was a combination of abrasion and corrosion.

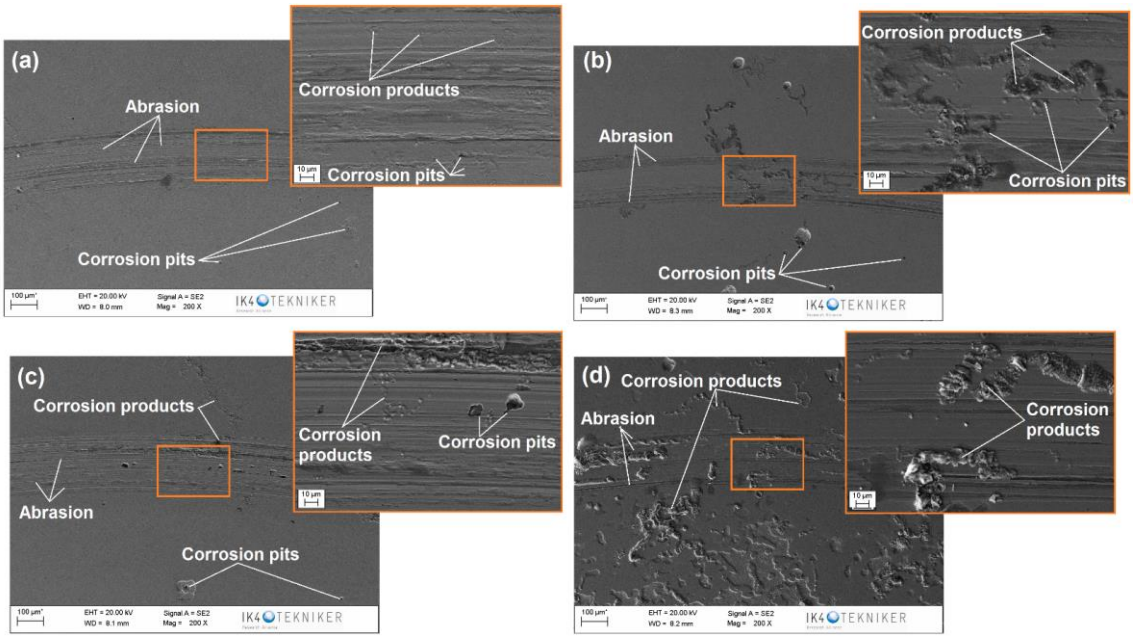

Fig. 5.3.6 SEM images showing the topography of the wear tracks of the R4 steel grade obtained in the tests with rotation just during sliding at (a) 50 and (b)100 rpm, and the rotating tests at (c) 50 and (d) 100 rpm

The degradation of both the wear track and the unworn surface seem to increase with increasing rotation speed. Furthermore, the damage is higher when comparing the samples that rotated during the whole test with those that rotated just during sliding. This is evinced in the topography images of the test surfaces obtained by confocal microscope depicted in Fig. 5.3.8, where the roughness of both the worn and unworn surfaces increases with sliding speed. The test that rotated during the whole test show higher roughness. The increase in roughness in the samples that were mirror polished before the tests is associated with the degradation of the samples by corrosion reactions. Therefore, the higher roughness confirmed a larger material loss in the samples that rotated during the whole test, as previously suggested in the current registered before, during and after the wear tests. This increase in roughness is not observed in the AISI 316 steel samples, where the surface remains smooth after all the tests. This is again related with the negligible corrosion taking place in the unworn protected surface.

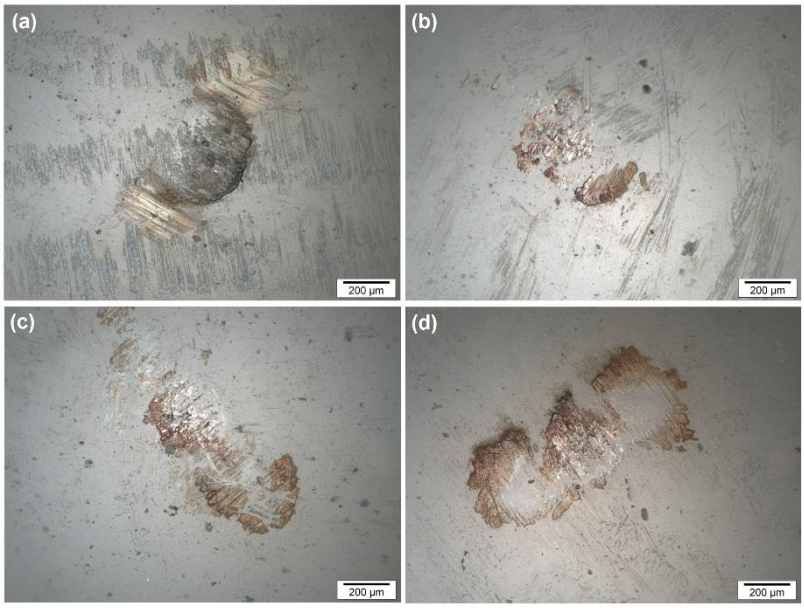

Fig. 5.3.7 Optical micrographs of the alumina counterbody surface after the tests for the AISI 316 at (a) 50 and (b) 100 rpm, and the R4 steel at (c) 50 and (d)100 rpm

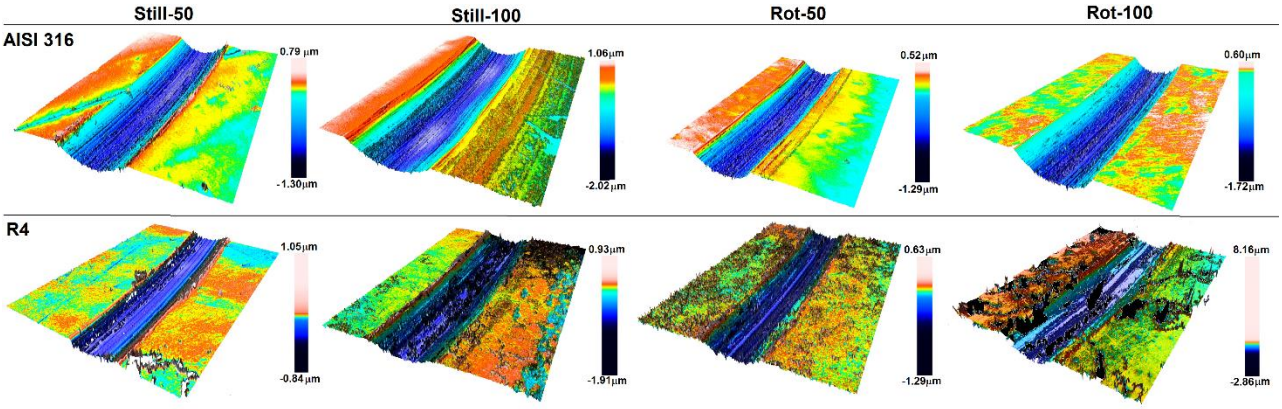

Fig. 5.3.8 Topography of the wear tracks generated in the AISI 316 and R4 steels, in the tests performed at different

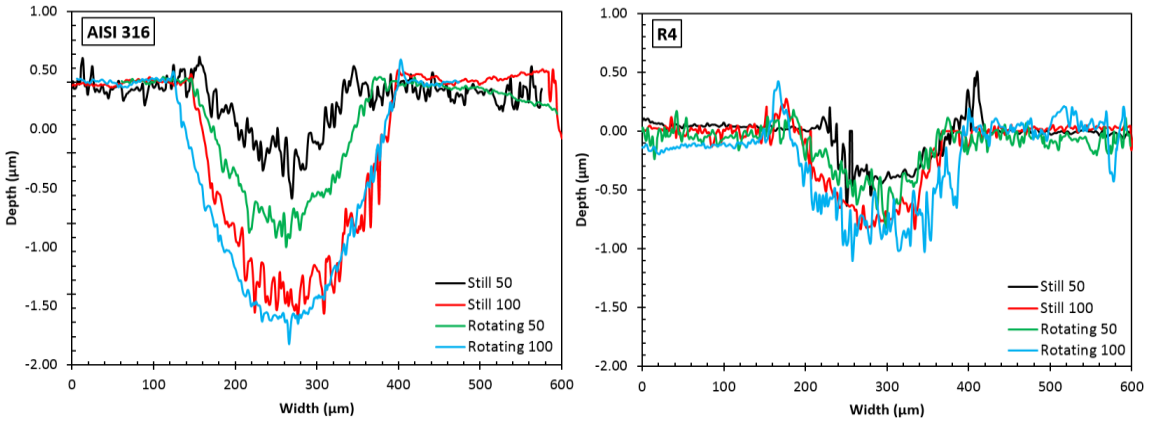

Fig. 5.3.9 Cross-section profiles of the wear tracks generated in the AISI 316 and R4 steels after the tribocorrosion tests

The wear track size of all the samples can be compared at a glance in the images presented in Fig. 5.3.8. In both materials, the tracks generated during the tests at 50 rpm is smaller. It can also be noticed that the tracks of the stainless steel seem to be bigger than those of the R4 steel. This is confirmed by the cross-section profiles of the wear tracks obtained from the topographies presented in Fig. 5.3.9. The bigger tracks in the AISI 316 samples can be ascribed to the lower mechanical resistance of the alloyed steel

in comparison with the low-alloyed one. When comparing the size of the tracks for the AISI 316 steel at the different tests, the bigger tracks correspond to the tests performed at 100 rpm, as a result of the higher number of cycles, i.e., the double, with the subsequent higher material removal. In the case of the R4 steel, the same trend is observed, although the difference is not so evident.

5.3.3.4 Material loss evaluation

As previously commented, the material loss in passive materials corresponds to the wear track volume, as a result of both chemical and mechanical interactions in the tribological contact due to depassivation of the surface. On the other hand, the material loss in an active material is the sum of the tribocorrosion in worn area, by both corrosion and mechanical interplay, and the corrosion in the unworn surface. This, in turn, is derived from two components: pure corrosion and wear-accelerated corrosion. Therefore, the procedures employed in passive materials to quantify the contributions of wear and corrosion to the total material loss cannot be used for passive materials, as already explained in previous works [38,44].

The material loss evaluation was made following the procedure employed in a previous study [38]. The total material loss (V_{tot}) was obtained by weighting the samples before and after each test and multiplying this value by the steels density. The material loss due to tribocorrosion (V_{tr}) was quantified by calculating the wear track volume from the cross-section profiles, as explained in section 5.3.2.4. Finally, the material loss due to corrosion in the unworn area (V_{corr}) was obtained by subtracting the wear track volume to the total material loss (Eq. 5.3.I). Even if the material loss evaluation of passive materials has been made differently [5,8,9], in this work, the same procedure has been employed for both steels in order to compare the results. The results are depicted in Fig. 5.3.10 and compiled in Table 5.3.2.

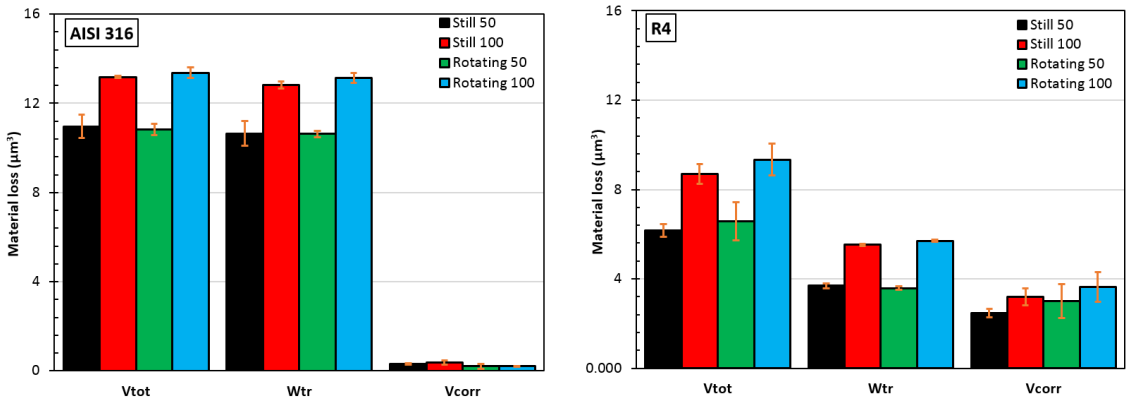

Fig. 5.3.10 Total material loss (V_{tot}), material loss due to tribocorrosion on the wear track (W_{tr}), and material loss due to corrosion in the unworn surface (V_{corr}) in volume

The results obtained for the AISI 316 stainless steel showed that the larger V_{tot} corresponds to the tests performed at 100rpm. This is in coherence with the cross-section profiles and topographies showing the greater wear tracks in these tests, with the double number of total sliding cycles. In fact, little difference can be noticed between V_{tr} and V_{tot}, which in turn leads to low V_{corr} values. This is a consequence of the little corrosion reactions taking place in the passive unworn surface before and during sliding, as previously explained. Furthermore, no significant difference is observed in the values obtained for the tests in static and rotating conditions, confirming the low influence of agitation on the tribocorrosion response of the stainless steel.

In the case of the R4 steel, the samples tested at 100 rpm also presented the larger V_{tot}. Besides, at both rotation speeds, V_{tot} was larger for the samples that rotated during the whole test. The V_{tr} values obtained for the samples showed similar values for each rotation speed. Therefore, the differences in the material loss for the static and rotating samples are related to the material loss due to corrosion on the unworn surface (V_{corr}), rather than tribocorrosion in the wear track. As it can be noticed, V_{corr} is higher in the rotating cells and increases with increasing rotation speed in both cases. These results are in coherence with that observed in the evolution of the corrosion currents in Section 5.3.3.2, that showed higher currents both before and during sliding as a consequence of higher corrosion rates on the steel in the rotating cells.

All these results evinced the wear-acceleration corrosion of the unworn surface and revealed high sensitivity to the agitation of the electrolyte on the tribocorrosion degradation of active materials.

5.3.4 **Conclusions**

This work aimed to compare the tribocorrosion behavior of a passive and an active material, i.e., an AISI 316 stainless steel and an R4 HSLA steel grade. Furthermore, the influence of the electrolyte agitation has been investigated for both materials. For this aim, unidirectional ball-on-disc tribocorrosion tests have been performed using the zero resistant ammetry (ZRA) electrochemical technique. The effect of agitation was evaluated by performing the tests at different rotation speeds, in the samples that rotated just during sliding and other that rotated during the whole test duration.

From the results obtained in this work, the following conclusions can be drawn:

- The potentiodynamic polarization tests showed little influence of agitation in the AISI 316 stainless steel but a significant influence of wear, since the curves obtained under tribocorrosion conditions were cathodically displaced as a consequence of the depassivation of the worn surface increasing corrosion reactions in the tribological contact.
- The results obtained for the R4 steel showed a high influence of agitation as a shift of the curves towards more positive potentials and higher currents, suggesting the increase in the corrosion rate by the electrolyte agitation. The curves under tribocorrosion conditions were even more displaced, indicating the acceleration of corrosion by wear process.
- The tribocorrosion tests showed completely different results for both materials, showing negligible currents before sliding for the passive alloy and an increase during sliding as a result of the activation of the material in wear track. No significant influence of agitation was observed from the results of the AISI steel.
- However, the results of the R4 steel showed considerable currents before sliding, indicating a high reactivity of the active steel, in which no passive layer is formed. The currents increased during sliding, as a consequence of the wear-accelerated corrosion of the unworn surface. The currents were observed to be higher in the rotating cells, suggesting a significant influence of the electrolyte agitation in the corrosion rate of the steel.
- The coefficients of friction registered during the tribocorrosion test did not present significant differences between the different test conditions for either material. In both cases, the wear debris that reacted with the solution and remained in the tribological contact led to an increase of the coefficient with sliding time.

- The superficial analysis and the material loss evaluation showed a negligible influence of agitation on the stainless steel, but a considerable effect on the material loss in the unworn surface of the active steel, coherently with the current evolution registered during the tests, confirming the detrimental effect of agitation.
- All these results evinced the wear-acceleration corrosion of the unworn surface and revealed high sensitivity to the agitation of the electrolyte on the tribocorrosion degradation of active materials.

5.3.5 **Acknowledgments**

This work was performed with the support of the FRONTIERS IV project (ELKARTEK 2018) financed by the Basque Country. Authors would also like to acknowledge the Education, Linguistic Politics and Culture Department of the Basque Government for its support through the grant “Programa Predoctoral de Formación de Personal Investigador No Doctor (PRE_2017_2_0088)” awarded to the first author.

5.3.6 **References**

[1] D. Landolt, S. Mischler (Eds.). *Tribocorrosion of Passive Metals and Coatings*. Woodhead Publishing, Cambridge, 2011, ISBN: 978-1-84569-966-6

[2] S. Mischler, E.A. Rosset, D. Landolt. *Effect of Corrosion on the Wear Behaviour of Passivating Metals in Aqueous Solutions*. Tribology Series 25 (1993) 245-253

[3] D. Landolt. *Electrochemical and materials aspects of tribocorrosion systems*. Journal of Physics, D 39 (2006) 3121-3127

[4] D. Landolt, S. Mischler, M. Stemp. *Electrochemical methods in tribocorrosion: a critical appraisal*. Electrochimica Acta 46 (2001) 3913-3929

[5] J.-P. Celis, P- Ponthiaux (Eds.). *Testing Tribocorrosion of Passivating Materials Supporting Research and Industrial Innovation: Handbook*. Maney Publishing, UK, 2012, ISBN: 978-1-907975-20-2

[6] M.T. Mathew, P. Srinivasa Pai, R. Pourzal, A. Fischer, M.A. Wimmer. *Significance of Tribocorrosion in Biomedical Applications: Overview and Current Status*. Advances in Tribology (2009) doi:10.1155/2009/250986, article ID 250986

[7] S. Mischler. *Triboelectrochemical techniques and interpretation methods in tribocorrosion: A comparative evaluation*. Tribology International 41 (2008) 573-583

[8] N. Diomidis, J.-P. Celis, P. Ponthiaux, F. Wenger. *A Methodology for the Assessment of the Tribocorrosion of Passivating Metallic Materials*. Lubrication Science 21 (2009) 53-67

[9] N. Diomidis, J.-P. Celis, P. Ponthiaux, F. Wenger. *Tribocorrosion of Stainless Steel in Sulfuric Acid: Identification of Corrosion-Wear Components and Effect of Contact Area*. Wear 269 (2010) 93-103

[10] S. Mischler, P. Ponthiaux. *A round robin on combined electrochemical and friction tests on alumina/stainless steel contacts in sulphuric acid*. Wear 248 (2001) 211-225

[11] G. Stachowiak, M. Salasi, G. Stachowiak. *Three-Body Abrasion Studies of High-Cr Cast Irons: Benefits and Limitations of Tribo-electrochemical Methods*. Journal of Bio- and Tribo-Corrosion (2015) 1:6

[12] R.I. Trezona, D.N. Allsopp, I.M. Hutchings. *Transitions between two-body and three-body abrasive wear: influence of test conditions in the microscale abrasive wear test*. Wear 225-229 (1999) 205-214

[13] D. Landolt, S. Michler, M. Stemp, S. Barril. *Third body effects and material fluxes in tribocorrosion systems involving a sliding contact*. Wear 256 (204) 517-524

[14] N. Diomidis, S. Mischler. *Third body effects on friction and wear during fretting of steel contacts*. Tribology International 44 (2011) 1452-1460

[15] S.W. Watson, F.J. Friedersdorf, B.W. Madsen, S.D. Cramer. *Methods of measuring wear-corrosion synergism*. Wear 181-183 (1995) 476-484

[16] M. Stemp, S. Mischler, D. Landolt. *The effect of contact configuration on the tribocorrosión of stainless steel in reciprocating sliding under potentiostatic control*. Corrosion Science 45 (2003) 625-640

[17] S. Mischler, A. Spiegel, M. Stemp, D. Landolt. *Influence of passivity on the tribocorrosion of carbon steel in aqueous solutions*. Wear 251 (2001) 1295-1307

[18] P. Jemmely, S. Mischler, D. Landolt. *Electrochemical modelling of passivation phenomena in tribocorrosion*. Wear 237 (2000) 63-76
[19] Y. Sun, R. Bailey. *Improvement in tribocorrosion behavior of 304 stainless steel by surface mechanical attrition treatment*. Surface & Coatings Technology 253 (2014) 284-291
[20] A.C. Vieira, A.R. Ribeiro, L.A. Rocha, J.P. Celis. *Influence of pH and corrosion inhibitors on the tribocorrosion of titanium in artificial saliva*. Wear 261 (2006) 994-1001
[21] Y. Sun, V. Rana. *Tribocorrosion behaviour of AISI 304 Stainless steel in 0.5M NaCl solution*. Materials Chemistry and Physics 129 (2011) 138-147
[22] R. Pileggi, M. Tului, D. Stocchi, S. Lionetti. *Tribo-corrosion behavior of chromium carbide based coatings deposited by HVOF*. Surface & Coatings Technology 268 (2015) 247-251
[23] X. Luo, X. Li, Y. Sun, H. Dong. *Tribocorrosion behaviour of S-phase surface engineered medical grade Co-Cr alloy*. Wear 302 (2013) 1615-1623
[24] Z. Guo, X. Pang, Y. Yan, K. Gao, A.A. Volinsky, T-Y Zhang. *CoCrMo alloy for orthopedic implant application enhanced corrosion and tribocorrosion properties by nitrogen ion implantation*. Applied Surface Science 347 (2015) 23-34
[25] A.M. Ribeiro, A.C. Alves, L.A. Rocha, F.S. Silva, T. Toptan. *Synergism between corrosion and wear on CoCrMo-Al2O3 biocomposites in a physiological solution*. Tribology International 91 (2015) 198-205
[26] Z. Doni, A.C. Alves, F. Toptan, J.R. Gomes, A. Ramalho, M. Buciumeanu, L. Palaghian, F.S. Silva. *Dry sliding and tribocorrosion behavior of hot pressed coCrMo biomedical alloy as compared with the cast CoCrMo and Ti6Al4V alloys*. Materials and Design 52 (2013) 47-57
[27] V.G. Pina, A. Dalmau, F. Devesa, V. Amigó, A.I. Muñoz. *Tribocorrosion behavior of beta titanium biomedical alloys in phosphate buffer saline solution*. Journal of the Mechanical Behavior of Biomedical Materials 46 (2015) 59-68
[28] I. Hacisalihoglu, A. Samancioglu, F. Yildiz, A. Alsaran. *Tribocorrosion properties of different type titanium alloys in simulated body fluid*. Wear 332-333 (2015) 679-686
[29] Y. Yan (Ed.). *Bio-Tribocorrosion in Biomaterials and Medical Implants*. Woodhead Publishing (2013), ISBN: 978-0-85709-540-4
[30] A. de Frutos Rozas. *Tribocorrosión de biomateriales metálicos modificados superficialmente mediante técnicas de vacío*. Ph.D. Thesis, Universidad autónoma de Madrid, Facultad de ciencias, June 2010
[31] M. Azzi, J.A. Szpunar. *Tribo-electrochemical technique for studying tribocorrosion behaviour of biomaterials*. Biomolecular Engineering 24 (2007) 443-446
[32] J. K. Saha. *Corrosion of Constructional Steels in Marine and Industrial Environment*. Springer India (2013). ISBN: 978-81-322-0719-1
[33] K. Xiao, C.F. Dong, X.G. Li, F.M. Wang. *Corrosion Products and Formation Mechanism during Initial Stage of Atmospheric Corrosion of Carbon Steel*. Journal of Iron and Steel Research International 15 (2008) 42-48
[34] J.G. Castaño, C.A. Botero, A.H. Restrepo, E.A. Agudelo, E. Correa, F. Echeverría. *Atmospheric corrosion of carbon steel in Colombia*. Corrosion Science 52 (2010) 216-223
[35] H. Möller, E.T. Boshoff, H. Froneman. *The corrosion behaviour of a low carbon steel in natural and synthetic seawaters*. The Journal of The South African Institute of Mining and Metallurgy, Volume 106 (August 2006) 585-592
[36] Joint Industry Project Steering Committee. *Mooring Integrity for Floating Offshore Installations Joint Industry Project Phase 2: The effect of wear and corrosion of steel components on the integrity of mooring systems for floating offshore installations*. Health & Safety Executive (HSE) (2017). Research report 1096
[37] A. López, R. Bayón, F. Pagano, A. Igartua, A. Arredondo, J.L. Arana, J.J. González. *Tribocorrosion behaviour of mooring high strength low alloy steels in synthetic seawater*. Wear 338-339 (2015) 1-10
[38] A. López-Ortega, R. Bayón, J.L. Arana, A. Arredondo, A. Igartua. *Influence of temperature on the corrosion and tribocorrosion behavior of High-Strength Low-Alloy steels used in offshore applications*. Tribology International 121 (2018) 341-352
[39] A. López-Ortega, R. Bayón, J.L. Arana. *Evaluation of protective coatings for offshore applications. Corrosion and tribocorrosion behavior in synthetic seawater*. Surface & Coatings Technology 349 (2018) 1083-1097
[40] M.R. Dhanak, N.I. Xiros (Eds.). *Springer Handbook of Ocean Engineering*. Springer (2016) ISBN: 978-319-16648-3

[41] M. Lannuzzi, A. Barnoush, R. Johnsen. *Materials and corrosion trends in offshore and subsea oil and gas production*. NPJ Materials Degradation (2017) 2
[42] Y. Weng, H. Dong, Y. Gan (Eds.). *Advanced Steels. The Recent Scenario in Steel Science and Technology*. Springer (2011) ISBN: 978-3-642-17664-7
[43] P. Ault. *The use of coatings for corrosion control on offshore oil structures*. Journal of Protective Coatings and linings 23 (2006) 42-47
[44] A. López-Ortega, J. L. Arana, and R. Bayón. *Tribocorrosion of Passive Materials: A Review on Test Procedures and Standards*. International Journal of Corrosion, vol. 2018, Article ID 7345346, 24 pages, 2018
[45] ASTM G119-09(2016). *Standard guide for determining synergism between wear and corrosión*. ASTM International, West Conshohocken, PA, 2016
[46] UNE 112086:2016. *Ensayos de tribocorrosión en materiales pasivos*. 07 September 2016
[47] Offshore Standard DNVGL-OS E302, Det Norske Veritas, Offshore Mooring Chains, July 2018
[48] G.W. Stachowiak, A.W. Batchelor. *Engineering Tribology*. Butterworth Heinemann, UK (2005) ISBN: 978-0-7506-7836-0
[49] N. Espallargas, C. Torres, A.I. Muñoz. *A metal ion release study of CoCrMo exposed to corrosion and tribocorrosion conditions in simulated body fluids*. Wear 332-333 (2015) 669-678
[50] N. Espallargas, R. Johnsen, C. Torres, A.I. Muñoz. *A new experimental technique for quantifying the galvanic coupling effects on stainless steel during tribocorrosion under equilibrium conditions*. Wear 307 (2013) 190-197
[51] E. McCafferty. *Introduction to Corrosion Science*. Springer (2010) ISBN:978-1-4419-0454-6
[52] J.O. Bello, R.J.K. Wood, J.A. Wharton. *Synergistic effects of micro-abrasion-corrosion of UNS S30403, S31603 and S32760 stainless steels*. Wear 263 (2007) 149-159
[53] K.V.S. Ramana, T. Anita, S. Mandal, S. Kaliappan, H. Shaikh, P.V. Sivaprasad, R.K. Dayal, H.S. Khatak. *Effect of different environmental parameters on pitting behavior of AISI type 316L stainless steel: Experimental studies and neural network modelling*. Materials and Design 30 (2009) 3770-3775
[54] Y. Yi, P. Cho, A. AlZaabi, Y. Addad, C. Jang. *Potentiodynamic polarization behavior of AISI type 316 stainless steel in NaCl solution*. Corrosion Science 74 (2013) 92-97
[55] W. Liu, Q. Zhou, L. Li, Z. Wu, F. Cao, Z. Gao. *Effect of alloying elements on corrosion behavior of the huge crude oil storage tank steel in seawater*. Journal of Alloys and Compounds 598 (2014) 198-204
[56] J. Chen, Q. Zhang, Q.A. Li, S.L. Fu, J.Z. Wang. *Corrosion and tribocorrosion behaviors of AISI 316 stainless steel and Ti6Al4V alloys in artificial seawater*. Transactions of Nonferrous Metals Society of China 24 (2014) 1022–1031. doi:10.1016/S1003-6326(14)63157-5.
[57] R. Priya, C. Mallika, U. Kamachi Mudali. *Wear and tribocorrosion behaviour of 304L SS, Zr-702, Zircaloy-4 and Ti-grade2*. Wear. 310 (2014) 90–100.
[58] Y. Sun, V. Rana. *Tribocorrosion behaviour of AISI 304 stainless steel in 0.5M NaCl solution*. Mater. Chem. Phys. 129 (2011) 138–147
[59] Dr. Shih (Ed.). *Corrosion Resistance*. In Tech (2012) ISBN: 978-953-51-0467-4
[60] J.P. Celis, P. Ponthiaux, F. Wenger. *Tribo-corrosion of materials: Interplay between chemical, electrochemical, and mechanical reactivity of surfaces*. Wear 261 (2006) 939–946
[61] R.E. Melchers, T. Moan, Z. Gao. *Corrosion of working chains continuously immersed in seawater*. J Mar Sci Technol (2007) 12:102-110
[62] R.E. Melchers, R. Jeffrey. *Early corrosion of mild Steel in seawater*. Corrosion Science 47 (2005) 1678-1693
[63] R.E. Melchers. *Effect of marine immersion corrosion of carbon content of low alloy Steels*. Corrosion Science 45 (2003) 2609-2625
[64] J. Bhandari, F. Khan, R. Abbassi, V. Garaniya, R. Ojeda. *Modelling of pitting corrosion in marine and offshore Steel structures-A technical review*. Journal of Loss Prevention in the Process Industries 37 (2015) 39-62
[65] Joint Industry Project Steering Committee. *Mooring Integrity for Floating Offshore Installations Joint Industry Project: Phase 2 Summary*. Health & Safety Executive (HSE) (2017). Research report 1090.

[66] S.B. Pitchuka, B. Boesl, C. Zhang, D. Lahiri, A. Nieto, G. Sundararajan, A. Agarwal. *Dry sliding wear behavior of cold sprayed aluminum amorphous/nanocrystalline alloy coatings*. Surface & Coatings Technology 238 (2014) 118–125

Part II

Protective coatings: evaluation and development of new solutions

Contribution 4

Evaluation of protective coatings for offshore applications: Corrosion and tribocorrosion behavior in synthetic seawater

Surface & Coatings Technology 349 (2018) 1083-1097

Contribution 4: Surface & Coatings Technology 349 (2018) 1083-1097

5.4. EVALUATION OF PROTECTIVE COATINGS FOR OFFSHORE APPLICATIONS. CORROSION AND TRIBOCORROSION BEHAVIOUR IN SYNTHETIC SEAWATER

A. López-Ortega[a], R. Bayón[a], J.L. Arana[b]

[a] *IK4-TEKNIKER, Eibar, Spain*
[b] *Department of Metallurgical and Materials Engineering, University of the Basque Country, Spain*

ABSTRACT

Coatings have been widely used in the corrosion protection of metallic materials in marine environments. In this work, the corrosion and tribocorrosion behavior of three potential coatings employed in offshore applications has been evaluated. The coatings studied were a Thermally Sprayed Carbide coating with an organic sealant (C1), a Thermally Sprayed Aluminum with an organic topcoat (C2), and an epoxydic organic coating reinforced with ceramic platelets (C3). Electrochemical Impedance Spectroscopy and Potentiodynamic Polarization techniques have been employed to assess the corrosion performance of the coatings in synthetic seawater. Furthermore, unidirectional ball-on-disc tribocorrosion tests were performed to study the response of the coatings subjected to the simultaneous action of wear and corrosion. The coatings were found to provide to the steel substrate with enhanced corrosion resistance, both in the absence and during wear process, and to improve the tribological properties with lower coefficients of friction in seawater. The coating less affected by sliding in terms of corrosion resistance was the C2 coating, which also showed the lowest coefficient of friction.

Keywords: *Offshore; Corrosion; Tribocorrosion; Coatings; Seawater*

5.4.1 Introduction

Corrosion is one of the phenomena that worst affect the deterioration of materials in offshore applications. 30% of failures in ships and other marine equipment are the consequence of marine corrosion, with an annual cost of over EUR 1.5 trillion[vi] [1]. Marine corrosion is particularly aggressive, due to the high salt content and low electrical resistivity of seawater [2]. The chlorides present in seawater depassivate metal and alloys such as stainless steels, aluminum alloys or titanium alloys; even in the absence of oxygen. Chlorides are also present in marine atmospheres, which can lead to corrosion of non-submerged materials and structures [3]. The maximum corrosion rate of steel has been observed to be at a NaCl content of 3% in weight, which corresponds to the salinity of seawater (around 3.5wt%) [1,4]. There are other factors affecting corrosion in seawater and marine environments, e.g., temperature, dissolved oxygen concentration, pH, the presence of microorganisms, and so on [1,5-7]. Temperature and salinity of seawater, as well as dissolved oxygen concentration, vary depending on the geographical location. Furthermore, temperature and oxygen concentration also vary with water depth [1,5,6,8,9]. On the other hand, there are specific applications, e.g., mooring line systems, where the movement of seawater due to waves, wind and ocean currents, generates a relative movement between components that leads to a continuous

[vi] *Currency expressed in American trillion (10^{12})*

wear in the contact [7,10,11]. When wear and corrosion take place simultaneously, the phenomenon is known as tribocorrosion [12-14].

The most employed structural material is steel, usually mild or low-alloyed, which easily corrodes in the marine environment or submerged in seawater. These steels are relatively cost-effective, compared to other more corrosion resistant steels and alloys [1]. High-Strength Low-Alloyed (HSLA) steels, for instance, are widely used due to their high mechanical properties, with yield strengths in the range of 460-960 MPa, and relatively low weight [15,16]. The use of HSLA steels in offshore applications has increased from less than 10% to over 40% in less than a decade [17]. They are used in the fabrication of offshore structures such as jack-ups and legs, also in pipelines and tethering attachments for floating structures in tension leg platforms (TLPs), or mooring lines of semi-submersible structures, among others [15,18,19]. The corrosion rate of mild steel in seawater has been measured to be 250 microns per year [20,21]. This high dissolution rate involves elevate costs on maintenance and replacement of damaged surfaces, and what is worse, the risk of premature deterioration of infrastructures or components that can lead to catastrophic failures, even taking human lives in the worst-case scenario.

In order to avoid or prevent such unpredictable failures, coatings have been successfully used to minimize corrosion losses in steel structures. Protective coatings selected for marine environment strongly depend on the exposure zone, i.e., considering whether the protected system will be subjected to the marine atmosphere (atmospheric zone), continuous immersion (immersed zone), or intermittent exposure to marine atmosphere and seawater (splash and tidal zones) [22]. Depending on the exposure zone, the coatings must provide the system with specific properties to assure infrastructures durability.

The most widely employed corrosion-control solution for metallic materials in marine environments are organic coatings (250-300 µm thick), due to their high corrosion resistance [22,23]. However, the low wear resistance of these coatings is a drawback in specific applications. On the other hand, Thermally Sprayed Coatings (TSC) have recently been used in offshore applications [24,25]. For instance, Thermally Sprayed Aluminum (TSA) coatings with organic topcoat systems (250-300 µm thick) have widely been applied in submerged components [20,22,26], providing an effective service life of coated systems for 30 years in different exposure zones [26-28]. The aluminum layer deposited on top of the steel provides the substrate with an additional cathodic protection via the sacrificial anodic reaction of the aluminum. The NORSOK M-501 [29] standard recommends the use of an organic sealant on top of the sprayed aluminum to fill the pores and irregularities present in the coating and enhance the coating lifetime. When an additional wear resistance was required, Thermally Sprayed Carbide Coatings (TSCC) have also been used. This kind of coating protects the substrates against wear due to their high hardness, also providing the system with enhanced corrosion resistance.

In this work, three commercial coatings currently used for the protection of submerged steel components in mooring line systems have been evaluated in terms of corrosion and wear-corrosion behavior. For this aim, electrochemical corrosion tests consisting of electrochemical impedance spectroscopy and potentiodynamic polarization measurements were performed in synthetic seawater. Furthermore, the wear-corrosion (tribocorrosion) behavior of the coatings was evaluated by performing unidirectional ball-on-disc sliding tests in synthetic seawater, monitoring both electrochemical and tribological responses. The corrosion and tribocorrosion results of the coatings were

compared with the uncoated steel to confirm the actual improvements provided by the coatings.

5.4.2 **Experimental procedure**

5.4.2.1 Materials and sample preparation

In the present work, the corrosion and wear-corrosion behavior of three commercial coatings used in the protection of submerged components has been evaluated. The selected coatings are used in the protection of offshore mooring line components. The chain links and accessories that compose mooring lines are manufactured of High-Strength Low-Alloy steels, which are classified into five grades depending on their ultimate strength: R3, R3S, R4, R4S and R5[30]. In this study, R4 steel grade samples were coated with the following systems:

- Thermally Sprayed Carbide (WC-CrCo) with an organic sealant (**C1**)
- Arc Thermally Sprayed Aluminum with an organic topcoat (**C2**)
- Epoxy based organic coating reinforced with ceramic particles (**C3**)

The coatings were applied by the client in the frame of an industrial project, and the information on the coatings preparation is confidential. The test samples were R4 steel grade panels of 30x40 mm^2, which were coated after machining the plates from real chain components. For both corrosion and tribocorrosion tests, an exposed area of 2.31 cm^2 was created by using an insulating wax. The results of the coatings were compared with the un-coated steel samples, which were mirror polished (Ra<0.05 µm) before testing.

5.4.2.2 Coatings characterization

The roughness of the coatings was measured according to the DIN EN-ISO 4288:1998 standard, in a Perthometer M2 (Mar GmbH) profilometer. The cross-section of the coatings was analyzed in an Olympus GX71 optical microscope, and the coating thickness was measured in accordance to the UNE-EN ISO 1463:2005 standard. The morphology of C1 and C2 metallic coatings was assessed by Field Emission Scanning Electron Microscope (FE-SEM) equipped with Energy Dispersive X-ray Spectrometer (EDS), from OXFORD INCA Synergy. The porosity degree was obtained from the SEM cross-sectional images by image analysis software (AnalySIS pro). Finally, the hardness of the three coatings was measured in an Akashi AVK-A tester, equipped with Vickers indentation equipment, following the UNE-EN ISO 6507-1:2006 standard. The measurements were performed with a Vickers diamond pyramid indenter, with an indentation time of 10 s, under a load of 1 Kg for C1 coating, and 100 g for C2 and C3 coatings.

5.4.2.3 Electrochemical corrosion tests

The electrochemical corrosion tests were performed in a three-electrode cell, connected to an Autolab-Metrohm PGSTAT302N potentiostat, equipped with a FRA32M and EDC modules. A commercial Ag/AgCl (KCl 3M) and a platinum wire were used as the reference and counter electrodes. The test samples were connected as the working electrodes. The potential of the reference electrode is of 207 mV with respect to the Standard Hydrogen Electrode (SHE), and all the potentials in this work are referred to the Ag/AgCl electrode. The test solution was synthetic seawater with heavy metals prepared in accordance with the ASTM D 1141 standard. For each test, the cell was filled with 50 ml of this solution. The tests were performed at room temperature (23±2 ºC) and aerated conditions. The exposed surface of all the samples was circular and of 2.31 cm^2.

The samples were horizontally placed in the corrosion cell. All the tests were triplicated to ensure the reproducibility of the results.

The first series of electrochemical corrosion tests consisted of obtaining the polarization curve of the materials in synthetic seawater. The samples were immersed in synthetic seawater during 60 minutes for potential stabilization, during which the Open Circuit Potential (OCP) was recorded. Then, a potentiodynamic polarization measurement was carried out in the potential range from -400 mV to +1600 mV with respect to the open circuit potential (OCP vs. Ag/AgCl), at a sweep rate of 0.166 mV/s (ASTM G5).

In the second series of experiments, new samples were immersed in the electrolyte for 500 hours, and periodic Electrochemical Impedance Spectroscopy (EIS) measurements were performed to evaluate the evolution of coatings performance with immersion time. The impedance data was registered after 24, 168, 336 and 504 hours in synthetic seawater. The measurements were made under a sinusoidal perturbation of ±10 mV amplitude, at a frequency range from 10 kHz to 1 mHz, with 10 points per frequency decade.

5.4.2.4 Tribocorrosion tests

The tribocorrosion tests were performed in a unidirectional MicroTest MT/10/SCM tribometer under ball-on-disc configuration, as schematically shown in Fig. 5.4.1. The test samples were fixed in a three-electrode electrochemical cell, placed in the rotatory plate of the tribometer, and connected to an Autolab-Metrohm PGSTAT302N potentiostat, equipped with a FRA32M and EDC modules. This configuration allows the simultaneous control of both electrochemical and mechanical parameters during the tests.

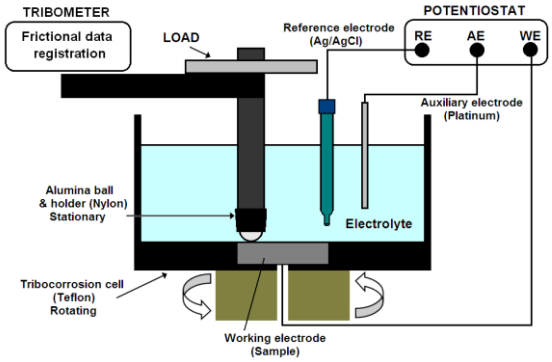

Fig. 5.4.1 Unidirectional tribocorrosion ball-on-disc experimental setup employed in this work

A commercial Ag/AgCl (KCl 3M), a platinum wire, and the test samples were connected as the reference electrode, the counterelectrode, and the working electrode, respectively. The test solution was synthetic seawater with heavy metals prepared in accordance with the ASTM D 1141 standard. For each test, 150 ml of this solution was employed.

In these tests, sliding represents the wear conditions between chain links and accessories with relative movement to one another. The contact conditions were calculated using the Hertzian Contact Theory [31], considering the real contact pressure between links in real applications, as already performed in a previous work [10]. The normal load was of 5 N, corresponding to an average Hertzian pressure of 930 MPa with a contact radius of 50.5 µm. The wear track was of 5 mm and the rotation speed 100 rpm. An alumina ball of 10 mm in diameter (G28) was used as the countermaterial.

The samples were immersed in the electrolyte, and after an hour of immersion, an Electrochemical Impedance Spectroscopy measurement was made. After the impedance measurement, a sliding wear test of 4000 cycles was performed, during which the coefficient of friction (COF) and a second EIS were simultaneously recorded. The EIS measurements were performed under a sinusoidal perturbation of ±10 mV amplitude, at a frequency range from 10 kHz to 10 mHz, with 10 points per frequency decade. The tests were performed at room temperature (23±2 ºC) and aerated conditions. The exposed surface of the samples was circular, of 2.31 cm^2. All the tests were performed by triplicate to ensure the reproducibility of the results.

After the tests, the surface of the samples was examined in an optical microscope (Olympus GX71), and the cross-section profiles of the wear tracks were obtained with a confocal microscope (Nikon ECLIPSE ME600). The material loss due to tribocorrosion in the wear track was quantified by calculating the wear track volume from the cross-section profiles, as described elsewhere [10-12,32]. The contact area of the alumina ball was also examined, but the wear of the balls was negligible, so no further mention is made in this work.

5.4.3 **Results and discussion**

5.4.3.1 Coatings characterization

Fig. 5.4.2 shows the cross-section morphologies of the three coatings. From the micrographs, it can be observed that the three coatings are well-bonded to the substrate, since no distinctive irregular interface is detected. The difference in thickness between the thee coatings can be clearly observed in these images, obtained with different magnitude. The organic sealant applied on C1 coating was not distinguished in the micrographs, whereas the organic topcoat applied on C2 coating was considerably thick.

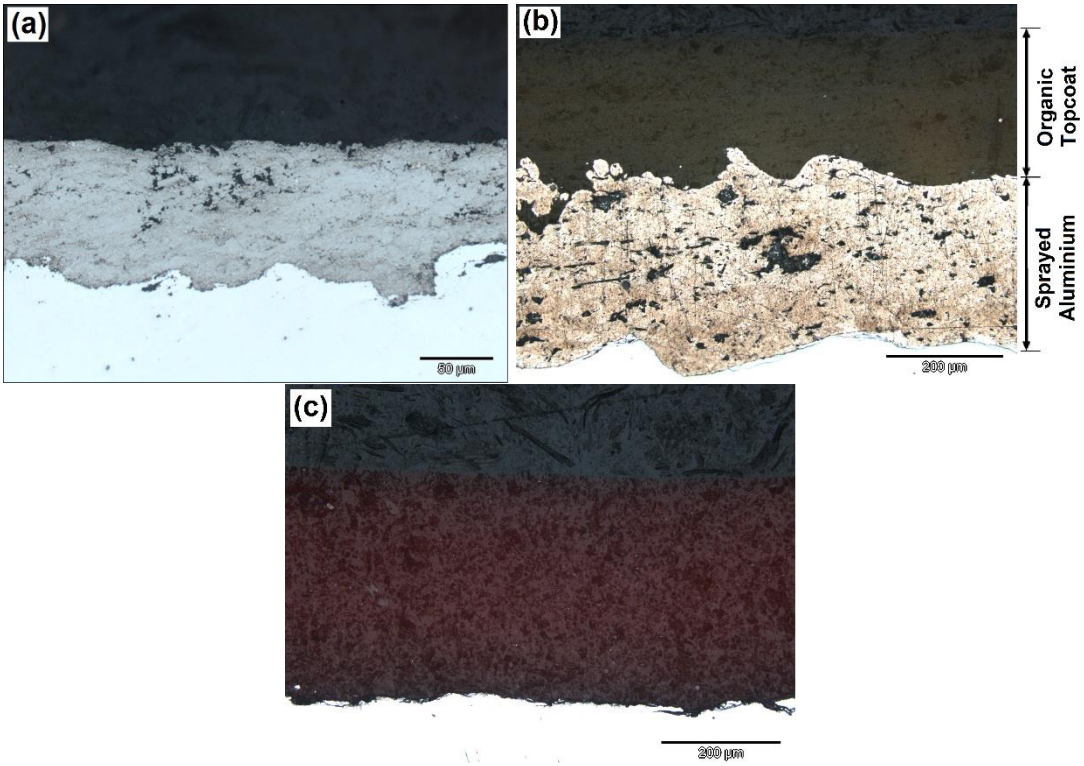

Fig. 5.4.2 Transversal micrographs of the (a) C1, (b) C2, (c) and C3 coatings applied on the R4 steel grade

The roughness and thickness of the coatings are compiled in Table 5.4.1. The higher roughness corresponds to the C3 coating, whereas the lower one was measured for the

C1 coating with values of 0.36 µm (Ra). C1 coating is the thinner of the three coatings, with the highest hardness values, in the typical hardness range of thermally sprayed WC-CrCo coatings [33-39]. The thickness of the organic sealant of C1 coating was measured with a Fischer Dual-Scope non-destructive portable thickness meter (ISO 2178, ISO 2360), and it was found to be of few microns (9±3 µm). The total thickness of C2 coating was around 533±14 µm, corresponding to the sum of the sprayed aluminum layer and the organic paint applied on top, as clearly observed in Fig. 5.4.2. The hardness of each layer is presented in Table 5.4.1. The hardness measured for C2 coating is also in accordance with that observed in literature for aluminum sprayed coatings [40,40]. C1 coating hardness is two orders of magnitude higher than those of C2 and C3 coatings. The hardness values of C3 coating are not far from those of C2 coating, which can be attributed to the presence of the ceramic platelets in the polymeric matrix, providing the coating with higher hardness than that of the un-reinforced polymer.

Table 5.4.1 Mean roughness, thickness, hardness and porosity values for the three coatings

Coating	Roughness, Ra (µm)	Thickness (µm)		Hardness (HV)	Porosity (%)
		Organic sealant	Sprayed metal		
C1	0.36±0.06	9.30±3.50	190.73±14.35	1269.00±30.00	1.90±0.38
C2	1.29±0.20	239.02±8.12	283.89±13.51	40.17±13.19	4.69±0.24
C3	3.34±0.24	430.20±14.94*		28.30±2.32	-

**The thickness of C3 coating corresponds to the total thickness of the epoxydic layer with ceramic platelets*

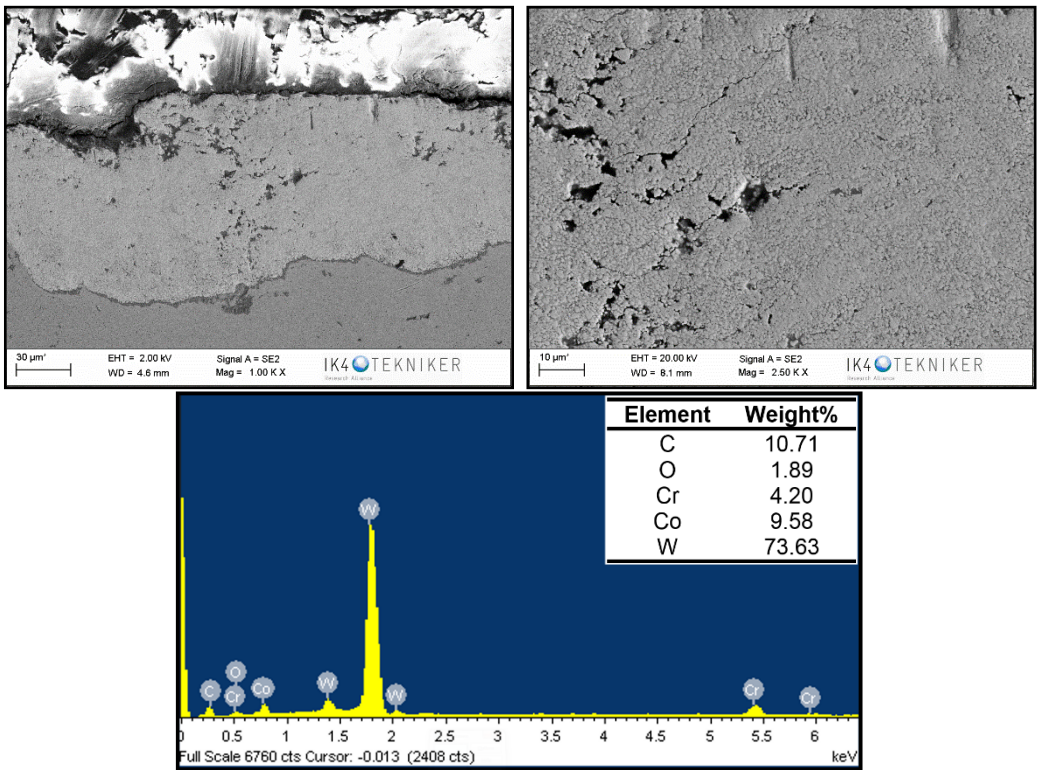

Fig. 5.4.3 Cross section SEM images and EDS analysis of C1 coating applied on the R4 steel grade

The SEM images and the results of EDS analyses of C1 and C2 coatings are shown in Fig. 5.4.3 and Fig. 5.4.4, respectively. From the SEM images, it can be observed that the coatings present typical morphology structure of thermally sprayed coatings, containing defects such as pores and cracks [42-46]. These defects are the consequence of the solidification of the sprayed material between successive splats, and to thermal stresses generated during the spray process [43,45,46]. In both cases, the coating consists of a dense matrix with some voids. The results obtained by EDS indicate that the dense (bright) regions in C1 coating are 11.25wt% C, 4.08wt% Cr, 10.07wt%

Co, and 74.60wt% W; whereas the chemical composition of the lighter (dark) regions corresponding to pores or cracks is 56.98wt% C, 12.61wt% O, 2.64wt% Cr, 8.54wt% Co, and 19.04wt% W. In the case of C2 coating, the dense (bright) regions are 3.74wt% O, and 96,26wt% Al; whereas the lighter (dark) regions are 50.47wt% C, 22.21wt% O, and 27.32wt% Al. The higher oxygen content in the dark regions of both thermally sprayed coatings indicates the presence of oxides coming from the in-flight particles oxidation during the spraying process [43,47,48]. The porosity percentages of coatings C1 and C2 were estimated from the SEM images, and were around 1.90% and 4.69%, respectively.

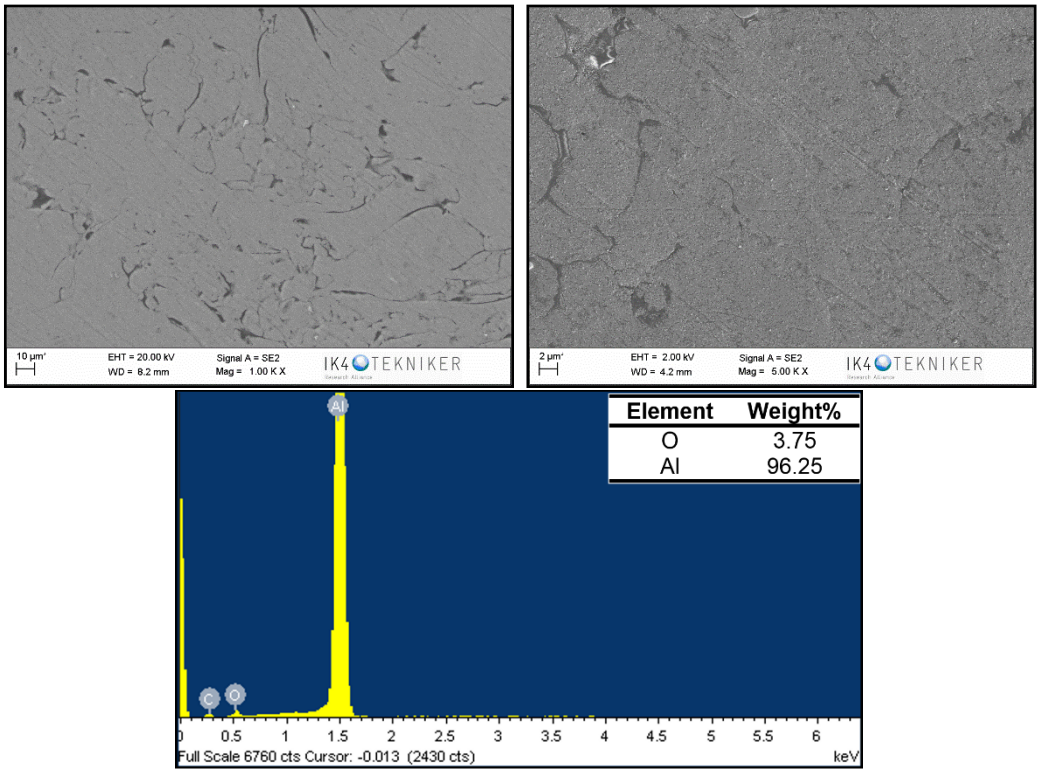

Fig. 5.4.4 Cross section SEM images and EDS analysis of C2 coating applied on the R4 steel grade

5.4.3.2 Electrochemical corrosion tests

Fig. 5.4.5 depicts the evolution of the open circuit potential of the samples during the first hour of immersion in synthetic seawater. In the case of the uncoated steel, there is an initial decrease in the potential and a stabilization after 1500 seconds. The potential drop towards negative values indicates corrosion of the steel. During this stage, known as phase 0 or activation control [7,49-51], the surface of the steel is exposed to the whole oxygen concentration of the electrolyte, and corrosion takes place by activation control. After several minutes, the oxygen close to the steel/electrolyte interface is consumed, and a diffusion of oxygen present in the bulk electrolyte to the corroding surface is required to give continuity to corrosion. This is known as phase 1 or concentration control [7,49-51], and is observed as a change in the slope of potential in Fig. 5.4.5. During this stage, the corrosion products generated lead to the formation of a rust layer, composed mainly of ferric oxyhydroxide (FeOOH) compound. This rust layer is known to be porous with week adhesion bounds [52-55] and, therefore, allows the penetration of the electrolyte to reach the substrate. However, the presence of the rust layer hinders the access of oxygen, which must diffuse through this layer to reach the steel surface. This phase is known as phase 2 or non-linear diffusion control [7,49-51], which takes place when the potential reaches more stable values around -0.65V in Fig. 5.4.5. The potentials registered for the three coatings are nobler than that of the uncoated steel. The potential of C1 coating remains almost constant around -0.12 V during the whole

hour of immersion. According to literature, the potential of WC-CrCo coatings in seawater is close to -0.4 V [39,56]. Similarly, the potential registered for C2 coating (-0.14 V) differs from that observed for aluminum in seawater, which is usually around to -1 V [47,57-59]. The nobler potential registered for C1 and C2 coating is ascribed to the presence of the organic layers that act as barriers impeding the access of electrolyte to the metallic coatings surfaces. The potential of C3 coating is close to 0, which is attributed to the non-conductive nature of the organic components of the coating, with high electrical resistance impeding the charge transfer between the electrolyte and the substrate [60,61]. Any potential lecture in the organic coating C3 or the organic layers used in C1 and C2 coatings is due to the penetration of electrolyte through the defects and pores of the organic layer, and the subsequent contribution of the substrate to the lecture. Therefore, the potentials in the C1 and C2 coatings of -0.12 V and -0.4 V, respectively, suggest that the electrolyte has reached the sprayed metal layers. In the case of C3 coating, no contribution of the substrate is observed.

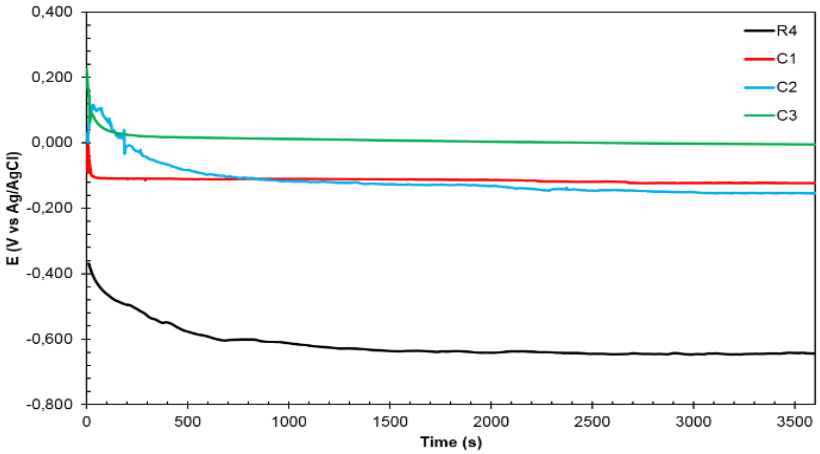

Fig. 5.4.5 Evolution of the open circuit potential during the first hour of immersion in synthetic seawater for the R4 steel grade and the three coatings

The polarization curves obtained in the potentiodynamic tests for the uncoated steel and the three coatings are presented in Fig. 5.4.6, and the electrochemical data obtained from the curves by standard Tafel extrapolation is compiled in Table 5.4.2. In the curve of the R4 steel, a great activation stretch is observed in the anodic branch above the corrosion potential (E_{corr}) (-0.659 V). In this region, the current increases sharply for small potential variations. Furthermore, no passive region is observed, indicating that the steel is very active in seawater. The curve corresponding to C1 coating is anodically displaced with respect to that of the R4 steel, with more positive corrosion potential (-0.275 V). In this case, a more stable anodic region is observed, where the current increases slightly with the potential increase. Above 0.5 V, the current increases more rapidly, and the transpassive region is observed close to 1 V. The corrosion current (i_{corr}) of C1 coating is one order of magnitude smaller than that of the R4 steel, and a difference of two orders of magnitude is observed in the anodic currents. Furthermore, the polarization resistance (R_p) of the coating is close to 3 x10^4 Ω cm^2, whereas that of the steel is considerably lower, of 690 Ω cm^2. The curves obtained for C2 and C3 coatings were found to be very similar. In both cases, the curves are anodically shifted with respect to that of the uncoated sample. Besides, the corrosion current and anodic currents are six orders of magnitude smaller than those of R4 and C1 coating, and the polarization resistances over 10^9 Ω cm^2. In both C2 and C3 coatings, the high corrosion resistance registered is attributed to the presence of a non-conductive component as the organic topcoat in C2, and the organic coating itself in C3. The corrosion potential of the aluminum in seawater is known to be close to -0.9 V [47,57-59,62], and the values registered for C2 coating of

0.02 V suggest a low porosity of the topcoat and, thus, a weak contribution of the aluminum layer to the lecture. Therefore, the three coatings provide the steel with an enhanced corrosion resistance in synthetic seawater, especially in the case of C2 and C3 coatings, due to the presence of a non-conductive organic layer.

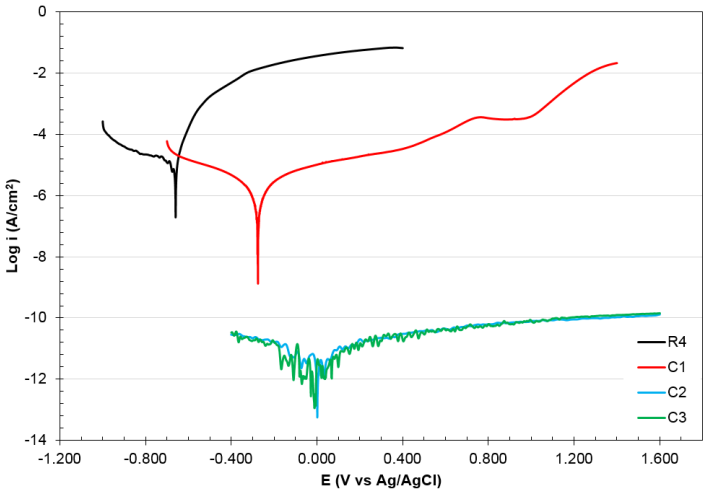

Fig. 5.4.6 Potentiodynamic curves obtained for the R4 steel grade and the three coatings in synthetic seawater under a sweep rate of 0.5 mV/s

Table 5.4.2 Electrochemical data obtained from the potentiodynamic curve by standard Tafel extrapolation

Material	Electrochemical parameters		
	i_{corr} (A/cm^2)	E_{corr} (V vs Ag/AgCl)	R_p (Ω cm^2)
R4	2.77 x10^{-5}	-0.659	0.96 x10^3
C1	1.83 x10^{-6}	-0.275	30.12 x10^3
C2	1.74 x10^{-12}	+0.002	33.5 x10^8
C3	1.50 x10^{-12}	-0.004	25.87 x10^9

In the second test series, electrochemical impedance spectroscopy measurements were performed at different immersion times. The results are presented in Fig. 5.4.8, in the form of Nyquist and Bode plots for the uncoated steel and the three coatings. The experimental data was analyzed with the NOVA 2.1 software. The quality of the obtained results was evaluated using Kramers-Kroing transformation (complex fit). The results showed an excellent fit for the substrate and C1 coating (χ^2<10^6), and a reasonable fit quality for C2 and C3 coatings (10^5 <χ^2<10^6). The impedance data was fitted using the Electrical Equivalent Circuits (EEC) shown in Fig. 5.4.7. The circuit represented in Fig. 5.4.7a, known as the simple Randles circuit, is employed to represent a coating or an uncoated corroding metal. The EEC represented in Fig. 5.4.7b is typically used to describe a coating on a metallic substrate, and that in Fig. 5.4.7c is used to describe the coating when there is a diffusion-limited reaction in the substrate/coating interface, e.g., due to the presence of corrosion products coming from substrate corrosion. Finally, the circuit in Fig. 5.4.7d can be used to represent a two-layer coating system on a metallic substrate. In all circuits, R_1 represents the resistance of the electrolyte between the reference and the working electrodes. In Fig. 5.4.7a, R_2 is associated with the resistance of the coating, or with the charge transfer resistance (polarization resistance) in the case of a corroding metal. The Constant Phase Element (CPE_1) represents the double layer capacitance at the electrolyte/coating or the electrolyte/steel interface. Constant phase elements are used for replacing simple capacitances for a better fit quality of the experimental data. The impedance of a CPE element can be represented as: $Z_{CPE} = 1/Y0\,(i\omega)^n$, where ω is the angular frequency, and i the imaginary number. Y0 and n (n≤1) are the admittance and the empirical exponent of the CPE, respectively. Whenever the surface acts as an ideal capacitor n is equal to unity and Y0 is identical to the double

layer capacitance. CPE_2 in Fig. 5.4.7b represents the double layer capacitance of the electrolyte/substrate interface, R_2 is the pore resistance of the coating, and R_3 is related to the polarization resistance of the substrate. The diffusion in Fig. 5.4.7c is represented by the Warburg diffusional element, which impedance can be expressed as: $Z_W = \sigma\omega^{1/2}(1-i)$. σ is the Warburg coefficient, which is inversely proportional to the diffusion coefficient. In Fig. 5.4.7d, R_2 and R_3 are the pore resistances of the two coating layers, and R_4 represents the resistance of the substrate. After several fitting processes, these circuits were selected as they gave the best fitting parameters with the smallest error, based on the chi-squared values (χ^2). This represents the square of the standard deviation between the original data and the calculated spectrum. The χ^2 values obtained were below 10^{-3}, showing an adequate fitting quality. Furthermore, the relative error of each element in the circuit was below 10%. The fitting curves are presented as solid lines in Fig. 5.4.8 for each spectrum, and the fitting process results are summarized in Table 5.4.3 for the different immersion times.

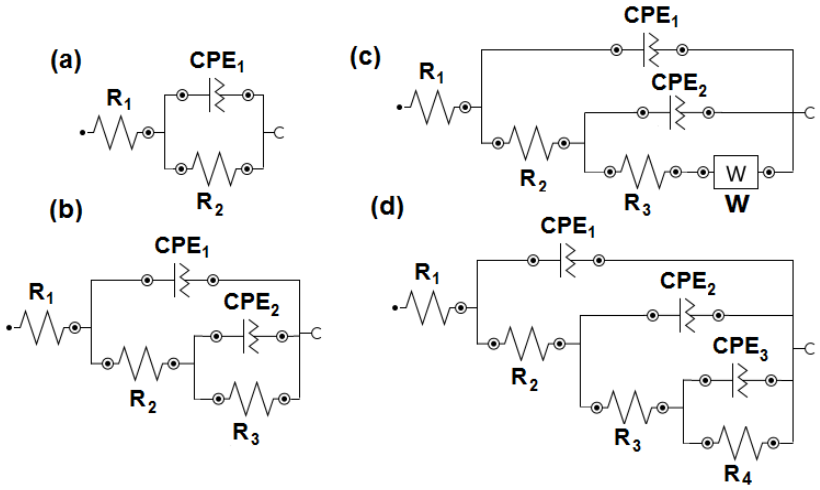

Fig. 5.4.7 Electrical equivalent circuits used to fit the electrochemical impedance spectroscopy data: (a) to represent a coating or a corroding metal, (b) to represent a coating with a corroding substrate, (c) to represent a coating with a corroding substrate with diffusion-controlled reactions, and (d) to represent a two-layer coating system with a corroding substrate

In the results obtained for the uncoated steel, two capacitive loops are observed in the Nyquist plot and in accordance, two inflection points in the Bode plot. The big capacitive loop at medium-frequency (MF) is physically related to the charge transfer process of the corrosion reaction of the steel [63]. The second time constant present in the impedance plots is related to a corrosion product layer that is formed on the surface [64]. The enlargement of the semicircle in the Nyquist plot with immersion time, is attributed to an increase in the corrosion resistance of the steel. Accordingly, an increase in the impedance modulus in the Bode plot is observed with higher exposure time. After 168 h, the phase angle maximum at MF ranges has shifted to lower frequencies (LF). The phase angle at high frequencies (HF) reaches values close to 0º, which is characteristic of purely resistive behavior [65,66]. The increase in the capacitive loop, the impedance modulus, and the phase angle at LF indicates an enhancement in the corrosion resistant response of the steel, as a result of the surface changes undergone during immersion [67]. The incomplete capacitive loop in the Nyquist plot at 168, 336, and 504 hours, and the increase in the phase angle values at LF, correspond to a more capacitive response of the system, as a consequence of the corrosion product layer presence [63]. The thickness of this layer increases with exposure time, hindering the access of electrolyte to the substrate surface and slowing down corrosion reactions, leading in turn to slightly higher corrosion resistance. The corrosion resistance of the uncoated steel (R_3) increases with immersion time up to values close to 3.5 x10^3 Ω cm^2. Even if the rust layer

impedes the dissolution of the substrate to some extent, the low resistance of this layer (R_2) confirms its poor barrier effect in the long-term corrosion protection of the steel in seawater [52-55]. The slight increase in the CPE_2-Y0 values indicates an increase in the exposed steel surface, as a result of an increase in the roughness due to corrosion degradation [68].

In the case of C1 coating, two semicircles in the Nyquist diagram and two inflection points in the Bode plot are observed, corresponding to two-time constants. The HF loop is related to the electrolyte/coating interface, whereas the LF loop corresponds to the electrolyte/substrate interface (corrosion process in the substrate) [47]. The electrolyte penetrates through the organic sealant pores, reaching the sprayed. The phase angle values close to zero at HF in all the measurements indicate an ohmic behavior of the system, corresponding to the WC-CrCo layer. Therefore, the organic sealant does not provide an effective barrier but allows the penetration of electrolyte from the beginning of immersion. In contact with seawater, the tungsten carbides form a galvanic couple with the metallic binder of the sprayed layer, leading to a selective dissolution of the CrCo matrix [24,36,46,56,69,70]. Eventually, the chromium oxides formed from the matrix dissolution, mainly Cr_2O_3 [38,71], block the pores and defects of the thermally sprayed layer, leading to lower corrosion rates and a stable behavior. This is observed as an improvement of the corrosion resistance (R_2) after 168 hours of immersion. At this stage, the phase maximum at MF has increased, indicating an enhancement of the capacitive behavior of the WC-CrCo layer, due to the passivation of the coating through the formation of chromium oxides. Furthermore, the phase maximum at LF also increases, indicating a higher capacitive response in the electrolyte/substrate interface, as a consequence of the presence of corrosion products coming from substrate corrosion. In fact, the shape of the phase at LF suggests the occurrence of diffusion-controlled reactions. This is often related to the presence of pores and the opening of pinholes in the coating [72], and the accumulation of products in these defects that delay the reactant migration to the corroding surface [47,53,72-74]. The increase of the pore resistance (R_2) and the decrease of W-Y0 parameter with immersion time confirm the accumulation of substrate corrosion products, which in turn lead to slightly higher corrosion resistance of the substrate (R_3), since corrosion is delayed by diffusion processes. The results obtained after 336 and 504 hours were very similar, and the values of CPE_1 remain almost constant, revealing low changes in the sprayed layers due to corrosion or passivation processes, and, therefore, good stability in seawater.

The Nyquist plot obtained for C2 coating at 24 hours presents two capacitive loops. The high impedance modulus measured for the coating close to 10^{11} Ω cm^2, and the highly capacitive response with a phase angle maximum of 90º at HF, evinces that the organic topcoat provides an effective barrier to corrosion. Similar resistance results have been observed for organic coatings with excellent resistant properties in seawater [75-77]. In spite of the high resistance of the system, the second capacitive loop at LF indicates a slight contribution of the aluminum layer from the early stages of immersion, as a result of the penetration of the electrolyte through the pinholes of the topcoat. The values of the phase maximum in the MF range close to 80º show a highly capacitive response of the electrolyte/aluminum interface. This is attributed to the passivation of the aluminum in contact with seawater, as confirmed by the high R_3 values. In the results obtained at 168, 336 and 504 hours, three capacitive loops and three inflection points are observed in the Nyquist and Bode plots, respectively. After 168 hours, the pore resistance of the topcoat (R_2) is considerably reduced, indicating an opening of pinholes in the organic layer. At this stage, the electrolyte has also penetrated through the pores and defects of the aluminum layer, causing the dissolution of active zones inside the coating. This is

observed as a decrease in the impedance modulus in two orders of magnitude, and a reduction of the capacitive loop at HF in the Nyquist Plot. The decrease of the phase maximums in the HF and MF denote a reduction in the capacitive responses of both the organic topcoat and the aluminum layer. Accordingly, the increase of CPE_2-Y0 and the decrease in CPE_2-n are related to a greater exposed surface of aluminum [72], as a consequence of topcoat delamination and penetration of electrolyte through the aluminum layer defects. The apparition of a phase maximum at LF range of around 30º confirms the presence of a third interface, corresponding to the electrolyte/substrate. The steel is nobler than the aluminum in seawater, which potential is around -1 V [47,57-59], and thus, a galvanic corrosion reaction is generated between the two metals. The aluminum dissolves protecting the steel substrate by a sacrificial cathodic protection mechanism [47,63]. At 336 hours, the capacitive loop at LF and the impedance modulus have increased, indicating a slight enhancement in the corrosion resistance of the system. The aluminum corrosion products are accumulated in the pores, hindering electrolyte penetration and leading to higher resistances (R_3) with time. These oxides block the pinholes and defects in the aluminum layer [43,47,59,63], hindering the electrolyte access and delaying the substrate corrosion. This is known as 'plugging effect' [47], and is confirmed by the increase of the substrate resistance (R_4). At 504 hours, the Nyquist semicircle at LF, the impedance modulus, and the phase maximum at LF increase again. This is again attributed to the higher amount of corrosion products delaying the further corrosion of the substrate, leading to slightly higher corrosion resistance of the system, as confirmed by the higher values of R_3 and R_4 after 504 h in Table 5.4.3.

C3 coating shows two-time constants after 24 hours of immersion, with high impedance modulus and a phase angle of 90 º in the HF range. This high resistance close to 10^{10} Ω cm^2 and the capacitive response, confirm the excellent barrier properties of the organic coating [75-77]. After 168 hours, a depletion in the semicircle and the impedance modulus decrease is observed, along with a shift of the phase angle plot towards HF. The electrolyte has permeated through the pinholes of the coating reaching the substrate, leading to a decrease in the corrosion resistance. The decrease in the substrate resistance value (R_3), as well as the increase of W-Y0, suggest the enlargement of the exposed surface of the steel. This observation is in coherence with the increase of CPE_2-Y0 and the decrease of CPE_2-n, indicating a higher roughness of the substrate generated by corrosion, which leads to a greater substrate exposed surface. Accordingly, the decrease in the pore resistance of the coating (R_2) and CPE_1-n value, and the increase in CPE_1-Y0, indicate a loss of capacity of the coating due to an increase of revealed pinholes and pathways for the electrolyte to the corroding substrate. Therefore, the coating becomes more conductive, and its performance is weakened [72,73]. Additionally, the oxides coming from substrate corrosion block the electrolyte pathways, leading to a diffusion-controlled reaction, which is clearly observed in the Nyquist plot at LF as a straight line of slope equal to 45º. The substrate corrosion and the formation of corrosion products can cause some coating delamination [4,27,60]. The increase of CPE_2-Y0, and decrease of CPE_2-n and R_2, can be related to a greater steel surface exposed due to coating delamination [60,78,79]. The resistance of the system continues to decrease with time, and the phase angle at HF range decreases up to 80º after 504 hours. This decrease indicates a loss in the capacitive behavior of the coating, which can be attributed to a greater delamination of the coating. Furthermore, the greater amount of corrosion products leads to an increase in the phase values at LF range.

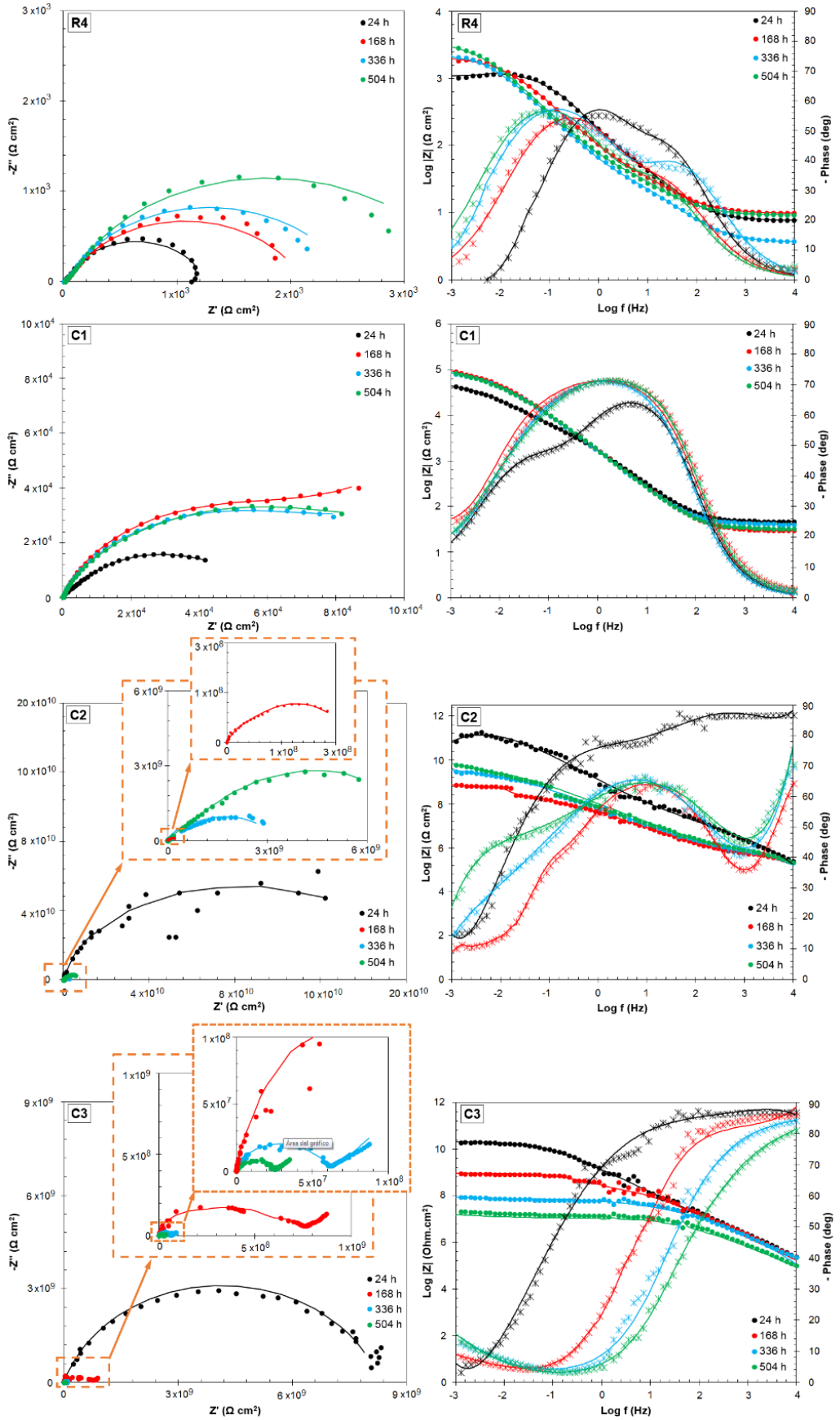

Fig. 5.4.8 Electrochemical Impedance Spectroscopy results obtained for the R4 steel and three coatings at different immersion times, where the solid lines represent the fitting curves obtained with the equivalent circuits

Table 5.4.3 Equivalent circuit parameters obtained from the impedance data fitting at different immersion times in synthetic seawater for the R4 steel and the three coatings

Material and exposure period		R_1 (Ω cm^2)	CPE_1-Y0 (F cm^{-2} s^{-n})	CPE_1-n	R_2 (Ω cm^2)	CPE_2-Y0 (F cm^{-2} s^{-n})	CPE_2-n	R_3 (Ω cm^2)	CPE_3-Y0 (F cm^{-2} s^{-n})	CPE_3-n	R_4 (Ω cm^2)	W-Y0 (F cm^{-2} s$^{-1/2}$)
R4	24 h	10.65	8.62×10^{-4}	0.765	1.14×10^{2}	5.43×10^{-4}	0.839	1.14×10^{3}	-	-	-	-
	168 h	13.55	1.41×10^{-3}	0.719	0.59×10^{2}	1.65×10^{-3}	0.740	2.05×10^{3}	-	-	-	-
	336 h	15.03	1.67×10^{-3}	0.710	0.38×10^{2}	3.19×10^{-3}	0.741	2.50×10^{3}	-	-	-	-
	504 h	17.78	1.96×10^{-3}	0.698	0.66×10^{2}	2.62×10^{-3}	0.759	3.50×10^{3}	-	-	-	-
C1	24 h	46.20	1.15×10^{-4}	0.813	5.80×10^{3}	1.86×10^{-4}	0.648	4.67×10^{4}	-	-	-	3.52×10^{-3}
	168 h	29.57	1.28×10^{-4}	0.822	4.23×10^{4}	4.94×10^{-5}	0.675	3.83×10^{4}	-	-	-	3.19×10^{-4}
	336 h	41.35	1.31×10^{-4}	0.827	4.07×10^{4}	1.09×10^{-4}	0.680	4.50×10^{4}	-	-	-	5.67×10^{-4}
	504 h	32.34	1.25×10^{-4}	0.831	3.33×10^{4}	9.74×10^{-5}	0.607	6.91×10^{4}	-	-	-	8.35×10^{-4}
C2	24 h	26.80	8.79×10^{-11}	0.965	1.10×10^{11}	2.74×10^{-11}	0.901	4.16×10^{8}	-	-	-	-
	168 h	128.67	1.26×10^{-10}	0.945	5.73×10^{5}	4.76×10^{-9}	0.766	1.67×10^{8}	1.40×10^{-8}	0.973	1.20×10^{8}	-
	336 h	117.12	1.94×10^{-10}	0.936	8.82×10^{5}	4.72×10^{-9}	0.785	5.34×10^{8}	1.25×10^{-9}	0.970	1.33×10^{9}	-
	504 h	95.17	1.32×10^{-10}	0.948	8.20×10^{5}	2.91×10^{-9}	0.757	6.54×10^{8}	5.11×10^{-10}	0.834	6.51×10^{9}	-
C3	24 h	3.86	9.44×10^{-11}	0.975	1.40×10^{8}	2.66×10^{-10}	0.850	1.85×10^{10}	-	-	-	-
	168 h	21.14	1.29×10^{-10}	0.945	1.15×10^{8}	8.66×10^{-13}	0.619	6.56×10^{8}	-	-	-	7.88×10^{-8}
	336 h	21.27	1.54×10^{-10}	0.936	1.64×10^{7}	5.32×10^{-10}	0.780	4.30×10^{7}	-	-	-	3.19×10^{-7}
	504 h	21.39	1.39×10^{-10}	0.949	2.33×10^{6}	1.61×10^{-9}	0.590	2.31×10^{7}	-	-	-	9.31×10^{-7}

The evolution of the OCP during the 504 hours of immersion is plotted in Fig. 5.4.9. The potential of the uncoated steel slightly decreases during the first 24 hours in seawater, and then remains constant around -0.67 V. In the case of C1 coating, the potential decreases from -0.03 V at 24 hours to -0.15 V at 168 hours and stabilizes in this value. This decrease can be attributed to the gradual dissolution of the CoCr matrix observed in the EIS results. Eventually, the matrix passivates forming Cr_2O_3 oxides, giving stable potential lectures. The results of C2 coating show a sharp decrease of potential after 168 hours. This is coherent with the EIS results, that showed the contribution of the aluminum layer as a consequence of electrolyte permeation through the organic topcoat. The potential lecture close to -1 V corresponds to the aluminum in seawater [47,57-59]. The increase in potential up to -0.88 V at 504 hours is attributed to the passivation of the aluminum, and the pinhole blockage by aluminum corrosion products as described in the impedance results. Finally, the results of C3 coating exhibit a slight reduction in the OCP, as a consequence of the penetration of electrolyte through the pinholes. After 24 hours the potential remains almost constant around -0.04 V.

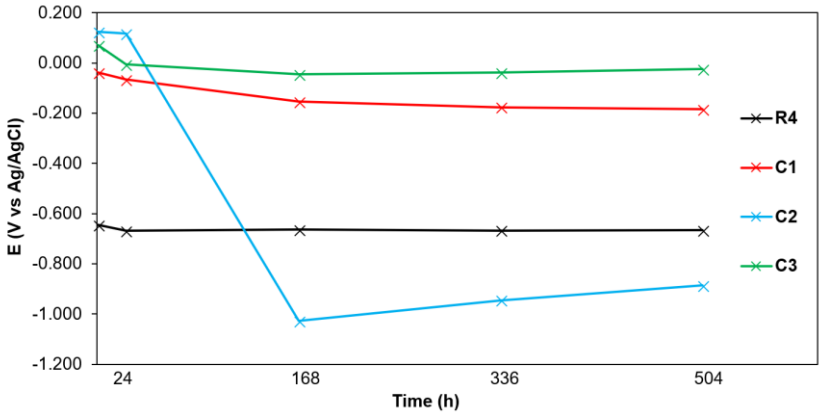

Fig. 5.4.9 Evolution of the open circuit potential during the 504 hours of immersion in synthetic seawater for the R4 steel and the three coatings

5.4.3.3 Tribocorrosion tests

Fig. 5.4.10 shows the results of the EIS measurements performed before and during wear sliding test, in the form of Bode Plots. The quality of the obtained results was analyzed using Kramers-Kroing transformation (complex fit). An excellent fit was obtained for the substrate and C1 coating ($\chi^2<10^6$) before sliding, and a reasonable fit quality during sliding ($10^5 <\chi^2<10^6$). C2 and C3 coatings showed reasonable fit quality both before and during sliding ($10^5 <\chi^2<10^6$). In all the samples, the corrosion resistance is affected by sliding, decreasing during wear. The impedance experimental data of the R4 steel was fitted with the EEC in Fig. 5.4.7a, whereas the results of the coatings were analyzed with the circuit in Fig. 5.4.7b. The χ^2 values obtained with these circuits were below 10^{-3}, and the relative error of each element in the circuit was below 10%, showing an adequate fitting quality. The fitting curves as presented as solid lines in Fig. 5.4.10 for each spectrum and the fitting process results are compiled in Table 5.4.4.

R4 steel shows one time constant, in a typical curve shape of a corroding metal where a charge transfer reaction is taking place in the electrolyte/metal interface. During sliding, the impedance modulus decreases one order of magnitude and the phase maximum decreases from 70º to 20º shifting to HF. This indicates a reduction of the corrosion resistance of the steel during the sliding process. The CPE-Y0 value increases as a consequence of the increase in the roughness of the steel surface due to corrosion [68]. Furthermore, the decrease in the CPE-n parameter indicates a loss in the capacitive response, since the surface becomes more conductive as a result of the greater number

of corrosion processes taking place. Therefore, the corrosion of the steel is accelerated during sliding, in accordance with the results observed in previous studies [10,11].

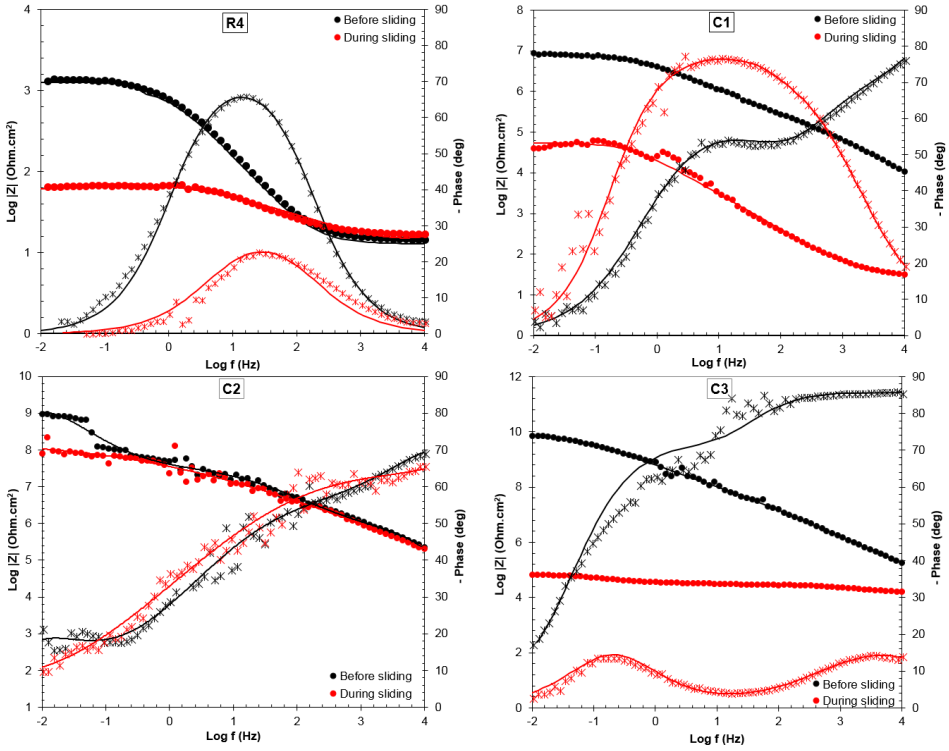

Fig. 5.4.10 Electrochemical Impedance Spectroscopy results obtained for the R4 steel and three coatings before and during sliding process in synthetic seawater, where the solid lines represent the fitting curves obtained with the equivalent circuits

C1 coating exhibits two-time constants, one in the HF limits with phase angle values of 80º, characteristic of capacitive films, and a second maximum of 50º in the MF range. The former is related to the sealant/electrolyte interface, whereas the latter corresponds to the WC-CrCo/electrolyte interface. Unlike the results obtained in the previous electrochemical corrosion tests, the organic sealant is contributing to this lecture. The existence of a second time constant evinces the penetration of electrolyte through the sealant reaching the sprayed carbide metal. Therefore, the sealant seems to be present during the first hours of immersion, but it is removed or delaminated from the surface with higher exposures, and its contribution is not detected after 24 hours in seawater. During sliding, the impedance modulus is reduced in three orders of magnitude. The phase angle at HF decreases from 80 º to 20º, indicating a more ohmic response of the system, as a consequence of the removal of the organic sealant and the exposure of a greater WC-CrCo area to the electrolyte. This is confirmed by the decrease of the pore resistance of the sealant (R_2) with sliding in three orders of magnitude, and the increase of CPE_2-Y0 parameter. The corrosion resistance of the carbide layer (R_3) before sliding is high, of 8.27 x10^6 Ω cm^2, and it is reduced in three orders of magnitude during sliding. This is attributed to the removal of the chromium oxides present in the tribological contact, which are formed in the absence of sliding when the CrCo matrix reacts with the electrolyte [38,71], leading to exposure of the fresh material to seawater. The unworn surface is still coated with the organic sealant, but its presence seems to be masked in the plots with the contribution of the metallic coating to the lecture.

C2 coating also shows two-time constants, corresponding to the electrolyte/ organic topcoat and electrolyte/aluminum interfaces. The phase angle at HF limit is 70º, slightly smaller than that observed after 24 hours in the electrochemical corrosion test results,

where the values were close to 90º. The lower capacitive response in this test is related to a greater contribution of the aluminum due to a greater number of pores present in the organic layer of this sample. During sliding, the impedance modulus decreases in nearly an order of magnitude. However, the resistance during sliding of C2 coating remains high, with values close to 10^8 Ω cm^2, being the coating less affected by sliding. The pore resistance (R_2) remains similar during the wear process, and the corrosion resistance of the aluminum layer (R_3) decreases from 1.22 x10^9 to 1.45 x10^8 Ω cm^2. These results suggest that the organic topcoat resists the action of the countermaterial, without considerable acceleration of the aluminum layer corrosion. The results were in coherence with the optical analysis of the samples, where no detachment of the topcoat was observed after the tests (see Section 5.4.2.4).

C3 coating also presents high corrosion resistance before sliding, in the order of 10^{10} Ω cm^2. The system shows two-time constants, corresponding to the coating/electrolyte and the steel/electrolyte interfaces. The phase angle before sliding presents values close to 90º in the HF limit. This indicates a highly capacitive behavior of the coating, coherently with its polymeric nature. The high resistance registered due to the good protective properties of the organic coating mask the contribution of the substrate corrosion. During the wear process, the two-time constants are more evident. The resistance of the coating is highly affected by sliding, as observed by the great decrease in the impedance modulus at LF limit to values close to 10^5 Ω cm^2. The pore resistance (R_2) of C3 coating decreases considerably. The decrease in the phase angle maximum at HF from 90º to 15º, and the reduction in the CPE_1-n value from highly capacitive values close to 1 to values around 0.5, indicate a reduction in the capacitive response of the coating, showing a more ohmic behavior. This is attributed to an increase in the number of pinholes and a weakening of the protective performance of the coating which has become more conductive [68,73]. This can be the consequence of certain coating delamination and exposure of the underlying steel. The decrease in the phase angle at LF to values close to 20º, the increase in the CPE_2-Y0 parameter and the substantial reduction in the corrosion resistance of the steel substrate (R_3), indicate a greater exposed area of the corroding substrate due to the coating delamination [68,73].

Table 5.4.4 Equivalent circuit parameters obtained from the impedance data fitting before and during sliding in synthetic seawater for the R4 steel and the three coatings

Material	Condition	R_1 (Ω cm^2)	CPE_1-Y0 (F cm^{-2} s^{-n})	CPE_1-n	R_2 (Ω cm^2)	CPE_2-Y0 (F cm^{-2} s^{-n})	CPE_2-n	R_3 (Ω cm^2)
R4	**Before sliding**	16.74	1.73 x10^{-4}	0.855	1.45 x10^3	-	-	-
	During sliding	18.62	6.54 x10^{-4}	0.741	0.10 x10^3	-	-	-
C1	**Before sliding**	24.67	1.29 x10^{-8}	0.798	3.56 x10^5	3.73 x10^{-8}	0.673	8.27 x10^6
	During sliding	27.26	6.23 x10^{-6}	0.850	0.26 x10^3	8.66 x10^{-6}	0.878	8.36 x10^4
C2	**Before sliding**	97.48	1.15 x10^{-10}	0.886	9.22 x10^6	1.04 x10^{-8}	0.874	1.22 x10^9
	During sliding	54.10	7.66 x10^{-11}	0.935	9.31 x10^6	5.32 x10^{-8}	0.616	1.45 x10^8
C3	**Before sliding**	119.19	1.49 x10^{-10}	0.956	1.64 x10^8	2.30 x10^{-10}	0.702	8.09 x10^9
	During sliding	101.64	3.23 x10^{-10}	0.537	2.19 x10^6	3.22 x10^{-5}	0.735	3.74 x10^4

The coefficients of friction (COF) registered for the uncoated steel and the three coatings are plotted together in Fig. 5.4.11, and the mean coefficient values are presented in Table 5.4.5. There is a slight increase in the coefficient of the R4 steel with sliding time, as a consequence of the superficial modifications that are taking place in the tribological contact. Furthermore, some fluctuations can be observed in the results, which are attributed to the detached particles and oxides that can remain in the contact [10,11,80]. The coefficients of the three coatings are considerably smaller than that of the R4 steel. At the beginning of the test, C1 coating presents values close to 0.18, increasing to 0.36

after 1000 seconds. This is the result of the removal of the organic sealant during the first cycles of sliding, leading to an alumina/WC-CrCo contact and, thus, to an increase in the coefficient value. The lower coefficient of friction corresponds to the C2 coating, with values close to 0.19 during the whole test duration. This is ascribed to the organic topcoat, which resists the tribological conditions imposed and is not removed from the surface. The coefficient registered for C3 coating is also low, close to 0.23. The fluctuations of the COF in this case can be attributed to the interactions of the alumina ball with the ceramic platelets present in the coating.

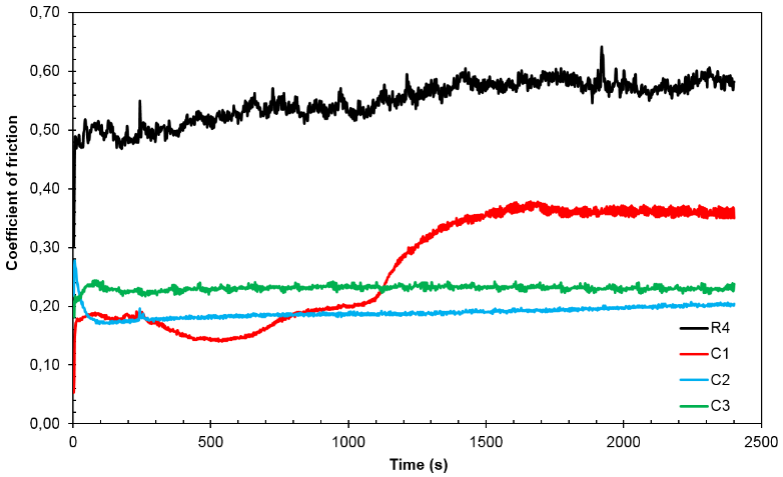

Fig. 5.4.11 Evolution of the coefficient of friction with sliding time for the R4 steel grade and three coatings in synthetic seawater

Table 5.4.5 Average coefficient of friction, total wear track volume (W_{tr}) and wear coefficient (K) for the R4 steel and the three coatings

Material	R4	C1		C2	C3
		Sealant	WC-CrCo layer		
Mean COF	0.49	0.18	0.36	0.19	0.23
W_{tr} (x10^{-5} cm^3)	1.28		12.75	4.01	2.45
K (x10^{-14} m^3 N^{-1} m^{-1})	2.04		20.28	6.38	3.89

5.4.3.4 Surface analysis and material loss evaluation

After the tests, the surface of the samples was analyzed by several microscopic techniques. The optical micrographs in Fig. 5.4.12 show the wear tracks of the R4 steel and the three coatings.

In the micrograph of the R4 steel grade, deep abrasion lines parallel to the sliding direction can be clearly observed. Furthermore, some corrosion in the form of pits can also be distinguished inside the track. The unworn surface of the sample is entirely covered by a homogeneous layer of corrosion products. As already observed in previous studies [10,11], sliding promotes the corrosion of the unworn surface, as a consequence of the coupling generated between the wear track and the unworn surface. In the wear track, however, less corrosion is observed as the countermaterial is continuously removing the corrosion products that may form.

In the case of C1 coating, the micrograph reveals the presence of pores in the unworn surface where the organic sealant is intact. The presence of these pores in the sealant was already observed in the EIS measurement obtained before sliding, where the penetration of electrolyte through the pores led to the contribution of the WC-CrCo metallic layer to the lecture. In the worn surface, the sealant has been completely removed, and some deformation of the sealant can be observed in the edges of the wear track. The straight lines present in the worn surface can also be observed in the wear

track, with the same direction. As it can be observed in Fig. 5.4.13, the lines are perpendicular to sliding direction, and they are visible under the organic sealant as well. Therefore, these lines are not abrasion lines generated by the sliding of the alumina ball but a consequence of the surface finishing of the sprayed coating. No significant wear is observed in the track, and no ferric corrosion products are detected neither in the worn or the unworn areas.

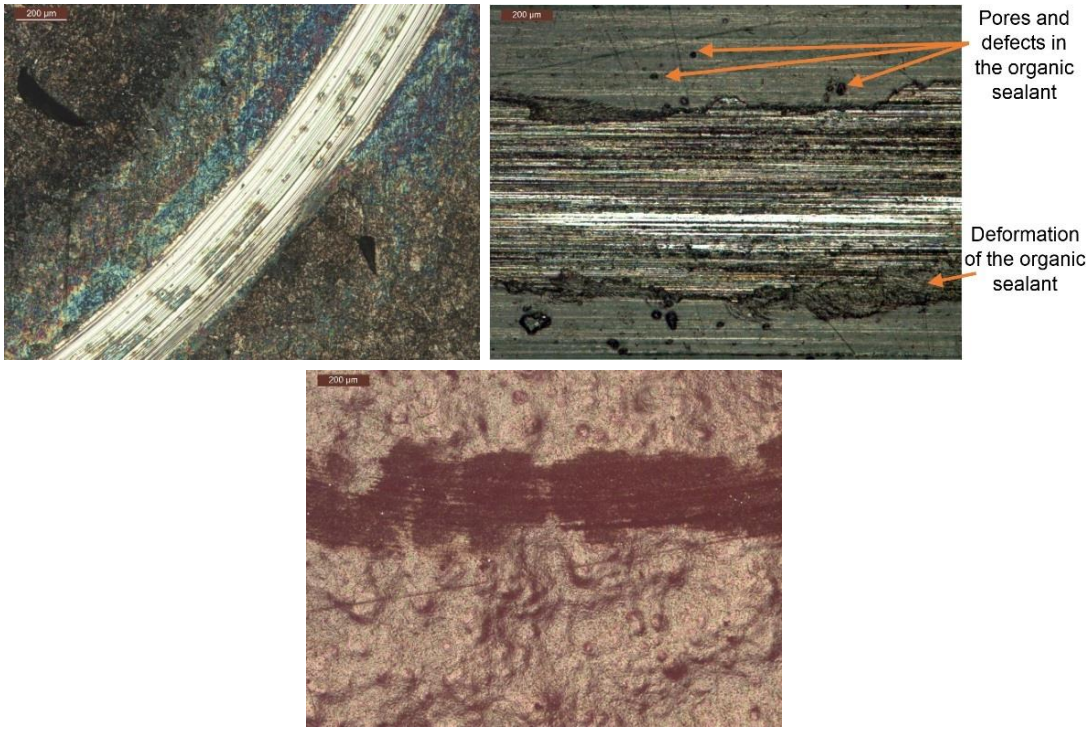

Fig. 5.4.12 Optical micrographs of the wear tracks of (a) R4 steel, (b) C1 coating, (c) C2 coating, and (d) C3 coating after the tribocorrosion test in synthetic seawater

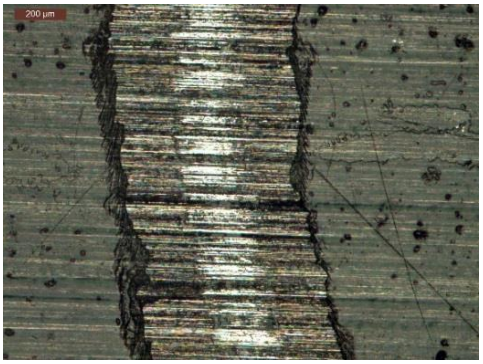

Fig. 5.4.13 Optical micrograph of C1 coating showing lines perpendicular to sliding direction, resulting from the surface roughness of the samples

The wear tracks of coatings C2 and C3 are similar. In both cases, abrasion lines can be clearly observed, and both worn and unworn areas are free of corrosion products. The organic topcoat in the case of C2 coating, and the C3 coating itself, seem to have resisted the tribological conditions imposed, without being removed or delaminated from the surface exhibiting the underneath aluminum layer or steel substrate, respectively. Therefore, the contributions of the metallic materials to the electrochemical measurements observed in previous impedance tests, are consequence of the access of electrolyte through the pores and defects present in the organic topcoat (C2) and in the organic coating (C3), rather than exposure of the underneath metallic material as a consequence of the elimination of the coating during sliding.

The topographies and the cross-section profiles of the wear tracks obtained in the confocal profilometer are shown in Fig. 5.4.14 and Fig. 5.4.15, respectively. The topography of R4 steel wear track reveals deep abrasion lines generated during the sliding test, and a high roughness of the unworn surface as a consequence of the severe degradation of the steel due to the wear-accelerated corrosion. The wear track morphology observed in C1 coating, and its rectangular shape (see Fig. 5.4.15), indicates that it was generated in the sealant rather than in the metal sprayed layer. The deep lines present in the track are not abrasion caused but surface roughness generated in the mechanization of the test samples. The same lines are clearly observed in the organic sealant, confirming the previous statement. The wear tracks of coatings C2 and C3 are visibly smaller than that of C1 coating, showing some abrasion lines.

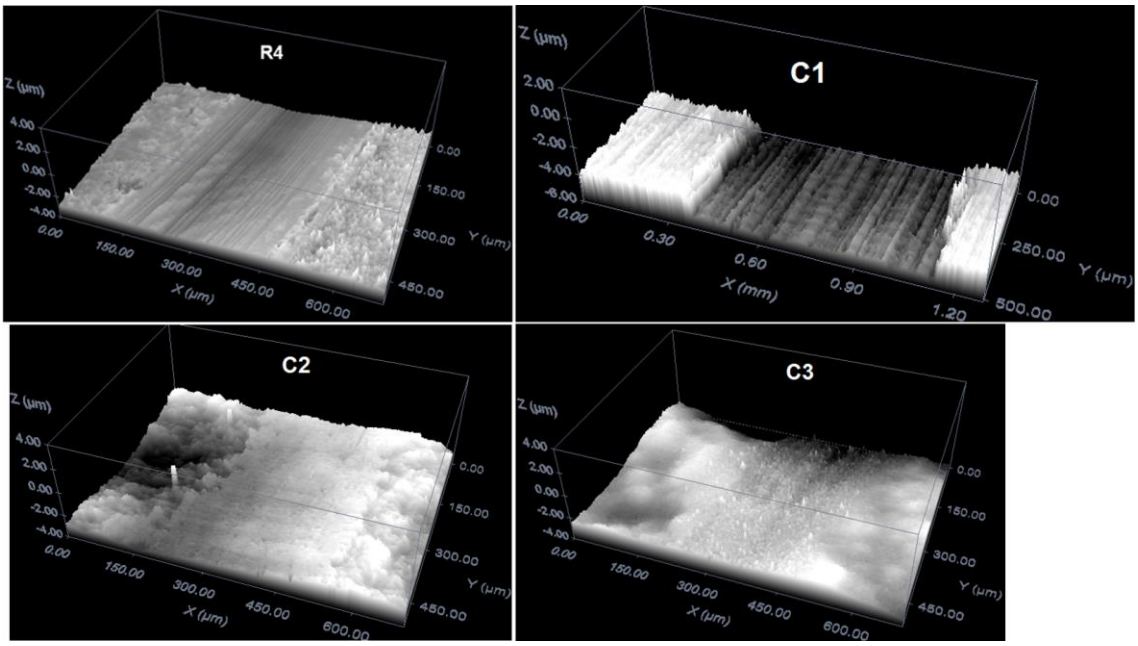

Fig. 5.4.14 Topography of the wear tracks generated in the sliding test in synthetic seawater for the R4 steel and the three coatings

As it can be observed in Fig. 5.4.15, the bigger track corresponds to C1 coating. However, the depth of the track close to 6 µm coincides with the thickness of the organic sealant deposited on top of the sprayed layer. Therefore, the material removed during the wear test is the organic sealant, whereas the WC-CrCo layer resists the conditions of the test, and no great wear is observed in its surface. The wear tracks of coatings C2 and C3 are similar and slightly bigger than that generated in the R4 steel grade. In both cases, the wear track depth is close to 4 µm, which is considerably smaller than the thickness of the organic topcoat of C2 coating and the thickness of C3 coating (see Table 5.4.1). Therefore, the organic layers in C3 and C3 coatings are not removed from the surface during the test.

The wear track volume is obtained from the profilometry analysis, and the wear coefficient (K) can be obtained by dividing the wear volume between the applied normal force and the sliding distance as follows:

$$K = \frac{Wear\ volume}{applied\ normal\ force\ .\ sliding\ distance} m^3 N^{-1} m^{-1} \qquad (5.4.I)$$

The results are compiled in Table 5.4.5. The smaller wear track has been found to be that of the R4 steel. However, the metal sprayed layer in C1 coating has not suffered any wear degradation. On the other hand, the tracks of C2 and C3 coatings are consequence of both the material removal in the tribological contact and some material plastic

deformation that took place under the applied load. Therefore, the coatings have resisted the tribological conditions imposed in the tribocorrosion test, without being removed from the contact exposing the bare material.

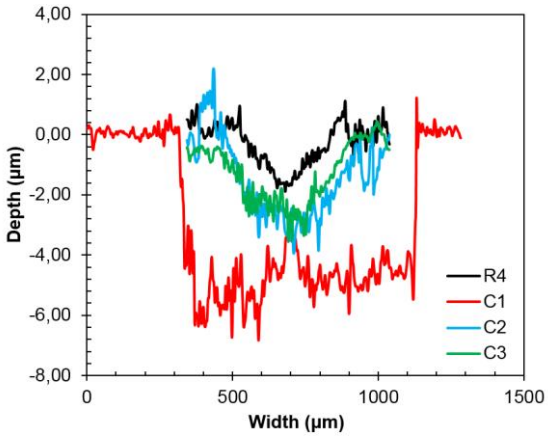

Fig. 5.4.15 Cross-section profiles of the wear tracks obtained in the tribocorrosion test of 4000 cycles at 100 rpm under 5N

5.4.4 Conclusions

In this work, three protective coatings used in offshore component protection have been evaluated in terms of corrosion and wear-corrosion behavior. For this aim, electrochemical corrosion tests and unidirectional tribocorrosion tests have been performed, comparing the behavior of the coatings with the un-coated R4 steel grade. From the results obtained in the tests, the following conclusions can be drawn:

- The corrosion tests showed a poor corrosion resistance and high corrosion rates for the R4 steel, and an enhancement of corrosion response for the three coatings. C2 and C3 presented the higher resistances, due to the polymeric nature of the topcoat in C2 and the organic layer of C3 coating.
- In the tribocorrosion tests, the corrosion resistance of the steel and the three coatings was found to be affected by sliding, decreasing in several orders of magnitude during wear process. C2 coating was observed to be the less affected sample, with corrosion resistances above 10^8 Ω cm^2.
- Furthermore, the three coatings improved the tribological response of the steel in synthetic seawater, presenting lower coefficients of friction than the uncoated sample. The smallest coefficient was obtained for C2 coating with values close to 0.19.
- Microscopy of the R4 steel samples showed deep abrasion lines with small corrosion pits in the wear track, and a significant amount of corrosion degradation undergone in the unworn surface. The coatings did not present ferric corrosion products either in the track or the unworn surface.
- The higher material loss corresponded to C1 coating, which was attributed to the organic sealant removal, with low abrasion and material loss from the hard WC-CrCo layer. C2 and C3 coatings presented similar material loss values, which was the sum of material removal and plastic deformation that took place under the applied load.
- Therefore, the three coatings were found to improve the corrosion performance also providing the steel with improved tribological response in synthetic seawater.

- The coating that showed the best performance with higher corrosion resistance and lower coefficient of friction was C2 coating. C3 coating presented high corrosion resistance, slightly lower than those of C2, a low coefficient of friction and small material loss due to the presence of ceramic platelets reinforcing the organic layer. Finally, C1 coating exhibited a good tribological response as a consequence of its high hardness, but the corrosion resistance was considerably lower than that of C2 and C3 coatings.

5.4.5 Acknowledgments

This work was performed with the support of the EMAITEK Initiative financed by the Basque Country. Authors would also like to acknowledge the Education, Linguistic Politics and Culture Department of the Basque Government for its support through the grant "*Programa Predoctoral de Formación de Personal Investigador No Doctor (PRE_2017_2_0088)*" awarded to the first author.

5.4.6 References

[1] M.R. Dhanak, N.I. Xiros (Eds.). *Springer Handbook of Ocean Engineering*. Springer (2016) ISBN: 978-319-16648-3

[2] R.W. Revie, H.H. Uhlig. *Corrosion and Corrosion Control. An Introduction to Corrosion Science and Engineering (4th edition)*. Wiley-Interscience (2008) ISBN: 978-0-471-73279-2

[3] L.L. Shreir, R. A. Jarman & G.T. Burstein (Eds.). *Corrosion. Volume 2, Corrosion Control (3rd edition)*. Butterworth-Heinemann (1994) ISBN: 0-7506-1077-8

[4] P.R. Roberge. *Corrosion Engineering. Principles and Practice*. Mc Graw Hill (2008) ISBN: 0-07-164087-8

[5] R. Baboian (Ed.). *ASTM corrosion tests and standards. Application and Interpretation (2nd edition)*. ASTM International (2006) ISBN: 0-8031-2098-2

[6] ASM Handbook. *Volume 13. Corrosion*. ASM International (1987) ISBN: 0-87170-007-7

[7] R.E. Melchers, T. Moan, Z. Gao. *Corrosion of working chains continuously immersed in seawater*. Journal of Marine Science and Technology (2007) 12:102-110

[8] D. Talbolt, J. Talbolt. *Corrosion science and technology*. CRC Press US (1998). ISBN: 0-8493-8224-6

[9] C. Guedes Soares, Y. Garbatov, A. Zayed. *Effect of environmental factors on steel plate corrosion under marine immersion conditions*. Corrosion Engineering, Science and Technology (2011) Vol 46, No 4

[10] A. López, R. Bayón, F. Pagano, A. Igartua, A. Arredondo, J.L. Arana, J.J. González. *Tribocorrosion behaviour of mooring high strength low alloy steels in synthetic seawater*. Wear 338-339 (2015) 1-10

[11] A. López-Ortega, R. Bayón, J.L. Arana, A. Arredondo, A. Igartua. *Influence of temperatura on the corrosion and tribocorrosion behavior of High-Strength Low-Alloy steels used in offshore applications*. Tribology International 121 (2018) 341-352

[12] J.-P. Celis and P. Ponthiaux (Eds.). *Testing tribocorrosion of passivating materials supporting research and industrial innovation: Handbook*. Maney publishing (2012). ISBN: 978-1-907975-20-2

[13] D. Landolt, S. Mischler, M. Stemp. *Electrochemical methods in tribocorrosion: a critical appraisal*. Electrochimica Acta 46 (2001) 3913-3929

[14] S. Mischler. *Triboelectrochemical techniques and interpretation methods in tribocorrosion: A comparative evaluation*. Tribology international 41 (2008) 573-583

[15] M. Lannuzzi, A. Barnoush, R. Johnsen. *Materials and corrosion trends in offshore and subsea oil and gas production*. NPJ Materials Degradation (2017) 2

[16] Y. Weng, H. Dong, Y. Gan (Eds.). *Advanced Steels. The Recent Scenario in Steel Science and Technology*. Springer (2011) ISBN: 978-3-642-17664-7

[17] J. Billingham, J.V. Sharp, J. Spurrier, P.J. Kilgallon. *Review of the performance of high strength steels used offshore*. Research Report 105. Prepared by Crandfield University for the Health & Safety Executive. ISBN: 0-7176-2205-3 (2003)

[18] H. Zhang, X. Wang, R. Jia, J. Hou, W. Guo. *Investigation on stress corrosion cracking behavior of welded High-Strength Low-Alloy steel in seawater containing various dissolved oxygen concentrations*. International Journal of Electrochemical Science 8 (2013) 1262-1273
[19] D.A. Skobir. *High-Strength Low-Alloy (HSLA) Steels*. Materials and technology 45 (2011) 294-301
[20] A.W. Momber, P. Plagemann, V. Stenzel. *Performance and integrity of protective coating system for offshore wind power structures after three years under offshore site conditions*. Renewable Energy 74 (2015) 606-617
[21] P. Ault. *The use of coatings for corrosion control on offshore oil structures*. Journal of Protective Coatings and linings 23 (2006) 42-47
[22] X. Sun, D. Huang, G. Wu. *The current state of offshore wind energy technology development*. Energy 41 (2012)298-312
[23] M.A. Alam, E.S.M. Sherif, S.M. Al-Zahrani. *Fabrication of various epoxy coatings for offshore applications and evaluating their mechanical properties and corrosion behavior*. Int. J. Electrochem. Sci. 8 (2013) 3121-3131
[24] R.J.K. Wood. *Tribocorrosion of coatings: a review*. Journal of Physics D: Applied Physics 40 (2007) 5502-5521
[25] R.J.K. Wood, J.A. Wharton. *Coatings for tribocorrosion protection, in Tribocorrosion of Passive Metals and Coatings*. D. Landolt and S. Mischler (Eds.), Woodhead Publishing (2011), ch. 11, pp. 296-333, ISBN: 978-1-94569-966-6
[26] S. Shrestha, A. Sturgeon. *Characteristics and electrochemical corrosion behaviour of thermal sprayed aluminium (TSA) coatings prepared by various wire thermal spray processes*. Eurocorr Proceedings, 2005
[27] Myer Kutz (Ed.). *Handbook of environmental degradation of materials (2nd edition)*. Elsevier (2012) ISBN: 978-1-4377-3455-3
[28] K.P. Fisher, W.H. Thomanson, T. Bosbrook, J. Murali. *Performance of Thermal-Sprayed Aluminium Coatings in Offshore Service*. Materials Performance 34 (1995) 27-35
[29] NORSOK M-501. *Surface preparation and protective coating*. Sixth edition, February 2012
[30] Offshore Standard DNVGL-OS E302, Det Norske Veritas, Offshore Mooring Chains, July 2015
[31] G.W. Stachowiak, A.W. Batchelor. *Engineering Tribology*. Butterworth Heinemann, UK (2005) ISBN: 978-0-7506-7836-0
[32] Y. Sun, E. Haruman. *Effect of electrochemical potential on tribocorrosion behaviour of low temperature plasma carburized 316L stainless steel in 1 M H2SO4 solution*. Surface & Coatings Technology (2015) 4280-4290
[33] G.C. Saha, T.I. Khan. *The Corrosion and Wear Performance of Microcrystalline WC-10Co-4Cr and Near-Nanocrystalline WC-17Co High Velocity Oxy-Fuel Sprayed Coatings on Steel Substrate*. Metallurgical and Materials Transactions A 41 (2010) 3000-3009
[34] D.W. Wheeler, R.J.K. Wood. *Erosion of hard surface coatings for use in offshore gate valves*. Wear 258 (2005) 526-536
[35] C. Zhang, M. Fujii. *Tribological behavior of thermally sprayed WC coatings under water lubrication*. Materials Sciences and Applications 7 (2016) 527-541
[36] R.J.K. Wood. *Tribology of thermal sprayed WC-Co coatings*. Int. Journal of Refractory Metals & Hard Materials 28 (2010) 82-94
[37] D. Toma, W. Brandl, G. Marginean. *Wear and corrosion behavior of thermally sprayed cermet coatings*. Surface and Coatings Technology 138 (2001) 149-158
[38] Q. Wang, S. Zhang, Y. Cheng, J. Xiang, X. Zhao, G. Yang. *Wear and corrosion performance of WC-10Co4Cr coatings deposited by different HVOF and HVAF spraying processes*. Surface & Coatings Technology 218 (2013) 127-136
[39] L. Fedrizzi, L. Valentinelli, S. Rossi. S. Segna. *Tribocorrosion behaviour of HVOF cermet coatings*. Corrosion Science 49 (2007)2781-2799
[40] I.C. Park, S.J. Kim. *Electrochemical Characteristics in Seawater for Cold Thermal Spray-Coated Al–Mg Alloy Layer*. Acta Metall. Sin (Eng. Lett.), 2016, 29 (8), 727-734
[41] T.C. Chen, CC. Chou, T.Y. Yung, J.Y. Huang. *Wear behavior of thermally sprayed Zn/15Zl, Al and Inconel 625 coatings on carbon steel*. Surface & Coatings Technology 303 (2016) 78-85
[42] M. Campo, M. Carboneras, M.D. López, B. Torres, P. Rodrigo, E. Otero, J. Rams. *Corrosion resistance of thermally sprayed Al and Al/SiC coatings on Mg*. Surface and Coatings Technology 203 (2009) 3224-3230

[43] H.-S. Lee, J.K. Singh, M.A. Ismail, C. Bhattacharya. *Corrosion Resistance Properties of Aluminum Coating Applied by Arc Thermal Metal Spray in SAE J2334 Solution with Exposure Periods*. Metals 2016, 6, 55; doi:10.3390/met6030055

[44] M.S. Han, Y.B. Woo, S.C. Ko, Y.J. Jeong, S.K. Jang, S.J. Kim. *Effects of thickness of Al thermal spray coating for STS 304*. Transactions of Nonferrous Metals Society of China 19 (2009) 925-929

[45] S. Deshpande, A. Kulkarni, S. Sampath, H. Herman. *Application of image analysis for characterization of porosity in thermal spray coatings and correlation with small angle neutron scattering*. Surface & Coatings Technology 187 (2004) 6-16

[46] P. Fauchais and A. Vardelle (2012). *Thermal Sprayed Coatings Used Against Corrosion and Corrosive Wear, Advanced Plasma Spray Applications*, Dr. Hamid Jazi (Ed.), ISBN: 978-953-51-0349-3, InTech, Available from: http://www.intechopen.com/books/advanced-plasma-spray-applications/thermal-sprayed-coatings-usedagainst-corrosion-and-corrosive-wear

[47] E.A. Esfahani, H. Salimijazi, M.A. Golozar, J. Mostaghimi, L. Pershin. *Study of Corrosion Behaviour of Arc Sprayed Aluminium Coating on Mild Steel*. Journal of Thermal Spray Technology 21 (2012) 1195-1202

[48] H.-S. Lee, J.K. Singh, J.H. Park. *Pore blocking characteristics of corrosion products formed on aluminum coating produced by arc thermal metal spray process in 3.5 wt.% NaCl solution*. Construction and Building Materials 113 (2016) 905-916

[49] R.E. Melchers, R. Jeffrey. *Early corrosion of mild Steel in seawater*. Corrosion Science 47 (2005) 1678-1693

[50] R.E. Melchers. *Effect of marine immersion corrosion of carbon content of low alloy Steels*. Corrosion Science 45 (2003) 2609-2625

[51] J. Bhandari, F. Khan, R. Abbassi, V. Garaniya, R. Ojeda. *Modelling of pitting corrosion in marine and offshore Steel structures-A technical review*. Journal of Loss Prevention in the Process Industries 37 (2015) 39-62

[52] J.K. Saha. *Corrosion of Constructional Steels in Marine and Industrial Environment*. Springer India (2013), ISBN: 978-81-322-0719-1

[53] K. Xiao, C.F. Dong, X.G. Li, F.M. Wang. *Corrosion Products and Formation Mechanism during Initial Stage of Atmospheric Corrosion of Carbon Steel*. Journal of Iron and Steel Research, International 2008, 15(5): 42-48

[54] J.G. Castaño, C.A. Botero, A.H. Restrepo, E.A. Agudelo, E. Correa, F. Echeverría. *Atmospheric corrosion of carbon steel in Colombia*. Corrosion Science 52 (2010) 216-223

[55] H. Möller, E.T. Boshoff, H. Froneman. *The corrosion behaviour of a low carbon steel in natural and synthetic seawaters*. The Journal of The South African Institute of Mining and Metallurgy, Volume 106 (August 2006)

[56] C. Monticelly, A. Frignani, F. Zucchi. *Investigation on the corrosion process of carbon steel coated by HVOF WC/Co cermets in neutral solution*. Corrosion Science 46 (2004) 1225-1237

[57] H. Ezuber, A. El-Houd, F. El-Shawesh. *A study on the corrosion behavior of aluminum alloys in seawater*. Materials and Design 29 (2008) 801-805

[58] R. Baboian (Ed.). *NACE Corrosion Engineer's Reference Book. (3rd edition)*. NACE International (2002) ISBN: 978-1-57590-127-5

[59] H.S. Lee, J.K. Singh, M.A. Ismail. *An effective and novel pore sealing agent to enhance the corrosion resistance performance of Al coating in artificial ocean water*. Sci. Rep. 7, 41935; doi: 10.1038/srep41935 (2017)

[60] D. Landolt. *Corrosion and Surface Chemistry of Metals*. CRC Press (2007) ISBN: 978-0-8493-8233-8

[61] A. Forsgren. *Corrosion Control Through Organic Coatings*. Taylor & Francis (2006) ISBN: 978-0-8493-7278-0

[62] U. Trdan, J. Grum. *Evaluation of corrosion resistance of AA6082-T651 aluminium alloy after laser shock peening by means of cyclic polarisation and EIS methods*. Corrosion Science 59 (2012) 324-333

[63] Q. Jiang, Q. Miao, F. Tong, Y. Xu, B.L. Ren, Z.M. Liu, Z.J. Yao. *Electrochemical corrosion behaviour of arc sprayed Al-Zn-Si-RE coatings on mild steel in 3.5 % NaCl solution*. Transactions of Nonferrous Metals Society of China 24 (2014) 2713-2722

[64] W. Liu, Q. Zhou, L. Li, Z. Wu, F. Cao, Z. Gao. *Effect of alloy element on corrosion behavior of the huge crude oil storage tank steel in seawater*. Journal of Alloys and Compounds 598 (2014) 198-204

[65] N. Imaz, M. Ostra, M. Vidal, J.A. Díez, M. Sarret, E. García-Lecina. *Corrosion behaviour of chromium coatings obtained by direct and reverse pulse plating electrodeposition in NaCl aqueous solution*. Corrosion Science 78 (2014) 251-259

[66] F. El-Taib Heakal, N.S. Tantawy, O.S. Shehta. *Influence of chloride ion concentration on the corrosion behavior of Al-bearing TRIP steels*. Materials Chemistry and Physics 130 (2011) 743-749

[67] D. Yang, O. Rosas, H. Castaneda. *$FeCO_3$ layer evolution for API 5L X52 steel in carbon dioxide saturated NaCl brine in the presence of 1-decyl-3-methylimidazolium chloride*. Corrosion Science 87 (2014) 40-50

[68] E. Barsoukov, J.R. Macdonald (Eds.). *Impedance Spectroscopy: Theory, Experiment and Applications*. Wiley-Interscience (2005) ISBN: 0-471-64749-7

[69] M. Rahkes, E. Koroleva. Z. Liu. *Improvement of Corrosion Performance of HVOF MMC Coatings by Laser Surface Treatment*. Surface Engineering 27 (10) (2011) 729-733

[70] S. Brioua, K. Belmokre, V. Debout, P. Jackuot, E. Conforto, S. Touzain, J. Creus. *Corrosion behavior in artificial seawater of thermal-sprayed WC-CoCr coatings on mild steel by electrochemical impedance spectroscopy*. Journal of Solid State Electrochemistry 16 (2012) 633-648

[71] V.A.D. Souza, A. Neville. *Corrosion and synergy in a WC-CoCr HVOF thermally spray coating- understanding their role in erosion-corrosion degradation*. Wear 259 (2005) 171-180

[72] D. Yang, C. Liu, X. Liu, M. Qi, G. Lin. *EIS diagnosis on the corrosion behavior of TiN coated NiTi surgical alloy*. Current Applied Physics 5 (2005) 417-421

[73] C. Liu, Q. Bi, A. Matthews. *EIS comparison on corrosion performance of PVD TiN and CrN coated mild steel in 0.5 N NaCl aqueous solution*. Corrosion Science 43 (2001) 1953-1961

[74] M.M. Verdian, K. Raeissi, M. Salehi. *Corrosion performance of HVOF and APS thermally sprayed NiTi intermetallic coatings in 3.5% NaCl solution*. Corrosion Science 52 (2010) 1052-1059

[75] N. Fredj, S. Cohendoz, X. Feaugas, S. Touzain. *Aging of marine coating in natural and artificial seawater under mechanical stresses*. Progress in Organic Coatings 74 (2012) 391-399

[76] S. Touzain, Q. Le Thu, G. Bonnet. *Evaluation of thick organic coatings degradation in seawater using cathodic protection and thermally accelerated tests*. Progress in organic coatings 52 (2005) 311-319

[77] Q. Le Thu, H. Takenouti, S. Touzain. *EIS characterization of thick flawed organic coatings aged under cathodic protection in seawater*. Electrochimica Acta 51 (2006) 2491-2502

[78] D. Loveday, P. Peterson, B. Rodgers. *Evaluation of Organic Coatings with Electrochemical Impedance Spectroscopy*. JCT Coatings Tech (August 2004).

[79] B.R. Hinderliter, S.G. Croll, D.E. Tallman, Q. Su, G.P. Bierwagen. *Interpretation of EIS data from accelerated exposure of coated metals based on modeling of coating physical properties*. Electrochimica Acta 51 (2006) 4505-4515

[80] J.G. Castaño, C.A. Botero, A.H. Restrepo, E.A. Agudelo, E. Correa, F. Echeverría. *Atmospheric corrosion of carbon steel in Colombia*. Corrosion Science 52 (2010) 216-223

Contribution 5

Evaluation of protective coatings for offshore applications: Validation for high corrosivity category atmospheres

Submitted for publication in Marine Structures

Contribution 5: Submitted for publication in Marine Structures

5.5. EVALUATION OF PROTECTIVE COATINGS FOR OFFSHORE APPLICATIONS. VALIDATION FOR HIGH CORROSIVITY CATEGORY ATMOSPHERES

A. López-Ortega[a], R. Bayón[a], J.L. Arana[b]

[a] *IK4-TEKNIKER, Eibar, Spain*
[b]*Department of Metallurgical and Materials Engineering, University of the Basque Country, Spain*

ABSTRACT

The interest in renewable energies obtained from the resources availed in the ocean has increased during the last years. However, the harsh atmospheric conditions in marine environments is a major drawback in the design of offshore structures. The protective systems employed to preserve offshore steel structures are regulated by several standards (ISO 12944, NORSOK M-501), which classify the corrosivity category of offshore installations as C5-M and Im2. In this work, three coatings employed in offshore components protection have been evaluated according to these standards, by performing aging tests in different climatic cabinets. The coatings studied were a Thermally Sprayed Carbide coating with an organic sealant (C1), a Thermally Sprayed Aluminum (TSA) with an organic topcoat (C2), and an epoxydic organic coating reinforced with ceramic platelets (C2). The only coating that reached the higher categories in all the tests was C2 coating. C1 coating presented ferric corrosion products coming from the substrate in some of the tests, and blistering was detected in C3 coating.

Keywords: *Offshore; Corrosion; Coatings; Weathering*

5.5.1 Introduction

Marine environment is a very aggressive working atmosphere, where structural materials and components are exposed to ultraviolet radiation, chloride-rich salty environment, frequent wetting and drying cycles, high humidity, the attack of biological microorganisms and marine bacteria, etc. [1-5]. Furthermore, there is also abrasion and severe wear caused by sand, ocean currents, floating wastes and contamination [1,5-8]. As schematically depicted in Fig. 5.5.1, offshore materials and structures are exposed to five corrosion zones, with different material corrosion rates [3,6,9-11]:

- **Atmospheric zone:** it is located above the sea level, and the severity of corrosion is related to the time of wetness, during which electrochemical processes take place. There is a direct relationship between atmospheric salt content and corrosion rate. Materials are also exposed to solar radiation, which deteriorates the performance of organic coatings.
- **Splash zone:** the section in the structure that is intermittently wetted, due to tides and the wind. The corrosion rate of metals in this zone is the higher, due to the aerated condition, which makes the access of dissolved oxygen for electrochemical reactions easy. Since it is continuously being wetted, chlorides can concentrate on the surface while the water films dry. Furthermore, the impinging of seawater containing sand and other flowing matter adds a mechanical component to the materials deterioration in this exposure zone.
- **Tidal zone:** the materials are alternately submerged and exposed to the splash zone, as the tide fluctuates. In the submerged condition, materials are exposed to a

well-aerated seawater, which favors the attachment and growth of biofouling. The corrosion rate is influenced by the tidal flow, with higher corrosion rates with increasing movements.

- **Submerged zone:** the section of the structure that is always immersed in the sea. The corrosion rate in this zone depends on the availability of oxygen to be transported to the cathodic sites of materials surfaces. As oxygen concentration varies with depth, decreasing with increasing distance to the surface, the corrosion rate is also slower at higher depths.
- **Subsoil:** In the buried structure, the oxygen concentration is low and hydrogen sulfide may be present.

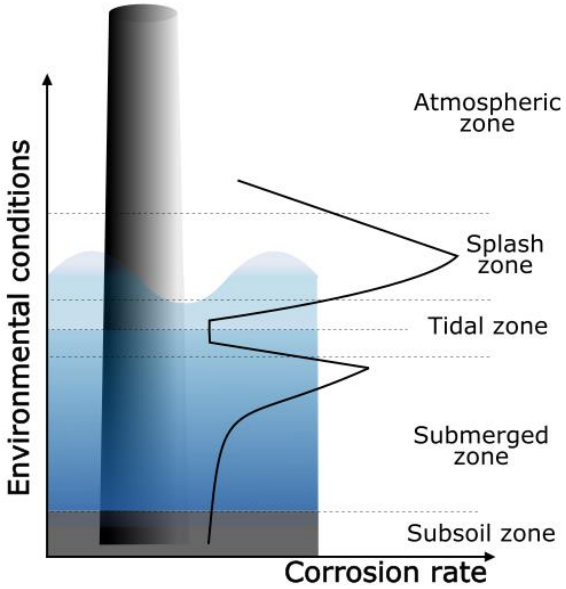

Fig. 5.5.1 Zones of corrosion and relative corrosion rate depending on the exposure zone (based on [8])

The most employed structural material in offshore applications is steel, usually mild or low-alloyed, due to their superior mechanical properties [1,13,14]. However, this kind of steels possess low corrosion resistance in seawater and corrode relatively fast. The corrosion rate of mild steel in seawater has been measured to be 250 microns per year [15,16]. In order to avoid or prevent premature failures due to high corrosion rate of structural steel, coatings have been successfully used. The requirements of protective coatings and their application procedures vary significantly depending on the installation location, i.e., onshore or offshore. Currently, the protection systems used in offshore structures are regulated by several standards, among which the ISO 12944:1-9[17] and the NORSOK M-501 [18] can be found. The selection of the protective system deeply depends on the location of the component. According to ISO 12944 (part two) and ISO 9223 [19], there are five corrosivity categories; from the C1 corresponding to a non-corrosive atmosphere, to industrial and marine corrosive categories (C5-I and C5-M). There are also IM1 and IM3 categories, to describe the water and soil corrosivity, respectively. The first edition of the ISO 12944-9 [20] published in January 2018, adds new categories for offshore related atmospheres: CX-offshore (atmospheric), Im4 (immersion), and CX-Offshore/Im4 for the splash and tidal exposure zones. ISO 12944 also classifies the durability, or the time for the first major maintenance as:

- **Low (L):** 2 to 5 years
- **Medium (M):** 5 to 15 years
- **High (H):** 15 to 25 years
- **Very High (VH):** >25 years

The categories required for a protective system in an offshore installation are C5-M and Im2, for non-submerged and submerged components, respectively. In order to obtain these protection grades, the ISO 12944 standard recommends employing multilayer coatings with thickness between 320 and 500 µm for a C5-M category in the atmospheric zone, and between 480 and 1000 µm for the splash zone and submerged components (Im2). According to the standard, these specifications should be enough to assure a component durability of 15 years [17]. On the other hand, the NORSOK standard does not specify a coating thickness range, but a minimum thickness. Therefore, a coating requiring a C5-M category should be at least 280 µm, whereas submerged components should have a minimum of 350 µm for an Im2 category [18].

Protective coatings selected for marine environment strongly depend on the exposure zone and must provide the system with specific properties to assure infrastructures durability. Typical coating systems employed in offshore applications [21] with the desired properties depending on the exposure zone are compiled in Table 5.5.1.

Table 5.5.1 Typical coating systems employed in offshore applications in the different exposure zones [21], with the desired properties and corrosivity category required (ISO 12944 [17])

Exposure zone	Coating system		Desirable coating properties
Atmospheric C5-M (ISO 12944)	Zinc rich epoxy primer Epoxy intermediate layer Polyurethane top-coat	(60-100 µm) (100-120 µm) (50-80 µm)	Corrosion-resistant, erosion-resistant, anti-icing, UV-resistant
Splash and tidal C5-M and Im2 (ISO 12944)	Two or three epoxy-based coats Polyurethane top-coat	(>1000 µm in total) (50-80 µm)	Combination of atmospheric and submerged coatings´ properties
Submerged Im2 (ISO 12944)	Two or three epoxy-based coats	(>450 µm in total)	Corrosion-resistant, antifouling, wear-resistant

In this work, three coatings used in offshore component protection have been evaluated. The selected coatings are commercial coatings currently used in the protection of steel submerged components in mooring line systems. In a previous work, the corrosion and tribocorrosion (wear+corrosion) behavior of the three coatings was evaluated [22]. Furthermore, the characterization of the coatings, in terms of thickness, hardness, porosity and microscopic analysis of the morphologies, was included in the first part of this work [22]. In the second part of the study, compiled within this document, the corrosion protection effectiveness of the coatings was assessed according to the ISO 12944 and NORSOK M-501 standards by performing aging tests on different cabinets. This work was carried out before the ISO 12944-9 was published, so the conditions and exposure times employed were those in the ISO 12944-6, for the C5-M/Im2 (high) category. On the other hand, the combined aging test performed in this work was performed according to the ISO 20340 and NORSOK M-501. However, after the publication of the ISO 12944-9, where this test procedure is recommended, ISO 20340 was withdrawn. Therefore, no longer mention to the ISO 20340 is made throughout the document, and these tests are referred to the new ISO 12944-9.

5.5.2 Experimental procedure

5.5.2.1 Materials and sample preparation

In the present work, the effectiveness of three coatings for offshore structural steel protection has been evaluated. The coatings studied in this work were the following:

- Thermally Sprayed Carbide (WC-CrCo) with an organic sealant (**C1**)
- Arc Thermally Sprayed Aluminum with an organic topcoat (**C2**)
- Epoxy based organic coating reinforced with ceramic particles (**C3**)

The coatings were applied on R4 [23] steel grade panels of 100x150 mm^2, which were mechanized to obtain samples of 100x75 mm^2. The uncoated backside and edges of the panels were isolated with an insulating wax to avoid corrosion of the steel substrate to affect the results. The exposed area of these samples was of 71 cm^2.

5.5.2.2 Corrosion-aging tests

The ISO 12944 and the NORSOK M-501 standards propose several accelerated aging tests such as immersion (ISO 2812-2[24]), water condensation (ISO 6270[25]) or salt-fog exposure (ISO 9227[26]); and the minimum time for the protective system to be effective depending on the corrosivity category and durability. The NORSOK M-501 and the ISO 12944-9 also propose an accelerated test combining UV irradiation (ISO 11507[27]), salt spray (ISO 9227) and low-temperature exposure in different chambers, to reproduce the aging conditions of the marine atmosphere. The exposure times that the coatings must fulfill without losing their protective effectiveness to achieve the C5-M and Im2 categories, according to the ISO 12944 standard, are listed Table 5.5.2 for the different aging tests.

Table 5.5.2 Minimum exposure time for the coatings to achieve the C5-M and Im2 categories according to the ISO 12944 standard [17]

Category	Durability ranges	ISO 2812-2 [24] (Immersion in water)	ISO 6270-2 [25] (Water condensation)	ISO 9227 [26] (Salt spray test)
C5-M	Low	-	240	480
	Medium	-	480	720
	High	-	720	1440
Im2	Low	-	-	-
	Medium	2000	-	720
	High	3000	-	1440

In all the tests, visual inspections were performed periodically, so as to detect the presence of any defect such as blisters, cracks, delamination of the coating or corrosion of the substrate. All the samples were exposed in the chamber for the maximum duration to achieve the C5-M High category, unless premature failure of the coating due to the appearance of defects was detected (ISO 4628 1-5 [28]).

Immersion tests (ISO 2812-2)

The resistance of the coatings to immersion was analyzed according to the ISO 2812-2 [24] standard (Table 5.5.3). The test was performed in a Julabo ED thermostatic bath. The temperature of the bath was fixed at 40 ºC, and the circulation and aeration system of the water was activated during the whole test duration. The total duration of the test was of 3000 hours (Im2-High category). Three samples of each coating were tested.

Water condensation tests (ISO 6270)

A water condensation test was performed according to the ISO 6270-2 standard to analyze the resistance of the coatings to humidity under water condensation conditions. The standard describes three water atmospheres:

- Condensation atmosphere with constant humidity (CH)
- Condensation atmosphere with alternating humidity and air temperature (AHT)

- Condensation atmosphere with alternating air temperature (AT)

The conditions of the three tests are summarized in Table 5.5.3. The test cycles were repeated until a total duration of 720 hours was completed. The test was performed in a Kesternich HK300-800 S/M humidostatic chamber. Three samples of each coating were introduced in the chamber, for each test alternative.

Salt spray tests (ISO 9227)

Corrosion-aging tests in neutral salt spray chamber were performed under the conditions specified in the ISO 9227 standard (Table 5.5.3) in an ASCOTT 2000S chamber. Six test samples were prepared for each coating. In three of these samples, an X-shaped incision that reached the steel substrate was made (ISO 17872 [29]). No incision was made in the C1 coating, due to the high hardness of the tungsten carbide, and the six samples were introduced in the chamber without an incision. According to EN ISO 12944-6 standard, the corrosion from the scratch in the samples with incision shall not exceed 1 mm, calculated as:

$$M = \frac{C-W}{2} \tag{5.5.I}$$

Where W is the original width of the scratch, and C the maximum width of corrosion across the scratch, in millimeters. In the samples with the incision, adhesion tests were performed at the end of the exposure, following the ASTM D3359 standard [30].

Combined-aging test (NORSOK M-501, ISO 12944-9)

The coatings were aged by combining the exposure to several climatic environments, in accordance with the procedure described in the NORSOK M-501 and ISO 12944-9 standards. The test consisted of combining the exposure to UV radiation and condensation (ISO 11507, A method), with the exposure to salt spray (ISO 9227) and low temperature. The duration of exposure to different conditions is presented in Table 5.5.3. The UV/condensation period was performed in an Atlas UVTest weathering device. The UV lamps employed in the test were type II UV lamps (UVA-340), of 340 nm (ISO 11507). The salt spray and low-temperature periods were carried out in an ASCOTT 2000S chamber and in a WEISS C340/70 climatic chamber, respectively. The UV/condensation period was started with the UV radiation and finished with condensation. The coatings were rinsed with deionized water between the salt spray and the low-temperature periods. The temperature of -20±2 ºC of the low-temperature period was reached in less than 30 minutes from the moment the samples were introduced into the chamber. The cycle was repeated 4 times, for a total duration of 720 h. The samples were evaluated three times per cycle after the samples were removed from each chamber.

Table 5.5.3 Summary of the corrosion-aging tests and their conditions in accordance with the different standards

Standard	Test type		Cycle duration		Conditions in the cabinet		Total duration of the test
			Test periods	Total	Temperature	Relative humidity	
ISO 2812[25]	Immersion test		-		(40±3) ºC	-	3000 h
ISO 6270[25]	Constant humidity condensation atmosphere (CH)		From warm-up to end of exposure		(40±3) ºC	100%	720 h
	Alternating condensation atmosphere	Alternating humidity and air temperature (AHT)	8 h including warm-up		(40±3) ºC	100%	
			16 h including warm-up		18-28ºC	Ambient	720 h
		Alternating air temperature (AT)	8 h including warm-up	24 h	(40±3) ºC	100%	
			16 h including warm-up	24 h	18-28ºC	100%	720 h
ISO 9227[26]	Salt spray		-		(35±3) ºC	-	1440 h
NORSOK M501[18] ISO 12944-9[20]	Ultraviolet radiation and condensation (ISO 11507[27])		4 h UV radiation (0.77 W/m^2)	72h	(60±3) ºC	-	
			4 h condensation		(50±3) ºC	100%	720 h
	Salt spray (ISO 9227)		72 h	168 h	(35±3) ºC	-	
	Low temperature		24 h		(-20±2) ºC	-	

5.5.3 Results and discussion

The results of the corrosion-aging tests for the three coatings in different climatic chambers, and their categorization in accordance with the ISO 12944 and NORSOK M-501 standards are briefly recapitulated within this section.

5.5.3.1 Immersion tests (ISO 2812-2)

Immersion tests were performed to evaluate the resistance of the coatings to water immersion. The final surface state of the samples is presented in Fig. 5.5.2, comparing the tested samples with an untested one.

In the first evaluation after 168 hours of immersion, C1 coating samples presented some decolorized zones in the surface. This could be a consequence of the partial removal of the organic sealant applied on top of the sprayed carbide. After 336 hours, two small ferritic pits were detected in one of the samples. The discoloration of the samples was more evident with increasing exposure time. In the evaluation performed at 1344 hours, ferric corrosion was observed in the edges of the samples, close to the insulating wax, which was formed due to cavitation effect, and by the possible penetration of water under the wax leading to corrosion of the underneath steel. This corrosion spread with time, but no corrosion sign was detected in the middle zone of the surface. At the end of the exposure, the tone of the tested samples was more brownish color, and several decolorized and brighter zones were distinguished as a consequence of the sealant loss. The corrosion present in the edges was not considered as a coating failure, since it was observed to be caused by a non-adequate insulating property of the organic wax. The microscopic analysis of the surface revealed some isolated pits along the surface, in a lower density than 1 % of the total surface (Fig. 5.5.3).

In the case of C2 coating, the presence of ferric corrosion pits was detected close to the edges in the first evaluation at 168 hours. These pits corresponded to the oxidation undergone by some metallic particles that were embedded in the surface of the coatings during machining processes, i.e., contaminants. After 672 hours, the apparition of white salts resulting from the oxidation of the aluminum layer beneath the organic topcoat was observed. The state of the coating remained unaltered in the following evaluations at longer immersion times. The final surface state of the coating was similar to that of the untested sample, in terms of color and bright, and no presence of ferric corrosion coming from the steel substrate was detected.

The samples of C3 coating presented a loss of brightness from the first evaluation at 168 hours of exposure, showing a considerably paler tone. After 504 hours, a blister appeared in one of the three samples (Fig. 5.5.4), which was removed from the chamber thereafter. The microscopic analysis of the transversal surface of the blister showed the presence of ferric corrosion products, revealing the underneath corrosion of the substrate by electrolyte penetration through the coating. In the next evaluation, at 672 hours, some blisters were detected in the other two samples. The samples were kept in the chamber until the 3000 hours of immersion were reached, and the blisters were observed to increase in size and number with higher exposure time. At the end of the test, the surface of both samples was covered with blisters (Fig. 5.5.2). In accordance with the UNE EN-ISO 4628-2 standard, the blistering grade of the three samples was the following:

- C3-sample No.1: 4(S4)
- C3-sample No.2: 2(S4) (removed from the chamber after 504 hours of immersion)
- C3-sample No.2: 4(S5)

C1 and C2 coatings passed the 3000 hours of immersion, achieving the Im2(High) category (ISO 12944-6), whereas C3 coating did not pass the immersion test, not even reaching the 2000 hours of immersion required for an Im1(Medium) category (Table 5.5.7).

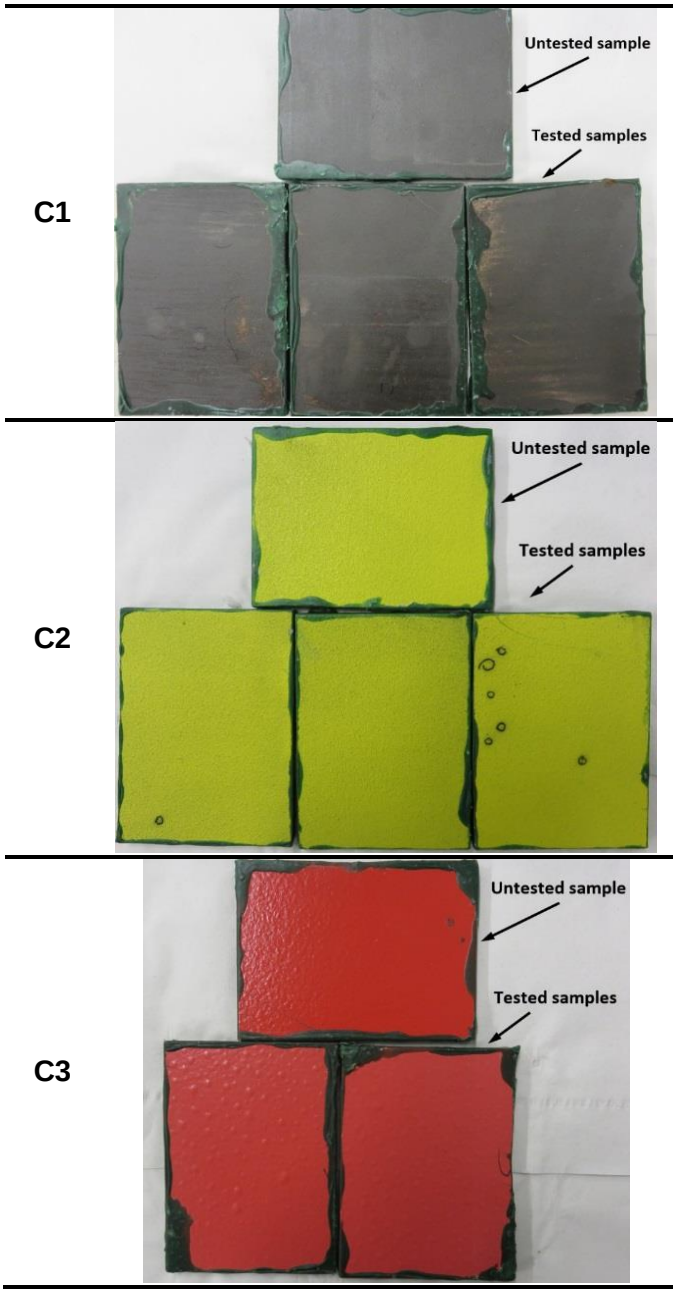

Fig. 5.5.2 Visual appearance of the R4-coated samples after 3000 hours of immersion in accordance with the ISO 2812 standard

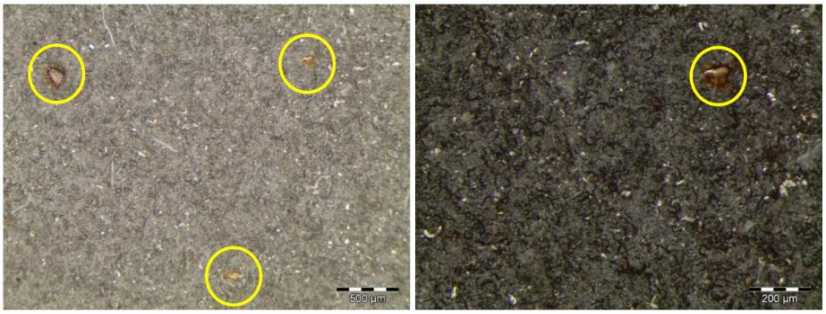

Fig. 5.5.3 Optical microscopies of the C1 coating surface showing corrosion pits

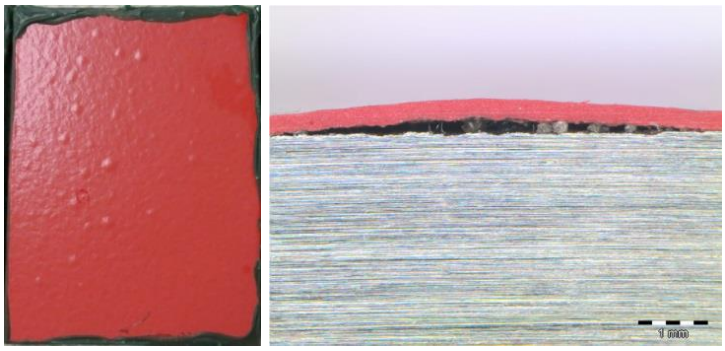

Fig. 5.5.4 Surface state of sample No.2 of the C3 coating showing blisters after 504 hours of immersion (left) and micrograph of the ferric corrosion products formed under the blister (right)

5.5.3.2 Water condensation tests (ISO 6270)

The resistance of the coatings to humidity under water condensation conditions was evaluated under three atmospheres, i.e., constant humidity (CH), alternating temperature and humidity (AHT), and alternating temperature (AT). The final surface appearance of the tested coatings compared with an untested sample is presented in Fig. 5.5.5. Table 5.5.4 summarizes the results obtained after the condensation tests, expressed as the surface percentage covered by ferric corrosion (FC), white salts (WS) and blistering grade.

In the three exposure atmospheres, C1 coating presented some decolorized zones in the surface after several hours in the cabinet, as a consequence of the partial elimination of the sealant applied on top of the sprayed carbide. This was observed after 110 in CH test, and after 278 hours in AHT and AT tests. Furthermore, ferric corrosion was observed to appear in all the samples close to edges. As previously explained in the immersion tests, this corrosion phenomenon was due to cavitation effects in the edges of the insulating wax and was not considered as a coating failure. The color of the coating changed with increasing exposure, as a consequence of the sealant degradation, acquiring a more reddish tone (Fig. 5.5.5). In the AHT test, some characteristic red/brown colored corrosion products were observed in the center of one of the samples, but the surface coverage by these corrosion products did not exceed the 1 %, so the coating was considered to pass the three tests successfully, with a C5-M(High) category (ISO 12944-6).

In the case of C2 coating, all the samples presented some red spots on the surface, corresponding to ferric oxides. These oxides, however, did not came from substrate corrosion but from corrosion of metallic particles that were embedded in the coating surface during sample machining process. No significant changes were observed in the coating during the exposure to the three condensation atmospheres in terms of ferric corrosion, blistering, cracking, or color change. In CH test, the presence of white salts resulting from the aluminum oxidation was detected after 614 hours. One of the samples for the AHT test was prepared with a smaller exposed surface, due to several imperfections presented in the top of the coating, in order to avoid the influence of those defects on the final results. No defects such cracks, ferric corrosion, or blisters were detected in any sample of AHT test, not even white salts from aluminum oxidation. Finally, in the AT test, white salts appeared after 336 hours just in one of the samples. Therefore, C2 coating passed the three condensation tests, achieving a C5-M(High) category (ISO 12944-6).

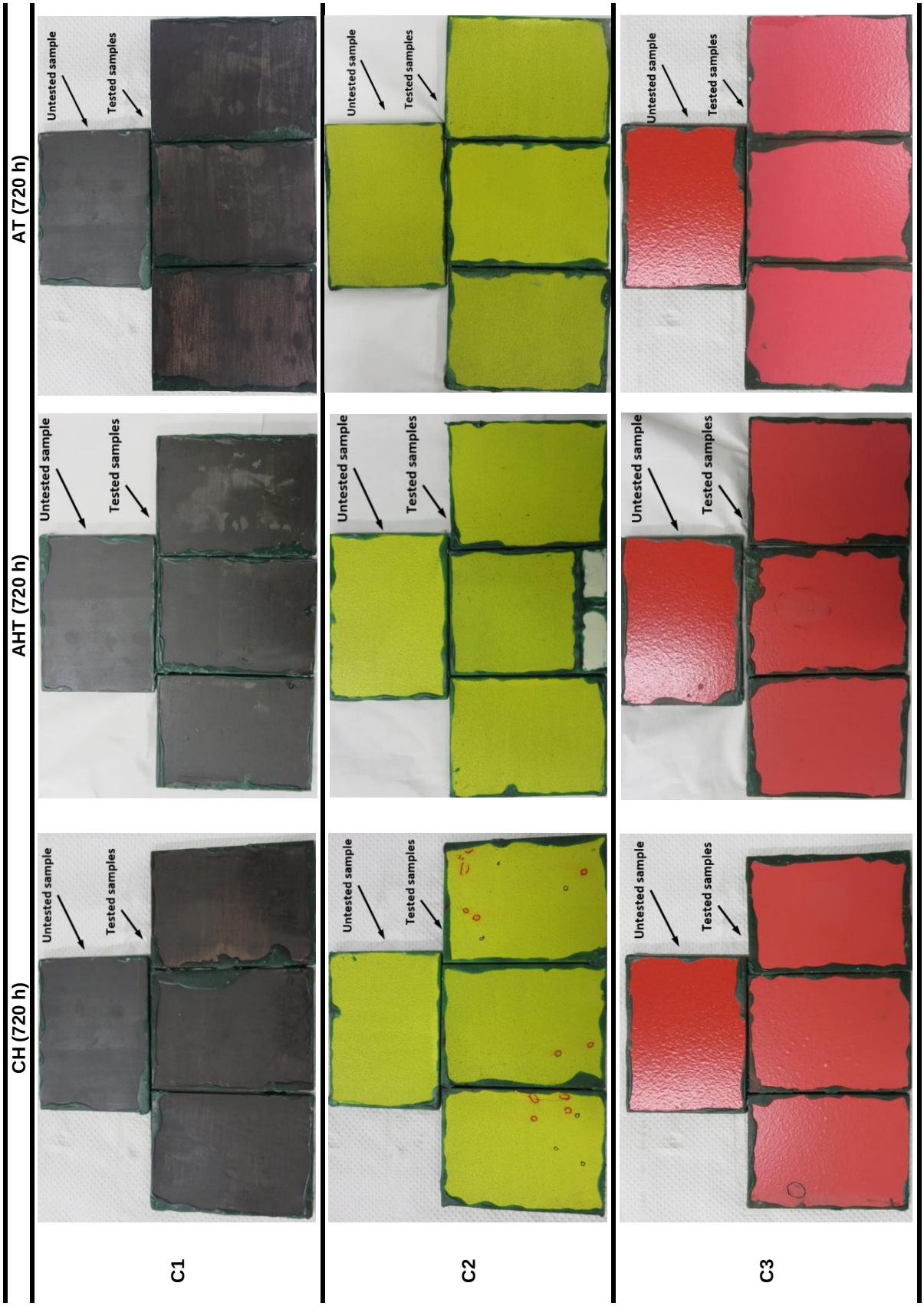

Fig. 5.5.5 Visual appearance of the coatings Surface after 720 hours of exposure to condensation tests at constant humidity (CH), alternating humidity and temperature (AHT) and alternating temperature (AT), according to the ISO 6270-2 standard

The samples of C3 coating showed color and brightness loss after several hours of exposure, but no presence of ferric corrosion, cracks, or other defects was detected during the evaluations. The only defects appeared in the CH test samples, which presented a significant part of the surface covered by blisters. According to the UNE EN-ISO 4628-2 standard, the blistering grade of the three samples was the following:

- C3-sample No.1: 2(S3)
- C3-sample No.2: 2(S4)
- C3-sample No.2: 2(S4)

Table 5.5.4 Summary of the oxidation and blistering grade of the coatings after the condensation tests in accordance with the ISO 6270-2 standard [25]

Coating		Oxidation grade			Blistering grade		
		CH	AHT	AH	CH	AHT	AH
C1	Sample 1	3%E*	2%E	3%E	0%	0%	0%
	Sample 2	3%E	2%E+1%C*	2%E	0%	0%	0%
	Sample 3	3%E	1%E	-	0%	0%	-
C2	Sample 1	1%WS*	0%	0%	0%	0%	0%
	Sample 2	1%WS	0%	1%(WS)	0%	0%	0%
	Sample 3	1%WS	0%	-	0%	0%	-
C3	Sample 1	0%	0%	0%	20%	0%	0%
	Sample 2	0%	0%	0%	30%	0%	0%
	Sample 3	0%	0%	-	30%	0%	-

(*) E: ferric corrosion at edges; C: ferric corrosion at the center; WS: white salts

Consequently, C3 coating was classified with C5-M(High) category for the AHT and AT tests, and with a C4(High)/C5-M(Medium) category for the CH test, corresponding to an optimal surface condition of the coating for 480 hours of exposure to constant humidity (ISO 12944-6) (Table 5.5.7).

5.5.3.3 Salt spray tests (ISO 9227)

The coatings were exposed to salt spray conditions to evaluate the resistance to saline corrosive environment. The final surface appearance of the tested samples with and without incision are presented in Fig. 5.5.6. In the case of C1, the six samples were tested without an incision, and just the final state of three of the samples are presented in Fig. 5.5.6, as representative of all the samples. Table 5.5.5 summarizes the degradation observed in the coatings along the different evaluations, in terms of percentage of ferric corrosion or white salts, and progression of ferric corrosion.

C1 coating remained unaltered for the first 504 hours of exposure, after which corrosion was observed to spread in all the samples. After 1440 hours in the chamber, four of the six samples presented a 25-30 % of the surface covered by ferric corrosion. The color of the coating changed with exposure time, acquiring a purple tonality. The surface evaluated with a magnifying glass revealed the presence of ferric pits along the whole exposed surface (Fig. 5.5.7). The oxidation grade of the coating was Ri4(S2), in accordance with the UNE-EN ISO 4628-3 standard.

	Without incision	With incision
C1	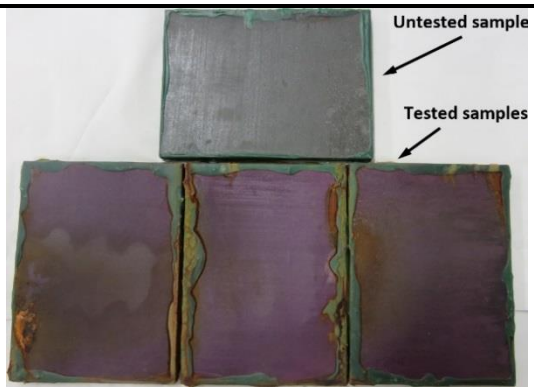	
C2	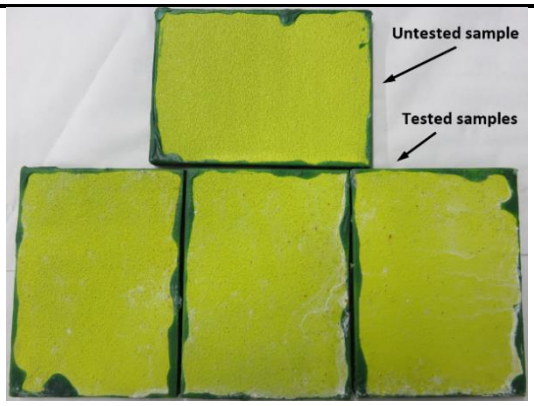	
C3	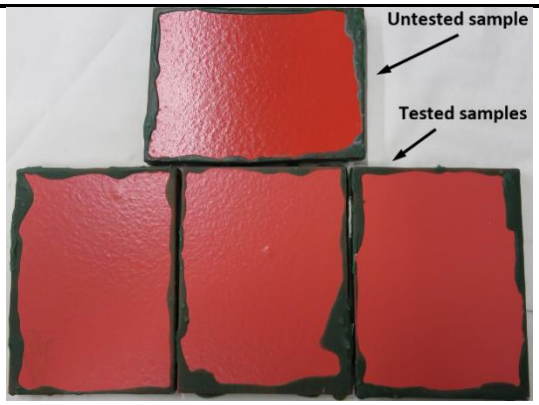	

Fig. 5.5.6 Visual appearance of the coatings surface with and without incision after 1440 hours of exposure to salt spray, according to the ISO 9227 standard

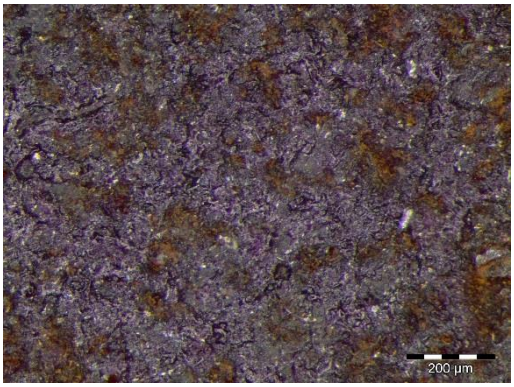

Fig. 5.5.7 Surface estate of C1 coating after 1440 hours of exposure to salt spray, showing ferric pits along the whole exposed surface

Table 5.5.5 Degradation observed in the three coatings samples with and without incision at different evaluation times during the exposure to salt spray chamber (ISO 9227 [26]) and adhesion test results of the samples with incision (ASTM D3359 [30])

Coat.	Incision	Sample No.	Exposure time (h)							Adhesion test
			504	672	840	1008	1178	1370	1440	
C1	No	1	~15%FC(*)	25%FC	25%FC	25%FC	25%FC	25%FC	25%FC	-
	No	2	~5%FC	5%FC	5%FC	5%FC	5-10%FC	5-10%FC	5-10%FC	-
	No	3	15-20%FC	25%FC	25%FC	25%FC	25-30%FC	~30%FC	~30%FC	-
	No	4	15%	20%	~20%	~20%	~30%	~30%	~30%	
	No	5	Isolated pits	<5%	<5%	<5%	<5%	<5%	<5%	
	No	6	10-15%	15-20%	20-25%	20-25%	20-25%	20-25%	20-25%	
C2	No	1	Unaltered	WS(*) P(*)	WS P	WS P	<5%WS	<5%WS	5-10%WS	-
	No	2	Unaltered	Unaltered	Unaltered	WS P	<5%WS	<5%WS	5%WS	-
	No	3	Unaltered	WS P	WS P	WS P	<5%WS	<5%WS	5-10%WS	-
	Yes	4	WS Np(*)	WS Np	WS Np	WS Np	WS Np	WS Np	WS Np	5A
	Yes	5	WS Np	WS Np	WS Np	WS Np	WS Np	WS Np	WS Np	4A
	Yes	6	WS Np	WS Np	WS Np	WS Np	WS Np	WS Np	WS Np	5A
C3	No	1	Unaltered	Unaltered	1 blister	1 blister	1 blister	1 blister	1 blister	-
	No	2	Unaltered	Unaltered	1 blister	1 blister	1 blister	1 blister	1 blister	-
	No	3	Unaltered	Unaltered	Unaltered	Unaltered	Unaltered	Unaltered	Unaltered	-
	Yes	4	0.4 mm PFC(*)	0.6 mm PFC	0.6 mm PFC	0.8 mm PFC	0.8 mm PFC	2 mm PFC	2 mm PFC	4A
	Yes	5	0.5 mm PFC	0.8 mm PFC	0.8 mm PFC	0.8 mm PFC	0.8 mm PFC	1.2 mm PFC	1.2 mm PFC	5A
	Yes	6	0.5 mm PFC	0.9 mm PFC	0.9 mm PFC	1 mm PFC	1 mm PFC	2.6 mm PFC +1 blister	2.6 mm PFC +1 blister	5A

(*) FC=Ferric corrosion; WS= White salts; P= Pits; Np=No progression; PFC=progress of ferric corrosion

In the case of C2 coating, the presence of white salts was detected after 672 hours in the chamber. These salts were observed in the form of small pits, which increased in size with exposure time. The surface percentage covered by white salts was of 5% after 1178 hours and increased reaching the 5-10 % at the end of the test. The samples of C2 coating with incision did not present ferric corrosion in either evaluation. White salts were observed from the first evaluation at 504 hours. The adhesion test results of the samples with incision was of 5A grade for two of the three samples, corresponding to the higher grade of the scale, with no detachment of the coating. The third sample was classified as 4A, since a small trace of the coating was removed with the adhesive tape.

C3 coating remained unaltered for 840 hours, when the presence of one blister was detected in two of the three samples without incision, but the apparition of new blisters or other defects was not observed in the following evaluations. The third sample remained unaffected until the end of the test. The samples with incision showed the progression of ferric corrosion from the first evaluation at 504 hours. Ferric corrosion spread with exposure time, exceeding the 2 mm in two of the three samples after 1370 hours. Furthermore, a blister was detected in one of these samples. The adhesion results were 5A grade for two of the samples, and 4A for the third one.

Considering the high amount of ferric corrosion in C1 coating, and the presence of a blister in C3 coating, the failure of these two coatings was estimated at 504 and 672 hours, respectively, so they were classified as C4(Medium)/C5-M(Low) category (ISO 12944-6). C2 coating, however, overcame the 1440 hours of exposure to salt spray with no ferric corrosion presence, and it was classified as C5-M(High) category (ISO 12944-6) (Table 5.5.7).

5.5.3.4 Combined-aging test (NORSOK M-501, ISO 12944-9)

In the combined-aging test, the coatings were exposed to different atmospheres, so as to reproduce climatic conditions. The samples were subjected to UV radiation and water condensation, salt spray, and low temperature. The visual appearance of the coatings at the end of the test is depicted in Fig. 5.5.8, and the degradation in terms of ferric corrosion coverage of the samples and blistering are summarized in Table 5.5.6.

Ferric corrosion was observed in coating C1 samples from the end of the first exposure to salt spray, covering a 1% of the exposed surface. This corrosion appeared close to edges of the samples, as a consequence of cavitation effects under the insulating wax employed. The samples lost their initial brightness, as a consequence of the degradation and elimination of the organic sealant. Ferric corrosion increased during the second test cycle, and the samples acquired a more reddish tone in the entire surface. The tonality change undergone by the coating was observed to be the consequence of the presence of ferric pits distributed along the exposed surface of the samples (Fig. 5.5.9).

In the case of C2 coating, oxides coming from metallic impurities were observed, similarly to the previous tests. Some white salts resulting from aluminum oxidation were detected in one of the samples during the second cycle, but no more changes were observed in any sample during the rest of the exposure. The color and appearance of the samples did not change during the test, and ferric corrosion or other defects were not detected.

C3 coating showed discoloration and brightness loss from the first exposure to UV radiation, especially in the center of the samples. The color change was more noticeable with increasing exposure, but no other defects such as blisters or ferric corrosion were observed in any sample.

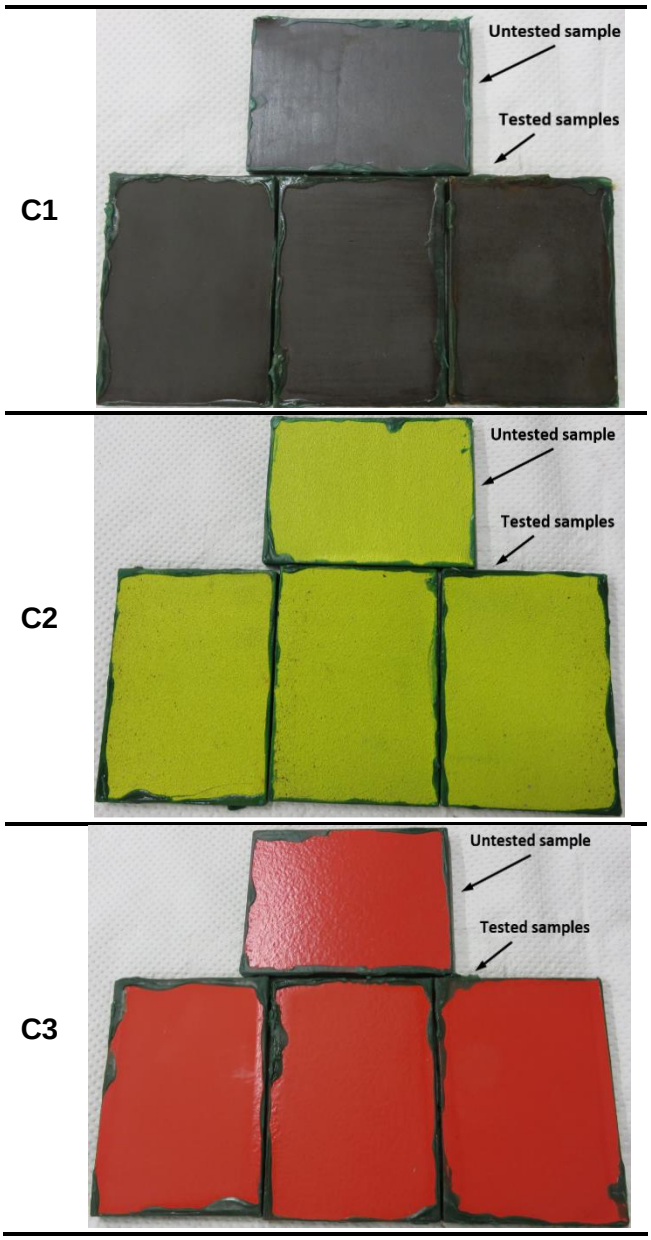

Fig. 5.5.8 Visual appearance of the coatings surface after 720 hours of exposure to combined aging according to the ISO 20340 and NORSOK M-501 standards

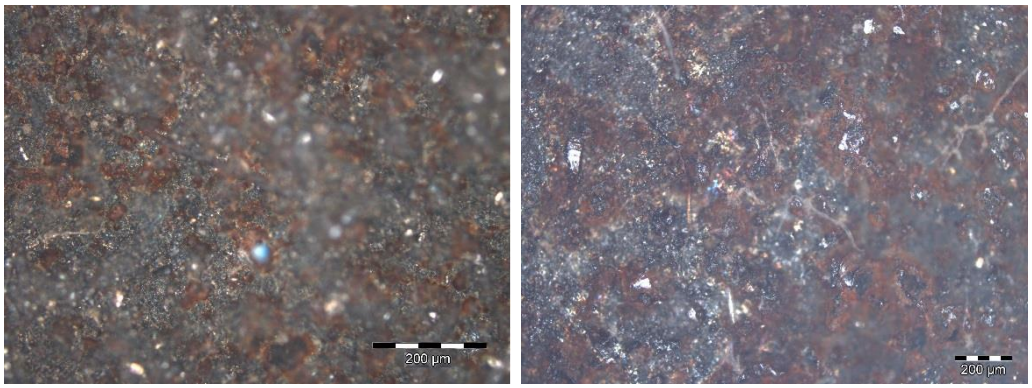

Fig. 5.5.9 Surface estate of C1 coating after 720 hours of exposure to combined aging, showing ferric pits along the whole exposed surface

Considering the significant number of ferric corrosion pits present in the surface of the samples, C1 coating did not pass the combined aging test. On the other hand, C2 and C3 coatings passed the test, showing just discoloration and brightness loss in the case

of C3 coating, which does not compromise the protective performance of the coating (Table 5.5.6).

Table 5.5.6 Summary of the oxidation and blistering grade of the coatings after the combined aging test in accordance with the ISO 12944-9[20] and NORSOK M-501[18] standards

Coating		Oxidation grade	Blistering grade
C1	Sample 1	16%	0%
	Sample 2	4%	0%
	Sample 3	12%	0%
C2	Sample 1	2% (Inclusions)	0%
	Sample 2	2% (Inclusions)	0%
	Sample 3	3% (Inclusions)	0%
C3	Sample 1	0%	0%
	Sample 2	0%	0%
	Sample 3	0%	0%

Table 5.5.7 Summary of the corrosivity categories of the ISO 12944-6[17] standard obtained for the coatings in the different corrosion-aging tests performed

Test/Standard	Type	Coating Category (ISO 12944-6)		
		C1	C2	C3
Immersion ISO 2812	-	Im2(High)	Im2(High)	No pass (Blistering)
Condensation ISO 6270	CH	C5-M(High)	C5-M(High)	C4(High)/C5-M(Medium)
	AHT	C5-M(High)	C5-M(High)	C5-M(High)
	AT	C5-M(High)	C5-M(High)	C5-M(High)
Salt spray ISO 9227	-	C4(Medium)/C5-M(Low)	C5-M(High)	C4(Medium)/C5-M(Low)
Combined aging ISO 12944-9 NORSOK M-501	-	Not passed	Passed	Passed

5.5.4 Conclusions

In the present work, the effectiveness of three coatings for the corrosion protection of offshore structural steel has been evaluated, according to the ISO 12944 and NORSOK M-501 standards. The corrosivity category of the coatings was determined for each aging test condition (ISO 12944). The conclusions of this work were the following:

- From the immersion tests (ISO 2812-2), the only coating that did not reach the 4000 hours of immersion was C3 coting. Blisters were detected to appear after 504 hours in one of the samples, and after 672 hours in the other two samples. C1 and C2 coatings were classified as IM2(High), overcoming the 4000 hours of exposure without the appearance of any defect.
- Regarding the water condensation tests (ISO 6270), C1 and C2 coatings obtained the C5-M(High) category in the three water atmospheres. C3, however, was classified as C5-M (High) in AHT and AT atmospheres, and as C4(High)/C5-M(Medium) due to the apparition of blisters after 614 hours of exposure.
- In the case of salt spray tests (ISO 9227), C2 was the only coating reaching the C5-M(High) category. C1 and C3 coatings were classified as C4(Medium)/C5-M(Low), after the presence of ferric corrosion (480 hours) in C1 coating and blisters (972 hours) in C3 coating were detected. The adherence measured for C2 and C3 coatings in the samples with incision was of 4A/5A, according to ASTM D3359

standard. The adherence of C1 coating was not measured, since the incision could not be made in the hard carbide layer.

- With respect to combined-aging tests (NORSOK M-501, ISO 12944), C1 coating did not pass the test since the surface of the samples was covered by a considerable amount of ferric corrosion at the end of the test. On the other hand, C2 and C3 coatings pass the test, showing just some discoloration and loss of brightness, maintaining the protective properties.
- Finally, the only coating that reached the higher category and overtook all the test atmospheres was C2 coating.

5.5.5 Acknowledgments

This work was performed with the support of the EMAITEK Initiative financed by the Basque Country. Authors would also like to acknowledge the Education, Linguistic Politics and Culture Department of the Basque Government for its support through the grant "*Programa Predoctoral de Formación de Personal Investigador No Doctor (PRE_2017_2_0088)*" awarded to the first author.

5.5.6 References

[1] M.R. Dhanak, N.I. Xiros (Eds.). *Springer Handbook of Ocean Engineering*. Springer (2016) ISBN: 978-319-16648-3

[2] R. Winston Revie, Hebert H. Uhlig. *Corrosion and Corrosion Control. An Introduction to Corrosion Science and Engineering (4th edition)*. Wiley-Interscience (2008) ISBN: 978-0-471-73279-2

[3] R. Baboian (Ed.). *ASTM corrosion tests and standards. Application and Interpretation (2nd edition)*. ASTM International (2006) ISBN: 0-8031-2098-2

[4] ASM Handbook. *Volume 13. Corrosion*. ASM International (1987) ISBN: 0-87170-007-7

[5] R.E. Melchers, T. Moan, Z. Gao. *Corrosion of working chains continuously immersed in seawater*. Journal of Marine Science and Technology (2007) 12:102-110

[6] A.W. Momber, P. Plagemann, V. Stenzel. *Performance and integrity of protective coating system for offshore wind power structures after three years under offshore site conditions*. Renewable Energy 74 (2015) 606-617

[7] A. López, R. Bayón, F. Pagano, A. Igartua, A. Arredondo, J.L. Arana, J.J. González. *Tribocorrosion behaviour of mooring high strength low alloy steels in synthetic seawater*. Wear 338-339 (2015) 1-10

[8] A. López-Ortega, R. Bayón, J.L. Arana, J.L. Arana, A. Arredondo, A. Igartua. *Influence of temperature on the corrosion and tribocorrosion behavior of High-Strength Low-Alloy steels used in offshore applications*. Tribology International 121 (2018) 341-352

[9] D. Santos, C. Brites, M.R. Costa, M.T. Santos. *Performance of Paint systems with polyurethane topcoats, proposed for atmospheres with very high corrosivity category*. Progress in Organic Coatings 54 (2005) 344-352

[10] ASM Handbook. *Volume 13. Corrosion*. ASM International (1987) ISBN: 0-87170-007-7

[11] M. Kutz (Ed.). *Handbook of environmental degradation of materials (2nd edition)*. Elsevier (2012) ISBN: 978-1-4377-3455-3

[12] R. Baboian (Ed.). *NACE Corrosion Engineer's Reference Book (3rd edition).* NACE International (2002) ISBN: 978-1-57590-127-5

[13] M. Lannuzzi, A. Barnoush, R. Johnsen. *Materials and corrosion trends in offshore and subsea oil and gas production*. NPJ Materials Degradation (2017) 2

[14] Y. Weng, H. Dong, Y. Gan (Eds.). *Advanced Steels. The Recent Scenario in Steel Science and Technology*. Springer (2011) ISBN: 978-3-642-17664-7

[15] A.W. Momber, P. Plagemann, V. Stenzel. *Performance and integrity of protective coating system for offshore wind power structures after three years under offshore site conditions*. Renewable Energy 74 (2015) 606-617

[16] P. Ault. *The use of coatings for corrosion control on offshore oil structures*. Journal of Protective Coatings and linings 23 (2006) 42-47

[17] ISO 12944:1-9. *Paints and varnishes. Corrosion protection of steel structures by protective paint systems*. November 2017-February 2018
[18] NORSOK M-501. *Surface preparation and protective coating*. Sixth edition, February 2012
[19] ISO 9223. *Corrosion of metals and alloys. Corrosivity of atmospheres. Classification, determination and estimation*. Second edition, February 2012
[20] ISO 12944-9. *Paints and varnishes. Corrosion protection of steel structures by protective paint systems. Part 9: Protective Paint systems and laboratory performance test methods for offshore and related structures*. First edition, January 2018
[21] K. Mühlberg. *Corrosion Protection of Offshore Wind Turbines. A Challenge for the Steel Builder and Paint Applicator*. Hempel Protective. Published in JPCL (2010)
[22] A. López-Ortega, J.L. Arana, R. Bayón. *Evaluation of protective coatings for offshore applications. Corrosion and tribocorrosion behaviour in synthetic seawater*. Surface & Coatings Technology 349 (2018) 1083-1097
[23] Offshore Standard DNVGL-OS E302, Det Norske Veritas, Offshore Mooring Chains, July 2018
[24] ISO 2812-2. *Paints and varnishes. Determination of resistance to liquids*. Second edition, January 2007
[25] ISO 6270. *Paints and varnishes. Determination of resistance to humidity.* Second edition, November 2017
[26] ISO 9227. *Corrosion tests in artificial atmospheres. Salt spray test*. Fourth edition, March 2017
[27] ISO 16474-3. *Paints and varnishes. Methods of exposure to laboratory light sources. Fluorescence UV lamps*. September 2014
[28] ISO 4628 1-5. *Paints and Varnishes. Evaluation of degradation of coatings. Designation of quantity and size of defects, and of density of uniform changes in appearance*. Forth edition, 2016
[29] ISO 17872. *Paints and Varnishes. Guidelines for the introduction of scribe marks through coatings on metallic panels for corrosion testing*. First edition, 2007
[30] ASTM D3359-17. *Standard Test Methods for Rating Adhesion by Tape Test*. ASTM International, West Conshohocken, PA, 2017

Contribution 6

Corrosion, wear and tribocorrosion behavior of a Thermally Sprayed Aluminum coating modified by Plasma Electrolytic Oxidation Technique for offshore submerged components protection

Corrosion Science 143 (2018) 258-280

Contribution 6: Corrosion Science 143 (2018) 258-280

5.6. CORROSION, WEAR AND TRIBOCORROSION PERFORMANCE OF A THERMALLY SPRAYED ALUMINUM COATING MODIFIED BY PLASMA ELECTROLYTIC OXIDATION TECHNIQUE FOR OFFSHORE SUBMERGED COMPONENTS PROTECTION

A. López-Ortega[a], J.L. Arana[b], E. Rodriguez, R. Bayón[a]

[a] *IK4-TEKNIKER, Eibar, Spain*
[b]*Department of Metallurgical and Materials Engineering, University of the Basque Country, Spain*
[c]*Vicinay Marine Innovación, Spain*

ABSTRACT

Thermally Sprayed Aluminum (TSA) coatings have been widely employed to protect steel components from corrosion in the marine environment. However, TSA is highly damaged in transport operations, due to the low wear resistance of aluminum, leading to a rapid coating deterioration during final service. In this work, the TSA properties have been improved by Plasma Electrolytic Oxidation (PEO) technique. The response of the newly generated TSA/PEO duplex system was investigated by means of sliding wear tests, electrochemical corrosion tests, and tribocorrosion tests in synthetic seawater. The study was completed with several characterization techniques, including SEM and confocal microscopy, and X-ray diffractometry.

Keywords: *Offshore; Corrosion; Tribocorrosion; Coatings; Thermally Sprayed Aluminum; Plasma Electrolytic Oxidation*

5.6.1 Introduction

Marine environment is a very aggressive working atmosphere, that comprises several phenomena that can accelerate the degradation of structural materials reducing their useful life. The exposition to ultraviolet radiation, chloride-rich salty environment, frequent wet-dry cycles, high humidity, low temperature, and the presence of marine bacteria and microorganisms are some examples. Corrosion is one of the phenomena that worst affect the deterioration of materials in offshore applications. The high salinity and low electrical resistivity of seawater make this environment especially aggressive [1]. In certain applications, materials are also subjected to mechanical stresses that can lead to premature failure of components and structures. This is the case of Oil&Gas platforms, wind towers, renewable energy extraction systems, and mooring lines, inter alia. Abrasion, impact, and wear generated by waves, wind, ocean currents, floating objects, sand, and heavy waves are the major stress types [2]. Mooring lines, for instance, are subjected to severe wear degradation in the connection between links and accessories, as a consequence of the relative movement generated between components by waves, wind, and ocean currents [3-7]. Offshore structures, as well as mooring lines, are also exposed to abrasion and impact in the splash zone generated by heavy waves, floating wastes, sand particles, and other contaminants present in seawater [2,8,9]. Corrosion is also more severe in the splash zone, where the concentration of oxygen is higher [3,9,10]. Wear and corrosion are two processes that lead to an irreversible degradation, and whenever they take place simultaneously, the process is known as tribocorrosion. Tribocorrosion involves a synergism between wear

and corrosion, since the total material loss when the two processes occur simultaneously is greater than when they act alone [6,7,11-13].

Steel is the most employed structural material in offshore applications, usually mild or low-alloyed, due to their good properties and relatively low cost compared to high-alloyed steels [8]. High-Strength Low-Alloyed (HSLA) steels, for instance, are widely used for their high mechanical properties, with yield strengths in the range of 460-960 MPa, and relatively low weight [14,15]. This kind of steels is used in jack-ups and legs, pipelines, tethering attachments for floating structures in Tension Leg Platforms (TLPs), mooring lines of semi-submersible structures, etc. [14,16,17]. However, due to their low alloying content, HSLA steels possess low corrosion resistance in seawater, with corrosion rates around 250 microns per year [9,18].

In order to save the elevate maintenance and replacement costs of damaged elements, and avoid premature failure of infrastructures or components, protective coatings have been widely used to protect steel in the marine environment. The selection of the appropriate coating strongly depends on the exposure zone, since the requirements and desirable properties of the coating vary with the degradation phenomena taking place in each exposure location [19]. In splash zone, for instance, the coating should provide the steel structures and components with both corrosion and wear resistance, whereas, in the atmospheric zone, the coating should also be resistant to UV radiation and icing conditions. Thermally Sprayed Aluminum (TSA) coatings have been widely used for the protection of submerged components [13,19,20], providing effective service life for 30 years in different exposure zones [10,13,21]. The aluminum deposited on steel substrate acts as a sacrificial anode, providing the steel with an additional cathodic protection. However, the poor wear resistance of the aluminum can be a major drawback [22]. The coatings in structural components and other elements are not applied in situ, due to the complexity of coating technologies and equipment dimensions. Some studies have revealed that the 45% of the damage in coatings by mechanical stresses is mainly generated during transport and erection operations [2]. Hence, if the TSA coating is damaged or partially removed before installed in the final application, the defects generated in the coating can accelerate the further dissolution of the aluminum by galvanic corrosion mechanism. On the other hand, in certain applications such as mooring lines, wear between links also leads to fast deterioration of the aluminum in working conditions. Therefore, the improvement of the wear resistance of the sprayed layer is a major concern to assure the durability of the coating.

In this work, a TSA coating has been treated by Plasma Electrolytic Oxidation (PEO) technique in order to provide the coating with an enhanced wear resistance. Plasma Electrolytic Oxidation, also named Micro Arc Oxidation (MAO) technique, is an electrochemical process of oxidation that allows the generation of ceramic oxide coatings with improved hardness, adhesion, wear and corrosion resistance [23-32]. The process involves an anodic polarization of the sample to high voltages, exceeding the dielectric breakdown voltage, so as to generate discrete short-lived plasma micro-discharges in the surface [23,24,26,29,32-34]. PEO technique is based on the conventional anodizing, with similar configuration, but higher voltages (300-600 V) and current densities (100-500 mA/cm2) are employed. The high voltages allow the generation of plasma micro-discharges, facilitating the diffusion of oxygen ions through the discharge channels present in the oxide film, to react with the substrate forming the anodic film [23,24,28,31-33,35]. Due to the rapid development and extinction of the discharges, within 10^{-4} and 10^{-5} seconds, the substrate is not subjected to thermal damage. The characteristics of PEO-generated coatings are superior to those of conventional and hard anodizing coatings, in terms of wear and corrosion resistance, and higher thickness [24]. The better

properties are associated with the presence of high-temperature phases, e.g., Al_2O_3, generated during PEO process by rapid melting by micro-discharges and cooling in contact with refrigerated electrolyte [29,32,33,35]. Another difference between the two processes, is the employment of environmentally friendly alkaline electrolytes in PEO, making it a more sustainable process, which has grown the interest in several industrial sectors to replace conventional anodizing [24-27,36]. This technique has widely been used for coating light metals such as aluminum, magnesium, titanium, and their alloys for a large number of applications, i.e., aerospace, automobile, biomedical, etc. [24,25,27,35]. Some researchers have developed ceramic PEO coatings on steel by using a pretreatment of the surface, such as hot-dipping in aluminum [37,38]. W. Gu, et al. prepared PEO coatings on arc-sprayed aluminum, and evaluated the corrosion response of the generated duplex-system [39]. While the corrosion behavior of PEO coatings generated in aluminum has been widely investigated [23,31-34], little investigation has been done on the tribocorrosion response of aluminum PEO coatings. Furthermore, the tribocorrosion response of PEO generated coatings on TSA has not been investigated yet.

The aim of this work is to enhance the wear and tribocorrosion performance of a TSA coating used in submerged component protection, modifying the aluminum layer by PEO technique. These components are exposed to wear conditions during transport and erection, and corrosion and tribocorrosion conditions during their service life while immersed in the ocean. Therefore, the corrosion, wear and tribocorrosion response of the generated duplex coating was investigated. For this aim, electrochemical corrosion tests consisting of electrochemical impedance spectroscopy and potentiodynamic polarization measurements were performed in synthetic seawater (ASTM D1141). The wear resistance was evaluated by performing dry abrasion tests under ball-on-disc configuration in a unidirectional tribometer. Finally, the wear-corrosion (tribocorrosion) behavior was studied using the same tribometer and configuration with the samples immersed in synthetic seawater, monitoring both electrochemical and tribological responses. The results of the developed duplex coating were compared with the as-sprayed coating and the steel substrate. The study was completed with several characterization techniques, including SEM and confocal microscopy, pull-off adhesion tests, hardness and roughness measurements, and X-ray diffractometry.

5.6.2 **Materials and methods**

5.6.2.1 Materials

In the present work, the response of a modified TSA coating by PEO technique was analyzed in terms of wear, corrosion, and tribocorrosion resistance. The selected coating system is used in the protection of offshore mooring line components, such as chain links and accessories. These elements are manufactured of High-Strength Low-Alloy steels, which are classified into five grades depending on their ultimate strength: R3, R3S, R4, R4S and R5[40]. In this study, R4 steel grade samples were used as substrates.

Steel panels were extracted from real chain components and coated by arc Thermal Spray technique with an aluminum layer. Prior to the spraying process, the panels were sand-blasted to remove any dust or impurities, and to provide the substrate with proper roughness to increase the coating bonding strength to the substrate [41,42]. The aluminum was deposited by arc spray method using a Margarido Mod-M45 equipment, using Al1050 wires of 1.60 mm in diameter (Oerlikon Metco). The optimized spraying parameters are listed in Table 5.6.1. With these process parameters, coating layers of 250-300 µm were reached.

Table 5.6.1 Deposition parameters of the arc spraying process

Air pressure	Spraying Voltage	Spraying Current	Spraying distance	Wire feed rate	Deposition rate
6-7 bar	30-32 V	90-150 A	30 cm	12.8 m/min	140 g/min

5.6.2.2 Plasma electrolytic oxidation

After the spraying process, the samples were subjected to a Plasma Electrolytic Oxidation (PEO) process. Prior to the PEO process, the TSA-coated panels were ground with 400 grit polishing paper to ensure reproducible initial surface conditions in all the samples. Then, the panels were cleaned in an ultrasonic bath with ether and acetone, rinsed with alcohol and dried with air. The treatments were performed in a commercial KERONITE KT 20-50 (20KW AC power supply) equipment. The electrolyte used was an aqueous standard aluminum electrolyte provided by KERONITE with a pH of around 2, and a conductivity of 6.82 mS/cm, which composition is confidential. After several trials, the more suitable process parameters to obtain thick oxide layers with low porosity in the TSA/PEO interface were selected: 25 A/dm^2 for 135 minutes. In this work, the results obtained in the optimization of process parameters are not presented. The test equipment is composed of a water-cooled bath with a stirring system that ensured the electrolyte temperature to be below 20 ºC in all the processes. A stainless steel mesh was used as the cathode, whereas the TSA-coated steel samples were connected as the anodes. The total area of the samples exposed in each process was of 69.12 cm^2. After the PEO process, the samples were cleaned ultrasonically with ether and acetone, rinse with alcohol and dried with compressed air.

5.6.2.3 Coatings characterization

The roughness of the as-sprayed and PEO-treated coatings was determined in a Perthometer M2 (Mar GmBH) profilometer (DIN EN-ISO 4288). The thickness of the coatings was measured from the cross-section profile in an Olympus GX71 optical microscope (UNE-EN ISO 1463). The hardness was assessed in a Future-Tech FM-700 microhardness tester, equipped with Vickers indentation equipment (UNE-EN ISO 6507-1). The measurements were performed using a Vickers diamond pyramid indenter, with an indentation time of 15 s, under a load of 100g for the R4 steel substrate and PEO layer, and under 25 g for the TSA coating.

The morphology of the coatings was analyzed by Field Emission Scanning Electron Microscope (FE-SEM) equipped with Energy Dispersive X-ray Spectrometer (EDS), from OXFORD INCA Synergy. The porosity degree was obtained from the SEM cross-sectional images by image analysis software (AnalySIS pro). The chemical composition of the samples was assessed by EDS. The phase structure of the PEO coatings was defined by X-ray diffraction (XRD) analysis in a D8 Advance diffractometer from Bruker, using a Cr-$K_{\alpha 1}$ radiation source operating at 40 mA and 40 kV, in the 2θ=5-160º range with steps of 0.06º and time step of 0.5 s. The results were analyzed with a DIFRAC.EVA software from Bruker.

Finally, the adhesion of the TSA and the TSA/PEO coating systems was analyzed by a pull-off adhesion test (PosiTest AT-A), with dollies of 20 mm in diameter at a tensile rate of 0.7 MPa/s (ISO 4624). The adhesive used in the tests was a methyl-based LOCTITE 496. Four repetitions were performed for each coating system, and the mean value was obtained. The fracture type was analyzed according to ISO 4624.

5.6.2.4 Electrochemical corrosion tests

For the electrochemical corrosion tests, a three-electrode set-up was used, with the test sample as working electrode, a platinum wire as counterelectrode, and a commercial Ag/AgCl (KCl 3M) as reference electrode (+207 mV/SHE). The electrodes were connected to an Autolab-Metrohm PGSTAT30 potentiostat equipped with FRA32M and EDC modules. Synthetic seawater with heavy metals (ASTM D 1141) was used as the electrolyte. 50 ml of this solution was employed in each test. The tests were performed at room temperature (23±2 ºC) and aerated conditions, and the exposed surface of all the samples was of 2.31 cm^2. The results of the coatings were compared with the un-coated steel samples, which were mirror polished (Ra<0.05 µm) before testing. All the tests were performed by triplicate to ensure the reproducibility of the results.

The corrosion tests consisted of two test series: potentiodynamic Polarization (PDP) and Electrochemical Impedance Spectroscopy (EIS) measurements. PDP tests were performed after one hour of immersion, once the potential of the samples was stabilized. The potential ranged from -400 mV to +1600 mV with respect to the open circuit potential (OCP vs. Ag/AgCl) of each sample, at a sweep rate of 0.166 mV/s. In the second test series, the evolution of coatings performance with immersion time was assessed by performing EIS measurements. The impedance data was registered after 24 hours, and weekly until 1512 hours (9 weeks) of immersion were completed. The measurements were registered under a sinusoidal AC perturbation of ±10 mV amplitude, at a frequency range from 10 kHz to 1 mHz, with 10 points per frequency decade. At the end of the tests, the surface of the samples was analyzed by scanning electron microscopy (FE-SEM / EDS).

5.6.2.5 Abrasion and tribocorrosion tests

Abrasion tests were performed in a unidirectional MicroTest MT/10/SCM tribometer under ball-on-disc configuration. In these tests, sliding represents the wear conditions between components in dry conditions, as in the case of transport and erection in the final location. The contact conditions were calculated using the Hertzian Contact Theory [43], considering the real contact pressure between links in real applications, as already performed in previous works [6,7,19]. The normal load was of 5 N, corresponding to an average Hertzian pressure of 930 MPa with a contact radius of 50.5 µm. An alumina ball of 10 mm in diameter (G28) was used as the countermaterial. The ball described a wear track of 10 mm in diameter at a rotation speed of 100 rpm. The duration of the sliding abrasion test was of 40 minutes, during which the coefficient of friction (COF) was registered.

The tribocorrosion experiments were conducted in the same unidirectional tribometer used for abrasion tests. The specimens were fixed in a three-electrode cell placed in the rotatory plate of the tribometer and connected to an Autolab-Metrohm PGSTAT30 potentiostat. This setup has been employed in previous studies and can be found elsewhere [6,7,19]. This configuration allows the simultaneous control of both electrochemical and mechanical parameters during the tests. A commercial Ag/AgCl (KCl 3M), a platinum wire, and the test samples were connected as the reference electrode, the counterelectrode, and the working electrode, respectively. For each test, 150 ml of synthetic seawater (ASTM D 1141) was employed. In these tests, sliding represents the wear conditions between chain links and accessories with relative movement to one another generated by wind, waves, ocean currents, and so on. The tribological conditions were the same as in the above-mentioned abrasion tests, with an alumina ball as countermaterial. The tests consisted of monitoring the Open Circuit Potential (OCP) during the first hour of immersion, followed by an EIS measurement.

Then, a sliding wear test of 4000 cycles was performed during which the OCP and the COF were simultaneously recorded. After the wear process, the potential was stabilized for fifteen minutes, and a second EIS was measured. Both EIS measurements were obtained under a sinusoidal AC perturbation of ±10 mV amplitude, at a frequency range from 10 kHz to 10 mHz, with 10 points per frequency decade. The tests were made at room temperature (23±2 ºC) and aerated conditions. The exposed surface of the samples was of 2.31 cm^2. The results of the coatings were compared with mirror polished steel specimens (Ra<0.05 µm). Three replicates of each material were tested to ensure the reproducibility of the results.

5.6.2.6 Morphology of the worn surface and material loss quantification

After the abrasion and tribocorrosion tests, the surface morphology of all the tested specimens was examined by optical microscopy and scanning electron microscopy (FE-SEM / EDS), to identify the wear mechanism and measure the dimensions of the wear tracks generated. The cross-section profile of the wear tracks was obtained with a confocal microscope (Sensofar S Neox). The material loss in the wear track was quantified by calculating the wear track volume from the cross-section profiles, as described elsewhere [6,11,19,44]. The contact area of the alumina ball was also examined by optical microscopy (Olympus GX71).

5.6.3 Results and discussion

5.6.3.1 Coatings characterization

Fig. 5.6.1 shows the cross-section morphologies of the as-sprayed and PEO-modified coatings. In both cases, the TSA coating is well-bonded to the substrate, since no distinctive irregularity is detected in the coating/steel interface. The PEO layer generated above the sprayed coating also shows good adhesion to the aluminum, without any discontinuity in the junction of the two coatings.

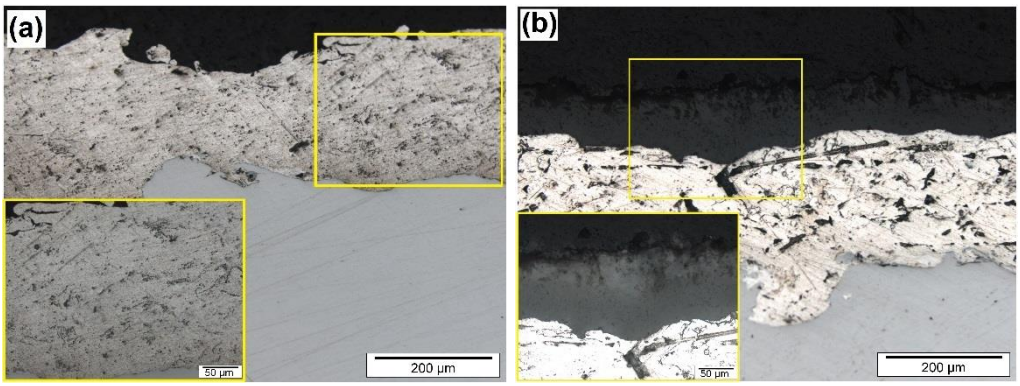

Fig. 5.6.1 Transversal micrographs of the (a) TSA and (b) TSA/PEO coatings applied on the R4 steel grade substrate

The roughness, thickness, and hardness measurements of both coatings are compiled in Table 5.6.2. In the duplex TSA/PEO system, the thickness of the aluminum layer prior to the PEO process was of 270±16 µm, and it was slightly reduced during the oxidation process to values close to 233 µm. The oxide layer obtained by PEO technique was of 103 µm. The hardness of the TSA layer was not affected by the plasma oxidation process, presenting values of around 45 HV in both specimens. The hardness of the oxide layer was considerably superior, with values of 25 times higher than those of the sprayed aluminum. The values obtained for both the TSA [45,46] and the PEO-generated aluminum oxide [28,31] are in accordance with that reported in the literature for this type

of coatings. The hardness of the substrate was also measured, giving values of 264.80±14.08 (HV 0.1).

Table 5.6.2 Mean roughness, thickness, hardness, porosity, and pull-off adhesion values obtained for the TSA and TSA/PEO coatings

Coating		Porosity (%)	Thickness (µm)	Hardness (HV)	Roughness, Ra (µm)	Pull-off (MPa)
TSA		4.11±0.97	273.95±47.95	44.10±2.49	2.24±0.12	21.49±0.49
TSA/PEO	TSA	4.17±1.82	233.95±25.68	45.33±3.28	5.69±0.64	21.07±0.70
	Inner dense layer	1.29±0.76	103.68±8.14	1187.00±31.17		
	Intermediate layer	5.10±2.22				
	Outer porous layer	11.27±3.78				

The SEM images and the results of EDS analysis of the TSA are shown in Fig. 5.6.2. The coating presents a typical morphology structure of a thermally sprayed coating, containing defects such as pores and cracks [47-51]. These defects are a consequence of the solidification of the sprayed material between successive splats, and to thermal stresses generated during the spray process [48,50,51]. The coating consists of a bright matrix with some dark voids. The EDS results indicate that the bright regions are mainly composed of aluminum. The dark regions corresponding to cracks and pores possess a higher oxygen content (52.86 wt% Al and 47.14 wt% O), corresponding to oxides coming from the in-flight particles oxidation during the spraying process [48,52,53]. The porosity of the TSA layer estimated from the SEM images was around 4.2%.

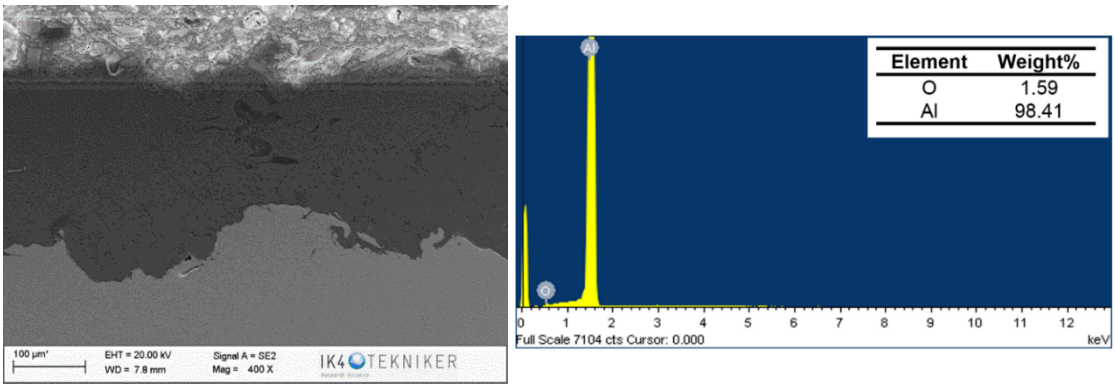

Fig. 5.6.2 Cross section SEM images and EDS analysis of TSA coating applied on the R4 steel grade

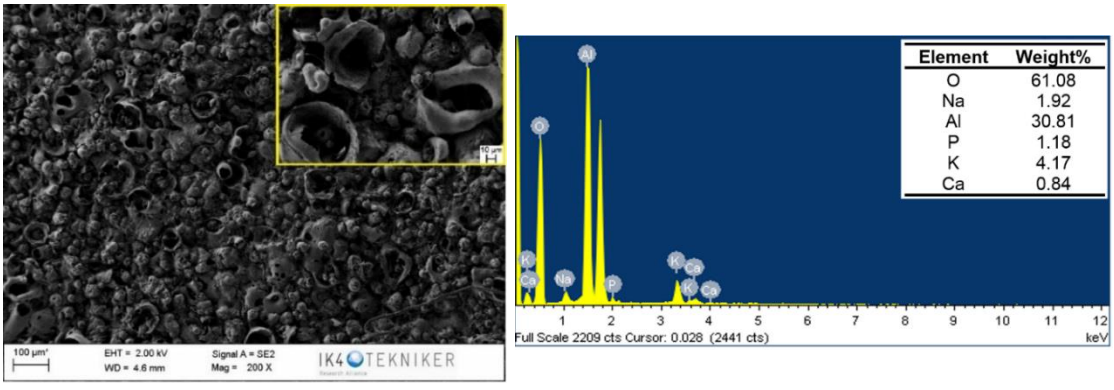

Fig. 5.6.3 SEM image showing the surface morphology of the PEO coating and EDS analysis obtained in the topmost surface

The SEM image in Fig. 5.6.3 shows the surface morphology of the PEO oxide layer generated on the TSA coating. The surface exhibits a typical PEO morphology, consisting of a large proportion of pores with high roughness, as a consequence of the gas evolution taking place in the molten oxide material during the process [23,25,30]. The air bubbles formed increase the turbulence in the electrolyte promoting the

homogeneous growth of the coating. The gas can be trapped into bubbles within the material, generating the characteristic porous morphology of PEO coatings. The high pressure in the trapped air generates the explosion of these bubbles, and the rapid cooling of the melted material in contact with the electrolyte results in a high roughness [28,30]. As observed in the cross-section images in Fig. 5.6.4, the PEO-generated oxide layer consists of three distinct regions characteristic of this kind of coatings [27,29-31,33]: a thin inner layer, an intermediate or functional layer, and an outer layer. The inner layer shows a dense appearance with low pore content. A greater pore content can be observed in the intermediate layer, while the outer layer presents a highly porous structure. The intermediate layer has been found to provide good mechanical properties against wear, and good corrosion protection, whereas the best corrosion performance is provided by the inner dense layer [27,29,33,35,36,]. In the intermediate layer, the pores are small with diameters no larger than 2 µm, and they are evenly distributed. The pores in the top layer are larger and randomly dispersed. The micropores present in the oxide layer are formed as a result of the plasma micro-discharges and the fast melting of the material in contact with the electrolyte, and the gas evolution in the plasma channels [34]. No columnar pores or cracks are observed across the different layers of the PEO coating. The thickness of each layer was measured, and the porosity percentage was estimated from the SEM images (Table 5.6.2). The inner layer was the thinner and denser layer, with 12.75±4.57 microns of thickness and a porosity of 1.3%. The intermediate layer thickness was of 47.75±5.32 microns, and its porosity of 5%. The outer layer was the thicker and the more porous layer, with 52.50±9.08 microns and 11% of porosity. The EDS spectra obtained on the topmost surface is presented in Fig. 5.6.3. The PEO layer is composed mainly of aluminum and oxygen. Some other elements such as sodium, phosphorous, potassium, and calcium coming from the electrolyte have also been detected in small percentages. The EDS analysis obtained in the cross-section of the PEO coating revealed the presence of these elements only in the outer layer, while the intermediate and inner layers were composed of aluminum and oxygen: 52.4 wt% Al and 47.59 wt% O for the inner layer, and 41.8 wt% Al and 58.20 wt% O for the intermediate one. Finally, the XRD spectrum showed that the PEO-generated aluminum oxide layer was mainly formed by α-Al_2O_3 and γ- Al_2O_3 (Fig. 5.6.5). The formation of these phases can be attributed to the high current densities at the vicinity of the micro-discharges sites, generating the rapid heating and cooling of the aluminum. The α-Al_2O_3 can be formed from γ- Al_2O_3 at high temperatures (1000-2000 ºC) [23,33]. The hard α-Al_2O_3 phase has been observed to be formed in intermediate layers and is responsible for the wear properties in PEO coatings [23,29,32,33,54].

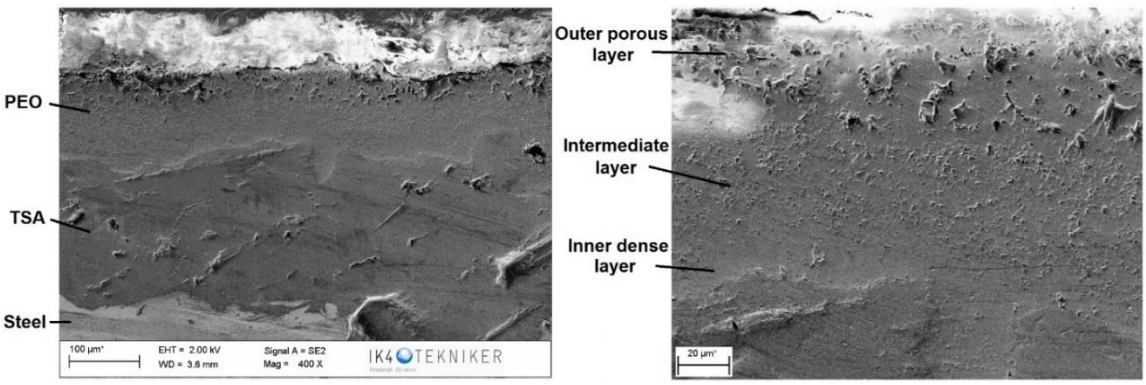

Fig. 5.6.4 Cross section SEM images of (left) the TSA/PEO coating system applied on the R4 steel grade and (right) the PEO layer in detail showing three distinct sub-layers

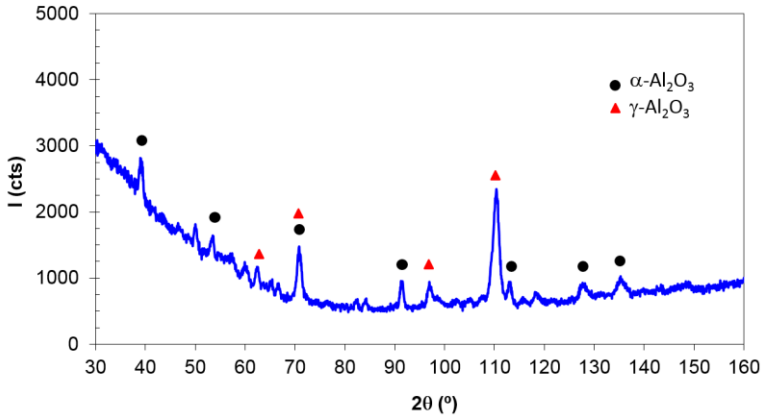

Fig. 5.6.5 XRD pattern of the PEO coating generated on the TSA

The pull-off adhesion test (ISO 4626) showed an adequate bonding strength of both the as-sprayed coating and the TSA/PEO duplex system, with values around 21 MPa (Table 5.6.2). According to the ISO 12944-9 [55] standard, the minimum pull-off test value for protective coatings in their initial performance, i.e., before any exposure to aggressive atmospheres, should be of 5 MPa for their use in splash and tidal zones (CX-offshore and Im4 categories [56]). Therefore, the results obtained for the coatings of this work exceed this value noticeably. Furthermore, the standard recommends a 0% adhesive failure between the substrate/metalized steel and the first coat, when the results are below 5 MPa. In this case, the fractures on the as-sprayed coating were a combination of adhesive fracture between the adhesive and the aluminum layer and adhesive between substrate and aluminum layer (Fig. 5.6.6a and b). On the other hand, the fracture in the TSA/PEO coating was cohesive within the oxide layer (Fig. 5.6.6c and d).

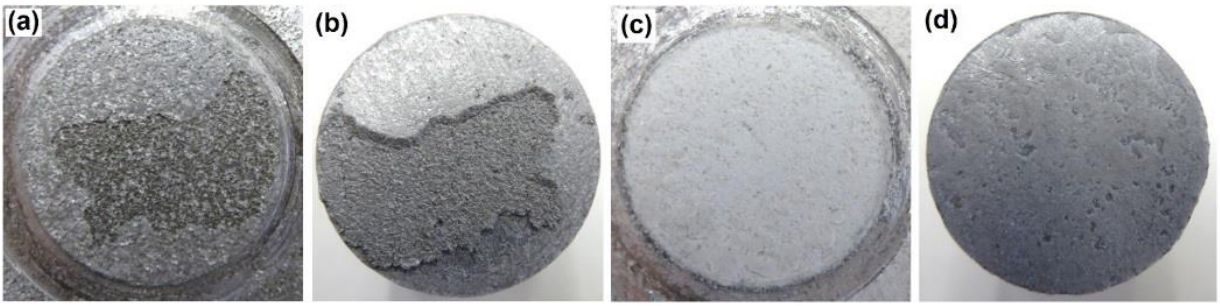

Fig. 5.6.6 Fracture surface of the coatings after pull-off adhesion test: TSA coated sample (a) and dolly (b), and TSA/PEO coated sample (c) and dolly (d)

5.6.3.2 Electrochemical corrosion tests

Fig. 5.6.7 shows the polarization curves obtained for the R4 steel grade and the two coating systems in synthetic seawater. The steel substrate shows a typical curve shape of an active material, characterized by a great activation stretch in the anodic branch and a lack of passive plateau [6,7,22,57]. There is a sharp increase in current values for small potential variations above the corrosion potential (E_{corr}). The curve of the aluminum shows a more negative corrosion potential close to -1 V, which is in accordance with the values reported in literature for aluminum in seawater [52,58-61]. In this case, four well-defined regions can be observed: the cathodic domain below E_{corr}, the cathodic-anodic transitions at potentials close to E_{corr}, a passive plateau (from -0.9 to -0.6 V), and a transpassive dissolution domain above -0.6 V. In the passive domain, the aluminum reacts with seawater to form a protective oxide layer that slows down corrosion processes and leads to constant corrosion currents, i.e. corrosion rates, in the whole domain. The corrosion current is limited to values of 0.2 µA/cm^2. In the transpassive domain, there is a sharp increase of the current density of almost two orders of

magnitude for small potential variations. This is attributed to the passive film breakdown leading to its transpassive dissolution, as well as water oxidation processes [62-64]. The breakdown of the passive layer is a consequence of the presence of aggressive ions in seawater, such as Cl^-. These ions can penetrate through the passive film due to their small size, generating the dissolution of the aluminum oxide and the localized corrosion of the bare aluminum beneath the passive film [22,31,65]. The current values at higher anodic potentials reach those of the substrate, suggesting that the fast dissolution of the aluminum leads to the exposition of the steel. Once the aluminum layer thickness is considerably reduced, the anodic polarization promotes the corrosion of the steel, and thus, the current values registered close to 0.3 A/cm^2 corresponds to the substrate corrosion. The curve registered for the TSA/PEO duplex system shows a corrosion potential between those of the uncoated steel and the as-sprayed coating. This sample presents lower currents in the whole anodic domain, and no sharp increase is observed but the current increases progressively with the potential increase. The currents registered at high anodic potentials are close to 0.13 µA/cm^2.

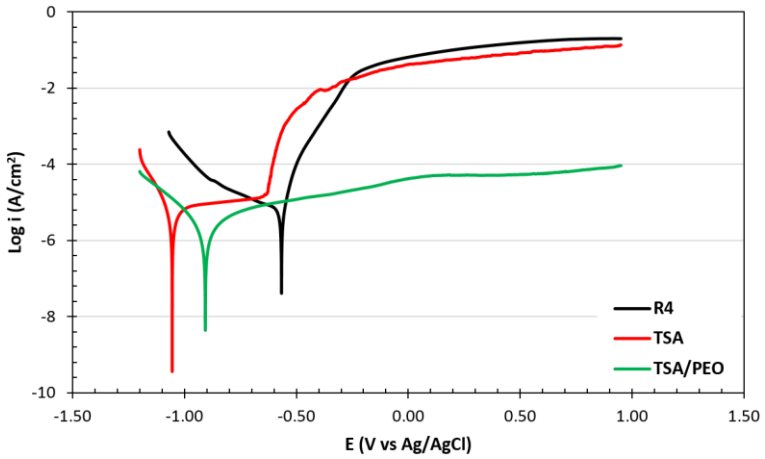

Fig. 5.6.7 Potentiodynamic curves obtained for the R4 steel grade, TSA, and TSA/PEO coating systems in synthetic seawater under a sweep rate of 0.166 mV/s

Table 5.6.3 Electrochemical data obtained from the potentiodynamic curve by standard Tafel extrapolation

Material	Electrochemical parameters			
	i_{corr} (µA/cm^2)	E_{corr} (V vs Ag/AgCl)	R_p (kΩ cm^2)	v_{corr} (mm/yr)
R4	27.02	-0.567	2.70	0.299
TSA	7.74	-1.056	5.06	0.085
TSA/PEO	4.55	-0.912	12.37	0.043

The electrochemical data obtained from the curves by standard Tafel polarization is collected in Table 5.6.3. From these values, it can be noticed that the corrosion current, corrosion resistance and corrosion rate obtained for the as-sprayed coating are not very far from those of the steel substrate, and being higher than those reported for bulk aluminum elsewhere[66]. This could be the consequence of the contribution of the steel across the cracks and defects of the aluminum layer, leading to higher aluminum dissolution through galvanic protection mechanism[47,52,66]. On the other hand, the TSA/PEO system exhibits lower corrosion currents, considerably higher corrosion resistance, and smaller corrosion rates. Therefore, the shift of corrosion potential in the noble direction of the PEO-modified TSA coating with respect to the as-sprayed coating, along with the better electrochemical data obtained from the curve, indicate that the PEO treatment improves the corrosion response of the sprayed aluminum coating in seawater. The better corrosion response of the duplex coating system can be attributed to the higher chemical stability of the PEO-generated thick oxide layer in seawater, due to its

ceramic nature, acting as an effective barrier to the underneath aluminum and steel substrate.

For the assessment of the corrosion performance of the coatings with prolonged exposition to seawater, EIS measurements were performed at different immersion times in synthetic seawater. The results obtained for the uncoated steel, the TSA coating, and the PEO-modified TSA coating are presented in Fig. 5.6.8, in the form of Nyquist and Bode plots. The corrosion degradation mechanism of the TSA and TSA/PEO coatings in synthetic seawater deduced from the impedance spectroscopy results, is schematized in Fig. 5.6.9.

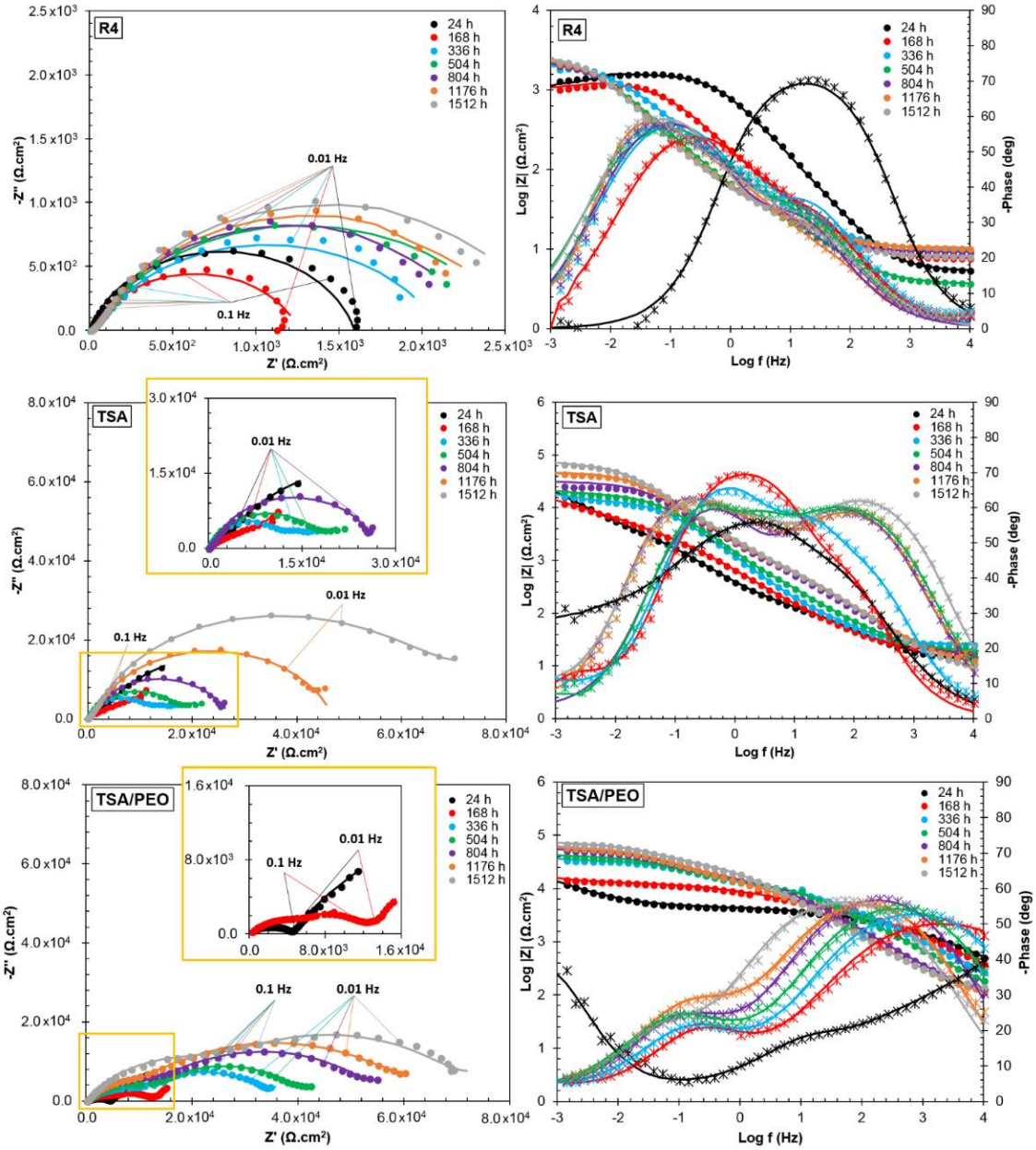

Fig. 5.6.8 Electrochemical Impedance Spectroscopy results obtained for the R4 steel, TSA, and TSA/PEO coating systems at different immersion times, where the solid lines represent the fitting curves obtained with the equivalent circuits

The diagrams of the uncoated steel show two capacitive loops in the Nyquist plot and two inflection points in the Bode plot. The big capacitive loop at medium-frequency (MF) range is physically related to the charge transfer process of the corrosion reaction taking place on the steel surface [67]. The second time constant at lower frequencies is related

to the corrosion product layer formed on the surface of the sample [68]. The phase angle values at high frequencies (HF) close to 0º is characteristic of purely resistive behavior [69,70]. In the first week of immersion, a decrease in the semicircle in the Nyquist plot and a reduction in the impedance modulus is observed, which is attributed to a reduction in the resistance of the steel. However, for larger immersion times the semicircle is enlarged, and the impedance modulus increases, indicating an enhancement in the corrosion resistance with immersion time [71]. The increase of the phase maximum at low frequencies (LF), its shifts to lower frequencies, and the form of the Nyquist diagram as an incomplete semicircle confirm the previous statement. These changes are related to the formation of a corrosion product layer on the surface, which shows a more capacitive response [67]. The increase in this layer thickness with immersion time leads to an increase in the corrosion resistance, as a consequence of the higher restriction of electrolyte access to the corroding surface with immersion time.

After 24 hours in seawater, the Nyquist plots of the TSA coating present two capacitive loops, and accordingly two inflection points in the Bode diagram. As a consequence of the non-homogeneous topography of the sprayed aluminum, which also contains pores, cracks, and other irregularities, the solution penetrates through the pores from the beginning of immersion, generating an increase in the exposed surface as it infiltrates through the defects (Stage 1 in Fig. 5.6.9). The depressed semicircle at middle-low frequencies is enlarged with immersion time, accordingly with the increase in the impedance modulus at LF, indicating an improvement in the corrosion response of the system with time. The phase maximum at MF increases from 58º at 24h to 70º after 168 hours of immersion, suggesting a more capacitive response as a consequence of the reactions taking place in the coating surface forming a thin oxide passive layer (Stage 2 in Fig. 5.6.9). The deviation of the phase maximum values from 90º indicate a non-ideal capacitor behavior. This dispersion can be attributed to inhomogeneities in the dielectric material, i.e., the passive layer, such as porosity, mass transport, and relaxation effects [72]. The presence of a second time constant is more evident above 336 hours, showing two-phase maximums in the medium-high and medium-low frequency ranges. The former is related to the oxide layer formed in the topmost surface of the coating, whereas the latter can be a consequence of the reactions taking place in the coating/substrate interface [53,61]. Due to inherent properties of the sprayed layer, with a considerable presence of pores and defects, the solution penetrates through these defects after hours of immersion. These defects form ion conducting paths across the coating, allowing aggressive species to reach the substrate surface. Since the steel is nobler than the coating, with more positive E_{corr} as previously observed polarization tests, a galvanic corrosion process is formed between the steel and the aluminum [22,52,67,73]. Therefore, the aluminum dissolves to provide the substrate with a sacrificial cathodic protection (Stage 3 in Fig. 5.6.9). After 504 hours in seawater, the two-phase maximums with values around 60º are more clearly distinguished at HF (~100Hz) and MF (~0.5Hz). Furthermore, a diffusion tale is detected in the LF range in the Nyquist plot. The second time constant at MF is related to the reaction of the aluminum to form corrosion products in the regions close to the substrate. In neutral chloride solutions, aluminum is known to dissolved forming Al^{3+} ions, which hydrolyze and precipitate as $Al(OH)_3$ on the coating walls [22,31]. These deposits can block the pinholes and defects in the aluminum layer [22,48,52,61,67,73], hindering the electrolyte access and delaying the further aluminum dissolution that requires diffusion of reactants through the oxides (Stage 3 in Fig. 5.6.9). This is known as ‘plugging effect’ [52]. The presence of white deposits was confirmed in the SEM-EDS analysis performed on the samples after the test, which is presented at the end of this section. No significant changes are observed thereafter in the corrosion response of the coating, but a slight increase in the impedance modulus at LF, indicating

the enhancement of the corrosion response with time. This is attributed to both the formation of the passive layer, and the blockage of conducting paths in the coating by aluminum corrosion products [22,60]. The contributions of the outer passive film oxides and the corrosion products closer to the interface have similar phase maximum values close to 60º. The further exposition of the system to seawater, would eventually lead to the TSA coating failure, due to aluminum dissolution by cathodic corrosion mechanism, protecting the steel substrate to a certain extent (Stage 5 in Fig. 5.6.9).

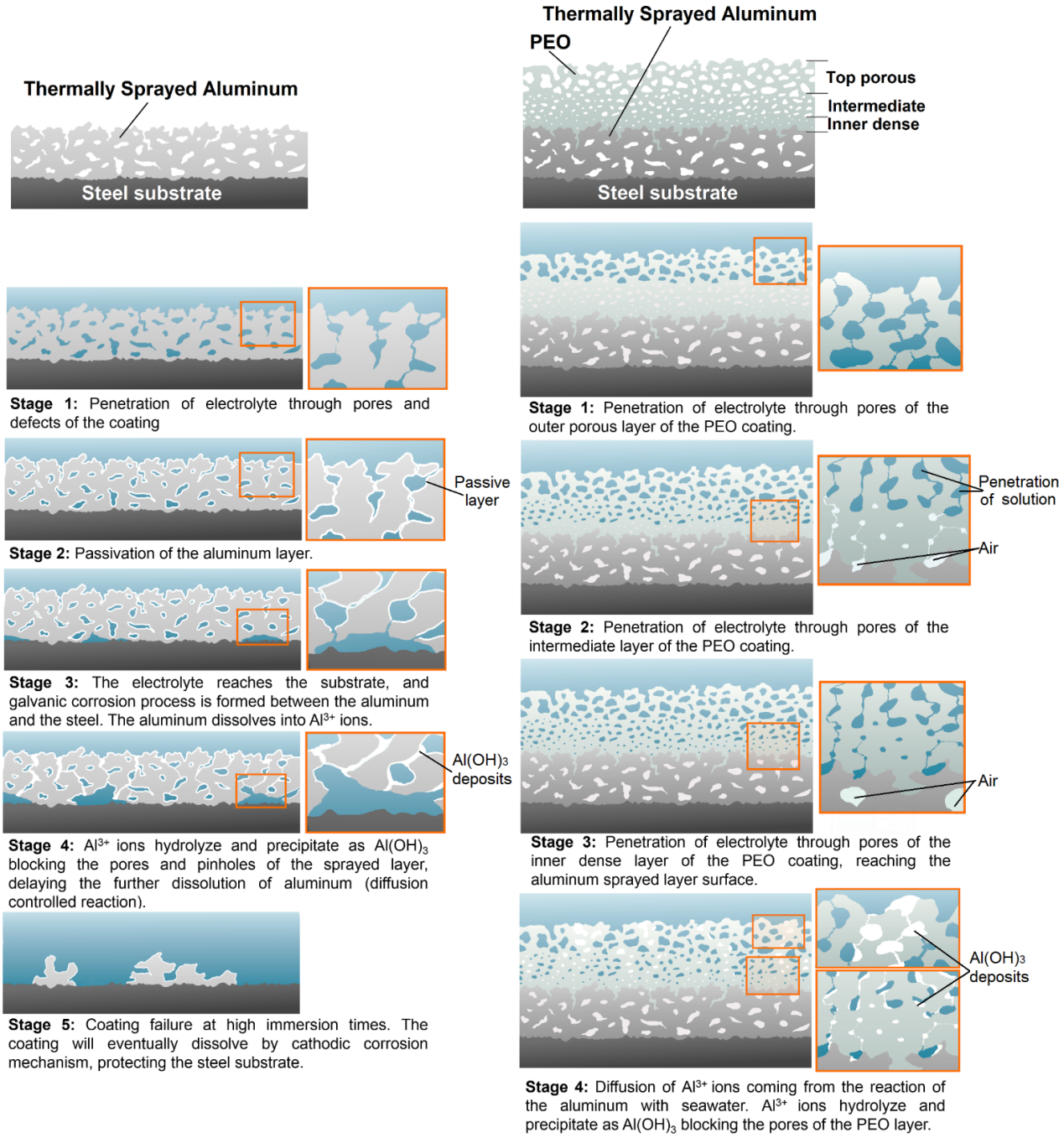

Fig. 5.6.9 Schematics of the corrosion mechanisms of the TSA (left) and TSA/PEO (right) coating systems in synthetic seawater

The impedance spectra obtained for the TSA/PEO coating exhibits two relaxation processes. This is coherent with that observed in literature for PEO coatings, where the time constant at HF has been attributed to the outer porous layer, and the time constant in MF range to the less porous inner layer [23,32,35,75,76]. The Nyquist plot at 24 hours

shows a small capacitive loop at HF and a bigger one for the LF range. This indicates that the corrosion resistance of the PEO layer in the early immersion stage is provided mainly by the inner barrier layer, by delaying the access of solution to the substrate surface [31]. The porous nature of the outer and the intermediate layers make them permeable by electrolyte [26], which reaches the inner barrier layer after 24 hours of immersion (Stage 1 and 2 in Fig. 5.6.9). After 168 hours, the two capacitive loops are more difficult to distinguish, and a diffusion tale appears in the LF range. In the Bode plot, two-phase maximums are clearly defined. The phase maximum in the HF range has shifted to lower frequencies from values above 10^4 Hz to 10^3 Hz, with values close to 50º. The maximum at MF also shifts to lower frequencies (from 26Hz-4Hz to 1.4Hz-0.13Hz) and increases from 17º to 20º. The impedance modulus at MF slightly increases, while no difference is observed at LF. All these variations suggest the infiltration of electrolyte through the small pores of the inner barrier, and exposure of underneath aluminum of the TSA layer (Stage 3 in Fig. 5.6.9). The diffusion tale at LF is associated with the diffusion of ions and corrosion products in the coating/surface interface. The reaction of the aluminum to form corrosion products that remain in the pores of the inner layer blocking the access of solution, leads to an increase in the corrosion resistance response of the system with higher exposure to seawater. This is observed as a gradual enlargement of the capacitive loops in the Nyquist diagram and the increase in the impedance modulus at MF and LF. Furthermore, the slight increase of the phase maximums and their shift to lower frequencies indicate a more capacitive response, which can be attributed to a more significant accumulation of corrosion products in the pores. Similar results were obtained by C. Liu et al. [31], who ascribed the improvement of the PEO coating with exposure time to diffusion of Al^{3+} ions and their hydrolyzation to form $Al(OH)_3$ deposits that blocked the coating defects (Stage 4 in Fig. 5.6.9). Coherently with their arguments, the EDS analysis performed in the TSA/PEO coating at the end of long-exposure test revealed the white deposits to be formed by Al and O, in an atomic ratio of 1:3 (Al:O), which corresponds to $Al(OH)_3$ compound[31] (see Fig. 5.6.12 and Fig. 5.6.13). G.-L. Song and Z, Shi [77] described the corrosion protection mechanism of anodized magnesium alloys by three different effects. These effects were also confirmed to occur in PEO coatings by C. Liu et al. [31], and are attributable to the PEO layer generated in this work. There is a "retarding" effect by delaying the infiltration of solution through the oxide layer defects, especially in the less porous inner barrier layer. There is also a "blocking" effect, which restricts the exposed area of the substrate surface in contact with the electrolyte. Finally, there is a "passivation" effect, where the active regions of the substrate through the defects of the PEO layer react to form a passive layer of corrosion products that eventually are accumulated in the small pores of the inner barrier layer of the PEO coating. Therefore, even if the solution reaches the TSA layer, the aluminum hydroxides formed impede the further penetration of electrolyte through the TSA pores and defects, improving the long-term response of this coating.

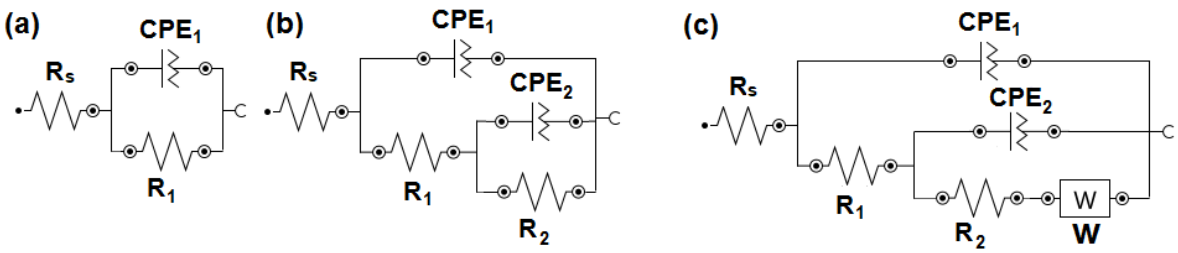

Fig. 5.6.10 Electrical equivalent circuits used to fit the electrochemical impedance spectroscopy data

Electrical Equivalent Circuits (EEC) are widely used for EIS modeling, which consist of an assembly of electrical elements that represent the physical and electrical characteristics of the electrochemical interface. The experimental data was analyzed

with NOVA 2.1 software, and the ECCs used are shown in Fig. 5.6.10. After several fitting processes, these circuits were selected as they gave the best fitting parameters with the smallest error, based on the chi-squared values (χ^2). This represents the square of the standard deviation between the original data and the calculated spectrum. The χ^2 values obtained were below 10^{-3}, showing an adequate fitting quality. Furthermore, the relative error of each element in the circuit was below 5%. The fitting curves are presented as solid lines in Fig. 5.6.8 for each spectrum. In the three circuits Fig. 5.6.10, R_s represents the solution resistance, and each CPE/R pair is used to represent a capacitance and a resistance in an interface, corresponding to a time constant. The Constant Phase Element (CPE) is widely used for replacing the simple capacitances for a better fit quality of the experimental data, when there is a deviation of the ideal capacitive behavior due to inhomogeneities, roughness, porosity, and other non-ideal dielectric properties [31,35,52,53,61,78]. The impedance of a CPE element can be represented as: $Z_{CPE} = 1/Y_0\,(i\omega)^n$, where ω is the angular frequency, and *i* the imaginary number. Y0 and *n* (*n*≤1) are the admittance and the empirical exponent of the CPE, respectively. Whenever the surface acts as an ideal capacitor *n* is equal to unity and Y0 is identical to the double layer capacitance. The circuit parameters obtained from the fitting process are compiled in Table 5.6.4.

In the case of the R4 steel, even if no coating is applied on top of the substrate, the corrosion products formed during immersion accumulate in the surface hindering the access of electrolyte to the corroding substrate, and the circuit in Fig. 5.6.10b can be used from the early immersion stage. The CPE_1/R_1 pair is used to describe the behavior of the rust film, which thickness increases with immersion time as the corrosion of the steel progresses. The second CPE_2/R_2 describes the double layer capacitance in the electrolyte/substrate interface and the charge transfer resistance, which is ascribed to the electrochemical reaction taking place in this interface. The corrosion resistance of the steel (R_2) increases with immersion time up to 2.85 kΩ cm^2. These values are in accordance with the results obtained in the polarization tests (2.74 kΩ cm^2), indicating a low corrosion resistance of the active R4 steel in synthetic seawater. The slight increase of R_1 is attributed to a thickening of the rust layer with immersion time, but its low value confirms the poor barrier effect of this film. Finally, the small increase in the CPE_2-Y0 values indicates an increase in the exposed steel surface, as a result of an increase in the roughness due to corrosion [79].

The circuit in Fig. 5.6.10b has been employed to describe passive materials, i.e., aluminum alloys in 3.5% NaCl solution [75], to represent the passive film generated as a spontaneous reaction of the surface with the electrolyte and the reactions taking place in the metal surface. In the case of TSA coating, where the aluminum is placed over a steel substrate, the same circuit can be employed to describe the dissolution of the aluminum layer by galvanic corrosion mechanism. In this case, the CPE_1/R_1 pair corresponds to the aluminum layer and represents the coating capacitance and pore resistance. The latter is ascribed to the ion conducting paths across the coating, i.e., pores and other defects, that allow the penetration of electrolyte, and gives information on the coating ability to protect the substrate in terms of corrosion resistance. The CPE_2/R_2 describe the double layer capacitance in the vulnerable regions of the exposed surface in the bottom of the coating, and the charge transfer resistance of the electrochemical reaction in these regions. As explained before, the nobler potential of the steel with respect to the aluminum leads to a galvanic dissolution of the latter and, thus, the CPE_2/R_2 in this case describes the reactions of the aluminum layer in the coating/substrate interface. The decrease in the pore resistance (R_1) and increase in CPE_2-Y0 observed from 24 to 168 hours, are a consequence of the increase in the

exposed area of the coating due to uncovering of porosity, and electrolyte penetration. At this stage, the higher CPE_1-n and CPE_2-n values in the range of 0.8 indicate a more capacitive response, as a consequence of higher aluminum corrosion products due to reactions that have taken place in the aluminum in contact with seawater. The EEC employed for 504 and longer exposure times is represented in Fig. 5.6.10c. Similarly to the previous circuit, CPE_1/R_1 and CPE_2/R_2 correspond to the aluminum layer and the coating/substrate interface, respectively. The Warburg diffusional element (W) is used to represent the diffusion-limited reaction in the TSA/steel interface, as a result of the presence of corrosion products coming from aluminum reaction with seawater. The impedance of the Warburg element can be expressed as: $Z_W = \sigma\omega^{1/2}(1-i)$, where σ is the Warburg coefficient, which is inversely proportional to the diffusion coefficient. The increase of pore resistance of the coating (R_1) with time indicates an enhancement of the aluminum layer resistance. The decrease in W-Y0 and increase in R_2 indicate a reduction of the exposed surface in the TSA/steel interface, as a consequence of the greater aluminum corrosion products coming from the galvanic reaction of the aluminum in contact with the steel substrate. The mass transfer reaction controlling the aluminum dissolution process leads to solution hindering by the mass transfer of corrosion products, increasing the provided protection of the coating against corrosion [53]. The gradual increase of both R_1 and R_2 with immersion time indicate an enhancement on the protection of the steel substrate, by both the galvanic dissolution of the aluminum in the vulnerable regions where the electrolyte reaches the substrate, and by the blockage of the ion conducting paths by the corrosion products formed in these electrochemical reactions.

The EEC circuit in Fig. 5.6.10b has been widely employed in literature for PEO coatings [23,32,35,74-76]. According to literature, due to the porous nature of the outer layer, it is unlikely to contribute to the corrosion resistance of the coating, and the EEC is composed of two relaxation processes [23,32,35,75,76]. The time constant at HF range (CPE_1/R_1) is related to the outer porous layers of the PEO coating (i.e., top porous and intermediate), whereas the second at LF (CPE_2/R_2) is associated with the inner barrier layer. R1 corresponds to the pore resistance of the topmost layers and is related to the pores and defects such as discharge channels generated in the outer and functional layers. CPE2 corresponds to the double layer capacitance in the electrolyte/inner layer interface, and R2 is the charge transfer resistance across the dense layer. The results obtained are consistent with those found in literature for PEO coatings generated in aluminum alloys for long exposure to 3.5% NaCl solutions (after 24 and 168) [23,75]. The higher R_2 values compared to R_1 confirm a poorer corrosion behavior of the outer porous layers and evince the corrosion protection of the system to be provided mainly by the inner layer [31]. The low CPE-n values for both layers, close to 0.6, can be attributed to the non-uniform porous nature of the oxide layer [75]. The EEC employed for longer exposure is represented in Fig. 5.6.10c. CPE_1/R_1 and CPE_2/R_2 correspond to the outer porous layer and the inner barrier layer, respectively. The Warburg diffusional element (W) is used to represent the diffusion-limited reaction in the PEO/TSA interface, as a result of the presence of corrosion products coming from the reaction of the aluminum sprayed layer with seawater. The increase in CPE2-Y0 and decrease in CPE_2-n and R2 values from 24 hours to 168 h, indicate an increase in the exposed surface of the inner barrier layer as a consequence of solution infiltration through its discharge channels. The increase in R_1 and R_2 with immersion time represents an improvement in the corrosion resistant response of the system. The gradual increase in CPE_1-n and CPE_2-n values, and the decrease in W-Y0 indicate a higher capacitive response due to greater accumulation of corrosion products in the pores of the PEO coating layers, hindering the further penetration of solution.

Table 5.6.4 Equivalent circuit parameters obtained from the impedance data fitting at different immersion times in synthetic seawater

Material and exposure period		R_s (Ω cm^2)	CPE_1-Y0 (F cm^{-2} s^{-n})	CPE_1-n	R_1 (kΩ cm^2)	CPE_2-Y0 (F cm^{-2} s^{-n})	CPE_2-n	R_2 (kΩ cm^2)	W-Y0 (F cm^{-2} s$^{-1/2}$)
R4	**24 h**	7.65	8.62 x10^{-04}	0.765	0.11	5.43 x10^{-04}	0.839	1.14	-
	168 h	9.73	1.41 x10^{-03}	0.710	0.06	1.65 x10^{-03}	0.740	2.05	-
	336 h	3.61	1.67 x10^{-03}	0.719	0.04	3.23 x10^{-03}	0.741	2.50	-
	504 h	9.17	1.96 x10^{-03}	0.698	0.06	2.62 x10^{-03}	0.759	3.50	-
	804 h	9.19	2.24 x10^{-03}	0.717	0.05	3.45 x10^{-03}	0.800	2.37	-
	1176 h	10.39	2.27 x10^{-03}	0.710	0.05	3.50 x10^{-03}	0.803	2.62	-
	1512 h	8.13	1.10 x10^{-03}	0.706	0.05	3.72 x10^{-03}	0.811	2.85	-
TSA	**24 h**	17.61	4.43 x10^{-04}	0.854	8.10	2.25 x10^{-03}	0.751	13.44	-
	168 h	25.77	1.19 x10^{-04}	0.823	1.18	6.40 x10^{-05}	0.882	13.59	-
	336 h	19.86	1.12 x10^{-04}	0.766	1.62	4.20 x10^{-05}	0.883	18.69	-
	504 h	8.94	9.23 x10^{-05}	0.743	2.57	3.53 x10^{-05}	0.944	24.96	1.07 x10^{-02}
	804 h	14.01	6.70 x10^{-05}	0.745	2.32	5.07 x10^{-05}	0.887	28.92	1.14 x10^{-02}
	1176 h	16.41	5.50 x10^{-05}	0.750	2.24	4.73 x10^{-05}	0.855	74.40	3.15 x10^{-03}
	1512 h	8.13	5.37 x10^{-05}	0.767	1.71	4.93 x10^{-05}	0.800	70.50	1.90 x10^{-03}
TSA/PEO	**24 h**	21.15	2.22 x10^{-07}	0.614	3.63	3.48 x10^{-05}	0.643	28.20	-
	168 h	33.70	4.78 x10^{-06}	0.608	12.75	6.00 x10^{-05}	0.699	21.25	4.48 x10^{-03}
	336 h	53.00	4.80 x10^{-06}	0.652	13.50	6.62 x10^{-05}	0.658	27.70	4.20 x10^{-03}
	504 h	80.50	4.62 x10^{-06}	0.678	16.30	5.68 x10^{-05}	0.635	49.70	4.30 x10^{-03}
	804 h	77.50	6.14 x10^{-06}	0.707	15.90	6.24 x10^{-05}	0.665	38.30	3.38 x10^{-03}
	1176 h	90.50	8.34 x10^{-06}	0.700	15.15	4.88 x10^{-05}	0.648	45.50	2.70 x10^{-03}
	1512 h	110.00	9.80 x10^{-06}	0.686	34.00	8.34 x10^{-05}	0.766	36.60	2.24 x10^{-03}

The main information on a coating performance in terms of corrosion (combination of capacitive and resistive behavior), is mainly reflected in the impedance at the lowest frequency ($|Z|_{f\to 0}$), where higher values correspond to lower corrosion rates [67]. Therefore, the modulus at LF such as 0.01Hz ($|Z|_{0.01Hz}$) is often used to evaluate the protection abilities of the coating system [36,67,80]. The modulus at 0.01Hz of the steel and the two coating systems are represented in Fig. 5.6.11a as a function of immersion time. The modulus of the two coatings are considerably higher than that of the steel substrate. In both coatings, the impedance modulus increases with immersion time. The sharp increase in the TSA/PEO coating above 168 h can be ascribed to the increasing presence of aluminum corrosion products blocking the pores in the PEO layer. In the case of the TSA, the increase is progressive, and is also attributed to the greater presence of aluminum corrosion products with increasing exposition to seawater.

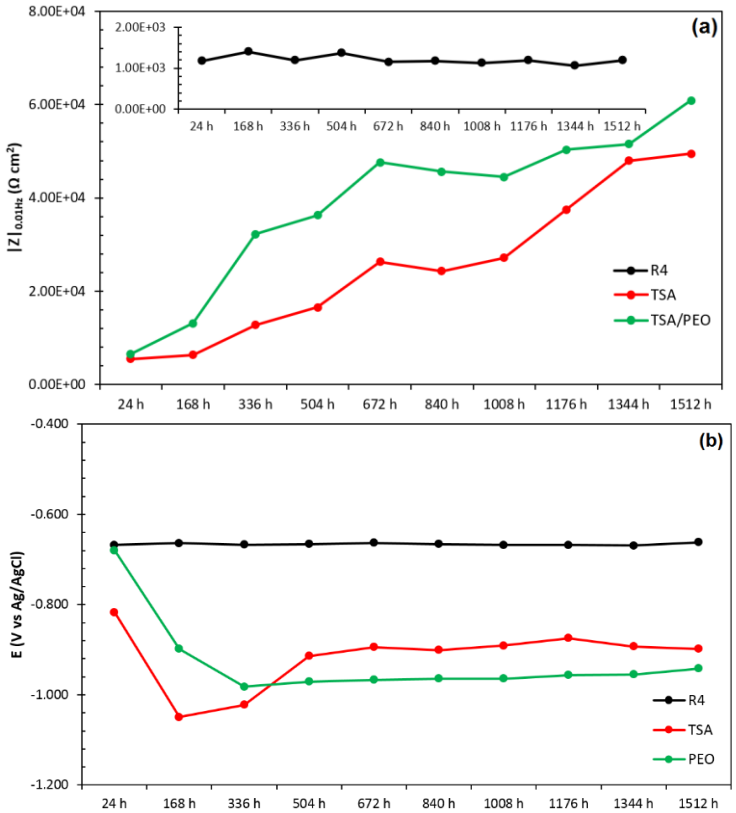

Fig. 5.6.11 Evolution of the impedance modulus at 0.01Hz (a) and OCP (b) with immersion time

The evolution of the OCP during the 1500 hours of immersion is plotted in Fig. 5.6.11b. The potential of the uncoated steel slightly decreases during the first 24 hours in seawater, and then remains constant around -0.67 V. In the case of the TSA coating, there is a drop in potential after the first week of immersion to values close to -1.1 V, and a progressive increase in the successive weeks to values around -0.9 V. The results are in coherence with the EIS evolution explained above. The decrease in potential is a consequence of the penetration of electrolyte through all coating defects, whereas the subsequent increase is related to the passivation of the aluminum and blockage of pores with aluminum corrosion products. Finally, the potential of the TSA/PEO decreases with time, reaching values close to those of aluminum in seawater. At the beginning of immersion, the PEO layer presents a barrier to electrolyte permeation due to the small pores of the intermediate and inner layers. Coherently with that observed in the EIS results, the potential drop around -0.9 V after 168 h indicate the penetration of solution which reaches the aluminum layer. The blockage of small PEO layer pores with

aluminum corrosion products leads to a slight increase in potential with time after the end of the test, presenting potential values close to those of the as-sprayed coating.

After corrosion tests, the surface of the specimens was analyzed by SEM-EDS microscopy. The SEM micrographs of the tree samples are depicted in Fig. 5.6.12 and the EDS analysis results are presented in Fig. 5.6.13.

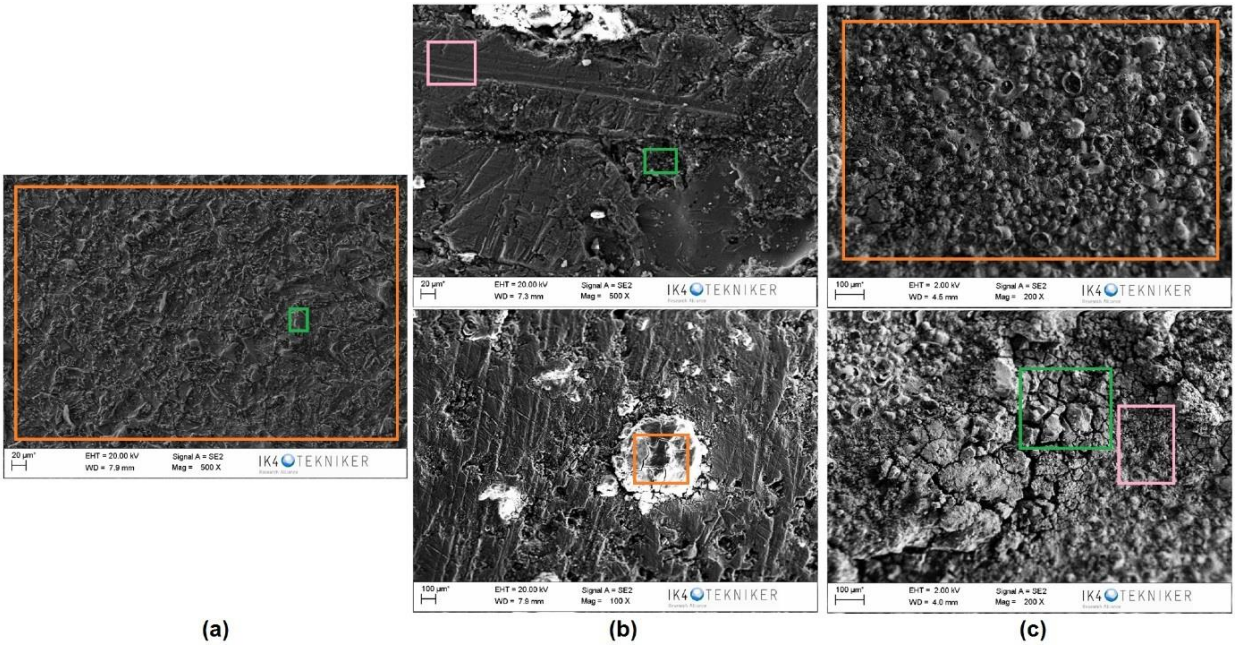

Fig. 5.6.12 SEM images of the specimens after long-term exposure to seawater: (a) uncoated steel, (b) TSA coating deposited on steel, (c) TSA/PEO duplex coating system

The high degradation of the uncoated steel is evident (Fig. 5.6.12a). The roughness of the previously mirror polished specimen has notably increased as a consequence of the high corrosion dissolution of the sample. The EDS analysis revealed the presence of chlorine (0.37 wt%) and oxygen (14.19 wt%) on the corroded surface of the steel, with a higher presence of these elements on the corrosion products (0.80 wt% Cl and 27.72 wt% O). The TSA coating (Fig. 5.6.12b) showed an inhomogeneous surface, presenting some smooth regions, with white deposits, and some rougher regions where the coating appeared to be damaged. The smoothest region of the surface was mainly composed of aluminum (47.14 wt%) and oxygen (22.5wt%), and a slight presence of chlorine was also detected (0.62 wt%). This region corresponded to the passive film formed as the spontaneous reaction of the aluminum with seawater. The white deposits, corresponded to aluminum oxides that might form as a consequence of the dissolution of aluminum close to the TSA/steel interface, that reacted with the solution to form complex oxides. The composition of this deposits contained some elements such as sodium, magnesium, and chlorine present in synthetic seawater (55.07 wt% O, 21.55 wt% Al, 2.39 wt% Mg, 1.69 wt% Ca, 0.76 wt% Na, 1.69 wt% Cl, and the rest C, Si and S). Finally, in the rough regions where the aluminum layer seems to be more damaged, a slight presence of iron was detected (4.21 wt% Fe, 18.42 wt% O, and 14.68 wt% Al, the rest C, Mg, Si, S, and Cl). This corroborates that solution reached the TSA/steel interface. In the TSA/PEO duplex system (Fig. 5.6.12c), the topmost surface of the PEO coating presented similar morphology to that before any corrosion test, showing negligible degradation (Fig. 5.6.3). The EDS analysis of the surface revealed the composition of this layer to be unchanged, just showing a slight amount of chlorine (61.04 wt% O, 33.31 wt% Al, 3.32 wt% K, 1.12 wt% Na, 0.88 wt% P, 0.33 wt% Cl, and 0.86 wt % C.). In a small region of the sample, the surface presented a brittle-like appearance. This region was found to be composed

mostly of aluminum and oxygen (66.42 wt% O, 31.78 wt% Al, 1.25 wt% Cl, and 0.56 wt% Si), in a 1:3 (Al:O) atomic ratio, confirming the presence of $Al(OH)_3$ compound blocking the pores of the PEO coating.

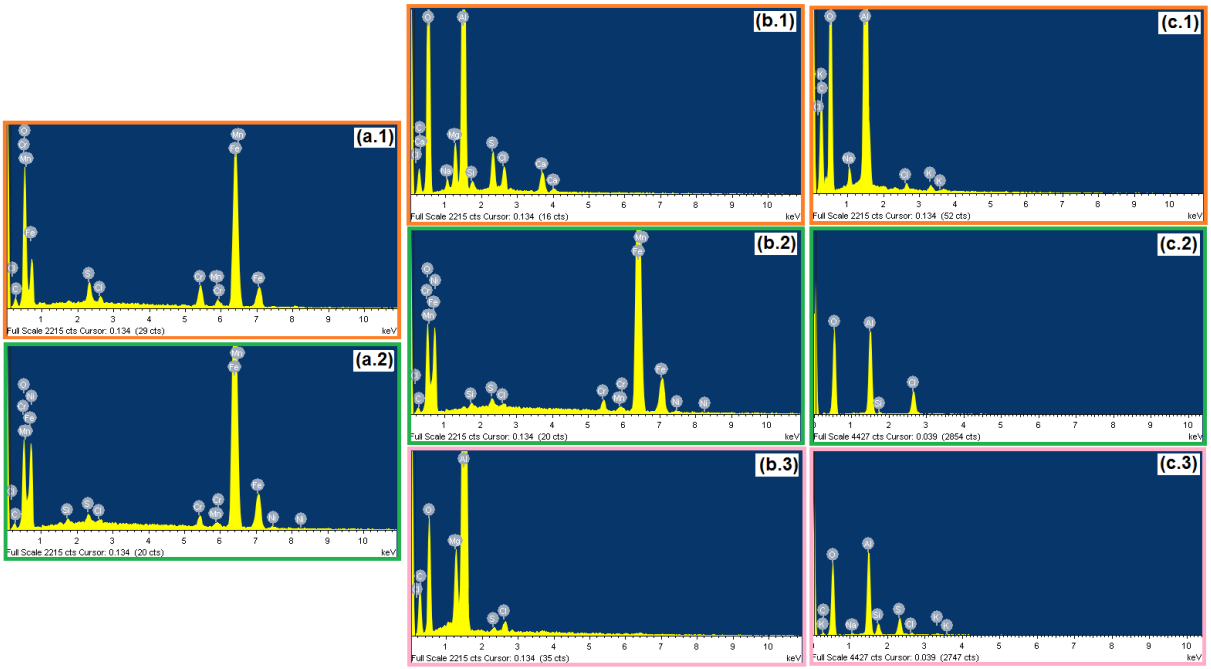

Fig. 5.6.13 EDS results of the specimens after long-term exposure to seawater: (a) uncoated steel, (b) TSA coating deposited on steel, (c) TSA/PEO duplex coating system

5.6.3.3 Abrasion and tribocorrosion tests

The evolution of the open circuit potential (OCP) of the specimens registered for the first hour of immersion is depicted in Fig. 5.6.14a. The potential of the uncoated steel decreases during the first minutes of immersion, and stabilizes in values close to -0.6 V. In this kind of steels, the potential drop is attributed to corrosion processes taking place in the surface [6,7,22], leading to the formation of a rust layer composed mainly of ferric oxyhydroxide (FeOOH) compound [81-84]. This rust layer is known to be porous and low adherent; thus, it does not constitute an effective barrier to the electrolyte. However, after acquiring a certain thickness after several minutes, the rust layer hinders the access of oxygen to the corroding surface [3,22,85-87], and the system reaches a stable state at -0.6 V. In the case of the TSA coating, the potential slightly increases during the first minutes of immersion. This is the typical response of a passive material, as a consequence of the formation of a protective oxide layer from the spontaneous reaction with the electrolyte [11-13,22]. The passive film, of few nanometers thick, acts as a barrier impeding the further access of electrolyte and protecting the aluminum layer from corrosion. The stable values obtained after the first hour around -0.9 V are in accordance with that measured for the aluminum in seawater [52,59-61], indicating that there is no contribution of the substrate to the potential lecture. Finally, the potential of the TSA/PEO decreases from values close to -0.2 V to stabilize at around -0.68V. The decrease in the potential might be ascribed to the porous nature of the PEO layer. As observed from the microscopical characterization, the outer layer is porous and loose, so the electrolyte easily penetrates through the pores of the outer layer, resulting in a decrease of potential. Once the electrolyte reaches the less porous intermediate layer, the system stabilizes giving steady potential values at the end of the curve. Although the potential is close to that of the uncoated steel, no contribution of the substrate is expected due to the good barrier effect provided by the PEO layer, as demonstrated from the long-term immersion tests of the previous section. Therefore, the higher potential of the TSA/PEO system in

comparison with the as-sprayed coating, indicates that the PEO layer provides the sprayed aluminum with an effective protection in seawater.

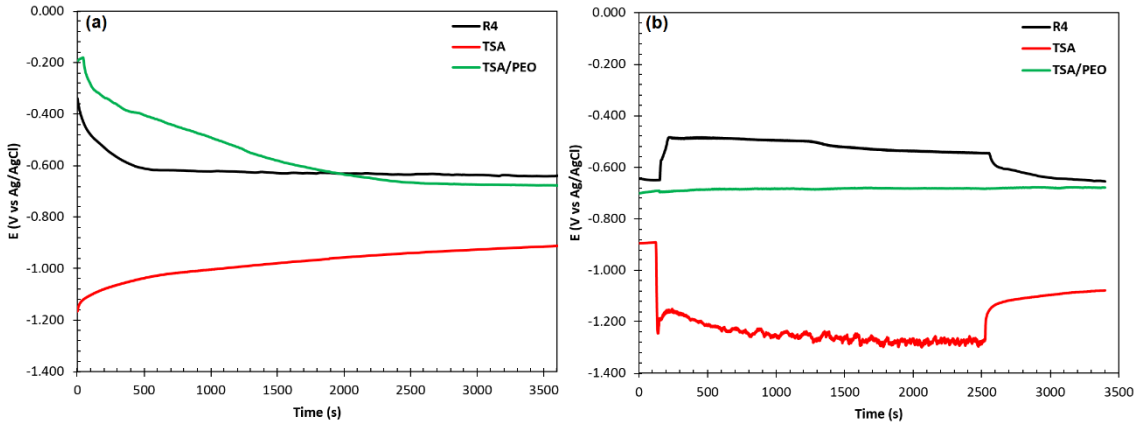

Fig. 5.6.14 Evolution of the open circuit potential during the (a) first hour of immersion in synthetic seawater and (b) during and after sliding wear test

The evolution of potential during the sliding is presented in Fig. 5.6.14b. Sliding generates a potential shift towards more positive values in the uncoated steel. According to the results obtained in previous studies [6,7], this change in the potential is attributed to the more positive potential of the material in the wear track, free of the rust that is removed from the contact, with respect to the unworn surface. At the end of sliding, the material in the worn surface reacts again to form a new rust layer, reaching potential values close to those before sliding. In the case of the TSA coating, the response registered during the sliding test is a potential drop to more cathodic values, as a consequence of the rupture and removal of the passive layer exposing the bare aluminum to the electrolyte [11-13]. During the whole wear test, the potential remains around -1.25 V, showing some fluctuations above 1000 seconds. These small potential variations can be the consequence of localized corrosion processes taking place in the depassivated surface (repassivation and depassivation events) [11-13,88-90], as well as to debris remaining in the contact or even some material adhesion that can lead to variations in the frictional response. Once sliding ends, the potential increases again indicating a repassivation of the worn surface, showing slightly lower values in comparison with those before the wear test. The potential of the TSA/PEO coating system is not affected by the mechanical effect imposed during sliding, remaining almost constant during the whole test around -0.7 V. Similar responses have been observed for hard ceramic coatings generated by PEO technique [89-91], indicating excellent stability under wear-corrosion solicitations. This behavior can be ascribed to the higher resistance to abrasion of the oxide layer which resists the mechanical stresses with no significant changes that can lead to variations in the corrosion response.

The EIS measurements obtained before and after wear process are presented in Fig. 5.6.15, and the fitted impedance values are collected in Table 5.6.5.The steel sample shows one capacitive loop in the Nyquist plot and one inflection point in the Bode plot, corresponding to a one time constant in both lectures. The shape of the curves is the typical response of a corroding metal with a charge transfer reaction in the electrolyte/metal interface. There is a small reduction in the impedance modulus, and a decrease in the phase maximum from 70º to 60º, indicating a decrease in the corrosion resistance of the steel after sliding wear test. The impedance data was fitted using the EEC in Fig. 5.6.10a, known as Randles simple circuit. The CPE_1 is the double layer capacitance in the electrolyte/steel interface, and R_1 is the charge transfer resistance. The higher CPE_1-Y0 value after sliding indicates an increase in the exposed surface of

the steel, as a consequence of the higher roughness of the sample due to corrosion [79]. The slight decrease in R_1 confirms the reduction of the resistance due to sliding.

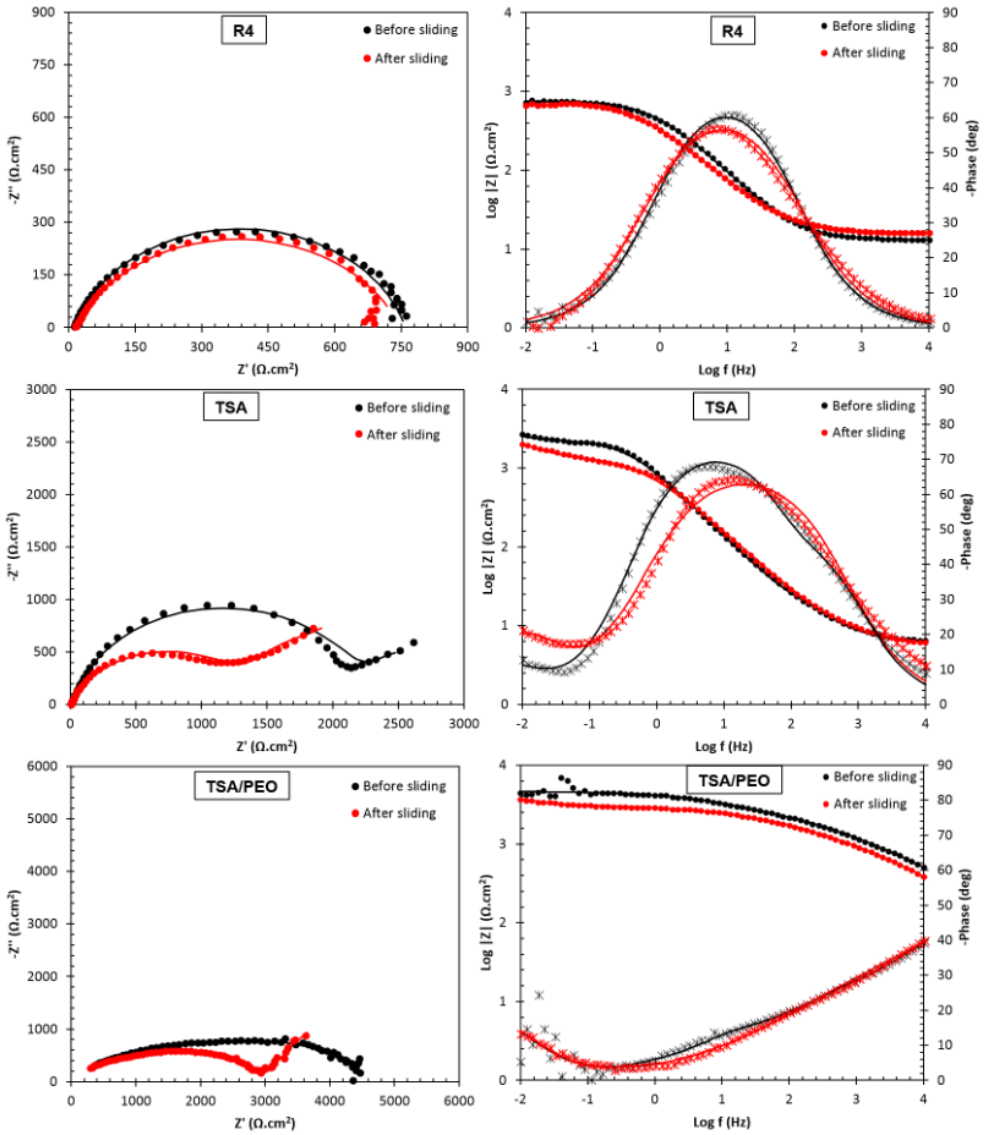

Fig. 5.6.15 Electrochemical Impedance Spectroscopy results obtained before and after sliding process in synthetic seawater for the steel and two coating systems, where the solid lines represent the fitting curves obtained with the equivalent circuits

The TSA-coated sample shows two capacitive loops, which correspond to the aluminum layer in the topmost surface at HF and within the ionic paths of the coating at LF. The capacitive loop at HF is more significant than that at LF, indicating that after an hour of immersion the electrolytes barely penetrates within the defects of the sprayed layer, and the exposed surface of aluminum in these regions is small in comparison with the topmost surface of the sample. After the test, there is a slight decrease in the impedance modulus at LF, and a reduction in the size of the capacitive loop at HF. The removal of the passivated aluminum in the tribological contact, and the successive material detachment during the whole test, leaves fresh material in the wear track to react at the end of the test. The depassivation of this surface, with not enough time to fully repassivate after sliding, leads to a decrease in the semicircle at HF. Furthermore, the considerable material removal in the contact makes it easier for the electrolyte to reach the TSA/steel interface, where the aluminum dissolves due to galvanic sacrificial protection mechanism.

The EEC used to fit the results of the coating was the same used in early corrosion stage (Fig. 5.6.10b). The decrease in CPE_1-Y0 and increase in CPE_1-n are attributed to a decrease in the topmost passive surface, which is also confirmed by a decrease in R_1. On the other hand, CPE_2-Y0 decreases and R_2 increases after sliding. This could be related to the wear debris that might be smeared and compacted in the wear track during the mechanical solicitation [92-94], filling the pores or paths to the substrate. Furthermore, the partial repassivation of the worn surface after the wear test might also be responsible for the increase of R_2. The overall effect of sliding in the system is a decrease in the protectiveness of the coating, due to the removal of the topmost passive layer, and generation of shorter paths for the solution to penetrate and reach the steel through the remaining TSA layer in the worn surface. Once the substrate is exposed, the galvanic reaction between the aluminum and steel begins, and the aluminum dissolves. Eventually, this would lead to a greater steel surface exposed, i.e., larger cathode size, which in turn, will accelerate the aluminum dissolution, causing the total coating failure.

The Nyquist diagram of the TSA/PEO duplex coating before sliding shows one capacitive loop. However, the impedance data was fitted with the EEC in Fig. 5.6.10b giving smaller fitting error than the circuit in Fig. 5.6.10a. Therefore, the second relaxation process at LF is masked by the great contribution at HF. In this case, CPE_1/R_1 represents the outer porous layer, and CPE_2/R_2 is the contribution of both the intermediate and inner layers. During the one hour of immersion before sliding, the electrolyte penetrates through the pores in the outer layer, reaching the intermediate layer. The smaller pore sizes of the latter, make it difficult for the solution to further penetrate and reach the inner barrier layer and, thus, the contribution at LF can be considered to correspond to this layer. During sliding, the topmost porous layer is partially removed, and greater intermediate layer surface is exposed. This leads to a decrease in the semicircle loop at HF, and an increase of that at LF. The partial removal of the top layer was confirmed in the surface analysis explained later in Section 5.6.3.4. The reduction in R_1 indicates a lower resistance of the ripped outer layer, whereas the decrease in CPE_2-Y0 and increase of R_2 could be related to the presence of corrosion products coming from the tribochemical reactions taking place during the wear process [95]. The presence of $Al(OH)_3$ deposits in the worn surface was confirmed in the surface analysis of the samples (see Section 5.6.3.4).

Table 5.6.5 Equivalent circuit parameters obtained from the impedance data fitting before and after sliding test in synthetic seawater

Material	Condition	R_s (Ω cm^2)	CPE_1-Y0 (F cm^{-2} s^{-n})	CPE_1-n	R_1 (kΩ cm^2)	CPE_2-Y0 (F cm^{-2} s^{-n})	CPE_2-n	R_2 (kΩ cm^2)
R4	**Before sliding**	13.10	3.53 x10^{-04}	0.822	0.75	-	-	-
	After sliding	16.05	5.97 x10^{-04}	0.767	0.73	-	-	-
TSA	**Before sliding**	5.96	2.56 x10^{-04}	0.773	1.43	1.01 x10^{-02}	0.888	1.56
	After sliding	6.21	1.26 x10^{-04}	0.846	0.03	1.06 x10^{-04}	0.853	2.33
PEO	**Before sliding**	10.79	1.48 x10^{-05}	0.517	4.02	3.48 x10^{-03}	0.813	0.84
	After sliding	8.38	1.84 x10^{-05}	0.521	3.26	8.44 x10^{-05}	0.841	3.51

Despite the physical modifications generated by sliding in the PEO layer, the overall corrosion resistance of the coating provided by the duplex system is affected by wear. The impedance modulus at LF remains similar, and no contribution of the aluminum of the sprayed layer is observed. Furthermore, the negligible variations in the OCP during sliding also confirms the good stability of the coating under wear-corrosion solicitations. Consequently, the PEO process seems to improve the tribocorrosion resistance of the aluminum sprayed coating.

The coefficients of friction registered for the dry abrasion test and the tribocorrosion test in synthetic seawater are plotted together in Fig. 5.6.16, and the mean values are compiled in Table 5.6.6. In the dry abrasion tests, the lowest COF corresponded to the TSA coating, whereas the highest was measured for the TSA/PEO system. In the tribocorrosion tests, however, the opposite situation was observed, being the COF of the TSA coating the higher and that of the TSA/PEO the lowest.

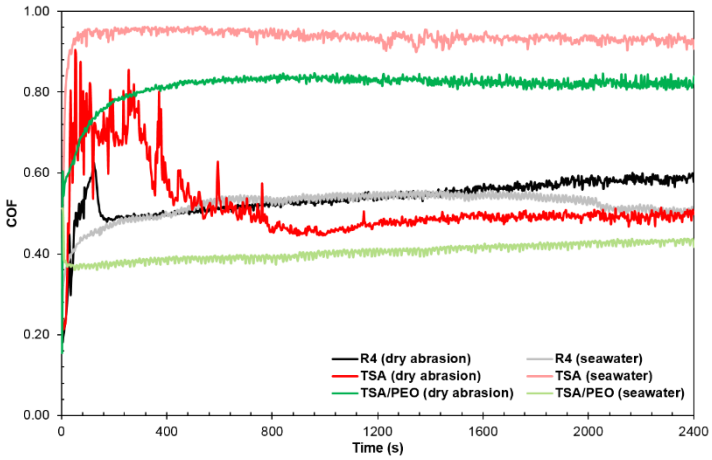

Fig. 5.6.16 Evolution of the coefficient of friction with sliding time for the steel and two coating systems in the dry abrasion and tribocorrosion tests

The coefficient of friction of the R4 steel in dry conditions has a greater running-in period compared to that of tribocorrosion conditions, but similar values are registered from 200 up to 1600 seconds of sliding. The gradual increase in the COF in dry sliding can be attributed to the more significant amount of debris remaining in the tribological contact [6,96]. On the other hand, the decrease in the coefficient observed for the tribocorrosion test above 1600 seconds can be a consequence of a slight lubrication effect of seawater [7,97], as well as to lower debris presence in the contact which are removed by the electrolyte movement.

In the case of the TSA coating, the COF in the tribocorrosion tests was considerably higher. The aluminum detached from the worn surface can react with the electrolyte to form oxides that remain in the contact acting as third body particles [98-100]. In dry conditions, the coating shows a running-in period during which the COF is higher, close to 0.7, with high fluctuations. This can be attributed to the detachment of aluminum particles which linger in the tribological contact, and to an increase in the contact surface with each cycle leading to higher COFs [101]. After several cycles, the wear debris can be smeared in the tribological contact providing some lubricating effect accommodating the sliding by shearing, reducing the coefficient and leading to more stable values [102].

Finally, the COF of the TSA/PEO duplex coating in dry and wet conditions are considerably different. The topmost porous layer of the PEO coating can be easily cracked and delaminated during the first test cycles, forming a smooth surface as the intermediate layer is exposed. The increase in the contact surface leads to an increase in the frictional force and the COFs registered during the first minutes of sliding [103]. Once the intermediate layer is reached, the coefficient is almost constant during the whole test. This transition is more evident in the dry tests, where the outer porous layer was removed entirely, as confirmed in the surface analysis in Section 5.6.3.4. The contact between two hard alumina materials, i.e., the counterbody and the PEO coating, leads to high coefficients at dry conditions. Similar COF values have been registered for Al_2O_3/Al_2O_3 contacts in dry conditions [100]. M. Treviño, et al. [30] attributed these high values in alumina-PEO contacts to the irregular topography, together with the edges

formed in the wear track that difficult the movement of the countermaterial, increasing the shear stresses in the surface and the COF. Furthermore, the easy removal of the porous and loose topmost layer can lead to debris formation, also increasing the resistance to countermaterial motion [105]. In tribocorrosion conditions, the coefficient is close to 0.42, being the lowest registered for all the materials and conditions tested, showing a good tribological response of the PEO-modified coating in seawater. Several researchers [106-109] have ascribed the low friction on Al_2O_3/Al_2O_3 contacts at wet conditions to the aluminum hydroxide that may form by a tribochemical reaction. Moreover, Wong et al. [110] stated that tribochemical wear resulted in surface smoothing, and the thin water film of low viscosity between the two hard materials provided a hydrodynamic lubrication. The apparition of aluminum hydroxides, i.e., $Al(OH)_3$, from the reaction of wear debris with seawater was confirmed in the surface analysis explained later in Section 5.6.3.4.

Table 5.6.6 Average coefficient of friction and total wear track volume (W_{tr}) obtained for dry abrasion and tribocorrosion tests of the R4 steel and the two coatings

	R4		TSA		TSA/PEO	
	Dry abrasion	**Seawater**	**Dry abrasion**	**Seawater**	**Dry abrasion**	**Seawater**
Mean COF	0.577±0.011	0.525±0.016	0.493±0.008	0.930±0.007	0.821±0.045	0.425±0.007
W_{tr} ($x10^{-3}$ mm^3)	83.16±2.16	0.91±0.06	739.55±28.33	646.73±14.75	120.88±3.79	Not measurable

5.6.3.4 Surface analysis and material loss evaluation

At the end of the tests, the surface of the specimens was analyzed by confocal and SEM-EDS microscopic techniques. The SEM micrographs obtained in dry abrasion and tribocorrosion tests in synthetic seawater are presented in Fig. 5.6.17, Fig. 5.6.19, and Fig. 5.6.21.

The images of the R4 steel substrate at 200 magnifications show an evident difference in the size and appearance of the wear track size generated after dry and tribocorrosion tests (Fig. 5.6.17). In dry abrasion tests, abrasion lines parallel to sliding direction can be observed. The steel removed from the track remaining in the tribological contact has been deformed and smeared under the applied load. The EDS analysis revealed the presence of some oxides in the worn surface (7.11 wt% C, 31.13 wt% O, 1.03 wt% Cr, 0.64 wt% Mn, and 60.09 wt% Fe), which might be formed as a consequence of the high temperatures reached in the contact during dry abrasion conditions. The rest of the worn surface presented similar EDS results as the unworn surface, with no oxygen at all (4.28 wt% C, 1.10 wt% Cr, 1.00 wt% Mn, and 93.62 wt% Fe). In tribocorrosion test specimens, however, abrasion grooves are more evident, and no smeared material is observed in the contact (Fig. 5.6.17b). Some corrosion products can be observed in the track, formed as a consequence of localized corrosion taking place in the worn surface. The EDS analysis revealed a considerable amount of oxygen along the whole wear track (5.95 wt% C, 14.83 wt% O, 1.06 wt% Cr, 0.71 wt% Mn, 2.02 wt% Na, 0.69 wt% Cl, and 75.72 wt% Fe), which could be consequence of crushing and spreading of the oxidized detached material remaining in the tribological contact. The material out of the wear track has also been highly corroded (Fig. 5.6.18). As previously observed for this kind of steels under tribocorrosion conditions, sliding promotes the corrosion of the unworn surface of the sample [6,7]. The EDS results of these region showing high oxygen content (11.88 wt% C, 32.91 wt% O, 2.02 wt% Na, 0.69 wt% Cl, 0.73 wt% Cr, and 51.77 wt% Fe), corresponding to a highly corroded surface, confirm the previous statement. The surface analysis performed in the countermaterial after the tests showed the presence of adhered steel in the alumina ball after dry abrasion test (Fig. 5.6.20a). Less transference of material is observed in the ball after tribocorrosion tests (Fig. 5.6.20b). In both tests,

the asperities of the hard ball generated grooves in the steel samples of lower hardness. No abrasion signs are observed in the ball indicating negligible wear damage of the countermaterial. The difference in the abrasion extent in the wear tracks, i.e., lower abrasion lines in dry condition, can be ascribed to a greater amount of steel adhered in the countermaterial filling its irregularities, which could eventually lead to a steel-steel contact.

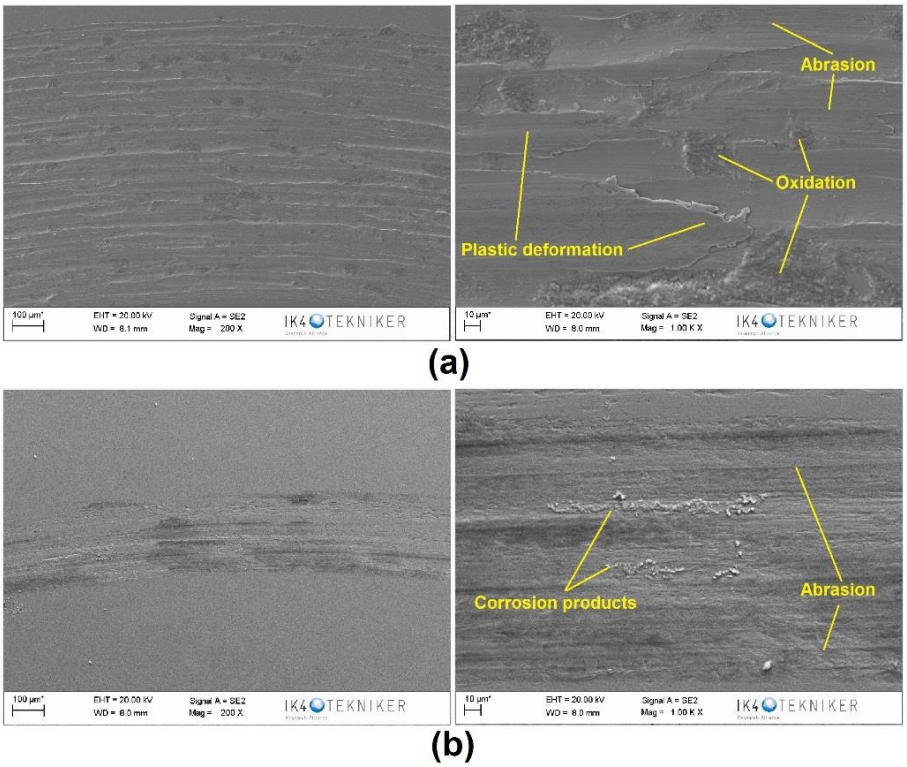

Fig. 5.6.17 SEM images showing the topography of the wear tracks of the steel samples after (a) dry abrasion and (b) tribocorrosion tests

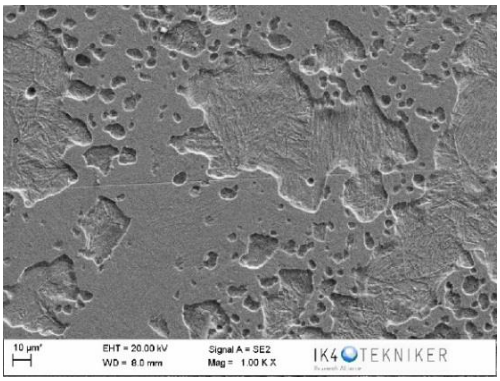

Fig. 5.6.18 SEM image showing the unworn surface topography of the R4 steel substrate after tribocorrosion test

The images of the wear track morphology of the TSA coating show severe damage and high roughness at both corrosion (Fig. 5.6.19a) and tribocorrosion (Fig. 5.6.19b) conditions. The worn surface in dry abrasion tests shows plowing, which led to delamination and material removal. This has been observed to be a common feature in soft metal wear mechanism [66,102]. The detached material is smeared and plastically deformed in the tribological contact under the stresses generated during the test, also showing abrasion lines in sliding direction. The results of the EDS analysis indicate that the deformed material is mainly composed of aluminum (97.83 wt % Al and 2.17 wt% O). A higher presence of oxygen is detected in the white regions around the smeared layers, indicating the oxidation of aluminum that might have occurred under high

temperatures reached during dry sliding conditions (56.36 wt% Al and 43.64 wt% O). The low abrasion resistance of the aluminum led to high delamination and eventual exposure of the steel substrate in certain regions of the wear track, as confirmed by EDS analysis in the whiter areas in Fig. 5.6.19(right) (5.58 wt% C, 1.74 wt% Mn, 5.90 wt% Al, and 86.78 wt% Fe). The worn surface morphology of the TSA coating in the tribocorrosion test is quite different, showing a more rough and brittle appearance than the dry test specimen. Material deformation is also observed in this sample, showing a tongue-shaped structure and shallower ploughing. The EDS revealed the main composition of the deformed layers to be aluminum (97.99 wt% Al and 2.01wt% O). The oxygen content in some regions of the track is higher (33.61 wt% O, 62.71 wt% Al, 0.56 wt% Na, 0.66 wt% S, 2.21 wt% Cl, and 0.25 wt% Ca), which can be attributed to a partial repassivation of the worn surface after sliding. The ploughed regions also presented oxides coming from aluminum reaction with the electrolyte (41.58 wt% O, 55.02 wt% Al, 2.05 wt% Cl, 0.68 wt% Na, and 0.68 wt% S). The passive layer in the unworn surface contained slight amounts of chlorine and sodium, and was mainly composed by aluminum and oxygen (41.84 wt% O, 54.34 wt% Al, 3.14 wt% Cl, 0.68 wt% Na). Contrary to the sample in dry conditions, no presence of iron was detected in the wear track of this specimen. The analysis of the countermaterial revealed a high transference of aluminum in dry sliding tests (Fig. 5.6.20c). The high hardness of the alumina ball results in adhesion of softer aluminum, which can oxidize after several cycles of sliding, acting as a third body particle and increasing the wear extent [111]. In tribocorrosion tests, however, less aluminum was adhered to the counterbody surface (Fig. 5.6.20d). The high difference in hardness between the hard countermaterial and soft aluminum layer resulted in negligible damage in the ball. Hence, the wear mechanism of the as-sprayed coating in dry conditions was a combination of adhesive, oxidative and abrasive wear, whereas the tribocorrosion mechanism was corrosive-adhesive.

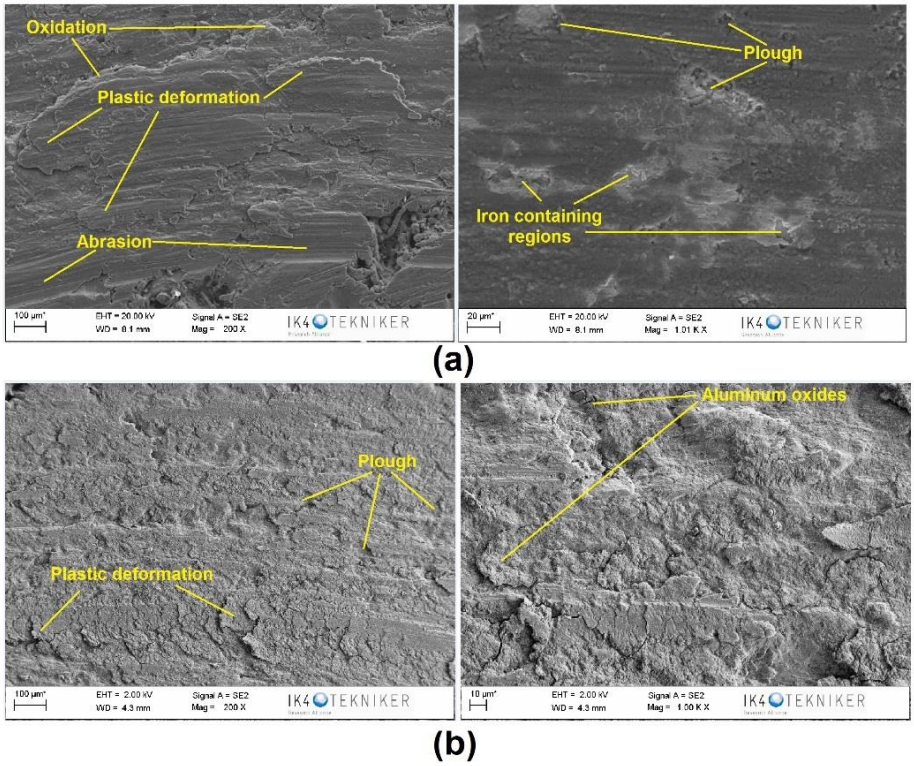

Fig. 5.6.19 SEM images showing the topography of the wear tracks of the TSA-coated steel samples after (a) dry abrasion and (b) tribocorrosion tests

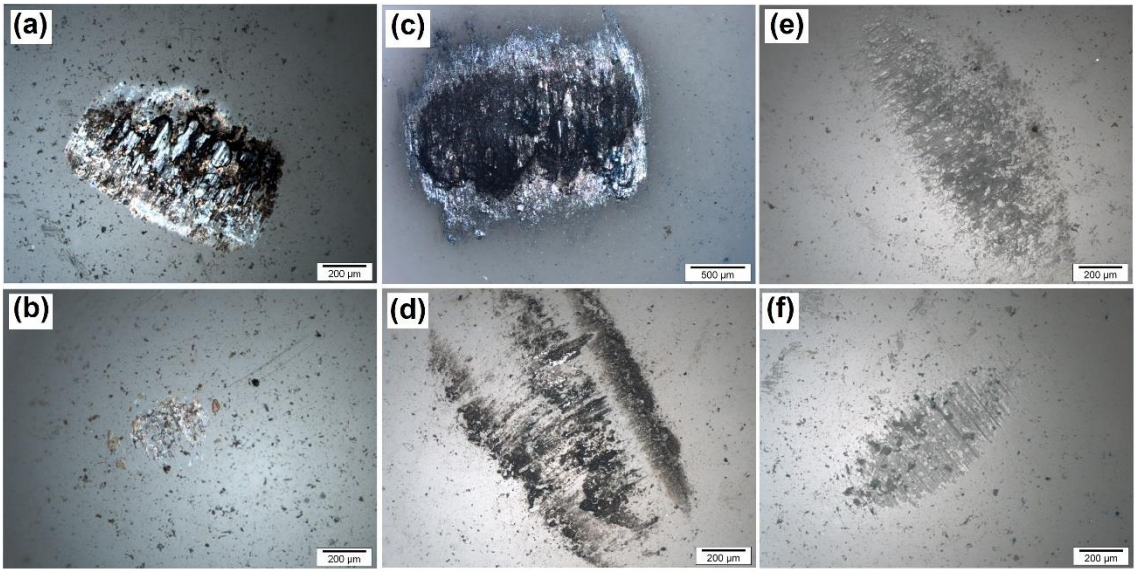

Fig. 5.6.20 Optical micrographs of the alumina counterbody surface after abrasion and tribocorrosion tests: steel dry abrasion (a) and tribocorrosion (b), TSA coating dry abrasion (c) and tribocorrosion (d), and TSA/PEO system after dry abrasion (e) and tribocorrosion (f)

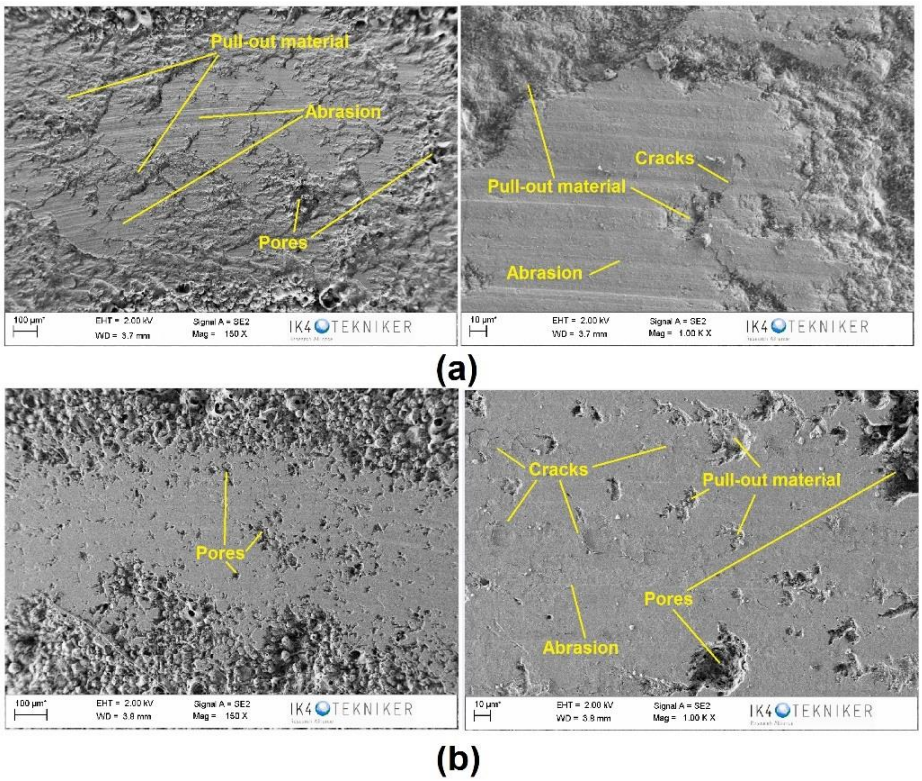

Fig. 5.6.21 SEM images showing the topography of the wear tracks of the TSA/PEO-coated steel samples after (a) dry abrasion and (b) tribocorrosion tests

The wear tracks generated in the TSA/PEO coating in dry and tribocorrosion tests are presented in Fig. 5.6.21. The wear and tribocorrosion mechanisms of the PEO layer of the duplex system are schematically depicted in Fig. 5.6.23 and Fig. 5.6.24, respectively. From the SEM images at 150 magnifications, a clear difference in the wear track size can be noticed, being considerably wider for the sample testes at dry conditions. In both cases, abrasion lines are observed parallel to sliding direction. During the first cycles in contact with the hard alumina countermaterial, the outer porous and loose oxide layer of the PEO coating can be easily removed (Stage 1 in Fig. 5.6.23 and Fig. 5.6.24). As this

layer is delaminated from the surface, a smoother surface is generated, corresponding to the intermediate functional layer. This layer, mainly composed of hard α-Al_2O_3 phase, decreases the wear ^{rate} [39,112]. The worn surface of the specimen at dry conditions shows low pore presence, which suggests the total removal of the topmost porous layer and deeper penetration of the countermaterial in the less porous intermediate layer, and thus, a greater material removal. The EDS results of the abraded regions in dry tests showed no presence of calcium, potassium, and phosphate, which were observed to be present in the outer layer of the coating (61.08 wt% O, 3.78 wt% K, 1.16 wt% Ca, 2.46 wt% P, and 30.82 wt% Al). This confirms the previous statement, as the composition of the worn surface in dry abrasion test (60.14 wt% O and 39.86 wt% Al) is in accordance with the intermediate layer composition measured in the coating characterization in Section 5.6.3.1. These elements were detected in the worn surface of the tribocorrosion test specimen (77.4 wt% O, 0.51 wt% K, 1.08 wt% P, 0.71 wt% Na, and 32.56 wt% Al), indicating a shallower penetration of the ball and just a partial removal of the top porous layer. A higher magnification analysis of the tracks revealed the presence of cracks in the worn surface of the samples (Fig. 5.6.22). These microcracks are created under the stresses generated by the successive passes of the countermaterial, due to the presence of pores beneath the worn surface (Stage 1 in Fig. 5.6.23 and Fig. 5.6.24). The cracks propagate generating the coarsening of pores (Stage 2 in Fig. 5.6.23 and Fig. 5.6.24) that eventually lead to material pull-out, leaving a brittle-like fracture appearance in several regions of the worn surface (Stage 3 in Fig. 5.6.23 and Fig. 5.6.24). This is more evident in the specimens tested at dry conditions, where a greater material detachment can be observed Fig. 5.6.22a. This is a typical wear model for ceramic brittle materials [28,113], and similar wear morphologies have been observed for dry Al_2O_3/Al_2O_3 contacts [114]. According to wear-regime maps of Al_2O_3/Al_2O_3 contacts at room temperature and dry conditions, under the speed and loads used in this study, the wear mechanism is localized microfracture [104], which is in accordance with the results obtained in this work. In the worn surface of the tribocorrosion test specimen in Fig. 21b, the initiation of crack generation above the pores and less pull-out material can be observed. In this case, the stable aluminum hydroxides, such as $Al(OH)_3$, formed from the reaction of wear debris with seawater (Stage 2 in Fig. 5.6.24) can provide the surface with a lubrication effect by shearing in the contact[106-109] (Stage 3 in Fig. 5.6.24). On the other hand, the slight lubricating ability of seawater [110] can also contribute to diminishing the material rate in wet conditions. The crack propagation is retarded, leading to lower material pull-out and shallower penetration of the countermaterial into the coating. Abrasion grooves are more evident in dry test sample, which can be ascribed to greater third body interaction resulting from more substantial detached material remaining in the tribological contact. In tribocorrosion tests, the wear debris can be more easily removed from the worn surface by seawater movement. The contact between two identical materials with similar hardness, i.e., alumina ball and alumina phases in the PEO layer, led to abrasion of the countermaterial at both test conditions (Fig. 5.6.20e and f). The wear extent was considerably higher in the ball used in dry conditions, which can be ascribed to a greater surface of contact with the hard intermediate layer. In spite of the evident abrasion of the ball, no wear could be measured in either case. Therefore, the wear mechanism of the PEO coating in dry conditions is a combination of abrasion and microfracture, whereas the tribocorrosion mechanism is composed of abrasion, microfracture and tribochemical wear (corrosion delamination fatigue).

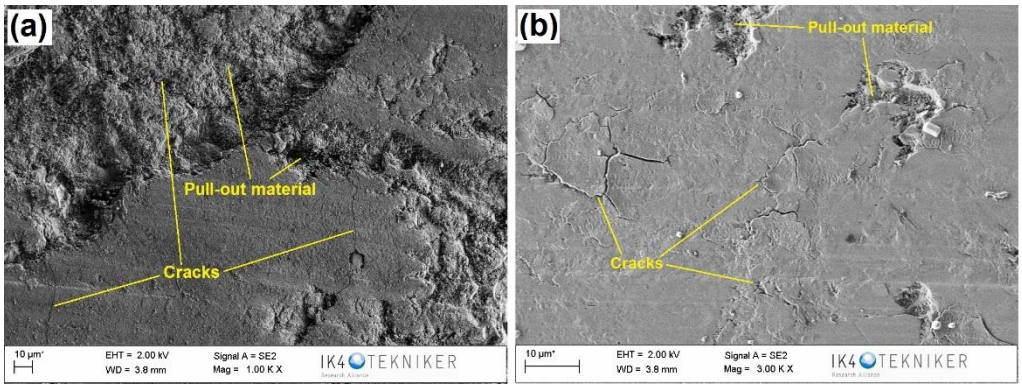

Fig. 5.6.22 SEM images of the TSA/PEO worn surface showing cracks and pulled-out material: (a) dry abrasion test and (b) tribocorrosion test specimens

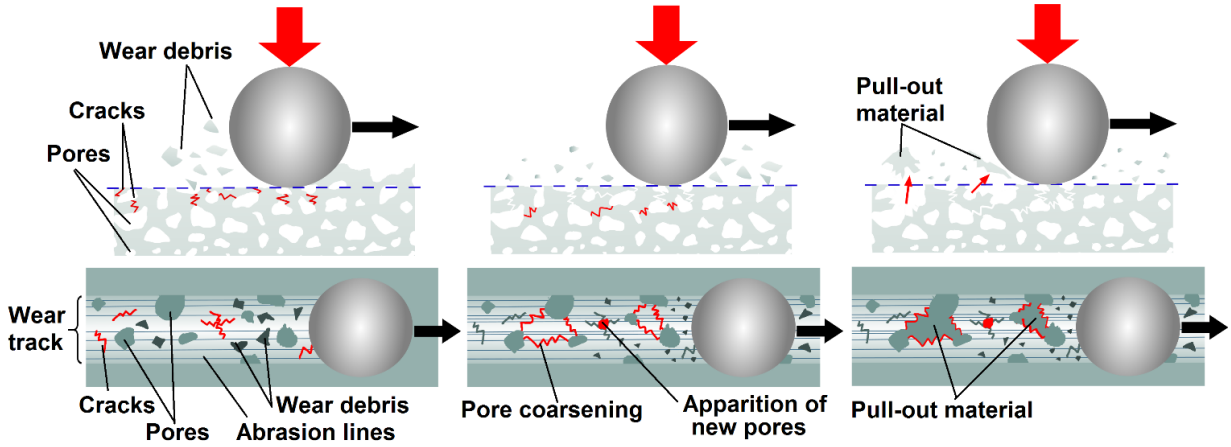

Stage 1: Removal of the topmost layer. Generation of wear debris, abrasion lines, uncovering of underneath porosity, and microcracks generation under the applied load due to pore presence beneath worn surface.

Stage 2: More abrasion lines are generated. Crack propagation leads to pore coarsening beneath the wear track. New pores are revealed.

Stage 3: Pore coarsening leads to material pull-out, leaving a brittle-like appearance.

Fig. 5.6.23 Schematic of the wear mechanism for the PEO layer of the TSA/PEO duplex coating at dry conditions

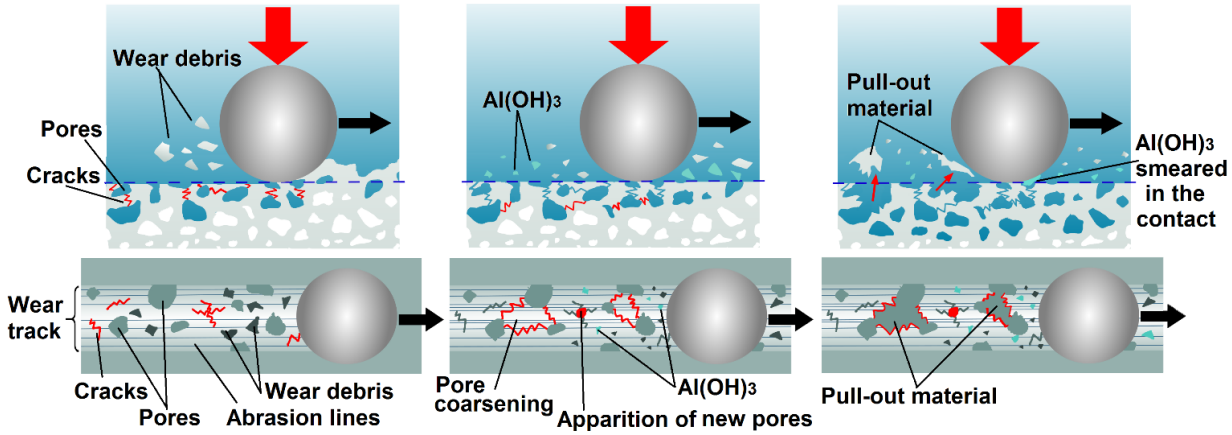

Stage 1: Removal of the topmost layer. Generation of wear debris, abrasion lines, uncovering of underneath porosity, and microcracks generation under the applied load due to pore presence beneath worn surface.

Stage 2: More abrasion lines are generated. Crack propagation leads to pore coarsening beneath the wear track. New pores are revealed. Penetration of electrolyte through cracks and pores. Reaction of wear debris to form aluminum hydroxides.

Stage 3: Pore coarsening leads to material pull-out, leaving a brittle-like appearance. Aluminum hydroxides are sheared in the contact providing certain lubricity to the system. Deeper penetration of electrolyte through the paths generated.

Fig. 5.6.24 Schematic of the tribocorrosion mechanism for the PEO layer in the TSA/PEO duplex coating in synthetic seawater

The topography of the samples surface is presented in the images obtained with the confocal microscope in Fig. 5.6.25, where the wear track size can be compared at a glance. In all cases, the wear track is wider and deeper in the dry tests. The topography of the unworn surface of the steel is different in both tests, showing a smooth surface in the dry abrasion test, and a rather rough appearance in the tribocorrosion test sample. The wear-accelerated corrosion undergone in seawater during the sliding tests led to an increase in roughness [6,7]. The porous surface of the TSA and TSA/PEO coatings is evident in the images, showing little difference between the dry and wet conditions in the duplex coating. In the TSA, however, greater and deeper porosity can be observed for the tribocorrosion specimen. This could be related with a certain dissolution of the aluminum reacting with seawater.

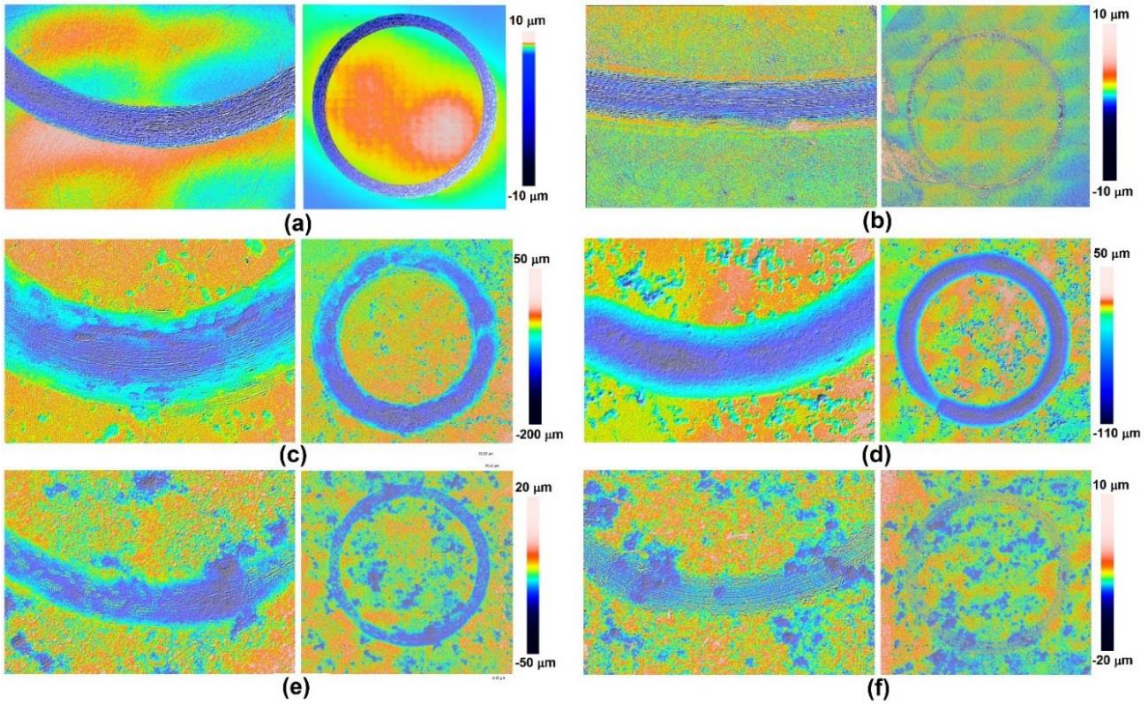

Fig. 5.6.25 Topography of the wear tracks generated in the (a) steel, (c) TSA, and (e) TSA/PEO in the dry sliding test, and in the (b) steel, (d) TSA, and (f) TSA/PEO in the tribocorrosion tests in seawater

The cross-section profiles of the wear tracks are plotted together in Fig. 5.6.26a, and the material loss obtained from the wear track volumes is represented in Fig. 5.6.26b and compiled in Table 5.6.6. The greater wear track, and accordingly the higher material loss, was measured for the TSA coating in dry abrasion test, followed by the TSA specimen tested in seawater. The depth of the track in dry conditions close to 200 microns confirms the removal of a great part of the sprayed layer, which original thickness was close to 270 microns (). The depth of the track in tribocorrosion conditions is around 120 microns. The tracks of the R4 steel and TSA/PEO coating in dry abrasion tests were very similar. The slightly greater material loss obtained for the latter can be attributed to a more brittle wear mechanism, and fast and easy removal of the outer porous layer. The track depth close to 50 microns coincides with the original thickness measured for the top porous layer (see Section 5.6.3.1), confirming the previous statement. The wear track of the steel in tribocorrosion tests was small in comparison with the dry condition sample. The material loss of the TSA/PEO coating could not be quantified, as the track depth was in the order of the roughness degree of the sample. A slight smoothing of the peaks in the wear track can be noticed in the cross-section, and abrasion lines are visible in the topography in Fig. 5.6.25d, but the wear was found to be negligible. This confirms that there was just a partial removal of the top porous layer in tribocorrosion test.

Consequently, the wear performance of the as-sprayed coating is considerably improved by PEO treatment, leading to lower material losses, especially in tribocorrosion conditions.

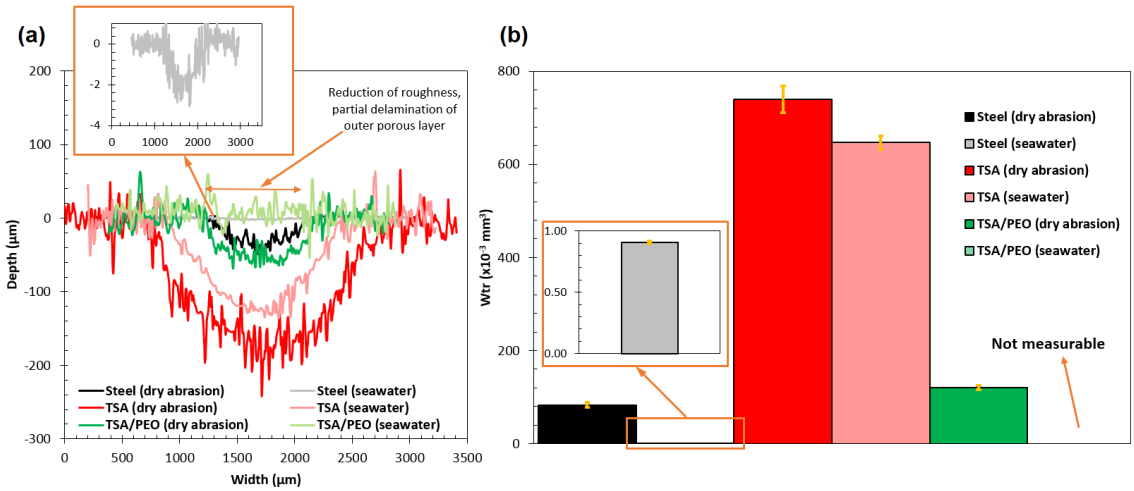

Fig. 5.6.26 Fig. 1 (a) Cross-section profiles of the wear tracks obtained in dry abrasion and tribocorrosion tests (4000 cycles at 100 rpm under 5N), and (b) material loss obtained from the wear track volume

5.6.4 **Conclusions**

The objective of this work was to investigate the enhancement of wear and tribocorrosion behavior of a PEO-modified TSA coating used in the protection of submerged components in offshore applications. For this aim, electrochemical corrosion tests, dry abrasion tests, and tribocorrosion tests have been performed comparing the results of the steel substrate, the as-sprayed aluminum coating, and the newly developed TSA/PEO duplex system. From the results obtained in this work, the following conclusions can be drawn:

- The PEO coating generated on top of the TSA presented a three-layered structure with a dense inner barrier in the interface with the TSA coating, showing an appropriate bonding strength to the sprayed layer.
- The corrosion tests confirmed the good barrier properties of the TSA/PEO duplex system, as a combination of the retarding and blocking effects provided by the PEO oxide layer, and the passivation given by the aluminum layer. The PDP and EIS results showed an improvement with respect to the as-sprayed coating, which durability could be expected to be lower due to aluminum dissolution through galvanic corrosion reaction with the steel substrate.
- The electrochemical response of the PEO coating was not affected by sliding, in terms of noticeable variations in the OCP and EIS results, indicating an improvement in the tribocorrosion resistance of the as-sprayed coating.
- The tribological behavior of the TSA coating was improved by the PEO treatment, showing smaller material losses at both dry and tribocorrosion conditions, and lower COF in tribocorrosion conditions. The high COF registered at dry abrasion tests was attributed to the contact between two hard Al_2O_3 materials. Nonetheless, the material loss was considerably smaller than that in the TSA coating.
- The wear mechanism of the PEO layer in the duplex coating was found to be a combination of abrasion and microfracture, whereas the tribocorrosion

mechanism was composed of abrasion, microfracture and tribochemical wear (corrosion delamination fatigue).

- Therefore, the TSA coating modified by PEO technique showed an improvement of the long-term corrosion behavior, and an enhancement of the wear and tribocorrosion resistance due to the high hardness and the ceramic nature of the generated oxide layer.

5.6.5 Acknowledgments

This work was performed with the support of the EMAITEK Initiative and the FRONTIERS project, both financed by the Basque Country. Authors would also like to acknowledge the Education, Linguistic Politics and Culture Department of the Basque Government for its support through the grant "*Programa Predoctoral de Formación de Personal Investigador No Doctor (PRE_2017_2_0088)*" awarded to the first author.

5.6.6 References

[1] R.W. Revie, H.H. Uhlig (Eds.). *Corrosion and Corrosion Control: An Introduction to Corrosion Science and Engineering (4th edition).* Wiley-Interscience, 2008. http://onlinelibrary.wiley.com/book/10.1002/9780470277270

[2] A.W. Momber, T. Marquardt. *Protective coatings for offshore wind energy devices (OWEAs): a review*. Journal of Coatings and Technology Research 15 (2018) 13–40

[3] R.E. Melchers, T. Moan, Z. Gao. *Corrosion of working chains continuously immersed in seawater*. Journal of Marine Science and Technology 12 (2007) 102–110

[4] A.O. Vazquez-Hernandez, G.B. Ellwanger, L.V.S. Sagrilo. *Reliability-based comparative study for mooring lines design criteria*. Applied Ocean Research 28 (2006) 398–406

[5] A.O. Vázquez-Hernández, G.B. Ellwanger, L.V.S. Sagrilo. *Long-term response analysis of FPSO mooring systems*. Applied Ocean Research 33 (2011) 375–383

[6] A. López, R. Bayón, F. Pagano, A. Igartua, A. Arredondo, J.L. Arana, J.J. González. *Tribocorrosion behaviour of mooring high strength low alloy steels in synthetic seawater*. Wear. 338-339 (2015) 1–10

[7] A. López-Ortega, R. Bayón, J.L. Arana, A. Arredondo, A. Igartua. *Influence of temperature on the corrosion and tribocorrosion behaviour of High-Strength Low-Alloy steels used in offshore applications*. Tribology International 121 (2018) 341–352

[8] M.N. Dhanak, I. Xiros (Eds.). *Springer Handbook of Ocean Engineering*. Springer Handbook (2016) ISBN 978-3-319-16649-0

[9] A.W. Momber, P. Plagemann, V. Stenzel. *Performance and integrity of protective coating systems for offshore wind power structures after three years under offshore site conditions*. Renewable Energy 74 (2015) 606–617

[10] M. Kutz (Ed.). *Handbook of environmental degradation of materials (2nd edition)*. Elsevier (2012) ISBN: 978-1-4377-3455-3

[11] J.-P. Celis, P. Ponthiaux (Eds.). *Testing tribocorrosion of Passivating Materials Supporting Research and Industrial Innovation: Handbook*. Maney Publishing UK (2012) ISBN 978-1-907975-20-2

[12] P. Ponthiaux, F. Wenger, J.-P. Celis. *Tribocorrosion: Material Behaviour Under Combined Conditions of Corrosion and Mechanical Loading*, Corrosion Resistance, in: Dr Shih (Ed.), In Tech (2012) ISBN: 978-953-51-0467-4

[13] D. Landolt, S. Mischler. *Tribocorrosion of Passive Metals and Coatings*. Woodheat Publishing (2011) ISBN 978-1-86469-966-6

[14] M. Iannuzzi, A. Barnoush, R. Johnsen. *Materials and corrosion trends in offshore and subsea oil and gas production*. Npj Materials Degradation 1 (2017)

[15] Y. Weng, H. Dong, Y. Gan (Eds.). *Advanced Steels. The Recent Scenario in Steel Science and Technology*. Springer (2011) ISBN: 978-3-642-17664-7

[16] H. Zhang, X. Wang, R. Jia, J. Hou, W. Guo. *Investigation on stress corrosion cracking behavior of welded High-Strength Low-Alloy steel in seawater containing various dissolved oxygen concentrations*. International Journal of Electrochemical Science 8 (2013) 1262-1273

[17] D.A. Skobir. *High-strength low-alloy (HSLA) steels*. Materials Tehnology 45 (2011) 295–301
[18] J.P. Ault. *The Use of Coatings for Corrosion Control on Offshore Oil Structures*. Journal of Protective Coatings and Linings. 23 (2006) 42–47.
[19] A. López-Ortega, R. Bayón, J.L. Arana. *Evaluation of protective coatings for offshore applications. Corrosion and tribocorrosion in synthetic seawater*. Surf. Coat. Technol. 349 (2018) 1083-1097
[20] R.J.K. Wood. *Tribo-corrosion of coatings: A review*. Journal of Physics D: Applied Physics 40 (2007) 5502–5521
[21] K. P. Fisher, W.H. Thomanson, T. Bosbrook, J. Murali. *Performance of Thermal-Sprayed Aluminium Coatings in Offshore Service*. Materials Performance 34 (1995) 27-35
[22] F.S. da Silva, J. Bedoya, S. Dosta, N. Cinca, I.G. Cano, J.M. Guilemany, A. V. Benedetti. *Corrosion characteristics of cold gas spray coatings of reinforced aluminum deposited onto carbon steel*. Corrosion Science 114 (2017) 57–71
[23] M. Mohedano, R. Arrabal, B. Mingo. *PEO of pre-anodized Al – Si alloys : Corrosion properties and influence of sealings*. Applied Surface Science 346 (2015) 57–67
[24] V. Dehnavi, B. Li, D.W. Shoesmith, X. Yang, S. Rohani. *Effect of duty cycle and applied current frequency on plasma electrolytic oxidation (PEO) coating growth behavior*. Surface & Coatings Technology 226 (2013) 100–107
[25] J. Martin, A. Melhem, I. Shchedrina, T. Duchanoy, A. Nominé, G. Henrion, T. Czerwiec, T. Belmonte. *Effects of electrical parameters on plasma electrolytic oxidation of aluminium*. Surface & Coatings Technology 221 (2013) 70–76
[26] G. Rapheal, S. Kumar, N. Scharnagl, C. Blawert. *Effect of current density on the microstructure and corrosion properties of plasma electrolytic oxidation (PEO) coatings on AM50 Mg alloy produced in an electrolyte containing clay additives*. Surface & Coatings Technology 289 (2016) 150–164
[27] R.O. Hussein, X. Nie, D.O. Northwood. *Production of high quality coatings on light alloys using Plasma Electrolytic Oxidation (PEO)*. WIT Transactions on Built Environment 166 (2017) 439-454
[28] Y. Jiang, Y. Zhang, Y. Bao, K. Yang. *Sliding wear behaviour of plasma electrolytic oxidation coating on pure aluminium*. Wear. 271 (2011) 1667–1670
[29] E. Matykina, R. Arrabal, A. Pardo, M. Mohedano, B. Mingo. *Energy-efficient PEO process of aluminium alloys*. Materials Letter 127 (2014) 13–16
[30] M. Treviño, N.F. Garza-Montes-de-Oca, A. Párez, M.A.L. Hernández-Rodíguez, A. Juárez, R. Colás. *Wear of an aluminium alloy coated by plasma electrolytic oxidation*. Surface & Coatings Technology 206 (2012) 2213–2219
[31] C. Liu, P. Liu, Z. Huang, Q. Yan, R. Guo, D. Li, G. Jiang, D. Shen. *The correlation between the coating structure and the corrosion behavior of the plasma electrolytic oxidation coating on aluminum*. Surface & Coatings Technology 286 (2016) 223–230
[32] E. Matykina, R. Arrabal, M. Mohedano, B. Mingo, J. Gonzalez, A. Pardo, M.C. Merino. *Recent advances in energy efficient PEO processing of aluminium alloys*. Transations of Nonferreous Metals Society of China 27 (2017) 1439-1454
[33] E. Matykina, R. Arrabal, P. Skeldon, G.E. Thompson. *Investigation of the growth processes of coatings formed by AC plasma electrolytic oxidation of aluminium*. Electrochimical Acta 54 (2009) 6767-6778
[34] V.S. Egorkin, S. V Gnedenkov, S.L. Sinebryukhov, I.E. Vyaliy, A.S. Gnedenkov, R.G. Chizhikov. *Increasing thickness and protective properties of PEO-coatings on aluminum alloy*. Surface & Coatings Technology 334 (2018) 29-42
[35] V. Dehnavi, D.W. Shoesmith, B. Li, M. Yari, X. Yang. *Corrosion properties of plasma electrolytic oxidation coatings on an aluminium alloy - The effect of the PEO process stage*. Materials Chemistry and Physics 161 (2015) 49–58
[36] B. Mingo, R. Arrabal, M. Mohedano, Y. Llamazares, E. Matykina, A. Yerokhin. *Influence of sealing post-treatments on the corrosion resistance of PEO coated AZ91 magnesium alloy*. Applied Surface Science 433 (2018) 653–667
[37] W.C. Gu, G.H. Lv, H. Chen, G.L. Chen, W.R. Feng, G.L. Zhang, S.Z. Yang. *Preparation of ceramic coatings on inner surface of steel tubes using a combined technique of hot-dipping and plasma electrolytic oxidation*. Journal of Alloys and Compounds 430 (2007) 308–312
[38] L. Lihong, S. Dejiu, Z. Jingwu, S. Jian, L. Liang. *Evolution of micro-arc oxidation behaviors of the hot-dipping aluminum coatings on Q235 steel substrate*. Applied Surface Science. 257 (2011) 4144-4150

[39] W. Gu, D. Shen, Y. Wang, G. Chen, W. Feng, G. Zhang, S. Fan, C. Liu, S. Yang. *Deposition of duplex Al_2O_3/aluminum coatings on steel using a combined technique of arc spraying and plasma electrolytic oxidation*. Applied Surface Science 252 (2006) 2927–2932

[40] Offshore Standard DNVGL-OS E302, Det Norske Veritas, *Offshore Mooring Chains*, July 2018

[41] D.J. Varacalle, D.P. Guillen, D.M. Deason, W. Rhodaberger, E. Sampson. *Effect of grit-blasting on substrate roughness and coating adhesion*. Journal Therm. Spray Technol. 15 (2006) 348-355

[42] D. Sen, N.M. Chavan, D.S. Rao, G. Sundararajan. *Influence of grit blasting on the roughness and the bond strength of detonation sprayed coating*. Journal of Thermal Spraying Technology. 19 (2010) 805-815

[43] Gwidon W. Stachowiak, Andrew W. Batchelor. *Engineering Tribology*. Butterworth Heinemann, UK (2005) ISBN: 978-0-7506-7836-0

[44] Y. Sun, E. Haruman. *Effect of electrochemical potential on tribocorrosion behavior of low temperature plasma carburized 316L stainless steel in 1M H2SO4 solution*. Surface & Coatings Technology 205 (2011) 4280–4290

[45] I.C. Park, S.J. Kim. *Electrochemical characteristics in seawater for cold thermal spray-coated Al-Mg alloy layer*. Acta Metallurgica Sinica (English Lett.) 29 (2016) 727–734

[46] T.C. Chen, C.C. Chou, T.Y. Yung, K.C. Tsai, J.Y. Huang. *Wear behavior of thermally sprayed Zn/15Al, Al and Inconel 625 coatings on carbon steel*. Surface & Coatings Technology 303 (2016) 78–85

[47] M. Campo, M. Carboneras, M.D. López, B. Torres, P. Rodrigo, E. Otero, J. Rams. *Corrosion resistance of thermally sprayed Al and Al/SiC coatings on Mg*. Surface & Coatings Technology 203 (2009) 3224–3230

[48] H.-S. Lee, J. Singh, M. Ismail, C. Bhattacharya. *Corrosion Resistance Properties of Aluminum Coating Applied by Arc Thermal Metal Spray in SAE J2334 Solution with Exposure Periods*. Metals (Basel). 6 (2016) 55

[49] M.S. Han, Y.B. Woo, S.C. Ko, Y.J. Jeong, S.K. Jang, S.J. Kim. *Effects of thickness of Al thermal spray coating for STS 304*. Transactions of Nonferrous Metals Society of China (English Ed. 19 (2009) 925–929

[50] S. Deshpande, A. Kulkarni, S. Sampath, H. Herman. *Application of image analysis for characterization of porosity in thermal spray coatings and correlation with small angle neutron scattering*. Surface & Coatings Technology 187 (2004) 6–16

[51] P. Fauchais and A. Vardelle (2012). *Thermal Sprayed Coatings Used Against Corrosion and Corrosive Wear, Advanced Plasma Spray Applications*. Dr. Hamid Jazi (Ed.), ISBN: 978-953-51-0349-3. InTech, Available from: http://www.intechopen.com/books/advanced-plasma-spray-applications/thermal-sprayed-coatings-usedagainst-corrosion-and-corrosive-wear

[52] E. Abedi Esfahani, H. Salimijazi, M.A. Golozar, J. Mostaghimi, L. Pershin. *Study of corrosion behavior of Arc sprayed aluminum coating on mild steel*. Journal of Thermal Spraying Technology. 21 (2012) 1195–1202

[53] H.S. Lee, J.K. Singh, J.H. Park. *Pore blocking characteristics of corrosion products formed on Aluminum coating produced by arc thermal metal spray process in 3.5 wt.% NaCl solution*. Construction and Building Materials 113 (2016) 905–916.

[54] X. Lu, M. Mohedano, C. Blawert, E. Matykina, R. Arrabal, K. Ulrich, M.L. Zheludkevich, *Plasma electrolytic oxidation coatings with particle additions – A review*. Surface & Coatings Technology 307 (2016) 1165–1182

[55] ISO 12944-9. *Paints and varnishes. Corrosion protection of steel structures by protective paint systems. Part 9: Protective Paint systems and laboratory performance test methods for offshore and related structures*. First edition, January 2018

[56] ISO 12944-1. *Paints and varnishes- Corrosion protection of steel structures by protective paint systems. Part 2: Classification of environments*. Second edition, November 2017

[57] T. V. Shibaeva, V.K. Laurinavichyute, G. a. Tsirlina, A.M. Arsenkin, K. V. Grigorovich. *The effect of microstructure and non-metallic inclusions on corrosion behavior of low carbon steel in chloride containing solutions*. Corrosion Sceince 80 (2014) 299–308

[58] U. Trdan, J. Grum. *Evaluation of corrosion resistance of AA6082-T651 aluminium alloy after laser shock peening by means of cyclic polarisation and EIS methods*. Corrosion Science 59 (2012) 324–333

[59] H. Ezuber, a. El-Houd, F. El-Shawesh. *A study on the corrosion behavior of aluminum alloys in seawater*. Materials & Design 29 (2008) 801–805

[60] R. Baboian (Ed.). *NACE Corrosion Engineer's Reference Book. (3rd edition)*. NACE International (2002) ISBN: 978-1-57590-127-5
[61] H.S. Lee, J.K. Singh, M.A. Ismail. *An effective and novel pore sealing agent to enhance the corrosion resistance performance of Al coating in artificial ocean water*. Scientific Reports 7 (2017)
[62] N. Espallargas, C. Torres, A.I. Muñoz. *A metal ion release study of CoCrMo exposed to corrosion and tribocorrosion conditions in simulated body fluids*. Wear 332-333 (2014) 669–678
[63] N. Espallargas, R. Johnsen, C. Torres, A.I. Muñoz. *A new experimental technique for quantifying the galvanic coupling effects on stainless steel during tribocorrosion under equilibrium conditions*. Wear 307 (2013) 190–197
[64] Y. Yan (Ed.). *Bio-Tribocorrosion in Biomaterials and Medical Implants*. Woodhead Publishing (2013), ISBN 978-0-85709-540-4
[65] E. McCafferty. *Introduction to corrosion science*. Springer (2010) ISBN 978-1-4419-0455-3.
[66] K. Spencer, D.M. Fabijanic, M.X. Zhang. *The use of Al-Al_2O_3 cold spray coatings to improve the surface properties of magnesium alloys*. Surface & Coatings Technology 204 (2009) 336–344
[67] Q. Jiang, Q. Miao, F. Tong, Y. Xu, B.L. Ren, Z.M. Liu, Z.J. Yao. *Electrochemical corrosion behavior of arc sprayed Al-Zn-Si-RE coatings on mild steel in 3.5% NaCl solution*. Transactions of Nonferrous Metals Society of China 24 (2014) 2713–2722
[68] W. Liu, Q. Zhou, L. Li, Z. Wu, F. Cao, Z. Gao. *Effect of alloy element on corrosion behavior of the huge crude oil storage tank steel in seawater*. Journal of Alloys and Compounds 598 (2014) 198–204
[69] N. Imaz, M. Ostra, M. Vidal, J.A. Díez, M. Sarret, E. García-Lecina. *Corrosion behaviour of chromium coatings obtained by direct and reverse pulse plating electrodeposition in NaCl aqueous solution*. Corrossion Science 78 (2014) 251–259
[70] F. El-Taib Heakal, N.S. Tantawy, O.S. Shehta. *Influence of chloride ion concentration on the corrosion behavior of Al-bearing TRIP steels*. Materials Chemistry & Physics 130 (2011) 743–749
[71] D. Yang, O. Rosas, H. Castaneda. *$FeCO_3$layer evolution for API 5L X52 steel in carbon dioxide-saturated NaCl brine in the presence of 1-decyl-3-methylimidazolium chloride*. Corrosion Science 87 (2014) 40–50
[72] U. Trdan, J. Grum. *SEM/EDS characterization of laser shock peening effect on localized corrosion of Al alloy in a near natural chloride environment*. Corrosion Science 82 (2014) 328–338
[73] N.M. Chavan, B. Kiran, A. Jyothirmayi, P.S. Phani, G. Sundararajan. *The corrosion behavior of cold sprayed zinc coatings on mild steel substrate*. Journal of Thermal Spraying Technology. 22 (2013) 463–470
[74] T. Arunnellaiappan, S. Arun, S. Hariprasad, S. Gowtham, B. Ravisankar, L. Rama Krishna, N. Rameshbadu. *Fabrication of corrosion resistant hydrophobic ceramic nanocomposite coatings on PEO treated AA7075*. Ceramics International 44 (2018) 874–884
[75] A. Venugopal, R. Panda, S. Manwatkar, K. Sreekumar, L.R. Krishna, G. Sundararajan. *Effect of micro arc oxidation treatment on localized corrosion behaviour of AA7075 aluminum alloy in 3.5 NaCl solution*. Transactions of Nonferrous Metals Society of China (English Ed. 22 (2012) 700–710
[76] J.B. Bajat, R. Vasilić, S. Stojadinović, V. Mišković-Stankovic. *Corrosion stability of oxide coatings formed by plasma electrolytic oxidation of aluminum: Optimization of process time*, Corrosion. 69 (2013) 693–702
[77] G.L. Song, Z. Shi. *Corrosion mechanism and evaluation of anodized magnesium alloys*. Corrosion Science 85 (2014) 126–140
[78] M. Gao, W. Lu, B. Yang, S. Zhang, J. Wang. *High corrosion and wear resistance of Al-based amorphous metallic coating synthesized by HVAF spraying*. Journal of Alloys & Compounds 735 (2018) 1363–1373
[79] E. Barsoukov, J.R. Macdonald (Eds.). *Impedance Spectroscopy: Theory, Experiment and Applications*. Wiley-Interscience (2005) ISBN: 0-471-64749-7
[80] M. Mohedano, R. Arrabal, B. Mingo, A. Pardo, E. Matykina. *Role of particle type and concentration on characteristics of PEO coatings on AM50 magnesium alloy*. Surface & Coatings Technology 334 (2018) 328–335

[81] J.K. Saha. *Corrosion of Constructional Steels in Marine and Industrial Environment.* Springer India (2013), ISBN: 978-81-322-0719-1
[82] K. Xiao, C. Dong, X. Li, F. Wang. *Corrosion Products and Formation Mechanism During Initial Stage of Atmospheric Corrosion of Carbon Steel*. Journal of Iron and Steel Research, International 15 (2008) 42–48
[83] J.G. Castaño, C. a. Botero, a. H. Restrepo, E. a. Agudelo, E. Correa, F. Echeverría. *Atmospheric corrosion of carbon steel in Colombia*. Corrosion Science 52 (2010) 216–223
[84] H. Möller, E.T. Boshoff, H. Froneman. *The corrosion behaviour of a low carbon steel in natural and synthetic seawaters*. The Journal of The South African Institute of Mining and Metallurgy, 106 (2006) 585–592.
[85] R.E. Melchers, R. Jeffrey. *Early corrosion of mild steel in seawater*. Corrosion Science 47 (2005) 1678–1693
[86] R.E. Melchers. *Effect of marine immersion corrosion of carbon content of low alloy Steels*. Corrosion Science 45 (2003) 2609–2625
[87] J. Bhandari, F. Khan, R. Abbassi, V. Garaniya, R. Ojeda. *Modelling of pitting corrosion in marine and offshore Steel structures-A technical review*. Journal of Loss Prevention in the Process Industries 37 (2015) 39-62
[88] M.R. Garsivaz Jazi, M.A. Golozar, K. Raeissi, M. Fazel. *Evaluation of corrosion and tribocorrosion of plasma electrolytic oxidation treated Ti-6Al-4V alloy*. Surface & Coatings Technology 244 (2014) 29–36
[89] V.S. De Viteri, R. Bayón, A. Igartua, G. Barandika, J.E. Moreno, C.P. Peremarch, M.M. Pérez. *Structure, tribocorrosion and biocide characterization of Ca, P and I containing TiO 2 coatings developed by plasma electrolytic oxidation*. Applied Surface Science 367 (2016) 1–10
[90] M. Fazel, H.R. Salimijazi, M.A. Golozar, M.R. Garsivaz Jazi. *A comparison of corrosion, tribocorrosion and electrochemical impedance properties of pure Ti and Ti6Al4V alloy treated by micro-arc oxidation process*. Applied Surface Science 324 (2015) 751–756
[91] S.A. Alves, R.B. V Saénz, D.V.M.P. Garcia. *Tribocorrosion Behavior of Calcium- and Phosphorous-Enriched Titanium Oxide Films and Study of Osteoblast Interactions for Dental Implants*. Journal of Bio- and Tribo- Corrosion 1 (2015) 1–21
[92] M.T. Mathew, M.J. Runa, M. Laurent, J.J. Jacobs, L.A. Rocha, M.A. Wimmer. *Tribocorrosion behavior of CoCrMo alloy for hip prosthesis as a function of loads: A comparison between two testing systems*. Wear. 271 (2011) 1210–1219
[93] M.J. Runa, M.T. Mathew, M.H. Fernandes, L.A. Rocha. *First insight on the impact of an osteoblastic layer on the bio-tribocorrosion performance of Ti6Al4V hip implants*. Acta Biomaterialia 12 (2015) 341–351
[94] S.A. Alves, A.L. Rossi, A.R. Ribeiro, F. Toptan, A.M. Pinto, T. Shoukuhfar, J.-P. Celis, L.A. Rocha. *Improved tribocorrosion performance of bio-functionalized TiO2 nanotubes under two-cycle sliding actions in artificial saliva*. Journal of Mechanical Behaviour of Biomedical Materials 80 (2018) 143-154
[95] M. Ghafaripoor, K. Raeissi, M. Santamaria, A. Hakimizad. *The corrosion and tribocorrosion resistance of PEO composite coatings containing α-Al2O3 particles on 7075 Al alloy*. Surface & Coatings Technology 349 (2018) 470-479
[96] S. Hiromoto, S. Mischler. *The influence of proteins on the fretting-corrosion behaviour of a Ti6Al4V alloy*. Wear 261 (2006) 1002–1011
[97] Y. Zhang, X. Yin, J. Wang, F. Yan. *Effect of halide concentration on tribocorrosion behavior of 304SS in artificial seawater*. Corrosion Science 99 (2015) 272–280
[98] R.I. Trezona, D.N. Allsopp, I.M. Hutchings. *Transitions between two-body and three-body abrasive wear: influence of test conditions in the microscale abrasive wear test*. Wear 225-229 (1999) 205–214
[99] D. Landolt, S. Mischler, M. Stemp, S. Barril. *Third body effects and material fluxes in tribocorrosion systems involving a sliding contact*. Wear 256 (2004) 517–524
[100] N. Diomidis, S. Mischler. *Third body effects on friction and wear during fretting of steel contacts*. Tribology International 44 (2011) 1452–1460
[101] S.B. Pitchuka, B. Boesl, C. Zhang, D. Lahiri, A. Nieto, G. Sundararajan, A. Agarwal. *Dry sliding wear behavior of cold sprayed aluminum amorphous/nanocrystalline alloy coatings*. Surface & Coatings Technology 238 (2014) 118–125
[102] D. Lahiri, P.K. Gill, S. Scudino, C. Zhang, V. Singh, J. Karthikeyan, N. Munroe, S. Seal, A. Agarwal. *Cold sprayed aluminum based glassy coating: Synthesis, wear and corrosion properties*. Surface & Coatings Technology 232 (2013) 33–40

[103] D. Cong, Z. Li, Q. He, H. Chen, Z. Zhao, L. Zhang, H. Wu. *Wear behavior of corroded Al-Al_2O_3 composite coatings prepared by cold spray*. Surface & Coatings Technology 326 (2017) 247–254
[104] B. Bhushan. *Introduction to tribology. Second Edition*. Willey (2013) ISBN: 978-1-119-94453-9
[105] Y. Erarslan. *Wear performance of in-situ aluminum matrix composite after micro-arc oxidation*. Transactions of Nonferrous Metals Society of China 23 (2013) 347–352
[106] M.G. Gee. *The formation of aluminium hydroxide in sliding wear of alumina.* Wear 153 (1992) 201-227
[107] T.E. Fischer, W. M. Mullins. *Chemical Aspects of Ceramic Tribology*. Journal of Chemistry and Physics 96 (1992) 5690-5701
[108] F. Zhou, Y. Wang, H. Ding, M. Wang, M. Yu, Z. Dai. *Friction characteristic of micro-arc oxidative Al_2O_3 coatings sliding against Si_3N_4 balls in various environments*. Surface & Coatings Technology 202 (2008) 3808–3814
[109] H. Ding, Z. Dai, S.C. Skuiry, D. Hui. *Tribology International Corrosion wear behaviors of micro-arc oxidation coating of Al_2O_3 on 2024Al in different aqueous environments at fretting contact*. Tribiology International 43 (2010) 868–875
[110] H.C. Wong, N. Umehara, K. Nato, K. Nii. *Fundamental study of water-lubricated ceramic bearings*. Transcactions of the Japan Society of Mechanical Engineers 61 (1995) 4073-4032
[111] M. Javidi, H. Fadaee. *Plasma electrolytic oxidation of 2024-T3 aluminum alloy and investigation on microstructure and wear behavior*. Applied Surface Science. 286 (2013) 212-219
[112] X. Nie, E.I. Meletis, J.C. Jiang, A. Leyland, A.L. Yerokhin, A. Matthews. *Abrasive wear y corrosion properties and TEM analysis of Al_2O_3 coatings fabricated using plasma electrolysis*. Surface & Coatings Technology 149 (2002) 245–251
[113] D. Schaupp, J. Schneider, K.H. Zum Gahr. *Wear mechanisms on multiphase Al_2O_3 ceramics during running-in period in unlubricated oscillating sliding contact*. Tribology Letters 9 (2001) 125–131
[114] B. Bushan (Ed.). *Modern Tribology Handbook. Volume one. Principles of Tribology*. CRC Press (2001) ISBN: 0-8493-8403-6

Contribution 7

Development of a superhydrophobic and bactericide organic topcoat to be applied on Thermally Sprayed Aluminum coatings in offshore submerged components

Submitted for publication in Progress in Organic Coatings

Contribution 7: Submitted for publication in Progress in Organic Coatings

5.7. DEVELOPMENT OF A SUPERHYDROPHOBIC AND BACTERICIDE ORGANIC TOPCOAT TO BE APPLIED ON THERMALLY SPRAYED ALUMINIUM COATINGS IN OFFSHORE SUBMERGED COMPONENTS

A. López-Ortega[a], O. Areitioaurtena[a], I. Elexpe[a], S. Alves[a], A.M. Goitandia[a], J.L. Arana[b], R. Bayón[a]

[a] *IK4-TEKNIKER, Eibar, Spain*
[b]*Department of Metallurgical and Materials Engineering, University of the Basque Country, Spain*

ABSTRACT

Marine environment is a very aggressive working atmosphere, where metals are subjected to corrosion and biological attacks, among other phenomena. The protection of steel components and structures has been achieved by means of protective coatings, including coatings with antifouling characteristics to avoid microbiological corrosion. In this work, an organic topcoat usually applied on top of Thermally Sprayed Aluminum (TSA) coatings has been functionalized. The paint was provided with superhydrophobic and antibacterial characteristics by the addition of SiO_2 nanoparticles and biocide agents to its composition. Three biocide agents were evaluated, and the best one was selected by means of wettability and bacterial activity tests. The adhesion of the paint was measured, and ecotoxicity of the paint was analyzed in aqueous marine environment. Finally, weathering aging tests were performed to evaluate the corrosion protection ability of the coatings for its use in aggressive atmospheres.

Keywords: *Offshore; Coatings; Antifouling; Ecotoxicity;*

5.7.1 Introduction

Marine environment is a very aggressive working atmosphere that comprises several phenomena that can accelerate the degradation of structural materials reducing their useful life. The exposition to ultraviolet radiation, chloride-rich salty environment, frequent wet-dry cycles, high humidity, low temperature, the presence of marine bacteria and microorganisms, are some examples. One of the phenomena that worst affect the deterioration of materials in offshore applications is corrosion. The high salinity and low electrical resistivity of seawater make this environment especially aggressive [1]. Along with marine corrosion, marine biofouling is another natural phenomenon representing the most significant problems in marine technology [2]. Offshore structures such as platforms, vessels, drilling pipes or mooring lines are subjected to biological attack [3]. Marine biofouling can be defined as the undesirable accumulation of microorganisms, algae, and animals on submerged structures in seawater [4-7]. When bacteria attach themselves onto metallic surfaces, they start to form a thin film known as biofilm, which can rapidly cover the surface of steel in natural environments [6,8]. The net result of the biofilm formation is that it usually creates concentration gradients of chemical species across its thickness, which can enhance corrosion on the metal surface [3,6-8]. The corrosion process that is initiated or accelerated by the activity of microorganisms is known as Microbiologically Influenced Corrosion (MIC). MIC has been reported to cause 2-3 mm of materials loss in the form of pits [9,10].

In order to prevent the colonization of microorganisms, antifouling (AF) paints have been widely employed in marine environments [4,5,11]. These paints were firstly used in boat

hulls, where the presence of fouling increases the drag friction and weight, thus, incrementing the fuel consumption up to a 40% [12] (around a 6% for every 100 µm increase in surface roughness [13]), and reducing the speed in a 70% [4,11]. AF paints have also been used in static structures such as buoys, pipelines and drilling platforms [14,15], in order to reduce MIC in submerged structures and components. The use of AF protection can save up to EUR 4.8 billion[vii] per year worldwide [4,16,17]. The former AF paints were formulated adding extremely toxic organotin, e.g., tributyltin oxide or TBT. These paints were characterized by a gradual release of biocide agents, also known as self-polishing [2]. However, TBT was found to be extremely toxic, and its use was banned in the EU in 2003, and globally in 2008 by the Maritime Organization [2,4,16,18,19]. Different formulations and technologies have been used thenceforth. The predominant biocide after the ban of TBT has been copper [2,5,17,16,20]. This element can be found naturally in marine environments, but it becomes toxic when exceeding the threshold of the organism tolerance of marine species [3,16]. The use of copper-based AF paints is regulated in some countries, according to the copper release rate. For instance, the allowance in Canada is of 40 µg/cm^2/day, whereas that in Denmark is 200 µg/cm^2 over the first 14 days [16]. Paints are usually loaded with high amounts of copper oxide (Cu_2O) and algaecide co-biocides or boosters, e.g., Irgarol 1051, diuron or chlorothalonil [4,11,15,16,19,21]. Currently, there are approximately 23 boosters in use [19], and some of them have been restricted in some countries [4,16,18]. Several studies have demonstrated that the addition of nanoparticles to paints formulation provide the paint with antibacterial ability. This is related to their peculiar physical, chemical, and biological properties, as well as to their high surface/volume ratio, which make their interaction with bacteria highly effective [22-24]. Three of the most promising nanoparticles for biocide applications are the copper oxide (CuO) [2], silicon dioxide (SiO_2) [25], and zirconium dioxide (ZrO_2) [26].

More recently alternatives in AF technologies include non-toxic formulations based on controlling the physicochemical and mechanical properties. This is achieved by controlling the surface free energy, surface topography or the wettability, modifying the interaction between the surface and marine microorganisms [2,3,27]. Hydrophobic surfaces, for instance, have been found to easily release bacteria and microorganisms from the surface inhibiting their settlement. Superhydrophobic surfaces prevent the sticking of organisms due to their low free energy surface. The minimization of intermolecular forces of interactions between microorganisms and the surface leads to an easy release of the adhered organisms under low shear stresses [28]. Superhydrophobic films have been achieved by using silica nanoparticles [25,27,29-31] or carbon nanotubes [27,32,33], among others. Furthermore, silica nanoparticles have been found to provide not only hydrophobicity properties but also bactericide ability [2] and corrosion resistance [34,35] to the paint.

The requirements of protective coatings and their application procedures vary significantly depending on the installation location, i.e., onshore or offshore. Currently, the protection systems used in offshore structures are regulated by several standards, among which the ISO 12944:1-9 (2018) [36] and the NORSOK M-501 (2012) [37] can be found. The selection of the protective system profoundly depends on the location of the component. According to the ISO 12944-2 and ISO 9223 [38], there are five corrosivity categories; from the C1 corresponding to a non-corrosive atmosphere, to industrial and marine corrosive categories (C5-I and C5-M). There are also IM1 and IM3 categories, to describe the water and soil corrosivity, respectively. The first edition of the

[vii] *Currency expressed in American billion (10^9)*

ISO 12944-9 [39] published in January 2018, adds new categories for offshore related atmospheres: CX-offshore (atmospheric), Im4 (immersion), and CX-Offshore/Im4 (splash and tidal exposure zones). The standard also classifies the durability or the time for the first major maintenance of the coatings as:

- Low (L): 2 to 5 years
- Medium (M): 5 to 15 years
- High (H): 15 to 25 years
- Very High (VH): >25 years

In previous works, the corrosion and tribocorrosion of several coating used in offshore applications have been assessed [40,41]. One of those coatings was a Thermally Sprayed Aluminum (TSA) with an organic topcoat. TSA coatings have been widely used for the protection of submerged components [42,43], providing effective service life for 30 years in different exposure zones [43-45]. The use of an organic layer on top of sprayed coatings is recommended to seal pores and defects, enhancing the coating lifetime [37]. The present study aims to functionalize the performance of both the TSA layer and the organic topcoat. In the first part of this work, the wear response of the TSA was enhanced by Plasma Electrolytic Oxidation (PEO) technique [46]. In the second part of the work, compiled within this paper, the organic topcoat paint is functionalized by means of nanoparticle incorporation to provide it with hydrophobic and antibacterial abilities, i.e., antifouling properties. The nanoparticles selected for this aim have already been employed to formulate hydrophobic or bactericide paints, but little is known on the properties of the paint when incorporating both nanoparticle types simultaneously. The paint obtained in this work was evaluated in terms of wettability, antibacterial activity, ecotoxicity, and weathering aging tests. The latter are currently employed to evaluate and validate the corrosion protection ability of coatings for their use in aggressive atmospheres. The coatings were aged in different cabinets according to ISO 12944 and NORSOK M-501 standards.

5.7.2 Materials and methods

5.7.2.1 Materials

The test samples were R4 steel grade [47] plates. This is a High-Strength Low-Alloyed steel usually used in the manufacturing of chains, connector and other accessories composing the mooring lines employed in offshore floating platforms. The test panels were extracted from real chain components and coated by arc Thermal Spray technique with an aluminum layer (TSA). Some of the panels were treated by Plasma Electrolytic Oxidation (PEO), in order to enhance the wear performance of the sprayed aluminum. All the details on the TSA and PEO processes parameters, coatings properties and morphologies were explained previously [46]. The dimensions of the panels were 50x75x8mm.

The topcoat paint selected for its functionalization was the Carboguard® paint from Carboline®. This paint is usually employed on top of TSA coatings for the protection of submerged components. For the different tests and evaluations carried out in this work, the original Carboguard coating was applied on the TSA coating, whereas the modified Carboguard paint was applied on top of the newly developed TSA/PEO duplex coating system.

Three different biocide agents were evaluated, and one of them was selected after a first characterization based on wettability and bacterial activity tests. For these tests, the paints were applied on flat aluminum 5005 H24 plates of 140x70x0.8 mm.

5.7.2.2 Organic topcoat paint functionalization

For the functionalization of the organic topcoat paint, a commercial paint Carboguard® 890 & 890 (LT) from Carboline® was selected. The paint consisted of three components, i.e., the binder (Carboguard-A), the hardener (Carboguard-B), and a thinner (C). The paint was prepared in a proportion of A/B/C=1/1/2, as recommended by the manufacturer. The nanoparticles were incorporated into the paint by dispersing them in the thinner.

For the hydrophobicity, silicon dioxide (SiO_2) nanoparticles from Evonic (Aerosil R 812) were used. The characteristics of the nanoparticles are presented in Table 5.7.1. A pre-dispersion of the SiO_2 nanoparticles was prepared in the thinner. In order to ensure the stability of the nanoparticles once added in the paint system, a Croda-KD3 surfactant was used in the pre-dispersion. The optimum concentrations of SiO_2 nanoparticles and Croda-KD3 surfactant were 25 wt% and 5 wt%, respectively. The pre-dispersion was prepared by mechanically agitating the solution for 15 minutes, followed by 30 minutes in an ultrasonic homogenizer (Vibracell-VCX750) at an operating frequency of 20kHz, pulsing operating mode of 1s on/1s off, and output power fixed at 750W at 60% amplitude. During this last operation, the nanoparticle size distribution was repeatedly measured by Laser Diffraction Spectrometry (LDS) in a Malvern Mastersizer 2000 instrument, until the optimum values were reached. Based on previous knowledge, the minimum nanoparticle size distribution to achieve a stable dispersion was set on 180 nm (see Fig. 5.7.1).

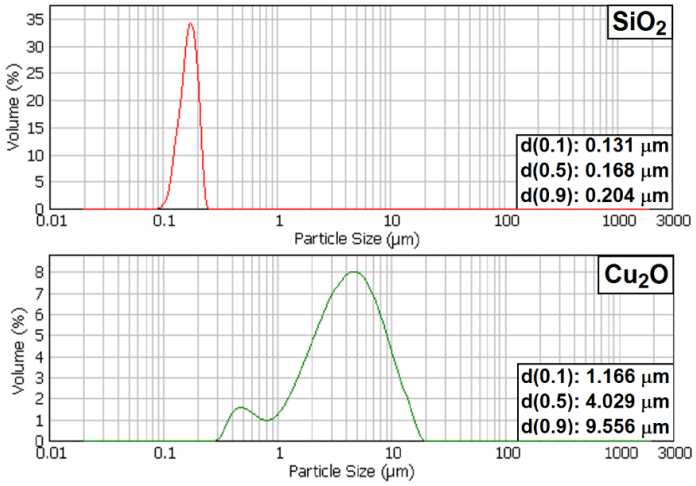

Fig. 5.7.1 Size distribution of the SiO_2 (top) and Cu_2O (bottom) nanoparticles pre-dispersions measured by LDS

For the antibacterial properties, three strategies were evaluated: two commercial biocides Econea (Tralopyril) from Sigma-Aldrich and Irgarol 1051 from Ciba Inc., and copper (II) oxide (Cu_2O) nanoparticles from Sigma-Aldrich (Table 5.7.1). The Econea and Irgarol biocides were directly incorporated in the thinner, whereas for the Cu_2O nanoparticles a pre-dispersion in the thinner was prepared. For this aim, the mixture was mechanically agitated for 15 minutes, for which a nanoparticle size distribution of 1-5 µm was obtained (see Fig. 5.7.1). For each of the three biocides evaluated, two concentrations were prepared: 1.5 wt% and 5 wt% in weight.

The paints were prepared by adding the 25wt% SiO_2 pre-dispersion with the dispersions containing the bactericide agents as the thinner, and applied by spray technique. For the first characterization of the different paint formulations, aluminum 5005 H24 plates were spray painted. The thickness of the coatings was of 100±20 µm. After the most effective combination of SiO_2 and biocide agent in terms of wettability and antibacterial ability was selected, the TSA/PEO samples were sprayed with this paint. The TSA samples were

coated with the non-modified topcoat, to use this system as the reference for the different tests performed within this work. In both cases, several spray passes were made to reach a coating thickness of around 250 microns, as recommended in the ISO 12944-9.

Table 5.7.1 Information of the nanoparticles employed for the paint functionalization

Nanoparticle	Size	BET (m^2/g)	Molecular weight (g/mol)	Company
Silicon dioxide (SiO_2)	10-30 nm	260±30	-	Evonik
Copper (II) oxide (Cu_2O)	≤5 µm	-	M_W= 143.09 (97% assay)	Sigma-Aldrich

5.7.2.3 Coatings characterization

Roughness, thickness, and adhesion

The roughness of the as-sprayed and PEO-treated coatings before and after applying the organic topcoats was determined in a Perthometer M2 (Mar GmBH) profilometer (DIN EN-ISO 4288). The thickness of the different layers composing the coatings was measured from the cross-section profile in an Olympus GX71 optical microscope (UNE-EN ISO 1463). Finally, the adhesion of the paints was analyzed by a pull-off adhesion test (PosiTest AT-A), with aluminum dollies of 20 mm in diameter at a tensile rate of 0.7 MPa/s (ISO 4624). The adhesive used in the tests was a methyl-based material (LOCTITE 496). Prior to the test, after the curing time of the adhesive, the coatings were cut to the substrate around the circumference of the dollies. Four repetitions were performed for each sample, and the mean value was obtained. The fracture type was visually estimated according to ISO 4624.

Surface hydrophobicity assessment

The hydrophobicity grade of the developed topcoat paint was evaluated by measuring the static contact angles formed by drops of synthetic seawater with heavy metals (ASTM D1141) on the tests sample surfaces at room temperature (23±2 ºC). The evaluation was carried out in a SURFTENS universal goniometer, with the SURFTENS 4.6 software, where the contact angle was measured by means of an optical camera.

5.7.2.4 Antibacterial activity assessment

To assess the antibacterial activity, the procedure described in JIS Z2801:2012 [48] and its equivalent ISO 22196:2011 [49] standards were followed. A bacterial suspension of a known concentration (2.5-10 $x10^5$ bacteria per mL) was prepared, and 400 µL were inoculated on the studied surfaces, followed by their incubation for 24 hours at an optimum temperature (35± 1ºC). The samples size was of 50x50 mm, and a cover film (parafilm) of 40x40 mm dimensions was placed on the top of the bacterial suspension inoculated on each surface, before the incubation step. The antibacterial activity was determined comparing the results of the modified topcoat paint with the non-modified one. After the incubation period, the bacterial suspension was recovered from each surface, followed by their quantification and calculation of the number of the viable bacteria recovered per cm^2. The number of viable bacteria was determined by performing 10-fold serial dilutions of the recovered bacterial suspension in phosphate-buffered physiological saline. The microorganism used for the study was the *Escherichia coli* ATCC 8739 (*E.Coli*). Prior to the tests, the surfaces and the parafilm were sterilized with UV radiation in a laminar airflow chamber for 15 minutes. Commercially pure titanium grade 4 (cpTi4) samples were used as a negative control, since this material allows the bacterial growth. Due to the high hydrophobicity of the testing samples, the bacterial inoculum viscosity was increased by adding agar as an inert thickener, as indicated in

the ISO 22196:2011 standard. The quantity of agar-agar is not specified in the standard, so its preparation was made according to the ASTM E2180-18 [50] standard guideline: 0.85 g of NaCl and 0.3 g of agar-agar in 100 mL of distilled water. Three replicates were tested for each coating system.

The first test series consisted of a qualitative approach, comparing the bacterial growth for the topcoat paint modified with the three different biocides at two concentrations. The results of the different formulations were compared with those of the paint with a 25 wt.% of SiO_2, in order to evaluate just the influence of the biocide on the bacterial growth. From these results, the best paint formulation was selected, and a quantitative study was performed comparing the modified paint with the original paint. Finally, the quantitative tests were repeated for the topcoat paints applied on real samples, i.e., non-modified paint on the TSA-coated steel, and the modified paint on the TSA/PEO coating.

5.7.2.5 Marine aquatic ecotoxicity tests

For the evaluation of the new paint formulation toxicity, marine algal growth inhibition tests were performed according to the ISO 10253 [51] standard and using the MARINE ALGALTOXKIT recommended. *Phaeodactylum tricornutum* algae were purchased from MICROBIOTESTS Inc. The culturing was conducted in synthetic seawater mixed with a stock solution of nutrients prepared in accordance with ISO 10253. The algae concentration in the initial culture inoculum was adapted to 10^4 cell/mL three days before the tests, to ensure they were in the exponential growth phase. The incubation was made by maintaining the cultures at 20±2 ºC, with a constant lateral illumination of around 10000 lux for three days.

The toxicity tests were performed by using the leachate obtained from stirring the coated panels in synthetic seawater (ISO 10253), in accordance to the OECD no 23 guidance [52] for non-soluble substances. The panels were immersed in 1L of synthetic seawater and agitated during 28 days in a magnetic stirring. The leaching was collected and analyzed by Inductively Coupled Plasma Optical Emission Spectroscopy (ICP-OES) in an ULTIMA 2 HORIBA Jobin Yvon equipment every 24 hours to measure the release rate of copper and other main elements present in the painted samples. After analyzing the results, new samples were immersed and agitated during the time in which the metal release was observed to be the maximum. The leachates obtained in this second series were used to culture the *Phaeodactylum tricornutum* and analyze the paint toxicity. Algal growth inhibition was registered every 24 hours, measuring the optical density (OD) at 670 nm in a Jenway 6300 spectrophotometer. With the optical density, it was possible to calculate the EL_{50}, which is the concentration of leachate that causes a decrease of 50% in the algal growth. This terminology is employed instead of the standard EC_{50} (concentration of test substance resulting in algae growth reduction of 50%) when the test material is not completely soluble, as the substances studied in this work.

5.7.2.6 Evaluation of the coatings for high corrosivity category atmospheres

To compare and evaluate the corrosion protection performance of the two coating systems, accelerated weathering tests were performed in different climatic chambers. The test conditions were selected based on the ISO 12944-6 [53] and ISO 12944-9 [39] standards. The conditions and duration proposed by these standards for the C5-M (VH) (ISO 12944-6) and CX-offshore/Im4 (ISO 12944-9) categories are specified in Table 5.7.2. For the water condensation and salt spray tests, the samples were aged for the maximum duration set by the ISO 12944-6 to achieve the C5-M(VH) category. In the case of the immersion test and combined aging test, the duration of the tests was reduced to 2000 h.

Table 5.7.2 Summary of the corrosion-aging tests and their conditions in accordance with the different standards

Standard	Category	Test type	Cycle duration			Conditions in the cabinet		Total duration of the test
			Test periods		Total	Temperature	Relative humidity	
ISO 2812[54] ISO 12944-9 [39]	CX-Offshore/Im4	Immersion test	-			(40±3) ºC	-	4200 h
ISO 6270[26] ISO 12944-6 [53]	C5-M(VH)	Constant humidity condensation atmosphere (CH)	From warm-up to end of exposure			(40±3) ºC	100%	720 h
ISO 9227[27] ISO 12944-6 [53]	C5-M(VH)	Salt spray	-			(35±3) ºC	-	1440 h
NORSOK M-501[37] ISO 12944-9[39]	CX-Offshore/Im4	Ultraviolet radiation and condensation (ISO 11507[28])	4 h UV radiation (0.77 W/m^2)	72h	168 h	(60±3) ºC	-	4200 h
			4 h condensation			(50±3) ºC	100%	
		Salt spray (ISO 9227)		72 h		(35±3) ºC	-	
		Low temperature		24 h		(-20±2) ºC	-	

The resistance to water immersion was performed in a Julabo ED thermostatic bath, at 40 ºC (ISO 2812-2 [55]). The water condensation tests were performed according to the ISO 6270-2 [56], under constant humidity conditions at 40 ºC, in a Kesternich HK300-800 S/M humidostatic chamber. Salt-fog tests were carried out in an ASCOTT 2000S chamber, under the conditions specified in the ISO 9227 [56] standard. For this test, six samples of each coating systems were introduced in the chamber. In three of the specimens, an X-shaped incision that reached the steel substrate was made (ISO 17872 [57]). According to EN ISO 12944-6 standard, the rust coming from substrate corrosion from the scratch in the samples with incision shall not exceed 1 mm, calculated as:

$$M = \frac{C-W}{2} \quad \text{(5.7.I)}$$

Where W is the original width of the scratch, and C the maximum width of corrosion across the scratch, in millimeters. In the samples with the incision, adhesion tests were performed at the end of the exposure, following the ASTM D3359 standard [58].

Finally, the combined cycle aging test was performed based on the procedure described in the ISO 12944-9 [39] and NORSOK M-501 [37] standards. The test consists of combining the exposure to UV radiation and condensation (ISO 16474-3 [59], A method), with the exposure to salt spray (ISO 9227) and low temperature. The UV/condensation period was performed in an Atlas UVTest weathering device. The UV lamps employed in the test were type II UV lamps (UVA-340), of 340 nm (ISO 16474). The salt spray and low-temperature periods were carried out in an ASCOTT 2000S chamber and in a WEISS C340/70 climatic chamber, respectively.

For all the tests, three replicates of each coating system were evaluated, in order to ensure the repeatability of the results. The panels were periodically examined to detect the appearance of any defect such as blisters, cracks, delamination of the coating or corrosion of the substrate (ISO 4628 1-5 [60]). At the end of the aging tests, pull-off adhesion tests were repeated upon the tested samples under the above-mentioned conditions (ISO 4624). According to the ISO 12944-9 standard, the minimum pull-off value before artificial aging must be of 5 MPa. After aging, the adhesion should not be reduced more than the 50%. The fracture should show 0% of adhesive failure between the substrate and the first coating layer, unless the pull-off values are above 5 MPa, in which case the failure type required is not specified.

5.7.3 Results and discussion

5.7.3.1 Selection of the biocide agent

The static water contact angles of the flat aluminum 5005 H24 samples with and without the paint containing the three biocides in different concentrations is shown in Fig. 5.7.2. The images of the water droplets are presented on top of the results for each paint composition. The non-coated sample and the sample with the non-modified commercial paint presented hydrophilic behavior with contact angles below 90º. The addition of SiO_2 was confirmed to provide the paint with superhydrophobic character, showing contact angles above 150º. The incorporation of biocides modifies the wettability reducing the contact angles to values between 136 and 140º. The only system showing little variation on the contact angle with values close to those of the superhydrophobic composition with SiO_2 was the one containing a 1.5 wt% of Cu_2O.

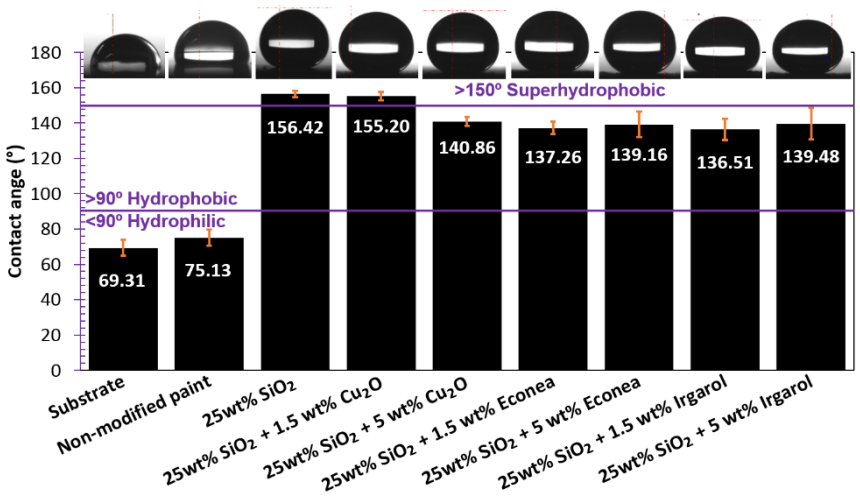

Fig. 5.7.2 Contact angles measured with synthetic seawater (ASTM D1141) on the aluminum substrate, the reference paint and the modified paint with different biocides and concentrations

Fig. 5.7.3 shows the results of the qualitative analysis of bacterial growth carried out on the paint with SiO_2, and the paint with SiO_2 and the three bactericides in two concentrations.

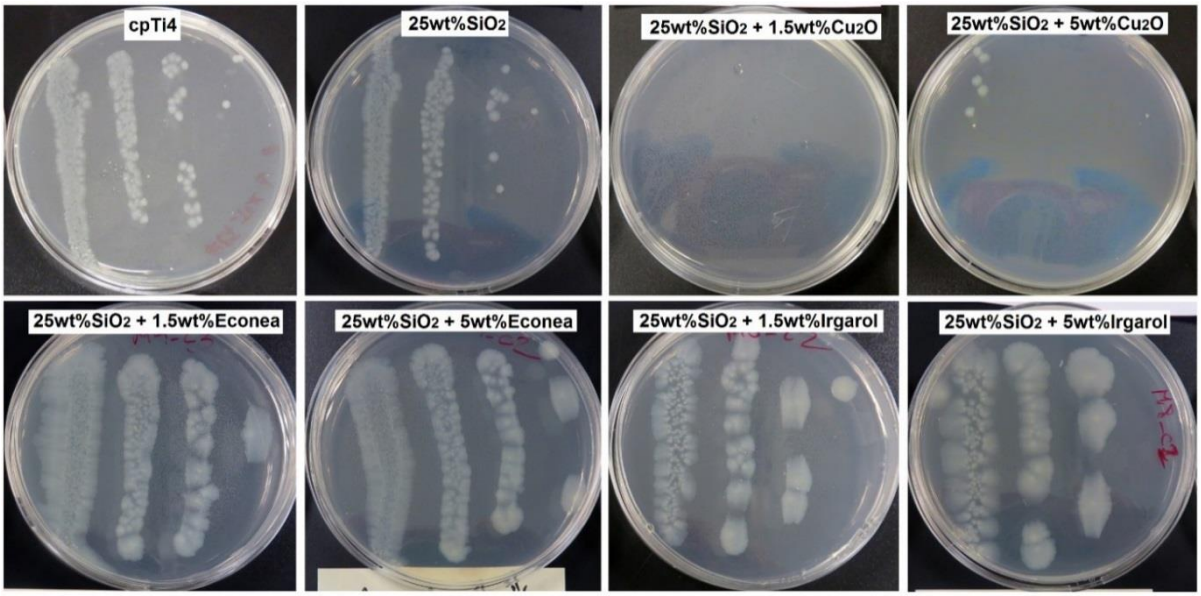

Fig. 5.7.3 Bacterial growth after 24 hours obtained for the cpTi4 reference, the paint with 25wt% SiO_2, and the paint with 25wt%SiO_2 and the different biocides in two concentrations

From the image, it can be noticed that the modified paints showed dissimilarities in the bacterial growth for the different biocides. The paint modified with SiO_2 exhibited a slight reduction of bacteria presence with respect to the cpTi4 reference sample. Some authors have already reported the antibacterial character of SiO_2 in AF paints [25]. However, the paints with silicon oxide combined with Irgarol or Econea did not present any biocide effect, in either concentration evaluated. The biocide agent that showed the best antibacterial performance was the copper oxide, especially for the lowest concentration (1.5 wt%). Comparing the results of the paint with SiO_2 and the paint with SiO_2 and 1.5 wt% Cu_2O, the former showed a slight decrease in the bacterial growth whereas the latter completely avoided the bacterial growth, most likely because of its bactericidal effect. Therefore, this paint was selected as the most promising one to perform the rest of the characterization within this work. Thenceforth, the non-modified paint and the modified one (25 wt% SiO_2+1.5 wt% Cu_2O) will be referred to as C and CM, respectively.

5.7.3.2 Coatings characterization

Fig. 5.7.4 shows the cross-section profile of the two coating systems, i.e., the TSA with the non-modified topcoat (TSA+C) and the TSA treated by PEO technique with the modified topcoat (TSA/PEO+CM). Both paints seem to be well bonded to the TSA and TSA/PEO coatings, showing no appreciable irregularity on the interface. The roughness of the samples before and after the spraying of the paints are presented Table 5.7.3,along with the thickness of each coating layer. The roughness of the TSA+C coating system shows little variation before and after painting. In the case of the TSA/PEO system, the initial roughness was higher, around 5 microns, due to the high porosity of the topmost layer of the PEO layer [46]. This value was reduced to 3.5 microns after applying the modified paint. Regarding the thickness of the coatings, the lower thickness of the TSA layer in the sample treated by PEO technique is attributed to the transformation of part of the aluminum to aluminum oxide during the process. The thickness of the PEO layer was around 95 microns, obtained with the process parameters described in the previous work [46]. In the case of the organic topcoats, the layer thickness acquired after several spraying passes was around 250 microns.

Table 5.7.3 Mean thickness and roughness values obtained for the TSA+C and TSA/PEO+CM coating systems

	TSA+C		TSA/PEO+CM		
	TSA	**C**	**TSA**	**PEO**	**CM**
Roughness, R_a (µm)	2.3±0.6	2.1±0.3	-	5.3±0.3	3.5±.3
Thickness (µm)	254±22	255±11	148±17	94±9	248±11

The values of the table were obtained from three samples of each material

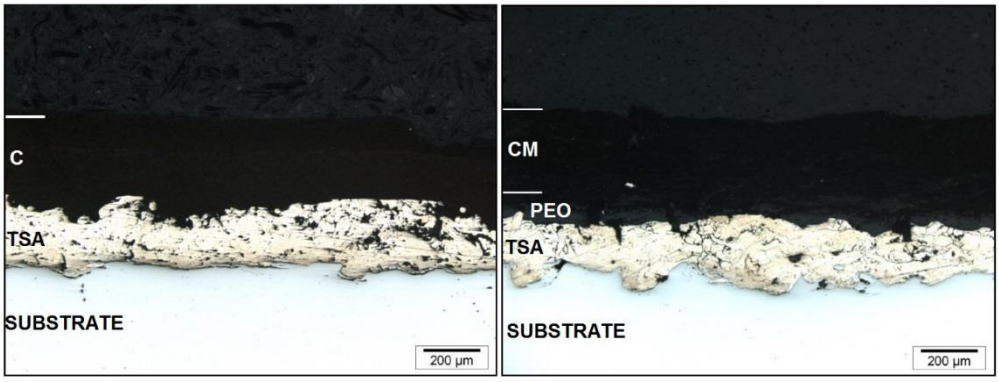

Fig. 5.7.4 Transversal micrographs of the TSA+C (left) and TSA/PEO+CM (right)coating systems applied on the R4 steel grade substrate

The adhesion of the two coating systems was evaluated by means of a pull-off test (ISO 4624). Both systems showed adequate bonding strength, with similar results: 8.78±0.28 MPa for the TSA+C and 8.03±0.10 MPa for the TSA/PEO+CM. According to the ISO 12944-9 [39] standard, the minimum pull-off test value for protective coatings in their initial performance, i.e., before any exposure to aggressive atmospheres, should be of 5 MPa for their use in splash and tidal zones (CX-offshore and Im4 categories). Therefore, the results obtained for the coatings are considered appropriate. Furthermore, the standard recommends a 0% adhesive failure between the substrate/metalized steel and the first coat, when the results are below 5 MPa. A representative fracture surface of each coating sample and the respective dolly is presented in Fig. 5.7.5. In both cases, the fracture type was generally cohesive within the paint, showing in some punctual cases an adhesive failure between the adhesive and the coating in areas below the 20% of the test surface.

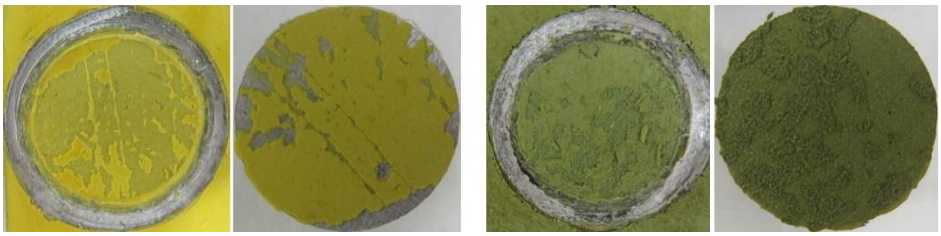

Fig. 5.7.5 Fracture surface of the coatings after pull-off adhesion test: TSA+C coated sample and dolly (left), and TSA/PEO+CM coated sample and dolly (right)

Wettability tests were repeated comparing the results for the non-modified and modified topcoat applied on flat aluminum samples (C and CM), for the TSA and TSA/PEO samples with no paint, and the non-modified and modified topcoats applied on the TSA and TSA/PEO specimens, respectively. The results are presented in Fig. 5.7.6, showing the contact angle values and the water drop shape. The TSA and TSA/PEO samples show low contact angles, especially in the case of the TSA/PEO sample, due to the high porosity and roughness of the topmost layer of the oxide layer. The contact angles of the non-modified topcoat are close to 75º in both the flat and the TSA+C samples, indicating a small influence of the sample roughness or topography on the wettability of the topcoat. Similarly, the modified topcoat presents a superhydrophobic behavior in both the flat sample and the high-porous TSA/PEO coating. The considerable increase of the contact angle from 16.30º to 152.42º, and the similar results in the smoother and rougher samples, suggest that the topography of the substrate does not affect the superhydrophobic character of the modified paint.

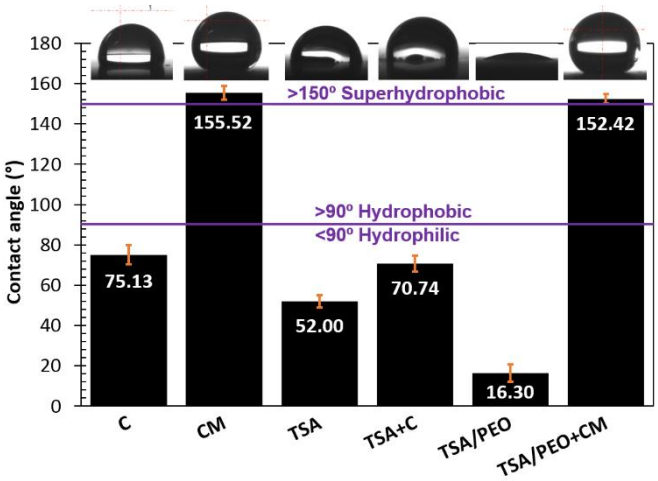

Fig. 5.7.6 Contact angles measured on the non-modified (C) and modified (CM) paints applied on the flat aluminum 5005 H24 samples, TSA coating with no paint, TSA coating with the non-modified paint (TSA+C), TSA/PEO duplex coating system with no paint, and TSA/PEO coating with the modified paint (TSA/PEO+CM). The liquid used in the measurements was Synthetic seawater (ASTM D1141)

5.7.3.3 Antibacterial activity assessment

The quantitative bacterial assessment was carried out for the topcoat paints applied on both the flat aluminum 5005 H24 samples and the real samples, i.e., TSA and TSA/PEO coatings, to evaluate the influence of the topography on the antibacterial ability of the topcoat. Fig. 5.7.7 shows the lowest dilution (1/10) at which a representative difference on the bacterial growth was observed. The non-modified Carboguard paint showed an appreciable decrease on the bacteria content after 24 hours with respect to the cpTi4 reference. On the other hand, no bacteria could be detected in the CM sample, confirming the effective antibacterial character achieved by means of the addition of Si_2O and specially Cu_2O to the paint formulation.

The results obtained for the non-modified paint applied on the TSA coating, the modified paint applied on the TSA/PEO coating, and the cpTi4 reference after 24 hours of incubation are depicted in Fig. 5.7.8. The images correspond to the lowest dilution at which a representative difference could be observed between the different materials (1/10). A decrease in the bacterial growth can be noticed in the non-modified paint with respect to the reference. In turn, there is a further bacterial growth decrease in the modified topcoat. However, there is a noticeable difference between the results obtained for the flat samples, which display greater growth inhibition.

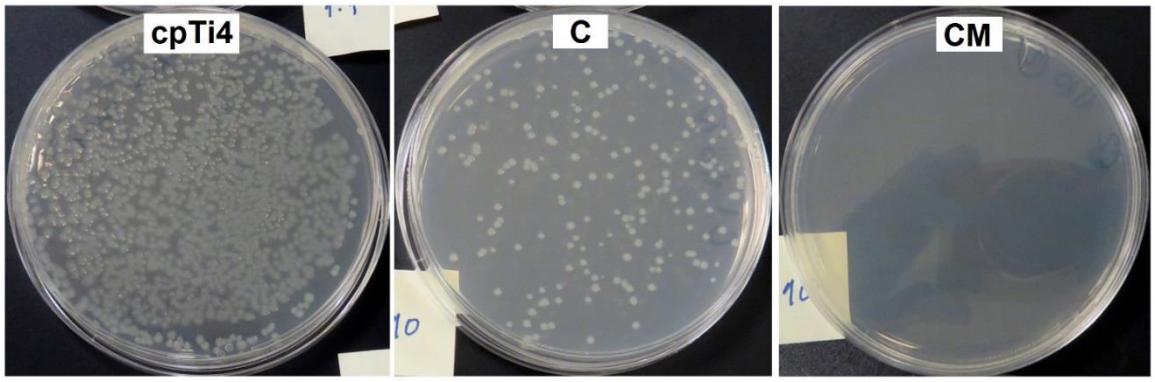

Fig. 5.7.7 Bacterial growth after 24 hours obtained for the cpTi4 reference (left), and the non-modified paint (middle) and modified paint (right) applied in the flat aluminum 5005 H24 samples, for the 1/10 dilution

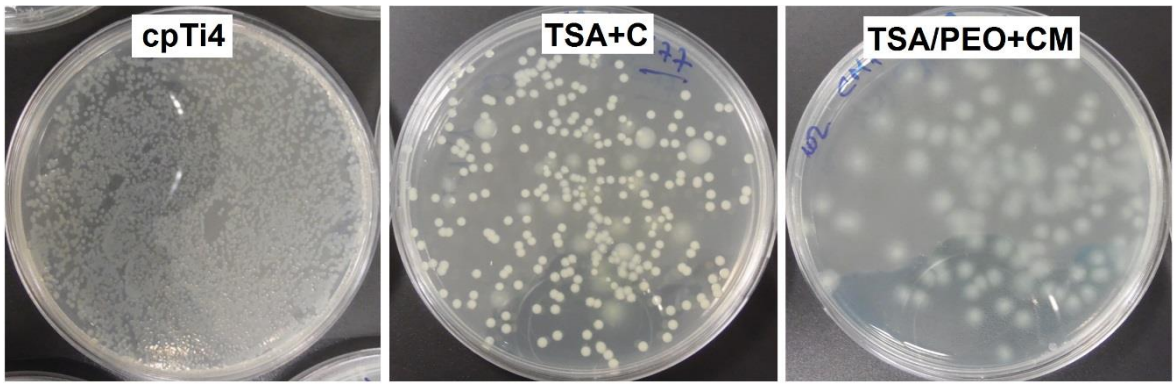

Fig. 5.7.8 Bacterial growth after 24 hours obtained for the cpTi4 reference (left), the non-modified paint on the TSA coating (middle) and the modified paint on the TSA/PEO coating (right), for the 1/10 dilution in the real samples

The antibacterial activity (R) was calculated according to ISO 22196 with the following equation:

$$R = U_t - A_t \qquad (5.7.II)$$

Where U_t and A_t are the average of the common logarithm of the number of viable bacteria (bacteria/cm^2) recovered after 24 hours from the untreated and treated test specimens, respectively.

The antibacterial activity after 24 hours of incubation can also be expressed as a microorganism percentage reduction (R%), as follows:

$$R\ (\%) = \frac{C-control(bacteria/cm^2)-CM(bacteria/cm^2)}{C-control(bacteria/cm^2)}\ x100 \qquad (5.7.III)$$

The results obtained for the C and CM paints are presented in Fig. 5.7.9. The diagram on the left corresponds to the paints applied on the flat aluminum 5005 H24 samples, whereas the figure on the right shows the result of the C and CM applied on top of the

TSA and TSA/PEO coatings, respectively. From the results, it can be noticed that there is a reduction on the number of bacteria after 24 hours for the paint containing the biocide agents, especially in the flat samples. This confirmed the enhancement of bactericide behavior of the paint with the addition of SiO_2 and Cu_2O nanoparticles.

The bacteria reduction of the modified paint in the flat aluminum sample was of the 99.72%, whereas that of the one applied on top of the TSA/PEO coating was of 64.53%. Therefore, the effective antibacterial ability of the topcoat was confirmed to be considerably high in both cases. On the other hand, the difference on the results indicated an influence of the surface topography on the antibacterial activity, showing a decrease on the growth inhibition in the paint applied on the real TSA/PEO coating system of high roughness. Similar trends have been previously reported, in which the infectious bacterial adhesion and growth was enhanced in rougher substrates [61-64]. Nevertheless, the results still showed an efficient antibacterial ability with a decrease of 64.53% of viable bacteria.

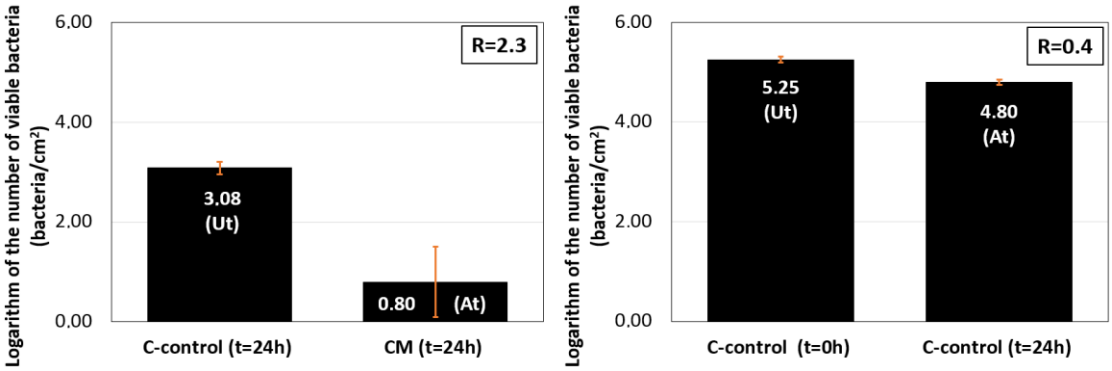

Fig. 5.7.9 Mean viable bacteria recovered per cm^2 in the non-modified sample at 0 and 24 h, and the modified topcoat at 24 h, and antibacterial activity (R)

5.7.3.4 Marine aquatic ecotoxicity tests

Fig. 5.7.10 shows the release of the main elements present in the painted samples during the 28 days that the specimens were stirred in synthetic seawater. In both coating systems, i.e., TSA+C and TSA/PEO+CM, the release trends for the different elements are very similar. The higher concentration in both cases corresponded to silicon, which was reduced with increasing immersion time. Manganese was detected during the first 14 days, but its presence was negligible henceforth. Finally, the concentration of the other two main elements, i.e., titanium from the base paint composition and copper from the nanoparticles incorporated in this study, was negligible and could not be quantified in either evaluation. This indicated a good bonding and stability of copper nanoparticles in the paint, with low release rate, which could enlarge the antibacterial ability of the coating. On the other hand, the more substantial silicon content obtained for the modified paint during the initial days could be attributed to the higher concentration of this element due to the addition of Si_2O nanoparticles. Nevertheless, the silicon content in the modified paint decreases with time to lower values than those of the original paint at the end of the test.

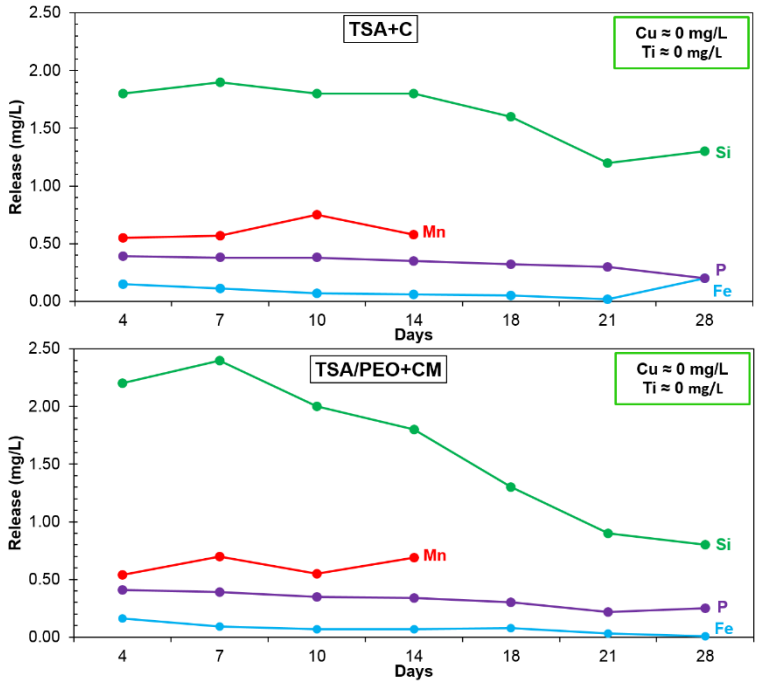

Fig. 5.7.10 Metal release in mg/L obtained from the leachates of the TSA+C and TSA/PEO+CM coating systems agitated during 28 days in synthetic seawater. The release of copper and titanium was negligible in both samples.

From the previous results, the solubility of elements was observed to be critical after 96 hours. New samples were immersed in seawater and stirred for 96 hours to perform the ecotoxicity tests with the *Phaeodactylum tricornutum* algae. Aslo, a second series of ecotoxicity tests were performed for the leachates obtained after 28 days of stirring, to compare the results obtained at the two stirring times. From these leachates, the concentrations bringing the decrease of 50% in the algal growth (EL_{50}) as well as their associated 95% confidence limits were determined. The results obtained for the TSA+C and the TSA/PEO+CM systems are compiled in Table 5.7.4. For the leachates obtained after 96 hours of stirring, the EL_{50} of both coatings are above 100%, indicating that the toxicity of the coatings at this stage is negligible. The results obtained for the leachates after 28 days, however, show higher toxicity levels, especially for the non-modified paint, which are more than the double of that of the modified-paint. This interesting result could be related to the higher concentration of both silicon on the base paint leachate. The EL_{50} obtained for the TSA/PEO+CM system indicates that it is necessary a 61.78 vol. % of the substances present in the leachate to inhibit the algal growth.

Table 5.7.4 EL_{50} values and lower and upper 95% confidence limits obtained for the algal growth inhibition test of 72 hours with Phaeodactylum tricornutum. The studied leachates were obtained after stirring the TSA+C and TSA/PEO+CM for 96 hours and 28 days in synthetic seawater

Stirring time	Sample	$EL_{50,\ 72h}$ (vol. %)	95% Confidence limits
96 hours	TSA+C	>100	-
	TSA/PEO+CM	>100	-
28 days	TSA+C	23.77	23.66- 24.82
	TSA/PEO+CM	61.78	58.22-82.89

5.7.3.5 Evaluation of the coatings for high corrosivity category atmospheres

Fig. 5.7.11 contains one representative image of the coated samples before and after the weathering aging tests in the different atmospheric conditions: salt fog with and without the scribe, water condensation, immersion, and the combined cycle. As it can be

noticed from the images after aging, neither coating system presented severe degradation showing rusting or underrusting, chalking, or delamination.

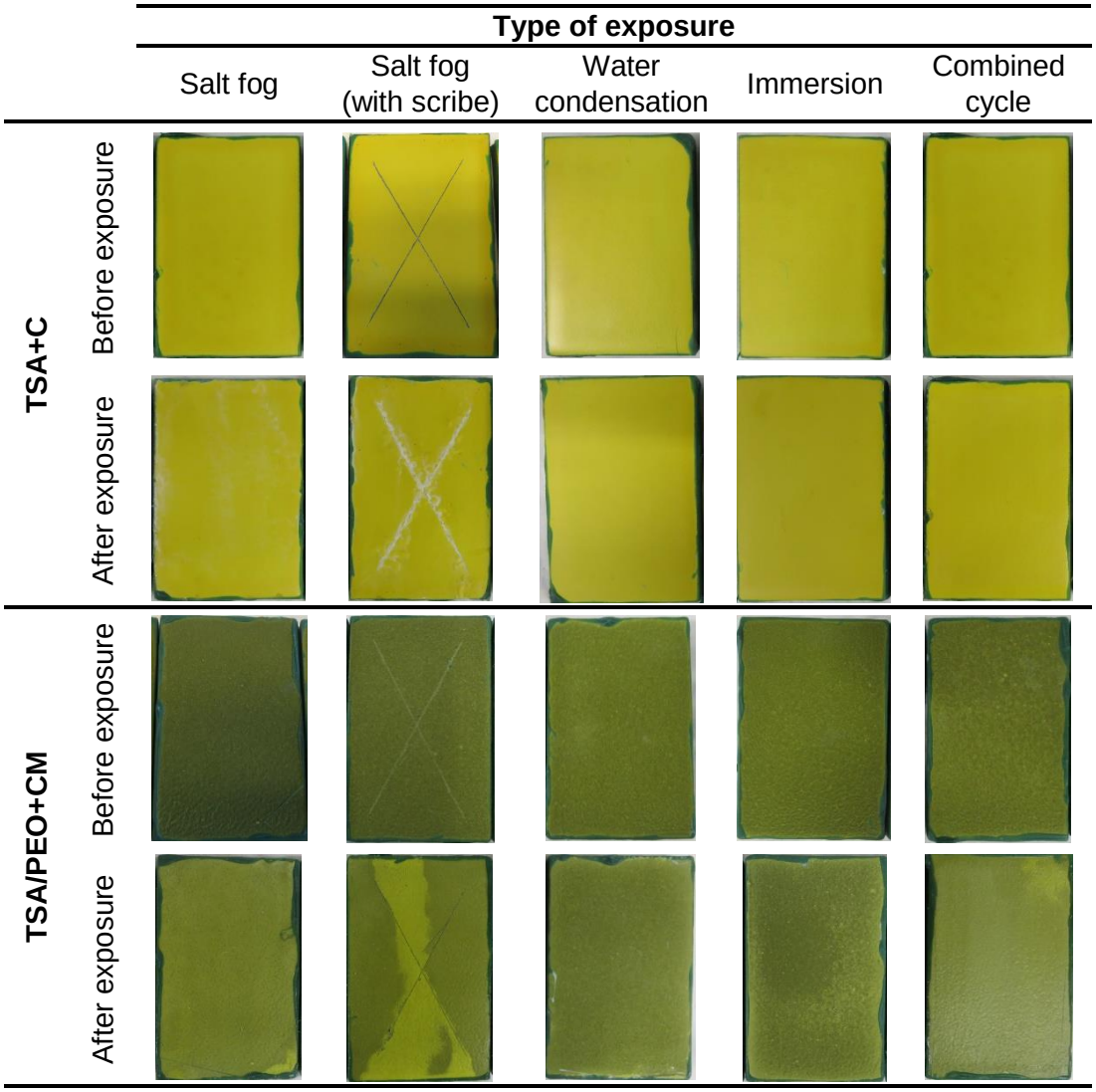

Fig. 5.7.11 Accelerated aging tests results showing the surface state of one representative sample for each exposure type

In the case of the non-modified topcoat applied on the TSA, no discoloration or brightness loss was observed, presenting a similar appearance from that prior to the tests. The only samples showing a deterioration in the form of blisters where those tested in the salt fog chamber. The samples with no incision presented one or two blisters, which appeared after 840 hours of exposure increasing in size up to 15 mm in diameter (Fig. 5.7.12a). In the case of the samples with the scribe, white salts coming from the underneath aluminum layer reaction was observed from the beginning of the test. The white salts spread with the exposure time, to an extent up to 2mm. Furthermore, the blisters appeared in the vicinity of the scribe after 168 h, increasing in size and number, up to sizes of 14 mm in diameter the (Fig. 5.7.12b). The samples of the water condensation test, immersion test, and combined cycle presented no blister or any other relevant defect. In the case of the CM topcoat applied on top of the TSA/PEO system, an evident discoloration can be noticed in all the samples from the images in Fig. 5.7.11. The discoloration was more evident in the samples tested in the salt fog chamber. In the samples tested with the scribe, an isolated blister was detected in one of the samples close to the scribe. The blister appeared after 1300 hours in the chamber and increased in size up to 6 mm in diameter at the end of the test (Fig. 5.7.12c). In the rest of the

samples, apart from the color loss, no rust, blistering, cracking or delamination was observed. Therefore, the results obtained for both coating systems showed a good performance of both paints, showing little deterioration such as discoloration in the case of the CM paint. The samples with higher deterioration in both coatings were those exposed to the salt spray, presenting blisters both in the scribed and non-scribed samples in the original paint, and a noticeable discoloration and an isolated blister in the case of the CM paint.

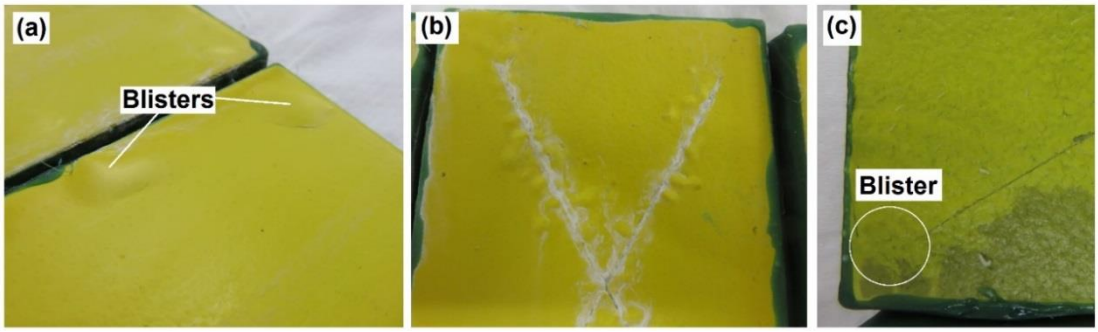

Fig. 5.7.12 Images showing in detail the blisters that appeared in the TSA+C samples (a) without and (b) with scribe, and (c) TSA/PEO+CM sample with scribe after the salt-fog exposure

The results of the pull-off adhesion tests performed in the two coating systems after the weathering aging tests are collected in Table 5.7.5. A representative fracture surface of the samples and the respective dollies are presented in Fig. 5.7.13 for each atmospheric condition.

Table 5.7.5 Pull-off adhesion test results performed on the TSA+C and TSA/PEO+CM coating systems after the weathering aging tests in different atmospheric conditions.

	Pull-off adhesion (MPa)	
Type of exposure	**TSA+C**	**TSA/PEO+CM**
Reference	8.78±0.28	8.03±0.10
Salt-fog	5.78±0.28	6.52±0.10
Water condensation	7.31±0.47	7.96±0.24
Immersion	8.06±0.24	5.40±0.12
Combined cycle	7.78±0.28	7.77±0.16

As recommended in the ISO 12944-9 standard, the minimum pull-off value before artificial aging must be of 5 MPa, and it should not be reduced more than the 50% after aging. According to the results in Table 5.7.5,all the values exceeded the 5 MPa specified on the standard, with reductions with respect to the initial results lower than the 35%. Therefore, both coating systems fulfill the requirements of the ISO 12944-9 standard. On the other hand, different fractures types were found depending on the aging atmosphere. In the case of the TSA+C coating, for instance, the fracture observed in most cases was cohesive within the organic sealant, with isolated regions showing adhesive failure between the adhesive and the paint. In the case of the samples from the water condensation and immersion tests, the fractures were mainly adhesive between the TSA layer and the paint. In the case of the TSA/PEO+CM system, the fracture in all the samples was cohesive within the modified paint. Just one case of adhesive failure between the PEO layer and the paint in a small region of the surface took place. This was found in one of the samples after the combined cycle aging test and is presented in Fig. 5.7.13. Finally, from the adhesion tests performed on the samples with scribe aged in the salt-fog chamber, both coating systems presented good adhesion showing no delamination. According to the ASTM D3359 standard classification, the samples were classified as 5B, which corresponds to the higher level of adhesion.

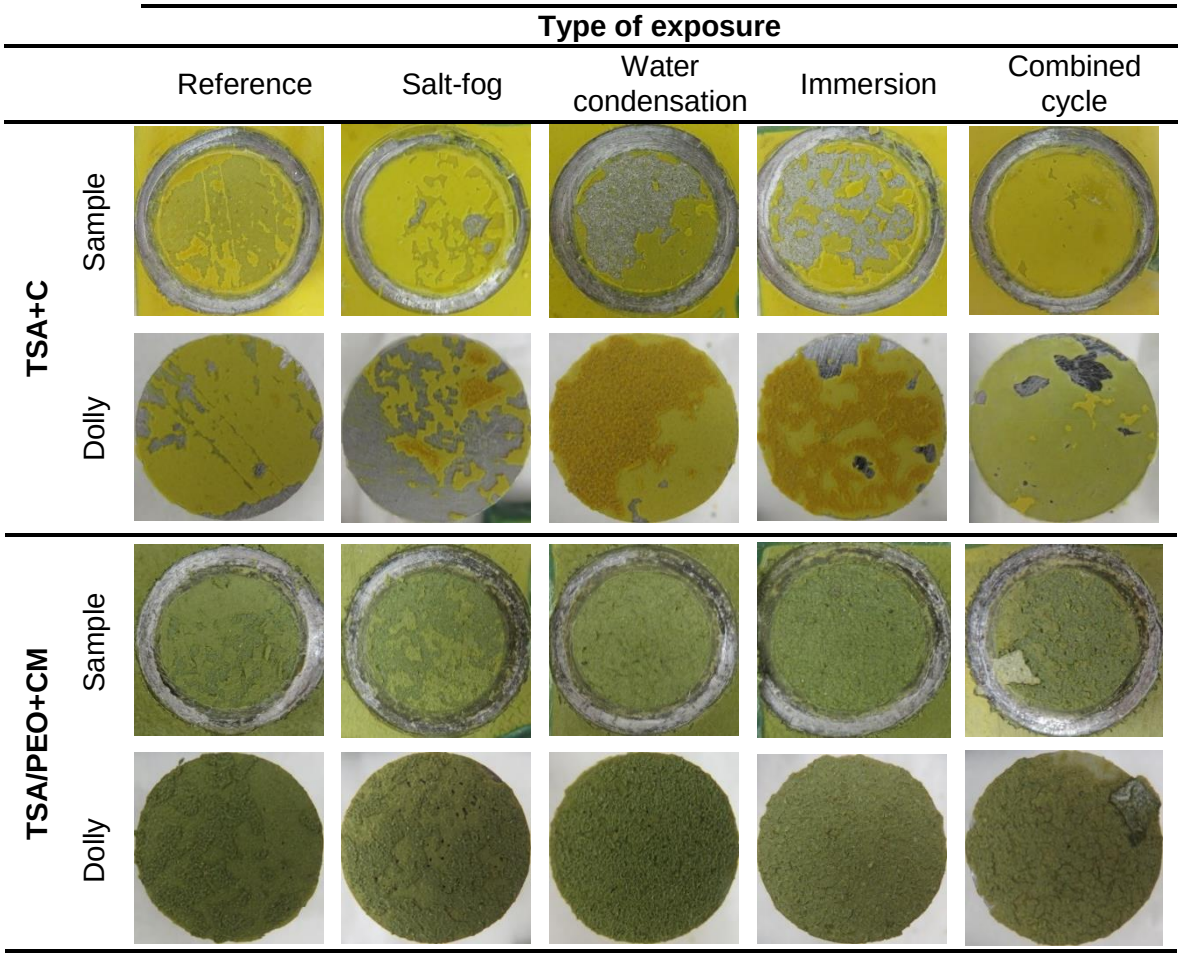

Fig. 5.7.13 Fracture surface of the two coating systems after weathering aging tests in different atmospheric conditions

5.7.4 Conclusions

In the present work, the organic topcoat paint used on top of TSA coatings for the protection of offshore submerged components has been functionalized, to provide it with antifouling properties. For this aim, SiO_2 and Cu_2O nanoparticles have been incorporated into the paint formulation. The former aimed to increase the hydrophobicity of the paint to minimize the attachment of bacteria and microorganisms to the surface, whereas the latter are intended to make the paint bactericide. From the results obtained in this work, the following conclusions can be drawn:

- From the initial wettability and antibacterial activity assessment tests, the paint containing a 25wt% of Si_2O and a 1.5wt% of Cu_2O was found to be the most promising, with high hydrophobicity and antibacterial characteristics.
- The wettability tests performed on the original paint and the modified paint in the flat samples showed an increase in the hydrophobicity of the paint by the addition of the silica nanoparticles, with values above 150°. After applying the modified paint on real samples, the topography of the rough TSA/PEO substrate did not show any detrimental effect on its superhydrophobicity.
- From the antibacterial activity assessment, however, an influence of the surface topography was found, showing a slight decrease in the antibacterial activity of the modified paint when applied on the rough TSA/PEO sample. Nevertheless, the system exhibited an efficient antibacterial ability decreasing 64.53% of viable bacteria.

- The ecotoxicity tests confirmed a low toxicity of both the original paint and the modified one after the first 4 days of immersion. The toxicity of both systems increased after 28 days, especially for the original paint, which presented a toxicity three times higher than the non-modified paint.
- The artificial aging tests performed in different atmospheres revealed the appearance of blisters in some samples of TSA with the original paint, whereas no defects were detected for the TSA/PEO and modified-paint system apart from a discoloration.
- The adhesion pull-off tests revealed an adequate bonding strength for both non-modified and modified paints with their respective substrates, with values above the 5 MPa recommended on the ISO 12944-9 standard. Furthermore, the reduction in the adhesion after the weathering aging tests was below the 35%, fulfilling the requirements of the standard for a CX-offshore/Im4 category.

5.7.5 Acknowledgments

This work was performed with the support of the FRONTIERS IV project (ELKARTEK 2018, KK-2018/00108) financed by the Basque Country. Authors would also like to acknowledge the Education, Linguistic Politics and Culture Department of the Basque Government for its support through the grant "*Programa Predoctoral de Formación de Personal Investigador No Doctor (PRE_2017_2_0088)*" awarded to the first author.

5.7.6 References

[1] R.W. Revie, H.H. Uhlig. *Corrosion and Corrosion Control. An Introduction to Corrosion Science and Engineering (4th edition)*. Wiley-Interscience (2008) ISBN: 978-0-471-73279-2

[2] E.K. Oikonomou, Z. Iatridi, M. Moschakou, P. Damigos, G. Bokias, J.K. Kallitsis. *Development of Cu^{2+}- and/or phosphonium-based polymeric biocidal materials and their potential application in antifouling paints*. Progress in Organic Coatings 75 (2012) 190-199

[3] L.D. Chambers, K.R. Stokes, F.C. Walsh, R.J.K. Wood. *Modern approaches to marine antifouling coatings*. Surface and Coatings Technology 201 (2006) 3642-3652

[4] C. Hellio, D. Yebra (Eds.). *Advances in marine antifouling coatings and technologies*. Woodhead publishing (2009) ISBN: 978-1-84569-631-3

[5] I. Amara, W. Miled, R.B. Slama, N. Ladhari. *Antifouling processes and toxicity effects of antifouling paints on marine environment. A review*. Environmental Tocixology and Pharmacology 57 (2018) 115-130

[6] R. Javaherdashti. *Microbiologically Influenced Corrosion. An Engineering Insight*. Springer (2008) ISBN: 978-1-84800-073-5

[7] D. Feron (Ed.). *Nuclear corrosion science and engineering*. Woodhead Publishing Series in Engineering (2012). ISBN: 978-1-84569-765-5. Chapter 8: *Microbiologically influenced corrosion (MIC) in nuclear power plant systems and components*. B. Tribollet. Pages 230-261

[8] K.M. Usher, A.H. Kaksonen, I. Cole, D. Marney. *Critical Review: Microbially Influenced Corrosion of Buried Carbon Steel Pipes*. International Biodeterioration & Biodegradation 93 (2014) 84-106

[9] Noble Denton Europe Limited. *Floating production systems*. *JIP FPS mooring integrity*. Health & Safety Executive (SHE) (2006). Research report 444

[10] E. Fontaine, A.E. Potts, R.E. Melchers. *Investigation of Severe Corrosion of Mooring Chain in West Africa Waters*. Proceedings of the 22nd International Offshore and Polar Engineering Conference, ISOPE (2012), Rhode, Greece

[11] R. Parks, M. Donnier-Marechal, P.E. Frickers, A. Turner, J.W. Readman. *Antifouling biocides in discarded marine paint particles*. Marine Pollution Bulletin 60 (2010) 1226-1230

[12] D.M. Yebra, S. Kiil, K. Dam-Johansen. *Antifouling technology- past, present and future steps towards efficient and environmentally friendly antifouling coatings*. Progress in Organic Coatings 50 (2004) 75-104

[13] N. Voulvoulis, M.D. Scrimshaw, J.N. Lester. *Comparative environmental assessment of biocides used in antifouling paints*. Chemosphere 47 (2002) 789-795
[14] A. Turner. *Marine pollution from antifouling paint particles*. Marine Pollution Bulletin 60 (2010) 159-171
[15] D. Carteau, K. Vallée-Réhel, I. Linossier, F. Quiniou, R. Davy, C. Compère, M. Delbury, F. Faÿ. *Development of environmentally friendly antifouling paints using biodegradable polymer and lower toxic substances*. Progress in Organic Coatings 77 (2014) 485-493
[16] K. A. Dafforn, J.A. Lewis, E.L. Johnston. *Antifouling strategies: History and regulation, ecological impacts and mitigation*. Marine Pollution Bulletin 62 (2011) 453-465
[17] D.M. Yebra, S. Kiil, K. Dam-Johansen, C. Winell. *Reaction rate estimation of controlled-release antifouling paint binders: Rosin-based systems*. Progress in Organic Coatings 53 (2005) 256-275
[18] J. Wang, T. Shi, X. Yang, W. Han, Y. Zhou. *Environmental risk assessment on capsaicin used as active substance for antifouling system on ships*. Chemosphere 104 (2014) 85-90
[19] S. Soroldoni, F. Abreu, I.B. Castro, F.A. Duarte, G.L. Pinho. *Are antifouling paint particles a continuous source of toxic chemicals to the marine environment?*. Journal of Hazardous Materials 330 (2017) 76-82
[20] M. Lagerström, J.F. Lindgren, A. Holmgvist, M. Dahlström, E. Ytreberg. *In situ release rates of Cu and Zn from commercial antifouling paints at different salinities*. Marine Pollution Bulletin 127 (2018) 289-296
[21] B.T. Watermann, B. Daehne, S. Sievers, R. Dannenberg, J.C. Overbeke, J.W. Klijnstra, O. Heemken. *Bioassays and selected chemical analysis of biocide-free antifouling coatings*. Chemosphere 60 (2005) 1530-1541
[22] K.M. Reddy, K. Feris, J. Bell, D.G. Wingett, C. Hanley, A. Punnoose. *Selective Toxicity of Zinc Oxide Nanoparticles to Prokaryotic and Eukaryotic Systems*. Applied Physics Letters 90 (2007) 1-3
[23] A. Azam, A.S. Ahmed, M. Oves, M.S. Khan, S.S. Habib, A. Memic. *Antimicrobial activity of metal oxide nanoparticles against Gram-positive and Gram-negative bacteria: a comparative study*. International Journal of Nanomedicine 7 (2012) 6003-6009
[24] M. Mishra, J.S. Paiwal, S.K. Singh, E. Selvarajan, C. Subathradevi, V. Mohanasrinivasan. *Studies on the inhibitory activity of biologically synthesized and characterized zinc oxide nanoparticles using Lactobacillus sporogens against Staphylococcus aureus*. Journal of Pure and Applied Microbiology 7 (2013) 1-6
[25] H. Wang, X. Zhao, C. He. *Enhanced antifouling performance of hybrid PVDF ultrafiltration membrane with the dual-mode SiO_2-g-PDMS nanoparticles*. Separation and Purification Technology 166 (2016) 1-8
[26] O.F. Obidi, S.C.U. Nwachukwu. *The Antibacterial Activity of ZrO_2 Nanoparticles on Biocide Resistant Bacilli in Paints*. Journal of Advanced Biotechnology and Bioengineering 2 (2014) 60-64
[27] I. Banerjee, R.C. Pangule, R.S. Kane. *Antifouling coatings: Recent developments in the design of surfaces that prevent fouling by proteins, bacteria and marine organisms*. Advanced Materials 23 (2011) 690-718
[28] S. Krishnan, C.J. Weinman, C.K. Ober. *Advances in polymers for anti-fouling surfaces*. Journal of Materials Chemistry 18 (2008) 3405-3413
[29] H.M. Shang, Y. Wang, S.J. Limmer, T.P. Chou, K. Takahashi, G.Z. Cao. *Optically transparent superhydrophobic silica-based films*. Thin solid Films 472 (2005) 37-43
[30] X.Y. Ling, I.Y. Phang, G.J. Vansco, J. Huskens, D.N. Reinhoudt. *Stable transparent superhydrophobic nanoparticle films*. Langmuir 25 (2009) 3260-3263
[31] W. Dou, P. Wang, D. Zhang, J. Yu. *An efficient war to prepare hydrophobic antireflective SiO_2 film by sol-gel method*. Materials Letters 167 (2016) 69-72
[32] J. Yang, Z. Zhang, X. Men, X. Xu. *Fabrication of stable, transparent and superhydrophobic nanocomposite films with polystyrene functionalized carbon nanotubes*. Applied Surface Science 255 (2009) 9244-9247
[33] Z. Wu, Q. Xi, J. Wang, J. Ma. *Preparation of large area double-walled carbon nanotube macro-films with self-cleaning properties*. Journal of Materials Science & Technology 26 (2010) 20-26
[34] S. Shi, Z. Zhang, L. Yu. *Hydrophobic polyaniline/modified SiO_2 coatings for anticorrosion protection*. Synthetic Metals 233 (2017) 94-100

[35] S. Ammar, K. Ramesh, I.A.W. Ma, Z. Farah, B. Vengadaesvaran, S. Ramesh, A.K. Arof. *Studies on SiO_2-Hybrid polymeric nanocomposite coatings with superior corrosion protection and hydrophobicity*. Surface & Coatings Technology 324 (2017) 536-545
[36] ISO 12944:1-9. *Paints and varnishes. Corrosion protection of steel structures by protective paint systems*. November 2017-February 2018
[37] NORSOK M-501. *Surface preparation and protective coating*. Sixth edition, February 2012
[38] ISO 9223. *Corrosion of metals and alloys. Corrosivity of atmospheres. Classification, determination and estimation*. Second edition, February 2012
[39] ISO 12944-9. *Paints and varnishes. Corrosion protection of steel structures by protective paint systems. Part 9: Protective Paint systems and laboratory performance test methods for offshore and related structures*. First edition, January 2018
[40] A. López-Ortega, R. Bayón, J.L. Arana. *Evaluation of protective coatings for offshore applications. Corrosion and tribocorrosion behaviour in synthetic seawater*. Surface & Coatings Technology 349 (2018) 1083-1097
[41] A. López-Ortega, R. Bayón, J.L. Arana. *Evaluation of protective coatings for offshore applications. Validation for high corrosivity category atmospheres*. Under review in Marine Structures
[42] R.J.K. Wood. *Tribocorrosion of coatings: a review*. Journal of Physics D: Applied Physics 40 (2007) 5502-5521
[43] R.J.K. Wood, J.A. Wharton. *Coatings for tribocorrosion protection, in Tribocorrosion of Passive Metals and Coatings*, (eds.) Landolt D. And Mischler S, Woodhead Publishing (2011), ch. 11, pp. 296-333, ISBN 978-1-94569-966-6
[44] Myer Kutz (Ed.). Handbook of environmental degradation of materials (2nd edition). Elsevier (2012) ISBN 978-1-4377-3455-3
[45] K.P. Fisher, W.H. Thomanson, T. Bosbrook, J. Murali. *Performance of Thermal-Sprayed Aluminium Coatings in Offshore Service*. Materials Performance 34 (1995) 27-35
[46] A. López-Ortega, J.L. Arana, E. Rodríguez, R. Bayón. *Corrosion, wear and tribocorrosion performance of a thermally sprayed aluminum coating modified by plasma electrolytic oxidation technique for offshore submerged components protection*. Corrosion Science 143 (2018) 258-280
[47] Offshore Standard DNVGL-OS E302, Det Norske Veritas, Offshore Mooring Chains. July 2018
[48] JIS Z2108:2012. *Antibacterial Products-Test for antibacterial activity and efficacy*. May 21, 2012
[49] ISO 22196:2011. *Measurement of antibacterial activity on plastics and other non-porous surfaces*. August 1, 2011
[50] ASTM E2180-18. *Standard Test Method for Determining the Activity of Incorporated Antimicrobial Agent(s) In Polymeric or Hydrophobic Materials*. ASTM International, West Conshohocken, PA, 2018
[51] ISO 10253. *Water quality: Marine algal growth inhibition test with Skeletonema sp. And Phaeodactylum tricornutum*. Third edition, Novemebr 2011
[52] OEDC Series on testing and assessment. No 23. *Guidance document on aquatic toxicity testing of difficult substances and mixtures*. ENV/JM/MONO (2000) 6, December 2000
[53] ISO 12944-6. *Paints and varnishes. Corrosion protection of steel structures by protective paint systems. Part 9: Laboratory performance test methods*. Second edition, January 2018
[54] ISO 2812-2. *Paints and varnishes. Determination of resistance to liquids*. Second edition, January 2007
[55] ISO 6270-2. *Paints and varnishes. Determination of resistance to humidity*. Second edition, November 2017
[56] ISO 9227. *Corrosion tests in artificial atmospheres. Salt spray test*. Fourth edition, March 2017
[57] ISO 17872. *Paints and Varnishes. Guidelines for the introduction of scribe marks through coatings on metallic panels for corrosion testing.* First edition, 2007
[58] ASTM D3359. *Standard Test Methods for Measuring Adhesion by Tape Test*. ASTM International, West Conshohocken, PA, 2017
[59] ISO 16474-3 *Paints and varnishes. Methods of exposure to laboratory light sources. Fluorescence UV lamps.* September 2014
[60] ISO 4628 1-5. *Paints and Varnishes. Evaluation of degradation of coatings. Designation of quantity and size of defects, and of density of uniform changes in appearance*. First edition, 2007

[61] K. Hori, S. Matsumoto. *Bacterial adhesion: From mechanism to control*. Biochemical Engineering Journal 48 (2010) 424-434

[62] K. Anselme, P. Davidson, A. Popa, M. Giazzon, M. Liley. L. Ploux. *The interaction of cells and bacteria with surfaces structured at the nanometre scale*. Acta biomaterialia 6 (2010) 3824-3846

[63] A. Han, J.K.H. Tsoi, F.P. Rodrigues, J.G. Leprince, W.M. Palin. *Bacterial adhesion mechanisms on dental implant surfaces and the influencing factors*. International Journal of Adhesion and Adhesives 69 (2016) 58-71

[64] S.A. Alves, A.R. Ribeiro, S. Gemini-piperni, R.C. Silva, A.M. Saraiva, P.E. Leite, G. Perez, S.M. Oliveira, J.R. Araujo. *TiO_2 nanotubes enriched with calcium, phosphorous and zinc: promising bio-selective functional surfaces for osseointegrated titanium implants*. RSC Advances 7 (2017) 49720–49738

Chapter 6

Discussion and final conclusions

Discussion

Chapter 6: Discussion and final conclusions

6.1 DISCUSSION

PART I. Tribocorrosion of HSLA steels (active materials) in offshore applications

In the present thesis, one of the main challenges that have been overcome is the assessment of the tribocorrosion behavior of active materials. This work was focused on the specific case study of offshore mooring lines. These elements are manufactured with HSLA steels of low corrosion resistance in the aggressive marine environment, and they are subjected to tribocorrosion solicitations during their service life. In fact, wear and corrosion and, thus, their interaction, has been reported to highly accelerate the degradation of this components, increasing the probability of failure by fatigue-corrosion.

The first investigations of this study revealed that the tribocorrosion response of the active HSLA steels strongly differed from that of passive alloys, in terms of potential and current evolution during sliding and degradation synergisms. In passive materials, there is a decrease in the potential and an increase in the current as a consequence of the rupture of the passive layer in the tribological contact. As the passive layer is removed, the wear track is activated and reacts with the electrolyte, which is reflected in an increase in the current. In this case, the material in the worn surface dissolves during continuous sliding whereas the area outside the track remains under passive state.

However, the behavior of HSLA steels was found to be somewhat different, and the potentials registered in the different experiments carried out increased during sliding. In these steels of low corrosion resistance in seawater, the surface is not passivated, and it is corroding the whole time that it is in contact with the aggressive environment. The oxides formed on the surface of the steel, mainly ferric oxyhydroxides (FeOOH), can slow down corrosion to some extent by impeding the access of oxygen to the corroding surface. Nevertheless, when this corrosion product layer is removed by sliding, and the fresh alloy is exposed in the wear track, two electrochemically different regions are generated in the surface of the steel: the worn and the unworn surfaces. The former presents more positive potential than the latter, which makes the potential shift to more positive values as soon as it is created during the wear test. This potential difference generated makes the surface of the steel to behave as a macrobattery. The nobler worn surface constitutes the cathode of the reaction, whereas the outer part of the track behaves as an anode. This leads to a wear-accelerated corrosion of the unworn surface during tribocorrosion.

The evolution of the current and thus the corrosion kinetics for the HSLA steels was different depending on the test type performed, i.e., under applied potential in the potentiostatic tests (chapter 5.1) or at open circuit potential conditions with the ZRA configuration (chapter 5.3). In the former, the samples are kept at the same potential during the whole test, whereas in the latter the potential is not fixed but varies depending on the electrochemical state of the surface. In the potentiostatic tests, both at anodic and cathodic potentials, the current was found to decrease during sliding. This peculiar response indicated that the corrosion kinetics in the newly generated wear track was different from that of the rest of the surface. Since the corrosion current is directly related with the corrosion rate, this decrease confirmed the worn material to have lower corrosion rate. On the other hand, in the tests performed at open circuit potential conditions with the ZRA configuration, the current increased during sliding. This indicated an increase in the overall corrosion rate of the sample. Since the wear track was

observed to have lower corrosion kinetics, the rise in the current was related to the wear-accelerated corrosion of the unworn region.

The superficial analyses and the material loss quantifications carried out after the different tests, evinced the considerable material loss due to wear-accelerated corrosion of the unworn surface. In fact, the quantifications carried out in chapter 5.2 demonstrated the material loss due to wear-accelerated corrosion in the outer part of the track to be quadruplicated at room temperature.

Another interesting finding was the strong dependence of the coefficient of friction as well as the material loss on the applied potential and the corrosion products formed in each electrochemical situation. At cathodic potentials, where corrosion was inhibited, the metal particles detached from the surface were deformed on the tribological contact, accommodating the sliding by shearing and leading to low coefficients and low material losses. At high anodic potentials, the oxide products formed a film with a certain lubricating ability that reduced the coefficient of friction. The high material losses at anodic potentials were a consequence of the fast dissolution of the steel enhanced by the potentials applied. Finally, the higher coefficients always corresponded to the tests performed at open circuit potential conditions, mainly due to the third-body effect generated by the material particles detached that remained in the tribological contact.

The tribocorrosion behavior of the active steels was found to be influenced by several parameters, as the temperature and electrolyte agitation. In chapter 5.2, the influence of temperature was evaluated. The results showed that the increase in the electrolyte temperature led to more substantial material loss due to corrosion in the unworn surface, encouraged by the easiest diffusion of oxygen to the corroding surface. Similarly, the investigations on the effect of agitation in chapter 5.3 confirmed that this parameter also enhanced corrosion through a greater oxygen supply towards the sample surface. In the case of tests in chapter 5.3, the influence of agitation was negligible for the passive AISI 316 steel. Therefore, the tribocorrosion behavior of the active steels was found to be highly dependent on these variables that can affect the corrosion rate, which in the case of passive materials seem to have little or, at least, less influence. These factors are variable in real applications and, thus, their impact on the response of the material should be taken into consideration to avoid premature failures of steel components.

Finally, for the studies performed within the first part of this thesis concerning active materials, different test methodologies were used, based on previous investigations and protocols employed in the assessment of passive materials. With the procedure described in the ASTM G119 standard used in chapter 5.1, the synergism between wear and corrosion could be quantified for the R4 and R5 steel grades. Nevertheless, this procedure has been questioned by experts, since it consists of performing individual tests either avoiding corrosion or wear, and the influence of one another can be thus neglected. The second test protocol employed in chapter 5.2 was the one of the UNE 112086 standard. With this practice, the effect of wear on corrosion and vice versa could be evaluated, since the tests were performed at open circuit potential conditions. However, the quantification of the mechanical and electrochemical parameters to the total material loss described in this protocol was found to be unsuitable for active materials. In this kind of materials, the unworn surface is not protected by the passive layer, but it is actively dissolving during the whole test. Therefore, the electrochemical contribution is the sum of the corrosion taking place in the wear track and the wear-accelerated corrosion of the unworn surface, which cannot be separated following the above-mentioned protocol. The last test procedure proposed in chapter 5.3 comprised the ZRA technique to register the potential and current evolution simultaneously, gaining

information on both thermodynamics and the kinetics of the reactions taking place in the steel. Therefore, this technique presented certain advantages with respect to the two former procedures. Firstly, the tests are performed at open circuit potential conditions, without applying any potential that could hinder the effect of wear on corrosion, or vice versa. And secondly, since both potential and current responses are registered simultaneously, it takes just one experiment to gain information of both parameters.

PART II. Protective coatings: evaluation and development of new solutions

The second part of this thesis dealt with the evaluation of tribocorrosion performance of coatings employed in the protection of steel components and structures in offshore applications. Also, new developments have been proposed to enhance the existing solutions against tribocorrosion in order to enlarge their durability in such harsh conditions.

The three commercial coatings of different nature evaluated in chapter 5.4 were confirmed to improve the corrosion response of the steel substrate, especially when organic layers were involved, as in the case of the organic topcoat applied on the TSA (C2) and the organic coating C3. However, the performance of the coatings was affected by wear, which reduced their resistance and accelerated their degradation by mechanical removal. The coatings showed low coefficients of friction and resisted the tribological conditions imposed. Therefore, the three commercial coatings selected in this work presented adequate tribological performance, due to the high hardness of the TSC coating (C1), the ceramic reinforcement of the organic coating (C3), and the high solid contents of the organic topcoat applied on the TSA (C2). In both C3 and C2 coatings, the organic component withstood the tribological conditions. In fact, the TSA coating without the organic topcoat was confirmed to be highly damaged in the tests performed in chapter 5.6 during both dry abrasion and tribocorrosion in seawater. The low abrasion resistance of aluminum could lead to fast degradation of the coating losing its protecting purpose faster than expected. Therefore, further considerations should be taken into account in the selection of coatings that will be subjected to wear and corrosion solicitations.

On the other hand, the new solution proposed in chapter 5.6 to enhance the performance of the TSA coating by PEO treatment was found to be very promising. The duplex TSA/PEO system presented appropriate bonding strength exceeding the recommendations of the offshore standards considerably. The long-term corrosion behavior of the TSA was also improved after the treatment. While the durability of the aluminum layer can be reduced through sacrificial dissolution when it is protecting the steel substrate by galvanic corrosion mechanism, the PEO layer provided a combination of retarding and blocking effects that lowered the corrosion rate of the system. The inner dense layer of the PEO coating hindered the infiltration of electrolyte through the coating, and once seawater reached the TSA layer, the aluminum passivated blocking the small pores of the PEO oxide layer. The results of the tribocorrosion tests showed that the PEO layer was not mechanically affected by sliding, presenting low material losses and, thus, improving the tribocorrosion response of the TSA coating. Also, the higher wear resistance in dry conditions after the treatment could enlarge the life of the coating reducing the damage of the component during transport or assembly operations.

The second strategy proposed in chapter 5.7 as a new coating solution was the functionalization of the organic topcoat applied on top of the TSA. For this aim, nanoparticles were incorporated into the Carboguard® paint to provide it with antifouling properties. SiO_2 and Cu_2O nanoparticles were selected to achieve hydrophobic and

bactericide properties, respectively. Although these nanoparticles have been previously used to get these properties separately, little information has been found on the effect of the addition of both on the resulting paint properties. The paint obtained in this work was superhydrophobic with high bactericide ability, and no detrimental effect on either property was observed by the simultaneous addition of both nanoparticle types. The topography of the coated substrate, in terms of roughness, was found to affect the antibacterial ability of the paint, whereas the superhydrophilicity was not influenced by this parameter. The topcoat was able to decrease the *E. Coli* bacteria in a 64.53%, showing an effective biocide ability against this bacterium, and its ecotoxicity was also proven to be low. No copper release was observed from these analyses, which could be interesting considering the acceptance levels of this element in certain countries (e.g., 40 µg/cm^2/day in Canada or 15 µg/cm^2/day in Denmark).

Finally, the new coating system consisting of the TSA/PEO with the functionalized organic topcoat showed a good performance in all the weathering aging tests, with no degradation signs, and proper adherence after the prolonged exposure in the different climatic chambers. Therefore, from the results of chapters 5.6 and 5.7, the functionalization of the TSA/organic-topcoat was successfully accomplished. The steel substrate was protected from corrosion by the three-layered coating system, the wear resistance of the TSA layer was highly improved, and the whole system was provided with additional properties by the incorporation of nanoparticles in the organic topcoat.

Final conclusions

Chapter 6: Discussion and final conclusions

6.2 FINAL CONCLUSIONS

The first part of the present thesis was focused on the evaluation of tribocorrosion of active materials, such as the HSLA steels employed in offshore applications, exposed to the aggressive marine environment. The main outcomes of this investigation are summarized as follows:

- The tribocorrosion behavior of the active HSLA steels has been evaluated, and a closer understanding of the phenomena has been achieved:
  - During the wear test, a potential difference between the worn and unworn surfaces was created. The registered potential increased indicating that the worn surface generated was more cathodic than the rest of the surface, which led to the formation of a macrobattery on the surface of the sample.
  - On the other hand, the current in potentiostatic tests decreased during sliding. The corrosion rate on the worn material was found to be slower than that on the rest of the surface.
  - In the tests at open circuit potential conditions, the current increased indicating an increase in the overall corrosion rate of the sample. Since the corrosion rate in the wear track was lower, the increase should be taking place on the unworn surface.
  - Therefore, it was found that during tribocorrosion tests, there was a wear accelerated-corrosion of the unworn surface of the steels, which increased their degradation considerably.
- The coefficient of friction was found to depend on the electrochemical potential and the corrosion products formed. At anodic and cathodic potentials, the formation of corrosion products layer or their absence, respectively, led to lower coefficients. On the other hand, the higher coefficients were registered at open circuit potential conditions, where third-body effect took place.
- The tribocorrosion behavior of HSLA steels was highly influenced by the electrolyte temperature and the agitation, which can ease the oxygen supply to the corroding surface affecting the corrosion rate.
- The protocols available for the assessment of passive materials can be used to evaluate the behavior of active materials, with some limitations:
  - With the ASTM G119 standard, the synergism can be quantified, but the influence of wear in corrosion and vice versa can be neglected.
  - With the UNE 112086, the effect of wear on corrosion and vice versa can be evaluated, but the material loss protocol is not suitable.
  - Finally, the ZRA configuration proposed in the thesis allowed to register both the potential and current evolution simultaneously and could be an interesting route to evaluate this kind of materials.

The second part of this thesis, regarding protective coatings, has allowed achieving the original conclusions summarized below:

- The tribocorrosion behavior of three commercial coatings currently employed in offshore submerged components was evaluated. The three coatings enhanced the corrosion response of the steel substrate, but their performance was affected by wear. Their corrosion resistance was reduced, and their degradation was accelerated by mechanical removal.

- The coatings resisted tribological conditions imposed, presenting low coefficients of friction. This was ascribed to the high hardness of C1 and the reinforcements in C2 and C3 coatings.
- The new solution proposed to enhance the performance of the TSA coating by PEO treatment was found to be very promising. The PEO layer improved the corrosion, wear and tribocorrosion resistances of the TSA in synthetic seawater.
- The addition of SiO2 and Cu2O nanoparticles to the Carboguard® paint provided it with superhydrophobicity and highly bactericide ability against E. Coli bacterium. The copper release of the paint was negligible, and its ecotoxicity was low.
- Finally, the three-layered coating system consisting of the TSA/PEO with the functionalized organic topcoat showed a good performance in all the weathering aging tests.

Summarizing, the findings of this thesis have evinced the importance of the synergism between wear and corrosion on the degradation of HSLA steels. There is a complex interaction that depends on several variables as temperature, salinity, mechanical loads, and so on. This investigation has demonstrated the considerable acceleration of material loss by corrosion during wear. In turn, the occurrence of this synergism emphasizes the necessity of considering this material loss by wear-accelerated corrosion in the design codes which, at present, underestimate this phenomenon. Furthermore, the importance of evaluating the tribocorrosion performance of protective coatings is also manifested. Finally, this study highlights the necessity of using this kind of methodology for the evaluation of the materials performance under wear-corrosion requirements, and to increase the knowledge on the synergism between both phenomena.

Chapter 7

Future work

Chapter 7: Future work

After the development of the present thesis, and taking into account all the results and the knowledge acquired during its execution, the following four future lines of investigations are proposed:

Extrapolation to other applications

On the basis of the importance of the evaluation of tribocorrosion for the design of components, as it has been highlighted in this thesis for offshore mooring lines, the extrapolation of the knowledge acquired to other offshore sectors would be of great interest. This would be the case of renewable energies, such as wind, wave, or tidal power. The further development of all these technologies will imply the use of high-performance steels in their installations, which will be subjected to similar threats as those of Oil&Gas mooring lines. Based on the course of action followed to date, the knowledge from Oil&Gas should be employed to further develop these offshore technologies. The methodology and the test protocols employed in this work could be used for the assessment of other high-performance, adapting the test procedures to the different materials and working conditions of each application, to gain information on this phenomenon.

Improve paint formulations for wear-corrosion requirements

In the studies carried out for the different coatings currently used in the protection of steel components and structures against wear-corrosion requirements, the reinforced organic layers were found to perform satisfactorily. Therefore, another future work in the field would be the functionalization of new paint systems by the incorporation of different agents, to increase their wear resistance and simultaneously provide other functionalities. For instance, the addition of nanomaterials could highly improve the performance of the paints, due to the interaction of these nanoparticles with the polymeric matrix. For this aim, ceramic oxides such as silicon oxide, titanium oxide, aluminum oxide, zirconium oxide, or graphene could be used. Also, the simultaneous addition of different nanoparticles that could lead to the achievement of combined properties, such as hydrophobicity, bactericide ability, and improved wear performance should be investigated. In this context, the reinforcement of the self-healing paints that are currently gaining attention in the field could also be a matter of interest.

Scalability of the Plasma Electrolytic Process

The modification of the TSA coating by the PEO process was found to be very promising, in terms of both abrasion and tribocorrosion resistance. Notwithstanding the findings of this work, further efforts should be made to evaluate the scalability of this process to be implemented on the fabrication chain. This would entail proving the effectivity of the process when moving from small test samples at laboratory scale to real components at industrial scale, to ensure the convenience of the process implementation both at technical and economic levels.

Validation of the functionalized organic topcoat

After functionalizing the Carboguard® paint and confirming the resulting topcoat to present superhydrophobic and bactericide ability against *E. Coli* bacterium, further investigations should be made to validate its performance as a proper antifouling paint. On the one hand, the antibacterial properties of the paint should be studied against another wild range of bacteria present in seawater environments, e.g., crustaceans and

algae. On the other hand, after validating the corrosion protection ability of the coatings in climatic chambers, long-term exposure tests in real marine environment would be necessary to really confirm the performance of the paint.

ANNEX I

Instrumental techniques

Annex I: Instrumental techniques

A.I.1 CORROSION TESTS

The experimental dispositive used in the corrosion tests performed in this thesis was a three-electrode electrochemical cell. The cell is composed by a reference electrode (RE), a counterelectrode (CE), and a working electrode (WE). The RE is a non-polarizable electrode, used to measure the potential variations occurring in the working electrode. Typical reference electrodes are Saturated Calomel Electrodes (SCE) and Silver/Silver Chloride electrodes (Ag/AgCl). The CE is the one used to polarize the working electrode. This electrode is usually made of platinum, gold, graphite, or another inert material, to avoid producing any distortion in the system. Finally, the metal which corrosion rate is the aim of the study is connected as the WE. The electrodes are connected to a potentiostat, to register the potential between the RE and the WE, or the current between the CE and the RE.

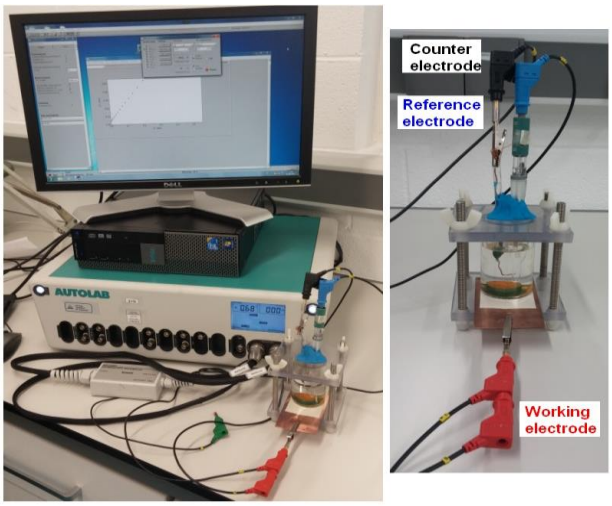

Fig. A.I.1 Experimental set-up of the corrosion tests

The experimental setup used in this work is presented in Fig. A.I.1. A commercial Ag/AgCl (KCl 3M) electrode and a platinum wire of 1 mm in diameter were employed as the reference and the counter electrodes, respectively. The electrodes were connected to an Autolab-Metrohm PGSTAT302N potentiostat [1] with which the electrochemical parameters were both controlled and registered. This potentiostat is equipped with a FRA32M and EDC modules, which allow the registration of currents up to 100 pA in systems with high impedances, i.e., protective coatings with high resistances (>100 GΩ). All the corrosion tests were performed in synthetic seawater with heavy metals, prepared in accordance with the ASTM D1141 standard [2], and on aerated conditions and room temperature. The electrochemical techniques employed within this thesis were the following:

- **Open Circuit Potential (OCP) monitoring:** is the simplest electrochemical method. It provides information on the electrochemical reactivity of the material in the test solution, but it does not give quantitative information on the kinetics of the reactions, i.e., corrosion rates.
- **Potentiodynamic Polarization (PDP) technique:** is one of the most widely-used test methods to evaluate corrosion and consists of performing a potential sweep in the range from cathodic to the anodic domain while registering the current produced.

This technique allows evaluating the active/passive behavior of the materials at different potentials and determining the kinetics of ongoing reactions, i.e., the corrosion rate.

- **Potentiostatic polarization:** it is used to simulate the oxidizing action of a corrosive environment. This technique consists of imposing a fixed potential between the reference and the working electrodes. The current is measured as a function of time, to evaluate the evolution of electrochemical kinetics of reactions occurring on the electrode surface.
- **Electrochemical Impedance Spectroscopy (EIS) measurements:** it consists of exciting the system using an AC potential or small amplitude current sinusoidal signal over a wide range of frequencies and measuring the current or potential response obtained. The impedance spectrums give information on the elementary steps occurring in the electrochemical reactions, and their kinetics can also be obtained from these diagrams.
- **Electrochemical noise (EN) analysis:** it can be defined as the spontaneous potential and current fluctuations taking place in a metal exposed to an aggressive medium. This technique allows potential and current fluctuations to be registered simultaneously, so it is possible to obtain information on the thermodynamics from the potential noise, and kinetics information from the current noise.

A.I.2 TRIBOCORROSION TESTS

For tribocorrosion assessment, the test equipment shall allow controlling and monitoring both mechanical and electrochemical parameters. The apparatus used to measure tribological properties is named tribometer. A tribometer generates a relative motion, either unidirectional (rotatory) or bidirectional (reciprocating), rubbing two surfaces against each other. On the other hand, the electrochemical parameters are controlled and registered with electrochemical cells, as the one previously explained. Tribocorrosion tests consist of performing wear tests under certain mechanical conditions of normal load and speed or frequency, while performing electrochemical techniques to evaluate the response of the system before, during and/or after the wear process.

The tribocorrosion tests were performed in a rotatory MicroTest MT/10/SCM tribometer [3]. The tribometer is adapted so an electrochemical cell can be placed above the rotatory plate (Fig. A.I.2). The machine allows applying a load in the range of 1 to 20 N and rotation speeds from 10 to 500 rpm. In the case of the work presented in chapter 5.2, the tests were performed in a UMT-CETR3 reciprocating tribometer [4], with loads in the range of 0.05 to 1000 N, and frequencies from 0.1 to 30 Hz. For both tribometers, the electrodes were connected to an Autobal-Metrohm PGSTAT302N potentiostat. Similarly to those in electrochemical corrosion tests, the electrodes used were a commercial Ag/AgCl (KCl 3M) as the RE, a platinum wire as the CE, and the test sample as the WE. The tests were performed under ball-on-disc configuration, using an alumina ball of 10 mm in diameter (G28) as the countermaterial. The tests conditions, in terms of applied load, were selected to be close to those in real applications. The contact conditions were calculated using the Hertzian Contact Theory, considering the contact pressure between links and accessories. The normal load was 5 N, corresponding to an average Hertzian pressure of 930 MPa with a contact radius of 50.5 µm. The electrochemical techniques employed in tribocorrosion tests consisted of a combination of the previously explained techniques.

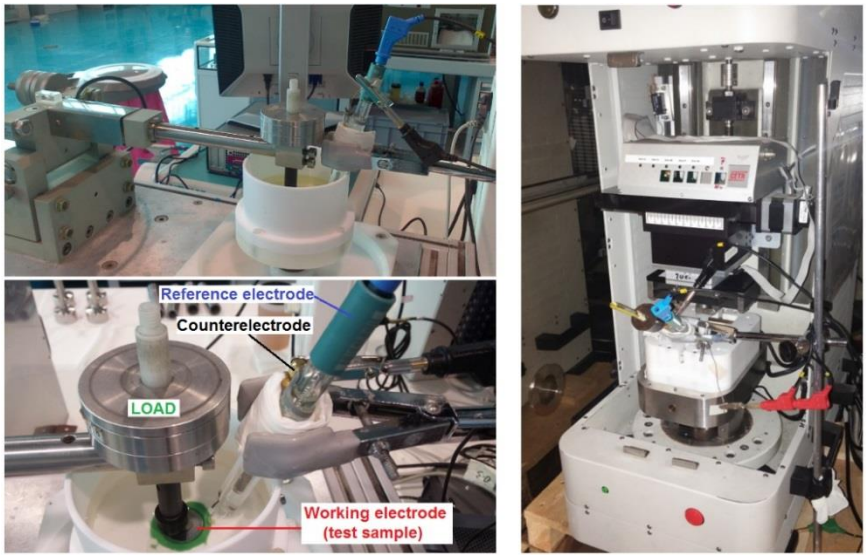

Fig. A.I.2 Tribocorrosion test set-up, showing the electrochemical cell disposition in detail in the MicroTest rotatory (right) and CETR reciprocating (left) tribometers used in this work

A.I.3 WEATHERING AGING TESTS

Weathering aging tests were performed according to several standards (ISO 6270 [5], ISO 2812 [6], ISO 9227 [7], ISO 16474 [8], etc.) to evaluate the effectiveness of different coatings for the protection of steel components, as regulated by the current classification societies (ISO 12944 [9] and NORSOK M501 [10] standards).

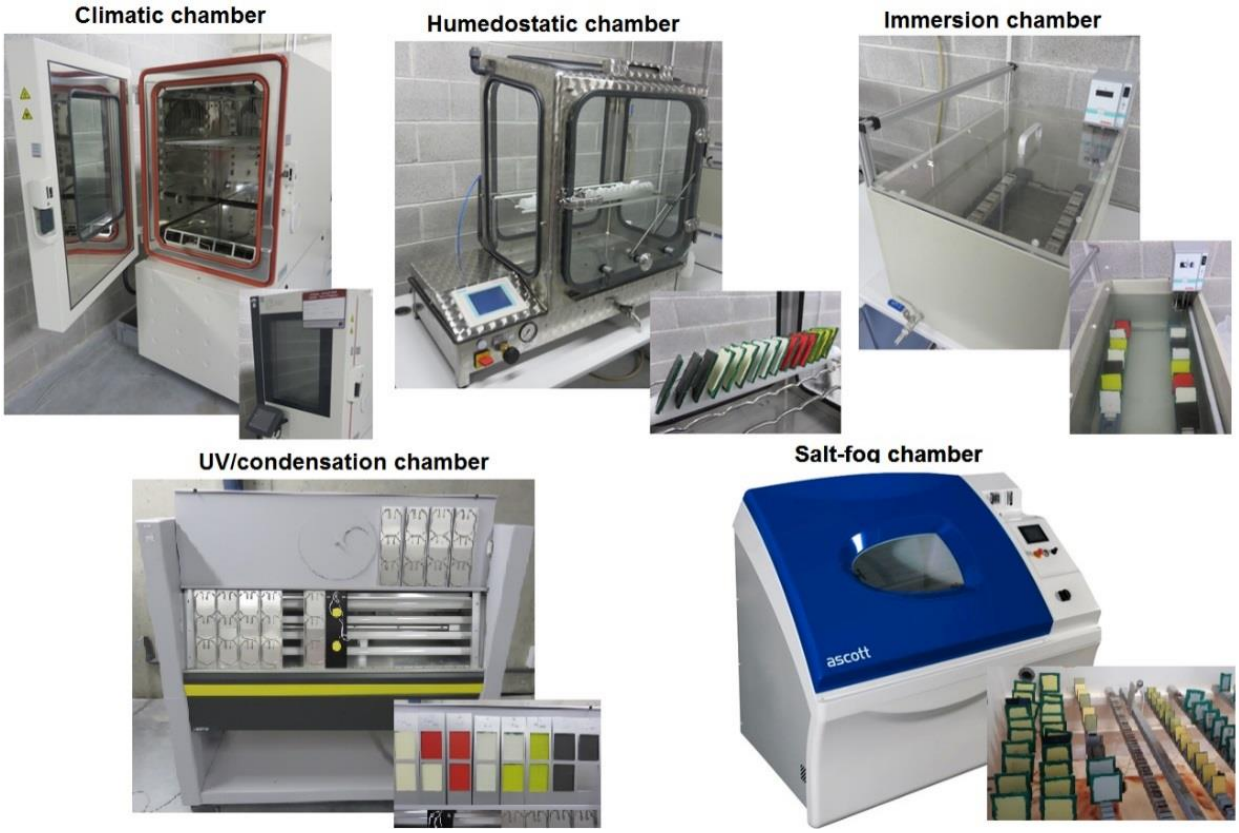

Fig. A.I.3 Climatic chambers employed in the ageing tests

The climatic chambers employed in the evaluation of coatings in chapters 5.5 and 5.7 are presented in Fig. A.I.3. The immersion tests were performed in a Julabo ED

thermostatic bath [11], the salt spray tests in a neutral salt fog chamber ASCOTT 2000S [12], and the condensation tests in a Kesternich HK300-800 S/M humidostatic chamber [13]. The climatic chamber WEISS C340/70 [14] was used to reproduce low-temperature conditions, and the Atlas UVTest weathering device [15] to perform UV radiation and water condensation cycles.

A.I.4 PLASMA ELECTROLYTIC OXIDATION TECHNIQUE

The Plasma Electrolytic Oxidation (PEO) process involves the application of a modulated voltage to the component in an electrolyte bath agitated using compressed air and under temperature control. The sample acts as an anode while the stainless steel mesh placed in the bath acts as a cathode. The process involves an anodic polarization of the sample to high voltages, exceeding the dielectric breakdown voltage, so as to generate discrete short-lived plasma micro-discharges in the surface. This results in oxidation of the component surface (plasma electrolytic oxidation) as well as elemental co-deposition from the electrolyte solution, which creates a hard ceramic oxide layer on the substrate alloy. The process schematic is presented in Fig. A.I.4.

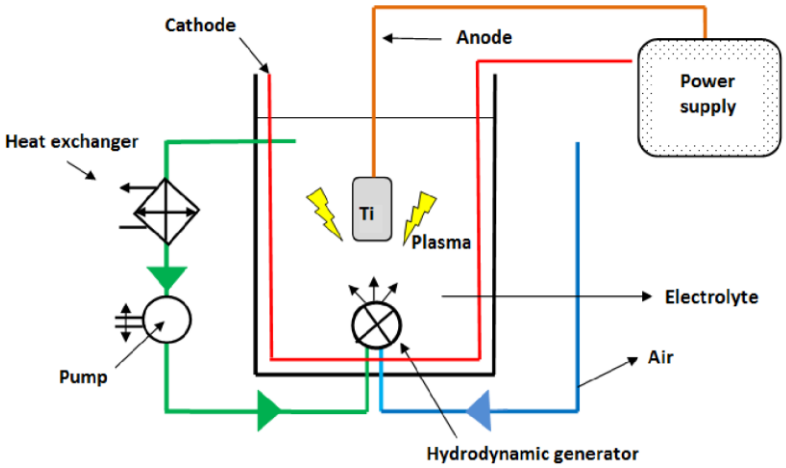

Fig. A.I.4 Schematic illustration of the Plasma Electrolytic Oxidation (PEO) process

The equipment used in this work was a commercial KERONITE KT 20-50 (20KW AC power supply) instrument [16]. The PEO coatings were generated above a Thermally Sprayed Aluminum (TSA) coating, to enhance the wear and tribocorrosion behavior of the aluminum layer. The coating system developed by PEO technique and its characterization are presented in chapter 5.6.

A.I.5 SURFACE CHARACTERIZATION TECHNIQUES

A.I.5.1 Optical microscopy

The optical microscope is one of the oldest microscopic techniques used in the characterization of surfaces. This useful tool allows the observation of the surface at high magnifications in order to make a first characterization of the surface. The microscope used in this work was the Olympus GX71 [17], equipped with the AnalySIS pro image software (Fig. A.I.5).

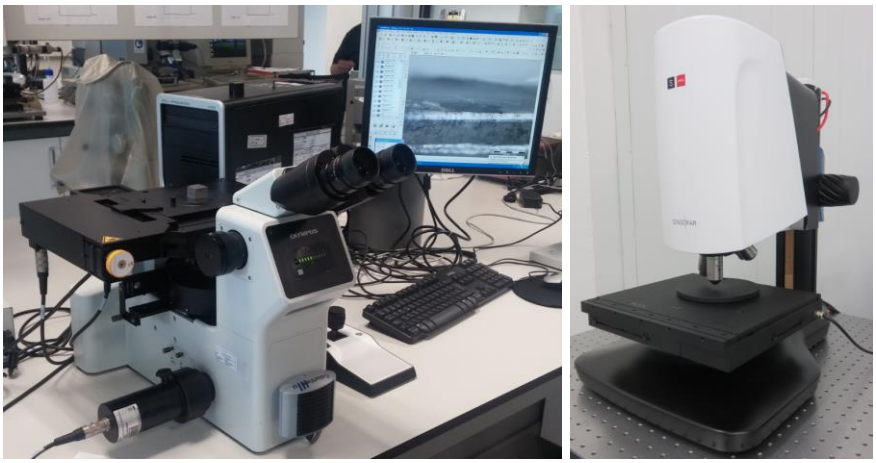

Fig. A.I.5 Olympus GX71 optical microscope (left) and Sensofar S Neox confocal microscope (right)

A.I.5.2 Confocal microscopy

Confocal microscopy is an optical imaging technique used to increase optical resolution and contrast of a micrograph by using point illumination and a spatial pinhole to eliminate out-of-focus light in specimens that are thicker than the focal plane. It enables the reconstruction of three-dimensional structures from the obtained images. This technique has gained popularity in the scientific and industrial communities, and typical applications are in life sciences, semiconductor inspection, and material science. The devices used in this work were a Nikon ECLIPSE ME600 (Z resolution 10 nm) and a Sensofar S Neox [18] confocal (Z resolution 3 nm) microscopes (Fig. A.I.5).

A.I.5.3 Scanning Electron Microscopy and Energy-Dispersive X-ray Spectroscopy

Scanning Electron Microscopy (SEM)

A scanning electron microscope (SEM) is a type of electron microscope that images a sample by scanning it with a high-energy beam of electrons in a raster scan pattern. The electrons interact with the atoms that make up the sample producing signals that contain information about the sample surface topography, composition, and other properties such as electrical conductivity. The types of signals produced by a SEM include secondary electrons, back-scattered electrons (BSE), characteristic X-rays, light (cathodoluminescence), specimen current and transmitted electrons. The signals result from interactions of the electron beam with atoms at or near the surface of the sample. In the most common or standard detection mode, secondary electron imaging (SEI), the SEM can produce very high-resolution images of a sample surface, revealing details less than 1 nm size. Due to the very narrow electron beam, SEM micrographs have a large depth of field yielding a characteristic three-dimensional appearance useful for understanding the surface structure of a sample.

Energy-Dispersive X-ray Spectroscopy (EDS)

EDX or EDS is an analytical technique used for the elemental analysis or chemical characterization of a sample. It is one of the variants of X-ray fluorescence spectroscopy which relies on the investigation of a sample through interactions between electromagnetic radiation and matter. Its characterization capabilities are in large part due to the fundamental principle that each element has a unique atomic structure allowing X-ray that are characteristic of an element's atomic structure to be identified uniquely from one another. To simulate the emission of characteristic X-rays from a specimen, a high-energy beam of charged particles such as electrons or protons, or a

beam of X-rays, is focused into the sample being studied. At rest, an atom within the sample contains ground state (or unexcited) electrons in discrete energy levels or electron shells bounds to the nucleus. The incident beam may excite an electron in an inner shell, ejecting it from the shell while creating an electron hole where the electron was. An electron from an outer, higher-energy shell then fills the hole, and the difference in the energy between the higher-energy shell and the lower energy shell may be released in the form of an X-ray. The number and energy of the X-rays emitted from a specimen can be measured by an energy-dispersive spectrometer. As the energy of the X-rays is a characteristic of the difference in energy between the two shells, and of the atomic structure of the element from which they were emitted, this allows the elemental composition of the specimen to be measured.

Fig. A.I.6 ZEISS ULTRA plus SEM microscope (left) and D8 Advance X-ray diffractometer (right)

The equipment used in this work was the ZEISS ULTRA plus Field Emission Scanning Electron Microscope with EDS and BSE microanalysis from OXFORD INCA synergy [19] (Fig. A.I.6). The equipment has a controlled field emission source with incorporated GEMINI® patented column, for high resolution and analysis from ZEISS Company.

A.I.5.4 X-ray diffraction

X-rays are electromagnetic radiation with the wavelength (λ) of the same order as the cell parameters of crystals. This makes crystalline substances able to diffract X-rays. When the radiation strikes on the atoms electronic cloud of a crystal lattice, these become on-time emitters of that radiation. The emitted radiation of each atom is expanded in the form of a spherical wave and interferes with that created by bordering atoms. This interference can be either destructive or constructive. The directions in which the interference is constructive follow Bragg's law:

$$n\lambda = 2d_{hkl}\sin\theta \qquad \text{(A.I.I)}$$

Where n is a natural number, λ the wavelength of the used X-rays, d_{hkl} the distance between two consecutive planes defined by a components vector hkl, and θ the radiation incidence angle.

X-ray diffraction (XRD) can be used to qualitatively analyze the phases present in a polycrystalline material, i.e., a material formed by a large number of small crystals randomly arranged. A sample with these features will always present a certain number of crystallites that fulfill Bragg's law when irradiated with a beam of X-rays. The diffractometers allow the accurate determination of the direction in which the diffraction occurs.

In the present thesis, X-ray measurements were performed to characterize the phase structure of the PEO coating developed in chapter 5.7. The analyses were carried out in a D8 Advance diffractometer from Bruker [20], equipped with a Cr-Kα1 radiation source (Fig. A.I.6). The measurements were carried out from5 to 160º in 2θ, with steps of 0.06º and time counting of 0.5 s. The results were analyzed with the DIFRAC.EVA software from Bruker.

A.I.5.5 Surface roughness measurements

Surface roughness, often shortened to roughness, is a measure of the texture of a surface. The tracing method is employed to determine the roughness of a surface, and it is an inspection method for the two-dimensional tracing of the surface. It requires a surface pick-up to be traversed horizontally across the surface at a constant speed. The traced profile is the surface profile, and it is quantified by the vertical deviations of a real surface from its ideal form. When the deviations are significant, the surface is rough, and, on the other hand, if the deviations are small, the surface is smooth.

Fig. A.I.7 Perthometer M2 profilometer of Mahr

In this work, the Marh Perthometer M2 [21] was used to measure the roughness of different surfaces (Fig. A.I.7). This equipment has a maximum measuring range of 150 µm, with a maximum cut off length of 17.5 mm. The evaluation and selection of the measurement length can be made according to different standards (ISO, JIS, CNOMO). For the calculation of the arithmetic average roughness (R_a) values, the equipment followed the DIN EN ISO 4288 and DIN EN ISO 4287 standards [22].

A.I.5.6 Vickers hardness tests

In this work, the hardness of different materials has been measured by Vickers indentation method, also referred as to microhardness test method. The test consists of making an indentation on the material, using a diamond pyramid, by applying a specific load at a controlled speed. The pyramid impresses a geometrical form in the surface, which size depends on the materials ability to resist the load imposed. The results are obtained in what is known as Vickers Hardness (HV), which can be converted to pascals or other hardness units, e.g., Rockwell or Brinell. After the indentation, the diagonals of the impressed diamond are measured and converted to HV by the following equation:

$$HV = \frac{F}{A} \approx \frac{0.1591\,F}{d^2} \qquad \text{(A.I.II)}$$

Where F is the applied force in newtons, A the surface area of the indentation in square millimeters, and d the diagonals of the impressed diamond in millimeters.

The macro and microhardness tests in this thesis have been performed in an Akashi AVK-A and a Future-Tech FM-700 testers, respectively (Fig. A.I.8). Both apparatuses are equipped with a Vickers indentation device, following the UNE-EN ISO 6507-1 [23]

standard. The applied loads were in the range of 0.025 to 1 Kg, depending on the test material nature, and the indentation time was set to 15 seconds.

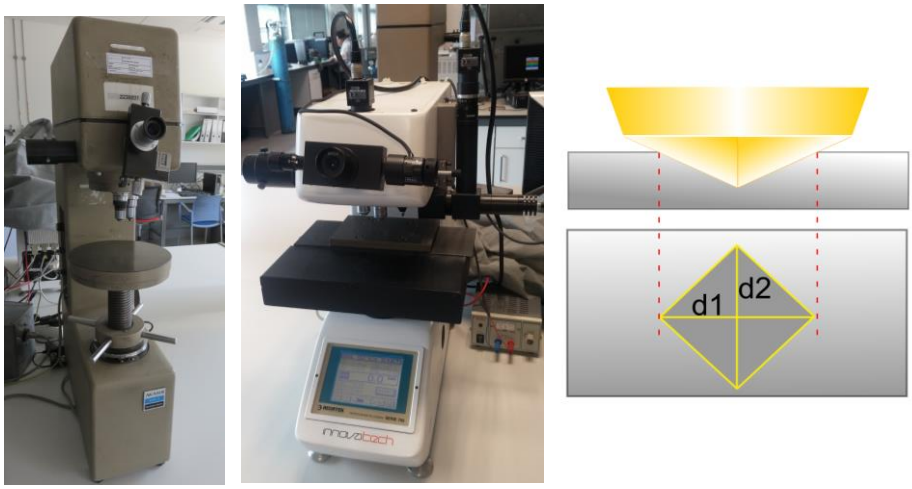

Fig. A.I.8 Akashi AVK-A tester, Future-Tech FM-700 tester, and schematic of the indentation made by the diamond indenter

A.I.5.7 Goniometer

The SURFTENS universal goniometer [24] was used to investigate the wetting behavior of the samples, i.e., to evaluate the hydrophilic/hydrophobic grade of the studied surfaces (Fig. A.I.9). This evaluation is based on the measurement of the static contact angle of a drop of water on the surface investigated.

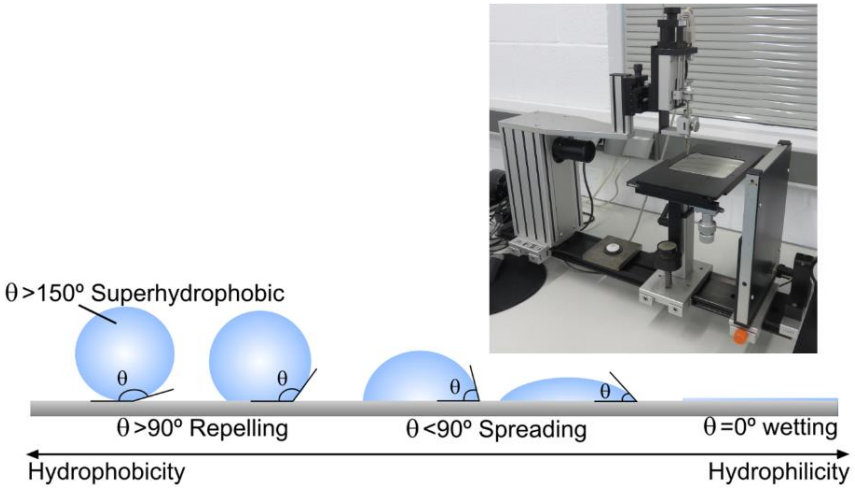

Fig. A.I.9 Schematic of the water drop shape and contact angle in solid surfaces with different hydrophobicity-hydrophilicity gradients, and SURFTENS universal goniometer

For the evaluation of the hydrophobicity of the coatings in chapter 5.7, synthetic seawater (ASTM D1141) was employed as the test liquid. The contact angle is measured by means of an optical system which calculates the values. The higher the contact angle value, the higher the hydrophobicity of the studied surface.

A.I.5.8 Pull-off adhesion tests

Adhesion tests consist of measuring the force required to pull the coating away from the substrate, by applying a specific pressure. The breaking points, i.e., the detachment of the coating, takes place along the weakest interface within the system composed by the substrate, the single or multi-layered coating, the glue, and the dolly. The fracture type can be determined by analyzing the test surface of both the coated substrate and the

dolly, and it can be either cohesive or adhesive (Fig. A.I.10). A cohesive fracture takes place within a coating layer, showing the same material in both the dolly and the coated substrate. On the other hand, an adhesive fracture occurs at the interface between layers, leaving different materials on the dolly and the coated substrate. The failure can also combine cohesive and adhesive fractures in different proportions along the different layers.

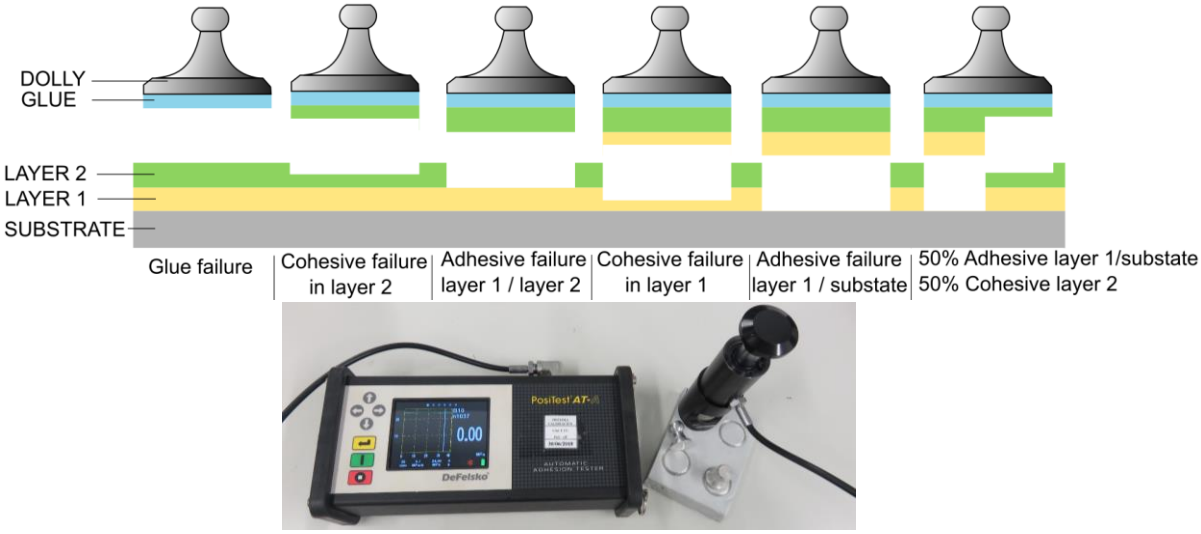

Fig. A.I.10 Schematic of the failure types in a pull-off adhesion test and PosiTest AT-A automatic equipment

The adhesion tests carried out in the characterization of coatings in chapters 5.6 and 5.7 were performed with a PosiTest AT-A automatic equipment from DeFelsko [25] (Fig. A.I.10). Aluminum dollies of 20 mm in diameter were stuck in the test surface with a methyl-based LOCTITE 496 adhesive and pulled-off after 48 hours of curing at a tensile rate of 0.7 MPa/s (ISO 4624 [26]).

A.I.6 CHEMICAL CHARACTERIZATION TESTS

A.I.6.1 Inductively Coupled Plasma Optical Emission Spectroscopy

The Inductively Coupled Plasma (ICP) associated with the Optical Emission Spectrometry (OES) is a multielement technique for the determination of 70 types of elements from the µg/L to the percent level without dilution. The technique is based upon the spontaneous emission of photons from atoms and ions that have been excited in a radio frequency (RF) discharge. Liquid and gas can be directly injected into the instrument, whereas solid samples require extraction or acid digestion so that the analytes will be present in a solution. The sample solution is converted to an aerosol and directed into the central channel of the plasma. At its core, ICP sustains a temperature of approximately 10000 K, which quickly vaporizes the aerosol. Analyte elements are then liberated as free atoms in the gaseous state. Further collisional excitation within the plasma imparts additional energy to the atoms, promoting their excited states. Sufficiently energy is often available to convert the atoms into ions and subsequently promote the ions to their excited states. Both the atomic and ionic excited state species may then relax to the ground state via the emission of a photon. These photons have characteristic energies that are determined by the quantized energy levels of the structure for the atoms or ions. Thus, the photons wavelengths can be used to identify the elements from which they originated, and the total number of photons is directly proportional to the concentration of the original element in the sample.

The ICP-OES in this work was used in the leaching obtained from superhydrophobic and bactericidal paint developed in chapter 5.7, in order to measure and quantify the copper and other main element release. The equipment used was an ULTIMA 2 HORIBA Jobin Yvon instrument [27].

A.I.7 ENVIRONMENTAL CHARACTERIZATION TESTS

A.I.7.1 Antibacterial activity tests

The antibacterial activity tests were performed in chapter 5.7 to evaluate the antifouling ability of the paint modified with nanoparticles incorporation. These tests consist of incubating a bacterial inoculum of a known concentration on the studied surfaces. The bacteria colonies are quantified in viable bacteria recovered per square centimeter after 24 hours of incubation at optimum temperature (35±2 ºC).

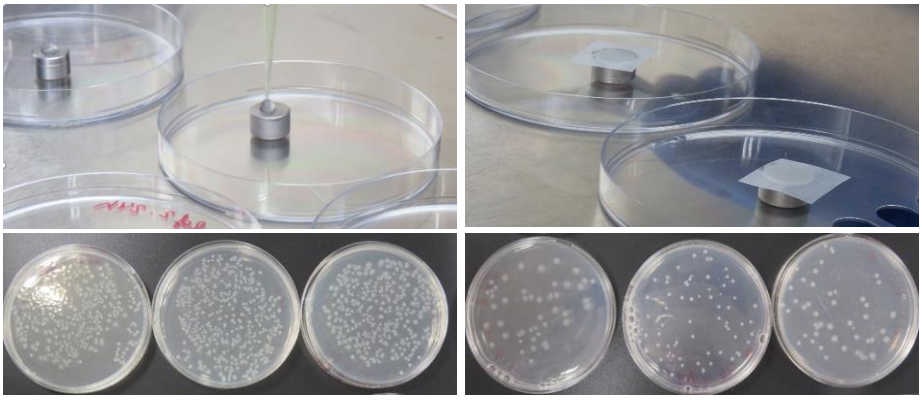

Fig. A.I.11 Image showing different steps of the antibacterial assessment test and different bacterial growth in the suspension incubated on the studied surfaces

The test procedure used in this thesis is based on the JIS Z2801 [28] standard, and its equivalent ISO 22196 [29]. The microorganism used for the study was the *Escherichia coli* ATCC 8739 (*E.Coli*). Prior to the tests, the surfaces were sterilized with UV radiation in a laminar airflow chamber for 15 minutes. The results are always contrasted with a negative control that allows the bacterial growth, to compare the ability of the test sample to reduce the bacterial activity. When evaluating hydrophobic surfaces such as the paints developed within this work, the bacteria inoculum viscosity should be increased by adding agar-agar, as indicated in the ISO 22196:2011 [30] standard.

A.I.7.2 Ecotoxicity tests

Ecotoxicity tests were performed to evaluate the toxicity of the paints with nanoparticles developed in chapter 5.7. The test procedure selected to analyze the antifouling coatings were marine algal growth inhibition tests following the ISO 10253 [31] standard using the MARINE ALGALTOXKIT [32] recommended. The marine algae used in the tests was *Phaeodactylum tricornutum* (MICROBIOTESTS Inc.), which were cultured in synthetic seawater mixed with nutrient containing solutions. The incubation of the algae culture was made three days before the tests, at a controlled temperature (20±2 ºC) with a constant lateral illumination of 100000 lux.

The evaluation of the paint toxicity was made by using the leaching obtained after stirring coated panels in synthetic seawater for several days (OECD no 23 guidance). The leaching was collected and analyzed by ICP-OES to measure the release rate of the main elements present in the samples every 24 hours for 28 days. The leachates in

which the release was observed to be the maximum was then selected to perform the ecotoxicity tests. The algal growth inhibition in the leachates was registered every 24 hours by measuring the optical density (OD) at 670 nm in a Jenway 6300 spectrophotometer [33]. With the optical density, it is possible to calculate the EL_{50}, which is the concentration of the leachate that causes a decrease of 50% in the algal growth.

Fig. A.I.12 Phaeodactylum tricornutum from the AGALTOXIKIT (left), algal growth (middle) and Jenway 6300 spectrophotometer

A.I.8 REFERENCES

[1] Information on the potentiostat and modules available at Atulolab's website (September 2018): http://www.metrohm-autolab.com/Products/Echem/NSeriesFolder/PGSTAT302N

[2] ASTM D1141. *Standard Practice for the Preparation of Substitute Ocean Water*. July 2012

[3] Information on the MicroTest tribometer available at (September 2018): http://www.microtest-sa.com/en_US/productos/equipos-de-ensayo/tribometros-indentadores/

[4] Information on the UMT series tribometers available at (September 2018): https://www.bruker.com/products/surface-and-dimensional-analysis/tribometers-and-mechanical-testers/umt-tribolab/overview.html

[5] ISO 6270-2. *Paints and varnishes. Determination of resistance to humidity*. Second edition, November 2017

[6] ISO 2812-2. *Paints and varnishes. Determination of resistance to liquids*. Second edition, January 2007

[7] ISO 9227. *Corrosion tests in artificial atmospheres. Salt spray test*. Fourth edition, March 2017

[8] ISO 16474-3 *Paints and varnishes. Methods of exposure to laboratory light sources. Fluorescence UV lamps.* September 2014

[9] ISO 12944:1-9. *Paints and varnishes. Corrosion protection of steel structures by protective paint systems*. November 2017-February 2018

[10] NORSOK M-501. *Surface preparation and protective coating*. Sixth edition, February 2012

[11] Information on the Julabo ED thermostatic bath available at (September 2018): https://www.julabo.com/en/products

[12] Information on the ASCOTT 2000S chamber available at (September 2018): https://www.ascott-analytical.com/salt-spray-key-features/

[13] Information on the Kesternich HK300-800 S/M humidostatic chamber available at (September 2018) (September 2018): https://www.cts-clima.com/en/corrosion/kesternich-and-humidostatic-chamber.html

[14] Information on the WEISS C340/70 climatic chamber available at (September 2018): https://testlab.amtest.eu/en/our-test-equipment/climate-chambers-c340-40-and-c340-70

[15] Information on the Atlas UVTest chamber available at (September 2018): https://www.atlas-mts.com/products/standard-instruments/fluorescent-uv

[16] Information on the KERONITE KT 20-50 equipment manufacturer available at (September 2018): https://www.keronite.com/

[17] Information on the Olympus GX71 optical microscope available at (September 2018): https://www.olympus-ims.com/es/microscope/gx71/
[18] Information on the Sensofar S Neox confocal microscope available at (September 2018): https://www.sensofar.com/metrology/sneox/
[19] Information on the ZEISS ULTRA plus SEM microscope available at (September 2018): https://www.zeiss.com/microscopy/int/products/scanning-electron-microscopes.html
[20] Information on the D8 Advance diffractometer available at (September 2018): https://www.bruker.com/es/products/x-ray-diffraction-and-elemental-analysis/x-ray-diffraction/d8-advance/technical-details.html
[21] Information on the Perthometer M2 profilometer available at (September 2018): http://surfacefinishequipment.com/mahr-m1-mahr-m2.html
[22] DIN EN ISO 4288. *Geometrical products specifications (GPS). Surface texture: Profile method. Rules and procedures for the assessment of surface texture*. July 2008
[23] UNE-EN ISO 6507-1. *Metallic materials. Vickers hardness tests. Part I: Test method*. Third edition, November 2006
[24] Information on the SURFTENS universal goniometer available at (September 2018): http://www.optophase.com/Brochure/OEG/SurfTens/Surftens_universal_e.pdf
[25] Information on the PosiTest AT-A equipment available at (September 2018): https://www.defelsko.com/positest-at#at-a
[26] ISO 4624. *Paints and varnishes. Pull-of test for adhesion*. February 2016
[27] Information on the ULTIMA 2 HORIBA instrument available at (September 2018): http://www.horiba.com/fileadmin/uploads/Scientific/Documents/Emission/JY20002.pdf
[28] JIS Z2108:2012. *Antibacterial Products-Test for antibacterial activity and efficacy*. May 21, 2012
[29] ISO 22196:2011. *Measurement of antibacterial activity on plastics and other non-porous surfaces*. August 1, 2011
[30] ISO 22196:2011. *Measurement of antibacterial activity on plastics and other non-porous surfaces*. August 1, 2011
[31] ISO 10253. *Water quality: Marine algal growth inhibition test with Skeletonema sp. And Phaeodactylum tricornutum*. Third edition, November 2011
[32] Information on the MARINE ALGALTOXIKIT available at (September 2018): http://www.microbiotests.be/toxkits/marine%20algaltoxkit.pdf
[33] Information on the Jenway 6300 spectrophotometer available at (September 2018): http://www.jenway.com/product.asp?dsl=289

ANNEX II

Publications and dissemination activities

Annex II: Publications and dissemination activities

A.II.1 PUBLICATIONS

Publications of the author related with the subject of the thesis

A. López, R. Bayón, F. Pagano, A. Igartua, A. Arredondo, J.L. Arana, J.J. González *Tribocorrosion behaviour of mooring High Strength Low Alloy steels in synthetic seawater*. Wear 339-339 (2015) 1-10

A. López-Ortega, R. Bayón, J.L. Arana, A. Arredondo, A. Igartua. *Influence of Temperature on the Corrosion and Tribocorrosion Behaviour of High Strength Low Alloy Steels used in offshore applications*. Tribology International 121 (2018) 341-352

A. López-Ortega, J.L. Arana, R. Bayón. *Tribocorrosion of passive materials: a review on test procedures and standards*. International Journal of Corrosion, vol 2018, article ID 7345346, 24 pages, 2018

A. López-Ortega, R. Bayón, J.L. Arana. *Evaluation of protective coatings for offshore applications. Corrosion and tribocorrosion behavior in synthetic seawater*. Surface & Coatings Technology 349 (2018) 1083-1097

A. López-Ortega, J.L. Arana, E. Rodríguez. R. Bayón. *Corrosion, wear and tribocorrosion performance of a Thermally Sprayed Aluminum coating modified by Plasma Electrolytic Oxidation for offshore submerged components protection*. Corrosion Science 143 (2018) 258-280

A. López-Ortega, R. Bayón, J.L. Arana. *Evaluation of protective coatings for offshore applications. Validation for high corrosivity category atmospheres*. Under review (Marine Structures)

A. López-Ortega, J.L. Arana, R. Bayón. *Effect of agitation on the tribocorrosion behavior of active materials*. Under review (Corrosion Science)

A. López-Ortega, O. Areitioaurtena, S. Alves, I. Elexpe, A.M. Goitandia, J.L. Arana, R. Bayón. *Development of a superhydrophobic and bactericide sealant to be applied on thermally sprayed aluminum coatings for offshore submerged components protection*. Under review (Progress in Organic Coatings)

Other publications of the author related with tribocorrosion

L. Mendizabal, **A. López**, R. Bayón, J. Barriga, A. Igartua. *Tribocorrosion response of multilayer TaN coatings deposited by HPPMS technology in biological environments*. Surface and Coatings Technology 295 (2016) 60-69

A.II.2 DISSEMINATION ACTIVITIES

Contributions of the author to international conferences related with the subject of the thesis

Ainara López, Francesco Pagano, Raquel Bayón, Amaya Igartua. *Tribocorrosion effects on offshore mooring chain steel*. Eurocorr 2014, Pisa (Italy), 08-12/09/2014

Ainara López, Raquel Bayón, Jose Luis Arana, Francesco Pagano, Amaya Igartua. *Tribocorrosion behavior of mooring HSLA steel in synthetic seawater under bidirectional sliding*. Ibertrib 2015, Cartagena (Spain), 18-19/06/2015

Ainara López, Raquel Bayón, Jose Luis Arana, Francesco Pagano, Amaya Igartua. *Tribocorrosion behavior of mooring HSLA steel in synthetic seawater under bidirectional sliding*. Eurocorr 2015, Graz (Austria) 6-10/09/2015

Raquel Bayón, **Ainara López-Ortega**, E. Rodriguez. *Tribocorrosion behavior of mooring high strength low alloy steels in synthetic seawater with and without protective coatings*. NACE Milano Italia Section-Conference & Expo 2016, Genoa (Italy), 29-31/05/2016

Ainara López-Ortega, Raquel Bayón, Elena Rodríguez, Amaya Igartua, Jose Luis Arana. *Tribocorrosion behavior of coated and uncoated high-strength low-alloy steel in sea-water environment*. Lubmat 2016, Bilbao (Spain), 7-8/06/2016

Raquel Bayón, **Ainara López-Ortega**, Roman Nevshupa, Isabel Martinez. *Corrosion and corrosion-wear behavior of high-strength low-alloy steel in offshore environment*. XIV CNMAT 2016, Gijón (Spain), 8-10/06/2016

Ainara López-Ortega, Raquel Bayón, Alberto Arredondo, Jose Luis Arana, Amaya Igartua. *Evaluation of the corrosion and tribocorrosion behavior of potential coatings in offshore applications*. Nordtrib 2016, Hämeenlinna (Finland), 13-17/06/2016

Raquel Bayón, **Ainara López-Ortega**, Amaia Martinez, Iker Elexpe, Elena Rodríguez. *Advanced protection solutions for increasing the durability of mooring lines* (Poster). Marine Energy Week 2017, Bilbao (Spain), 27-31/03/2017

Ainara López-Ortega, Raquel Bayón, Alberto Arredondo, Jose Luis Arana, Amaya Igartua. *Influence of temperature on the corrosion and tribocorrosion behavior of high-strength low-alloy steels used in offshore applications* (Oral & Poster). Ecotrib 2017, Ljubljana (Slovenia), 07-09/06/2017. *Best student poster award, second place*.

Ainara López-Ortega, Raquel Bayón, Jose Luis Arana. *Influence of agitation and rotation speed on the tribocorrosion behaviour of a HSLA steel in seawater environment*. Eurocorr 2017, Prague (Czech Republic), 04-07/09/2017

Ainara López-Ortega, Raquel Bayón, Jose Luis Arana. *Wear and corrosion performance of a modified TSA coating for offshore submerged components*. NACE Milano Italia Section-Conference & Expo 2018, Genoa (Italy), 27-29/05/2018

Ainara López-Ortega, Raquel Bayón, Jose Luis Arana. *Corrosion and wear-corrosion behavior of protective coatings for offshore applications* (Poster). NACE Milano Italia Section-Conference & Expo 2018, Genoa (Italy), 27-29/05/2018

Ainara López-Ortega, Jose Luis Arana, E. Rodriguez, Raquel Bayón. *Enhancement of the wear-corrosion behavior of a Thermally Sprayed Aluminum coating for offshore submerged components by Plasma Electrolytic Oxidation Technique*. Lubmat 2018, San Sebastián (Spain), 05-06/06/2018

Ainara López-Ortega, Jose Luis Arana, Raquel Bayón. *Tribocorrosion of steel and coatings in offshore*. SMT32 2018, San Sebastian (Spain), 27-29/06/2018

Ainara López-Ortega, Jose Luis Arana, E. Rodriguez, Raquel Bayón. *Tribocorrosion behavior of a modified TSA coating employed in offshore submerged components*. XV CNMAT 2018, Salamanca (Spain), 04-06/07/2018

Contributions of the author to international conferences related with corrosion or tribocorrosion

L. Mendizabal, **A. López**, R. Bayón, J. Barriga, A. Igartua. *Tribocorrosion response of multilayer TaN coatings deposited by HPPMS technology in biological environments*. ICTF 2014, Dubrovnik (Croatia), 13-16/10/2014

L. Mendizabal, **A. López-Ortega**, R. Bayón. *Tribocorrosion response of multilayer TaN coatings deposited by HPPMS technology in biological environments.* E-MRS 2015, Lille (France), 11-15/05/2015

V. Sáenz de Viteri, R. Bayón, **A. López-Ortega**, A. Vela, A. Cimpean, D. Stanciu. *Multifunctional TiO2 coatings by Plasma Electrolytic Oxidation on TiNbZrTa alloy for dental applications*. Lubmat 2018, San Sebastián (Spain), 05-06/06/2018

Borja Zabala, Amaya Igartua, Txomin Goitia, Javier Calvo, Ana García, Xana FernándeZ, **Ainara López-Ortega**, Juan Carlos Rodriguez, Frank Girot. *Experimental study on plastic injection moulding moulds wear*. Lubmat 2018, San Sebastián (Spain), 05-06/06/2018

L. Mendizabal, **A. López-Ortega**, J. Barriga. *High Performance antibacterial thin films for titanium biomedical components*. 16th International Conference on Plasma Surface Engineering 2018, Garmisch-Partenkirchen (Germany), 17- 21/09/2018

Relevant journal publications

Hindawi
International Journal of Corrosion
Volume 2018, Article ID 7345346, 24 pages
https://doi.org/10.1155/2018/7345346

Review Article

Tribocorrosion of Passive Materials: A Review on Test Procedures and Standards

A. López-Ortega,[1] **J. L. Arana**,[2] **and R. Bayón**[1]

[1]*IK4-TEKNIKER, Eibar, Spain*
[2]*Department of Metallurgical and Materials Engineering, University of the Basque Country, Spain*

Correspondence should be addressed to A. López-Ortega; ainara.lopez@tekniker.es

Received 31 January 2018; Accepted 29 April 2018; Published 7 June 2018

Academic Editor: Ramesh Chinnakurli

This paper reviews the most recent available literature relating to the electrochemical techniques and test procedures employed to assess tribocorrosion behaviour of passive materials. Over the last few decades, interest in tribocorrosion studies has notably increased, and several electrochemical techniques have been adapted to be applied on tribocorrosion research. Until 2016, the only existing standard to study tribocorrosion and to determine the synergism between wear and corrosion was the ASTM G119. In 2016, the UNE 112086 standard was developed, based on a test protocol suggested by several authors to address the drawbacks of the ASTM G119 standard. Current knowledge on tribocorrosion has been acquired by combining different electrochemical techniques. This work compiles different test procedures and a combination of electrochemical techniques used by noteworthy researchers to assess tribocorrosion behaviour of passive materials. A brief insight is also provided into the electrochemical techniques and studies made by tribocorrosion researchers.

1. Introduction

In accordance with the ASTM G 40 Standard [1], tribocorrosion can be defined as a synergetic process involving the simultaneous action of contact between surfaces in relative motion with the chemical reactions in the environment, where each process is affected by the action of the other and, in many cases, accelerated.

The first steps in the field of tribocorrosion date back to 1875, when Edison observed alterations in the coefficient of friction with different applied potentials [2]. The effect of surface chemistry on the mechanical response of materials has been investigated since the beginning of the twentieth century [3]. Between the late 1970s and early 1980s, the effect of wear on corrosion was studied by several researchers in different industrial application systems, i.e., abrasion-corrosion, erosion-corrosion, or sliding-corrosion [4]. But it was not until the 1990s that tribocorrosion mechanisms in sliding contact were proposed by Mischler et al. (1993) [5] and Madsen (1994) in a standard form [6].

Tribocorrosion encompasses several industrial sectors, e.g., material processing, energy conversion, transportation, oil and gas exploration, medical and dental implants, surgical devices, among others [2, 7, 8]. Due to its impact on daily life and potential economic benefits, interest in the study of tribocorrosion phenomenon has increased over the last few decades [3, 9, 10]. As a consequence, several electrochemical techniques have been adapted to be applied to tribocorrosion research. Thus, crucial improvements in the study of tribocorrosion have been achieved through a better interpretation of triboelectrochemical results [7, 11].

Despite growing interest and the enhancement of electrochemical techniques, standardized testing methodology for tribocorrosion evaluation has only been made available recently. Prior to 2016, the only existing standard was the ASTM G119 [6], which describes a method to determine the synergism between wear and corrosion. However, this standard has drawn criticism from several authors who developed different approaches to study the tribocorrosion behaviour of passive materials [3, 12, 13]. In 2016, a new standard (UNE 112086 [14]) was published, with a different

Wear 338-339 (2015) 1–10

Contents lists available at ScienceDirect

Wear

journal homepage: www.elsevier.com/locate/wear

Tribocorrosion behaviour of mooring high strength low alloy steels in synthetic seawater

A. López [a,*], R. Bayón [a], F. Pagano [a], A. Igartua [a], A. Arredondo [b], J.L. Arana [c], J.J. González [c]

[a] IK4-Tekniker, Eibar, Spain
[b] Vicinay Innovación, Bilbao, Spain
[c] Department of Metallurgical and Materials Engineering, University of Basque Country, Spain

ARTICLE INFO

Article history:
Received 29 December 2014
Received in revised form
2 May 2015
Accepted 6 May 2015
Available online 14 May 2015

Keywords:
High strength steel
Tribocorrosion
Corrosion
Seawater

ABSTRACT

Offshore components of High-Strength Low-Alloy Steel (HSLA) are frequently exposed to tribological and corrosion effects during their working life. In the present work, several experiments have been performed to study the tribocorrosion behaviour of two steel grades, under unidirectional sliding in synthetic seawater. Sliding wear tests were performed under potentiodynamic and potentiostatic conditions at different applied potentials. The wear tracks were analysed by means of optical microscope and profilometry. The wear-corrosion synergism was quantified according to the ASTM G119 standard. Sliding promotes the wear accelerated corrosion of the unworn area in both alloys. Furthermore, the coefficient of friction of the steels is strongly influenced by the corrosion products and the applied potential.

1. Introduction

The main energetic sources used nowadays are oil and gas, especially those generated offshore. The platforms used for this aim have a great impact at environment, social and economic levels. Offshore platforms are tied up to the sea bottom through mooring systems, which are composed of chains, anchor systems and connectors.

High strength steels (yield strength from 460 MPa to 960 MPa) are increasingly being used in offshore structural applications. These steels offer some advantages over conventional steels, especially when the weight plays an important role.

When immersed in the ocean, the chains are subjected to high corrosion rates [1] especially in the splash zone, where the concentration of oxygen is high. Moreover, the floater motions induced by the environmental actions due to waves, wind and current movements of the sea [2,3] involves the links to be in relative motion with each other leading to a continuous wear in the surfaces in contact [1]. Wear and corrosion are two processes that lead to a surface damage due to a progressive material loss as a result of mechanical and electrochemical processes, respectively [4]. When this two degradation processes occur in a simultaneous way, it is known as tribocorrosion.

In accordance with the ASTM G40 Standard [5], tribocorrosion can be defined as a form of solid surface alteration that involves the joint action of relatively moving mechanical contact with chemical reaction in which the result may be different in effect than either process acting separately. In other words, it is the process leading to an irreversible transformation of the material resulting from the simultaneous physic-chemical and mechanical surface interactions occurring at a tribological contact [6–11]. In passive materials, the origin of tribocorrosion is closely related to the presence of a protective oxide film of few nm thick on material surfaces [11–13]. Under tribocorrosion conditions two main mechanisms contribute to material removal from the surface of the material: wear accelerated corrosion and mechanical removal from the sliding contact [4,7,13–15]. Tribocorrosion involves numerous synergy effects between mechanical and chemical or electrochemical phenomena [6–11].

The tribocorrosion behaviour of passive materials such as stainless steels or titanium has been widely studied [16–18] during years in different solutions. It is well known that these passive materials form a protective layer of few nanometres thick, which is mostly composed by oxides as a consequence of a spontaneous reaction when immersed in aqueous solutions [11–13].

As for low alloy steels, as those used in mooring line chains, the content in alloy elements is not enough to form such protective layer, and the major oxide formed is the ferric oxyhydroxide (FeOOH). The rust layer formed in carbon steels has a complex morphology and it is generally porous, with poor adherence and cracked in the outer part [19–21]. Unlike that formed on stainless steels, the film is not protective in the presence of corrosive electrolytes and it usually breaks down [22], so the electrolyte and

* Corresponding author. Tel.: +34 943206744; fax: +34 551 943202757.
E-mail address: ainara.lopez@tekniker.es (A. López).

http://dx.doi.org/10.1016/j.wear.2015.05.004
0043-1648/

Tribology International 121 (2018) 341–352

Contents lists available at ScienceDirect

Tribology International

journal homepage: www.elsevier.com/locate/triboint

Influence of temperature on the corrosion and tribocorrosion behaviour of High-Strength Low-Alloy steels used in offshore applications

A. López-Ortega [a,*], R. Bayón [a], J.L. Arana [b], A. Arredondo [c], A. Igartua [a]

[a] IK4-TEKNIKER, Eibar, Spain
[b] Department of Metallurgical and Materials Engineering, University of Basque Country, Spain
[c] Vicinay Marine Innovación, Bilbao, Spain

ARTICLE INFO

Keywords:
High Strength Low Alloy steel
Tribocorrosion
Seawater
Offshore

ABSTRACT

Tribocorrosion is an important failure cause of High-Strength Low-Alloy steel (HSLA) components in offshore applications due to the synergistic effect of wear and the corrosiveness of seawater. In this work, the effect of temperature on the tribocorrosion behaviour of two steel grades has been investigated by performing tribocorrosion tests under reciprocating sliding at two electrolyte temperatures. The total material loss due to corrosion in the unworn surface and due to tribocorrosion in the wear track was quantified. Sliding was found to accelerate the corrosion in the unworn area. Furthermore, temperature was confirmed to have an important effect on the tribocorrosion behaviour of the steels, in terms of higher material losses due to corrosion at higher test temperature.

1. Introduction

The materials working in offshore applications, are subjected to very harsh environmental conditions that accelerate their degradation. In marine environments, several phenomena take place simultaneously, which can shorten the useful life of structural materials leading to unpredicted failures. In the case of mooring systems, for instance, tribocorrosion plays an important role in terms of premature failure of components [1]. On one hand, the relative motion between chain links and connectors generated by waves, wind and ocean currents [2,3] leads to a continuous wear process in the contact surfaces. Moreover, corrosion is another important phenomenon to take into consideration in marine environments. The components that are continuously submerged or located in the splash zone of offshore structures, are subjected to high rate corrosion processes [4]. When wear and corrosion take place simultaneously, the process is known as tribocorrosion. There is a synergism between wear and corrosion, since the material loss when the two processes are occurring simultaneously, is greater than when they act separately [5,6].

Tribocorrosion of passive materials, e.g., stainless steels and titanium alloys, has been widely studied during the last decades for different applications and corrosive environments. It is well known that passive materials form a protective oxide layer of few nanometres in the surface [5–7], and that wear locally destroys and removes this layer, exposing the underlying fresh material to the electrolyte. The unprotected material in the track generated by wear undergoes corrosion while the intact protective film in the unworn surface remains undamaged [5–8]. However, the use of passive materials in offshore applications is limited, due to their high cost in comparison with lower alloyed steels, that meet the mechanical requirements at the expense of a higher corrosion resistance. For instance, High Strength steels (HSS), with yield strength values ranging from 460 to 960 MPa, are commonly used in offshore structural applications due to the high resistance/weight ratio. Submerged structures, anchor systems, chains and connectors composing mooring systems of offshore oil and gas platforms are predominantly manufactured with HSS steels. This kind of low-alloyed steels do not grow a protective oxide layer in the surface as a consequence of their low content in alloying elements precursors of passive film formation (Cr, Ni, Mo, etc). The dominant oxide formed on their surface is the ferric oxyhydroxide (FeOOH) compound. This rust film is highly porous and presents week adhesion bonds [9–12], allowing the electrolyte to penetrate though and reach the bare steel leading to continuous corrosion processes and high rates of material loss. Therefore, unlike passive alloys, low alloy steels are subjected to corrosion not only in the regions where the rust layer has been removed due to wear, but also in the remainder surface where the oxide layer does not form an effective barrier. Consequently, the surface degradation experienced in these steels is the sum of the material loss resulting from tribocorrosion in the contact area and the

* Corresponding author.
E-mail address: ainara.lopez@tekniker.es (A. López-Ortega).

https://doi.org/10.1016/j.triboint.2018.01.049
Received 1 August 2017; Received in revised form 17 November 2017; Accepted 22 January 2018
Available online 2 February 2018

Surface & Coatings Technology 349 (2018) 1083–1097

Contents lists available at ScienceDirect

Surface & Coatings Technology

journal homepage: www.elsevier.com/locate/surfcoat

Evaluation of protective coatings for offshore applications. Corrosion and tribocorrosion behavior in synthetic seawater

A. López-Ortega[a,*], R. Bayón[a], J.L. Arana[b]

[a] IK4-TEKNIKER, Eibar, Spain
[b] Department of Metallurgical and Materials Engineering, University of the Basque Country, Spain

ARTICLE INFO

Keywords:
Offshore
Corrosion
Tribocorrosion
Coatings
Seawater

ABSTRACT

Coatings have been widely used in the corrosion protection of metallic materials in marine environments. In this work, the corrosion and tribocorrosion behavior of three potential coatings employed in offshore applications has been evaluated. The coatings studied were a Thermally Sprayed Carbide coating with an organic sealant (C1), a Thermally Sprayed Aluminum with an organic sealant (C2), and an epoxydic organic coating reinforced with ceramic platelets (C3). Electrochemical Impedance Spectroscopy and Potentiodynamic Polarization techniques have been employed to assess the corrosion performance of the coatings in synthetic seawater. Furthermore, unidirectional ball-on-disc tribocorrosion tests were performed to study the response of the coatings subjected to simultaneous action of wear and corrosion. The coatings were found to provide to the steel substrate with enhanced corrosion resistance, both in absence and during wear process, and to improve in the tribological properties with lower coefficients of friction in seawater. The coating less affected by sliding in terms of corrosion resistance was C2 coating, which also showed the lowest coefficient of friction.

1. Introduction

Corrosion is one of the phenomena that worst affects the deterioration of materials in offshore applications. A 30% of failures in ships and other marine equipment are consequence of marine corrosion, with an annual cost of over $1.8 trillion [1]. Marine corrosion is particularly aggressive, due to the high salt content and low electrical resistivity of seawater [2]. The chlorides present in seawater depassivate metal and alloys such as stainless steels, aluminum alloys or titanium alloys; even in absence of oxygen. Chlorides are also present in marine atmospheres, which can lead to corrosion of non-submerged materials and structures [3]. The maximum corrosion rate of steel has been observed to be at a NaCl content of 3% in weight, which corresponds to the salinity of seawater (around 3.5wt%) [1, 4]. There are other factors affecting corrosion in seawater and marine environments, e.g., temperature, dissolved oxygen concentration, pH, presence of microorganisms, and so on [1, 5–7]. Temperature and salinity of seawater, as well as dissolved oxygen concentration vary depending on the geographical location. Furthermore, temperature and oxygen concentration also vary with water depth [1, 5, 6, 8, 9]. On the other hand, there are certain applications, e.g. mooring line systems, where the movement of seawater due to waves, wind and ocean currents, generates a relative movement between components that leads to a continuous wear in the contact [7, 10, 11]. When wear and corrosion take place simultaneously, the phenomenon is known as tribocorrosion [12–14].

The most employed structural material is steel, usually mild or low-alloyed, which easily corrodes in marine environment or submerged in seawater. These steels are relatively cost-effective, compared to other more corrosion resistant steels and alloys [1]. High-Strength Low-Alloyed (HSLA) steels, for instance, are widely used due to their high mechanical properties, with yield strengths in the range of 460–960 MPa, and relatively low weight [15, 16]. The use of HSLA steels in offshore applications has increased from less than 10% to over 40% in less than a decade [17]. They are used in the fabrication of offshore structures such as jack-ups and legs, also in pipelines and tethering attachments for floating structures in tension leg platforms (TLPs), or mooring lines of semi-submersible structures, among others [15, 18, 19]. The corrosion rate of mild steel in seawater has been measured to be 250 μm per year [20, 21]. This high dissolution rate involves elevate costs on maintenance and replacement of damaged surfaces, and what is worse, the risk of premature deterioration of infrastructures or components that can lead to catastrophic failures, even taking human lives in the worst-case scenario.

In order to avoid or prevent such unpredictable failures, coatings have been successfully used to minimize corrosion losses in steel structures. Protective coatings selected for marine environment

* Corresponding author.
E-mail address: ainara.lopez@tekniker.es (A. López-Ortega).

https://doi.org/10.1016/j.surfcoat.2018.06.089
Received 12 January 2018; Received in revised form 15 May 2018; Accepted 27 June 2018
Available online 01 July 2018

Corrosion Science 143 (2018) 258–280

Contents lists available at ScienceDirect

Corrosion Science

journal homepage: www.elsevier.com/locate/corsci

Corrosion, wear and tribocorrosion performance of a thermally sprayed aluminum coating modified by plasma electrolytic oxidation technique for offshore submerged components protection

A. López-Ortega[a,*], J.L. Arana[b], E. Rodríguez[c], R. Bayón[a]

[a] IK4-TEKNIKER, Eibar, Spain
[b] Department of Metallurgical and Materials Engineering, University of the Basque Country, Spain
[c] Vicinay Marine Innovación, Spain

ARTICLE INFO

Keywords:
Offshore
Corrosion
Tribocorrosion
Coatings
Thermally sprayed aluminum
Plasma electrolytic oxidation

ABSTRACT

Thermally Sprayed Aluminum (TSA) coatings have been widely employed to protect steel components from corrosion in marine environment. However, TSA is highly damaged in transport operations, due to the low wear resistance of aluminum, leading to a rapid coating deterioration during final service. In this work, the TSA properties have been improved by Plasma Electrolytic Oxidation (PEO) technique. The response of the newly generated TSA/PEO duplex system was investigated by means of sliding wear tests, electrochemical corrosion tests, and tribocorrosion tests in synthetic seawater. The study was completed with several characterization techniques, including SEM and confocal microscopy, and X-ray diffractometry.

1. Introduction

Marine environment is a very aggressive working atmosphere, that comprises several phenomena that can accelerate the degradation of structural materials reducing their useful life. The exposition to ultraviolet radiation, chloride rich salty environment, frequent wet-dry cycles, high humidity, low temperature, and the presence of marine bacteria and microorganisms are some examples. Corrosion is one of the phenomena that worst affect the deterioration of materials in offshore applications. The high salinity and low electrical resistivity of seawater makes this environment especially aggressive [1]. In certain applications, materials are also subjected to mechanical stresses than can lead to premature failure of components and structures. This is the case of Oil & Gas platforms, wind towers, renewable energy extraction systems, and mooring lines, inter alia. Abrasion, impact, and wear generated by waves, wind, ocean currents, floating objects, sand, and heavy waves are the major stress types [2]. Mooring lines, for instance, are subjected to severe wear degradation in the connection between links and accessories, as consequence of the relative movement generated between components by waves, wind, and ocean currents [3–7]. Offshore structures, as well as mooring lines, are also exposed to abrasion and impact in the splash zone generated by heavy waves, floating wastes, sand particles, and other contaminants present in seawater [2,8,9]. Corrosion is also more severe in the splash zone, where the concentration of oxygen is higher [3,9,10]. Wear and corrosion are two processes that lead to an irreversible degradation, and whenever they take place simultaneously, the process is known as tribocorrosion. Tribocorrosion involves a synergism between wear and corrosion, since the total material loss when the two processes occur simultaneously is greater than when they act alone [6,7,11–13].

Steel is the most employed structural material in offshore applications, usually mild or low-alloyed, due to their good properties and relatively low cost compared to high-alloyed steels [8]. High-Strength Low-Alloyed (HSLA) steels, for instance, are widely used for their high mechanical properties, with yield strengths in the range of 460–960 MPa, and relatively low weight [14,15]. This kind of steels are used in jack-ups and legs, pipelines, tethering attachments for floating structures in Tension Leg Platforms (TLPs), mooring lines of semi-submersible structures, etc [14,16,17]. However, due to their low alloying content, HSLA steels possess low corrosion resistance in seawater, with corrosion rates around 250 microns per year [9,18].

In order to save the elevate maintenance and replacement costs of damaged elements, and avoid premature failure of infrastructures or components, protective coatings have been widely used to protect steel in marine environment. The selection of the appropriate coating strongly depends on the exposure zone, since the requirements and desirable properties of the coating vary with the degradation phenomena taking place in each exposure location [19]. In splash zone, for

* Corresonding author.
E-mail address: ainara.lopez@tekniker.es (A. López-Ortega).

https://doi.org/10.1016/j.corsci.2018.08.001
Received 7 June 2018; Received in revised form 24 July 2018; Accepted 1 August 2018
Available online 07 August 2018
0010-938X/